BIOLOGICAL EVALUATION AND MECHANISTIC INSIGHTS OF TARGETED NANO-FORMULATION FOR COMBINATORIAL CANCER THERAPY

By

NEENA GIRISH SHETAKE

Enrolment No. : LIFE01201404004

Bhabha Atomic Research Centre, Mumbai

A thesis submitted to the

Board of Studies in Life Sciences

In partial fulfillment of requirements

for the Degree of

DOCTOR OF PHILOSOPHY

of

HOMI BHABHA NATIONAL INSTITUTE

December, 2020

Homi Bhabha National Institute

Recommendations of the Viva Voce Committee

As members of the Viva Voce Committee, we certify that we have read the dissertation prepared by **Mrs. Neena Girish Shetake** entitled "**Biological Evaluation and Mechanistic Insights of Targeted Nano-formulation for Combinatorial Cancer Therapy**" and recommend that it may be accepted as fulfilling the thesis requirement for the award of Degree of Doctor of Philosophy.

Chairman – Dr. Rajiv Sarin	Signature with date	12.4.2021
Guide / Convener – Dr. Badri N. Pandey	Signature with date	12.4.2021
Co-guide -		
Examiner - Prof. Deepa Ghosh	Signature with date	12.4.2021
Member 1- Dr. A. K. Tyagi	Signature with date	12/04/2021
Member 2- Dr. Santosh Kumar	Signature with date	12/4/2021
Member 3- Dr. B. S. Patro	Signature with date	03.05.2021

Final approval and acceptance of this thesis is contingent upon the candidate's submission of the final copies of the thesis to HBNI.

I/We hereby certify that I/we have read this thesis prepared under my/our direction and recommend that it may be accepted as fulfilling the thesis requirement.

Date: 12.4.2021

Place: Mumbai

Signature
Co-guide (if any)

Signature
Guide

BIOLOGICAL EVALUATION AND MECHANISTIC INSIGHTS OF TARGETED NANO-FORMULATION FOR COMBINATORIAL CANCER THERAPY

By

NEENA GIRISH SHETAKE

Enrolment No. : LIFE01201404004

Bhabha Atomic Research Centre, Mumbai

A thesis submitted to the

Board of Studies in Life Sciences

In partial fulfillment of requirements

for the Degree of

DOCTOR OF PHILOSOPHY

of

HOMI BHABHA NATIONAL INSTITUTE

December, 2020

STATEMENT BY AUTHOR

This dissertation has been submitted in partial fulfillment of requirements for an advanced degree at Homi Bhabha National Institute (HBNI) and is deposited in the Library to be made available to borrowers under rules of the HBNI.

Brief quotations from this dissertation are allowable without special permission, provided that accurate acknowledgement of source is made. Requests for permission for extended quotation from or reproduction of this manuscript in whole or in part may be granted by the Competent Authority of HBNI when in his or her judgment the proposed use of the material is in the interests of scholarship. In all other instances, however, permission must be obtained from the author.

Neena Girish Shetake

DECLARATION

I, hereby declare that the investigation presented in the thesis has been carried out by me. The work is original and has not been submitted earlier as a whole or in part for a degree / diploma at this or any other Institution / University.

Neena Girish Shetake

LIST OF PUBLICATIONS ARISING FROM THE THESIS

Journal:

1. **Neena G. Shetake**, Amit Kumar, Snehal Gaikwad, Pritha Ray, Sejal Desai, Raghumani Singh Ningthoujam, Rajesh Kumar Vatsa and Badri N. Pandey. Magnetic Nanoparticle mediated Hyperthermia Therapy induces tumor growth inhibition by apoptosis and HSP90/AKT modulation, *International Journal of Hyperthermia* (2015); 31: 909-19.

2. **Neena G. Shetake**, Amit Kumar and B. N. Pandey. Iron-oxide nanoparticles target intracellular HSP90 to induce tumor radio-sensitization. *BBA General Subjects* (2019); 1863: 857-869.

3. **Neena G. Shetake,** B. N. Pandey. Hyperthermia therapy of cancer: Need for deeper biological insights for improved therapeutic outcome. *Journal of Radiation and Cancer Research* (2020); 10(4): 170-173 (*review article).*

Conferences:

1. **Neena G. Shetake**, Amit Kumar, B. N. Pandey, Iron oxide based Magnetic Nano-formulation for Improvement of Cancer Radiotherapy, *IAHOM*, Nanavati Hospital, India, Feb 15–16, 2020. **(Invited Talk).**

2. **Neena G. Shetake**, Amit Kumar, B. N. Pandey, Enhancement of Tumor Radio-sensitivity by Iron oxide nanoparticles : role of HSP90, DNA repair and apoptosis *ICRR-HHE 2018*, University of Hyderabad, India Feb, 1-4, 2018. **(Oral Presentation).**

3. **Neena G. Shetake**, Amit Kumar, B. N. Pandey, Iron oxide nanoparticles target intracellular HSP90 to induce tumor radio-sensitization, *(ICN:3I 2017)*, IIT-Roorkee, Dec 6-8 2017. **(Oral Presentation).**

4. **Neena G. Shetake**, Amit Kumar, B. N. Pandey, Magnetic Nanoparticles in combination with gamma radiation induce G2-M arrest and mitotic catastrophe mediated cell death, *ICRR-HHE-2016*, Feb.11-13, 2016, BARC, India. **(Best Oral Presentation Award).**

DEDICATIONS

Dedicated to Aai and Pappa

ACKNOWLEDGEMENTS

I wish to express my sincerest gratitude to my mentor and guide, Dr. B. N. Pandey, Head, Radiation Signaling and Cancer Biology Section, RB&HSD, BARC, for introducing me to this immensely growing and fascinating field of 'nano-biotechnology'. His constant motivation, support, encouragement and valuable suggestions has helped me throughout my PhD duration. I would like to specially acknowledge Dr. Amit kumar, RB&HSD, BARC, for his critical scientific suggestions and constant encouragement and motivation for completion of this thesis work. I take this opportunity to acknowledge Dr. S. Chattopadhyay and Dr. Venugopalan, Ex-Directors, Biosciences Group, Dr. Vinay Kumar, Ex-Head, RB&HSD and Dr. S. K. Ghosh, Ex-Associate Director, Biosciences Group, for facilitating and supporting this research activity. I express my deepest sense of gratitude to all the members of the Doctoral Committee - Dr. Rajiv Sarin (Ex-Director, ACTREC), Dr. A. K. Tyagi (Associate Director, Chemistry Group), Dr. B. S. Patro (Head, Chemical Biology Section, BOD) and Dr. Santosh Kumar (Head, Free Radical Biology Section, RB&HSD), for their timely and valuable suggestions for improving this thesis work. I would like to specially acknowledge Dr. Hema Rajaram, Dean-Life Sciences, HBNI, for her invaluable support throughout my PhD duration.

I am grateful to Dr. Raghumani S. Ningthoujam, Chemistry Division, for teaching the basics of nanoparticle synthesis and helping me understand the basic concepts of nanoparticle chemistry. I would like to acknowledge Dr. R. K. Vatsa (Head, Cluster Chemistry Section, Chemistry Division) and Dr. P. A. Hassan (Head, Nanotherapeutics and Biosensors Section, Chemistry Division) for facilitating the fruitful collaborations and providing the infrastructure and scientific expertise in the field of nano-biotechnology. I am highly indebted to Dr. K. C. Barick and Dr. Gunjan Verma (Chemistry Division) for their valuable scientific suggestions and

helping me with the bio-physical characterization of my nano-formulation for this thesis work. I deeply acknowledge Dr. Jayesh Bellare (Department of chemical Engineering, IIT-Mumbai) and Ms. Shobha (IIT-Mumbai) for extending their support for Cryo-TEM and ED-XRF analysis. I am highly grateful to Mrs. Chiplunkar (Ex-Director, ACTREC) and Mrs. Sharda Sawant, ACTREC for providing the TEM facility. I would like to acknowledge Dr. N. L. Misra (Head, X-ray Spectroscopy Section, FCD) and Dr. Sangeeta Dhara, FCD, for providing the T-XRF facility. I am grateful to my colleagues from RB&HSD-Mr. Prayag Amin, Mrs. Jisha Menon and Mrs. Binita for helping with flow cytometry analysis and Dr. M. K. Tyagi, BOD and Mr. Rajesh, RPAD for their help during confocal microscopy studies. I would like to acknowledge all my lab members, especially Mr. Manjoor Ali, Mrs. Vasumathy and Mrs. Deepika Bhange for assisting in fluorescence microscopy and animal studies, Mrs. Hansa Yadav for her assistance during animal imaging studies and Mr. Manjoor Ali and Mr. Sourav Das for criticially reviewing this thesis. I am grateful to Dr. H. D. Sarma and Mr. Swami, Animal House Facility, for providing the infrastructure and technical support for animal experiments.

Finally, I wish to express my sincerest gratitude and indebtedness to my mother, father, brother, parent-in-laws, my husband and my son, Mihit, for their unconditional support. Without their co-operation and blessings, I would have not been able to complete my thesis work in time.

Thank You All !

Neena Girish Shetake

CONTENTS

SUMMARY

Currently, according to the WHO report, cancer is the second leading cause of death globally, following cardio-vascular diseases. Conventional cancer treatment modalities (viz. chemo-, radio- and hyperthermia therapy) mainly suffer the limitations of being non-specific to tumor cells and hence the associated normal tissue toxicity. Therefore, development of more effective cancer treatment strategies has become in-dispensable. With the advent of nanotechnology, different nanoparticle systems have been explored to develop targeted cancer treatment nano-agents, to improve the therapeutic index of conventional therapies. Amongst the nanoparticles, liposomes and super-paramagnetic iron oxide nanoparticles (SPIONs) have been extensively used for anti-cancer applications in clinic. Although these nano-formulations were found to significantly reduce the normal tissue toxicity as compared to the free drug, the improvement in anti-cancer efficacy was marginal. Thus, there is a scope for development of better nano-based agents for further improving the therapeutic ratio of cancer treatment modalities. In the present thesis, I have combined the virtues of two types of nanoparticle systems, namely, liposomes and SPIONs to design a novel liposomal nano-formulation for active tumor targeting and enhanced combinatorial chemo-, radio- and magnetic hyperthermia therapy of cancer.

Present thesis discusses the synthesis of two types of nano-formulations of SPIONs and describes the evaluation of their combinatorial cancer therapy efficacy in cultured cells and fibrosarcoma tumor model. Initially, I synthesized oleic acid coated SPIONs, referred to as 'MN-OA' and then to make it tumor targeted, MN-OA was co-encapsulated in a liposomal nano-formulation along with doxorubicin (Dox) for improved combinatorial cancer therapy application. The liposomal formulation was further conjugated with cyclic RGD (cRGD) peptide

for tumor targeting and is referred as 'T-LMD'. Both the nano-formulations were characterized for size, shape, surface charge, encapsulation efficiency and stability using suitable bio-physical techniques. MN-OA was found to have significant radio-sensitization and magnetic hyperthermia efficacy in murine fibrosarcoma (WEHI-164) cells and its tumor model. The mechanism of MN-OA induced cyto-toxicity was found to involve interaction of MN-OA with intra-cellular HSP90. This results in inhibition of HSP90 and down-regulation of its client proteins, playing role in cell cycle progression, DNA repair and cell survival.

The tumor targeted liposomal nano-formulation, T-LMD was also found to show significant anti-cancer efficacy in several (six) cancer cell lines and was more effective as compared to commercial formulation of liposomal Dox (Lippod^{TM}) at equivalent drug concentration. Intra-cellular uptake studies in U373MG cell line (over-expressing the cRGD specific αvβ3 integrin receptor) confirmed the contribution of cRGD tagging on T-LMD for targeted uptake in cells by receptor mediated endocytosis. *In vivo* as well, T-LMD showed significant targeting in fibrosarcoma tumors as compared to unconjugated liposomal formulation and showed very low accumulation in other organs in mice. T-LMD showed significant anti-cancer efficacy in combination with radiation and magnetic hyperthermia therapy, both in cultured cells and fibrosarcoma tumor model. Moreover, toxicological evaluation in tumor bearing and healthy BALB/c mice using histopathological studies and serum/whole blood analysis suggested the in-significant/no-observable toxicity of T-LMD in mice as compared to Lippod^{TM} or free Dox. These results demonstrate the potential of T-LMD for clinical translation as an anti-cancer agent for targeted and combinatorial cancer therapy applications.

SYNOPSIS

1. **Name of the Student:** Mrs. Neena Girish Shetake
2. **Name of the Constituent Institution:** Bhabha Atomic Research Centre
3. **Enrolment No. :** LIFE01201404004
4. **Title of the Thesis:** Biological Evaluation and Mechanistic Insights of Targeted Nano-formulation for Combinatorial Cancer Therapy
5. **Board of Studies:** Life Sciences

Cancer is an alarming word and brings out the darkest fear in most of our minds. Currently, it is the second leading cause of death globally, after cardio-vascular diseases[1]. In spite of the advances in the therapeutic modalities and development of novel strategies for the treatment, cancer still remains one of the major causes of death all over the world. Current cancer treatment strategies involve mainly chemotherapy, radiotherapy or a combination of the two modalities[2] and with hyperthermia, which is used as an adjuvant cancer therapy[3]. However, most of these treatment modalities are non-specific/non-targeted to the tumor cells, which in turn contributes to the normal tissue damage and a range of associated side effects including acute toxicities (such as xerostomia, mucositis, dysphagia, etc) and/or severe organ dysfunction[4]. Moreover, chemo- and radio-resistance is a recurring problem in these modalities[4] which significantly hampers their therapeutic efficacy. Thus, development of alternate strategies for the effective cancer treatment is highly warranted.

With the development of nanotechnology, nanomaterials with radio-sensitizing capabilities (such as gold and iron oxide) have been explored for drug delivery and anti-cancer applications. Amongst these, super-paramagnetic-iron oxide nanoparticles (SPIONs) have been

found to be most suitable for anti-cancer applications[5,6]. This is attributed to their super-paramagnetic behavior, high surface area to volume ratio and amenability to be conjugated with different functional groups. Moreover, the suitability of SPIONs as an MRI contrast agent, makes them an excellent candidate for theranostic applications[6]. In addition to inorganic nanoparticles, organic nanoparticles, such as liposomes have the added advantages of bio-compatibility, capability to deliver both hydrophilic and hydrophobic drugs, better temporal and thermal stability and controlled release of encapsulated content[7]. Liposomal anti-cancer formulations such as Doxil® and Lipo-Dox® have been approved by FDA and are in clinical use for several cancer types (metastatic breast and ovarian cancers, multiple myeloma, etc). However, their efficacy is limited due to their toxicities (hand and foot syndrome and stomatitis), relatively lower efficacy than free doxorubicin and non-targeted nature[8]. On the contrary, most of the SPIONs-based nano-formulations, currently in clinical use are approved for imaging applications (as a MRI contrast agent)[9]. There are very limited reports for the use of SPIONs for combinatorial therapy of cancer[10]. Moreover, most of these studies use non-targeted formulation of SPIONs and combine them with either chemo- or radio- or hyperthermia. Besides, validation of their therapeutic efficacy in animal models and detailed mechanistic insights are lacking in the literature. Therefore, there is a scope to develop a targeted nano-formulation, utilizing the virtues of both nanoparticle systems (viz. liposomes and SPIONs), for multi-mode combinatorial cancer therapy and a deeper mechanistic insight for their anti-cancer action.

Thus, in the present thesis, I have designed, synthesized and characterized two SPIONs based nano-formulations. Further their chemo-, radio- and hyperthermia abilities were evaluated in cancer cells *in vitro* as well as in a suitable tumor model. The first nano-formulation of SPIONs (average size 10 nm) is coated with oleic acid and is referred to as 'MN-OA'[11]. The

second nano-formulation is a tumor targeted liposomal nano-formulation co-encapsulated with MN-OA and doxorubicin, and functionalized for active targeting. This nano-formulation is an improvised form of MN-OA and referred to as 'T-LMD'. The novel aspects of the thesis include (i) co-encapsulation of Dox and MN-OA in liposomes along with its functionalization for active tumor targeting, (ii) studying the radio-sensitizing as well as magnetic hyperthermia efficacy of the formulation (T-LMD) and elucidation of the underlying mechanism, (iii) demonstration of tumor targeting efficacy of T-LMD in fibrosarcoma tumor model and (iv) validation of the combinatorial therapeutic efficacy in tumor model along with the assessment of toxicity parameters in healthy mice treated with T-LMD.

Thesis Objectives :

Objective I: To evaluate the radio-sensitizing ability of MN-OA under *in vitro* and *in vivo* conditions and elucidate the underlying mechanism of action.

Objective II: To synthesize and characterize PEGylated liposomes co-encapsulated with MN-OA and anti-cancer drug (doxorubicin).

Objective III: To functionalize the liposomes with suitable ligand and evaluate their *in vitro* efficacy, toxicity and mechanism for combinatorial cancer therapy.

Objective IV: To study the toxicological aspects and therapeutic efficacy of the targeted liposomes for combinatorial cancer therapy in animal model.

Organization of Thesis

The thesis is organized into five chapters which include an introduction (chapter one) and materials and methods (chapter two). Chapter three includes the results with relevant discussion. A general discussion is mentioned in chapter four. The conclusion and future directions of the thesis are mentioned in chapter five, followed by a list of references in the order of citation.

Chapter One: Introduction

The first chapter provides an overview of cancer with emphasis on cancer treatment modalities and their limitations, along with relevant examples of drugs in clinical use. A review of different types of nanoparticle systems used for bio-medical applications and their shortcomings has been provided. SPIONs mediated MHT, the mechanism of heat generation and pre-clinical and the clinical status of SPIONs have been reviewed in this chapter. Lastly, the chapter also includes the relevance, rationale and scope of the thesis.

Chapter Two: Materials and methods

This chapter provides the details of the materials (chemical reagents, antibodies, drugs, cell lines and animal systems), methodologies and techniques used for the thesis. Briefly, this chapter provides the details of synthesis of MN-OA and T-LMD and their characterization by different bio-physical techniques such as dynamic light scattering (DLS), zeta sizer, transmission electron microscopy (TEM), cryo-TEM, total-reflection-X-Ray fluorescence (T-XRF), Fourier-transform infrared spectroscopy (FT-IR) and fluorescence spectroscopy. Details of the assays used for the determination of *in vitro* anti-cancer efficacy of MN-OA and T-LMD (such as MTT, trypan blue dye exclusion assay, flow cytometry analysis, Western blotting and immuno-cytochemistry) have

been included. Details of development of fibrosarcoma tumor model, treatment schedule and endpoints used for evaluation of anti-tumor efficacy (such as tumor growth measurements, live animal imaging using luciferase-transfected WEHI-164 cells, histopathology, immuno-fluorescence and Western blotting studies) have been provided. Details of toxicity studies using serum/whole blood analysis and histopathological examination have been included in this chapter of the thesis.

Chapter Three: Results and Discussion

This chapter is divided into following three sections that mention the findings with relevant discussion:

Section 3.1 *In vitro* and *In vivo* Evaluation of Hyperthermia and Radio-sensitizing efficacy of Iron oxide Magnetic Nanoparticles (MN-OA) in mouse fibrosarcoma: *In vitro* studies showed heating ability of MN-OA to hyperthermic temperature (42 °C) within 4 min under alternating current (*AC*) magnetic field. In WEHI-164 cells, MN-OA showed an intra-cellular uptake of ~ 60 % as measured by Nile blue A staining and T-XRF. MN-OA showed significant killing of WEHI-164 cells when combined with magnetic hyperthermia (MN-OA + H, ~ 4 fold) as compared to MN-OA (~ 2 fold). MN-OA + H also showed significant inhibition of tumor growth [Tumor growth delay (TGD) of ~ 3 days] as confirmed by bio-luminescence imaging of luciferase transfected WEHI-164 tumor cells and manual measurement of tumor volume. The mechanism of tumor growth inhibition was found to involve apoptosis and inhibition of HSP90.

Clonogenic cell survival assay and sub-G1 analysis suggested significant radio-sensitization efficacy of MN-OA with a dose enhancement factor of 2.1. Cell cycle analysis

showed induction of G2-M arrest at 48 h and induction of apoptosis at late time points i.e. 96 and 144 h. Role of alternate cell death mechanism i.e. mitotic catastrophe was confirmed by polyploidy and presence of multiple spindle poles. Furthermore, the magnitude of DNA-double strand breaks (DSBs) measured by γH2AX foci at different time points showed a significantly higher intensity of γH2AX fluorescence in both MN-OA and MN-OA + 2 Gy groups. Interestingly, MN-OA + 2 Gy showed longer persistence of γH2AX foci up to 96 h as compared to control or 2 Gy or MN-OA. Western blot analysis of MN-OA + 2 Gy showed significant accumulation of HSP90 and a down-regulation of its client proteins involved in DNA repair (BRCA1, RAD51 and CHK1), which may be contributing to the observed higher DNA damage and its longer persistence. The possible interaction of MN-OA with HSP90 was studied by isolation of MN-OA-bound proteins from the cell lysates by magnetic separation followed by native PAGE and Western blot analysis. Results showed presence of HSP90 and HSP60 but not its client proteins (BRCA1 or RAD51) in the isolated fraction suggesting binding of MN-OA to HSP90 and HSP60. Moreover, SiRNA knock-down of HSP90 in WEHI-164 cells followed by treatment with MN-OA ± 2 Gy showed ~ 2 fold increase in the cell death as measured by MTT assay.

The radio-sensitizing potential of MN-OA was validated in fibrosarcoma tumor model, wherein a TGD of 4.4 and 2.1 was observed for MN-OA + (2+2+2 Gy) and MN-OA treatments, respectively. The enhanced inhibition of tumor growth was corroborated by an increase in apoptosis [~ 4 fold higher in MN-OA + (2+2+2 Gy) as compared to 2.5 fold in (2+2+2 Gy) and ~ 2 fold in MN-OA].

Section 3.2 Synthesis of targeted nano-formulation: evaluation of anti-cancer efficacy and mechanism of combinatorial cancer therapy: Although MN-OA showed promising magnetic hyperthermia and radio-sensitizing efficacy, it needed further improvements for making it tumor targeted. Therefore, I designed a tumor targeted liposomal nano-formulation (T-LMD) of MN-OA. Initially, PEGylated liposomes co-encapsulated with MN-OA and Dox (PEG-Lipo-MN-Dox) were synthesized (as non-targeted nano-formulation) which was compared with targeted nano-formulation (T-LMD), wherever required. TEM analysis confirmed the synthesis of spherical liposomes with MN-OA. PEG-Lipo-MN-Dox showed a hydrodynamic size of 158 nm ± 0.23 by DLS and a surface charge of -7.3 ± 2.1 mV by zeta sizer. MTT assay showed significantly higher (~ 7 fold) cyto-toxicity of PEG-Lipo-MN-Dox as compared to ~ 2 fold for clinical formulation of liposomal Dox (Lippod^{TM}, Celon Labs, India). TEM analysis of WEHI-164 cells treated with PEG-Lipo-MN-Dox showed presence of dark deposits of Fe in the cell cytosol either inside or outside membrane bound vesicles. Moreover, treated cells showed apoptotic morphology such as nuclear shrinkage and alterations in shape/size of the mitochondria.

For the synthesis of targeted nano-formulation (T-LMD) a post-insertion approach was employed. Initially, the phospholipid (DSPE-PEG-maleimide) was conjugated with a targeting agent followed by confirmation of the conjugation by HPLC and FT-IR. The conjugated phospholipid was further used for the synthesis of T-LMD. DLS showed a hydrodynamic size of ~ 170 nm for T-LMD with a surface charge of -21.3 ± 2.5 mV. Moreover, T-LMD showed ~ 40 % uptake in U373MG cells (over-expressing the αvβ3 integrin receptor), which was reduced to ~ 20 % in case of cells with the pre-blocked receptors. The receptor mediated uptake of T-LMD in U373MG cells was validated by the co-localization of Dox with the early endosomes marker

(EEA-1). On the contrary, WEHI-164 cells (marginal expression of αVβ3 integrin receptor) showed a diffused localization of Dox fluorescence in the cytoplasm and the nuclei suggesting a non-receptor mediated uptake of T-LMD (~ 25 %). MTT analysis of cancer and normal cell lines validated the significant anti-cancer efficacy of T-LMD, which was more towards cancer than normal cells, with the highest IC50 of 207.7 nM in WI26VA4 (normal human lung fibroblast) cells. Whereas other cell lines showed a much lower IC50 values (in ascending order): MDAMB-231 (99.9 nM) < WEHI-164 (109.2 nM) < MCF-7 (111.96 nM) < U373MG (116.21 nM) < WRL68 (138.54 nM) < A549 (152.6 nM).

Sub-G1 analysis and clonogenic cell survival assay showed significant radio-sensitizing potential of T-LMD, which was found to be dose dependent and mediated via G2-M arrest (shown by increased expression of P-CDC2, CDC2, Cyclin B1, P-CDC25C and CDC25C). Furthermore, γH2AX staining showed slower repair kinetics in T-LMD + 2 Gy (peak intensity at 3 h as compared to 30 min. in 2 Gy treatment) and persistence of foci upto 72 h, which was corroborated by increased expression of P-ATR, P-CHK1 and P-RAD51. T-LMD ± 2 Gy showed increased expression of P-JNK, Beclin-1, LC3B(II), apoptotic proteins (cleaved Caspase 3, cleaved PARP and BAD) and down-regulation of anti-apoptotic proteins (BCL2, AKT and Survivin) suggesting the role of JNK pathway and autophagy in the mechanism of radio-sensitization. In addition, T-LMD also showed significant killing (~ 5 fold) of WEHI-164 cancer cells in combination with magnetic hyperthermia. The mechanism was found to be mediated via induction of G2-M arrest and apoptosis (shown by increased expression of CDC2, Cyclin B1, cleaved Caspase 3 and cleaved PARP).

Section 3.3 Evaluation of toxicity and therapeutic efficacy of targeted liposomal nano-formulation (T-LMD) for combinatorial cancer therapy: To determine the tumor targeting efficacy of T-LMD under *in vivo* conditions, a traceable form of the nano-formulation was synthesized by labeling it with indo-cyanine green (ICG), a near-infrared dye for fluorescence based live animal imaging. Live animal imaging after *i.v.* administration of ICG labeled nano-formulations (PEG-Lipo-MN-Dox and T-LMD) showed their significant accumulation at the tumor site as early as at 15 min, which further increased by 48 h. On day 7, significant retention of ICG signal was observed in the tumor and was ~ 4 fold higher in ICG-T-LMD as compared to ICG-PEG-Lipo-MN-Dox. Major organs (viz. intestine, kidney, liver, spleen, lungs and heart) showed ~ 5 fold lower signal of ICG than the tumor. Anti-tumor efficacy of T-LMD was evaluated in fibrosarcoma tumor model either alone or in combination with radiation (R) or MHT (H) or both. Lippod^{TM} was used as a comparative clinical formulation control. A TGD of ~ 7 days was observed for T-LMD + H + R as compared to ~ 4 days for T-LMD + R, 3 days for T-LMD + H, 2 days for T-LMD, 0.2 days for Lippod^{TM} and ~ 2 days for Lippod^{TM} + R treatments. The increased tumor growth inhibition in combinatorial treatment was also corroborated by increased expression of TUNEL positive foci and decreased expression of Ki-67 (cell proliferation marker). To study the toxicological parameters, healthy BALB/c mice were treated with T-LMD or Lippod^{TM} or Dox at 3 mg/Kg dose for 4 days, followed by sacrifice of animals, analysis of whole blood/serum parameters and histopathology of major organs. Dox at 20 mg/Kg was used as a positive control. Serum analysis showed increased expression of liver function marker, ALT and cardiac damage marker, CK-MB in Lippod^{TM} and Dox (20 mg/kg) group but not in T-LMD. Histopathological examination validated the in-significant toxicity of T-LMD.

Chapter Four: General Discussion

There are limited reports in literature on the radio-sensitizing and magnetic hyperthermia potential of SPIONs. However, most of these studies lack a thorough understanding of the mechanisms by which these nano-formulations exert their anti-cancer effect either alone or in combination therapy. In the present thesis, I have synthesized, characterized and evaluated the anti-cancer efficacy of two nano-formulations, namely, MN-OA and T-LMD, both of which are made up of SPIONs. Moreover, a deeper understanding of the mechanism by which these nano-formulations exert their anti-cancer effect with identification of key molecular players (HSP90 or JNK) has been accomplished. The first nano-formulation, MN-OA (a non-targeted nano-formulation of SPIONs) showed significant combinatorial cancer therapy efficacy via induction of apoptosis, mitotic catastrophe and modulation of HSP90. MN-OA was found to inhibit HSP90 and its function of client protein folding, several of which are known to play crucial roles in cell survival, cell proliferation and DSBs repair.

To further improve the anti-cancer efficacy of MN-OA, a targeted liposomal based nano-formulation of MN-OA and Dox was designed (T-LMD) for active targeting of tumor cells and tumor neo-vasculature. T-LMD showed significant anti-cancer efficacy in several cancer cell lines and was found to be further enhanced when combined with gamma radiation or MHT. The mechanism of radio-sensitization by T-LMD was found to be mediated via induction of enhanced DSBs, activation of JNK pathway and apoptosis. Live animal imaging showed significant targeting of fibrosarcoma tumor by ICG-T-LMD with relatively lower accumulation in other organs. Moreover, T-LMD showed significantly higher anti-tumor efficacy as compared

to Lippod™ and in-significant toxicity, particularly cardiac toxicity (a major side effect of free Doxorubicin) in healthy mice.

Chapter Five: Conclusion and Future directions

T-LMD was established as a targeted nano-formulation with potential for enhanced efficacy for combinatorial chemo-, radiation and hyperthermia therapy of cancer. Based on *in vitro* and *in vivo* results, the present thesis opens many new arenas for basic and applied research. Firstly, the mechanistic insights of HSP90 regulation in nano-formulation mediated radio-/thermo-sensitization need to be established using suitable inhibitors and molecular docking studies. A clinical validation of modulation of HSP90 levels in cancer patients would facilitate exploring its prognostic value in hyperthermia therapy. Secondly, optimization of conditions for freeze-drying/re-constitution and stability parameters is warranted for long term storage/transportation of nano-formulation. Thirdly, a thorough evaluation of the toxicity and pharmacokinetics of T-LMD in healthy rodents/pre-clinical animals in GLP laboratory and validation of anti-tumor efficacy of T-LMD in other human xenograft models are required for its further clinical safety/efficacy evaluation before clinical trials of the nano-formulation.

List of Figures

	Kidney : glomeruli (G), tubules (T), Bone: spongy bone (B), marrow cells (BM), osteoblasts (O), Brain : neuronal cells (N), capillaries (C), Intestine: mucosal epithelium (M), villi (V), submucosa (S), muscularis (MS), lamina propria (L) and Muscle: myocyte (M)].

List of Schemes

List of Tables

Abbreviations

17-AAG	17-N-AllylAmino-17-demethoxyGeldanamycin
6-MP	6-MercaptoPurine
ABC transporters	The ATP-Binding Cassette transporters
ADCC	Antibody-Dependent Cell mediated Cytotoxicity
AKT/PKB	Protein Kinase B
ALK receptor	Anaplastic Lymphoma Kinase receptor
ALL	Acute Lymphocytic Leukemia
AMF	Alternating current Magnetic Field
APC	Adenomatosis Polyposis Coli
BAEC	Bhabha Atomic Research Centre Animal Ethical Committee
BBB	Blood Brain Barrier
BCR-Abl	Breakpoint Cluster Region-Abelson oncogene locus
BRCA1	Breast Cancer Susceptibility Gene
CA	Carcinoma
CART	Chimeric Antigen Receptor T-cell therapy
CD19	Cluster of Differentiation 19
CD20	Cluster of Differentiation 20
CD38	Cluster of Differentiation 38
CDC2	Cell-Division Cycle 2
CDR	Complementarity Determining Regions
CHK1	Checkpoint kinase-1
CLSM	Confocal Laser Scanning Microscopy
CMC	Critical Micellar Concentration
C-Met	Mesenchymal-Epithelial Transition factor
c-myc	Avian Myelocytomatosis virus oncogene Cellular homolog
CNT	Carbon Nanotubes
CPT	Charged Particle Therapy
CRS	Cyto-Reductive Surgery
CTL4A	Cytotoxic T-lymphocyte Antigen-4
CTLA-4	Cytotoxic T-lymphocyte-associated protein 4
DAPI	4′,6-Diamidino-2-PhenylIndole
DLS	Dynamic Light Scattering
DMEM	Dulbeccos Modified Eagle's Media
DMSO	Dimethyl Sulfoxide
DNA	DeoxyriboNucleic Acid
DOPC	1,2-Dioleoyl-*sn*-glycero-3-phosphocholine
DOPS	1,2-Dioleoyl-*sn*-glycero-3-phosphoserine
Dox	Doxorubicin

DPPC	1,2-Dipalmitoyl-*sn*-glycero-3-phosphocholine
DPPG	1,2-Dipalmitoyl-*sn*-glycero-3-phosphoglycerol
DSB	Double Strand Breaks
DSPC	1,2-Distearoyl-*sn*-glycero-3-phosphocholine
DSPE	1,2-Distearoyl-*sn*-glycero-3-phosphoethaolamine
EBRT	External Beam Radiotherapy
ECACC	European Collection of Authenticated Cell Cultures
EDTA	EthyleneDiamineTetraAcetic acid
EDX	Energy-Dispersive X-ray spectroscopy
EEA-1	Early Endosomal Marker
EGFR	Epidermal Growth Factor Receptor
EPC	Egg Phosphatidyl Choline
EPR	Electron Paramagnetic Resonance spectroscopy
FCS	Fetal Calf Serum
FDA	Food and Drug Administration
FT-IR	Fourier Transform-Infrared Spectroscopy
FWHM	Full Width Half Maxima
GAPDH	GlycerAldehyde 3-Phosphate DeHydrogenase
GM-CSF	Granulocyte-Macrophage Colony-Stimulating Factor
GNP	Gold NanoParticle
GnRH	Gonadotropin Releasing Hormone
GO	Graphene Oxide
HA	Hydroxy Apatite
Hck	Hematopoietic Cell Kinase
HCl	Hydrochloric acid
HER2	Human Epidermal growth factor Receptor 2
HIFU	High Intensity Focused Ultra-sound
HIPEC	Hyperthermic Intraperitoneal Chemotherapy
HPV	Human Papilloma Virus
HRT	Hormone Replacement Therapy
HR-TEM	High Resolution-Transmission Electron Microscopy
HSP	Heat Shock Protein
HUVECs	Human Umbilical Vein Endothelial Cells
IARC	International Agency for Research on Cancer
ICG	Indocyanine Green
ICMR	Indian Council of Medical Research
IgG1	Immunoglobulin G1
IGRT	Image Guided Radiation Therapy
IL	Interleukin
IMPT	Intensity Modulated Proton Therapy

IMRT	Intensity Modulated Radiotherapy
INF	Interferon
IONP	Iron Oxide Nanoparticles
LINAC	Linear particle Accelerator
LTSL	Low Temperature Sensitive Liposomes
Lyn	Lck/Yes novel tyrosine kinase
MAC	Membrane Attack Complex
mEHT	Modulated Electro-Hyperthermia Therapy
MFH	Magnetic Fluid Hyperthermia
MHT	Magnetic Hyperthermia Therapy
MLV	Multi-lamellar Vesicles
MN-OA	Magnetic Nanoparticles coated with Oleic Acid
MNP	Magnetic Nanoparticles
MPS	Mono-nuclear Phagocytic System
MRgHIFU	Magnetic Resonance Imaging-Guided High Intensity Focused Ultrasound
MSN	Mesoporous Silica Nanoparticles
mTOR	Mammalian Target Of Rapamycin
MTT	3-(4,5-diMethylThiazol-2-yl)-2,5-diphenyl Tetrazolium bromide
MWCO	Molecular Weight Cut Off
MWNT	Multi-Walled Nanotubes
NaCl	Sodium Chloride
NIR	Near-Infra Red
NK	Natural killer cells
NLC	Nano-structured Lipid Carriers
PAA	Poly Acrylic Acid
PAMAM	PolyAmidoAmines
PARP	Poly-ADP Ribose Polymerase
PBS	Phosphate Buffered Saline
PC	Phosphatidyl Choline
PD-1	Programmed cell Death protein-1
PDT	Photo-Dynamic Therapy
PE	Phosphatidyl Ethanolamine
PEG	Poly Ethylene Glycol
PG	Phosphatidyl Glycerol
PGA	PolyGlycosides
P-gp	Permeability Glycoprotein
PHFI	Public Health Foundation of India
PLA	Poly Lactic Acid
PoP	Porphyrin phospholipids

POPC	1-palmitoyl-2-oleoyl-sn-glycero-3-phosphocholine
PPMS	Physical Property Measurement System
PTA	Phospho-Tungstic Acid
PTT	Photo Thermal Therapy
QDs	Quantum Dots
ras	Rat Sarcoma
rb	Retinoblastoma
RES	Reticulo-Endothelial System
RGD	Arginine-Glycine-Aspartic Acid
RLU	Relative Luminescence Units
RNA	Ribo Nucleic Acid
ROS	Reactive Oxygen Species
SAR	Specific Absorption Rate
SDS-PAGE	Sodium Dodecyl Sulfate-PolyAcrylamide Gel Electrophoresis
SEM	Scanning Electron Mciroscopy
SERD	Selective Estrogen Receptor Degraders
SERM	Selective Estrogen Receptor Modulators
SLN	Solid Lipid Nanoparticles
SOBP	Spread-Out Bragg's Peak
SPION	Super-Paramagnetic Iron oxide Nanoparicles
SRT	Stereotactic Radiotherapy
TAA	Tumor Associated Antigenic peptides
TEM	Transmission Electron Microscopy
TGD	Tumor Growth Delay
TGDI	Tumor Growth Delay Index
TGI	Tumor Growth Inhibition
Tm	Phase transition temperature
TME	Tumor Micro-Environment
TRITIC	Tetramethyl Rhodamine Iso-Thiocyanate
TSLs	Temperature Sensitive Liposomes
T-Vec	Talimogene laherparepvec
T-XRF	Total Reflection-X-Ray Fluorescence
ULV	Uni-Lamellar Vesicles
VEGF	Vascular Endothelial Growth Factor
VSM	Vibrating Sample Magnetometer
WBH	Whole body hyperthermia
WHO	World Health Organization
XRD	X-Ray Diffraction
γ-H2AX	Phosphorylation of the Ser-139 residue of the histone variant H2AX

CHAPTER 1

INTRODUCTION

Introduction

Cancer is an alarming word and brings out the darkest of the fear in the minds of most of the people. Despite of the advances in therapeutic modalities in various directions, cancer still accounts for the second highest number of deaths after heart diseases, all over the world. According to World Health Organization (WHO) and International Agency for Research on Cancer (IARC), the global cancer burden is estimated to have increased to 18.1 million new cases and 9.6 million deaths in 2018, worldwide[1,12]. According to a statistical study led by Indian Council of Medical Research (ICMR) and Public Health Foundation of India (PHFI) the cancer incidence in India has increased by 28 ±% between 1990 and 2016[13,14]. In 2018, cancer took more than seven million lives in India, excluding those 2 million patients which continue to live with the deadly disease. Worryingly, according to ICMR, this death toll is expected to increase to 8.8 million by 2020 and double by 2040[14,15]. Hence, there is dying need to develop strategies for early detection or diagnosis and effective treatment of cancer.

Current cancer management strategies mainly involve use of surgery, chemotherapy, radio-therapy or a combination of these modalities. Alternative treatment approaches such as hyperthermia therapy have also been found to be effective as an adjuvant therapy in combination with chemo- or radiotherapy. However, most of these treatment modalities suffer from the limitations of being non-specific or non-targeted to tumor. The non-specificity contributes to the associated normal tissue damage and can result in a range of side effects including self-limited acute toxicities (such as xerostomia, mucositis, dysphagia, dermatitis, pneumonitis, proctitis, and cystitis), mild chronic symptoms, or severe organ dysfunction[16–18]. This in turn reduces the therapeutic index of chemo- or radio-therapy and limits the continuation of treatment[17]. In

addition, due to the heterogeneity and complexity of the tumor and its micro-environment, most of the cancers develop resistance to chemo or radiotherapy during course of treatment[4]. Despite the associated limitations, radiotherapy is regarded as one of the most important treatment modalities for cancer. The main objective of radio-therapy is to maximize the damage to tumor cells and at the same time minimize the normal tissue associated toxicity, thereby increasing the therapeutic ratio/index. This can be achieved by either focused delivery of the radiation to tumor site/tumor cells and minimizing the exposure to the normal tissue. However, this approach does not work well in case of tumors that are deep seated or near critical organs. Another approach to enhance the therapeutic ratio involves use of suitable molecules or drugs that can augment the efficacy of radio-therapy, such as radio-protectors, radiation mitigators or radio-sensitizers[19,20]. Radio-protectors (e.g. amifostine, tempol) are mostly anti-oxidants or free radical scavengers, which are administered before or during the radiation therapy and are intended to reduce the damage to surrounding normal tissues during radio-therapy, by scavenging the free radicals. On the contrary, radiation mitigators can be administered during or shortly after radiation treatment to re-populate certain cell populations, such as mucosa or bone marrow (e.g., G-CSF can effectively reduce the lethality of total body radiation exposure by assisting in marrow recovery)[20,21]. Radio-sensitizers, on the contrary, are intended to sensitize the tumor cells to radiation mainly by two modes : (i) enhancement of radiation induced DNA damage by using DNA intercalating, cross-linking or alkylating agents or (ii) impairment of radiation induced - DNA damage repair. The latter effect is usually mediated through inhibition of proteins that are involved in maintaining the genome integrity or play pivotal role in DNA-Damage-Response (DDR) signaling[22]. Moreover, based on mode of action, the radio-sensitizing agents can also be classified into five types: (i) suppression of intra-cellular thiols or other endogenous radio-

protective substances (e.g. N-Ethylmalemide, diamide, and diethyl maleate), (ii) formation of cytotoxic substances by radiolysis of the radio-sensitizer (e.g. iodoacetamide), (iii) inhibitors of repair pathways (e.g. topoisomerase inhibitors like camptothecin and topotecan), (iv) thymine analogs that can incorporate into DNA (e.g. bromo-deoxyuridine and iodo-deoxyuirdine), and (v) oxygen mimics (metronidazole and its analogs) that have electrophilic activity[23]. However, most of these molecules target one or a few oncoproteins and therefore have limited success in clinics. Therefore, development of better targeted strategies of cancer management has become indispensable.

With the advent of nanotechnology, nanomaterials with better radio-sensitizing capabilities (such as gold and iron oxide) have been developed. Amongst these, iron oxide nanoparticles (IONPs) have been found to be most suitable for bio-medical applications. This is mainly due to their super-paramagnetic behavior, by virtue of which they can be used as a MRI contrast agent and sensitize tumors cells by magnetic hyperthermia. This novel property of super-paramagnetism, makes IONPs, an excellent candidate as cancer theranostic agents[5,6,24]. In addition to inorganic nanoparticles, organic nanoparticles (such as liposomes) have the added advantage of bio-compatibility. Liposomes are excellent systems for targeted delivery of chemotherapeutic drugs to the tumor site, due to several advantages, such as; (i) minimizing the drug toxicity, (ii) better biocompatibility, (iii) ability to encapsulate hydrophilic/hydrophobic drugs and (iv) amenable to surface modifications for tumor targeting applications[25–27]. Thus, the virtues of both nanoparticles systems can be combined to develop a better and more effective anti-cancer agent for targeted and improved cancer hyperthermia and chemo-radiotherapy. In the following sections, I would be briefly describing the conventional and improved therapeutic modalities of cancer treatment that are either being practiced clinically or under clinical

development.

1.1 Overview of Cancer

Cancer is the second leading cause of death all over the world, after cardio-vascular diseases[28]. Even more agonizing than the mortality, it is the emotional and psychological toll that the disease takes on the person inflicted with the disease as well as on their well-wishers. Thus, in the Introduction Section of thesis, I would be addressing a few common queries related to this disease, which are as follows: (1.1) What is this disease ?, (1.2) What are the causative factors for cancer ?, (1.3) What is the status of cancer in India ? and (1.4) What are the current treatment options available?

1.1.1 What is cancer?

Normally, healthy cells divide and replace the lost or damaged cells and then stop dividing, either when they have reached a finite cell density (density dependent inhibition) or have reached their limit or boundary (contact dependent inhibition)[29]. Cancerous cells, on the contrary, multiply uncontrollably and can overgrow the surrounding normal tissues or spread to distant body parts in a process called as metastasis. Cancer is not one disease but many disorders that share profound growth dys-regulation. Hanahan and Weinberg have comprehensively conceptualized and described the eight hallmark capabilities that are common to many, if not all forms of human cancers[30–32]. The cancer cells should acquire these hallmarks to sustain uncontrolled growth, which are namely, (1) sustained growth-proliferative signaling, (2) evasion of growth suppressors, (3) avoiding immune destruction, (4) enabling replicative immortality,(5) activating invasion and metastasis, (6) inducing angiogenesis, (7) resisting cell death and (8) de-regulating cellular energetics. Additionally, the authors also highlight two facilitators, namely,

(1) tumor promoting inflammation and (2) genomic instability and mutation that aids the acquisition of these cancer cell hallmarks. The uncontrolled division of cancer cells eventually forms a visible lump called as tumor. However, not all tumors are cancerous, they can be benign as well.

1.1.2 Benign and Malignant tumors

An abnormal growth of cells or lump is called as tumor. When the cells of the tumor are normal, it is called as benign tumor. Pathological examination of benign tumors will show cells normal in size, shape and having normal chromosome number. Although, the cause for development of benign tumors is unknown, several factors (such as environmental toxins or radiation, spontaneous mutations, diet, stress, local injury or trauma or inflammation or infection) may induce the cells to just overgrew in some location, resulting in a benign tumor. Benign tumors do not spread to the neighboring body parts (do not metastasize) and are less worrisome unless they are pressing on nearby healthy organs, blood vessels or nerves, obstructing important body functions, or causing damage to normal body activity. Fibroids in the uterus are examples of benign tumors[33]. Malignant or cancerous tumors on the other hand are comprised of abnormal cells and can invade the surrounding healthy tissues or spread to distant organs through blood vessels or lymphatic system, a process called as metastasis. Pathological examination of malignant tumors shows presence of cells abnormal in size and shape and have abnormal chromosomes characterized by dark and large sized nuclei[34].

1.1.3 Types of cancer

Based on tissue origin cancers can be broadly categorized into following types (31,33,35):

A. Carcinomas

B. Sarcomas

C. Leukemia

D. Melanomas and

E. Lymphomas

A. **<u>Carcinomas:</u>** These are the cancers that originate in the skin or tissues that line body's organs, tubes, cavities and passageways and form solid tumors.

(i) **Adenocarcinomas:** This is a sub-type of carcinoma that originates in the cells of the glandular tissues that secretes mucus or fluids, such as the lungs, breast, colon and the prostate.

(ii) **Basal cell carcinoma:** It originates in the cells lining the deepest part of skin's outer layer and rarely a cause of concern as it not commonly observed to spread to other body parts.

(iii) **Squamous cell carcinoma:** It usually develops on the skin but can also involve cells lining certain organs or digestive and respiratory tracts. Unlike, basal cell carcinoma, it can spread to other body parts.

(iv) **Renal cell carcinoma:** This type of cancer grows in the kidney

(v) **Ductal carcinoma in-situ:** It is a type of breast cancer, wherein the cancer cells grow inside the ducts of the breast. However, since it does not spread to other areas, it is highly treatable and curable.

(vi) **Invasive ductal carcinoma:** It is type of breast cancer that initiates in the milk ducts and spread to the fatty tissue and can spread to other body parts through lymphatics and bloodstream.

B. **<u>Sarcomas:</u>** This is the cancer of the connective tissue or cells that make supporting

structures, such as bones, cartilage, cells that make the walls of the blood vessels or lymph vessels, muscle, fat or fibrous tissue and form solid tumors. Based on the cell type of origin they are further categorized into the following sub-types:

(i) Bone cancer: This originates in the cells that make up the bones of the body. The most common sub-types are as follows:

a. Osteosarcoma: This involves the uncontrolled growth of the bone cells that are mainly located at the end of long bones such as thigh and shin bone and bone around the knee and the upper arm. Most common in young adults of less than 25 years of age, making up ~ 30 % of all bone sarcoma cases and affects males more commonly than females.

b. Chondrosarcoma: This is also a type of bone cancer that originates in the cartilage cells and most common sites are upper arm, pelvic and thigh bones. More common in adults above 40 years of age and makes upto 37 % of bone sarcoma diagnosis.

(ii) Soft tissue sarcoma: This is a rare type of cancer that involves cells that form tissues that connect, support and surround other body structures, such as the muscles, fat, blood vessels, nerves, tendons and the lining of the joints. The most common sub-types are:

a. Leiomyosarcoma: This is a rare type of cancer that develops in the smooth or involuntary muscles and most common in the abdomen and the uterine muscles.

b. Rhabdomyosarcoma: This is also a rare type of sarcoma affecting more children than adults and originates in the skeletal or voluntary muscles of mainly the head and neck and the abdomen.

c. Synovial sarcoma: Most common in young adults and involves the cells around joints

and tendons, often near the knee.

d. **Liposarcoma:** Type of soft tissue sarcoma that originates in the fat cells of the body, mostly around the trunk, limbs and the retroperitoneum.

(iii) **Angiosarcoma:** This type of cancer develops in the inner lining of the blood vessels and the lymph vessels and most common in the skin, breast, liver, spleen and deep tissue.

(iv) **Fibrosarcoma or Fibroblastic sarcoma:** This type of cancer develops in the fibrous connective tissue, mesenchymal in origin and is characterized by immature proliferating fibroblasts or un-differentiated anaplastic spindle shaped cells arranged in a storiform pattern. Most common in males aged 30 to 40 years. Most commonly found in the limbs, skin (dermatofibrosarcoma) and the trunk and comprise of 5 % of the bone sarcoma cases.

C. **Leukemias:** This type of cancer originates in the blood or bone marrow and mainly affects the white blood cells or leucocytes. Leukemias are usually categorized as acute or chronic based on the speed of progression of the disease. In case of acute leukemia, the immature blood cells (blast cells) do not function properly and divide at a very fast pace. Whereas, in case of chronic leukemia, the mature blood cells become cancerous and divide at a slightly accelerated pace. Based on the type of cells involved, leukemias are classified as lymphocytic or myelogenous. Lymphoid cells or lymphocytes forms the lymphatic system which acts as the body's immune system, whereas, the myeloid cells form the blood cells such as red blood cells, macrophages, monocytes, neutrophils, basophils and eosinophils.

D. **Melanomas:** These are a type of skin cancer that involves the melanocytes, the cells that secrete the melanin pigment which gives the skin its brown or dark color. Most likely develops on the trunk in men and legs in women. The other common sites are face and neck.

E. **Lymphomas:** This cancer originates in the immune cells of the body (lymphocytes) that make up the lymphatic system of the body. This comprises of the lymph nodes, spleen, thymus and the bone marrow. These lymphocytes begin to grow uncontrollably, forming solid tumors and are categorized mainly into two types:

(i) **Hodgkin lymphomas:** This is less common type of lymphoma and is characterized by the presence of Reed-Sternberg cells, large atypical cells that do not contribute to immune protection.

(ii) **Non-Hodgkin Lymphomas:** This is more common type of lymphoma and based on the involvement of B or T lymphocytes is further categorized as (1) B-cell Non-Hodgkin Lymphoma or (2) T-cell Non-Hodgkin Lymphoma.

1.2 Causes or risk factors for development of Cancer

As we have discussed in **Section 1.1**, cancer is a result of uncontrolled cell division. The cell division is controlled by a dense orchestrated network of cell cycle regulators, which in turn are governed by the genes that code for these cell cycle proteins. Any disturbance in this network makes the cell cancerous. These genes can be mainly categorized into two types, namely, (1) proto-oncogenes and (2) tumor suppressor genes. A gain of function (activating) mutation in the proto-oncogenes (e.g. ras, her2, c-myc or cyclin D) or a loss of function (in-activating) mutation in the tumor suppressor genes (e.g. p53, rb, p16 or apc) can lead to development of cancerous phenotype. These mutations can be a result of random errors during DNA replication (sporadic) or caused by certain factors or a combination of these factors which can be briefly categorized as following[29,36]:

1. **Genetic factors:** Overall, 5 to 10 % of all cancers are due to mutations in the genes and

these genetic mutations are inheritable, contributing to the genetic pre-disposition to cancer. However, an inherited genetic defect is not necessarily passed on to all members of the same family, and not everyone who receives the same defective gene will develop cancer. Such cancers tend to occur earlier in life. Examples include mutations in the BRCA1 and BRCA2 genes contributing to ~ 10 % of the cases of breast or ovarian cancers and are attributable to inherited genetic mutations in these genes.

2. **Behavior or lifestyle related factors:** This includes smoking that can increase the risk of lung cancer. Other factors include:

2.1 Excessive consumption of alcohol

2.2 Tobacco chewing

2.3 Diet (excessive consumption of red or processed meat)

2.4 Inflammatory conditions: such as ulcerative colitis or obesity. The mechanism of obesity induced increased risk of cancer may be associated with the abnormal levels of metabolic proteins (insulin-like growth factor) or hormones (oestrogen and progesterone) or increased adipose tissue that contributes to an inflammatory environment.

3. **Environmental factors:** This includes exposure to certain environmental chemicals that can cause damage to the DNA and are called as carcinogens (cancer promoting agents). These includes:

3.1 Environmental pollutants like asbestos and tar

3.2 Excessive exposure to X-rays (in case of healthcare workers) or sun's UV rays

3.3 Some plastic chemicals (e.g. vinyl chlorides) and polynuclear hydrocarbons (e.g. benzopyrene)

3.4 Air pollution and radon gas that can increase the risk of lung cancer

3.5 Hormone replacement therapy (HRT) such as oestrogen is shown to increase the risk of uterine cancer.

4. **Infections (viral or bacterial):** This includes bacteria like *Helicobacter pylori* for increased risk of gastric cancers and viral infections such as Hepatitis B and C for risk of liver cancers. Human papilloma virus (HPV) is known to increase the risk of cervical, anal, penile and several head and neck cancers. Other viruses known to increase the risk of certain types of cancers are[37–39]:

4.1 **Epstein-barr virus:** Burkitts lymphoma, some types of Hodgkin and non-Hodgkins lymphoma and stomach cancers

4.2 **Human T-lymphotropic virus :** adult T-cell leukemia or lymphoma

4.3 **Kaposis sarcoma associated herpes virus**

4.4 **Merkel cell Polyoma virus :** rare skin cancer known as Merkel cell carcinoma

5. **Age:** Aging process is known to lead to accumulation of many molecular and cellular changes in the body which eventually increases the risk of cancer.

1.3 Cancer Epidemiology in India

According to the data published on May 2019 by Globocan (Global Cancer Observatory), out of the total 135,40,51,855 population (both male and female) screened, the number of new cases registered for cancer in India were 11,57,294 with 7,84,821 reported deaths due to cancer[1,40]. In India (in 2018), the top five most frequent cancers in all age groups excluding the non-melanoma skin cancers were found to be: cancer of the lip or oral cavity (16.1 %), lung (8.5 %), stomach (6.8 %), colorectum (6.4 %) and oesophagus (5.9 %) in males and breast (27.7 %), cervix and uteri (16.5 %), ovary (6.2 %), lip or oral cavity (4.8 %) and colorectum (3.4 %) in females. Other types of cancers contributed to 56.1 % and 41.5 % cases in males and females, respectively **(Fig.**

1.1). According to a study published by Rajpal et al., the estimated overall cancer prevalence in India is 83 per 1,00,000 persons (95% CI: 73.2; 92.7) and is significantly higher in elderly (> 70 years of age) population[41]. According to a review article by Smith et al, the mortality rate due to cancer in India has doubled from 1990 to 2016 and the cancer incidence in India is estimated to be doubled by 2040, which is currently at 1.15 million (as per 2018 statistics)[14]. (*Note: Cancer* ***prevalence*** *is defined as the proportion of the population found to be affected by the cancer at a particular time whereas* ***incidence*** *is the number of new individuals developing cancer during a particular period of time*[1]*).*

A.

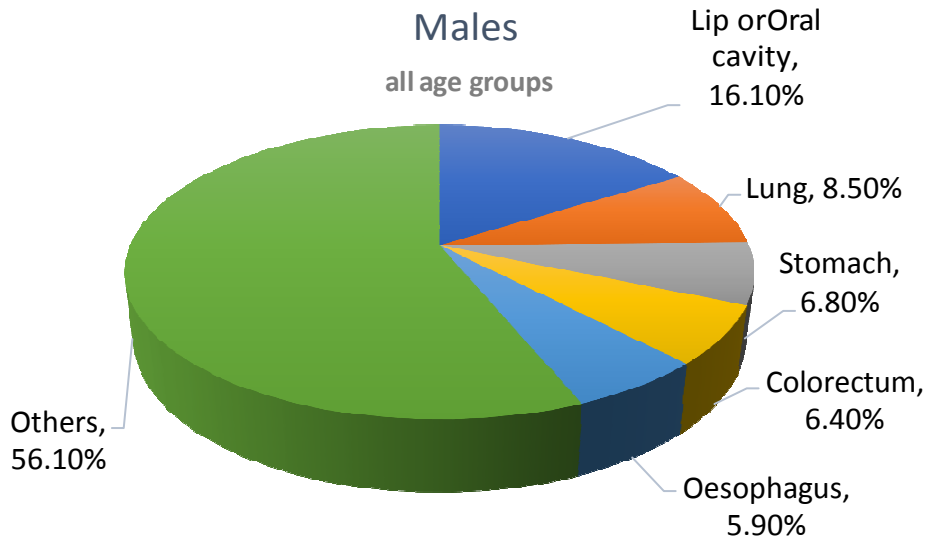

B.

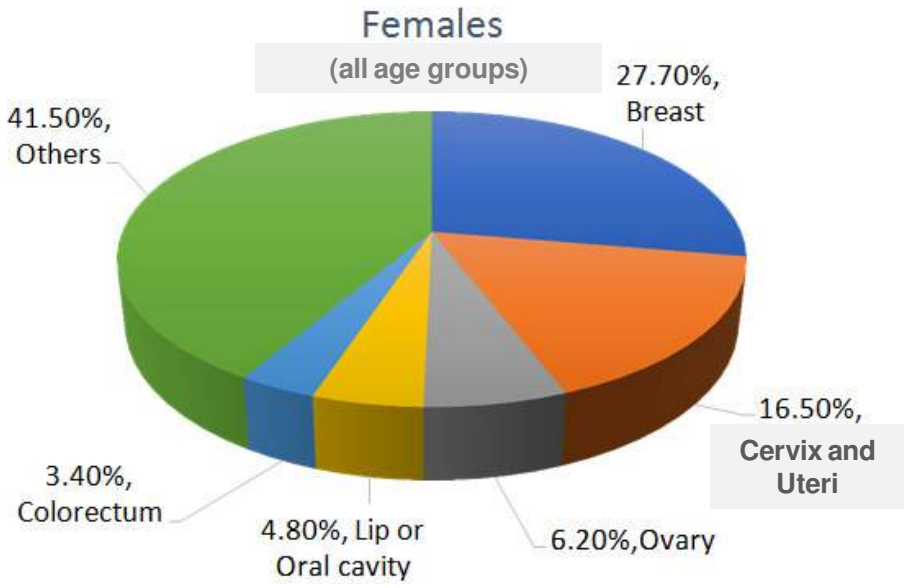

Fig. 1.1 *Pie chart for the top five most frequent cancers in India in males (A) and females (B) of all age groups (Source: Globocan 2018).*

1.4 Cancer treatment or modalities for cancer management

Depending on the location of cancer and its grade (highly proliferative or slowly progressing) and its staging (localized or metastasized to distant locations in the body), usually a combination of treatments are used for treatment. The ultimate goal of effective cancer treatment is to maximize the killing or removal of cancer cells with minimum or no damage to the normal tissues. The types of cancer treatments can be broadly categorized into following types **(Scheme 1.1)**[16,17,35]:

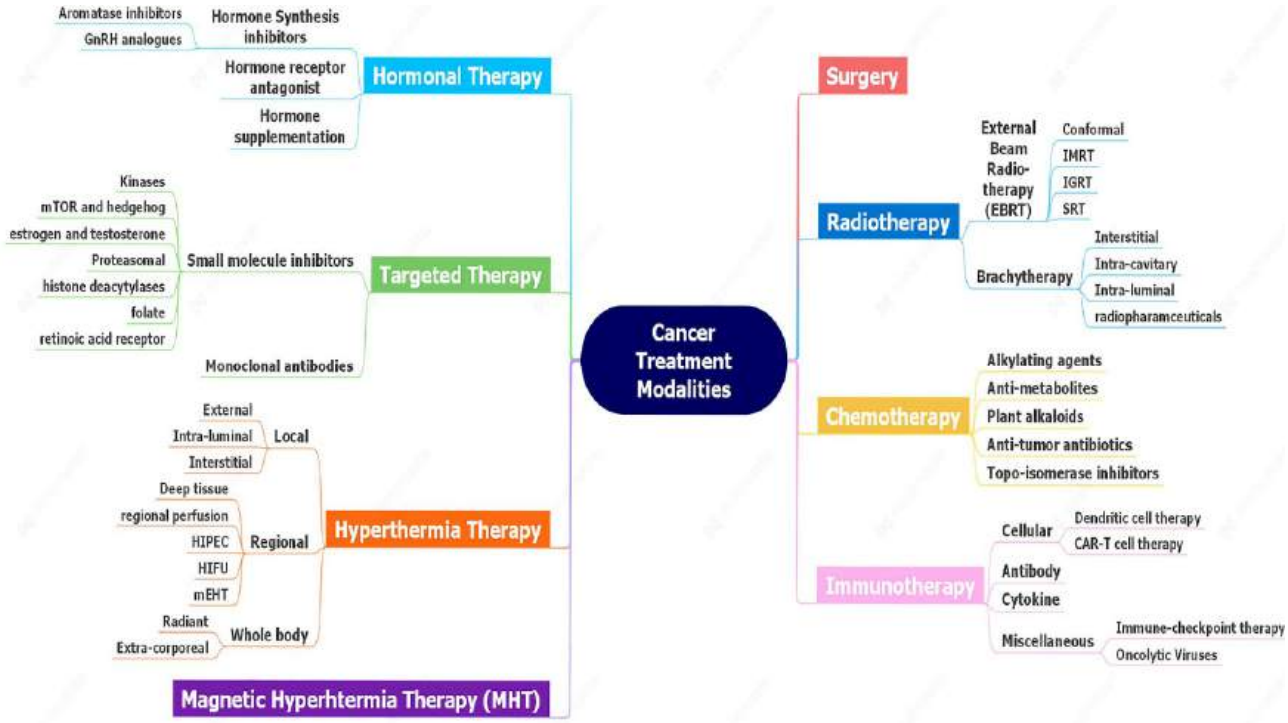

Scheme 1.1 *Scheme for the different types of cancer treatment modalities.*

1.4.1 Surgery: This involves surgical removal of the tumor region usually with a margin of normal healthy tissue adjacent to the tumor site being removed. This is followed by microscopic examination of the excised tissue to ensure that a margin of healthy tissue is also removed along with the tumor. This decreases the chance of tumor recurrence due to presence of tumor cells at the affected site. However, this is possible in case of tumor sites that are not located at critical locations or organs, such as in case of breast cancer or prostate cancer. Occasionally, surgery is used as a palliative treatment option for removal of tumors that obstruct or hinder important body functions, such as spinal cord compression or bowel obstruction[42]. Surgery is usually combined with radio- or chemotherapy to improve the therapeutic index.

1.4.2 Radiotherapy: Of all the cancer treatment options, radiotherapy is considered most effective for treatment of malignant lesions due to several advantages: (i) ability to modulate the radiation to the tumor region, thereby minimizing the normal tissue damage, (ii) radiation causes almost irreparable damage to the cancer cells by inflicting DNA strand breaks either directly or indirectly via generation of reactive oxygen species (ROS), (iii) the radiotherapy procedure is usually fast, painless and completed within 30 to 60 min without the need for hospitalization, thereby preserving the quality of life and (iv) radiation therapy can help relieve pain and control symptoms in case of advanced cancers[43–45]. Radiation therapy usually involves use of ionizing radiation, primarily gamma radiation or X-ray radiation. Other types of radiations used for treatment of cancers includes charged particles like proton beam and carbon ions, called as charged particle therapy (CPT)[46,47]. The CPT is better at sparing the damage to the normal tissue as compared to photons (γ or X-rays) due to their characteristic Bragg's peak. Moreover, the Bragg's peak can be widened to create a spread-out Bragg's peak (SOBP) to cover the 3D structure of the target tumor[48,49]. More recently, pencil beam scanning and intensity modulated proton therapy (IMPT) are used which enables high precision delivery of the radiation dose to the tumor tissue with minimum exposure to the surrounding normal tissue[50]. Albeit the several advantages of CPT, photon (γ or X-rays) based radiation therapy remains a preferred choice mainly, due to the cost factor which is extremely (~ 2 to 3 times) high for CPT. Another reason is the complexity and cost required to build the set up for the irradiator, which is very high for CPT as compared to photon-based radiotherapy. The photon based radiotherapy can be further classified into two types based on the mode of delivering the radiation as (A) External Beam Radiation Therapy (EBRT) or Teletherapy and (B) Internal Radiation Therapy or Brachytherapy:

(A) External Beam Radiation Therapy (EBRT) or Teletherapy: In this modality of

radiotherapy, the radiation is delivered from a distant source outside the body and is focused on the tumor site. Different machines such as orthovoltage X-ray machines, Cobalt-60 machines (such as Bhabhatron), linear accelerators (LINACs), proton or neutron beam machines are used to deliver the radiation[51]. For precise and accurate deposition of radiation at the tumor sites, which can be superficial (e.g. skin cancer) or deep seated (e.g. prostate), the radiotherapy beam can be modulated using different methods. Based on the method used, the different types of EBRT are as below[45,52,53]:

(i) Conformal Radiotherapy: Also called as 3D conformal radiotherapy, it shapes the radiation beam to closely match the patient's tumor geometry.

(ii) Intensity Modulated Radiotherapy (IMRT): This is also a type of conformal radiotherapy and it can modulate the energy of the radiation beam to deliver different energies of radiation to different parts of the tumor.

(iii) Image guided Radiotherapy (IGRT): This utilizes scanning or imaging data (e.g. by X-rays) to ensure that the patient is at the correct position for accurate delivery of the radiation to the tumor.

(iv) Stereotactic Radiotherapy (SRT): This enables to deliver the radiation to the tumor from different directions, thereby limiting the dose to normal tissue. Gamma knife is a stereotaxic radiotherapy applicator which uses a total of 201 beams of γ-radiation, that intersect to form a powerful tool or knife that can be focused to the tumor located in critical sites such as the brain.

(B) Internal Radiotherapy or Brachytherapy: Brachytherapy involves implanting the radiation source directly at the tumor site or as close to the tumor as possible. Contrary to EBRT, brachytherapy uses beta emitting radio-isotopes for treatment, which can deliver dose to the

tumor cells in the immediate vicinity, thereby minimizing the dose to the normal tissue. The radiation source or radioactive isotopes can be implanted in the form of seeds, wires or rods and is based on the method of implantation. It can be further classified as follows:

(i) Interstitial brachytherapy: In this, the radioactive seeds or wires are placed directly at the tumor site and can be removed on the same day, or removed after few days of treatment or may remain permanently in the patient.

(ii) Intra-cavitary brachytherapy: This method, involves the placement of an applicator (either plastic or metal) inside body cavities such as vagina, larynx or uterus, to irradiate the walls of the cavities or nearby tissues. The radioactive source may be placed after the applicator is positioned at the target site and removed after the desired dose is administered to the target site.

(iii) Intra-luminal brachytherapy: This method is used to treat hollow organs such as the oesophagus, wherein the radioactive source is placed inside the applicator that is positioned in the lumen of the oesophagus.

(iv) Radioactively tagged tracer molecules (radio-pharmaceuticals) administered intra-venously: This method is used to treat metastatic sites, wherein the radioactive isotopes can be labeled with tracer molecules that can specifically target the tumor cells and deposit the radioactivity to the cells that have actively taken up the radio-tracer. E.g. octreotide labeled Lu-177 used to treat somatostatin receptor over-expressing neuro-endocrine tumors[54].

Possible side-effects of radiotherapy: In-spite of the technological advances made in the way radiation is delivered to the target tumor site, some exposure to the normal tissue is un-avoidable, which in turn is associated with some discomforts or side-effects, which are as follows[18,55]:

1. Fatigue
2. Nausea and vomiting
3. Loss of appetite
4. Emotional distress
5. Skin erythema : dryness, itching, blistering or redness of the skin, if it is exposed to radiation during treatment.
6. Xerostomia : dry mouth, mouth or gum swelling, difficulty in swallowing, stiffness of the jaws, hair loss or tooth decay in cases of treatment of head and neck cancers.
7. Radiation fibrosis or pneumonitis, particularly during treatment of lung cancers where the chest is exposed to radiation.
8. Diarrhea, rectal bleeding, incontinence and bladder irritation, when the pelvic region is exposed to radiation.

These side effects are largely dependent on the location of the tumor in the body which is exposed to radiation and the modality of radio-therapy used and may or may not occur in all patients.

1.4.3. Chemotherapy: Chemotherapy is another modality of cancer treatment that is used for treatment of variety of cancers, especially those where surgery or radiotherapy is difficult or risky. The term ‘chemotherapy’ was coined by German chemist Paul Ehrlich in the early 1900s and defined chemotherapy as the use of chemicals to treat cancer. However, serious investigations of chemotherapy started during world war II, after observations of serious health implications (depletion of WBC count) of nitrogen mustards during the warfare. This initiated the era of chemotherapy in the 1940s with the use of nitrogen mustards and folic acid as

antagonist anti-neoplastic agents[56,57]. This modality of cancer treatment makes use of chemicals or drugs either singly or a cocktail of two or more drugs that selectively kills the fast-growing cells in the body and thus target the cancer cells more as compared to other normal cells of the body. Based on the type of cancer and the types of chemo-therapeutic drugs used for treatment, these drugs can be administered either orally, or intra-muscularly or intra-venously or sub-cutaneously (under the skin) or intra-thecally (injected in the fluid around the spine). Intra-venous route is most efficient as the bio-availability of the drug in 100 %, but oral route is most convenient and less painful for the patients. Most of the chemotherapeutic drugs act by two ways :(1) they either damage the DNA directly by intercalating or inducing DNA strand breaks or indirectly by inducing ROS or (2) they inhibit the repair of the damaged DNA by inactivating important repair enzymes or proteins in the cancer cell[56,58]. Based on the mechanism of action, the chemotherapeutic drugs can be broadly classified as follows:

(A) Alkylating agents: These agents act by covalently binding to the DNA by their alkyl group, resulting in intra-strand and inter-strand DNA cross-links, abnormal base pairing and DNA strand breaks, eventually terminating the replication of DNA and subsequent cell division. They are most effective on the slow growing cancer cells and are cell phase independent. There are several types of alkylating agents such as[18]:

(i) Mustard gas derivatives: Cyclophosphamide, Melphalan, Ifosfamide, Mechlorethamine and Chlorambucil

(ii) Ethylenimines : Thiotepa and hexamethyl melamine

(iii) Alkylsulfonates: Busulfan

(iv) Hydrazines and Triazines: Altretamine, Procarbazine, Dacarbazine and Temozolomide

(v) Nitrosureas: Carmustine, Lomustine and Streptozocin. Nitrosureas are unique because, unlike most types of chemo treatments, they can cross the blood-brain barrier. They can be useful in treating brain tumors.

(vi) Metal salts: Carboplatin, Cisplatin, and Oxaliplatin.

(B) Anti-metabolites: Anti-metabolites are analogs of natural substances that the cells need to divide and metabolize. They usually mimic building blocks of DNA and proteins, due to which the cells are tricked into incorporating the anti-metabolites in their DNA or proteins, but however, are not able to metabolize them further. These are cell cycle specific and are most effective in the S-phase of the cell cycle, when the DNA is actively replicating. Anti-metabolites are further classified as follows based upon the substances with which they interfere[58–60]:

(i) Folic acid antagonist: Methotrexate.

(ii) Pyrimidine antagonist: 5-Fluorouracil, Floxuridine, Cytarabine, Capecitabine, and Gemcitabine.

(iii) Purine antagonist: Fludarabine.

(iv) Purine analogs : 6-Mercaptopurine (6-MP), Azathioprine (pro-drug for6-MP), Cladribine and 6-Thioguanine.

(v) Adenosine deaminase inhibitor: Nelarabine and Pentostatin.

(vi) Ribonucleotide reductase inhibitors: Hydroxyurea.

(C) Plant Alkaloids: These are the anti-tumor agents derived from plants and are cell cycle specific. They usually act by blocking the cell division by various mechanism. A few examples are given below[61–63]:

(i) Vinca alkaloids : They are derived from periwinkle plant (*Catharanthus roseus*) and act by binding to tubulin, thereby inhibiting the microtubule polymerization resulting in cell cycle arrest in the metaphase. Ex. : Vincristine, Vinblastine and Vinorelbine.

(ii) Taxanes: Derived from the bark of pacific yew tree (*Taxus*) and acts by stabilizing the GDP-bound tubulins, resulting in inhibition of cell division by inhibiting the de-polymerization of microtubules. Ex. : Paclitaxel and Docetaxel.

(iii) Podophyllotoxins : They are derived from the May apple plant and act by de-stabilizing the microtubules and inhibiting the action of topoisomerase (II), thus inhibiting cell division during late S and G2 phases of cell cycle. Ex.: Etoposide and Tenisopide.

(iv) Camptothecan analogs : They are derived from the Asian "Happy tree'' (*Camptotheca acuminate*). They act by forming a ternary complex with topoisomerase (I), preventing the re-ligation of DNA, and hence DNA damage and induction of apoptosis. Ex: Irinotecan and Topotecan.

(D) Anti-tumor Antibiotics: These are compounds usually isolated from the fungi, *Streptomyces sp.* and are different from the antibiotics used for treating bacterial infections. They are cell cycle non-specific and exhibit their action by binding to the DNA and inhibiting DNA replication, resulting in inhibition of cell division and induction of apoptosis. They can be further categorized as follows[64]:

(i) Anthracyclines: Doxorubicin, Daunorubicin, Epirubicin, Mitoxantrone and Idarubicin. Doxorubicin and daunorubicin are isolated from *Streptomyces peucetius var. caesius* and exhibit the widest spectrum of anti-tumor activity against various human cancers. Owing to their planar structure consisting of a tetracycline ring bound to a daunosamine group through a glycoside

bond, they are known to intercalate into the DNA. The quinone and hydroquinone groups of these molecules act as electron donors and acceptors, thereby contributing to cellular damage through redox changes.

(ii) Chromomycins: Dactinomycin and Plicamycin. Dactinomycin is derived from *Streptomyces parvullus*, and it is known to inhibit DNA dependent RNA synthesis through stable complexes formed with DNA through intercalation. Plicamycin is derived from *Streptomyces plicatus* and is presumed to inhibit both cellular and enzymic RNA synthesis through forming stable complexes with DNA.

(iii) Miscellaneous: Mitomycin and bleomycin. Mitomycin is produced by *Streptomyces caespitosus* and is a pro-drug, which gets activated inside the cell into a bi- or tri- functional alkylating agent which cross-links the DNA and inhibits its synthesis. Bleomycin is derived from *Streptomyces verticillus* and is a glycopeptide antibiotic. It binds to the guanosine-cytosine-rich portions of the DNA via association of the S-tripeptide and by partial intercalation of the bi-thiazole rings. It produces DNA single strand breaks via generation of ROS which is molecular oxygen and Fe dependent. It shows highest toxicity in the G2 phase of cell cycle.

(E) Topoisomerase Inhibitors: This includes compounds that exhibit their cellular toxicity by interfering with the action of DNA topoisomerases (I or II), which play important role in manipulating the DNA structure necessary for DNA replication[65,66].

(i) Topoisomerase I inhibitors: Irinotecan, Topotecan.

(ii) Topoisomerase II inhibitors: Amsacrine, Etoposide, Etoposide phosphate, Teniposide and Doxorubicin.

(F) Miscellaneous: Several other chemotherapeutic drugs have unique mechanism of action and to name a few, such as (i) Mitotane which acts as a adrecortical steroid inhibitor[67,68] and (ii) bacterial enzymes such as asparaginase, isolated from *Escherichia coli* and *Erwinia chrysanthemi,* and its modified form PEG-asparagase which show their anti-neoplastic effects by inhibiting protein synthesis[69,70]. Asparaginase mainly catalyzes the conversion of L-asparagine into L-aspartic acid and ammonia, thereby depriving the tumor cells of the essential amino acid, L-asparagine. It is most effective in the G1 phase and is currently used for treatment of acute lymphocytic leukemia. PEG-asparagase is used in patients that show hypersensitivity reactions to other forms of L-asparaginase.

Probable side effects of chemotherapeutic drugs: Chemotherapeutic drugs have the ability to inhibit the fast dividing cells of the body (which is mostly comprised of the cancerous tissue). However, there are normal cells which also divide relatively fast and can get killed by the chemotherapeutic drugs. The most important decision of an oncologist is to optimize the dose for chemotherapy, because under-dosing may increase the chances of failure of the therapy and over-dosing can have serious health implications due the toxicity to the normal cells. The usual practice is to use the maximum effective safe dose even at the cost of some temporary side effects. However, not all patients have all or the same degree of the side effects and is usually dictated by the overall health parameters of the patient, such as renal function, liver function, complete blood count, etc. The most common side effects associated with this modality of cancer treatment can be summarized as but not limited to as follows[71,72]:

1. Fatigue

2. Nausea and vomiting
3. Diarrhoea
4. Mouth sores
5. Hair loss and
6. Anemia

Cells in the bone marrow, digestive tract, inner lining of the intestines, reproductive system and the hair follicles are relatively fast growing normal cells in body and get affected by the chemotherapeutic drugs.

1.4.4 Immuno-therapy: Immunotherapy is a growing sub-specialty of oncology and involves the application of fundamental knowledge of cancer immunology to boost or stimulate one's immune system to fight against cancer. In the year 2018, two immunologists (James P. Allison, America and Tasuku Honjo, Japan) received the Noble prize in physiology for the discovery of cancer therapy by the inhibition of the negative immune regulation by CTLA-4 and PD-1, respectively[73,74]. Immunotherapy action is based on the basic concept that the body's own immune system is capable of detecting and eliminating the cancer cells. This is done through the fundamental property of the immune system which enables it to discriminate the self from 'non-self' cells. Amongst immune cells, T-cells are a key player in this defense, which together with the antigen presenting cells can bind to non-self-antigens via T-cell receptors. However, in addition to this interaction, the discriminate elimination of the non-self (cancer) cells requires an intricate balance between proteins that functions as the T-cell accelerators and brakes. This fine balance enables a tight control over the T-cell action which ensures that only the non-self cells (pathogens or cancer cells) are eliminated, while the normal cells of the body are spared.

However, the identification of cancer cells by immune cells is difficult in some instances as cancer cells originate from mutations in the normal cells and may not always have a distinct surface marker. In some instances, although the immune cells have recognized the cancer cells, the immune response is not strong enough to eliminate them. Additionally, in certain cases the cancer cells themselves release certain molecules that make their detection and elimination by the immune system difficult. Thus, based on the approaches used to strengthen the detection and immune response against cancer cells, immunotherapy can be broadly categorized as active, passive or hybrid (both active and passive)[75–77]. Active immunotherapy directs the immune system to actively kill the cancer cells by targeting tumor antigens. Passive immuno-therapy on the other hand encompasses use of monoclonal antibodies, cytokines or immune cells (lymphocytes) to stimulate or enhance the already active anti-tumor immune response. Whereas, hybrid approach utilizes a combination of the above mentioned responses. Depending on the cells or molecules used, immunotherapy can also be further categorized as follows:

A. Cellular Immunotherapy: This involves activating the immune cells (dendritic or T-cells) of the body to elicit an anti-tumor response.

(i) Dendritic cell therapy: Dendritic cells are the antigen presenting cells (APC) in the body that can process the tumor cells antigen and differentiate into a mature APC which can prime the immune cells (T-lymphocytes) to kill other cells (cancer cells) presenting the same antigen. The activation of the dendritic cells *in vivo* can be done by either injecting autologous tumor tissue lysates (vaccination) or tumor associated antigenic (TAA) peptides in combination with an adjuvant [such as granulocyte and macrophage-colony stimulating factor (GM-CSF)] to increase the immune and anti-tumor responses[78,79]. Another strategy is to remove the dendritic

cells from the blood by leukapaeresis and activating them in presence of tumor antigens (whole tumor lysates or peptides) and re-introducing them in the body of the cancer patient to obtain an anti-tumor response. Sipuleucel-T (Provenge) for the treatment of asymptomatic or minimally symptomatic metastatic castration-resistant prostate cancer is one such clinically approved dendritic cell immunotherapy (2010). It involves activating the dendritic cells outside the body using a fusion protein of GM-CSF and prostate specific prostatic acid phosphatase (PAP) followed by re-introduction into the body[80].

(ii) CAR-T cell therapy: In CAR-T cells therapy (CART), the T cells are engineered (either using a virus or other gene editing methods) to express a chimeric antigen receptor (CAR), which specifically recognizes a tumor cell surface antigen. However, as against dendritic cell therapy, CAR-T cell therapy always requires, ex-vivo engineering and activation of the T-cells. Once activated, the T-cells are proliferated in culture conditions, prior to re-introduction into the patient. Before, re-introduction, the patients are subjected to routine chemotherapy, so as to increase the acceptance of the engineered T-cells and improve the anti-tumor response[81–83]. CART is a possible option in cases of cancer without much treatment options such as relapsed pediatric acute lymphoblastic leukemia (ALL). Infact, in 2017, FDA approved the use of CART for treatment of pediatric ALL and for adults with advanced lymphomas[84,85]. Several clinical trials with CD19-targeting (B cell specific surface antigen in ALL) CART in children with ALL, have shown promising results with almost complete remission and disease-free survival for several years in more than 80 % of the patients[82,85,86].

B. Antibody Therapy: Antibody therapy utilizes antibodies that are specially engineered to bind to the antigens on the tumor cells and elicit an anti-tumor immune response. The antibodies can be used as it is, without addition of any toxic elements called as 'naked antibodies'. Another approach is to tag the antibodies to a cytotoxic agent (either a chemotherapeutic drug or a toxin) or radioactive agent for immuno-radiotherapy of cancer. The antibodies used are mostly monoclonal, produced by hybridoma technology and can be of murine, chimeric or humanized types[87,88]. Initially, murine antibodies were used but they carried the risk of an immunogenic response in human patients, compromising the success of the therapy and risking the patient's life due to induction of allergic reactions or anaphylactic shock. Therefore, recently chimeric or humanized antibodies are used for cancer therapy. Chimeric antibodies (*suffix : ximab*) contains murine variable regions fused onto human constant regions making them 60 % human. This reduces the immunogenicity of the chimeric antibodies, thus increasing the serum half-life. Few examples of FDA approved chimeric antibodies includes, cetuximab targeting the EGFR in human metastatic colorectal cancers, rituximab targeting CD20 in B-cell non-Hodgkin's lymphoma and dinutuximab targeting GD2 in pediatric high risk neuroblastoma[89]. Humanized antibodies (*suffix : zumab*) are produced by grafting murine hypervariable regions on amino acid domains into human antibodies and are ~ 95 % human origin. However, they tend to have weaker affinities for their antigens as compared to parent murine antibodies, which however can be improved by introducing mutations into the complementarity determining regions (CDR) using error prone polymerase chain reaction (PCR), site directed mutagenesis and E. Coli mutator strains[90]. A few FDA approved humanized antibodies for cancer therapy includes, bevacizumab, targeting VEGF in metastatic colorectal cancers, elotuzumab targeting SLAMF7 in multiple myeloma and trastuzumab, targeting HER2 receptors in metastatic breast cancers[91].

Another type of antibody that is used for targeted antibody therapy of cancer is called as human monoclonal antibodies (*suffix : umab*). They are developed in transgenic mice or by using phage display libraries to produce human antibodies in mice by transferring the human immunoglobulin genes in mice genome and vaccinating the mice against a human antigen[90,92]. This includes FDA approved products such as avelumab targeting PD-L1 for treatment of metastatic merkel cell carcinoma, daratumumab targeting CD38 for treatment of multiple myeloma and durvalumab targeting PD-L1 for treatment of urothelial carcinomas[92]. The anti-cancer antibodies, be it chimeric, humanized or human monoclonal antibodies, kill the tumor cells mainly by two mechanism, i.e. antibody-dependent cell-mediated cytotoxicity (ADCC) or via activation of the classical complement pathway. Both the mechanisms require the presence of Fc portion of the therapeutic antibodies which is detected by the immune cells via their Fc receptors, once the therapeutic antibody binds to its target on the cancer cells. Once bound to immune cells (NK cells) they release perforin and granzyme B enzymes to kill the tumor cells. Complement activation requires the presence of IgG1 Fc region in the therapeutic antibodies which is activated by the binding of C1 fragment to the therapeutic antibodies bound to the cancer cells followed by the formation of membrane attack complex (MAC) which kills the tumor cells by pore formation[88].

C. Cytokine Therapy: Cytokines are membrane bound or secreted proteins that act as mediators of intercellular signaling and have significant role in immuno-modulation of the tumor micro-environment (TME). Of the several cytokines, interleukins (IL) and interferons (INF) have shown promising anti-cancer efficacy. The mechanism of cytokine therapy, although not thoroughly understood, primarily includes improving the efficacy of antigen priming, increasing the number of effector immune cells (T-cells and NK cells) and enhancing their cytolytic activity

in the TME[93,94]. To date, two cytokines have been approved by FDA for anti-cancer immunotherapy and includes IL-2 for metastatic melanoma and renal cell carcinoma[95,96] and INF-α for adjuvant therapy of stage III melanoma[97]. IL-2 promotes the proliferation of the effector and regulatory T-cells, but the exact mechanism of action is still unknown. IFN-α can induce direct caspase-dependent apoptosis in tumor cells and can also act as anti-angiogenic agent at low doses.

D. Miscellaneous Immuno-therapies: This includes therapies which are still undergoing pre-clinical research or are in clinical trials. A few are listed below:

(1) Immune checkpoint therapy: Immune check-points can be either stimulatory or inhibitory in nature and the tumor cells can modulate them to protect themselves from attack by the immune system. By blocking the negative feedback signaling to the immune cells in the TME can improve/enhance the immune response against tumors[98,99]. One such molecule is programmed cell death protein 1 (PDI) which is bound by its ligand PD-L1. Tumor cells are known to over-express PD-L1 on their surfaces, which by binding to PD-1 on activated T-cells, suppress their immunogenic anti-cancer response. PD-L1 on cancer cells also inhibits Fas and interferon dependent apoptosis, protecting themselves from the cyto-toxic molecules produced by T-cells. Thus, by blocking the PD-1 receptors on the T-cells using therapeutic antibodies (nivolumab and pembrolizumab)[99], the anti-tumor response of the tumors can be improved.

(2) Oncolytic viruses: This therapy includes the use of specially engineered viruses (adenoviruses, measles, herpes simplex virus, vaccinia virus, etc.) that can specifically target the tumor or cancer cells, while sparing the normal non-neoplastic cells and kill them by oncolysis. During oncolysis, new virions are released in the TME which can further kill more tumor cells

and also elicit an anti-tumor immune response[100,101]. Talimogene laherparepvec (T-vec) was the first FDA approved oncolytic virus for treatment of melanoma[102].

Limitations or side effects of Immuno-therapy: Similar to other cancer treatment modalities, immuno-therapy is also known to show side effects and in some cases can turn out to be fatal. For instance, the most common side effect of CART- cell therapy is cytokine release syndrome (CRS), which is a result of the primed T-cells releasing these chemical messengers (cytokines) that stimulate and direct the immune response. CRS, mostly mediated by IL-6 (inflammatory cytokine) can cause severely high fever and precipitous drop in blood pressures[103]. FDA has approved the use of anti-IL6 drug, tocilizumab (Actemra®), to manage the CRS during CART[104]. Other side effects include B-cell aplasia (mass killing of B-cells) as even the normal B-cell expressing the CD19 antigen get killed by the primed CAR expressing T cells. This is usually managed by a concomitant immunoglobulin therapy that provides the necessary antibodies to fight off infections[105]. A less common, but potentially lethal side effect is swelling in the brain (cerebral edema), the cause of which is still unknown[106]. Other less severe side effects can be listed as follows[107]:

1. Skin reactions: reddening, blisters and dryness of the skin
2. Fatigue, fever, chills and nausea
3. Muscle aches
4. Shortness of breath
5. Swelling of legs (edema)
6. Sinus congestions, headaches
7. Diarrhea and cough

1.4.5. Hormonal therapy: This modality of cancer therapy is usually employed in the treatment of cancers that depend on certain hormones for their uncontrolled growth, such as breast, endometrium, adrenal cortex and prostate cancers. It involves the use of inhibitors of hormone synthesis or drugs that act as hormone receptor antagonist to slow the growth of cancer cells or kill them. They basically modulate the endocrine system of the tumors, which are highly dependent on these abruptly expressed levels of hormone for their uncontrolled growth[108–111]. The hormonal therapy can be broadly categorized into three types:

A. Hormone synthesis inhibitors: This uses drugs that inhibit the synthesis of hormones in the organs where the tumor originates, to inhibit or slow down its growth. These drugs are of two types:

1. Aromatase inhibitors: This class of drugs inhibit the aromatase enzyme in the adrenal glands that is necessary for the synthesis of estrogen from androgens. Examples include letrozole and anstrozole, which are used for treatment of breast cancer in menopausal women. Tamoxifen can be used in both pre- and post-menopausal women with breast cancers[112].

2. Gonadotropin releasing hormone (GnRH) analogues: The drugs that acts as analogues of GnRH can cause complete suppression of the release of estrogen and progesterone in ovaries in females or testosterone in the male testes. Leuprorelin and goserelin in this category are used for the treatment of hormone responsive prostate cancer[113,114].

B. Hormone receptor antagonist: These drugs bind to the hormone receptors, which are expressed on the cancer cell surface or may be intra-cellular and prevent the activation of the bound receptors. Toremifene and fulvestrant that act as antagonists of estrogen receptor, are used in the treatment of metastatic breast cancer[115].

C. Hormone Supplementation: While most anti-neoplastic hormonal therapies depend on inhibiting the action of hormones supporting the tumor growth, there are certain hormone agonist, which can have anti-proliferative or even cytotoxic effect on the tumors. Examples include fluoxymesterone, an anabolic steroid, used for the treatment of advanced breast cancer[116] and estrogen diethylstilbestrol used for treatment of prostate cancer through suppression of testosterone production[117].

Possible side effects of hormonal therapy:

Since, hormone therapy blocks the production of certain hormones or interferes with how they function in the body, it is ought to have some side effects. Not all patients experience the side effects or to the same extent and depends on the type of cancer/medication. Some common side effects for men treated for prostate cancer by hormonal therapy includes[118]:

1. Hot flashes
2. Weakened bones
3. Diarrhea
4. Nausea and fatigue

Some common side effects for females being treated with hormonal therapy for breast cancer includes[119]:

1. Hot flashes
2. Vaginal dryness
3. Mood changes
4. Changes in menstrual periods in case of pre-menopausal women

5. Nausea and fatigue

1.4.6. Targeted therapy: Unlike chemotherapy, which targets all the fast dividing cells (normal or cancerous), targeted therapy directs the drugs specifically to cancer cells. These drugs utilize the definitive genetic features of the cancer cells, thereby minimizing the normal tissue injury. Targeted therapy is generally used for patients which do not respond to routine cancer therapies (like chemo- or radio-therapy) or is inoperable or spread to distant organs. Usually, patients are subjected to advanced genome testing to know about the genetic disposition, protein composition and other traits that the tumor exhibits. Using this knowledge the appropriate drugs are prescribed by the oncologists[120–122]. Targeted therapy is occasionally combined with radio-, chemo- or hormonal therapies and with surgery. Targeted therapy can be grouped in two types namely (i) small molecules inhibitors, which can enter the cells and bind to and hamper the action of molecules (signal transduction messengers or kinases) which are key to the growth of cancer cells[123] or (ii) monoclonal antibodies which bind to the cell surface targets on the cancer cell to exhibit their anti-tumor action[88,124]:

A. Small molecule inhibitors: This includes inhibitors of cellular kinases or other proteins such as proteasomes, folate, retinoic acid and hormones that play important role in cellular signal transduction pathways and cellular growth and are abruptly functioning in the cancerous cells.

a. Kinase inhibitors: Most kinase inhibitors target the receptor tyrosine kinases, some examples of inhibitors used for the treatment of different types of cancers (mentioned in parenthesis) are as below[123,125,126]:

(i) Bosutinib: blocks the action of BCR-Abl, Src, Lyn, and Hck cytoplasmic tyrosine kinases (acute lymphoblastic leukemia and chronic myelogenous leukemia).

(ii) Crizotinib: inhibits the action of ALK, ROS1 and c-Met receptor tyrosine kinases (non-small cell lung cancer and sarcomas).

(iii) Erlotinib: blocks the action of EGFR tyrosine kinase (bone, esophageal, kidney, pancreatic and non-small lung cancers).

(iv) Axitinib: blocks the action of VEGF 1/2/3 receptor tyrosine kinases (kidney cancers).

b. Inhibitors of mTOR and hedgehog signaling pathways: Some small molecule inhibitors (e.g. Sirolimus, Everolimus and Temsirolimus, used for the treatment of bone cancers, breast and neuroendocrine cancers and kidney and uterine cancers, respectively) inhibit the action of mTOR protein kinases[127]. While others (Vismodegib) block the action of proteins (e.g. smoothened) playing important role in the hedgehog pathway[128,129].

c. Inhibitors of estrogen and testosterone hormones: Certain small molecule inhibitors act by inhibiting the hormones secreted by the cancerous cells that are needed for sustaining continuous proliferation of the tumor cells. This includes selective estrogen receptor modulators (SERM) that attach to estrogen receptors and block action of estrogen, or selective estrogen receptor down-regulators (SERD), that block and reduce the number of estrogen receptors[130,131]. Some examples of SERM are Raloxifene (used to reduce the risk of breast cancer), tamoxifen citrate and toremifene citrate therapeutic agent for breast, ovarian and uterine cancers and soft tissue sarcomas[132]. Fulvestrant is a SERD for breast cancer treatment[130]. Some drugs inhibit the synthesis of estrogens by inhibiting the enzymes required for their synthesis such as aromatase inhibitors (for example anastrozole and exemestane) employed for treatment of breast and

uterine cancers. Some examples of testosterone inhibitors includes Abiraterone acetate (an inhibitor of androgen biosynthesis)[133], and Bicalutamide, Enzalutamide, Flutamide and Nilutamide (non-steroidal anti-androgens)[134].

d. Proteasomal inhibitors: They block the action of proteasome which leads to cell death. Ex: bortezomib (for multiple myeloma and non-Hodgkin lymphoma)[135] and carfilozomib for multiple myelomas[136].

e. Histone Deacetylase inhibitors: This includes romidepsin and vorinostat blocking the action of histone deacetylases and used for non-Hodgkin lymphomas treatment[137].

f. Folate inhibitors: Folate is needed for DNA synthesis and the rapidly growing cancer cells are highly dependent on the folate supply for their growth. Pralatrexate is a dihydrofolate reductase inhibitor, which is needed for folate synthesis and is used for treatment of non-Hodgkin lymphoma[138].

g. Retinoic acid receptor targets: Retinoids are small molecules binding to retinoic acid receptors and foster the growth of an immature cell into a mature cell and can help stopping the growth of some cancer types. Exisotretinoin and acitretin used for treatment of non-Hodgkin lymphoma[139] and non-melanoma skin cancers[140].

B. Monoclonal antibodies: This includes monoclonal antibodies that bind to growth promoting receptors expressed on the surface of cancer cells such as EGFR (Cetuximab and panitumumab) and HER2 (transtuzumab and pertuzumab). These receptors are mutated to always stay 'ON' is some cancers (such as colon and rectal cancers show over-expression of EGFR[141] and breast and gastric cancers show the continued expression of HER2 receptors)[142].

Some monoclonal antibodies bind to cell surface molecules of immune cells (T or B cells) that modulates the function of this immune cells and enhances the anti-tumor immune response. This includes rituximab (anti-CD20 antibody) used for therapy of ALL, Hodgkin and non-Hodgkin lymphomas[143]. Ipilimumab is a CTL4A-blocking antibody showing promising clinical potential in melanomas[144]. Others such as Bevacizumab and Ziv-aflibercept bind to VEGF and prevent it from attaching to its receptor. They act as anti-angiogenic molecules[145].

Limitations of targeted therapy

Although the targeted therapy is specific for the cancer cells, it still suffers certain limitations, mainly due to its targeting of one or a few molecular target(s) of cancer. However, the cellular signaling in cancer cells is governed by a complex network of signaling molecules. In addition, the tumor is not a homogenous population. Moreover, factors such as presence of alternate signaling pathways and the heterogenous population of tumor cells which may have chemo resistance, strongly impairs the efficacy of the targeted therapy. Hence, in most instances targeted therapy is often combined with radiotherapy or other cancer treatment modalities.

1.4.7 Hyperthermia therapy

1.4.7.1 History of Hyperthermia therapy: Hippocrates, an ancient Greek physician (479-377 B.C.), also known as 'Father of Medicine', in one of his famous quotes stated[146]:

> '*Those who cannot be cured by medicine, can be cured by surgery. Those who cannot be cured by surgery can be cured by fire (hyperthermia). Those, who cannot be cured by fire, are indeed incurable.*'

The term hyperthermia is a combination of two Greek words, 'hyper' means rise and 'therme' means heat. Hyperthermia literally means use of heat either locally or exposure of the whole body to heat to obtain therapeutic effects. The discovery of use of hyperthermia or heat for treatment of cancer was first published in the year 1866 by a German surgeon, Carl. D. W. Wusch[147]. He reported the regression of tumor in a 43-year old woman with a sarcoma on the face, who had contracted a streptococcal infection, erysipelas, following surgery. Dr. Wusch suggested that the bacterial infection resulted in severely high fever, which led to the shrinkage in the remaining tumor. On similar lines, in 1891, an American surgeon named Dr. William B. Coley developed a toxin that can induce erysipelas with typical high fever, which was used for treatment of several non-treatable cancers for almost a century[148]. Due to his discovery of the so called Coley's toxin and its use for cancer therapy, Dr. Coley is also called as the 'Father of modern use of hyperthermia and immunotherapy against cancer'[149]. This led to the foundation of the idea to use 'heat' for the treatment of cancer and later there were several reports by Dr. Westermark and Dr. Gottshchalk, who used prolonged heating upto 48 hours using metal coil with water circulation (thermo-couple based heating) or hot water tubs to treat varying types of gynecological tumors[150]. This was shortly followed by combining hyperthermia as an adjuvant therapy with radiation and chemotherapy. Later, the physiological advantages of combining hyperthermia with the conventional cancer therapy modalities became more promising and evident.

1.4.7.2 Mechanism of hyperthermia therapy: Hyperthermia therapy involves exposing the tumor region or a part of the body or whole body to elevated temperatures of ~ 42-43 °C, which

either kills the tumor cells directly or makes them more sensitive to subsequent concomitant chemo or radiotherapy of cancer. Although the mechanism of cell killing by heat is not well understood, there are several hypotheses for its mode of action. Predominantly, at cellular level, hyperthermia is known to cause denaturation of proteins, RNA and DNA (**Scheme 1.2**). It also affects the fluidity of cellular membranes resulting in altered cellular transport and membrane associated cellular signaling. It is also known to affect the important cellular functions, such as DNA replication, RNA and protein synthesis and repair of damaged DNA. Together these changes result in a significant decrease in tumor cell proliferation and increased induction of tumor cell death by apoptosis or necrosis, resulting in tumor regression. At a physiological level, hyperthermia is postulated to cause vasodilation, resulting in enhanced oxygen and drug supply at the tumor site, which in combination with concomitant radio or chemo-therapy results in enhanced tumor regression[151,152]. A scheme depicting the possible mechanisms of tumor cell killing by hyperthermia therapy is presented.

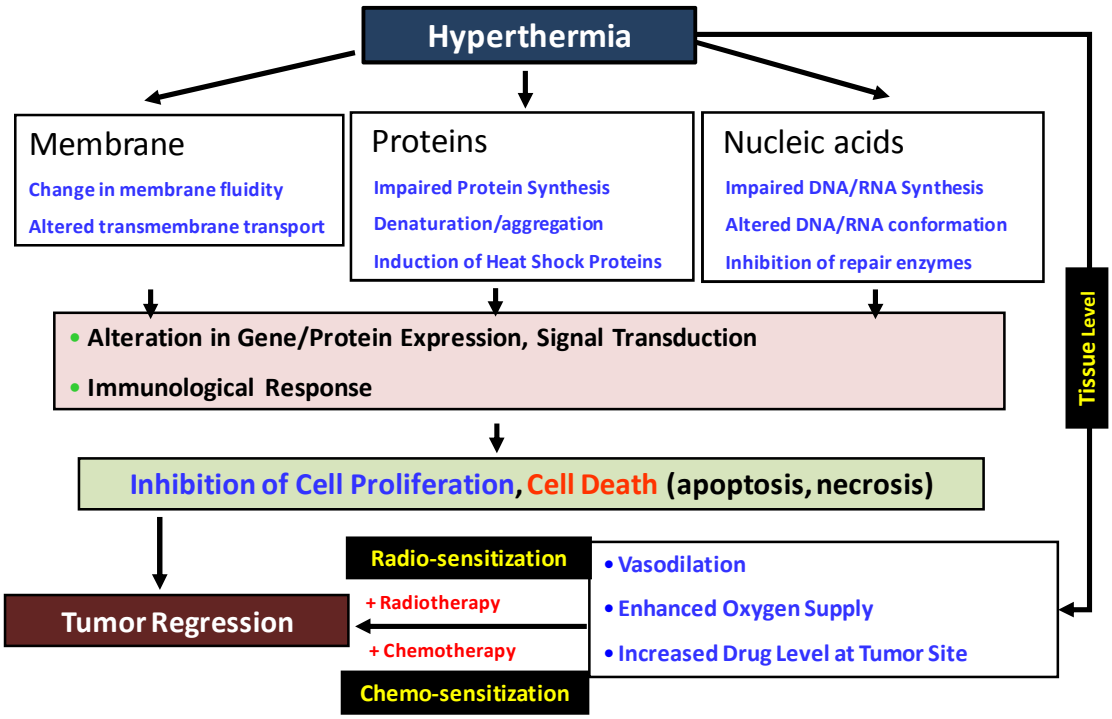

Scheme 1.2 *Scheme for probable mechanism of action of hyperthermia therapy.*

1.4.7.3 Types of hyperthermia therapy: Hyperthermia therapy can be administered using a variety of techniques, which can be broadly categorized as local, regional or whole body hyperthermia based on the area of body exposed to heat[150,153,154].

A. Local hyperthermia therapy: This modality is typically used for small tumors (> 3 cm and < 6 cm) located superficially i.e. on the skin or near the skin surface or in the vicinity of natural body cavities (such as esophagus or rectum). Different types of energies such as ultrasound, radio-waves or microwaves may be used to apply heat. Depending on the location of the tumor, local hyperthermia can be applied by following approaches:

1. External hyperthermia therapy: This is used for tumors located at or just near the skin and heat is applied using superficial applicators of different shapes and types (e.g. waveguide, spiral and current sheet). The applicators are positioned near the surface of the tumors using a contacting layer called as bolus. Water boluses are concurrently used to maintain the skin temperature ~ 37 °C to prevent any excess heating of the normal tissue and associated side effects. The boluses also help to mediate the electromagnetic linking from the applicators to the tissue. The temperature at the tumor site is monitored using thermometers placed in capillaries or tubes, inserted in the anesthetized tumor tissue[155].

2. Intra-luminal or endocavitary hyperthermia therapy: In this method, the tumors located near body cavities, such as rectum or esophagus, are treated using applicators that are inserted into the tumors through these cavities[156].

3. Interstitial hyperthermia therapy: This modality is used to treat tumors located deep inside the body such as brain tumors. This technique enables to heat the tumors to higher

temperatures as compared to other external heating techniques. In this method, the tumor region in anesthetized and the probes are inserted in the tumor region (e.g. brain tumor) followed by heating it to high temperatures (~ 60 °C using radio-frequency ablation). Ultra-sonography may be used to ensure appropriate positioning of the probes at the tumor site for efficient and accurate heating[157].

B. Regional hyperthermia therapy: In regional hyperthermia therapy, larger areas of the body, such as whole organs, body cavities or limb are heated using external applicators and micro-waves or radiofrequency energies. It is further categorized as follows[158]:

1. Deep tissue approaches: This is used for treatment of cancers located deep inside the body, such as bladder or cervical cancers. It uses external heat applicators that are placed inside the body cavity or around the organs, located nearest to the tumor site and heat is applied using micro-waves or radio-waves energies.

2. Regional perfusion techniques: It is used for treatment of cancers located near limbs, such as melanoma or liver or lung cancer. The patient's blood is removed, heated to hyperthermic temperatures and pumped (perfused) back into the limb or organs for the therapy[159].

3. Hyperthermic intra-peritoneal chemotherapy (HIPEC) and Hyperthermic intra-vesicular chemotherapy (HIVEC) : HIPEC is a type of regional perfusion and is used for tumors located in the peritoneal cavity, such as primary peritoneal mesothelia and gastric cancers. In this method, the chemotherapeutic drug (usually Cisplatin and Mitomycin C) is heated to hyperthermic temperature and then pumped back into the peritoneal cavity, so that the tumors receive the heated drug[160]. Heat ensures higher uptake of the chemotherapeutic drug inside the tumor cells, probably due to vasodilation caused by hyperthermia. The hyperthermic

temperature also sensitizes the tumor to the concurrent chemo-hyperthermia treatment. HIPEC is usually performed after a cyto-reductive surgery (CRS), which ensures the removal of macroscopic tumor sites[161]. Similarly, HIVEC has been used to treat bladder cancer and uses heated chemotherapeutic drugs similar to HIPEC.

4. **High-Intensity Focused Ultra-sound (HIFU):** This is a non-invasive technique that is used to heat the tumors by using low frequency (0.2 to 2 MHz) as compared to diagnostic medical ultra-sound (2 to 15 MHz) but high energy focused ultra-sound waves that can heat the tumors to very high temperatures of ~ 60 °C. At high enough acoustic intensities, cavitation can lead to formation of micro-bubbles, which can eventually implode (i.e., collapse) leading to very high temperature. HIFU is usually combined with magnetic resonance imaging (MRI) for imaging and thermometry purposes. MR-thermometry utilizes the shift in the proton resonance frequencies, which vary linearly and sensitively with change in temperature in the hyperthermia temperature range. Thus, HIFU is also called as MRI guided HIFU (MRgHIFU)[162].

5. **Modulated Electro-hyperthermia therapy (mEHT):** Modulated Electro-hyperthermia therapy utilizes capacitively (impedance) coupled 13.56 MHz amplitude-modulated radio-frequency energy. It can cause selective heating of tumor region due to the high ionic conductivity of cancer cells (high glycolysis due to Warburg effect) as compared to normal cells. mEHT is also called as oncothermia and has been used in clinics for more than 20 years for selective heating of the tumors to ~ 42 °C. Oncothermia is known to damage the tumor cell membranes, affecting the lipid rafts rich is several receptors required for sustaining tumor cell proliferation. Due to the elevated glycolysis, ionic concentration and permittivity of the tumor cells (compared to surrounding normal tissue), oncothermia is able to induce apoptotic cell death in the tumor tissue[163].

C. Whole body hyperthermia therapy (WBH): This is used for treatment of metastatic cancers and makes use of hot water blankets, inductive loops or thermal chambers (similar to large incubators) to raise the temperatures of the whole body to 41°C. WBH can be of two types based on the method of heating:

1. Radiant WBH: In this method, heat is superficially applied to the whole body using externally applied power absorption methods which utilizes non-ionizing electro-magnetic radiation for delivery of heat to the body. For example, Seimans's Hyperthermia Cabinet (Selmedic, Inc., Greensburg, PA), houses a 450 MHz microwave antenna capable of delivering 200 watts of power. Additionally, the patient can be heated from below using radiofrequency driven induction coils. In another examples, Heckel designed an IR chamber (1975) comprised of a series of IR lamps placed within a close system. This system was capable of emanating photons that can penetrate the skin to a depth of 1 to 2 mm and subsequently transfer heat to the patient's body. Similarly, Homback et al, reported the use of 433 MHz diathermy antennae arranged in a series of concentric rings, capable of delivering about 1800 watts of power to raise the core temperature of the patient to 41.2°C[164].

2. Extra-corporeal WBH: This system was developed by Parks et al. and heats blood which is passed through a high-flow arterial-venous shunt (capable of handling up to 1.2 to 2.1 liters of blood per minute) between femoral artery and vein. Blood is passed from the femoral artery through a pump and into a heat exchanger, which is capable of heating blood to temperature up to 42°C. This system enables rapid temperature control of externally heated blood. The anticipated body temperature is adjusted and measured by altering the current volume of the warmed injected blood[164].

1.4.7.4 Applicators for hyperthermia therapy: For application of heat, capacitive or inductive

- microwaves (100 MHz to 3000 MHz), radiowaves (500 KHz to 150 MHz) or ultra-sound (300 kHz to 2 MHz mechanical sound waves) and hot water perfusion, resisting wire beds, infrared radiators or ferro-magnetic seeds or nanoparticles are used. For deep seated tumors, radiofrequency at 8 – 12 MHz is useful, whereas microwaves of 434 to 915 MHz are used for superficial tumors[154]. All these techniques generate heat by three basic physical principles: (1) Thermal conduction of heat from higher to lower temperatures, using hot water or infrared chambers; (2) Resistive or dielectric losses from an applied electromagnetic field, such as radiofrequency waves and microwaves; (3) Mechanical losses due to molecular collisions from an ultrasound wave.

Limitations or side-effects of hyperthermia therapy

Conventional hyperthermia therapy suffers from several limitations, which has resulted in limited preference of hyperthermia as a therapeutic modality of cancer. Few side effects, which may not be common to all types of hyperthermia treatments can be listed as follows[3,150]:

1. In-homogenous heating of the tumor tissue as the heat is applied either from the surface or using probes inserted at specific locations inside the tumor.
2. Skin burns or blisters and pain due to heating of the skin. This happens as the skin surface is exposed to > 42 °C, for the tumor core to reach hyperthermia temperature of 42- 43°C.
3. Since, a gradient of temperature is usually formed at the tumor site due to the physical heating methods used, development of thermotolerance due to expression of heat shock proteins (particularly HSP70 and HSP90) has been reported in several studies[165,166].
4. The efficiency of whole-body hyperthermia is still debated in case of metastatic cancers.

5. Similar to other conventional cancer treatment modalities, hyperthermia therapy is also not a targeted cancer therapy and hence causes the associated side effects due to heating of normal tissues**.**

1.4.8 Magnetic Hyperthermia Therapy:

As discussed in **Section 1.4.7**, hyperthermia therapy has tremendous potential for cancer treatment but the major limitation of conventional hyperthermia therapy is the non-homogenous and non- targeted heating of the tumor cells. MHT, which is applied with the help of super-paramagnetic iron oxide nanoparticles (SPIONs), is an emerging cancer therapy modality with a potential to significantly overcome the limitations of conventional hyperthermia. It also facilitates for targeted and homogenous heating of the tumor tissue for better tumor control[167–169]. Other than SPIONs, two more modalities exist by which nanoparticle mediated hyperthermia therapy can be delivered to the cancer cells. One is optical heating using lasers[170,171] and another is ultra-sound heating due to collapse of small bubbles formed during cavitation[162,172]. Although these methods can generate significant heating at the tumor site, they have their own limitations that makes them less preferable as compared to SPIONs based MHT. Optical heating is severely affected by the significant attenuation of the laser light by the tissue. Whereas in case of ultra-sound heating, development of in-homogenous hotspots and variation in the speed of sound in most tissues and limited aperture of the applicator are a few limitations of this modality[173]. Thus, among the nanoparticle mediated modalities, SPIONs based MHT has better applicability and likelihood of success. As mentioned earlier, MHT utilizes specially designed super-paramagnetic nanoparticles (mostly of iron oxide) also called as ferro-fluids, which can be functionalized with tumor targeting agents (such as antibodies, tumor receptor specific ligands or peptides). These

targeted SPIONs can accumulate at the tumor site and induce localized heating of the tumor cells in presence of an externally applied alternating current (*AC*) magnetic field. Thus, the heating of the tumor tissue can be controlled externally by an *AC* magnetic field, which can be turned 'ON' several times even after a single injection of SPIONs for multiple heating sessions of the tumor **(Scheme 1.3)**.

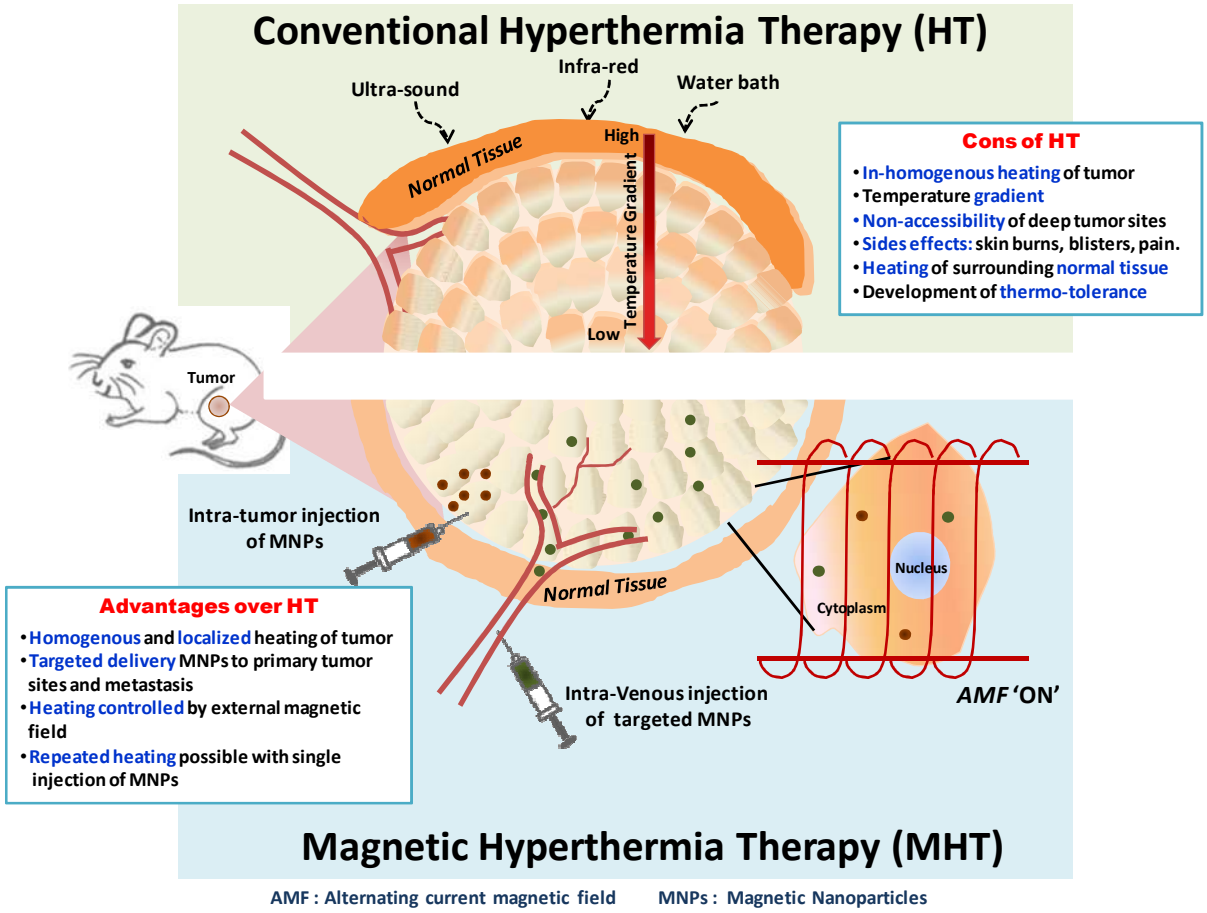

Scheme 1.3 *Scheme for comparison between conventional and magnetic hyperthermia therapy (Source: Shetake et, al, JRCR, 2020).*

1.4.8.1 Clinical status of MHT: MHT may be used as a sole anti-cancer technique or as an

adjuvant therapy in combination with radiation and cytotoxic chemotherapy. However, till now most of the anti-cancer applications of MHT have been evaluated only in a pre-clinical scenario with a very few reports of clinical application[174]. The first breakthrough step towards the clinical application of MHT was the development of a clinical magnetic fluid-based hyperthermia applicator (MFH 300F) by Gneveckow et al (MagForce Nanotechnologies, Germany) in 2004[175]. The first patient to be treated with a clinical MHT was a 67-year old male patient with locally recurrent prostate carcinoma. In 2005, Johannsen et al. treated this patient using the MFH 300 F and amino-silane coated magnetic nanoparticles and was well tolerated[176]. Another report is by Matsubara et al., who treated six patients with bone metastasis. MHT was applied using calcium phosphate cement containing magnetic nanoparticles and was combined with photodynamic therapy using acridine orange. The combination therapy was observed to preserve the limb function without local recurrences[177].

1.4.8.2 Challenges of MHT in clinical scenario

1. **Efficient tumor targeting of magnetic nanoparticles:** The major limitation of MHT under clinical scenario is the design and development of targeted magnetic nanoparticles, which can selectively accumulate at the tumor site, at sufficient quantities, for effective heating of the tumors upto hyperthermic temperatures. Albeit the nanoparticles can be injected intra-tumorally in case of superficial tumors, the distribution of nanoparticles inside the tumor is known to be quite in-homogenous[178]. This in-turn results in in-homogenous and in-sufficient heating of the tumor.

2. Design and development of clinical magnetic hyperthermia applicator: Till now, only one applicator for clinical application of MHT is known i.e. MFH 300 F developed by MagForce Nanotechnologies, Berlin, Germany. This instrument operates at 100 kHz radio-frequency with a magnetic field strength upto 18 kA/m[175]. These warrants the need of significantly higher quantities of MNPs at tumor site for efficient heating to hyperthermic temperature. However, in pre-clinical scenario, magnetic field intensities of upto 23 kA/m and radio-frequencies of 265 kHz have been safely used in mice for application of MHT, which can facilitate effective heating to 42-43 °C even in presence of moderate concentrations of MNPs[179–181].

1.4.8.3 Theory of heating by SPIONs

As mentioned above, a pre-requisite for MHT is the use of super-paramagnetic iron oxide nanoparticles. Now, what is meant by '*super-paramagnetism*' or '*super-paramagnetic nanoparticles'* ?

Super-paramagnetism is observed in nano-sized ferro and ferri-magnets. Super-paramagnetic nanoparticles are single domain magnetic nanoparticles and thus behave like tiny magnets. In case of bulk ferro or ferri-magnetic materials (which are composed of multiple magnetic domains), when they are reduced to nano-sizes (10 to 100 nm) they reach their single domain size. In these nano-size particles, the magnetization can flip direction under temperature influence. Thus, in the absence of any externally applied magnetic field (when the time for measurement of magnetization is sufficiently longer than the Néels relaxation time), these nanoparticles are all oriented in random directions and their net magnetic moment is 'zero'. Therefore, the nano-particles are said to be in a super-paramagnetic state, but unlike

paramagnetic materials, their magnetic susceptibility is very high[179,182–184]. However, when an external alternating current (*AC*) magnetic field is applied, super-paramagnetic nanoparticles generate heat mainly by two mechanisms: **(Scheme 1.4)**:

1. **Brownian relaxation:** It is the random motion of nanoparticles in the suspension. Heat is generated due to the frictional forces during the collision of these nanoparticles with each other and with the molecules of the suspension **(Scheme1.4)**.

2. **Néels relaxation:** This involves the rapid flipping of the magnetic domains (in case of the super-paramagnetic nanoparticles, the whole nanoparticles behaves like a single magnetic domain) in response to the external magnetic field. The frictional forces due to this rapid flipping motion, generates the heat **(Scheme1.4)**.

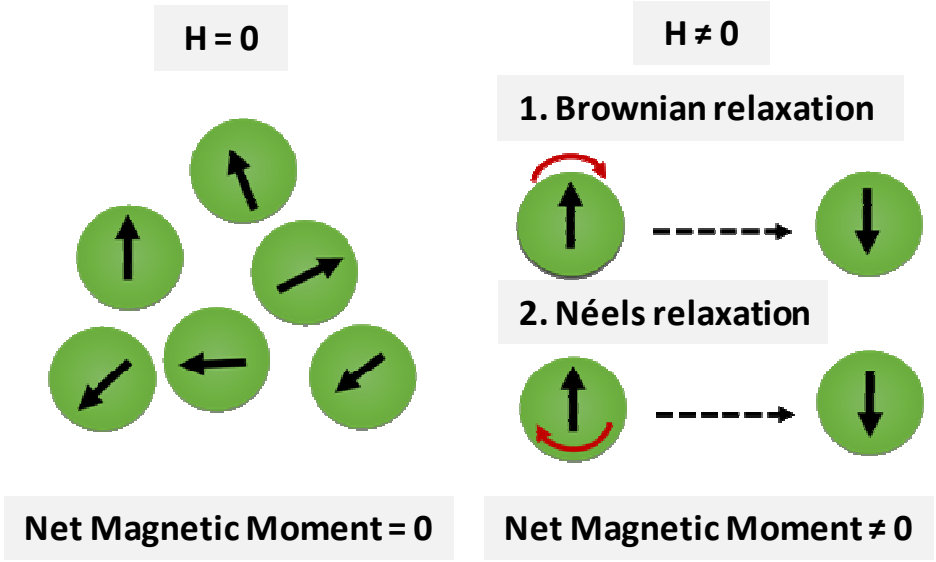

Scheme 1.4 *Scheme for heat generation by super-paramagnetic nanoparticles under alternating current (AC) magnetic field. H: Magnetic field intensity.*

The heat generation or power dissipation by super-paramagnetic nanoparticles under *AC* magnetic fields can be explained by the linear response theory (LRT) developed by Rosenzweig, in 2002. According to the LRT, power dissipation (*P*) is explained as[182] :

$$P = \mu_0 \pi \chi'' f H^2 \quad (1)$$

Where, μ_0 is the permeability of free space, Π is constant, f and H are the frequency and amplitude of *AC* magnetic field, respectively and χ'' is the out-of-phase component of *AC* magnetic field susceptibility of the colloidal magnetic fluid.

χ'' is further expressed as:

$$\chi'' = \frac{\omega\tau}{1 + (\omega\tau)^2} \chi_0 \quad (2)$$

Where, $\omega = 2\pi f$ *and* τ is the total relaxation (Brownian and Néels relaxation) and χ_0 is the actual susceptibility. The effective relaxation time is expressed as:

$$\frac{1}{\tau} = \frac{1}{\tau_N} + \frac{1}{\tau_B} \quad (3)$$

Wherein , τ_N is the Néels relaxation time due to internal rotation of the magnetic moment and is expressed as :

$$\tau_N = \left(\frac{\sqrt{\pi}}{2}\right) \tau_0 \frac{\exp\left(\frac{K_V}{K_B T}\right)}{\sqrt{\frac{K_V}{K_B T}}} \quad (4)$$

Wherein, K is the uniaxial magnetic anisotropy, H is the applied field, V is nanoparticle volume, K_B is Boltzmann's constant and T is the temperature.

The Brownian relaxation time, , τ_B is expressed as:

$$\tau_B = \frac{3\eta V_H}{K_B T} \quad (5)$$

Wherein, η is the dynamic viscosity and V_H is the hydrodynamic volume of the nanoparticles.

Thus, it can be stated that (from above equations) that the brownian relaxation time is directly proportional to nano-particle volume and viscosity of the medium. Thus, larger the particle or higher the viscosity of suspension medium, slower will the brownian motion and lesser will be the heat generated by the SPIONs under *AC* magnetic field conditions.

There are other mechanisms as well by which heat is generated by magnetic particles under *AC* magnetic fields, namely:

1. **Eddy currents:** Heat generation occurs due to the interaction of a conducting material with oscillating magnetic field. However, superparamagnetic nanoparticles, being semi-conducting in nature, they have a very high resistivity. Hence, under *AC* magnetic field, heat generation by superparamagnetic nanoparticles due to eddy currents is negligible[182].

2. **Hysteresis loss:** Heat generation by super-paramagnetic nanoparticles may occur by hysteresis loss at very high frequencies (> 100 kHz), when the magnetization response of the nanoparticles lags behind the applied field. The heat generation due to hysteresis is characterized by the blocking frequency, f_b, and when applied frequency is above the f_b, hysteresis is observed and at $f < f_b$, the nanoparticles are super-paramagnetic[182]. Hysteresis loss is *AC* magnetic field is expressed as:

$$\text{Area} = f \int M dH \quad (6)$$

Where, *f* and H are the frequency and amplitude of *AC* magnetic field and M is the magnetization of the SPIONs.

The heating efficiency of the super-paramagnetic nanoparticles in turn is represented by the specific absorption rate (SAR), which is expressed as:

$$SAR = C \frac{\Delta T}{\Delta t} \frac{1}{m_{magn}} \quad (7)$$

Wherein, C is the specific heat capacity of the sample (i.e. nanoparticles + diluent, in case of use of nanoparticles for biological application, the diluent is water). The specific heat capacity of nanoparticle is negligible, hence, C = 4.18 $Jg^{-1}K^{-1}$ (i.e. the specific heat capacity of water). $\Delta T/\Delta t$ is the initial slope of the time dependent-temperature curve of heat generation by nanoparticles under *AC* magnetic field. m_{magn} is the total amount of magnetic nanoparticle [182].

1.5 Nano-carriers or Nano-vehicles for targeted delivery of anti-cancer agents

Nanotechnology, is an expanding field and has revolutionized many areas of research, development and clinical applications including drug and gene delivery, gene therapy and diagnostics. In Greek, the word '*nano*' literally means '*dwarf*' and a nanoparticle typically has a size ranging from 1 to 100 nm[185,186]. The advent of nanotechnology and understanding of the unique characteristics of materials at the '*nano*-dimension' began with the famous lecture by Dr. Richard Feynman on December 29, 1959, where he stated[187]:

" there is plenty of room at the bottom"

Nanotechnology involves manipulation of materials at atomic and molecular scales to create

materials with remarkably different and new properties. This process of down-sizing the materials from a macro size to nano-size results in significant increase in the surface area to volume ratio, thus resulting in more number of atoms per unit surface in nanoparticles as compared to their bulk counterparts. Additionally, nanoparticles possess high surface energy, spatial confinement and reduced imperfections. Together, these feature imparts nanoparticles with dramatically unexpected and novel optical, physical and chemical properties, as they are small enough to confine their electrons and produce quantum effects[185,186]. In healthcare and medicine sector, there has been a tremendous increase in the use of nanoparticles for varied applications thereby, leading to the advent of the field of *'Nano-medicine'*[188]. Nano-medicine is defined by the European Science Foundation as *''the science and technology of diagnosing, treating and preventing disease and traumatic injury, of relieving pain, and of preserving and improving human health, using molecular tools and molecular knowledge of the human body'*[189]. The field of nano-medicine encompasses several application of nanoparticles for betterment of human health and well-being, such as (i) nano-delivery systems for drugs with better pharmacokinetic properties and bio-distribution, (ii) nano-delivery systems for gene therapy, (iii) nano-heating of tumors using SPIONs based MHT, (iv) nano-particles for tissue engineering applications (e.g. ceramic, polymeric and metal nanoparticles for bone injuries) and (v) as nano-theranostic agents for simultaneous detection and treatment of diseased conditions, such as in cancer[188]. Since the focus of my thesis is development of a nano-delivery system for cancer theranostic applications, I would focus mainly on the nanoparticles that have been used in cancer research (especially for targeted delivery of anti-cancer drugs).

Many nano-delivery systems such as nano-capsules, nano-spheres, polymeric nanoparticles, micro-bubbles, metallic nanoparticles (SPIONs, gold and silver nanoparticles),

quantum dots, etc. have been studied for targeted delivery of anti-cancer drugs. However, the lipid based delivery systems (niosomes, micelles and liposomes) are more explored due to their several advantages over the other delivery systems[190–192]. In the present chapter, I would briefly introduce the several nano-delivery systems which are being studied for cancer diagnostics and therapeutic applications.

1.5.1 Nano-delivery systems for targeted delivery of anti-cancer agents: Before going through the several nano-delivery systems available for drug delivery, I would like to address the basic question: *Why there is a requirement of a nano-delivery system in first place?* The ultimate purpose of a nano-delivery system is to:

(i) Enhance the efficacy of the entrapped drug and to minimize its inherent toxicity. This is achievable due to the altered optical, physical and chemical properties of nanoparticles, conducive for drug delivery. As already discussed, nanoparticles have a higher surface area to volume ratio, which significantly increases the number of surface atoms in a nanoparticle. This enhanced surface area to volume ratio can be utilized for higher ligand/drug binding to nanoparticle surface. Owing to this increase in the drug binding, the dosage and inherent toxicity of the drug can be significantly minimized[193,194].

(ii) A greater efficiency can be achieved by reducing the dosage or dosage frequency, as the mass of the nanoparticle per mass of drug can be lowered due to higher drug loading/encapsulation.

(iii) The efficacy of the drug can be further enhanced by co-functionalization of nanoparticles with ligands that enhance the drug binding, suppress immune response, enhance targeting and provide controlled release properties.

(iv) Decreasing the drug resistance by over-coming the rapid efflux of drugs due to over-expression of certain efflux pumps (e.g. P-glycoproteins and ABC transporters) in cancer cells. Nano-delivery systems can be designed to overcome the multi-drug resistance (MDR) phenomena, thereby increasing the therapeutic index of the chemo-therapy[195,196].

(v) Better targeting of the drug either passively due to the enhanced permeability and retention (EPR) effect or actively by receptor mediated endocytosis due to interaction between the cancer cell surface receptor/its ligand coated on the surface of the nano- carrier[197].

(vi) Improved pharmacokinetic properties (due to increased oral bio-availability), enhanced rate of drug dissolution and solubility[198].

(vii) Better stability of the drug when encapsulated in a nanocarrier as compared to free drug.

(viii) Increased patient compliance.

The nanoparticles in turn can be classified in different types based on their size, morphology, physical and chemical properties. Broadly, the nanoparticles can be classified into four main categories **(Scheme 1.5)**: (A) Organic, (B) In-organic, (C) carbon-based nanoparticles and (D) Nano-crystals. These in turn can be further classified as follows[199,200]:

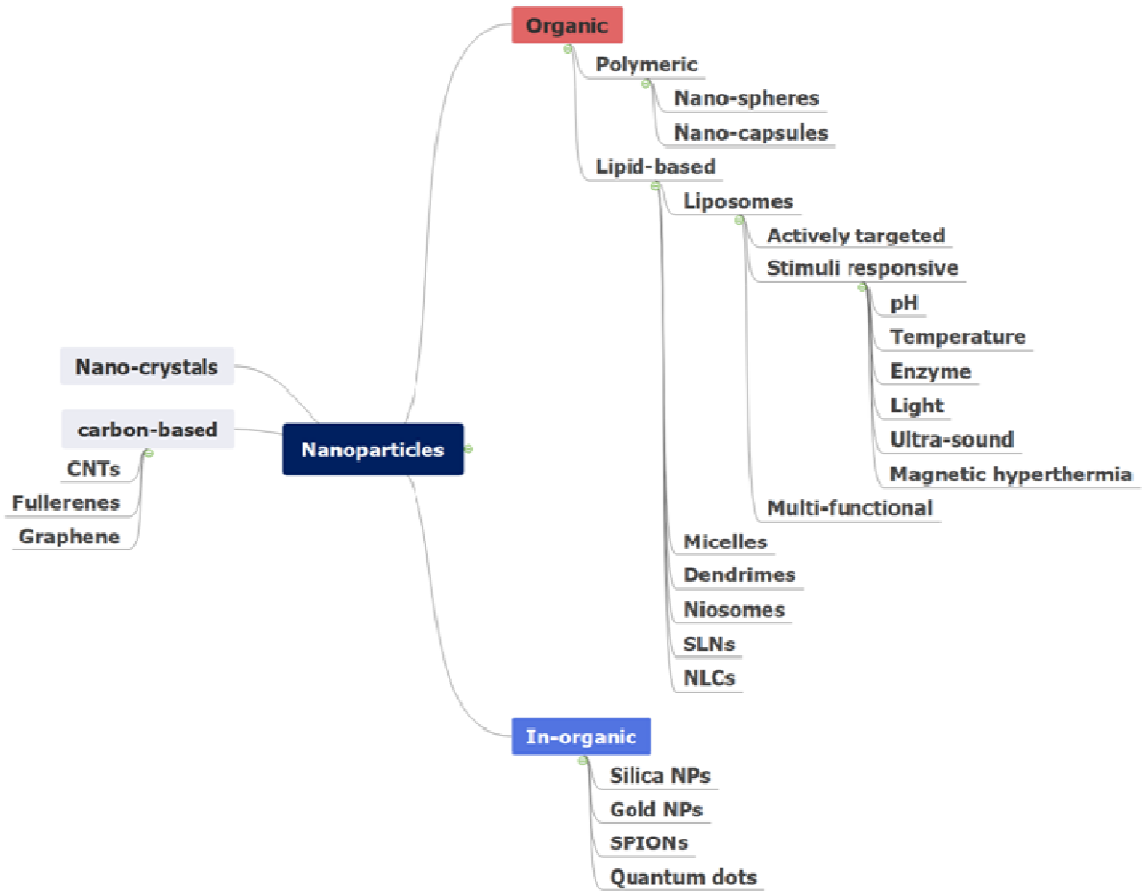

Scheme 1.5 *Scheme for classification of nanoparticles.*

A. Organic nanoparticles: Organic nanoparticles are solid particles templated upon natural or synthetic organic molecules including lipids or polymeric materials. They are further categorized based on their composition as:

(i) Polymeric nanoparticles: Polymeric nanoparticles are solid colloidal particles falling in the size range of 10 to 1000 nm and can be composed of either natural (such as chitosan, gelatin, sodium alginate and albumin) or synthetic [polylactides (PLA), polyglycosides (PGA), polyglutamic acid, etc.)] and bio-degradable (albumin, chitosan, gelatin, PLA, PGA, etc.) or non-

biodegradable [polymethylmethacrylates, polyamidoamines (PAMAM), etc.], polymers. Based on method of synthesis, polymeric nanoparticles are further classified as nanospheres and nano-capsules, wherein the drug can be either entrapped or encapsulated inside the polymer/within the carrier, physically adsorbed on the surface of the carrier or chemically linked to the surface[199]. A few examples of polymeric nanoparticles in clinical use are listed in **Table 1.1.**

(a) Nano-spheres: These are homogenous structures, typically consisting of the drug embedded in the polymer matrix of solid polymers.

(b) Nano-capsules: These are core-shell structures, consisting of a shell with an inner space, which is loaded with the drug of interest.

(ii) Lipid-based nanoparticles: Lipid based nanoparticles have been extensively exploited for *in vitro* and *in vivo* cancer therapy and have shown promising results in clinical trials. Their major advantages include (1) high temporal and thermal stability, (2) ease of preparation, (3) capacity to transport both hydrophilic and hydrophobic drugs, (4) display negligible toxicity and are highly bio-compatible, (5) facilitates increased time of drug action by favoring prolonged release or controlled release of the encapsulated drug, (6) high loading capacity, (7) low production cost and (8) capability of large Scale industrial production due to use of natural sources for synthesis. Some examples of lipid-based nanoparticles with promising applications in cancer diagnosis or treatment are discussed[201,202].

(A) Liposomes: Liposomes are spherical vesicles made of amphipathic phospholipid bilayers. They can be characterized based on their number of bilayers as (1) Uni-lamellar vesicles (ULVs) or (2) Multi-lamellar vesicles (MLVs). The ULVs or MLVs in turn can be of small (< 25 nm) or large size (25 to 250 nm). The phospholipids used for synthesis of liposomes

can be either from natural sources such as egg yolk, soya bean, canola seed or can be synthetically generated. A phospholipid typically consists of a glycerol back-bone that is esterified in positions 1 and 2, with fatty acids and in position 3 with phosphate group. In most of the membrane phospholipids, the phosphate group is further esterified with an additional alcohol, such as phosphatidyl choline (PC), phosphatidyl ethanolamine (PE) or phosphatidyl glycerol (PG), which in turn imparts neutral (PC and PE) or negative charge (PG) at pH 7.0[26,203]. Inspite of the similarity of the liposomal membranes to bio-membranes, they are still foreign to the body and tend to elicit an immune response, resulting in their clearance from blood following binding of plasma proteins and activation of the mono-nuclear phagocytic system (MPS) or reticulo-endothelial system (RES) of the body. To reduce their elimination by the body, the liposome membrane surface is often coated with amphipathic polyethylene glycol (PEG) or chitin derivatives or micro-encapsulated with gangliosides, resulting is synthesis of stealth liposomes[204]. The stealth property of the liposomes also enhances the blood circulation time of the drug, which otherwise due to its small size (free drug), would have been rapidly eliminated by the body. The passive accumulation of liposomal drug also enables decreasing the drug dosage and its inherent toxicity, as more normal cells are spared from contact with the drug. A few doxorubicin (Dox) loaded stealth liposomal formulations used in clinic for cancer therapy of solid tumors are Doxil® (Janssen Biotech, Inc., Horsham, USA) or Caelyx® (Schering-Plough Corporation, Kenilworth, USA)[205]. A few more clinically used liposomal formulations, which have shown better therapeutic efficacy than the drug in the free form are listed in **Table 1.1**. The liposomal membrane can be modified by different methods to impart unique properties or characteristics for (1) active targeting of tumor cells or tumor neo-vasculature, (2) stimuli-responsive release of the liposomal contents and (3) multi-functional liposomes to combine two

or more useful features for improved therapy. These sub-types are discussed briefly as follows[206]:

(1) Active targeting of tumor cells or neo-vasculature: The PEGylated or stealth liposomes as discussed above are known to accumulate at the tumor site, passively, due to the leaky vasculature and poor lymphatic drainage inside the solid tumors. The underlying mechanism facilitating drug accumulation due to the aberrant features of the tumor patho-physiology is called as enhanced permeability and retention (EPR) effect. A further enhancement of the accumulation of drug at the tumor site can be achieved by coating the liposomes with ligands for receptors that are known to be over-expressed on the surfaces of the tumor cells or tumor vasculature, and are referred to as actively targeted liposomes. The interaction of the targeting moiety or ligand with its receptor on the tumor cells or tumor endothelial cells, triggers rapid cellular uptake of the liposomal nano-formulation by receptor-mediated endocytosis[198]. The targeting moieties could be monoclonal antibodies, antibody fragments, peptides, proteins, nucleic acids, carbohydrates or small molecules. Few examples include liposomes (encapsulated with Dox, imatinib, docetaxel, or daunorubicin) labeled with the folic acid that actively target the folate receptors over-expressed on various malignant cells[207,208]. Similarly, transferrin receptor targeting by labeling the liposomes with transferrin protein has been evaluated for delivery of chemotherapeutic agents (vincristine, tetrandrine or temozolomide) across the blood-brain-barrier (BBB), for tumor therapy of gliomas[209,210]. Active targeting of the Epidermal Growth Factor Receptor (EGFR) over-expressing malignant cells has been achieved by the anti-EGFR-immunoliposomes. similarly, active delivery of Dox or oxaliplatin to cultured cells or animal tumor model of colon cancer could be achieved by modifying the already approved cetuximab or cetuximab fragments[206]. Till now, actively targeted liposomal nano-formulations have shown

better efficacy in *in vitro* and *in vivo* models or are currently in clinical trials; but no formulation has been approved for clinical application yet[211,212].

In addition to the tumor cells, tumor endothelial cells are also known to over-express receptors that are crucial for the angiogenesis process, such as the vascular endothelial growth factor (VEGF) receptor or the $\alpha_v\beta_3$ integrin receptors. These receptors have been exploited for active targeting of liposomes labeled with an anti-VEGF[165] monoclonal antibody for delivery of paclitaxel to human gastric cancer bearing nude mice[213] and arginine-glycine-aspartic acid (RGD) peptide labeled temperature sensitive liposomes (TSL) for targeted delivery of Dox to human Umbilical Vein Endothelial Cells (HUVECs) and B16Bl6/B16F10 melanoma xenograft tumor model in mice[214].

In addition to the long circulation and targeted delivery of the encapsulated drug, the liposomes can also be modified for sustained or prolong release of the drug over a period of few days. This is called as DepoFoam technology introduced by Pacira Pharmaceuticals, Inc., Parsippany, NJ, USA for extended release of the entrapped drugs[205].

(2) Stimuli responsive release of liposomal contents:

Triggered release of the entrapped contents from the liposomal carrier is desirable to ensure selective accumulation of the drug inside the tumor cells. This characteristic will also help in minimizing the toxicity of the drug and its dosage by facilitating prolong or sustained release of the drug at the target site. Stimuli responsive liposomes undergo morphological changes, such as aggregation, disruption or permeability changes in response to the tumor micro-environment. Utilizing the features of the tumor micro-environment, several strategies have been investigated

to stimulate the liposomes to release their contents in a controlled manner. These could be either internal stimuli (such as low pH, changes in redox potential, high temperature, higher activity of certain enzymes) inside the tumor cells/or its micro-environment or external stimuli (such as external application of magnetic fields, temperature or heat and ultrasound or light)[206,215].

(a) pH sensitive release of liposomal contents: These group of liposomal nano-formulations, utilizes pH labile linkers that are degraded in the acidic pH of endosomes or acidotic tumor mass resulting in a controlled or burst release of the entrapped drug at the target site. This strategy also benefits the unwanted degradation of the PEGylated liposomes that are not able to escape the endosomes, resulting in the degradation of the drugs inside the endosomes itself. An example is a bleomycin loaded liposomes composed of 2-carboxycyclohexane-1-carboxylated polyglycidol-having distearoyl phosphatidylethanolamine (CHexPG-PE) for pH sensitization. The CHexPG-PE-introduced liposomes show remarkable stability at physiological pH (7.3 to 7.5) but at pH < 7.2 rapid release of the drug was observed within 5 min. CHexPG-PE-introduced liposomes showed 2.5 times higher uptake in Colo-26 tumor bearing mice as compared to liposomes without the pH responsive group[216].

(b) Temperature triggered drug release from the liposomes: The phospholipids that are used in the synthesis of the liposomes impart fluidity or rigidity to the liposomal membrane and control their permeability due to the property of melting-phase transition temperature (Tm). At temperatures above their Tm, the liposome bilayers are highly leaky facilitating the release of the entrapped drug. Whereas at temperatures < Tm, the bilayers are pretty rigid and prevent any drug leakage. Using this property, temperature sensitive liposomes (TSLs) have been designed and used in several pre-clinical and clinical settings in combination with radio-frequency ablation or ultrasound and microwave heating of the tumor tissue[217,218].One such system is ThermoDox®

designed by Celsion Corporation (New Jersey, USA) and has been evaluated for its efficacy in phase III clinical trials for hepatocellular carcinoma[217].

(c) Enzyme responsive liposomes: Tumor cells have been known to over-express certain enzymes such as phospholipase A2 (PLA2), matrix metalloproteinases, alkaline phosphatase or transglutaminase etc. An example is a liposomal system designed by Tagami et al., which is composed of phospholipid (DPPC) and PEGylated block-copolymer (Poloxamer 188) and can rapidly release its encapsulated Dox in the presence of high levels of PLA2 in A549 lung cancer cells[219].

(d) Light-triggered drug release from the liposomes: External light source with appropriate adjustment of the amplitude, frequency, pulse duration and cycle has been investigated for controlled release of the drug from the light responsive liposomes, once they are accumulated at the tumor site. Due to its deeper penetration ability, near infrared (NIR) light has been investigated for this application. Dandon Luo and co-workers have demonstrated a NIR sensitive liposomal drug delivery system composed of 0.3 mole percent of porphyrin phospholipids (PoP) in a human pancreatic xenograft mice model. The tumor growth was found to be significantly delayed after following intravenous administration of 6 mg/kg doxorubicin, loaded in liposomes containing small amounts of DOPC and PoP[220].

(e) Ultra-sound mediated drug release from the liposomes: HIFU, as discussed in the earlier **Section 1.4.7.3.B.4** is known to induce significantly higher rise in temperature in an extremely focused area of the tumor. Thus, HIFU when combined with temperature sensitive liposomes can easily cause the phospholipids to reach their Tm, resulting in a significantly higher drug release at the heated tumor regions for enhanced therapeutic gain. Sergio Dromi and co-workers demonstrated the release of Dox from low temperature sensitive liposomes (LTSLs)

triggered by pulsed-HIFU, heating the tumors to 42 – 45 ^{o}C[221]. The excellent spatial resolution provided by MRI was coupled with HIFU and drug release was monitored in a murine mammary adenocarcinoma (JC) cell line and its tumor model. This study demonstrated rapid drug release at the tumor site following pulsed-HIFU and significant reduction in the tumor volumes using LTSLs[221].

(f) Magnetic hyperthermia triggered release of the liposomal contents: SPIONs can be co-encapsulated inside liposomes along with other anti-cancer drugs for controlled drug release applications in response to magnetic hyperthermia therapy. The liposome composition can be designed in such a way that the entrapped drug can be released at the target site in response to the hyperthermia temperatures attained by exposure of SPIONs to *AC* magnetic field. However, most of the magneto-liposomes designs are still at the pre-clinical stage and need further improvements for their translation to clinics[222,223].

No	Clinical product	Approval year	Company	Active Agent	Composition	Route of administration	Indications of use
FDA approved Liposomes for cancer treatment							
1.	Daunoxome®	1996	NeXstar Pharmaceuticals, Inc.	Daunorubicin-citrate salt	DSPC:chol (2:1)	*i.v.*	Kaposis sarcoma[205]
2.	Marqibo®	2012	Talon Therapeutics	Vincristine	Sphingomylein: Chol (60:40)	*i.v.*	Acute Lymphoblastic leukemia[205]
3.	DepoCyt®	1999	Sky Pharma Inc.	Cytosine arabinoside	DOPC: DPPG:chol:triolein	Spinally or intra-thecally	Neoplastic or lymphomatous meningitis[205]
4.	Doxil® or Caelyx® or Evacet® or Lipo-dox®	1995	Sequus Pharmaceuticals	Doxorubicin HCl	HSPC:Chol:mPEG-DSPE (56:38:5)	*i.v.*	Ovarian cancer, AIDS-related Kaposis Sarcoma, Multiple myeloma[205]
5.	Myocet®	2001	Cephalon	Doxorubicn hydrochloride	Chol:EPC (45: 55)	*i.v.*	Metastatic breast cancer[205]

6.	Mepacet®	2004	Takeda Pharmaceutical company	Mifamurtide	DOPS:POPC (3:7)	*i.v.*	High-grade, resectable, non- metastatic bone tumors[205]
7.	Onivyde™	2015	Merrimack Pharmaceuticals, Inc.	Irinotecan	DSPC:Chol:M-PEG-2000-DSPE (3:2:0.015)	*i.v.*	Metastatic adenocarcinoma of the pancreas[205]
8.	Vyxeos®	2017	Jazz Pharmaceutics	Daunorubici n and cytarabine	DSPC:DSPG:Chol (70:20:10)	*i.v.*	Acute Myeloid Leukemia in adults[224]
9.	Onpatro® (patisiran)	2018	Alnylam pharmaceuticals	SiRNA targeting the production of transthyretin (TTR) proteins	Chol:DLin-MC3-DMA:DSPC:PEG 2000 -C-DMG (6:2:13:3:3:1.6) per 2mg of SiRNA	*i.v.*	polyneuropathy caused by hereditary transthyretin- mediated amyloidosis (hATTR amyloidosis)[225]
FDA approved Liposomes for pain management							
1.	DepoDur™	2004	Sky Pharma Inc.	Morphine sulphate	DOPC: DPPG:chol:triolein	Epidural	Pain management[205]
2.	Exparel®	2011	Pacira Pharmaceuticals Inc.	Bupivacaine	DEPC: DPPG:chol:tricaprylin	*i.v.*	Pain management[205]
FDA approved Liposomes for fungal infections							
1.	Abelcet®	1995	Sigma-Tau Pharmaceuticals	Amphotericin B (AmB)	DMPC:DMPG (7:3)	*i.v.*	Invasive fungal infections refractory to conventional AmB deoxycholate therapy[205]
2.	Ambisome®	1997	Astellas Pharma	AmB	HSPC:Chol:DSPG: AmB (2:1:0.4:0.4)	*i.v.*	Fungal infections including leishmaniasis, aspergillosis, blastomycosis, coccidioidomycosis in febrile, neutropenic patients and a certain form of meningitis in people infected with HIV[205]
3.	Amphotec®	1996	Ben Venue Laboratories Inc.	AmB cholesteryl Sulphate	Sodium salt of cholesteryl sulphate:AmB (1:1)	*i.v.*	Serious fungal infections and leishmaniasis[205]

FDA approved Liposoms for viral infections							
1.	Epaxal®	1993	Crucell Berna Biotech	first virosome-adjuvanted vaccine for hepatitis A (HAV) strain RGSB	DOPE:DOPC (25:75)	*i.m.*	Vaccine for Hepatitis A virus (HAV) infection[205]
2.	Inflexal®	1997	Crucell Berna Biotech	Inactivated Hemagglutinin of influenza strains A and B	DOPE:DOPC (25:75)	*i.m.*	Influenza[205]
FDA approved Liposomes for photodynamic therapy (PDT)							
1.	Visudyne®	2000	Novartis AG	Verteporfin	DMPC: EPG1:8)	*i.v.*	subfoveal choroidal neovascularization due to age-related macular degeneration (AMD)[205]
FDA approved Liposomes for other applications							
1.	Diprivan® (lipid emulsion)	2013	Astra Zeneca Pharmaceuticals	Propofol	soybean oil (100 mg/mL), glycerol (22.5 mg/mL), egg lecithin (12 mg/mL); and disodium edetate (0.005%)	*i.v.*	anesthetic[226]
FDA approved micellar formulations							
1.	Estrasorb®	2003	Novavax Inc.	17β-estradiol hemihydrate	micellar	Topical application	Treatment of moderate vasomotor symptoms due to menopause[227]
FDA approved Metal based nanoparticles							
1.	Ferraheme® or Reinso®	2009	AMAG pharmaceuticals	Ferrumoxytol (Size: 17-30 nm)	SPIONS coated with polyglucose sorbitol carboxymethylether	*i.v.*	Treatment of anemia[228]
2.	INFeD®	2009	Actavis Pharma	Iron dextran	Iron-Dextran colloid	*i.m. or i.v.*	Iron deficiency in CKD (chronic kidney disease)[229]
3.	Dexferrum®	1957	American Regent	Iron dextran	SPIONs coated with Dextran	*i.v.*	Iron deficiency in CKD[229]
4.	Ferrlecit®	1999	Sanofi- Aventis	Sodium ferric gluconate	Sodium ferric gluconate complex in sucrose injection	*i.v.*	Iron deficiency in CKD[229]
5.	Venofer®	2000	Lutipold pharmaceutic als	Iron sucrose	Iron sucrose	*i.v.*	Iron deficiency in CKD[229]

6.	Nanotherm®	2010	Magforce Nanotechnologies	Iron oxide	Iron oxide SPIONs	Intra- tumoral	Glioblastoma[229]
7.	Ferridex® or Endorem	1996	AMAG pharmaceuticals	Ferrumoxide (Size: 80 - 150 nm)	Iron oxide SPIONs coated with dextran	Oral	Imaging agent[228]
8.	GastroMark® or Lumirem	2001	AMAG pharmaceutic als	Iron oxide	Iron oxide SPIONs coated with silicone	Oral	Imaging agent[229]
FDA approved nano-crystals for clinical applications							
1.	Emend®	2003	Merck and Co. Inc.	aprepitant	Nano-milled aprepitant with sucrose, microcrystalline cellulose, hydroxypropyl cellulose and sodium lauryl sulfate	Oral	Prevention of nausea and vomiting during cancer chemotherapy[9]
2.	Ostim®	2004	Osartis GmbH & Co. KG	Calcium hydroxyapati te (HA)	Nano-crystalline HA	Oral	Bone grafting material for orthopedic and dental surgical procedures[9]
3.	Rapamune®	2010	Wyeth Pharmaceutic als Inc.	Rapamycin (Sirolimus)	Amorphous nanoparticulate formulation of rapamycin	Oral	Treatment of lymphangioleiomyomatosis and prevention of rejection during Kidney transplant[9]
4.	Vitos®	2003	Orthovita Inc.	β-tricalcium phosphate	Calcium phosphate nano-crystals	Oral	Synthetic bone graft substitute[9]
5.	Ritalin®	1955	Novartis	Methylphenidate	Methylphenidate nanocrystals	Oral	Treatment of hyperactivity disorders in children such as ADHD[9]
6.	Tricor®	2004	Abbott laboratories	fenofibrate	Fenofibrate nano-crystals	Oral	Reduce triglyceride and cholesterol levels for prevention of atherosclerosis[9]
FDA approved polymeric nanoparticles							
1.	Cimzia® (certolizum ab pegol' (CZP)	2018	UCB, Brussels	PEGylated Fab fragment that binds to TNF-α	PEG (20 kDa)-humanized Fab' fragment against TNF-α	Sub-cutaneous injection	Treatment of rheumatoid arthritis, Crohn's disease, psoriatic arthritis and ankylosing spondylitis[9]

2.	Adagen® (Pegademase bovine)	1990	Enzon, Inc.	PEGylated adenosine deaminase (ADA)	PEG-5000-ADA	*i.v.*	Treatment of ADA deficiency[9]
3.	Neulasta® (Pegfilgrastim)	2002	Amgen Inc.	Filgrastim	Mono-methoxy PEG aldehyde chain (20 kDa) bound to N-terminalmethionine residue of filgrastim	*i.v.*	Treatment of febrile neutropenia[9]
4.	Oncaspar®	1994	Enzon Pharmaceuticals, Inc.	PEGylated L-asparaginase	mPEG(5 kDa)-L-asapraginase	*i.m.* or *i.v.*	Treatment of ALL and CML[9]
5.	Pegasys® (peginterferonalfa-2a)	2002	Genentech USA, Inc	PEGylated recombinant human alfa-2a interferon	Branched PEG(40 kDa)-recombinant human alfa-2a interferon	*i.v.*	Treatment of hepatitis C and HBeAg positive hepatitisB[9]
6.	Somavert® (pegvisomant (B2036-PEG)	2003	Pfizer pharmaceuticals	PEGylated analog of human growth hormone (hgh)	PEG(5 kDa)-hgh	Sub-cutaneous	Treatment of acromegaly[9]
7.	Macugen® (Pegatinib sodium)	2004	EyeTech Pharamaceuticals	PEGylated Anti-VEG aptamer	Two PEG moieties conjugated to the aptamer via amine groups of lysine residue	*i.v.*	Treatment of wet neo-vascular form of macular degeneration[9]
8.	Mircera® (epoetinβ or EPO0	2007	Vifor Pharma Inc.	PEGylated recombinant form erythropoietin	PEG(60 kDa) linked to butanoic acid and NHS modified structure linked to lysine moiety of EPO via amine groups	*i.v.* or sub-cutaneous	Treatment of anemia[9]
9.	SYLATRON™ (PEG-interferon alfa-2b)	2011	Schering Plough	PEGylated alpha interferon 2	Alpha interferon (INF) molecule conjugated to a mono PEG chain via succinimidyl carbonate (12 kDa)	Sub- cutaneous	Treatment of chronic hepatitis C[9]
10.	Krystexxa® (Pegloticase)	2010	Savient Pharmaceuticals	PEGylated recombinanat uricase	Four uniform chains, each of which are PEGylated	*i.v.*	Treatment of refractory chronic gout[9]
11.	Plegridy®	2014	Bio-gen Idec	PEGylated form of glycosylated recombinant interferon β	20 kDa methoxy-PEG-O-2-methylpropional dehyde(mPEG) conjugated to recombinant interferon β	Sub-cutaneous	Treatment of relapsing remitting multiple sclerosis (RRMS) in adult patients[9]

12.	Adynovate®	2015	Baxalta US Inc.	Recombinant PEGylated anti-hemophilic factor	PEG(20 kDa)-recombinant human coagulation factor VIII	*i.v.*	Treatment of hemophilia A[9]
DPPC (1,2-Dipalmitoyl-*sn*-glycero-3-phosphocholine), DSPE (1,2-Distearoyl-*sn*-glycero-3-phosphoethaolamine), DSPC (1,2-Distearoyl-*sn*-glycero-3-phosphocholine), mPEG (methoxy-polyethylene glycol), HSPC (hydrogenated soy phosphatidyl choline), Chol, DPPG (1,2-Dipalmitoyl-*sn*-glycero-3-phosphoglycerol), DOPC (1,2-Dioleoyl-*sn*-glycero-3-phosphocholine), EPC (Egg phosphatidyl choline), DOPS (1,2-Dioleoyl-*sn*-glycero-3-phosphoserine), POPC (1-palmitoyl-2-oleoyl-sn-glycero-3-phosphocholine), DMPC (1,2-Dimyristoyl-*sn*-glycero-3-phosphocholine), DMPG (1,2-Dimyristoyl-*sn*-glycero-3-phosphoglycerol), DSPG (1,2-Distearoyl-*sn*-glycero-3-phosphoglycerol), DEPC (1,2-Dierucoyl-sn-Glycero-3-Phosphatidylcholine), DOPE (1,2-Dioleoyl-*sn*-glycero-3-phosphoethanolamine), DLin-MC3-DMA (dilinoleylmethyl-4-dimethylaminobutyrate), *i.v.* (intravenous), *i.m.* (intra-muscular), ADHD (Attention Deficit Hyperactivity Disorder), CML (Chronic Myeloid Leukemia), ALL (Acute Lymphoid Leukemia)							

Table 1.1 *List of nano-formulations approved by FDA and in clinical use for various bio-medical applications.*

(B) Micelles: Micelles are also vesicular structures but unlike liposomes do not consist of lipid bi-layers. Instead they are nano-sized colloidal dispersions of amphiphilic lipid or surfactant molecules consisting of a hydrophilic head group and a hydrophobic tail group. Micelles form only when the surfactant concentration is greater than the critical micellar concentration (CMC) and the temperature of the system is greater than the 'krafft temperature'. Krafft temperature is the temperature at which the solubility of a surfactant is equal to the surfactant's CMC. Thus, micelles form spontaneously in aqueous media and are driven by the hydrophobic effect, wherein the entropy of the system is lost due to the ordering of the hydrophobic tails of the surfactant molecules into spherical shape at their CMC. This loss in entropy is balanced by a gain in entropy due to the release of solvation shells around the hydrophobic tails. Polymeric micelles made up of hydrophobic polymers such as PLA, polyamides, have been investigated for the delivery of poorly water soluble anti-cancer drugs[230]. A cholic acid (CA) conjugate of micelle made up of 8 molecules of CA and functionalized with PEG(5000) and loaded with paclitaxel (Paclitaxel-CA8-PEG5K) has been evaluated in murine models of ovarian cancer and was found

to show enhanced anti-tumor effect and less toxicity as compared to Taxol® and Abraxane® at equivalent paclitaxel doses[231].

(C) Dendrimers: Dendrimers are highly branched, three-dimensional, well-organized macroscopic nanostructures with a unique tree like branching structure and hence, the name 'dendrimers' (Greek word 'dendron' means 'tree'). They have been investigated immensely for their application in the emerging field of nano-medicine. Recently, lauryl modified-PAMAM dendrimers loaded with paclitaxel have been investigated for higher permeability across cell membranes of Caco-2 and porcine endothelial cells. They have been proposed to be potential nano-carriers for poorly water soluble P-gp efflux transporter drugs[232].

(D) Niosomes: Niosomes are also vesicular structures made up of bilayers. But unlike liposomes, the bilayers are composed of non-ionic single chain surface active agents and cholesterol and hence the name 'niosomes'. They are relatively more stable and in-expensive alternatives to liposomes, as the double chain phospholipids used for synthesis of liposomes are pre-disposed to oxidative degradation and requires special storage, handling and purity. Several anti-cancer drugs (such as Dox, paclitaxel) have been found to have better stability and release kinetics when entrapped inside niosomes instead of liposomes. However, the noisome technology is still in its infancy and needs more research for its evolution into a promising drug delivery technology[233].

(E) Solid Lipid Nanoparticles: Solid lipid nanoparticles (SLNs) are also a category of lipid carriers like liposomes but unlike liposomes they have a core made up of solid lipids, surrounded by a shell of stabilizing agents and usually dispersed in aqueous media. The solid lipid core is an improvement over the liquid or liquid crystalline core of liposomes. This enables encapsulation

of hydrophobic drugs and provides a potential for controlled or sustained drug release as against burst release in case of hydrophilic cores. Despite the advantages imparted by SLNs over liposomes, they are generally less stable and susceptible to rapid degradation by cellular lipases[234]. Daniela Chirio and co-workers investigated the cyto-toxicity of positively charged SLNs made up of behenic acid and loaded with paclitaxel, against NO3 glioblastoma cell line and was found to be more cyto-toxic and showed better *in vitro* blood-brain-barrier (BBB) permeability as compared to free paclitaxel[235].

(F) Nano-structured Lipid Carriers: Nano-structured lipid carriers (NLCs) are composed of a core of both solid and liquid lipids and are generally considered as improvised versions of lipid nano-carriers for targeted drug delivery applications. They are synthesized by mixing of solid lipids with liquid oils resulting in generation of special nanostructures in the matrix having an amorphous core or interior. Parenteral delivery and skin delivery of drugs are the most investigated applications of NLCs owing to their sustained release and retarded enzymatic attack in systemic circulation[236]. Yang et al., developed a hyaluronic acid coated and paclitaxel loaded NLCs system (HA-NLCs) and evaluated its anti-tumor efficacy in a B16 malignant melanoma mice model. HA-NLCs showed higher anti-tumor efficacy than taxol and prolonged blood circulation and increased accumulation of paclitaxel in tumor[237].

B. Inorganic nanoparticles: Inorganic nanoparticles have recently received immense attention as targeted drug delivery nano-carriers owing to their relatively higher stability than organic nanoparticles, less toxicity, high cellular uptake and non-immunogenic response, being some of the advantages.

(i) Silica nanoparticles: Mesoporous silica nanoparticles (MSNs) have been investigated as

an emerging drug delivery tool due to their high loading capacity for poorly water-soluble drugs. They have a solid framework with porous structure and large surface area, enabling functionalization with different targeting moieties for targeted drug delivery. Due to the strong Si-O bonds, these nanoparticles are highly resistive to physical and mechanical stresses as compared to lipid based nanocarriers[238]. A pH responsive MSNs system capped with chitosan and loaded with curcumin was investigated by Nasab and co-workers for sustained release and anti-cancer efficacy in U87MG glioblastoma cell line and was found to be more cyoto-toxic than the free curcumin[239].

(ii) Gold nanoparticles: Gold nanoparticles (GNPs) exhibit a combination of novel physical, chemical, optical and electronic properties, thus providing a highly multi-functional platform for imaging, diagnostics and therapeutics. GNPs have potential for multi-modal drug delivery applications, wherein enhanced drug pharmacokinetics or bio-distribution is coupled with simultaneous hyperthermia. GNPs also act as a contrast agent for radiation therapy, photo-imaging and spectrochemical diagnosis. Due to its unique property of Surface Plasmon Resonance (SPR), enabling the de-localization of the surface electrons, GNPs have the potential for photothermal therapy[240]. Farooq et al, synthesized highly stable colloidal suspension of GNPs for dual delivery of bleomycin and Dox to Hela Cells. The anti-cancer efficacy of the nano-hybrid system was found to be significantly higher than the single drug loaded GNPs or free drug[241].

(iii) SPIONs: SPIONs, as has been discussed in the previous **Section 1.4.8.3** of this Chapter, have been immensely studied as targeted drug delivery, imaging and therapeutic agents due to their super-paramagnetic behavior. The MHT capability of SPIONs combined with its amenability for functionalization with a range of targeting moieties, make SPIONs an excellent

choice as nano-carriers for targeted drug delivery and anti-cancer therapy applications. Moreover, SPIONs have improved bio-compatibilities due to their resemblance to cellular iron. Additionally, SPIONs can be tuned to accumulate in large quantities at target tumor site by application of strong permanent magnets, thus enhancing the cellular uptake of the SPIONs-drug complex. A list of commercially available formulations of SPIONs used for drug delivery or as MRI contrast agents is listed in **Table 1.1**. Although, the potential of SPIONs as MRI contrast agent is well established and utilized clinically, its therapeutic role for MHT of cancer still needs to be established at the patient level[242].

(iv) Quantum dots: Quantum dots (QDs) are basically semi-conductor crystals of nanometer size, with unique optical and electronic properties that can be utilized for imaging, drug delivery and bio-sensor applications. QDs exhibit bright intense fluorescence with size tunable light emissions and have good chemical and photo-stability. A three-in-one multifunctional theranostic system was designed by Guo et al. They developed a polyacrylic acid (PAA) coated $Cu_2(OH)PO_4$ QDs that shows a strong absorption in the NIR region. Post irradiation with NIR, local hyperthermia and reactive oxygen species (ROS) were generated, thus manifesting synergistic Photo-thermal therapy (PTT) and Photo Dynamic Therapy (PDT) applications. Moreover, these QDs showed excellent *in vivo* photo-acoustic imaging capabilities[243].

(C) Carbon based nanoparticles: Carbon based nanomaterials exhibit unique structural dimensions and excellent mechanical, electrical, thermal, optical and chemical properties that has attracted their utilization for bio-medical applications[244].

(i) Carbon nano-tubes: Carbon nanotubes (CNTs) are basically graphene sheets made up of carbon atoms rolled into seamless cylinders that can be either open or close ended and have a

high aspect ratio with diameters as small as 1 nm and length of several micrometers. CNTs can be made up of single or multiple graphene sheets rolled up into cylinders to form single walled nanotubes (SWNTs) or multi-walled nanotubes (MWNTs). CNTs have been of particular interest for application in the field of drug delivery due to their morphology (needle like shape), which warrants an enhanced intra-cellular uptake by direct penetration across the cell membrane. However, these are speculations/observations and detailed mechanism of uptake is still obscure[245]. In a recent study by Ji et al., Dox loaded MWNTs were found to show good activity against lymph node metastasis in EMT6 breast cancer model in mice[246].

(ii) Fullerenes: Fullerenes are nano-molecular carbon cages or hollow structures, which could be spherical, ellipsoidal or tubular in shape. The most well-known fullerene is buckyball or C_{60}, a spherical fullerene. Due to their unique physical, chemical, structural and electronic properties, they have attracted increasing attention for use as drug delivery vehicles and cancer therapy. Svitlana Prylutska and co-workers investigated the anti-cancer efficacy of a cisplatin-fullerene complex in chemotherapy resistant human leukemia cell sublines (HL-60/adr and HL-60/vinc, resistant to adriamycin and vincristine, respectively) as well as in Lewis lung carcinoma tumor model in mice. Their results showed significantly higher intra-cellular uptake and cyto-toxicity of the novel nano-formulation in *in vitro* as well as *in vivo* studies as compared to free drug or fullerenes alone[247]. However, detailed and extensive research is warranted for establishing the candidature of fullerenes for anti-cancer therapy and diagnostics.

(iii) Graphene: Graphene consists of a single layer of SP^2 hybridized carbon atoms arranged in a honey-comb two-dimensional (2D) crystal lattice. This 2D planar structure imparts unique properties of large surface area, great mechanical strength, superb conductivity and bio-compatibility, enabling utilization of graphene and graphene oxide (GO) for design of drug

delivery systems and other therapeutics. Graphene is the building block for CNTs or fullerenes. The surface area of graphene is four magnitudes higher (~ 2600 m^2g^{-1}) than any other nanomaterial explored for drug delivery[248]. Despite the several useful features their application is limited by poor aqueous solubility. However, graphene can be easily covalently or non-covalently modified with amphiphilic or hydrophilic polymers or linkers that can impart stimuli responsive release of conjugated drugs, in addition to improving its dispersibility in physiological conditions. Pei et al., reported synthesis of a PEGylated GO (pGO) for dual delivery of cisplatin and Dox for combination chemotherapy in a CAL-27, human squamous cell carcinoma model in nude mice. Authors demonstrated a significantly higher tumor control after treatment with the dual drug loaded pGO as compared to free drugs[249].

(D) Nanocrystals: These are nanoparticles with a crystalline character. For example a gold nanoparticle becomes a gold nano-crystal if the size of the nanoparticle is less than 100 nm and is composed solely of a single solid crystal of gold. Nanocrystals differ in properties from their bulk or larger counterparts in their physico-chemical properties. For example, silicon nano-crystal can provide efficient light emission, whereas bulk silicone cannot. Semi-conductor nanocrystals less than 10 nm are called as quantum dots. They have been utilized clinically to improve the dissolution rate of drugs, their saturation solubility, and to enhance the bio-availability of drugs[250]. Few examples of nano-crystals used in clinic are listed **(Table 1.1)**.

1.6 Background research done in laboratory related to thesis

As mentioned in previous **Section 1.4.8.3**, SPIONs, an important component of the nano-formulation in my thesis, has been studied in our laboratory. My research work on the synthesis of oleic acid coated SPIONs and their bio-physical characterization published previously in

'*Colloids and Surfaces B: Bio-interfaces, 2013*'[11] is not a part of the thesis but formed the foundation of the present thesis work. Hence, for easy reference of these details, I would like to briefly mention some of the basic characterization results of these SPIONs. These results ascertained the quality of nano-particles used in the present thesis pertaining to determination of their efficacy for combinatorial approaches and to further design and synthesize the targeted liposomal nano-formulation utilizing these SPIONs.

1.6.1 Synthesis of oleic acid coated iron oxide nanoparticles (MN-OA) and characterization of crystallite size and agglomeration

SPIONs were synthesized by chemical co-precipitation method and were subsequently functionalized with oleic acid (MN-OA). MN-OA was found to be crystalline in cubic phase with lattice parameters, a = 8.38 ± 0.01 and average crystallite size of 10 ± 2 nm. Transmission electron microscopy (TEM), selected area electron diffraction and high resolution-TEM (HR-TEM) obtained for MN-OA confirmed reduced agglomeration with an average particle size of 7 nm[11].

1.6.2 Magnetization study

Magnetization measurements were performed at room temperature by super-conducting quantum interference device magnetometer. Hysteresis loops showed clear saturation at 10 kOe. Saturation magnetization (Ms) was found to be 26.8 emu per gram of sample for MN-OA. MN-OA showed very low coercivity in the range of 10 – 20 Oe suggesting its superparamagnetic behavior[11].

1.6.3 FT-IR studies

The covalent conjugation of oleic acid to surface of IONPs was confirmed by Fourier transform-infrared (FT-IR) spectroscopy. FT-IR spectra of MN-OA was compared with only OA and uncapped MN by scanning the KBr pellets prepared for each sample. FT-IR spectra of OA showed peaks at 3005, 2925, 2855, 1710, 1462, 1285, 938 and 723 cm^{-1} which was in accordance with the reported values in literature. FT-IR spectra of uncapped MN showed broad doublets at 585 and 631 cm^{-1} due to combination of surface and core Fe-O bonds. Whereas, MN-OA showed a peak at 591 cm^{-1} and the shift in peak (from 631 cm^{-1} to 591 cm^{-1}) might be due to the interaction between Fe-O of MN and COO– of OA. MN-OA showed two distinct peaks at 1457 and 1557 cm^{-1}, attributed to symmetric and asymmetric COO– stretching vibrations, thus indicating that OA is chemically bound to MN. In addition, a peak at 1710cm^{-1} (corresponding to C-O stretching vibration), characteristic peak of unbound OA was also observed for MN-OA samples, indicating the presence of unbound or free OA in MN-OA preparations[11].

1.6.4 Thermo-gravimetric analysis (TGA) studies

As FT-IR analysis suggested the presence of unbound or free oleic acid (OA), I carried out TGA analysis to determine if the two components of OA (bound and un-bound) could be resolved and quantified. TGA was performed between room temperature and 800 ^{o}C for MN-OA and only OA samples. For OA, weight loss (90.8%) occurred in a single step between 170 and 366 ^{o}C. However, for MN-OA weight loss occurred in two steps, between 170 and 275 ^{o}C and 280 and 470 ^{o}C. The first weight loss may be attributed to the free or loosely bound OA, while the second transition may be due to the OA chemically bound to MN. In addition, a slight weight loss (1– 2 %) was observed in MN-OA below 150 ◦C due to water molecules adsorbed onto the MN

surface. The bound and unbound OA fractions were found to be 27.3 % and 19.7 %, respectively. The amount of OA optimized for functionalization of SPIONs was found to be 0.5 ml per 0.6 g of dried SPIONs powder. The minimization of free OA is required due to its cyto-toxicity[11].

1.7 Gap in knowledge in nanoparticle research areas and the relevance of present thesis work

Even though, extensive studies exist in literature in the area of nanoparticles, majority of known magnetic nano-formulations are either non-targeted or with poor efficacy. Moreover, studies are very limited in literature about actively targeted magnetic nanoparticles for improving the combinatorial cancer therapy approaches (especially radiotherapy, hyperthermia and chemo-therapy). Hence, in the present thesis, it is proposed to develop a targeted liposomal nano-formulation co-encapsulated with MN-OA and anti-cancer drug (Dox). In addition, the liposomes will be functionalized with polyethylene glycol (PEG) for improving the dispersibility and blood circulation period of the formulation. Further, the nano- formulation will also be conjugated with cyclic RGD (cRGD) peptide for active targeting of tumor cells and its neo-vasculature. Thus, the novel targeted liposomal nano-formulation (T-LMD) would enable targeted tumor delivery, combinatorial chemo-radiotherapy and magnetichyperthermia therapy of cancer. To achieve this, the proposed objectives of the present thesis are as following:

Objective I: To evaluate the radio-sensitizing ability of MN-OA under *in vitro* and *in vivo* conditions and elucidate the underlying mechanism of action.

Objective II: To synthesize and characterize PEGylated liposomes co-encapsulated with MN-

OA and anti-cancer drug (doxorubicin).

Objective III: To functionalize the liposomes with suitable ligand and evaluate their *in vitro* efficacy, toxicity and mechanism for combinatorial cancer therapy.

Objective IV: To study the toxicological aspects and therapeutic efficacy of the targeted liposomes for combinatorial cancer therapy in animal model.

1.8 Rationale of strategies used in the thesis

1. <u>Combining the virtues of liposomes and SPIONs:</u> As discussed above, lipid-based nano-carrier or nano-delivery systems, in particular liposomes, appear to have the multiple merits in terms of bio-compatibility, multi-functional applicability and conduciveness for design of a novel nano-delivery system for combinatorial cancer therapy application. Thus, in the present thesis, I decided to combine the merits of liposomes with SPIONs to design a novel drug delivery system with theranostic capabilities. There were two possible approaches to develop a tumor targeted nano-formulation: (i) Functionalization of the SPIONs surface with a tumor targeting ligand; (ii) Encapsulating the SPIONs inside a liposome, which in turn is functionalized with a tumor targeting agent. The first approach has the limitation of size (addition of functional groups may make the SPIONs very bulky) and availability of sufficient or appropriate functional groups for functionalization. The direct functionalization of SPIONs may also affect their dispersibility in physiological media, which is a pre-requisite for physiological applicability of SPIONs for anti-cancer therapy. However, in the second approach, SPIONs can be encapsulated inside liposomes. This approach may enable the preservation of the dispersibility issue of SPIONs (SPIONs with hydrophobic coating can be encapsulated inside the membrane region of

liposome). Moreover, liposomal encapsulation can offer the additional benefit of co-delivery of another anti-cancer agent along with SPIONs. Thus, through second approach, the virtues of both nanoparticles systems can be combined to develop a better and more effective targeted drug delivery system for improved hyperthermia and chemo-radiotherapy of cancer.

2. <u>Utilization of radio-sensitizing property of MN-OA:</u> Recent studies in our laboratory showed that oleic acid coated-iron oxide nanoparticles (MN-OA) resulted in down-regulation of several HSP90 client proteins which are involved in cell survival, cell cycle progression and DNA repair. Preliminary results showed that cancer cell treated with MN-OA and 2 Gy gamma radiation showed enhanced and persistent DNA damage. Based on these observations, we hypothesized that MN-OA could act as potential radio-sensitizer. Moreover, a much better/enhanced tumor control can be accomplished, if the MN-OA is combined with another anti-cancer (Dox) agent and both the compounds are co-delivered to the tumor cells in a targeted manner. Since, the mechanism of action of MN-OA (inhibition of DNA damage repair) and Dox (intercalation in DNA) involves modulation of DNA damage response pathways, the nano-formulation with both these agents may reduce the possibility of drug resistance and requirement of lower drug concentration and thus enabling improvement in outcome of chemo-radiotherapy.

Thus, the nano-formulation (NF) may result in enhanced tumor control due to following reasons: (i) due to the radio-sensitizing ability of MN-OA, the effective dose of Dox may be lowered, thereby minimizing its toxicity and side effects, (ii) this formulation will have the added advantage for theranostic application due to the presence of SPIONs (an established MRI contrast agent), (iii) the capping agent of SPIONs; oleic acid, is known to induce apoptosis in cancer cells and hence, will result in higher tumor toxicity, (iv) moreover, this NF may result in better therapeutic gain by targeted delivery of the nano-formulation to the tumor site, enhancing

the tumor cell killing due to a combination of increased DNA damage induced by Dox and impaired DNA repair caused by MN-OA.

1.9 Novelty of the Thesis

The novel aspects of the proposed thesis include (i) co-encapsulation of Dox in hydrophilic core and MN-OA in hydrophobic membrane of liposomes, (ii) studying the combinatorial chemo-radio- and hyperthermia therapy ability of this formulation (T-LMD) and (iii) active targeting of this formulation to tumor for better efficacy.

CHAPTER 2

MATERIALS AND METHODS

Materials and Methods

2.1 Reagents and chemicals

Ferric chloride ($FeCl_3.6H_2O$, 99.5 %), ferrous sulphate ($FeSO_4.7H_2O$, 98 %) and sodium carbonate anhydrous (Na_2CO_3, 99.5 %) were procured from Merck, Darmstadt, Germany. Oleic acid (OA, 99 %) and phosphate buffered saline (PBS) pellets were procured from Sigma-Aldrich, USA. Ammonium hydroxide (NH_4OH, minimum assay: 25 %) was obtained from Chemco Fine Chemicals, Mumbai. D-luciferin sodium salt was procured from Biosynth, Switzerland. Isoflurane was obtained from Neon labs, India. Dimethyl sulfoxide (DMSO) was procured from S. D. Fine-chemicals, India. Antibodies for HSP90, HSP70, HSP60, CHK1, CDC2, BRCA1, Ku70, Cyclin B1, α-tubulin, AKT and GAPDH were obtained from Cell Signaling Technology, USA and cleaved Caspase-3, cleaved PARP and Ki-67 from BD Pharmingen, USA. Antibody for RAD51 and γ-H2AX was obtained from Abcam, UK and Millipore, USA, respectively. G418 was obtained from Sigma, USA and Superfect transfection agent from Qiagen, USA. HSP90 SiRNA transfection kit was procured from Santacruz Biotech, USA. Phospholipids [(1,2-Distearoyl-*sn*-glycero-3-phosphoethanolamine-Polyethylene glycol (2000)-maleimide (DSPE-PEG (2000)-Maleimide] was purchased from Avanti Polar Lipids, USA and other phospholipids, viz. 1,2-Dipalmitoyl-*sn*-glycero-3-phoshocholine (DPPC), L-α-Phosphatidylethanolamine, distearoyl methoxy polyethylene glycol conjugate (DSPE-PEG) and cholesterol was procured from Sigma-Aldrich, USA. Cyclic RGD peptide (cRGDfC) was procured from Anaspec, USA, whereas indocyanine green (ICG) was purchased from Sigma Aldrich, USA. Chloroform was procured from S. D. Fine-chemicals, India. Anti-cancer drug doxorubicin hydrochloride (Dox, 98.0 to 102.0 % HPLC grade) was purchased from Sigma-

Aldrich, USA and Lippod™, a clinical formulation of liposomal doxorubicin was purchased from Celon labs, Hyderabad, India.

2.2 Synthesis of magnetic nanoparticles functionalized with oleic acid (MN-OA)

In literature, there are several methods to synthesize iron oxide nanoparticles (IONPs)[256,276]. In the present work, IONPs were synthesized by co-precipitation method. In a typical synthesis, $FeCl_3$ (0.25 M) and $FeSO_4$ (0.25 M) were mixed in a molar ratio of 2:1, followed by drop-wise addition of liquid ammonia (NH_4OH), till a dark black precipitate starts appearing. The solution was maintained at room temperature for 4 to 5 hours followed by removing the excess ammonia by washing with de-ionized water using a strong magnet (2.5 kOe). To remove the bound water, the washed black precipitate was further washed 2 to 3 times with acetone. The samples were air dried at room temperature for overnight to obtain a dried black precipitate of iron oxide.

The reaction between Fe+2/Fe+3 and OH- is given below:

$$Fe^{+2} + 2Fe^{+3} + 8\,OH^- \xrightarrow{pH\ 10} Fe_3O_4 + 4\,H_2O \qquad (1)$$

The dried precipitate of iron oxide was further crushed in a mortar and pestle to a fine powder followed by coating with oleic acid (1 : 0.8 w/v ratio). The samples were maintained at room temperature on a rocker for 12 h for the coating **(Scheme 2.1)**.

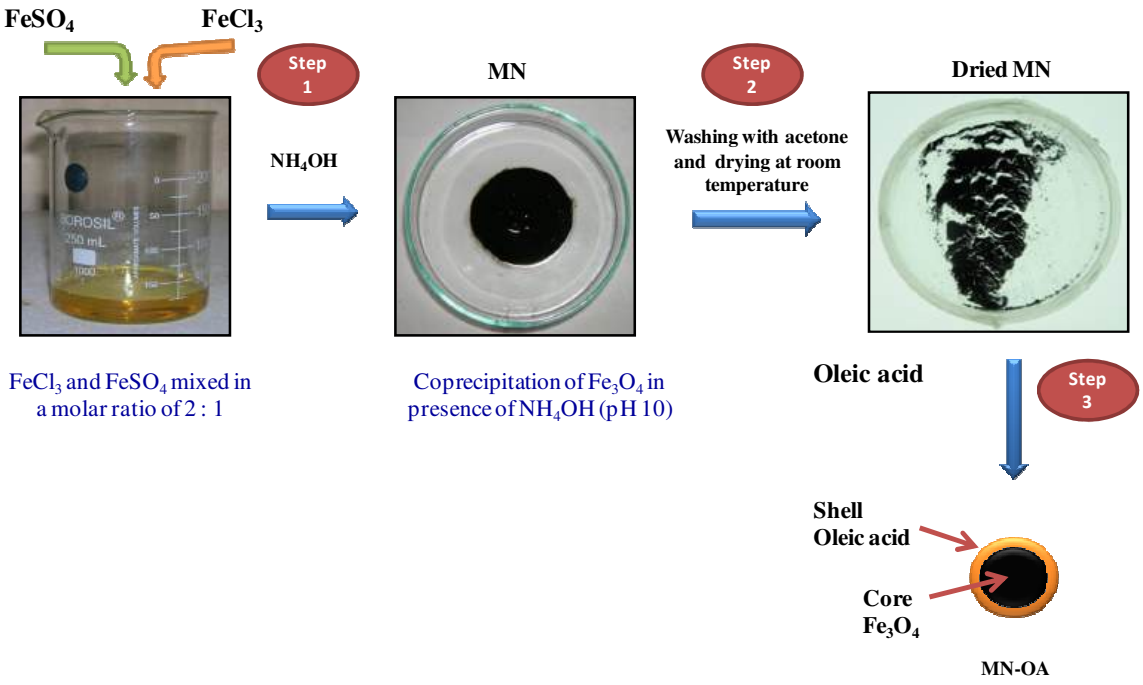

Scheme 2.1 *Scheme for synthesis of oleic acid coated iron oxide nanoparticles (MN-OA)*

For treatment of cell cultures, or wherever required, MN-OA was dispersed in 0.1 M Na_2CO_3 solution followed by dilution in phosphate buffered saline (PBS) (1:10). MN-OA forms a stable colloidal suspension in Na_2CO_3 (0.1 M) **(Scheme 2.2)**. The underlying reaction/interaction is as follows:

$$2CH_3(CH_2)_7CH{=}CH(CH_2)_7COOH + Na_2CO_3 \rightarrow 2CH_3(CH_2)_7CH{=}CH(CH_2)_7COO^- + Na^+$$

[Oleic acid] $+CO_2 + H_2O$ (2)

Addition of Na_2CO_3 helps in dissociation of COOH group of OA to COO^- and H^+. These ionized group/ions (COO^-) are useful in chemical interaction in polar medium (like water), where, Na^+ act as counter ions.

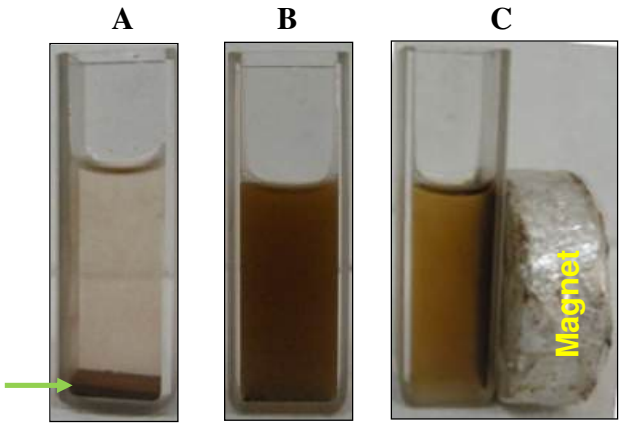

Scheme 2.2 *Representative digital photographs of MN-OA dispersed in* ***(A)*** *PBS or* ***(B)*** *solution of* Na_2CO_3 *(0.1 M) diluted in PBS (1:10). Green arrow indicates MN-OA agglomerated and settled at the bottom of the tube.* ***(C)*** *Image of MN-OA attracted to magnet (round) applied to the side of the tube.*

2.3 Characterization of MN-OA or liposomal nano-formulations: To confirm the synthesis of iron oxide (Fe_3O_4) nanoparticles and to determine its size, agglomeration, super-paramagnetic behavior and nature of conjugation with oleic acid, MN-OA was characterized by different bio-physical techniques. Liposomal nano-formulations [PEG-Lipo-MN-Dox and cRGD labeled PEG-Lipo-MN-Dox (T-LMD)] were also characterized by different bio-physical techniques as mentioned below: *[Please note: The XRD, TEM and FT-IR studies of MN-OA are not included in the thesis as these studies were done previously and are already published (Jadhav et al., 2013)*[11]*].*

2.3.1 X-Ray Diffraction (XRD) study: Confirmation of Fe_3O_4 synthesis and the average crystallite size and lattice parameters of MN-OA was determined by XRD study. Briefly, a suspension of MN-OA was prepared in chloroform and layer or coating of MN-OA was prepared

on a glass slide followed by air drying at room temperature to obtain a thin film of MN-OA on the slide. The crystal structure of the prepared samples was determined using a Philips powder X-ray diffractometer (PW1729, Phillips, Holland) with Ni-filtered Cu-Kα radiation. The X-ray tube was operated at 20 mA and 30 kV. The X-ray diffraction (XRD) pattern was recorded at scanning rate of 2^{o}/min. in 2Θ. The inter-planar distance (d_{hkl}) was calculated using

$$\text{Bragg's relation: } (2d_{hkl}).\sin\Theta = n\lambda \quad (3)$$

where n is a positive integer, λ is the wavelength of X-ray (1.5405 Å), Θ, Bragg's angle. The lattice parameters were calculated from the least square-fitting program of the diffraction peaks. The average crystallite size (t), after assuming spherical crystallites, was calculated from the diffraction line-width of XRD pattern, based on

$$\text{Scherrer's relation: } t\ 0.9\lambda/\beta\cos\Theta \quad (4)$$

where β is the full width at half maximum (fwhm).

2.3.2 Transmission electron microscopy (TEM): TEM (2000 FX, JEOL, Japan) was used for recording TEM images of MN-OA and PEG-Lipo-MN-Dox. For TEM, a suspension of MN-OA (0.5 mg/ml) was prepared in methanol by ultra-sonication. A drop of the dispersed MN-OA suspension was then put over the carbon coated copper (Cu) grid and evaporated to dryness at room temperature. In case of liposome samples (equivalent to 3.2 mg/ml of MN-OA), a drop of the liposome suspension was directly put over the carbon coated copper grid and a drop of phosphotungstic acid (PTA, 2 %) was added on it. PTA was used as a negative stain for liposomes to enhance the contrast of liposomal membrane. The PTA was left on the liposome sample for 45 secs and then blotted with a tissue paper. The PTA stained sample was then

evaporated to dryness at room temperature. Later the Cu grids containing the samples were mounted inside the sample chamber. HRTEM (high resolution transmission electron microscope) images of MN-OA were recorded using JEOL 2010 UHR TEM microscope. For PEG-Lipo-MN-Dox samples, energy dispersive-X-Ray (EDX) analysis was carried out on a few fields to determine its elemental composition. TEM and EDX studies on PEG-Lipo-MN-Dox were carried out at Indian Institute of Technology (IIT), Mumbai, India.

2.3.3 Cryo-TEM study: Cryo-TEM images were captured for T-LMD and Lippod^{TM} to visualize the encapsulation of Dox as it was not visible in case of TEM performed at room temperature. Cryo-mode imaging of vitreous samples of T-LMD or Lippod^{TM} were carried out at Indian Institute of Technology (IIT) – Mumbai, India.

2.3.4 FT-IR study: The conjugation of oleic acid (OA) with Fe_3O_4 (MN) was confirmed by Fourier Transform - Infrared (FT-IR) spectroscopy (Bomem FTIR, Switzerland). In case of MN-OA, FT-IR spectra were recorded using thin pellets of the samples made with KBr. For liposomal nano-formulation, FT-IR was used to confirm the conjugation of cyclic RGD (cRGD) peptide with DSPE-PEG-maleimide. Free cRGD and unconjugated DSPE-PEG-maleimide was used for comparison. Thus, in case of lipid samples, the liquid sample was placed in between a pair of calcium fluoride (CaF_2) windows and the FT-IR spectra was recorded in the transmittance mode (400 to 4000 cm^{-1}).

2.3.5 Reversed phase – High Performance Liquid Chromatography (RP-HPLC) study: To confirm the conjugation of cRGD to DSPE-PEG-maleimide, RP-HPLC analysis (Shimadzu, Japan) was carried out using C8 (Supelco®, Sigma-aldrich, USA) as stationary column and water as mobile phase. Briefly, 20 µl sample was injected into the HPLC and the retention time

and area under the curve (AUC) were determined from the graph. The peptide was detected using a UV/visible spectroscopic HPLC detector.

2.3.6 Magnetization study: Magnetization study was carried out to confirm the super-paramagnetic behavior of MN-OA. This was done using a Physical Property Measurement System (PPMS) (Model: 6000, Quantum Design) equipped with vibrating sample magnetometer (VSM) option and a superconducting magnet producing fields up to ± 9 Tesla.

2.3.7 Induction heating studies:

These studies were done to determine the heat generation ability of the nano-formulations (both MN-OA and liposomal nano-formulation) under alternating current (AC) magnetic field (AMF) conditions. Briefly, MN-OA (2-10 mg/ml in 1ml of 0.1 M Na_2CO_3) was placed in a 1.5 ml of micro-centrifuge tube and subjected to AMF conditions (265 kHz radio-frequency, 400 A current) using an induction heating instrument (Easy Heat 8310, Ambrell, UK and DM100 Nano-heating System, NB NanoScale Bio-magnetics, Spain) with 6 cm diameter (4 turns) coil. The magnetic field was calculated from the relationship:

$$H = 1.257\ ni/L \text{ (in Oe)} \quad (5)$$

Where, n, i and L denote the number of turns, applied current and the diameter of the turn in centimeters, respectively. Calculated values of the magnetic field (H) at 400 A was 335.2 Oe (equivalent to 26.7 kA mA^{-1}). Temperature in magnetic field was measured using glass fibre optic probe (Photon controls, USA).

2.3.8 DLS study: DLS was performed to determine the hydrodynamic size of MN-OA or liposomal nano-formulations. Briefly, a suspension of MN-OA (2 mg) was prepared in 1 ml of Na_2CO_3 (0.1 M), and further diluted (1 : 10) in PBS till a light-colored solution was obtained. 5 ml of sample was placed inside a quartz cuvette. In case of liposomal nano-formulations as well, 5 ml of sample (after appropriate dilution in PBS) was used for analysis. The DLS spectra was recorded using a Malvern 4800 Autosizer (UK) employing a 7132 digital correlator for the determination of hydrodynamic diameter.

2.3.9 Zeta potential measurement: To determine the charge on the surface of the liposomal nano-formulations (viz. PEG-Lipo-MN-Dox and T-LMD) and subsequently determine their colloidal stability, Zeta potential measurements were carried out on a Zetasizer nano series (Malvern Instruments, UK). In brief, a suspension of liposomes (equivalent to 0.3 mg/ml of MN-OA or 0.6 μM of Dox) was prepared in PBS and placed inside the cell of the zetasizer instrument. The samples were scanned for 30 cycles.

2.4 Synthesis of PEGylated liposomes co-encapsulated with MN-OA and Doxorubicin (Dox)

To synthesize PEGylated liposomes co-encapsulated with MN-OA and Dox (PEG-Lipo-MN-Dox), thin film hydration method was used. Briefly, phospholipids, viz. DPPC, DSPE-PEG and cholesterol were mixed in chloroform in a molar ratio of 6:1:2 in a glass tube. A 20 mg/ml of stock of MN-OA was prepared in chloroform and desired amount (viz. 300, 400, 500 μl of suspension corresponding to 6, 7 and 8 mg/ml of MN-OA) was added to the phospholipid mixture. The chloroform was then evaporated under a stream of nitrogen gas with constant swirling to obtain a thin film of phospholipids. The film was further dried under vacuum for 4 to 6 h. Dox was encapsulated by two methods: (i) thin film hydration and (ii) pH gradient method.

2.4.1 Thin film hydration method: In this method, the thin film of phospholipids was hydrated in 1 ml of PBS containing Dox (100 μM) using glass beads and mechanical shaking. The abrasion due to the glass beads during the mechanical shaking results in dislodgment of lipids from the tube surface. Due to the hydrophilic environment in the tube, the dislodged lipids tend to collapse into spherical structures resulting in formation of multi-lamellar liposomes (MLVs). The MLVs are then down-sized by sonication with a probe sonicator (Lab-line Instruments, Inc., India) for 15 secs, followed by heating in a water bath (at 55 ^{o}C) for 45 secs. The sonication and heating cycles are repeated several times to obtain a less viscous and more transparent suspension of uni-lamellar liposomes (ULVs). The ULVs are then subjected to gel permeation chromatography to remove the un-entrapped Dox using sephadex G-50 beads (pre-soaked with PBS for 24 h) by centrifugation at 2000 rpm for 5 min. An aliquot of the ULVs is taken before gel permeation chromatography for determination of encapsulation percentage of Dox **(Section 2.7)**. To efficiently remove the un-entrapped Dox, the eluent collected after gel permeation chromatography is dialyzed against saline for 4 to 6 h under constant stirring conditions using a 12 to 14 kDa Molecular Weight Cut-Off (MWCO) cellulose membrane (Spectrum Laboratories, USA). The ULVs thus formed are called as PEG-Lipo-MN-Dox **(Scheme 2.3)**.

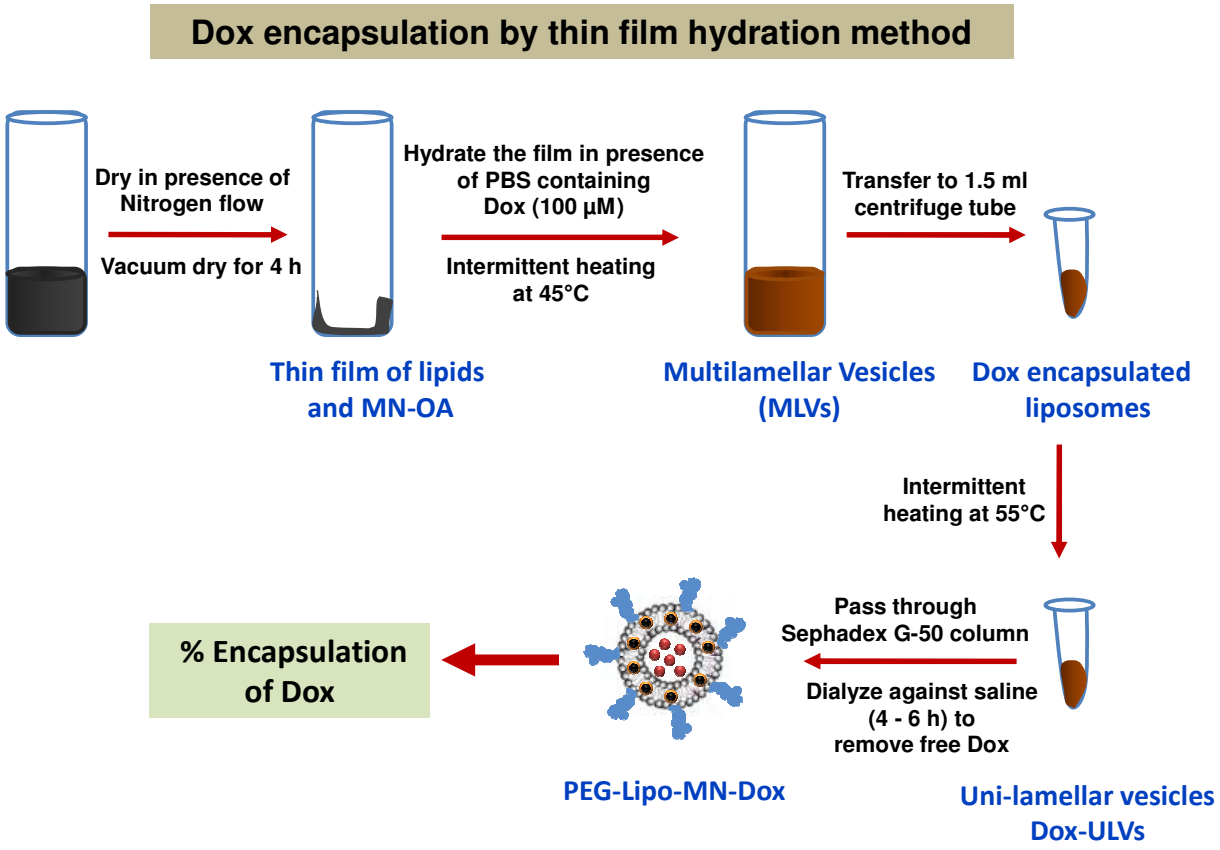

Scheme 2.3 *Schematic for synthesis of PEG-Lipo-MN-Dox by thin film hydration method*

2.4.2 pH gradient method: The principle of drug loading by pH gradient method relies on the development of a pH gradient across the membrane of the liposomes. Briefly, the thin film of lipids is first hydrated with 0.5 ml of citrate buffer (300 mM, pH 4.0). The formed MLVs are then subjected to rapid freezing in liquid nitrogen followed by thawing in room temperature water. These freeze-thaw cycles are repeated for 7-8 cycles to ensure substantial encapsulation of citrate buffer inside the liposomes, thus making the liposome interior acidic. The citrate encapsulated MLVs are then down-sized by sonication and subjected to gel permeation chromatography as discussed above to obtain citrate encapsulated ULVs. For encapsulating Dox, the citrate-ULVs are incubated with 0.5 ml of Dox (100 µM) solution prepared in PBS (pH 7.4

with 0.1 % DMSO) in a water bath maintained at 60 ^{o}C for 10 min **(Scheme 2.4)**. This is followed by again passing the Dox-ULVs through sephadex G-50 (Sigma-Aldrich, USA) column and dialysis as discussed above.

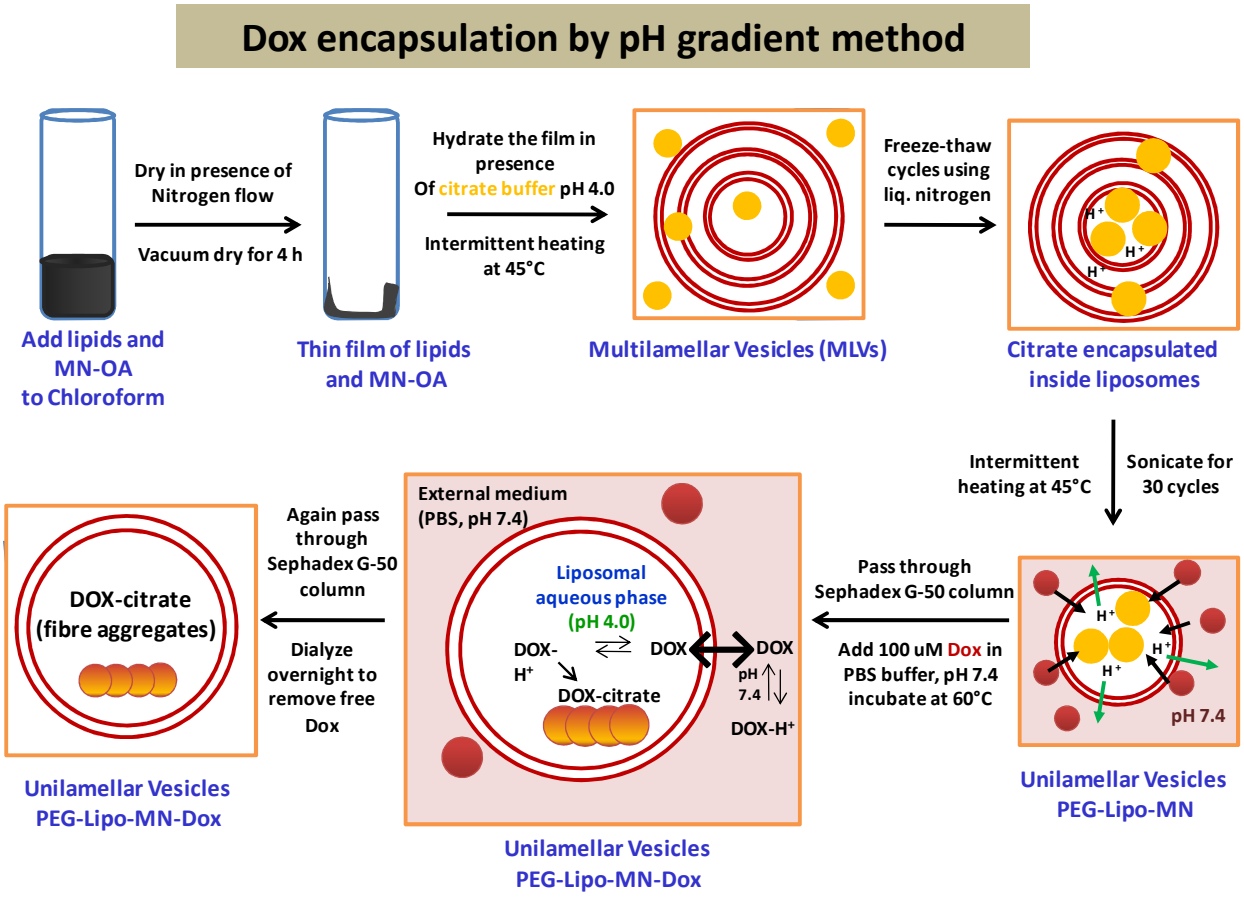

Scheme 2.4 *Schematic for synthesis of PEG-Lipo-MN-Dox by pH gradient method*

2.5 Synthesis of cRGD labeled PEG-Lipo-MN-Dox (T-LMD)

The tumor targeted liposomal nano-formulation, T-LMD was synthesized utilizing a pre-labeling and post-insertion approach. Briefly, cRGD was first chemically linked to PEG-DSPE-maleimide using maleimide-thiol click chemistry[251]. For this, cRGD peptide (1 mg/ml) and the

phospholipid (508 mg/ml) were dissolved separately in reaction buffer (50 mM triethanolamine HCl, 50 mM sodium phosphate, 150 mM NaCl and 1 mM EDTA). The cRGD solution was then mixed with the phospholipid solution in a molar ratio of 2 : 1 in a glass bottle at 4 °C for overnight. The free cRGD peptide was removed by dialysis using 3.5 kDa molecular weight cut off (MWCO) dialysis membrane (Spectrum Laboratories, USA). The coupling of cRGD to PEG-DSPE-maleimide was confirmed by Reverse phase-High Performance Liquid Chromatography (RP-HPLC) and Fourier Transform-Infrared Spectroscopy (FT-IR) studies.

2.6 Synthesis of indocyanine green (ICG) loaded liposomal nano-formulations

For determination of the tumor targeting efficacy of T-LMD and its bio-distribution in different organs of mice, the liposomal nano-formulation was loaded with near-infrared dye, ICG. For synthesis of ICG loaded T-LMD (ICG-T-LMD), ICG (10 mg/ml) was added to the thin film of phospholipids and MN-OA as shown in **Scheme 2.5**. The ICG containing film of phospholipids was then hydrated and processed further by pH gradient method as described in **Section 2.4.2**. To determine the encapsulation efficiency of ICG, fluorescence measurement method was used. Briefly, 10 µl aliquot of ICG-T-LMD, before and after dialysis was lysed with 10 µl triton X-100 (10 %) and further diluted with 980 µl of PBS. The fluorescence was measured in a micro-plate reader (Tecan infinite M200 Pro, Switzerland) at excitation and emission wavelength of 790 nm and 820 nm, respectively in a black well plate using top optics. % Encapsulation was determined by using the formula:

(%) Encapsulation = (average fluorescence intensity of ICG-T-LMD after dialysis/ average fluorescence intensity of ICG-T-LMD before dialysis) x 100. (6)

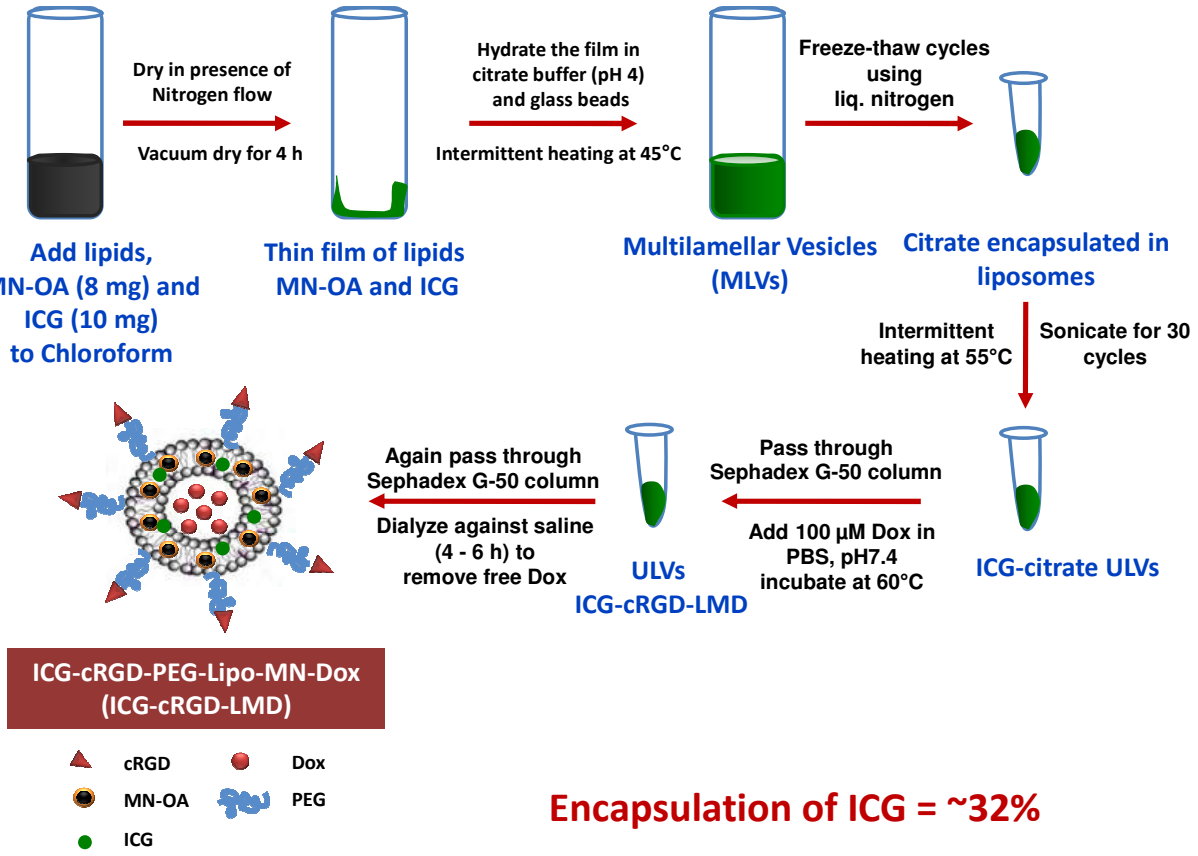

Scheme 2.5 *Scheme for synthesis of ICG loaded T-LMD.*

2.7 Estimation of encapsulation efficiency of Doxorubicin (Dox) and MN-OA in liposomes

To determine the percentage encapsulation of Dox and MN-OA, fluorescence measurement and Fe estimation by ortho-phenanthroline method[252] was used, respectively. Briefly, once, the liposomes were synthesized by thin film hydration method, an aliquot of liposomal sample (10 µl) was collected in triplicates just before and after dialysis (to remove the un-encapsulated Dox) of the liposomal nano-formulation. The entrapped Dox was released by adding 10 µl of triton X-100 (10 %) and vortexing for 30 secs. The sample was diluted with 980 µl of PBS, followed by

measurement of Dox fluorescence in a plate reader at Ex: 485 nm and Em: 585 nm. % encapsulation was measured using the formula:

(%) Encapsulation of Dox = (Average fluorescence intensity of Dox after dialysis/ Average fluorescence intensity of Dox before dialysis) x 100. (7)

For determination of percentage encapsulation of MN-OA, 50 µl aliquot of final liposomal suspension (after dialysis) was dissolved in 50 µl of conc. HCl by vortexing for 10 min. A suspension of 8 mg/ml of MN-OA was prepared in chloroform and 50 µl aliquot of this suspension was also dissolved in HCl as described earlier. Once, the MN-OA was completely solubilized resulting in a slightly yellow colored solution, a 10 µl aliquot was taken from each sample and Fe content was measured by ortho-phenanthroline method. In brief, 10 µl aliquot of sample was diluted with distilled water (490 µl). The diluted samples was further mixed with 500 µl of 10 % hydroxylamine hydrochloride solution, 250 µl of acetate buffer (0.1 M, pH 4.5), 150 µl ammonia : water (1:1) mixture and 500 µl of 1, 10-phenanthroline solution (0.25%) in the same order and incubated at room temperature for 15-20 min. The absorbance was measured at 510 nm. 70 PPM ferrous ammonium sulfate solution was used as a standard for Fe estimation. Percentage encapsulation of MN-OA was determined as:

(%) Encapsulation of MN-OA = (Fe content of liposomal sample in PPM/Fe content of 8 mg/ml MN-OA suspension in PPM) x100 (8)

2.8 Determination of stability of liposomes by dynamic dialysis method

To determine the stability of liposomes in PBS (pH 7.4) at 37 ^{o}C, dynamic dialysis method was used. Briefly, 100 µl of PEG-Lipo-MN-Dox sample was diluted in PBS (900 µl) and placed

inside a floating dialysis bag (Micro-Float-A-Lyzer, Spectrum Labs, USA) with MWCO of 8 to 12 kDa. Before initiating the dialysis, a 10 µL aliquot was removed from the dialysis bag and replaced with equal volume of buffer maintained at same temperature. The dialysis was carried in a water bath maintained at 37 ^{o}C. *(Note: In a separate tube, PBS was also maintained at the same temperature in the water bath and was used to maintain the volume of solution after removing an aliquot for estimation).* After defined time points (viz. 10 min., 1 h, 3h, 6h and 24 h), 10 µl aliquot of liposome sample was removed from the dialysis bag and replaced with PBS as described previously. To measure the amount of Dox in the aliquoted sample, the liposomes were lysed with 10 µl of triton X-100 (10 %) followed by dilution with 980 µL of PBS. The fluorescence intensity of Dox was measured using a plate reader at Ex: 485 nm and Em: 585 nm. The percentage release of Dox was determined using the formula:

% Release = 100 - (average fluorescence intensity of Dox at t_t – initial fluorescence intensity of Dox)/(average fluorescence intensity of Dox at t_0 - initial fluorescence intensity of Dox) x 100 (9)

Where, t_0 corresponds to zero time point and t_t corresponds to subsequent time points.

2.9 Determination of heat generation ability of MN-OA under alternating current (*AC*) magnetic field (AMF) conditions

Once the synthesis of MN-OA was confirmed by different bio-physical techniques, its heat generation ability under AMF conditions was tested. The heat generation ability of MN-OA is a measure of its specific absorption rate (SAR), which in turn dictates its suitability for MHT. Briefly, 10 mg of MN-OA was dispersed in 100 µl of Na_2CO_3 (0.1 M) by sonication in water bath for 10 min. The suspension was further diluted in PBS (900 µl) to obtain a 10 mg/ml

dispersion of MN-OA. The centrifuge tube containing the MN-OA suspension was placed in a holder and the assembly was placed inside the Cu coils of the induction heating instrument such that the sample lies at the center of the Cu coils without touching the sides. To measure the temperature rise in the MN-OA dispersion, a fibre optic temperature sensor probe (1 mm diameter, Photon Controls, USA) was dipped in the sample ensuring it does not touch the side or the bottom of the sample tube **(Fig. 2.1)**. The AMF was applied at 335 Oe magnetic field intensity, 265 kHz radio-frequency and 400 A current for 10 min. and the temperature rise per minute was noted. A graph of temperature vs time was plotted and the slope of the linear part of the curve was determined. SAR was determined using the formula:

$$SAR = C.(\Delta T/\Delta t).(1/m_{magn}) \quad (10)$$

where, C is the specific heat capacity of the sample (i.e. MN-OA + diluent, here the major component of the diluent is water). However, the specific heat capacity of MN-OA is negligible, hence, C = 4.18 $Jg^{-1}K\text{-}^{1}$ (i.e. the specific heat capacity of water). $\Delta T/\Delta t$ is the initial (usually first 5 min.) slope of the time dependent-temperature curve. m_{magn} is the total amount of Fe_3O_4 in (MN-OA + water). Since MN-OA contains 52.7 % of Fe_3O_4 (5.27 mg of Fe_3O_4 per 10 mg of MN-OA) and weight of water can be considered as 1 mg (equivalent to 1 ml), the total weight of Fe_3O_4 in 10 mg of MN-OA + water was calculated as 6.27 mg.

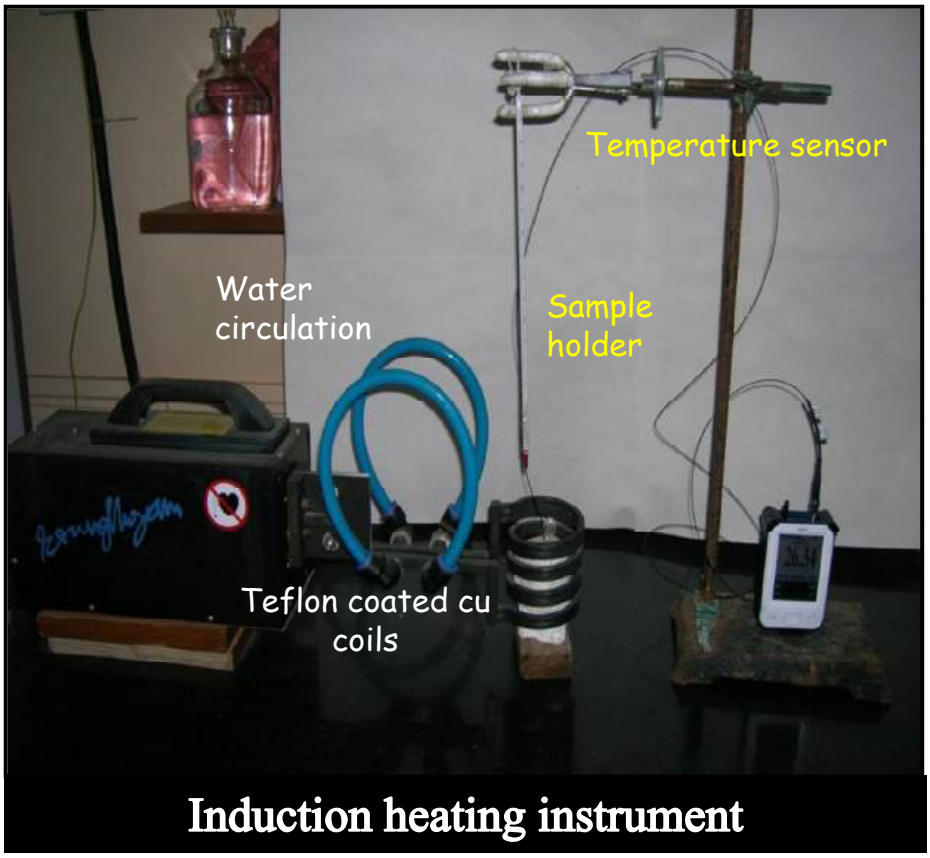

Fig. 2.1 *Induction heating instrument for determination of heat generation capacity of magnetic nanoparticles under AMF.*

2.10 Cell lines, animals and irradiation

Mouse skin fibrosarcoma (WEHI-164), human fibrosarcoma (HT-1080), human glioblastoma (U373MG), human lung adenocarcinoma (A549), human breast adenocarcinoma (MDAMB-231 and MCF-7), human hepatoma (WRL-68) cell lines were obtained from National Centre for Cell Sciences (NCCS), Pune, India and human normal lung cells (WI26VA4) was obtained from European Collection of Authenticated Cell Cultures (ECACC). Cells were cultured in Dulbecco's Modified Eagle Medium (DMEM; GIBCO, Invitrogen, CA, USA) supplemented with 10 % fetal bovine serum (FBS: Himedia Laboratories, Mumbai, India) and antibiotics (100

U ml^{-1} penicillin and 100 µg ml^{-1} streptomycin) in a humidified atmosphere of 5 % CO_2 at 37 °C.

For animal experiments, female BALB/c mice (6-8 weeks old) weighing ~ 20 g were obtained from the animal house facility of Bhabha Atomic Research Centre (BARC). The animals were housed in a solid floor cage with adequate bedding. The room temperature was maintained at 20-24°C, and a 14 h of light and 10 h of dark cycle was maintained. Animals received a diet of commercially available pellets and water *ad libitum*. All experiments were conducted adhering to the Institutional Animal Ethical Committee guidelines (BAEC/22/17 and BAEC/18/2019)

For irradiation, the cells were seeded in 60 mm Petri dishes to 50 % confluency for overnight at culture conditions. Further after treatment with MN-OA or liposomal nano-formulations (viz. PEG-Lipo-MN-Dox, T-LMD or Lippod^{TM}) the dishes were sealed with parafilm, wrapped in aluminum foil and subjected to radiation in a ^{60}Co gamma teletherapy irradiator (Bhabhatron II, Panacea Medical Technologies, Bangalore, India; dose rate: 1 Gy/min). Required dosimetry was performed using Farmers Ion Chamber (Scandatronix Wellhofer, Germany).

For irradiation of animals, they were restrained in a specially designed perspex cage with only the tumor bearing leg of mice being placed in the field for irradiation. Local irradiation to the tumor region was carried out using ^{60}Co teletherapy irradiatior (Bhabhatron-II mentioned above) with appropriate shielding.

For *in vivo* live animal imaging experiments, the animals were injected either with only indocyanine green (ICG) or ICG labeled PEG-Lipo-MN-Dox with or without cRGD conjugation

via the intra-venous route. Immediately after the dye/drug administration, the mice were transferred to an anesthesia chamber perfused with isoflurane : oxygen (5 % : 95 %) gas mixture [through in-built anesthesia set up of live animal imaging system (Photon Imager, Biospace Lab, France) till the animals were un-conscious (taking about 2 minutes)]. Once the mice were sedated, they were transferred to the imaging chamber of imaging system, wherein also isoflurane: oxygen gas mixture flow was maintained at 5 % concentration. The mice were imaged continuously for 45 min. followed by removal of mice from the imaging chamber and placement in open air till they are fully conscious. For further time points, viz. 3 h, 24 h, 48 h and 168 h, the mice were again anesthetized as described earlier. At a time, three mice were imaged in imaging chamber for each time point.

For magnetic hyperthermia therapy, a single BALB/c mouse was placed inside a plastic holder or restrainer with an insulated support. This assembly was then placed inside the copper (Cu) coils of the induction heating instrument, wherein the mouse was subjected to alternating current (*AC*) magnetic field (AMF) conditions (330 - 335 Oe magnetic field intensity, 265 kHz radio-frequency, 400 A current) for magnetic hyperthermia therapy (MHT) for 10 min. Only the lower body of the mouse including the tumor on the hind leg was placed inside the coil, whereas it was ensured that the head region of the mouse lies outside the Cu coils **(Scheme 2.6)**. During MHT, the mice were in a conscious state. The tumor volume was calculated using the formula,

$$\text{Tumor volume} = 0.523A^2C \qquad (11)$$

where, A: larger diameter and C: smaller diameter.

Tumor growth delay (TGD), tumor growth delay index (TGDI) and % tumor growth inhibition (% TGI) were calculated as follows:

TGD (for doubling of the tumor volume) = Difference in the no. of days required to reach double tumor volume for treated and control groups. (12)

TGDI = Ratio of no. of days required to reach double tumor volume for treated and control groups. (13)

TGI(%) = (Vc-Vt)/(Vc-Vo)*100, where Vc, Vt are the tumor volumes of control and treated groups at the respective days after start of the treatment and Vo, is the tumor volume of control at the start of the treatment. (14)

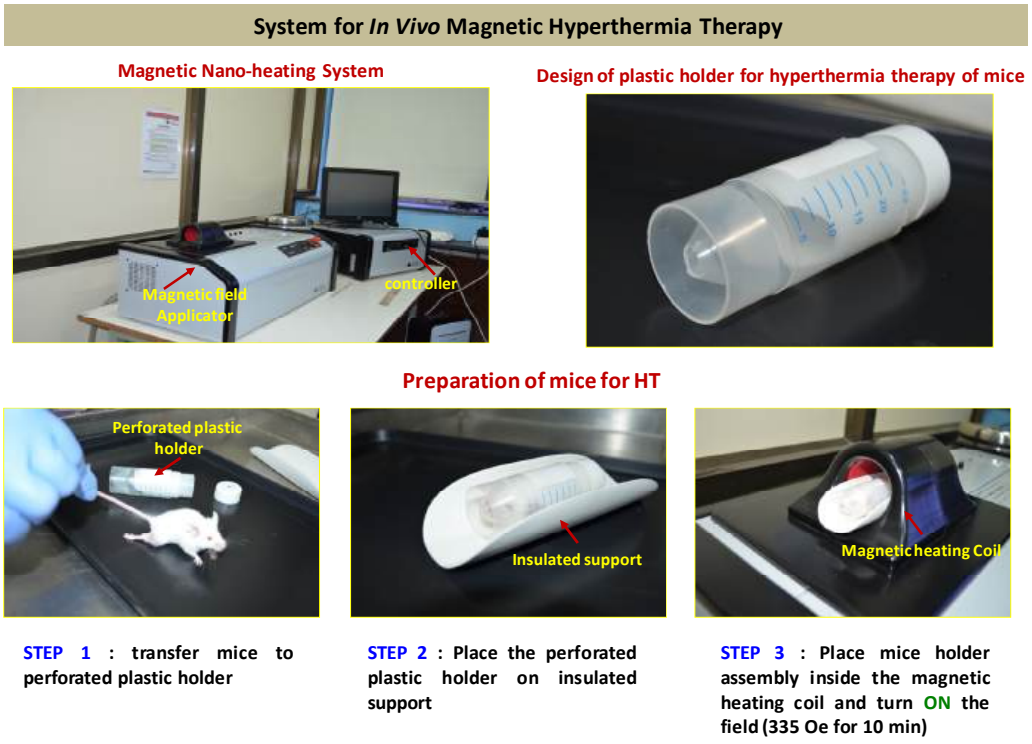

Scheme 2.6 *Steps for preparation of fibrosarcoma tumor bearing mice for MHT.*

2.11 Prussian blue and Nile blue staining for visualization of iron distribution in WEHI-164 cancer cells or fibrosarcoma tumors

2.11.1 Prussian blue staining

WEHI-164 cancer cells or tumors and other organ tissue sections were processed for Prussian blue staining of iron to determine the distribution of MN-OA. Principle of staining is based on reaction of potassium ferrocyanide with Fe^{3+} under acidic conditions to form ferric ferrocyanide; an insoluble blue colored complex, also called as Prussian blue[253]. Thus, blue spots correspond to presence of Fe^{3+}. In brief, WEHI-164 cells treated with MN-OA for 3 h were washed with PBS, followed by fixing in paraformaldehyde (4 %) at room temperature for 20 min. In case of tumor or organ tissue sections, the paraffin sections were de-waxed in xylene solution, twice for 10 min. each followed by re-hydration in decreasing grades of alcohol and washing with PBS. The fixed cells or tissue sections were then stained using Prussian blue staining kit (Polysciences, USA). Briefly, the samples were incubated with the staining solution [a 1:1 mixture of 4 % potassium ferrocyanide and 4 % hydrochloric acid (HCl)] at room temperature for 20 min. The slides were again washed with PBS and counter stained with 1 % nuclear fast red solution and then examined by light microscopy.

2.11.2 Nile blue staining

Nile blue sulphate or Nile blue A (Sigma, USA), a histological fat stain, was used to validate the interaction of MN-OA with WEHI-164 cells by staining the oleic acid coat of MN-OA. The principle of staining is based on the interaction of the blue oxazine form of Nile blue A with phospholipids and free fatty acids (such as oleic acid) resulting in a bright red fluorescence at 488 nm excitation wavelength and 545 nm emission wavelength [254]. The cancer cells (0.5×10^6)

were seeded on a glass coverslip and treated with MN-OA (0.22 and 0.44 mg/ml for 3 h) as described earlier. After fixing with paraformaldehyde, the cells were incubated with 10 µg ml^{-1} Nile blue A in PBS for 2 h in culture conditions followed by washing with PBS. The coverslips were mounted on slides and fluorescence was visualized by CLSM (LS510 Meta Carl Ziess, Germany) at 488 nm excitation wavelength and 575–615 nm emission wavelength.

2.12 Iron estimation for measurement of uptake of MN-OA or liposomal nano-formulation in cells or tumor tissues

To determine the uptake of MN-OA or liposomal nano-formulation in cancer cells, mainly two methods were followed. (i) Total reflection-X-ray fluorescence (T-XRF) spectroscopy or (ii) ortho-phenanthroline method for colorimetric detection of Fe in samples. However, due to the higher speed of detection and capability of simultaneous analysis of multiple samples at a time, ortho-phenanthroline method was used for further cell experiments as well as for detection of Fe in tissue samples due to the higher inherent iron content in tissues.

2.12.1 T-XRF method: Briefly, WEHI-164 cells treated with MN-OA (0.44 mg/ml MN-OA) or liposomal nano-formulation (equivalent to 0.017 to 0.17 mg/ml of MN-OA) for different time points. For each time point, the treated cells were washed with PBS twice, followed by harvesting the cells by trypsinization. The cell pellet was again washed with PBS and then 200 µl of supra-pure HCl was added to each cell pellet. The samples were then placed in a water bath maintained at 90 ^{o}C for 4 to 6 h. The acid was then evaporated in a fume hood using a heating block maintained at 90 ^{o}C till the volume in each sample reached 50 µl. The samples were then diluted in distilled water (950 µl) and processed for T-XRF analysis (TX2000, Ital Structures,

Italy) using Mo Kα radiation as excitation source. The samples were further diluted with distilled water and spiked with Gallium, which was used as an internal reference standard.

2.12.2 Ortho-Phenanthroline method: To study the uptake of MN-OA or liposomal nano-formualtion in different cell lines, the treated cancer cells were digested in concentrated HCl till a clear solution was obtained, followed by heating to evaporate the HCl. The samples were diluted in 10 ml of distilled water. The clear solution obtained after digestion was used for estimation of Fe content using ortho-phenanthroline method as discussed in **Section 2.7**.

2.13 Measurement of cancer cell cyto-toxicity by trypan blue dye exclusion and 3-(4,5-Dimethylthiazol-2-yl)-2,5-Diphenyltetrazolium Bromide (MTT) assay

The effect of MN-OA or liposomal nano-formulation on the viability of various cancer cells was studied by using either the trypan blue dye exclusion or the MTT assay

2.13.1 Trypan blue dye exclusion assay

To determine the effect of MN-OA on viability of WEHI-164 cancer cells either alone or in combination with MHT, the cancer cell viability was determined by trypan blue dye exclusion method. WEHI-164 Cells (0.5 X 10^6) were seeded overnight into 60 mm culture dishes in 4 ml complete DMEM. Then, the cells were treated with MN-OA (0.11, 0.22, 0.33 or 0.44 mg/ml) for 3 h at culture conditions (20 mg/ml stock of MN-OA was dispersed in 1 ml of 1:10 mixture of 0.1 M sodium carbonate : PBS followed by further dilution in complete DMEM to obtain the desired concentration). Treatment was followed by washing the cells with PBS (pre-warmed at 37 °C) and further replaced by pre-warmed DMEM with 10 % FBS. For induction heating, the 60 mm dishes were placed under a magnetic field of ~ 335 Oe at a current of 400 A and 265 kHz

radiofrequency for 10 min. Following induction heating, the dishes were transferred to humidified incubator at 37 °C for 24 h. Later the cells were trypsinized and the cell pellet was resuspended in equal volumes of PBS. 10 µl of the cell suspension was added to 10 µl of trypan blue (0.4 % prepared in PBS) and the cells were counted using a hemocytometer under a bright field microscope. The % viability was expressed as % Viability = (No. of live cells / Total No. of cells) X 100 (15)

2.13.2 MTT assay

To study the effect of MN-OA or various liposomal nano-formulations (viz. PEG-Lipo, PEG-Lipo-MN-OA, PEG-Lipo-Dox, PEG-Lipo-MN-Dox, T-LMD or Lippod^{TM}) on the viability of various cancer (viz. WEHI-164, HT-1080, A549, U373MG, MDAMB-231, MCF-7 and WRL68) and normal (WI26VA44) cells lines, either alone or in combination with MHT or 2 Gy γ-radiation, MTT cell proliferation assay was used. Briefly, various cancer cells were seeded in 96 well plates at a cell density of 1000 to 5000 cells (cell number was varied depending on the time point for MTT termination, viz. for 72 - 96 h time point 1000 cells were seeded, whereas for 24 – 48 h treatment 5000 cells were seeded). The cells were incubated at culture conditions for overnight followed by treatment with MN-OA or liposomal nano-formulation in the required concentration range (0.11 to 0.44 mg/ml for MN-OA and 25 to 400 nM equivalent concentration of Dox or 17.4 to 67 µg/ml of equivalent concentration of MN-OA for liposomal nano-formulation) after appropriate dilution in PBS or complete DMEM. *(Note: After synthesis, liposomal nano-formulations were sterile filtered by passing through 0.22 µm syringe filter. This was followed by determination of encapsulated concentration of Dox and MN-OA by fluorescence and colorimetric methods, respectively as discussed in* ***Section 2.7****. For treatment*

of cells the liposomal nano-formulations were diluted in PBS to desired concentrations). The cancer cells were further incubated at culture conditions for desired time points (viz. 24 to 96 h). For determination of cell viability or cell proliferation, the media containing the nano-formulation was removed by aspiration and replaced with fresh media containing MTT (0.5 mg/ml) followed by incubation under culture conditions for 3 to 4 h. This was followed by removal of the MTT containing media by aspiration and solubilization of the formazan crystal formed by addition of dimethyl sulphoxide (DMSO: 200 µl per well) to form a blue colored solution. After uniform solubilization by shaking on a rocker, the absorbance was measured in a plate reader (Tecan infinite Pro M200, Switzerland) at 544 nm. The percentage viability was determined by considering the absorbance of control as 100 %.

2.14 Cell cycle analysis by flow cytometry

The effect of different concentrations of MN-OA either alone or in combination with MHT (at 0.22 and 0.44 mg/ml) or in combination with 2 Gy (R) γ-radiation (at 0.55 mg/ml MN-OA concentration) in WEHI-164 cells on the different phases of cell cycle was determined by propidium iodide (PI) staining based flow cytometry analysis. The effect of liposomal nano-formulations, namely PEG-Lipo-MN-Dox (at 1000 nM equivalent Dox concentration in WEHI-164 cells) and T-LMD (at 25, 50, 75, 100, 200, 300 and 400 nM equivalent Dox concentration in WEHI-164 and U373MG cell lines) was also studied by PI based cell cycle analysis. Briefly, cancer cells (0.25×10^6) were seeded in 60 mm culture dishes in 4 ml media for overnight at culture conditions. This was followed by treatment with desired doses of MN-OA or liposomal nano-formulations for 3 h at culture conditions. In case of MN-OA treatment, the media was replaced with fresh medium and further incubation at culture conditions for 24 h or 48 h.

However, in case of liposomal nano-formulations, the drug containing media was not removed as the % uptake at 3h was significantly lower for liposomal nano-formulation (~ 20 to 25 %) as compared to MN-OA (~ 55 %). For combination treatment with MN-OA, the cells were first treated with different amounts of MN-OA for 3h followed by replacing the media and irradiation of cells with 2 Gy. Whereas in case of combination treatment with liposomal nano-formulations, the cells were irradiated after 3 h of treatment without any media removal step. For cell cycle analysis, the cancer cells were harvested by trypsinization after desired time points (24 h and 48 h for MN-OA or MN-OA + R or MN-OA + MHT) and (24 h for PEG-Lipo-MN-Dox and 24 and 72 h for T-LMD or T-LMD + R or T-LMD + MHT) followed by washing with PBS twice and fixing in ice cold absolute methanol. The fixed cells were stored at -20°C till further use. For flow cytometry analysis, the cells were first permeabilized (0.1% Triton X-100 and 1 mg/ml sodium citrate in PBS) followed by staining with PI [containing freshly added RNAse solution (50 µg/tube)]. The flow cytometry (Partec, Germany) was carried out at 488 nm excitation and 585 nm emission wavelengths.

2.15 Measurement of apoptosis in control and treated WEHI-164 cells: Cell death detection ELISA Assay

For determination of level of apoptosis in WEHI-164 cells after treatment with increasing concentrations of MN-OA (0.22 or 0.44 mg/ml) in combination with or without MHT, Cell death detection ELISA^{PLUS} kit (Roche, USA) was used. The assay is based on a quantitative sandwich-enzyme-immunoassay-principle using anti-DNA and anti-histone monoclonal antibodies. In this assay the magnitude of fragmented DNA and histone proteins in cytosolic fraction, the hallmark features of apoptosis, was determined. This allows specific determination of mono- and oligo-

nucleosomes in the cytosolic fraction of cell lysates. The assay was carried out following manufacturer's instructions. Briefly, the WEHI-164 cells were treated with MN-OA ± MHT as described in Section 2.13 followed by harvesting the cells by trypsinization. A defined number of cells (10^4) were lysed using cell lysis buffer provided with the kit followed by centrifugation at 200 x g for 15 min. to separate the cytoplasmic fraction containing the mono- or oligo-nucleosomes. Then, 20 µl of cytoplasmic fraction was transferred to each well of the microplate (in triplicates) pre-coated with anti-histone antibodies, followed by washing with wash buffer provided with the kit. This was followed by addition of anti-DNA antibody solution labeled with horse radish peroxidase (HRP). The amount of anti-DNA-HRP antibody binding was determined by addition of ABTS substrate and measurement of absorbance at 405 nm and 490 nm as reference wavelength.

2.16 Measurement of apoptosis in control and treated WEHI-164 cells: Annexin-V/PI Assay

To determine the percentage of early (annexin V+/PI-) or late apoptotic (annexin V+/PI+) cells or necrotic cells (annexin V-/PI+) after treatment with MN-OA ± 2 Gy, annexin V-FITC/PI staining kit (Roche diagnostics, USA) was used. Briefly, WEHI-164 cells (0.25 x 10^6) were seeded in 60 mm culture dishes for overnight at culture conditions followed by treatment with either MN-OA or 2 Gy or combination treatments as described above. For late time points, cells were harvested (2 h after treatment with MN-OA + 2Gy) counted and re-seeded in 60 mm Petri dishes at a density of 10,000-40,000 cells (for 144 and 96 h time points). Cells were later harvested after 24, 48, 96 and 144 h followed by counting the cells. The cell number was adjusted to 1 x 10^6 cells and then the cells were stained with annexin V-FITC/PI staining kit,

followed by observing the cells (~ 200) under 40 X magnification by fluorescence microscopy. % cells stained with only PI (necrotic cells), only FITC (early apoptotic cells) and both PI and FITC (late apoptotic cells) were determined.

2.17 Determination of radio-sensitization ability of MN-OA or liposomal nano-formulation using Clonogenic cell survival assay

To evaluate the radio-sensitization ability of MN-OA or liposomal nano-formulation (T-LMD), clonogenic cell survival assay was carried out. Briefly, WEHI-164 cells (0.25×10^6) were seeded in 60 mm Petri dishes with 4 ml of DMEM (containing 10% FCS) for overnight at culture conditions. Further, cells were treated with different doses of MN-OA (0.33, 0.44 and 0.55 mg corresponding to 82.5, 110 and 137.5 µg/ml, respectively) for 3h followed by replacing the media with fresh medium and then irradiation of cells with 2 Gy. The cells were further incubated under culture conditions for 2 h followed by trypsinization and cell counting. Cells (500 cells) were seeded in 60 mm culture dishes from each group [Control, 2 Gy, MN-OA (0.33, 0.44 and 0.55 mg) and MN-OA + 2Gy (0.33 + 2Gy. 0.44 + 2Gy and 0.55 + 2Gy)] followed by incubation under culture conditions for 9 days. In case of liposomal nano-formulation, the WEHI-164 cells were seeded at a cell density of 500 cells in 6 well plates containing 4 ml of complete media for overnight at culture conditions. The cells were then treated with different concentrations of T-LMD or Lippod^{TM} (at 25, 50, 75 and 100 nM equivalent Dox concentration) and incubated further at culture conditions for 9 days. As discussed in **Section 2.13.2**, a slight modification in treatment protocol was followed for liposomal nano-formulations mainly due to their difference in the percentage uptake (viz. ~ 55 % for MN-OA as against ~ 25 % for T-LMD). On 9th day, the colonies were washed with PBS, fixed with absolute ethanol for 30 secs

followed by staining with crystal violet (0.5% w/v) for 3 min. and de-staining with distilled water. The plates were then allowed to dry and then the colonies were counted. The colonies were considered with minimum 50 cells and counted. Plating efficiency (%) was determined by using the formula,

% Plating efficiency (PE) = (no. of colonies in control or treated group/no. of cells seeded) * 100 (16)

The % survival was determined by using the formula,

% Survival = (ratio of PE of treated and control group) * 100. (17)

Survival fraction was determined by using the formula,

Survival fraction = no. of colonies/(no. of cells plated/PE) (18)

2.18 Immuno-cytochemistry for actin, α-tubulin and γ-H2AX proteins: For immuno-cytochemistry experiments, the WEHI-164 cells ($0.25x10^6$) were seeded in 60 mm Petri dishes as described previously **(Section 2.14)**. For staining of actin and α-tubulin, the cells were trypsinized and counted after treatment with MN-OA or 2 Gy alone and in combination. 10,000 to 40,000 cells from each treatment group were re-seeded on glass coverslips in 60 mm Petri dishes and further incubated under culture conditions for required time (viz. 144 and 96 h). For staining of γ-H2AX foci, 0.25×10^6 WEHI-164 cells were seeded on glass coverslips for overnight in 60 mm Petri-dishes followed by treatment with MN-OA and/or 2Gy. For 96 h time point, 40,000 cells were re-seeded after treatments as described previously. In case of liposomal nano-formulation, WEHI-164 cells (0.2×10^6) were treated with T-LMD (200 nM equivalent concentration of Dox) for 3h followed by irradiation at 2 Gy (without removal or replacement of media). The samples were fixed with para-formaldehyde (4 %) at different time points post-

irradiation (viz. 5 min., 15 min. 30 min. 1 h, 3 h, 6 h, 24 h,48 h and 72 h) to determine the magnitude of γ-H2AX in cells. In case of MN-OA treatment also, after required period of incubation post-irradiation (i.e. 15 min, 30 min, 24 h and 96 h), the cells on the coverslips were washed with PBS followed by fixing in 4 % paraformaldehyde for 20 min at room temperature (RT). The cells were washed twice with PBS followed by permeabilization with 0.5% triton X-100 for 5 min, again washed twice with PBS followed by blocking with 5% FCS (at RT for 1h). Cells were further incubated with desired primary antibodies [α-tubulin or γ-H2AX (Millipore) 1:200 dilution] for 2 h at RT. The cells were washed with PBS containing 0.05 % Tween 20, thrice for 5 min each. Further, cells were incubated with appropriate secondary antibody labeled with Alex Fluor 488 (for α-tubulin and γ-H2AX). For labeling actin, cells were treated with phalloidin-tetramethyl rhodamine B isothiocyanate (phalloidin-TRITC) (Sigma, USA) for 1 h at RT. This was followed by washing twice with PBS for 5 min and mounting the cells with prolong gold antifade with DAPI (Molecular Probes, USA). Cells were visualized by fluorescence (Nikon Eclipse Ti, Japan) or confocal (Zeiss Meta 710, Germany) microscopy using appropriate filters.

2.19 Magnetic separation of proteins bound with MN-OA

To isolate the proteins that are bound to MN-OA, untreated control or treated cells were lysed using native lysis buffer [Tris (50 mM), pH 8.0, 0.8 % NP-40, NaCl (150 mM) and 10 % glycerol containing 1 mM PMSF and 0.5 mM sodium orthovanadate]. The tubes containing cell lysates were then placed on top of a magnet (field strength: ~ 0.5 kOe) to collect MN-OA associated/bound proteins (attracted towards the magnet). In control tubes, no protein pellet was found after applying magnet. The supernatant containing the unbound protein fraction was

removed. The MN-OA bound proteins fraction was washed 5–6 times (without centrifugation) with native lysis buffer to remove any unbound proteins using every time the same magnet. The MN-OA bound protein fraction was then used for identification of MN-OA bound proteins by SDS PAGE and Western blotting.

2.20 siRNA transfection

To confirm the role of HSP90 in MN-OA induced radio-sensitization in WEHI-164 cells, the cancer cells were transfected with HSP90 siRNA to knock down HSP90 expression using manufacturer's protocol (Santacruz biotech, USA). This was followed by treatment of cancer cells with MN-OA and radiation and determining the effect on percentage cell proliferation. At 48 h post transfection, untreated control group transfected with either HSP90 or control SiRNA was examined for the level of HSP90 and HSP60 proteins by Western blotting

2.21 TEM of WEHI-164 cells treated with PEG-Lipo-MN-Dox

For determination of sub-cellular distribution of PEG-Lipo-MN-Dox in WEHI-164 cells, the cancer (5×10^6) cells were treated with nano-formulation (1µM equivalent concentration of Dox) for different time points (viz. 3 h and 24 h). The samples were later processed for TEM. Briefly, the cells were harvested by using a cell scraper at the desired time points followed by washing twice with PBS by centrifugation at 1500 RPM for 3 min. The cell pellet was then fixed with glutaraldehyde (2.5 % made in 0.05 M sodium cacodylate buffer with 0.1 M sodium chloride, pH 7.5) for 20 min. at room temperature. The cell pellet was further washed with cacodylate buffer and maintained in the same buffer at 4 ^{o}C until further processing. The samples were further

processed and imaged by TEM facility (Zeiss EM, Germany) of ACTREC, Kharghar, Navi Mumbai, India.

2.22 Visualization of early endosomes and T-LMD in U373MG and WEHI-164 cells using supra-resolution confocal microscopy

To determine the mode of uptake of T-LMD in U373MG and WEHI-164 cancer cells, the cancer cells (0.2×10^6) were seeded on a glass coverslip at culture conditions for overnight. The cancer cells were then treated with 200 nM (equivalent concentration of Dox) of T-LMD or free Dox for different time points (viz. 1 h and 3 h). At desired time point, the media was removed and the cells were washed with PBS twice followed by fixing with ice-cold paraformaldehyde (4 %) at 4 ^{o}C for 30 min. The cancer cells were again washed with PBS and treated with permeabilization solution (0.5 % triton X-100) for 5 min at RT. The cancer cells were again washed with PBS and incubated with blocking solution (5 % FBS made in PBS) for 1 h at RT. The cells were further incubated with anti-EEA1 (early endosomal marker) anti-body (1 : 50 dilution in 1 % FBS) for overnight at 4 ^{o}C. The cells were then washed with 0.05 % tween-20 containing PBS for 5 min each (three washes). This was followed by incubation with Alexa fluor 488 labeled secondary antibody (anti-rabbit) at 1: 100 dilution in 1 % FBS for 1 h at RT. The cells were again washed in PBS (twice) and stained with DAPI (1 µg/ml) for 5 min. at RT followed by washing with PBS and mounting the cells on slides using Prolong Gold anti-fade mountant (Molecular probes, USA). The cells were imaged using CLSM (Leica SP8 STED, Singapore) in supra-resolution mode at Ex: 488 nm and Em: 543 nm for EEA-1 and Ex: 488 nm and Em: 650 nm for Dox.

2.23 Expression of $\alpha_v\beta_3$ integrin receptor on cell surface of multiple cancer cell lines

To determine the expression level of $\alpha_v\beta_3$ integrin receptor on the surface of multiple cancer (viz. WEHI-164, U373MG, A549, MCF-7, MDA-MB231, WRL68) and normal (WI26VA44) cell lines, flow cytometry analysis following antibody staining was carried out. Briefly, the cancer cells (1×10^6) were seeded in 6-well plate in 2 ml of media for overnight at culture conditions. The cells were then harvested by using a cell scraper and washed with PBS twice by centrifugation at 1500 RPM for 5 min. The cells were then fixed with paraformaldehyde (2 %) for 15 min. at RT, followed by washing with PBS (twice). Further, the cancer cells were treated with anti- $\alpha_v\beta_3$ integrin receptor antibody (Abcam, USA) for 1 h at RT followed by washing with PBS containing 0.05 % Tween 20. Alexa-fluor 488 labeled secondary anti-body (anti-mouse) was added to the cells and incubated at RT for 1 h followed by washing twice with PBS. The cells were finally suspended in PBS and acquired (20,000 cells per sample in triplicates) in the flow cytometer (Partec, Germany). Secondary antibody control (i.e. cancer cells were treated with only the secondary antibody) was used to normalize the fluorescence signal of non-specific binding of secondary antibody onto the cell surface.

2.24 Development of luciferase expressing WEHI-164 cells for *in vivo* imaging

The WEHI-164 cells were transfected with the CMV-FL2-eGFP-pcDNA 3.1(+) plasmid vector (available from Addgene, USA) by lipo-fection method. The transfected clones were selected using G418 selection medium. The luminescence of clones was measured in a luminometer at 550 nm and relative luminescence units (RLU) per µg protein were calculated. Clone expressing highest RLU per µg protein was further cultured in P-100 and maintained in selection medium containing 200 µg per ml of G418 **(Scheme 2.7)**. This clone was used for establishment of

fibrosarcoma tumors in BALB/c mice followed by injection of vehicle control or MN-OA and exposure to AMF as described earlier. *The transfection experiments were done in collaboration with Dr. Pritha Ray, Ray lab, ACTREC.* For *in vivo* imaging, 3 mg of D-Luciferin sodium salt (BIOSYNTH, USA; stock prepared in saline) was injected intra-peritoneally in animals. This was followed by sedation of mice using isoflurane as described previously. Once the animals were anesthetized (~ 5 min. after injection) the animals were imaged using the *in vivo* imaging system (Photon Imager, Biospace, France). Results were expressed as mean luminescence intensity (photons/s/cm^2/Sr) ± SEM.

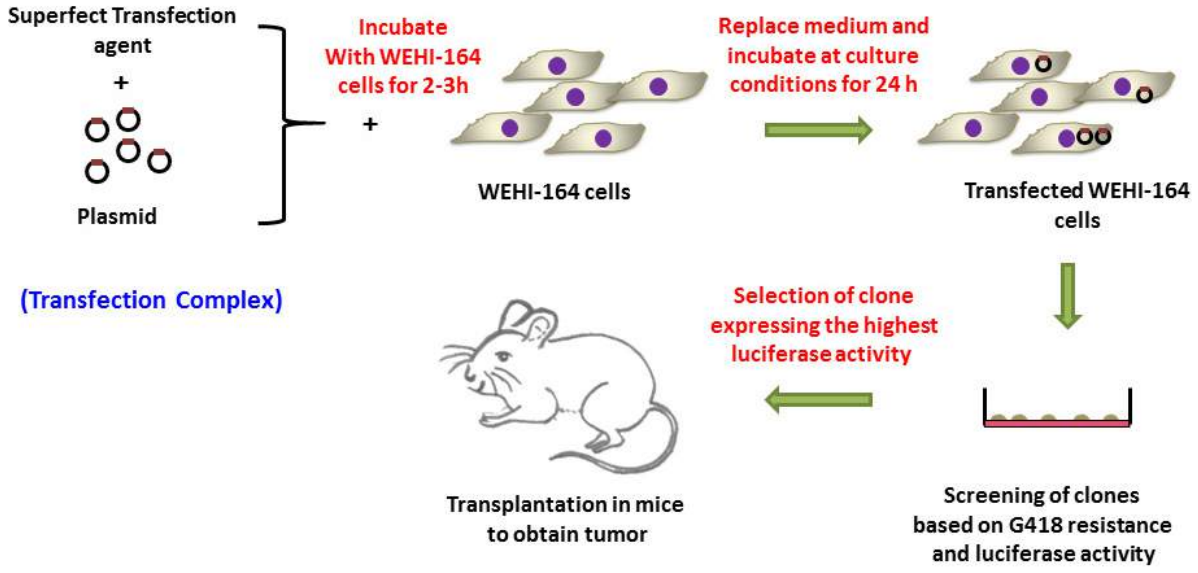

Scheme 2. *Scheme for transfection of WEHI-164 cells were luciferase gene for bio-luminescence imaging of tumors developed with luciferase transfected WEHI-164 cells. (Source: Shetake et al, 2015[178]).*

2.25 Establishment of fibrosarcoma tumor model

To establish a fibrosarcoma tumor model, WEHI-164 (mouse fibrosarcoma tumor cells; 1 x 10^6) were injected intramuscularly in the right hind leg of BALB/c mice. Palpable tumors (7-9 mm in diameter) were obtained on 8^{th} day after injection. On day 8 animals were injected, intra-tumoraly with vehicle control (3.5 µl oleic acid dispersed in 0.1 M sodium carbonate) or MN-OA (dispersed in 0.1 M sodium carbonate) as described previously **(Section 2.2)** followed by MHT as described in next section. For testing of liposomal nano-formulations, they were administered intravenously via tail vein injection, once the tumors were palpabale.

2.26 *In vivo* magnetic hyperthermia therapy (MHT)

For *in vivo* MHT using MN-OA, on day 8, 100 µl of MN-OA stock (~ 0.44 mg MN-OA) was injected in the tumor in 2 settings: twice on day 8 and twice on day 10 at an interval of 1h between the two injections. Thus, total 1.76 mg of MN-OA (equivalent to 69.6 µg Fe) was injected intra-tumoraly. The whole animal was treated four times (on days 8, 9, 10 and 11) with AMF (400 A, 265 kHz radiofrequency, 10 min; 2 h after the MN-OA injection) using specially designed plastic tubes with sufficient ventilation. The above treatment schedule consisted of four groups (8 tumor bearing mice in each group): Group I: vehicle control (C), Group II: vehicle control and exposed to AMF (C + H), Group III: MN-OA alone (MN-OA), and Group IV: MN-OA followed by exposure to AMF (MN-OA + H).

In case of liposomal nano-formulation, two injections (with a gap of 4 h) of 100 µl each of T-LMD (equivalent to 3 mg/kg of Dox) was administered intra-venously in BALB/c mice with palpable tumors (~ 8 mm diameter) on day 8 post implantation of WEHI-164 cells. The

mice were then subjected to MHT (400 A, 265 kHz radiofrequency, 10 min) for three consecutive days (day 2, 3 and 4) post intra-venous administration of T-LMD as described above. The above treatment schedule consisted of following four groups (8 tumor bearing mice in each group): Group I: vehicle control (C), Group II: vehicle control and exposed to AMF (C + H), Group III: T-LMD alone (T-LMD), and Group IV: T-LMD followed by exposure to AMF (T-LMD + H).

The tumor growth of control and treated animals was monitored for another 8 days by measuring the tumor diameter (small and large) using a Vernier caliper. Since, the tumor was an oblate spheroid; the volume was calculated using the formula:

$$\text{Tumor volume} = 4/3\ \pi\ abc$$

Since, for an oblate spheroid, a=b<c,

Therefore, formula used to calculate tumor volume = $4/3\ \pi\ a^2c$,

Where a: larger radius and c: smaller radius

Since, we measured the diameter using Vernier caliper, the formula modifies to

$$\text{Tumor volume} = 4/3\ \pi\ (A/2)^2\ (C/2)$$

$$= 0.523A^2C \qquad (19)$$

Where, A: larger diameter and C: smaller diameter

On day 9 after initiation of treatment, mice were sacrificed, tumors were excised and part of the tumor was fixed in formalin solution (10 %) for immuno-fluorescence and histopathological studies. The remaining part was snap frozen in liquid nitrogen and stored at -80°C till use.

2.27 *In vivo* Radiotherapy and combinatorial MHT and Radiotherapy

For *in vivo* radio-therapy, fibrosarcoma tumors were developed in BALB/c mice as discussed in **Section 2.25.** For radio-therapy, the mice were placed inside perpex cages with their tumor bearing leg stretched outside, such that only the tumor bearing leg gets exposed to gamma radiation during therapy. In case of radio-therapy by MN-OA, it was injected intra-tumoraly as discussed in **Section 2.25**. Whereas, in case of T-LMD, the nano-formulation was administered intra-venously as described in above section. In addition to T-LMD, Lippod^{TM} at equivalent concentration of Dox to T-LMD was also injected intra-venously in separate group of mice. Post drug administration (either MN-OA or T-LMD or Lippod^{TM}), the tumors were subjected to irradiation with 2 Gy dose for three consecutive days (day 2, 3 and 4) corresponding to a total fractionated dose of 6 Gy (2+2+2Gy)

Thus, the treatment groups for MN-OA were as follows (8 tumor bearing mice in each group):

Group I: vehicle control (C), Group II: vehicle control and exposed to fractionated 6 Gy radiation (C + R), Group III: MN-OA alone (MN-OA), and Group IV: MN-OA followed by exposure to fractionated 6 Gy (MN-OA + R).

Treatment groups for T-LMD and Lippod^{TM} were as follows (8 tumor bearing mice in each group):

Group I: vehicle control (C), Group II: vehicle control and exposed to fractionated 6 Gy radiation (C + R), Group III: T-LMD alone (T-LMD), and Group IV: T-LMD followed by exposure to fractionated 6 Gy (T-LMD + R).

Treatment groups for T-LMD in combination with MHT and radiotherapy were as follows (8 tumor bearing mice in each group):

Group I: vehicle control (C), Group II: exposed to AMF and fractionated 6 Gy radiation (H + R), Group III: T-LMD alone (T-LMD), and Group IV: T-LMD followed by exposure to AMF (T-LMD + H), Group V: T-LMD followed by exposure to fractionated 6 Gy (T-LMD + R) and Group VI: T-LMD followed by exposure to AMF and fractionated 6 Gy with an interval of 2 h between the two treatments (T-LMD + H + R).

As mentioned in **Section 2.26**, the tumor growth of control and treated animals was monitored for another 8 days by measuring the tumor diameter (small and large) using a Vernier and the tumor volume was measured by using the Formula No. 19.

2.28 Histopathology analysis of tumor and organ tissue sections

Formalin fixed tumor or organ tissues were embedded in paraffin wax to obtain tissue blocs, followed by microtomy to obtain 5 micron thick tumor tissue sections. These sections were mounted on pre-treated glass slides and further processed for H & E staining (outsourced to M/s Chaitanya laboratories, Pune). A preliminary report was also provided by the pathologist as per standard codes, which was again validated by analyzing more images under bright field microscopy in the laboratory. In brief, the sections were de-paraffinized in xylene (three changes of 5 min. each) followed by re-hydration (for 2 min. each) in decreasing grades of alcohol (viz.

95 % to 70 % to 50 % to 30 % to distilled water) and finally placed in PBS for 5 min before processing the slides for H & E staining.

2.29 TUNEL staining of tumor tissue sections

The tumor tissue sections were de-paraffinized and re-hydrated as mentioned above. For TUNEL assay, the rehydrated sections were permeabilized with 0.1 % triton X-100 and 0.1 % sodium citrate, followed by washing with PBS and incubation in TUNEL reaction mixture (50 µl enzyme + 450 µl label solution) in humidified atmosphere at 37 °C for 1 h. The slides were again washed in PBS followed by mounting with cover slips and observation by fluorescence microscopy at 40 X magnification.

2.30 Immuno-fluorescence staining for expression of Ki-67

The tumor tissue sections were de-paraffinized and re-hydrated as mentioned in **Section 2.28**. Further, antigen unmasking was performed by immersing the re-hydrated tumor tissue sections in 10 mM sodium citrate buffer at sub-boiling temperatures (~ 80 °C) for 10 min. The slides were allowed to cool at room temperature. Later the slides were immersed in permeabilization solution (0.1 % triton X-100, 0.1 % sodium citrate) for 5 min. and further washed with TBST (Tris buffered saline with Tween 20). The slides were blocked with 5 % normal goat serum (NGS) for 2 h at room temperature followed by incubation with appropriate primary antibody (1:50 dilution in 5% NGS) at 4 °C for overnight. The slides were washed with TBST thrice for 5 min followed by incubation with Alexa Fluor 568 labeled anti-mouse secondary antibody for 2 h. The slides were again washed with TBST thrice followed by mounting with anti-fade containing DAPI (Moelcular probes, USA). The slides were observed by fluorescence microscopy at 40 X

magnification. To subtract fluorescence due to non-specific binding of secondary antibody, tumor sections were treated with only secondary antibody and their mean fluorescence intensity (MFI) values were subtracted from the MFI of tumor sections treated with primary as well as secondary antibody. Fluorescence intensity was measured by using Image J software and expressed as MFI per field. The values were normalized with fluorescence intensity of DAPI and fold change was calculated as MFI of treated tumors/MFI of control tumors.

2.31 Preparation of tumor tissue lysates and Western Blotting

For preparation of tumor tissue lysates and protein extraction, the frozen samples were thawed on ice and then transferred to a pre-chilled mortar. The tissue was crushed in presence of liquid nitrogen to a fine powder. The powder was re-suspended in lysis buffer (20 mM Tris-HCl, 150 mM NaCl, 1 mM EDTA, 1 mM IGEPAL, 1 % sodium lauryl sulphate, 1 mM PMSF, pH 7.5) and subjected to 5-7 freeze-thaw cycles with intermittent vortexing (viz. freezing in liquid nitrogen for 30 sec. followed by thawing in water for 1 min.). Once the lysates appeared clear, it was centrifuged at 4°C at 32,000 x g for 15 min. The protein content in tissue lysates was determined by using the BIO-RAD protein estimation kit following manufacturer's instructions. Samples of cells/tissue lysates (50 µg of protein) were then subjected to 10 % sodium dodecyl sulfate polyacrylamide gel electrophoresis and Western blotting (WB) using desired primary antibody (1:1000 dilution) and appropriate secondary antibody (1:4000 dilution) conjugated with horse radish peroxidase. The bound secondary antibody was detected using chemiluminiscent detection kit (Roche diagnostics, USA) and gel documentation sytem (Syngene, USA). The intensity of each band was quantified using Image J software. Antibodies against GAPDH (1:4000; CST) were used as loading controls. Intensity of each protein band was divided with respective

GAPDH band intensity. The ratio obtained were used to measure fold change with respect to control.

2.32 Measurement of tumor surface temperature using infra-red (IR) camera

The temperature rise at tumor surface was measured by a high-resolution infra-red (IR) camera (Thermal Imager testo 875-1, USA) and the images were analysed by thermography software (Testo IR Soft Software, Version 3.1). The mean temperature of tumor surface before and after exposure to AMF in both control and treated groups was measured.

2.33 Serum biochemistry and whole blood analysis

Serum samples were analyzed for the levels of creatinine, Alanine Transaminase (ALT), Alkaline Phosphatase (ALP) and total glucose using automated serum biochemical analyzer, Rx Daytona + (Randox, Kearneysville, WV, USA). For determination of levels of creatinine kinase-MB (CK-MB), ELISA based kit (Roche diagnostics, USA) was used. Whole blood parameters were measured using an automated blood analyzer (Randox, UK).

2.34 Statistical analysis

All *in vitro* experiments were conducted at least thrice in triplicates. All values are presented as Mean ± SEM and wherever required data was analyzed using Student's t-test. Statistical significance was determined at $p < 0.05$. All *in vivo* experiments were repeated at least twice with minimum 6 to 8 mice per group. All values are presented as Mean ± SEM and wherever required data was analyzed using Student's t-test. Statistical significance was determined at $P < 0.05$.

CHAPTER 3

RESULTS AND DISCUSSION

Section 3.1 : *In Vitro* and *In Vivo e*valuation of Hyperthermia efficacy and Radio-sensitizing potential of Iron oxide Magnetic Nanoparticles (MN-OA) in mouse fibrosarcoma

SECTION 3.1 *IN VITRO* AND *IN VIVO* EVALUATION OF HYPERTHERMIA EFFICACY AND RADIO-SENSITIZING POTENTIAL OF IRON OXIDE MAGNETIC NANOPARTICLES IN MOUSE FIBROSARCOMA

The present chapter evaluates the cancer cell killing efficacy of oleic acid coated iron oxide magnetic nanoparticles (MN-OA) in combination with either magnetic hyperthermia therapy (MHT) or γ-radiation. Underlying mechanisms of cancer cell killing in combination with MHT or gamma radiation (radio-sensitization) have also been elucidated. The role of HSP90 has been identified as a key molecular player for MN-OA induced enhanced killing of cancer cells either individually or in combination treatment with MHT/γ-radiation. Moreover, the *in vitro* observations have been validated and the underlying mechanism has also been studied in a murine fibrosarcoma tumor model.

Super-paramagnetic iron oxide nanoparticles (SPIONs) were synthesized by chemical co-precipitation method and further functionalized with oleic acid (OA), resulting in synthesis of MN-OA **(Chapter 2, Section 2.2)**. OA was used as a capping agent mainly for three reasons. Firstly, the hydrophobic nature of OA prevents the agglomeration of as-synthesized SPIONs due to their strong magnetic dipolar interactions. Secondly, OA is known to induce apoptosis in tumor cells[254] and thirdly, it may contribute in the process of radio-sensitization through generation of ROS via lipid peroxidation. Thus, MN-OA was synthesized and characterized as mentioned in **Chapter 2 Section 2.2 & 2.3** and used for further experiments. Wherever required, especially for treatment of cell cultures, MN-OA was dispersed in 0.1 M Na_2CO_3 (Sigma, 99.0 % purity) solution prepared in de-ionised water, followed by dilution in PBS (1:10). MN-OA forms

stable colloidal suspension in Na_2CO_3 (0.1 M) and the underlying reaction/interaction is as follows:

$$2CH_3(CH_2)_7CH=CH(CH_2)_7COOH + Na_2CO_3 \rightarrow 2CH_3(CH_2)_7CH=CH(CH_2)_7COO^- + Na^+$$

[Oleic acid] $+CO_2 + H_2O$ (1)

Addition of Na_2CO_3 helps in dissociation of COOH group of OA to COO^- and H^+. These ionized group/ions (COO^-) are useful in chemical interaction in polar medium (like water), where, Na^+ act as counter ions.

3.1.1 DETERMINATION OF HEAT GENERATION BY MN-OA UNDER ALTERNATING CURRENT (*AC*) MAGNETIC FIELD CONDITIONS

For hyperthermia therapy applications, MN-OA should be able to raise the temperature of the cells to hyperthermia range (41-42 °C). To test the heating efficacy of MN-OA, 10 mg of the nanoparticles (MN-OA), were suspended in 1 ml (1.5 ml volume plastic centrifuge tube) of 0.1 M Na_2CO_3 buffer diluted in PBS (1:10), followed by placement of MN-OA suspension under *AC* magnetic field conditions (350 Oe magnetic field intensity, 400 A current and 265 Hz radio-frequency) for 10 min at room temperature using induction heating system (Easy Heat 8310, Ambrell, UK). The temperature of the suspension was measured using an optical sensor temperature probe (Photon Controls, USA). For this, probe was dipped in the centre of MN-OA suspension during induction heating and values were recorded in a display unit connected to the probe. Results showed a time dependent increase in the temperature of MN-OA suspension **(Fig. 3.1.1)**. The rise in temperature was rapid (reached 47.2 ± 1.4 °C in first 5 min.), followed by a slower increase in temperature in the next 5 min (reached a temperature of 52.5 ± 1.7 °C by 10

min). Hyperthermic temperature of 42 - 43 ^{o}C was attained at ~ 3 min, after application of the *AC* magnetic field. The SAR was calculated using the formula mentioned in **Chapter 2, Section 2.9,** and was found to be 66.09 Wg^{-1}.

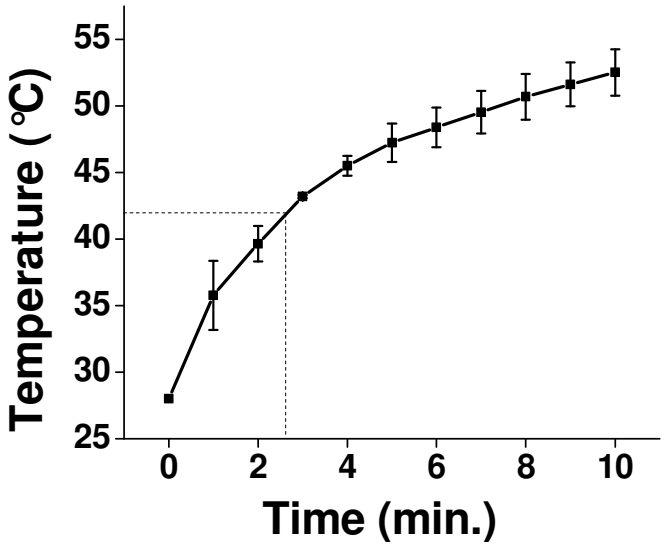

Fig. 3.1.1 *Time dependent change in temperature of MN-OA (10 mg/ml) under AC magnetic field conditions (350 Oe magnetic field intensity, 400 A, 265 kHz radio-frequency) for 10 min.*

3.1.2 CELLULAR INTERACTION AND CYTO-TOXICITY OF MN-OA

As mentioned in **Section 3.1.1**, MN-OA showed significant heating to hyperthermia temperature (42 °C) within 3 min of exposure to *AC* magnetic field conditions. Therefore, I evaluated its magnetic hyperthermia efficacy in WEHI-164 (murine fibrosarcoma) cancer cells. However, for efficient delivery of hyperthermia therapy to cancer cells, MN-OA should show significant internalization in cancer cells. Therefore, I also studied its internalization / interaction in WEHI-164 cancer cells by colorimetric assay and fluorescence based microscopy. The following sections discuss the cellular interaction and cyto-toxicity of MN-OA in combination with or without hyperthermia therapy.

3.1.2.1 MN-OA showed significant cellular interaction with WEHI-164 cells as studied by Prussian blue staining and fluorescence microscopy

For efficient magnetic hyperthermia therapy, MN-OA should have significant internalization inside the cancer cells. To determine their cellular interaction/internalization, MN-OA inside the cells was visualized by two methods. Firstly, the MN-OA localization in WEHI-164 cells was visualized by Prussian blue staining **(Fig. 3.1.2 A)** at 3 h post-treatment. However, due to the poor sensitivity of Prussian blue staining, a more sensitive fluorescence based detection method was also used. For this, the oleic acid component of MN-OA was stained by Nile blue A dye **(Fig. 3.1.2 B)**. Nile blue is known to spontaneously oxidize to a red and blue oxazine, out of which the blue oxazine is known to interact with phospholipids/free fatty acids and emit a red fluorescence after excitation at 488 nm[254]. Using Prussian blue and Nile blue A staining a significant internalization of MN-OA was observed in WEHI-164 cells. Nile blue staining showed increase in red fluorescence (as compared to control) in a concentration dependent manner in MN-OA treated cells and was mainly localized to membrane and cytoplasm. Whereas, OA treated controls (WEHI-164 cells treated with free OA at equivalent concentration to MN-OA-0.44 mg/ml) showed the red fluorescence mainly in the cytosolic region. For validation of these results, the uptake of MN-OA in WEHI-164 cells was also determined by Fe estimation by T-XRF method (as mentioned in **Chapter 2, Section 2.12.1**). For this, MN-OA treated WEHI-164 cells were harvested after 3h, followed by acid digestion of cells. Fe concentration in MN-OA treated cells was expressed in percentage considering the Fe content of equal concentration of MN-OA used for treatment as 100 %. The % internalization was found to be 44.8 ± 4.9 and 61.8 ± 1.2 % at 0.22 and 0.44 mg/ml treatment of MN-OA for 3 h, respectively **(Fig. 3.1.2 C)**.

A.

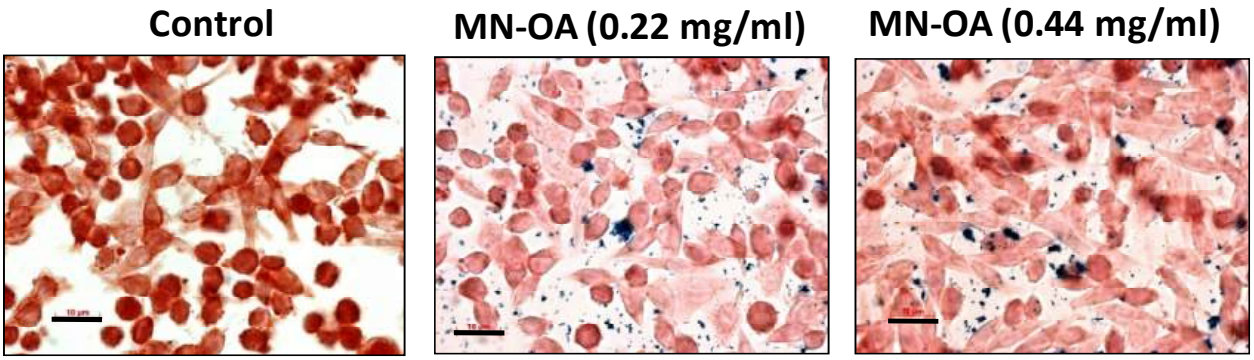
Control
MN-OA (0.22 mg/ml)
MN-OA (0.44 mg/ml)

B.

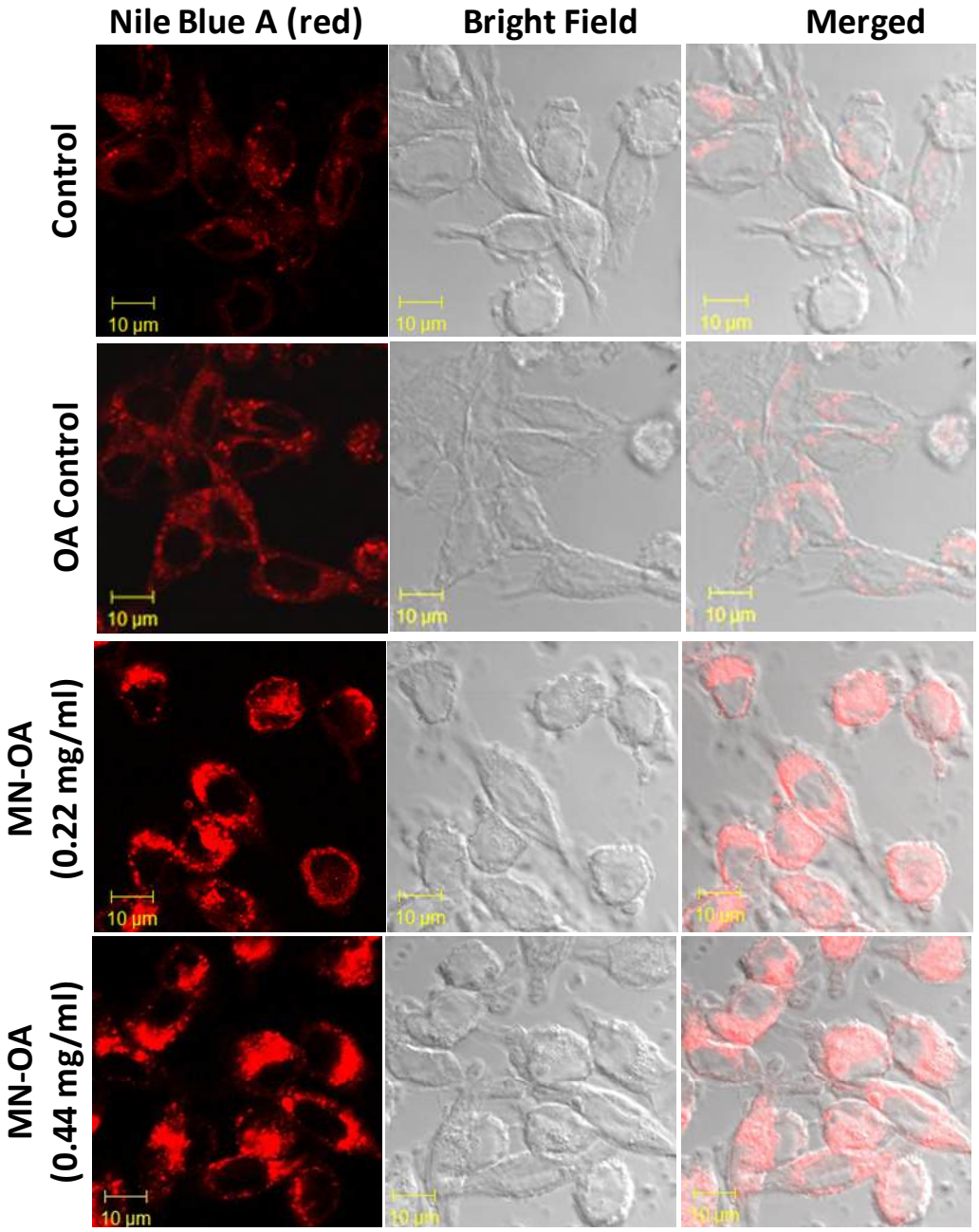
Nile Blue A (red)
Bright Field
Merged
Control
OA Control
MN-OA (0.22 mg/ml)
MN-OA (0.44 mg/ml)
10 µm

C.

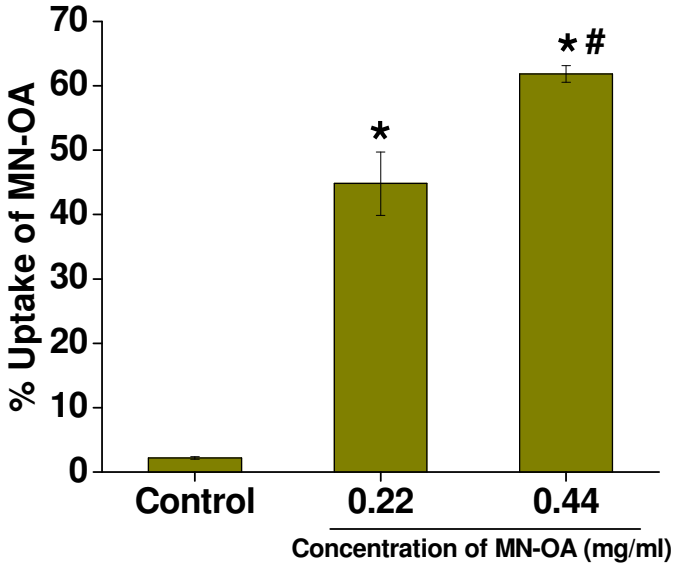

Fig. 3.1.2 ***(A)*** *Prussian blue staining of WEHI-164 cells at 3 h after treatment with MN-OA (Scale bar : 10 µm), dark blue spots show Fe localization,* ***(B)*** *Confocal laser scanning microscopy of WEHI-164 cells at 3 h post-treatment with free oleic acid (OA) at equivalent concentration to OA in MN-OA (same as 0.44 mg/ml) or 0.22 or 0.44 mg/ml concentrations of MN-OA (Scale bar : 10 µm). The red fluorescence was imaged at 488 nm excitation wavelength and 545 nm emission wavelength,* ***(C)*** *Percentage uptake of MN-OA in WEHI-164 cells as determined by total reflection X-ray fluorescence (T-XRF) method. * Significant at P<0.05 as compared to control and # indicates significant difference between 0.22 and 0.44 mg/ml of MN-OA treated WEHI-164 cells.*

3.1.2.2 MN-OA showed significant killing of cancer cells in a dose dependent manner as measured by trypan blue cell viability assay

Before studying the hyperthermia efficacy of MN-OA, firstly, the effect of different doses of MN-OA was evaluated on the cell viability of WEHI-164 cells by trypan blue cell viability assay. At lower concentration, *i.e.* 0.11 mg/ml, the cyto-toxicity didn't differ significantly (~ 3 to

% as compared to control) **(Fig. 3.1.3)**. However, at 0.22 and 0.33 mg/ml of MN-OA, the cyto-toxicity was found to be significantly increased to 21 ± 9 % and 38.35 ± 5.3 % and was further increased to 44.2 ± 5.1 % at 0.44 mg/ml concentration of MN-OA. These results suggest a threshold of MN-OA concentration required for induction of cell killing in WEHI-164 cells.

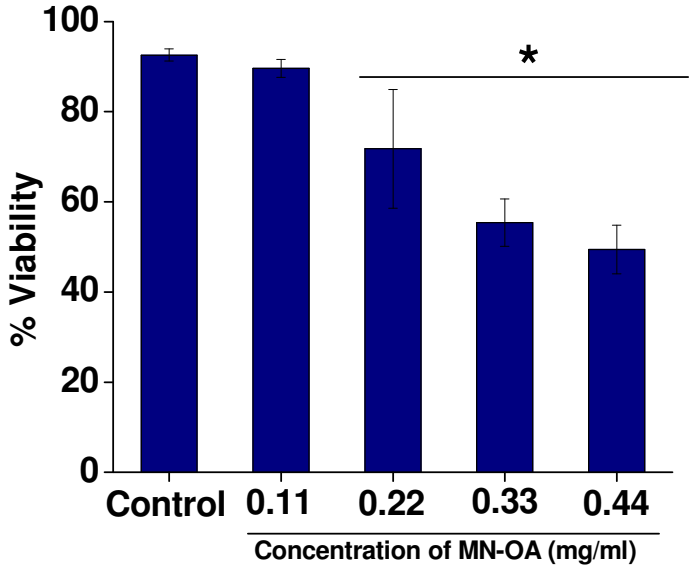

Fig. 3.1.3 *Determination of cell viability of WEHI-164 cells by trypan blue assay, after treatment with increasing concentrations (viz. 0.11, 0.22, 0.33 and 0.44 mg/ml) of MN-OA [dispersed in 0.1 M Na_2CO_3 diluted in PBS (1:10)] for 24 h.*

Rationale for combining MN-OA with MHT: SPIONs have been used for magnetic hyperthermia therapy applications due to their super-paramagnetic behaviour[184]. They can generate localized and focused heating inside the cells by different heating mechanisms when exposed to *AC* magnetic field conditions (as discussed in **Chapter 1, Section 1.4.8.3**). Therefore, after initial studies of cancer cell killing and internalization of MN-OA, the efficacy of nanoparticles in combination with hyperthermia was studied.

3.1.3 *IN VITRO* AND *IN VIVO* EVALUATION OF HYPERTHERMIA EFFICACY OF MN-OA

To determine the hyperthermia induced cancer cell killing efficacy of MN-OA, the effect of MN-OA treatment was evaluated in WEHI-164 cells subjected to *AC* magnetic field of 350 Oe, 400 A and 265 kHz radio-frequency for 10 min. The effect on cell viability and cell cycle were studied by trypan blue viability assay and PI staining based flow cytometry analysis, respectively. The contribution of apoptotic cell death was measured by cell death detection ELISA^{PLUS} kit.

3.1.3.1 MN-OA in combination with hyperthermia therapy showed significant killing of WEHI-164 cells

In order to evaluate the killing efficacy of MN-OA with or without hyperthermia treatment, % viability was determined by trypan blue assay in WEHI-164 cells treated with MN-OA ± MHT **(Fig. 3.1.4 A & B)**. Since, 0.22 and 0.44 mg/ml of MN-OA was found to induce lower and higher cell cyto-toxicity as studied earlier **(Fig. 3.1.3)**, these two concentrations were used for further experiments. WEHI-164 cells treated with 0.22 or 0.44 mg/ml of MN-OA showed a cell viability of 64.14 ± 0.24 and 59.2 ± 0.3 %, respectively at 24 h and was found to further decrease significantly to 53.44 ± 2.7 and 25.8 ± 1.5 %, respectively, when combined with hyperthermia therapy. The untreated control (92.03 ± 1.6 %) and hyperthermia control (90.2 ± 1.9 %) showed higher viability **(Fig. 3.1.4 B)**. *(Since, at 48 h time point, cellular clumping or aggregation increased in case of MN-OA + MHT treatment, trypan blue assay could not be performed reliably. Therefore data for 24 h is shown).* These results demonstrate the hyperthermia efficacy of MN-OA, which was found to be concentration dependent, with 0.44 mg/ml being the most

effective dose. WEHI-164 cancer cells treated with MN-OA (0.44 mg/ml) followed by MHT showed cellular detachment/rupture resulting in cellular debris **(Fig. 3.1.4 A)**

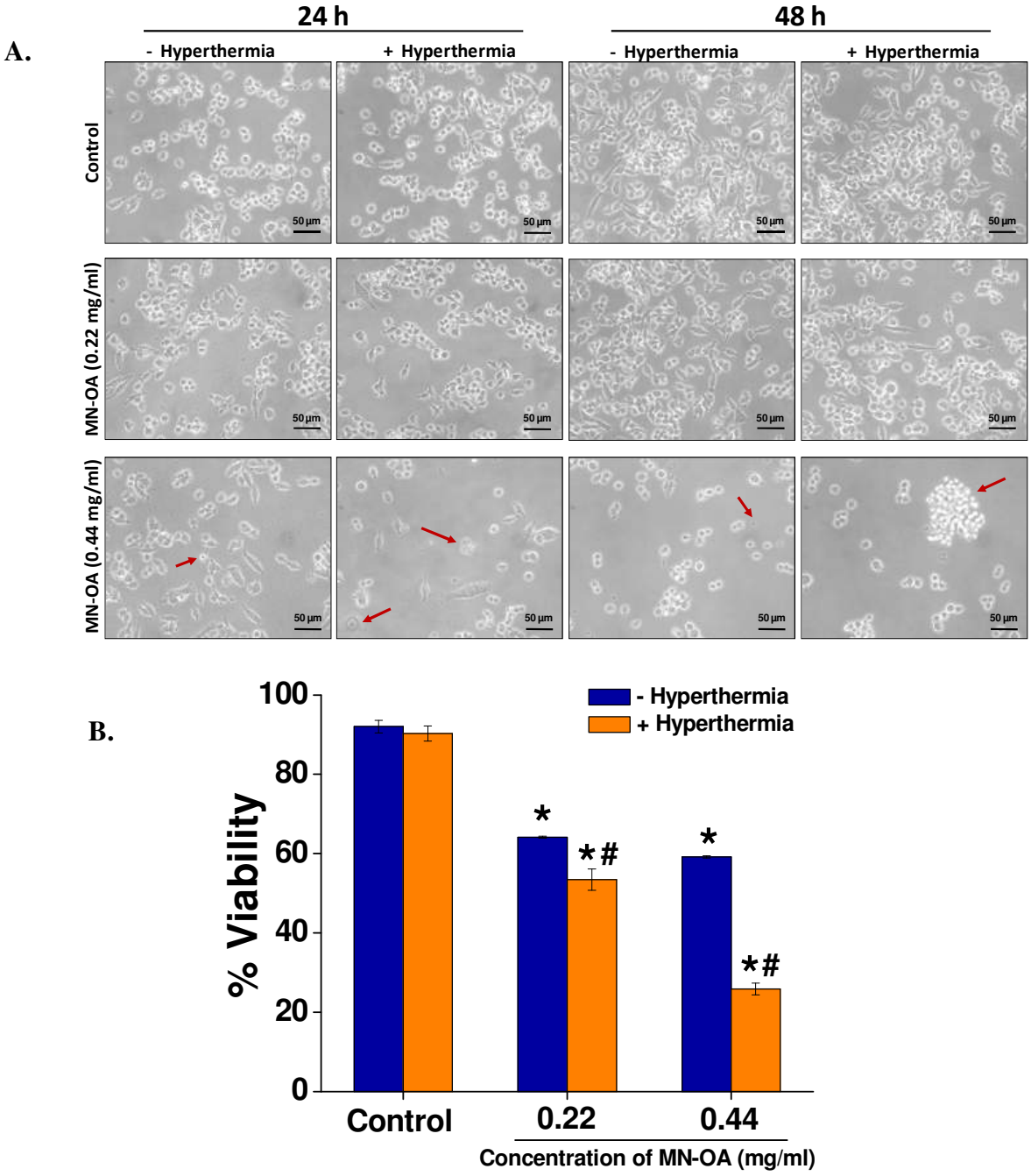

***Fig. 3.1.4** (A) Representative bright field microscopy images of WEHI-164 cells treated with 0.22 and 0.44 mg/ml concentration of MN-OA at 24 h and 48 h. Scale bar : 50 µm. Red arrows indicate cells showing apoptotic morphology (cell shrinkage, cell detachment and cellular*

debris). ***(B)*** *Cell viability at 24 h by trypan blue viability assay after treatment with MN-OA (0.22 or 0.44 mg) in combination with or without hyperthermia therapy (at 350 Oe magnetic field strength, 400 A AC current, 265 kHz radiofrequency for 10 min.). * Significant at P<0.05 as compared to control and # indicates significant difference between MN-OA treated groups in combination with or without hyperthermia therapy.*

3.1.3.2 MN-OA in combination with hyperthermia therapy showed significant modulation of cell cycle in WEHI-164 cells

To evaluate the hyperthermia efficacy of MN-OA, the effect of MN-OA (0.22 and 0.44 mg/ml) treatment in combination with or without magnetic hyperthermia therapy (MHT) was studied on different phases of cell cycle in WEHI-164 cells by PI staining based cell cycle analysis by flow cytometry. Briefly, WEHI-164 cells were treated with different concentrations of MN-OA, followed by replacing the nanoparticle containing medium with fresh media after 3h of treatment. The cells were further incubated at culture conditions for 24 and 48 h. The cell cycle distribution was studied by fixing the cells with ice cold methanol, followed by processing the cells for PI staining and acquiring by flow cytometry as mentioned in Materials and Methods **(Chapter 2, Section 2.14).** Results showed a significant increase in the sub-G1 population at 0.44 mg/ml (16.7 ± 1.2 %) concentration of MN-OA as compared to 0.22 mg/ml (4.7 ± 0.6 %) and control (3.22 ± 0.25 %). Moreover, the sub-G1 population was found to be further significantly increased in a concentration dependent manner in combination with hyperthermia therapy (H) to 8.9 ± 1.1 and 20.9 ± 0.2 %, respectively, for 0.22 and 0.44 mg/ml of MN-OA at 24 h, as compared to cells subjected to magnetic field only (H : 4.5 ± 0.2 %) **(Fig. 3.1.5 A)**. At 48 h, a significant increase in the G2-M population was observed at 0.44 mg/ml of MN-OA (34.9

± 1.1 %) as compared to control (21.17 ± 1.1) or only H (22.09 ± 2 %) treatments. However, the % cells in G2-M phase (36.4 ± 1.9 %), did not increase further significantly, in the combination treatment group (0.44 + H) **(Fig. 3.1.5 B)**.

A.

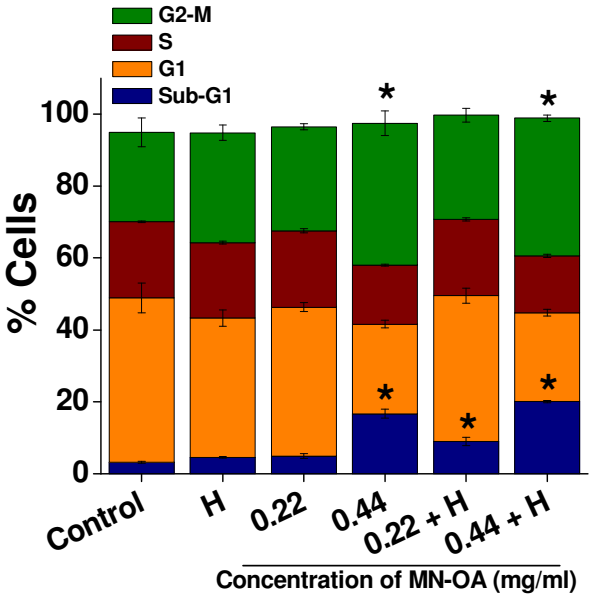

B.

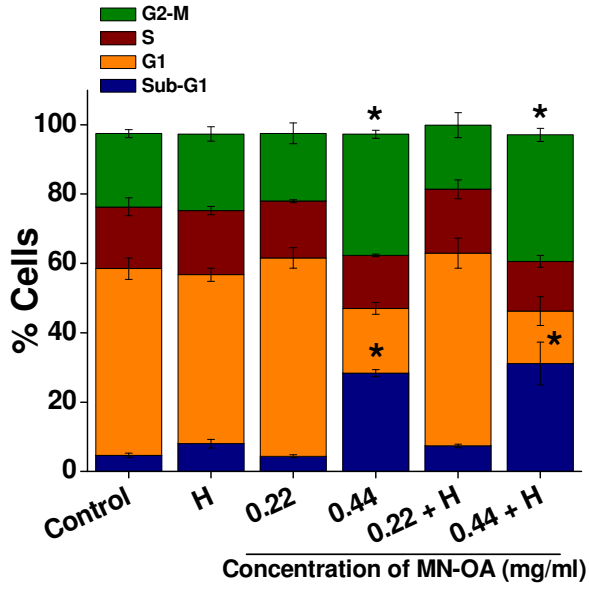

Fig. 3.1.5 *Distribution of WEHI-164 cells in different phases of cell cycle after treatment with different concentrations of MN-OA (0.22 and 0.44 mg/ml) at* ***(A)*** *24 and* ***(B)*** *48 h, respectively. (H: magnetic hyperthermia therapy). * Significant at P<0.05 as compared to control.*

3.1.3.3 MN-OA in combination with hyperthermia therapy showed significant increase in cell death by apoptosis

In order to further elucidate the mode of cell death in cancer cells after treatment with MN-OA, magnitude of apoptosis was determined using the Cell Death Detection ELISA^{PLUS} kit (**Fig. 3.1.6**). Compared to untreated control, the increase in relative apoptotic death was 2.7 ± 0.6 and 3.08 ± 0.3 fold, respectively in cells treated with 0.22 and 0.44 mg/ml of MN-OA. Whereas, after MHT, the relative apoptotic death was further enhanced significantly to 2.86 ± 0.1 and 4.85 ± 0.4 fold, respectively for cells treated with 0.22 and 0.44 mg/ml of MN-OA. These results indicate the role of apoptosis as one of the cell death mechanisms induced by MN-OA treatment in combination with MHT.

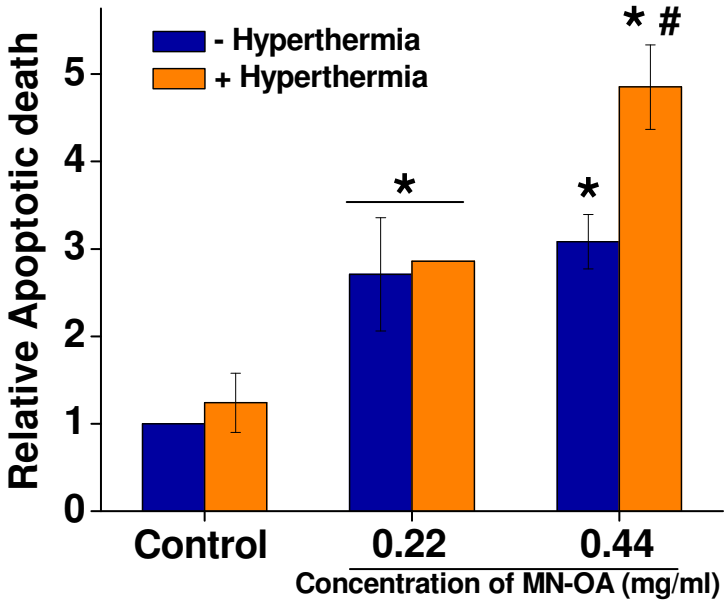

Fig. 3.1.6 *Relative apoptotic death after indicated treatments at 24 h. * Significant at P<0.05 as compared to control and # indicates significant difference between MN-OA treatment groups with or without magnetic hyperthermia therapy.*

3.1.3.4 MN-OA in combination with hyperthermia therapy induces down-regulation of HSP90 and its pro-survival client protein AKT

Conventionally, hyperthermia therapy is known to induce the expression of heat shock proteins (HSPs) in response to the heat stress[261]. However, very little is known in literature about the status of HSPs expression in response to MHT. Amongst HSPs, HSP90 is known to be elevated in several cancer cells and is an important target for cancer therapy. Moreover, structure of HSP90 in known to have large binding sites for hydrophobic residues[262]. Since, MN-OA has mainly hydrophobic character due to its oleic acid coat, some interaction may be possible between MN-OA and HSP90. Therefore, we determined the level of HSP90 in WEHI-164 cells after treatment with MN-OA ± MHT (H). Results showed a concentration dependent increase in the levels of HSP90 in cells treated with MN-OA, whereas, in case of MN-OA + H, a significant down-regulation of HSP90 was observed **(Fig. 3.1.7 A)**. Interestingly, MN-OA treatment showed a slight down-regulation of AKT, whereas in case of MN-OA + H treatment, the down-regulation of AKT was much more pronounced (1.5 and 5 fold decrease in the levels of HSP90 for 0.22 + H and 0.44 + H treatments, respectively). These results were suggestive of inhibition of HSP90 and subsequent down-regulation of its client protein (AKT). Therefore, to test this hypothesis we treated the WEHI-164 cells with a known small molecule inhibitor of HSP90, 17-AAG (17-N-allylamino-17-demethoxygeldanamycin). Interestingly, WEHI-164 cells treated with 17-AAG also showed up-regulation of HSP90 and down-regulation of AKT in a concentration dependent manner **(Fig. 3.1.7 B)**. These results further corroborate the MN-OA mediated inhibition of cellular HSP90 as one of mechanism playing a role in MHT induced cell death.

A.

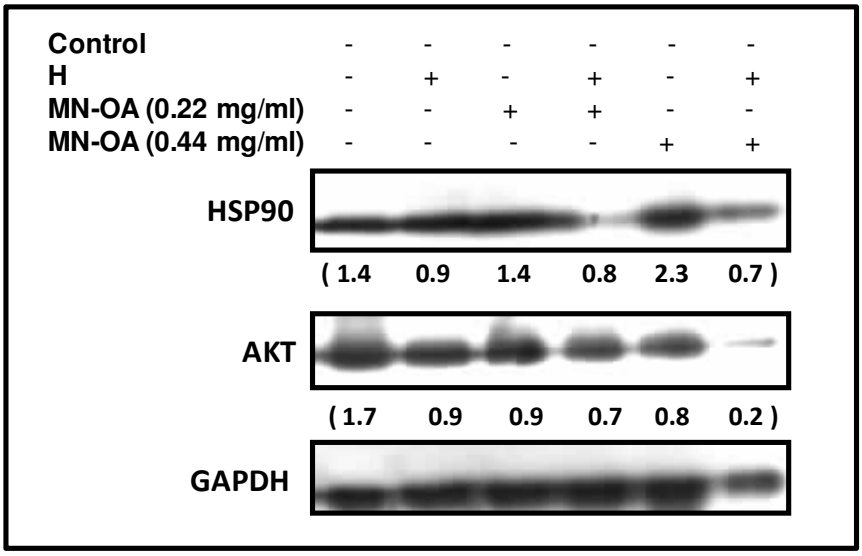

B.

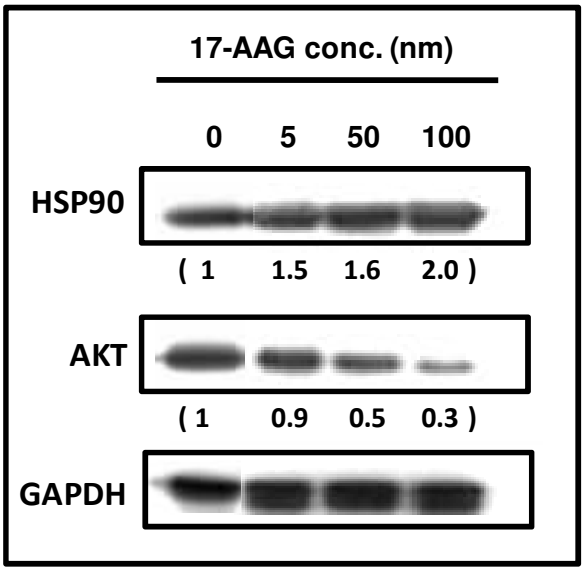

Fig. 3.1.7 (A) *Western blot analysis for expression of heat shock marker (HSP90) and cell survival marker (AKT) in WEHI-164 cells treated with MN-OA (0.22 and 0.44 mg/ml) or magnetic hyperthermia (H) or both. For MHT, cells were treated with 0.22 or 0.44 mg of MN-OA for 3 h followed by replacement of medium and exposure to AC magnetic field (350 Oe magnetic field intensity, 400 A, 265 KHz, 10 min.). Samples were harvested after 24 h and*

processed for Western blotting as mentioned in Materials and Methods. ***(B)*** *WEHI-164 cells were treated with increasing concentrations of 17-AAG (viz. 5, 50 and 100 nM) for 24 h followed by harvesting the cells for Western blotting. Values in parenthesis represent relative fold change in level of respective proteins as compared to control after normalizing with GAPDH.*

3.1.3.5 Validation of magnetic hyperthermia efficacy of MN-OA in murine fibrosarcoma tumor model

To determine the hyperthermic killing efficacy of MN-OA under *in vivo* conditions, fibrosarcoma tumor model was established in BALB/c mice **(Scheme 3.1.1)**. Briefly, 1 x 10^6 WEHI-164 cells were injected intra-muscularly in the right hind leg of BALB/c mice. Once the tumors were palpable (day 8, tumor diameter ~ 7-8 mm), MN-OA was injected intra-tumoraly at three distant spots in the tumor on day 8 and 10 (100 µl each, twice on each day, equivalent to total 1.76 mg of MN-OA per mice) followed by exposure to *AC* magnetic field (AMF) on days 8, 9, 10 and 11 **(Scheme 3.1.1)**.

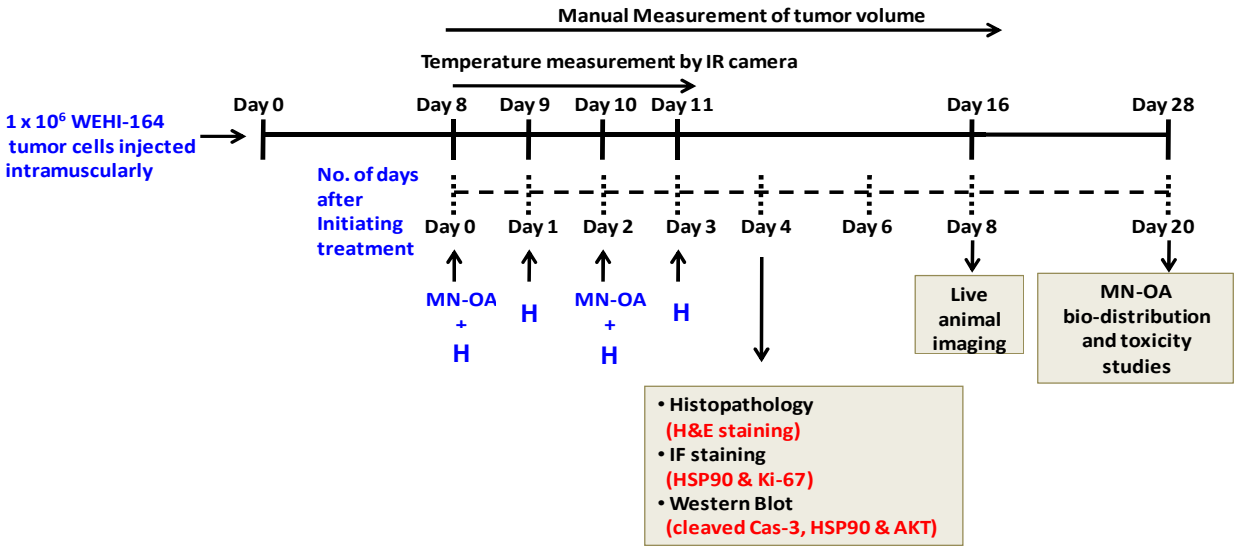

Scheme 3.1.1 *Schedule of MHT and analysis of tumor samples by different molecular techniques.*

When the tumor bearing mice were administered with MN-OA followed by MHT, it showed significant inhibition of tumor growth as determined by tumor volume measurement **(Fig. 3.1.8 A)**. Tumors treated either with MN-OA or MN-OA + H showed a significant ($P<0.05$) decrease in tumor growth kinetics and a tumor growth delay (TGD) of 1.5 and 3 days, respectively, as compared to control. However, there was no significant difference in the tumor volume of control and only hyperthermia (C + H) tumors upto 8th day of treatment. For a more sensitive measurement of tumor growth inhibition, stable transfectants of WEHI-164 cells expressing the luciferase enzyme, were transplanted into mice to obtain tumors. These animals were further subjected to MHT followed by *in vivo* imaging on day 8 after initiating the treatment. Tumors treated with MN-OA + H showed ~ 7 fold reduction in luminescence intensity as compared to control **(Fig. 3.1.8 B and C)**. Only MN-OA treatment and *AC* magnetic field (H) reduced the luminescence intensity by 1.5 and 1.2 fold, respectively.

A.

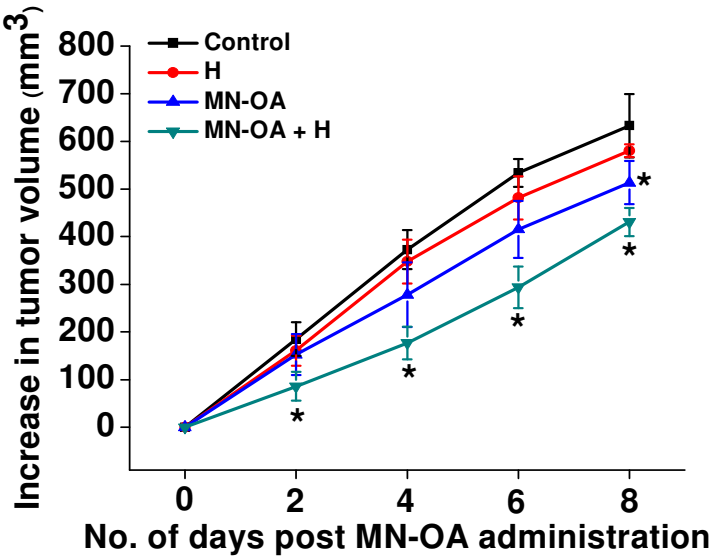

B.

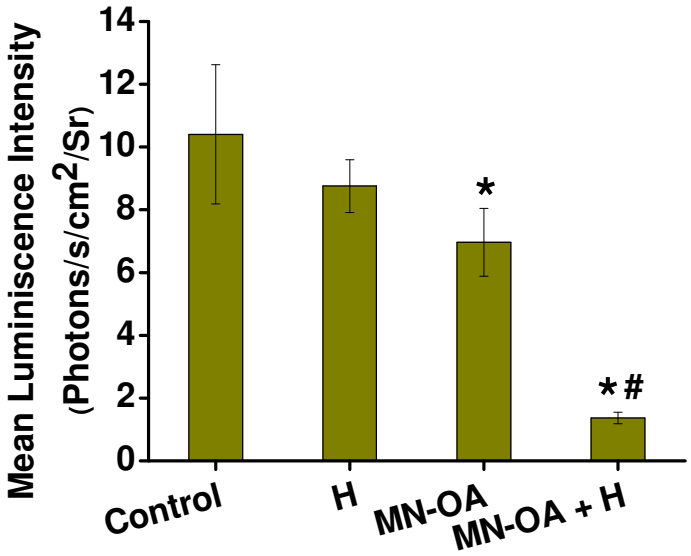

C.

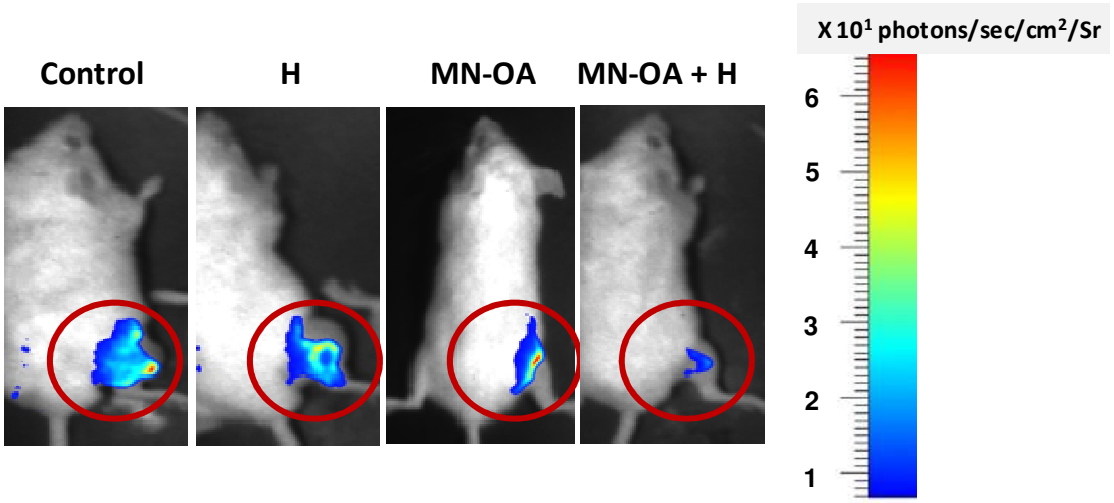

Fig. 3.1.8 ***(A)*** *Tumor growth kinetics after treatment with MN-OA with or without MHT measured by Vernier calliper (n=8).* ***(B)*** *WEHI-164 cells expressing the luciferase gene were transplanted in female BALB/c mice (n=6) to obtain tumors and further subjected to MHT. The luminescence intensity of tumors was measured on day 8 after initiation of treatment, using in vivo live animal imaging system (Photon Imager, Biospace Lab, France). Data is presented as Mean ± SEM, n=5. * Significant at P<0.05 as compared to control and # indicates significant difference between MN-OA treated groups with or without hyperthermia therapy.* ***(C)*** *Representative images of mice transplanted with luciferase expressing WEHI-164 cells by live in vivo animal imaging system on day 8 after indicated treatments.*

3.1.3.6 Thermal imaging showed increase in tumor surface temperature after MHT

As observed in **Fig. 3.1.8 A**, MN-OA + H showed higher anti-tumor efficacy as compared to only MN-OA. Therefore, we monitored the rise in tumor surface temperature using IR based thermal camera, just before and immediately after exposure of tumor bearing leg of mice to *AC* magnetic field. The temperature profile of the tumor region was determined using the Testo IRSoft thermography analysis software. Analysis of thermal images of treated tumors (MN-OA + H), captured immediately after MHT showed a significant temperature rise of ~ 3 ± 0.5°C ($P<0.05$) at the tumor surface as compared to control tumors exposed to *AC* magnetic field, which showed a lower temperature rise of 1.5 ± 0.4°C **(Fig. 3.1.9 A - D)**.

A.

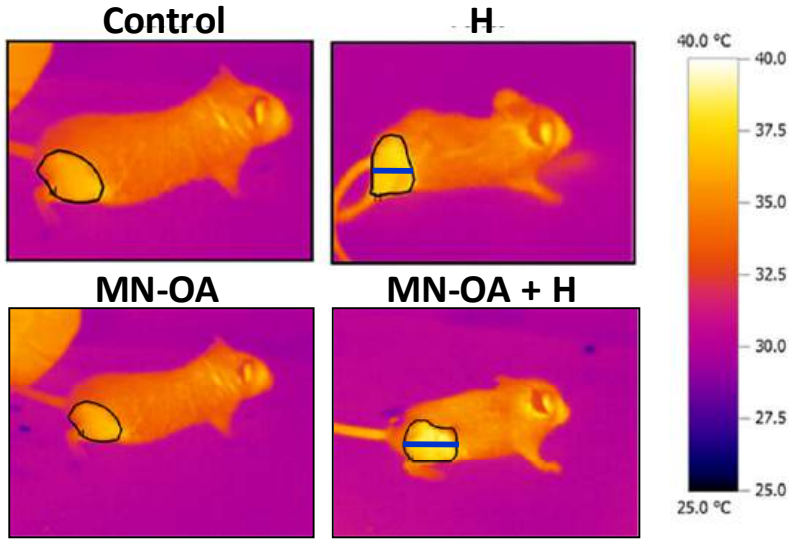

B.

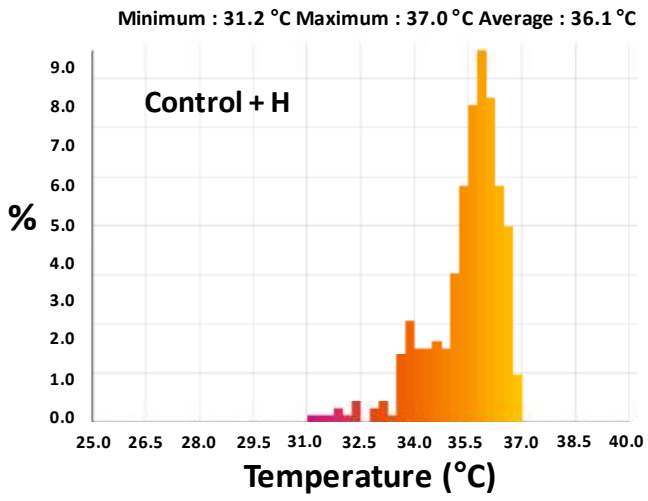

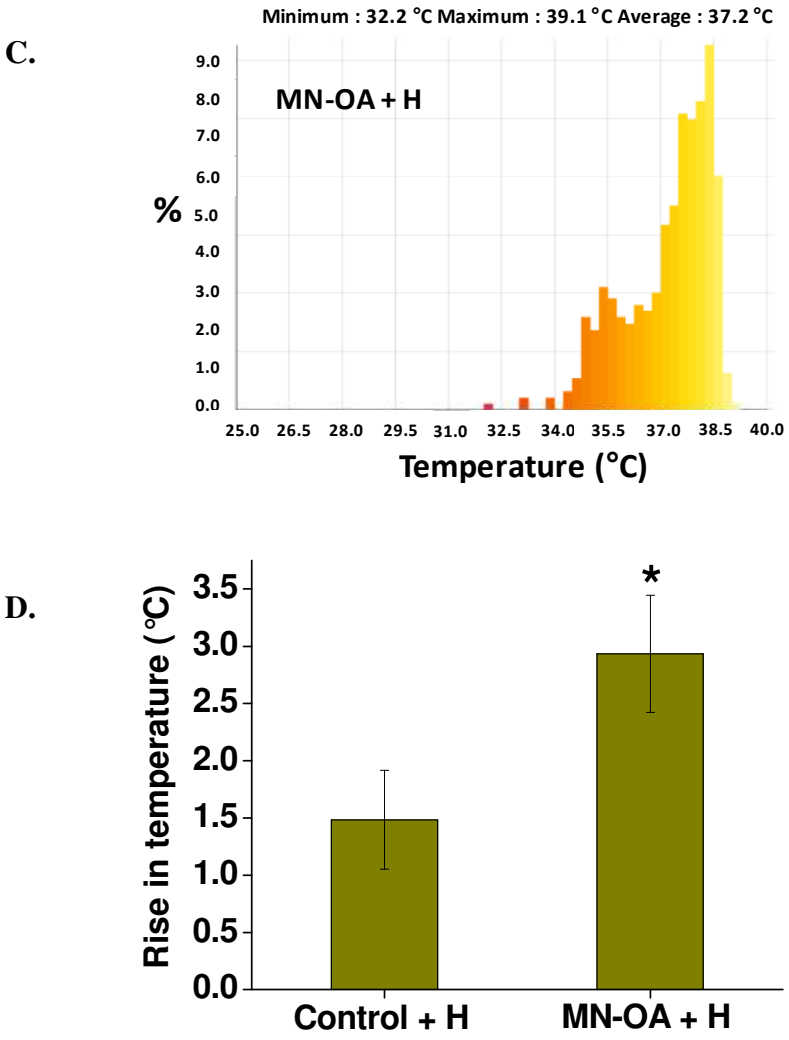

Fig. 3.1.9 *Measurement of tumor surface temperature using IR camera. (A) Representative images for temperature rise at surface of tumor region in mice treated with only AC magnetic field or MN-OA + H, before and after the therapy (blue line on the tumor region indicates the selected tumor region for determining the temperature distribution along the line using the Testo IRSoft thermography analysis software), (B) & (C) temperature distribution profile along the selected tumor region (indicated by blue line) for control and MN-OA treated mice, respectively, immediately after turning off the AC magnetic field. (D) Bar graph of temperature rise at the tumor region for control and treated mice. Values represent Mean ± SEM (n = 3) and * Significant at P<0.05 as compared to control.*

3.1.3.7 MN-OA ± H showed significant inhibition of tumor growth by induction of apoptosis

To determine the mechanism of tumor growth inhibition induced by MN-OA mediated MHT at tissue level, tumor tissue sections were processed by different molecular techniques. Histopathological analysis and immuno-fluorescence staining of tumor tissue sections for markers of apoptosis (TUNEL assay) and tumor cell proliferation (Ki-67), as well as Western blot analysis of tumor tissue lysates were performed. Histopathological analysis of control tumor tissue sections exhibited high mitotic index, mild apoptosis, mild hyperchromasia (increased staining intensity of cell nuclei) and anaplasia (reversion of cells to less differentiated state) with infiltration of polymorphonuclear immune cells. On the contrary, tumors treated with either MN-OA or MN-OA + H showed presence of moderate and severe apoptotic regions (fragmented nuclei stained with hematoxylin), respectively, along-with low mitotic index and moderate hyperchromasia and anaplasia **(Fig. 3.1.10 A)**. Results of TUNEL assay showed presence of severe apoptosis (69.3 ± 15.14 foci per field) in tumors treated with MN-OA + H, as against mild apoptosis in control (5.5 ± 0.07 foci per field) and C+H (3.5 ± 0.07 foci per field) tumors. In tumors treated with only MN-OA, moderate apoptosis (42 ± 2.0 foci per field) was observed **(Fig. 3.1.10 B)**. These results suggested the role of apoptotic cell death in MN-OA mediated MHT induced tumor growth inhibition. Furthermore, Western blot analysis showed enhanced level of expression of cleaved caspase-3 (~103 fold, average value of two mice) in tumors treated with MN-OA + H, but was substantially lower in tumors treated with only MN-OA or only *AC* magnetic field or control. Moreover, pro-survival marker, AKT and heat shock protein, HSP90 was found to be significantly down-regulated in MN-OA + H treatment groups **(Fig. 3.1.10 C)**.

This results are in agreement with our *in vitro* results, where WEHI-164 cells treated with MN-OA + H showed similar down-regulation of AKT and HSP90 **(Fig. 3.1.7 A)**.

A.

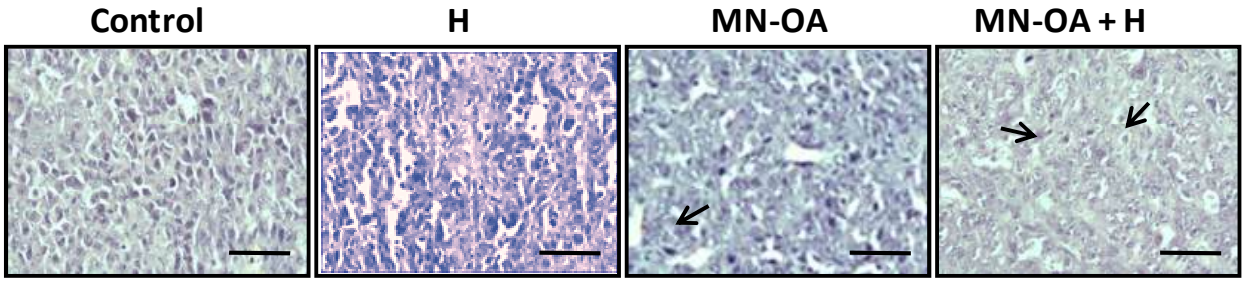

B.

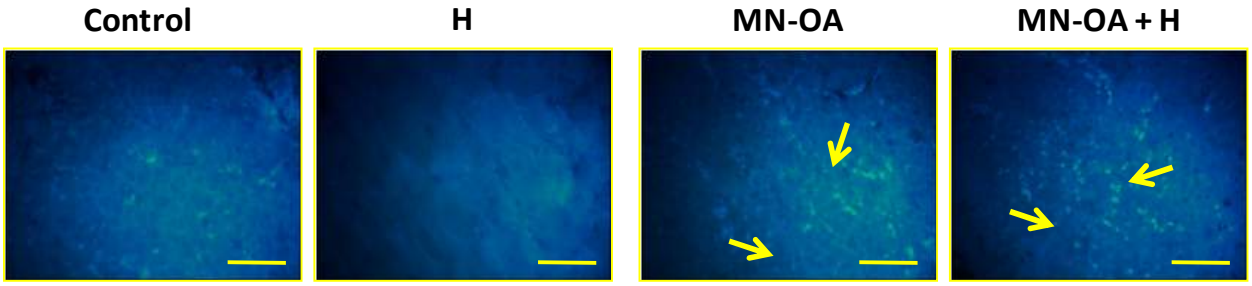

C.

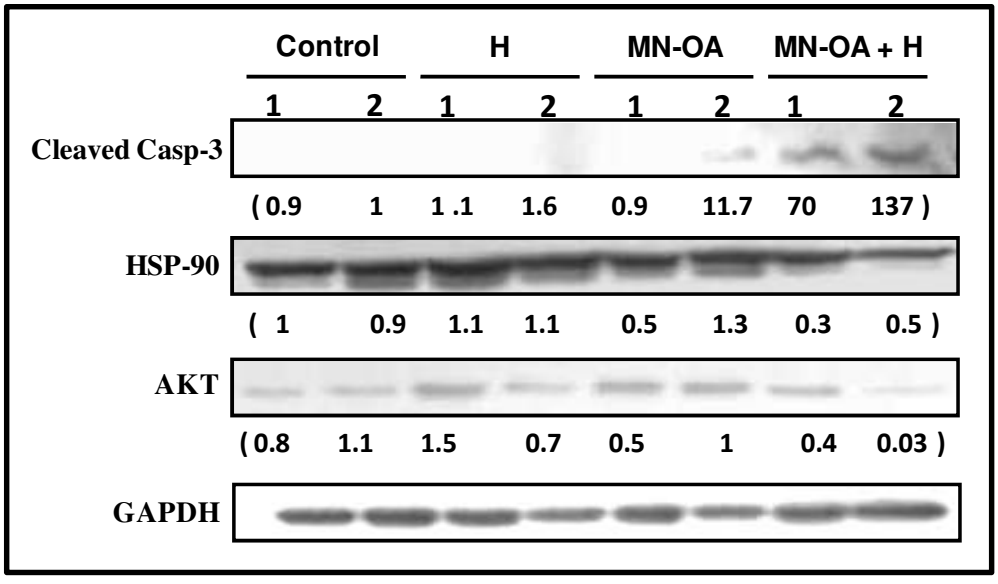

Fig. 3.1.10 (A) *Representative bright field microscopy images of tumor tissue sections subjected to indicated treatments and stained with hematoxylin and Eosin (H & E) to determine histopathological changes (magnification: 40X, Scale bar = 50 µm). Black arrows indicate tumor cells depicting apoptotic morphology* ***(B)*** *Representative fluorescence microscopy images of tumor tissue sections processed for TUNEL assay to determine the level of apoptosis after indicated treatments (Scale bar = 25 µm). Yellow arrows indicate TUNEL positive foci (green).* ***(C)*** *Western blot analysis for expression of apoptosis marker (cleaved caspase 3), heat shock marker (HSP90) cell survival marker (AKT/PKB) in tumor tissue lysates, on day 4 after initiating the treatment. Values in parenthesis represent relative fold change as compared to control after normalizing with GAPDH.*

3.1.4 *IN VITRO* AND *IN VIVO* EVALUATION OF RADIO-SENSITIZATION EFFICACY OF MN-OA

Rationale for combining MN-OA with radiation: Our results showed enhanced efficacy of MN-OA along with hyperthermia **(Section 3.1.3)**. Moreover, western blot experiments suggested modulation of intra-cellular HSP90, a chaperon protein involved in folding of several client proteins playing important role in cellular processes like cell cycle and DNA repair. Thus, MN-OA may contribute in radio-sensitization by down-regulating the HSP90 client proteins. SPIONs have been reported to induce radio-sensitization by oxidative stress due to presence of Fe^{2+} ions that can contribute in Fenton's reaction[263]. In addition, MN-OA has oleic acid as a capping agent, which is a mono-unsaturated fatty acid and can contribute to oxidative stress through lipid peroxidation. Moreover, oleic acid has been reported to induce apoptosis in cancer cells[254]. Hence, the radio-sensitization efficacy of MN-OA was studied in murine fibrosarcoma cells in combination with gamma radiation.

3.1.4.1 MN-OA inhibits proliferation of Human (HT-1080) and murine (WEHI-164) fibrosarcoma cells in combination with radiation

Effect of MN-OA treatment in combination with γ-radiation was studied in terms of cell proliferation of human (HT-1080) and mouse (WEHI-164) fibrosarcoma cell lines. **Table 3.1.1** shows the anti-proliferative activity of MN-OA at different concentrations (0.33 and 0.55 mg/ml) alone or in combination with gamma-radiation (2 Gy) in WEHI-164 and HT-1080 cells, as measured by MTT assay. MN-OA treatment itself reduced proliferation of HT-1080 and WEHI-164 cells in a concentration-dependent manner. Combination treatment of MN-OA with 2 Gy further inhibited the proliferation of both the cell lines as compared to individual treatments of

either MN-OA (at respective concentration) or 2 Gy. WEHI-164 cells were found to be resistant to radiation than the HT1080. Moreover, MN-OA in combination with 2 Gy, at all the tested concentrations produced significant anti-proliferative effect in WEHI-164 cells. WEHI-164 cells being syngenic to BALB/c mice, an immuno-competent fibrosarcoma tumor model could be established for evaluation of radio-sensitizing efficacy of MN-OA under *in vivo* scenario. Moreover, due to the immuno-competency, these tumor model can be easily handled for local tumor irradiation. For these reasons, WEHI-164 cancer cell model was selected for further *in vitro* experiments to determine the radio-sensitization efficacy of MN-OA and its underlying mechanism.

Treatment Groups	% Proliferation (MTT assay)	
	HT-1080	WEHI-164
	Average ± SD	Average ± SD
Control	100 ± 8.4	100 ± 0.7
2 Gy	88.6 ± 4.7	96.7 ± 2.7
MN-OA3	90.1 ± 4.2	96.2 ± 4.8
MN-OA3 + 2 Gy	43.2 ± 3.5*	88.5 ± 5.9*
MN-OA5	44.9 ± 4.4*	91.5 ± 5.1
MN-OA5 + 2 Gy	34.4 ± 0.8*	58.9 ± 7.1*

Table 3.1.1 *Effect of different concentrations of MN-OA either alone or in combination with gamma-radiation (2 Gy) on proliferation of human (HT1080) and murine (WEHI164) fibrosarcoma cells after 120 h of treatment. Data represents Mean ± SD from three independent replicates. MN-OA3 : 0.33 mg/ml of MN-OA, MN-OA4 : 0.44 mg/ml, MN-OA5 : 0.55 mg/ml. *Significantly different at $p<0.05$ as compared to control.*

3.1.4.2 MN-OA inhibits clonogenic survival of WEHI-164 cells in combination with gamma radiation

To evaluate the radio-sensitizing ability of MN-OA, WEHI-164 cells were treated with increasing concentrations of MN-OA (viz. 0.33, 0.44 and 0.55 mg/ml of MN-OA and referred to as MN-OA3, MN-OA4 and MN-OA5, respectively) in combination with 2 Gy of gamma radiation. Clonogenic assay was used to determine the radio-sensitizing potential of MN-OA in WEHI-164 cells. As compared to control, cancer cells treated with MN-OA3, MN-OA4 and MN-OA5 showed 78.4 ± 3.6, 80.9 ± 2.9 and 60.7 ± 3.1 % survival, respectively. Whereas cells treated with 2 Gy showed 54.1 ± 2.2 % clonogenic survival. (Values of treatment groups were normalized with control, considering it as 100 %). However, WEHI-164 cells treated with combination treatments viz. 0.33 + 2 Gy, 0.44 + 2 Gy and 0.55 + 2 Gy showed 45.2 ± 3.2, 34.2 ± 3.4 and 9.4 ± 1.9 % survival, respectively **(Fig. 3.1.11 A & B)**. Furthermore, the survival curve of irradiated (2, 4 or 6 Gy) WEHI-164 cells treated with or without MN-OA5 is shown in **Fig. 3.1.11 C**. Results showed that MN-OA significantly ($P<0.05$) decreased the survival fraction of irradiated cancer cells. To achieve 90 % decrease in survival fraction, radiation dose required was decreased from 4.9 Gy in MN-OA treatment group to 2.2 Gy in MN-OA + 2 Gy [dose enhancement factor (DEF) of 2.2]. These results suggest the radio-sensitizing ability of MN-OA in WEHI-164 cells. The survival curves were found to fit significantly (R^2 = 0.958 to 0.978) to the linear-quadratic equation and parameters α and β were also determined. **Table 3.1.2** shows a summary of LQ parameters. The value of α parameter was found to be significantly increased (~ 3 fold, p=0.008) from 0.134 ± 0.076 Gy^{-1} in 2 Gy alone to 0.448 ± 0.073 Gy^{-1} in MN-OA5 + 2 Gy. However, the quadratic parameter, β was found to be decreased from 0.104 ± 0.015 Gy^{-2} in 2 Gy alone to 0.054 ± 0.016 Gy^{-2} in combination treatment. The increase in α and decrease in β

parameter is suggestive of an enhanced direct potentially lethal damage (PLD). Since, 0.55 mg of MN-OA in combination with 2 Gy resulted in maximum decrease in clonogenic survival of WEHI-164 cells, this concentration was used for further experiments and unless otherwise stated is hereafter referred as '*MN-OA*'.

A.

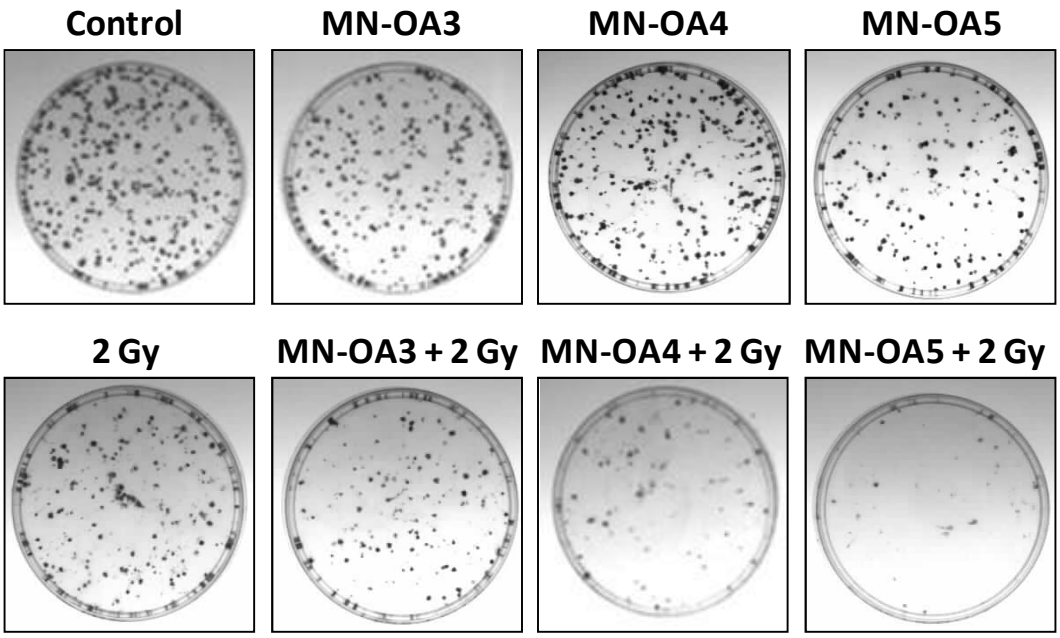

B.

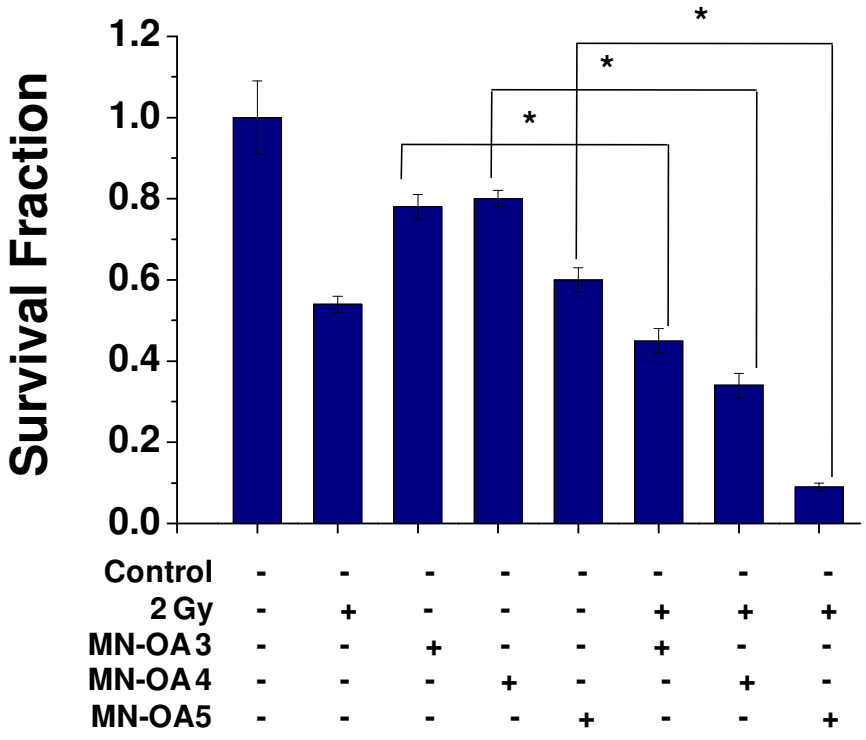

C.

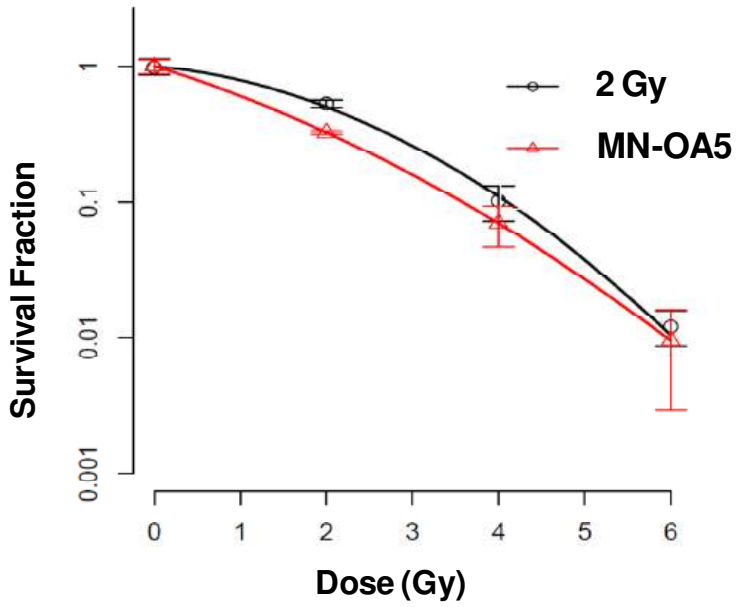

Fig. 3.1.11 *MN-OA in combination with 2 Gy induces significant decrease in the clonogenic survival of WEHI-164 cells.* ***(A)*** *Representative images for clonogenic survival of different treatment groups.* ***(B)*** *Percentage survival of WEHI-164 cells after treatment with different doses of MN-OA (0.33, 0.44 or 0.55 mg which corresponds to MN-OA3, MN-OA4 and MN-OA5, respectively) and/or 2 Gy of γ radiation alone and in combination.* ***(C)*** *Survival curves of WEHI-164 cells treated with MN-OA5 and/or different doses of γ radiation (2-6 Gy) alone and in combination. * Significantly different at P<0.05.*

	2 Gy	**MN-OA5 + 2 Gy**
α (Gy^{-1})	0.134 ± 0.076	0.448 ± 0.073*
β (Gy^{-2})	0.104 ± 0.015	0.054 ± 0.016*
α/β	1.289 ± 0.913	8.194 ± 3.66*
R squared	0.958	0.978

Table 3.1.2 *Values of linear-quadratic parameters α, β and α/β ratio obtained from the analysis of survival curves of murine fibrosarcoma cells (WEHI-164) treated with different doses of gamma-radiation alone or in combination with MN-OA5.Analysis was done using the RAD-ADAPT software. * Significant difference at P<0.05 as compared to 2 Gy.*

3.1.4.3 MN-OA induces G2-M arrest in WEHI-164 cells in combination with gamma radiation

To determine the mechanism of MN-OA induced radio-sensitization, cell cycle analysis was carried out by PI staining followed by flow cytometry. WEHI-164 cells were treated with 0.55 mg/ml of MN-OA without or with 2 Gy, followed by cell cycle analysis at 24 and 48 h. At 24 h, a significant increase in % cells in sub-G1 was observed in case of cells treated with MN-OA (17.9 ± 2.1 %) or combination treatment (22.8 ± 3 %) as compared to control (2.2 ± 0.3 %) or radiation (2.6 ± 0.4 %) **(Fig. 3.1.12 A)**. This was also accompanied by a slight decrease in G1, S and G2-M population for cells treated with MN-OA or MN-OA + 2 Gy as compared to control **(Fig. 3.1.12 A)**. However, after 48 h, the % cells in sub-G1 did not change significantly in the different treatment groups, viz. 2 Gy (8.2 ± 1.2 %) or MN-OA (7.3 ± 0.3 %) as compared to control (6.6 ± 1.8 %). Combination treatment showed significant change in sub-G1 (11.09 ± 1.7 %), albeit it was lower than at 24 h. Interestingly, after 48h, % cells in G2-M phase significantly increased from 28.1 ± 2.03 % in control to 32.4 ± 0.4 % and 33.6 ± 2 %, in MN-OA or MN-OA + 2 Gy treatments, respectively **(Fig. 3.1.12 B)**. To ascertain the induction of G2-M arrest, the effect of MN-OA or combination treatment on the levels of Cyclin B1 and CDC2 (markers of G2-M arrest) proteins was determined by Western blotting **(Fig. 3.1.12 C)**. Compared to control, a significant decrease in the levels of Cyclin B1 and CDC2 was observed in WEHI-164 cells

treated with MN-OA alone or combination treatment at 24 h. Since, both Cyclin B1 and CDC2 are known to be bonafide client proteins of HSP90, the level of HSP90 was determined after treatment with MN-OA or MN-OA + 2 Gy. Interestingly, the levels of HSP90 were found to be increased in case of both MN-OA and combination treatments as compared to control or radiation, suggesting an inhibition of HSP90, as observed previously (**Section 3.1.3.4 and Fig. 3.1.7**). Thus, probably the inhibition of HSP90 by MN-OA might have induced the down-regulation of its client proteins (viz. Cyclin B1 and CDC2), thereby resulting in arrest of cells in G2-M phase.

A.

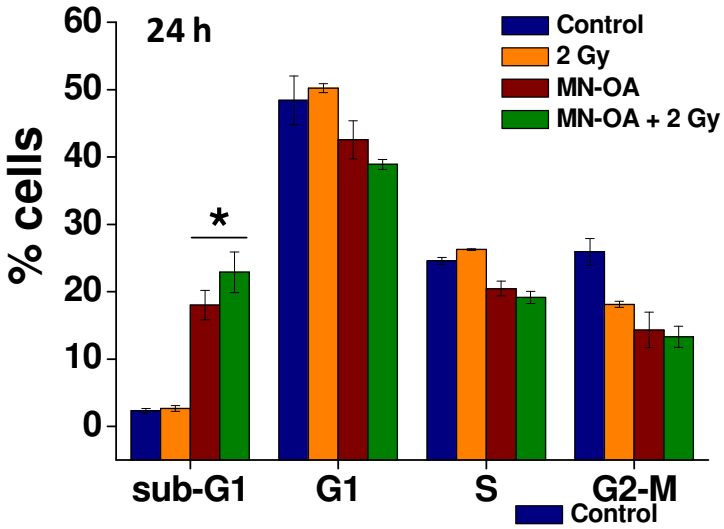

B.

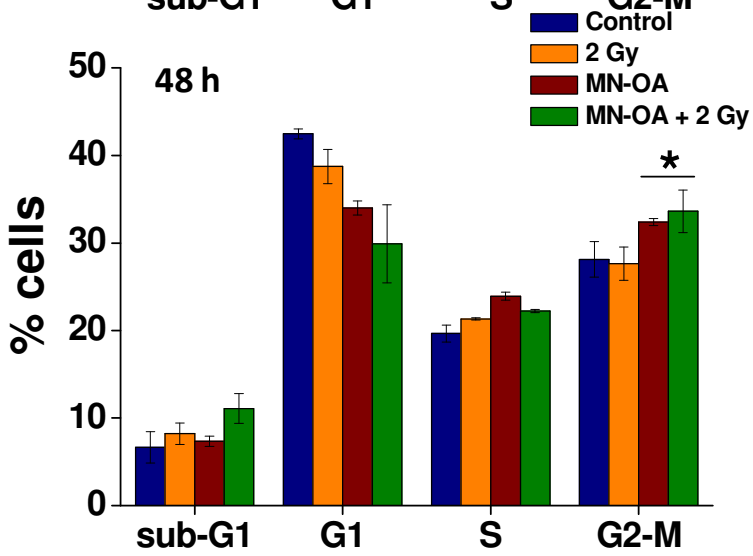

C.

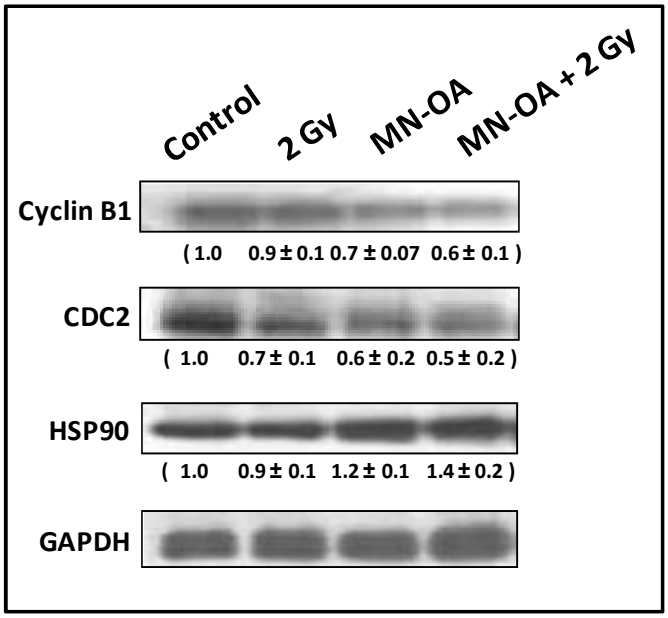

Fig. 3.1.12 *Cell cycle analysis at* ***(A)*** *24 and* ***(B)*** *48 h in WEHI-164 cells treated with MN-OA and 2 Gy alone or in combination, * Significantly different at P<0.05 as compared to control.* ***(C)*** *Western blot analysis of WEHI-164 cells after various treatments for determining the levels of G2-M cell cycle proteins (Cyclin B1 and CDC2) and HSP90. Values in parenthesis represent fold change compared to control after normalizing with GAPDH.*

3.1.4.4 MN-OA in combination with 2 Gy induces apoptosis at late time points

To study the mechanism of cell death induced by MN-OA in combination with 2 Gy, annexin V/PI staining assay was employed to determine the magnitude of apoptosis. Once the cells were stained with annexin V and PI staining kit (Roche diagnostics, USA), the measurement of early apoptotic (annexin-V-FITC positive cells), late apoptotic (annexin-V-FITC and PI positive cells) and necrotic (PI positive cells) cells was carried out at different time points (24, 72, 96 and 144 h) using fluorescence microscopy. Results showed that as compared to 2 Gy, combination treatment (MN-OA + 2 Gy) did'nt cause a significant increase in percentage of apoptotic/necrotic

cells at 24 h and 72 h. However, at later time point (96 h), combination treatment showed a significant ($P<0.05$) increase in the percentage of late apoptotic cells (58.13 ± 1.86 %) as compared to 2 Gy (25.1 ± 1.1 %), MN-OA (15.7 ± 2.8 %) or control (3.6 ± 0.6 %). At 144 h also, cells treated with combination treatment showed a significant increase in the percentage of late apoptotic cells (19.9 ± 2.2 %) as compared to 2 Gy (9.5 ± 2.8 %) or MN-OA (2.8 ± 0.9) or control (11.9 ± 2.9 %) **(Fig. 3.1.13 A to D)**. These results enticed us to understand the pathway or events (e.g. mitotic catastrophe) through which late apoptosis occurred in WEHI-164 cells treated with MN-OA + 2 Gy.

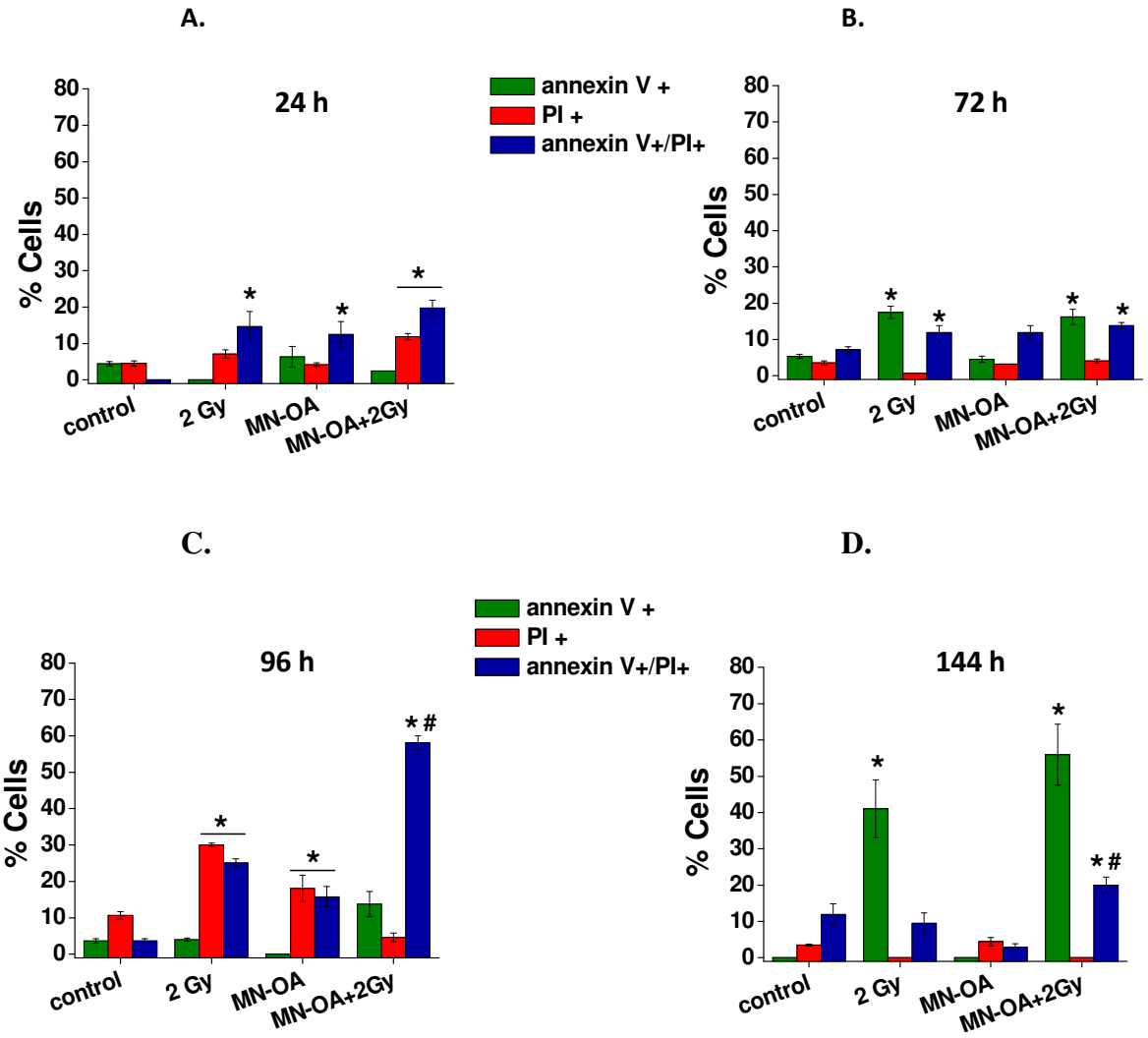

Fig. 3.1.13 *Determination of percentage apoptosis in WEHI-164 cells treated with MN-OA and/or 2 Gy at* ***(A)*** *24,* ***(B)*** *72,* ***(C)*** *96 and* ***(D)*** *144 h by annexinV/PI staining. * Significantly different at P<0.05 as compared to control and # significantly different at P<0.05 as compared to 2 Gy treatment.*

3.1.4.5 Combination treatment showed presence of few senescent cells

Since, MN-OA in combination with 2 Gy gamma radiation induced cell death at late time points, possibility of alternate cell death mechanisms (such as senescence) which might be playing a role in MN-OA induced radio-sensitization, was studied. For this, the WEHI-164 cells were stained for β-galactosidase activity using senescence staining kit (Roche diagnostics, USA). Results showed presence of a few senescent cells in combination treatment group (~ 2 fold) as compared to control or individual treatments (viz. 1.1 and 1.5 fold in 2 Gy and MN-OA treatments, respectively) **(Fig. 3.1.14)**. Typically, the cells with increased beta-galactosidase activity also showed an enlargement in size and increase in the number of cellular extensions. Moreover, the total cell number was also found to be decreased in MN-OA and MN-OA + 2 Gy treatments as compared to control or 2 Gy.

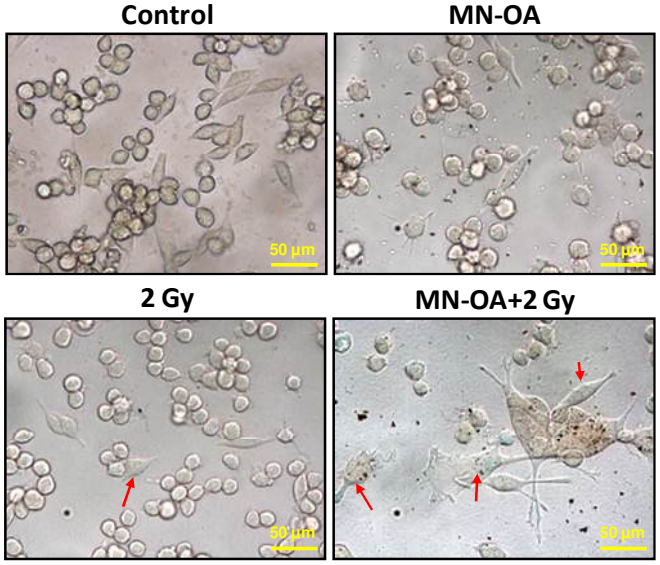

Fig. 3.1.14 *WEHI-164 cells stained for β-galactosidase activity using senescence staining kit. Red arrows indicate senescent cells (stained blue). Scale bar = 50 μm.*

3.1.4.6 Role of mitotic catastrophe in MN-OA induced radio-sensitization

In addition to senescence, another cell death mechanism which is usually followed by G2-M arrest is mitotic catastrophe[255]. As observed in **Section 3.1.4.3**, WEHI-164 cells treated with MN-OA or MN-OA + 2 Gy, showed induction of G2-M arrest at 48 h **(Fig. 3.1.12 A-C)**. Therefore, the expression of markers of mitotic catastrophe was studied in these treatment groups to ascertain its contribution to the observed cell death and decreased cell proliferation. Mitotic catastrophe was measured by quantification of polyploid cells (with > 2 nuclei) by DAPI staining and determination of the expression level of α-tubulin by immuno-cytochemistry. Results showed that the cells treated with MN-OA + 2 Gy exhibited a significant increase in the percentage of polyploid cells at the late time points (96 h and 144 h) as observed by staining the nuclei with DAPI **(Fig. 3.1.15 A)**. These results were further corroborated by the presence of multiple spindle poles in cells treated with combination treatment as visualized by staining with α-tubulin antibody **(Fig. 3.1.15 B)**. Furthermore, quantification/analysis of percentage of polyploid cells was carried out in ~ 500 cells per treatment group. Analysis at 96 h showed that as compared to control (3.2 ± 0.9 %), 2 Gy (10.5 ± 1.9 %) or MN-OA (7.3 ± 0.8 %) treatments, WEHI-164 cells treated with MN-OA + 2 Gy showed significant ($P < 0.05$) increase (17.5 ± 0.9 %) in the percentage of cells with > 2 nuclei **(Fig. 3.1.15 C)**. At 144 h, the polyploidy was further increased to 22 ± 1.09 % in case of combination treatment **(Fig. 3.1.15 D)**. These results indicate that mitotic catastrophe may be one of the possible modes of cell death through which MN-OA conferred radio-sensitization in WEHI-164 cells.

A.

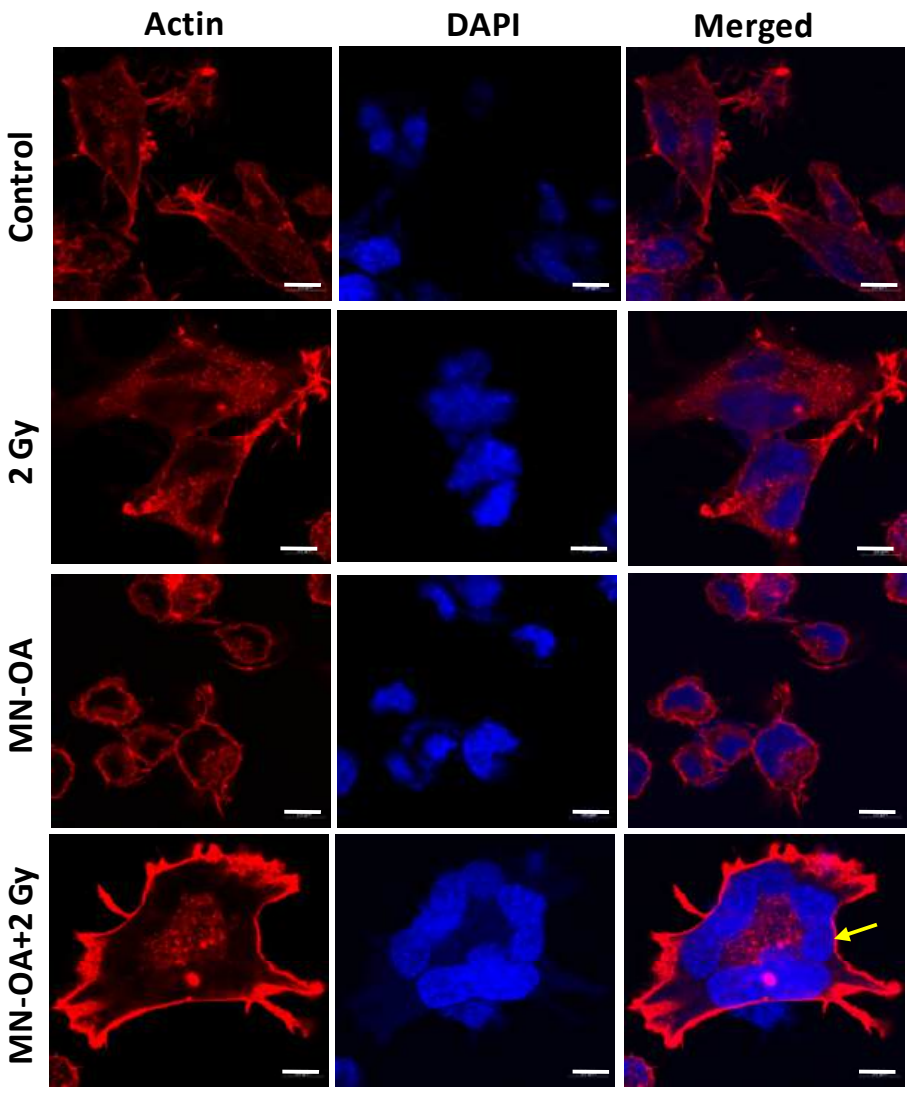

B.

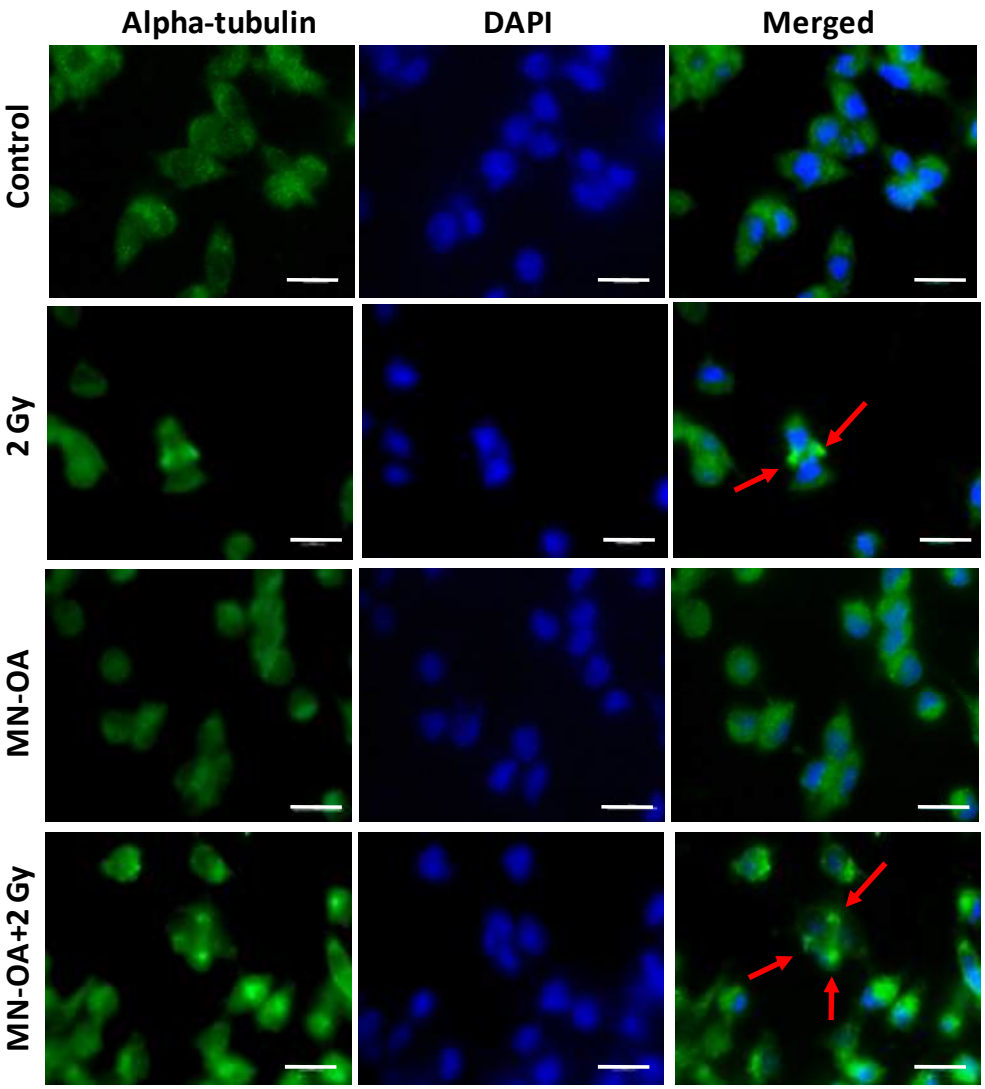
Alpha-tubulin
DAPI
Merged
Control
2 Gy
MN-OA
MN-OA+2 Gy

C.

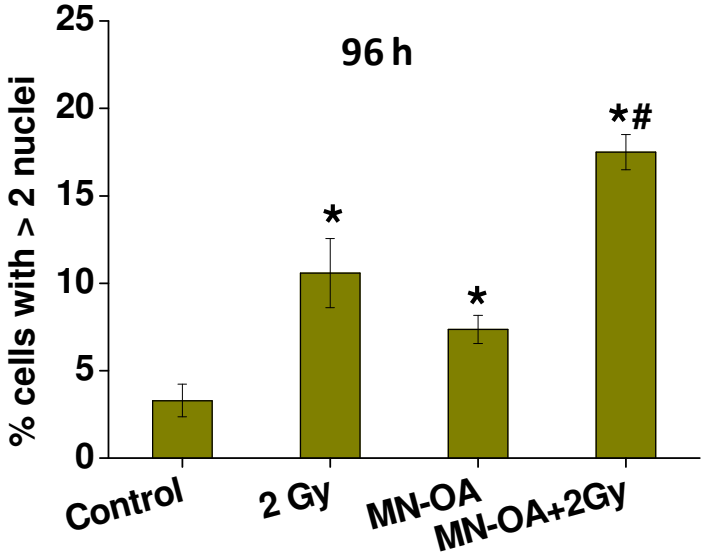
96 h
% cells with > 2 nuclei
25
20
15
10
5
0
*
*
*#
Control
2 Gy
MN-OA
MN-OA+2Gy

D.

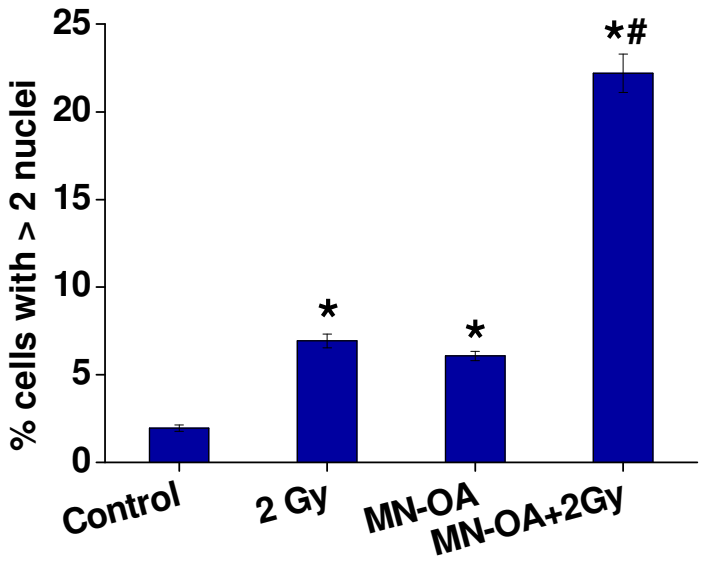

Fig. 3.1.15 *Effect of MN-OA treatment on markers of mitotic catastrophe in WEHI-164 cells.* ***(A)*** *Representative confocal laser scanning microscopic images of WEHI-164 cells stained with DAPI (nucleus; blue) and phalloidin-TRITC (actin; red), Scale bar = 10µm and* ***(B)*** *Representative fluorescence microscopic images for α-tubulin expression after indicated treatments (Scale bar = 10 µm). Arrows indicate cells expressing alpha-tubulin foci. Percentage of cells with more than 2 nuclei at* ***(C)*** *96 and* ***(D)*** *144 h, after indicated treatments. * Significantly different at P<0.05 as compared to control and # indicates significant difference between MN-OA treatment groups with or without 2 Gy.*

3.1.4.7 MN-OA in combination with 2 Gy interrupts the repair of damaged DNA

Results of cell cycle analysis **(Fig. 3.1.12 A & B)**, apoptosis **(Fig. 3.1.13)** and mitotic catastrophe **(Fig. 3.1.15)** indicated that MN-OA + 2 Gy treatment induces G2-M arrest, enhances apoptosis and induces mitotic catastrophe mediated cell death. Ionizing radiation is known to cause DNA double strand breaks (DSBs), which results in the induction of cell death. Therefore, the level of

radiation-induced DNA damage (double strand breaks) was determined by measuring the γ-H2AX foci formation at different time points (15 min, 30 min, 24 h and 96 h) **(Fig. 3.1.16 A & B)**. Results showed a significant increase in mean fluorescent intensity per field (MFI) for γ-H2AX foci measured after 15 and 30 min in combination treatment group. A similar magnitude of MFI was also observed in MN-OA treatment **(Fig. 3.1.16 B)**. The few γ-H2AX foci visible in control cells may be due to the basal level of DNA damage, which may have varied slightly during the cell cycle. At 24 h time point, the MFI of 2 Gy decreased to almost close to control cells but in case of MN-OA and MN-OA + 2 Gy, it remained higher. Moreover, at 96 h, the MFI of γ-H2AX foci was found to be persistent in combination treatment, which however became close to control cells in case of MN-OA treatment. These results suggested the effect of MN-OA on radiation induced DNA damage response and subsequent slow repair processes, which may be resulting in persistence of damage. One of the probable mechanism of induction of higher DSBs is via generation of ROS. Therefore, the levels of ROS was measured in WEHI-164 cells following treatment with MN-OA and gamma radiation using DCHFDA assay. Results showed no significant change in the levels of ROS after treatment with MN-OA or combination treatment. Whereas, a dose dependent increase in ROS was observed after treatment with increasing doses of gamma radiation alone **(Fig. 3.1.16 C)**. These results suggested some alternative mechanism for induction of DSBs by MN-OA. Therefore, further experiments were performed to study the effect of MN-OA + 2 Gy on DNA double stand break repair proteins (viz. Ku70, CHK1, RAD51 and BRCA1). Results showed significant down-regulation of DNA repair/damage signaling proteins (viz. CHK1, RAD51 and BRCA1) in cells treated with MN-OA or combination treatment. However, the level of Ku70 was found to be unchanged in all treatment groups **(Fig. 3.1.16 D)**. Interestingly, CHK1, RAD51 and BRCA1 are bonafide client

proteins of HSP90. However, Ku70 is not reported to be a client protein for HSP90[264]. Therefore, to ascertain the role of HSP90 in MN-OA mediated down-regulation of DNA repair proteins, MN-OA interaction with HSP90 was examined. For this as shown in **Fig. 3.1.16 E(i)**, using a strong magnet (strength: 0.5 kOe) the MN-OA bound proteins were separated from the lysate (obtained by using native lysis buffer) of MN-OA treated WEHI-164 cells. Western blotting of MN-OA bound proteins revealed the presence of HSP90 and HSP60. However, HSP70, CHK1 and RAD51 (other HSP90 client proteins) were not detected in the MN-OA bound protein fraction **Fig. 3.1.16 E(ii)**. Thus, these results suggest the interaction of MN-OA with HSP90 under intracellular conditions.

A.

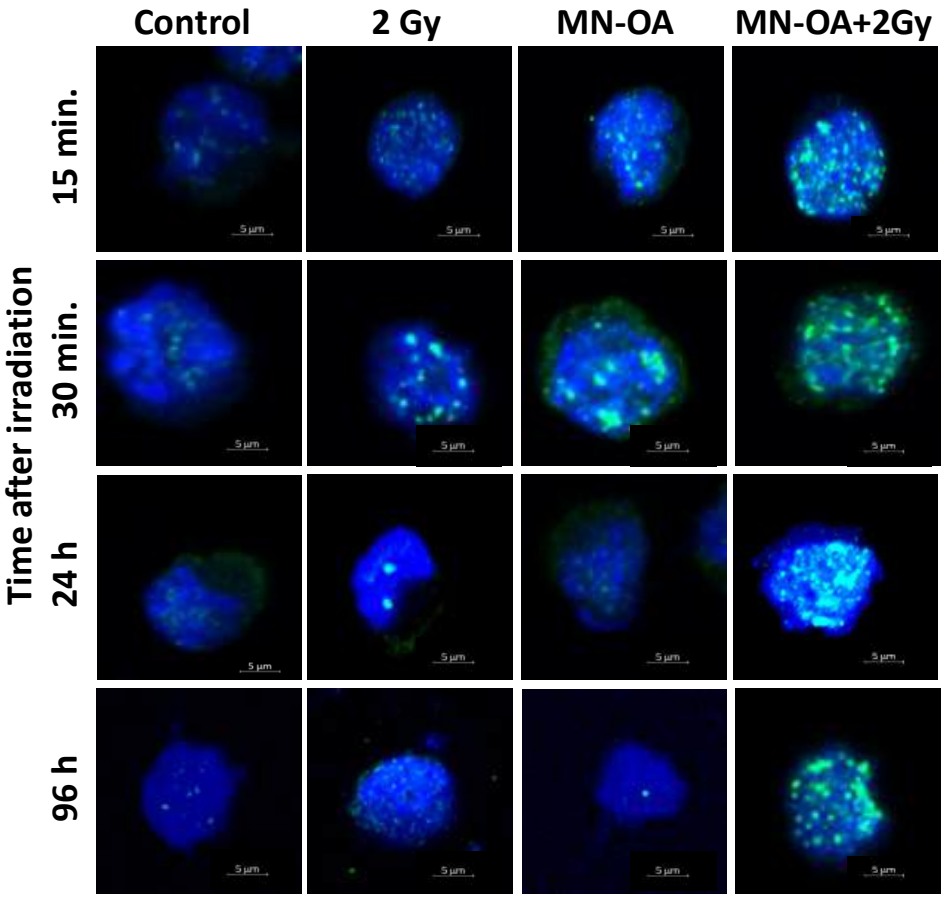

B.

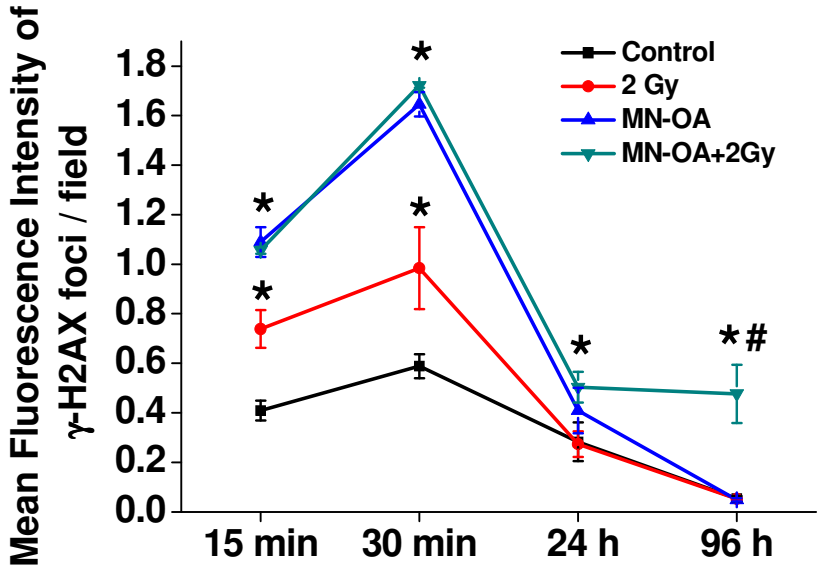
Mean Fluorescence Intensity of γ-H2AX foci / field
1.8
1.6
1.4
1.2
1.0
0.8
0.6
0.4
0.2
0.0
15 min
30 min
24 h
96 h
Control
2 Gy
MN-OA
MN-OA+2Gy
*
*
*
*
*
*#

C.

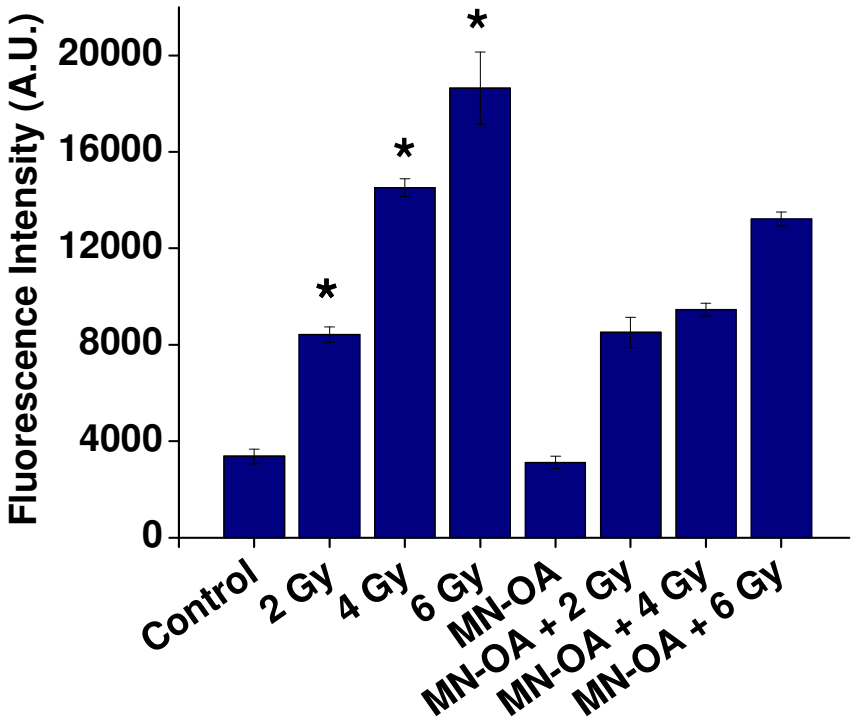
Fluorescence Intensity (A.U.)
20000
16000
12000
8000
4000
0
*
*
*
Control
2 Gy
4 Gy
6 Gy
MN-OA
MN-OA + 2 Gy
MN-OA + 4 Gy
MN-OA + 6 Gy

D.

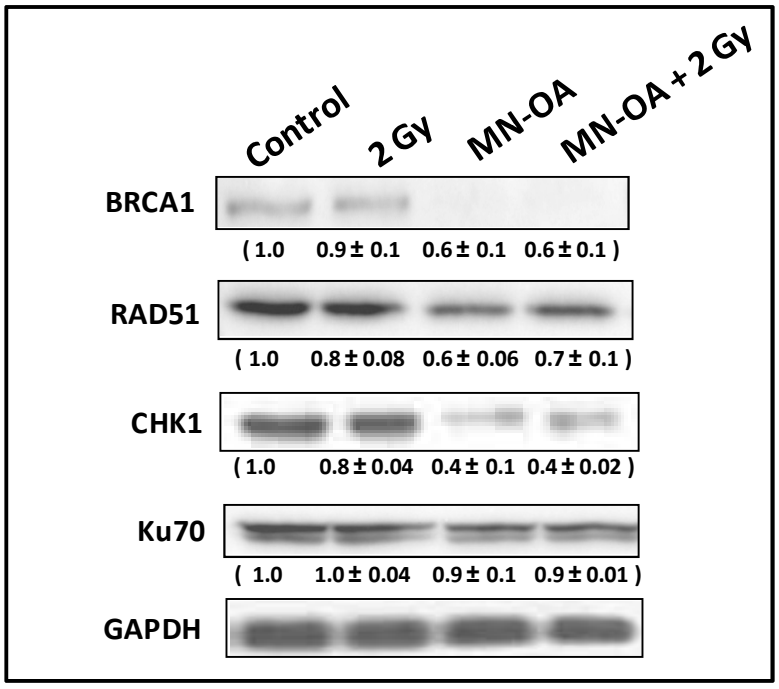
Control
2 Gy
MN-OA
MN-OA + 2 Gy
BRCA1
(1.0 0.9 ± 0.1 0.6 ± 0.1 0.6 ± 0.1)
RAD51
(1.0 0.8 ± 0.08 0.6 ± 0.06 0.7 ± 0.1)
CHK1
(1.0 0.8 ± 0.04 0.4 ± 0.1 0.4 ± 0.02)
Ku70
(1.0 1.0 ± 0.04 0.9 ± 0.1 0.9 ± 0.01)
GAPDH

E. (i)

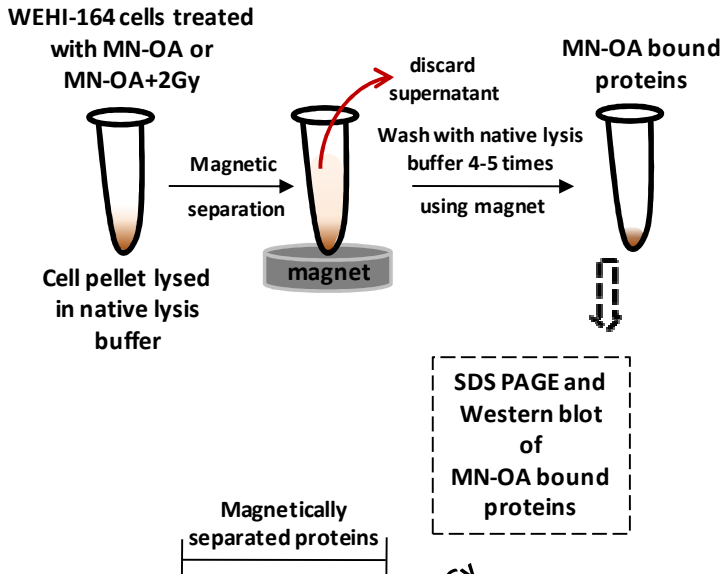
WEHI-164 cells treated with MN-OA or MN-OA+2Gy
Magnetic separation
discard supernatant
magnet
Wash with native lysis buffer 4-5 times using magnet
MN-OA bound proteins
Cell pellet lysed in native lysis buffer
SDS PAGE and Western blot of MN-OA bound proteins

E. (ii)

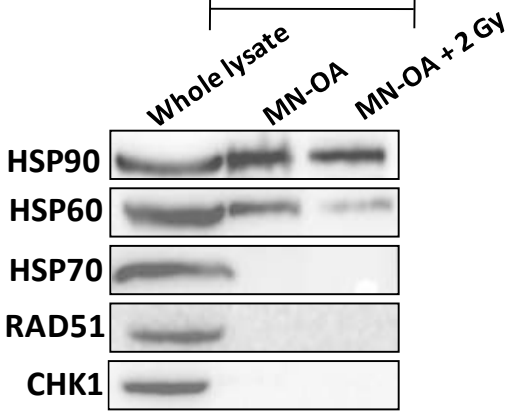
Magnetically separated proteins
Whole lysate
MN-OA
MN-OA + 2 Gy
HSP90
HSP60
HSP70
RAD51
CHK1

Fig. 3.1.16 *Effect of MN-OA in combination with 2 Gy on the magnitude of DNA damage and expression of DNA repair proteins.* ***(A)*** *Confocal microscopic images of cells for determination of γ-H2AX foci (magnification: 63 X, optical zoom: 3X, Scale bar = 5μm).* ***(B)*** *Mean Fluorescence Intensity/field of γ-H2AX foci in cells treated with MN-OA and 2 Gy alone and/or in combination. * Significantly different at P<0.05 as compared to control and # indicates significant difference between MN-OA treated groups with or without 2 Gy* ***(C)*** *Effect of indicated treatments on intracellular ROS generation in WEHI-164 cells (n=3) as assayed by H_2DCDFA fluorescence probe,* ***(D)*** *Western Blot analysis for the expression of DNA repair proteins.* ***(E)(i)*** *Scheme for native lysis of WEHI-164 cells treated with MN-OA either alone or in combination with 2 Gy and separation of MN-OA bound proteins by using a magnet.* ***(E)(ii)*** *Western blot analysis of MN-OA bound protein samples. Values in parenthesis represent fold change compared to control after normalizing with GAPDH.*

3.1.4.8 Knock-down of cellular HSP90 using siRNA enhanced MN-OA mediated radio-sensitization in WEHI-164

To further validate the role of HSP90 in MN-OA induced radio-sensitization, we generated HSP90 knocked-down-WEHI-164 cells and studied the effect of MN-OA or 2 Gy or combination treatment on the proliferation of cells transfected with HSP90-siRNA **(Fig. 3.1.17 A)**. The knock down and specificity of HSP90-siRNA was confirmed by Western blotting of transfected samples **(Fig. 3.1.17 B)**. MN-OA + 2 Gy treatment in HSP90-siRNA transfected WEHI-164 cells showed a significant decrease in percentage cell proliferation to 10 ± 1.3 % as compared to scrambled siRNA transfected cells (22 ± 2.8 %) at 96 h. Only MN-OA treatment as well showed a significant decrease in percentage cell proliferation to 17 ± 2% in HSP90 siRNA-

transfected cells as compared to scrambled siRNA-transfected cells (32 ± 2.1 %). However, only radiation (2 Gy) treatment didn't show significant difference in the percentage proliferation of cancer cells in HSP90-siRNA-transfected (64 ± 5.4%) and scrambled siRNA-transfected (53 ± 2.4 %) conditions (**Fig. 3.1.17 B**). These results suggest that knock-down of HSP90 increases the sensitivity of WEHI-164 cells to treatment with MN-OA alone and in combination with radiation. Thus, these results further validate the role of HSP90 in MN-OA induced radio-sensitization.

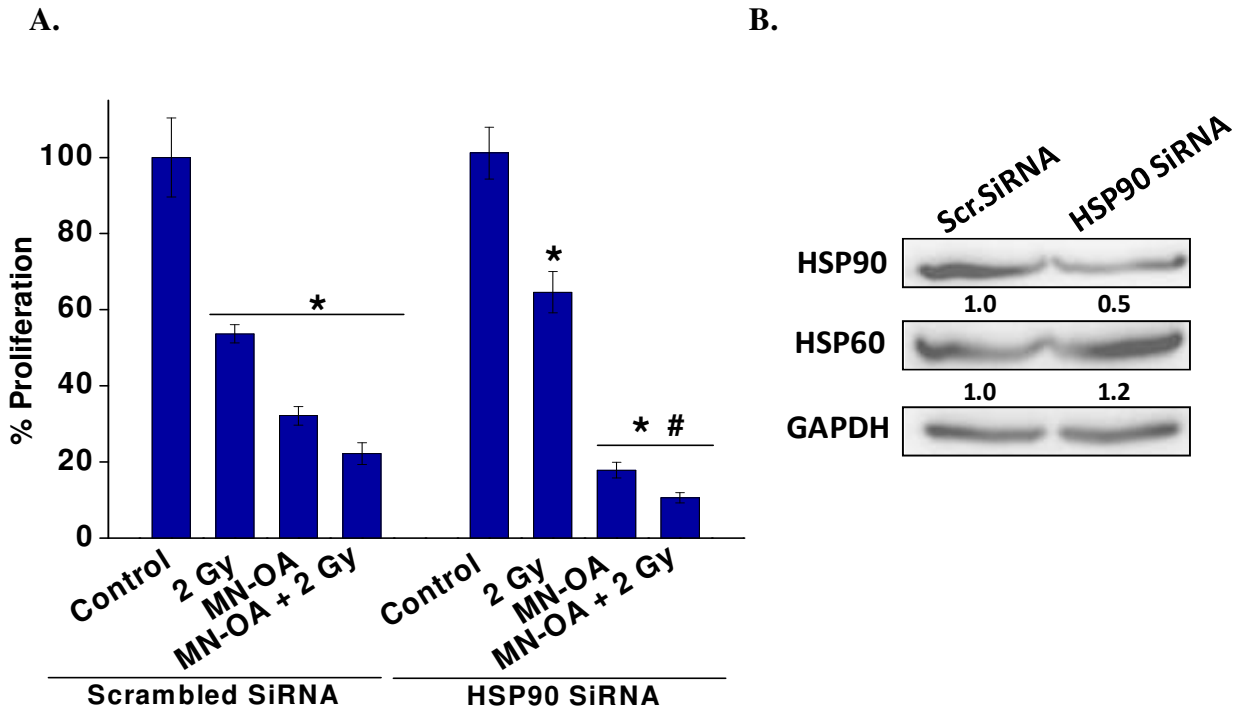

Fig. 3.1.17 ***(A)*** *Percentage cell proliferation of WEHI-164 cells at 96 h after knock-down of HSP90 using SiRNA transfection followed by treatment with MN-OA and/or 2 Gy, either alone or in combination. * Significantly different at P<0.05 and # indicates significant difference between MN-OA treated groups with or without 2 Gy following HSP90 knock-down* ***(B)*** *Western*

blot image for expression of HSP90 protein after siRNA transfection. Level of HSP60 was also examined for the specificity of HSP90-siRNA. (Scr.SiRNA: Scrambled SiRNA).

3.1.5.1 *IN VIVO* VALIDATION OF RADIO-SENSITIZING ABILITY OF MN-OA IN FIBROSARCOMA TUMOR

In vitro results demonstrated the radio-sensitizing ability of MN-OA in WEHI-164 cells. To further validate these results, the radio-sensitizing ability of MN-OA was evaluated in a fibrosarcoma tumor model. Fibrosarcoma tumors were obtained as discussed earlier **(Section 3.1.3.5)**. Once the tumors were palpable MN-OA was injected intra-tumorally, followed by irradiation of the tumor bearing leg with gamma radiation using Bhabhatron (^{60}Co-teletherapy machine). **Scheme 3.1.2** describes the schedule of MN-OA injection and irradiation of tumors. The effect of various treatments (viz. MN-OA or 3 x 2Gy, alone or in combination) on tumor growth was monitored from day 1 to day 21 as shown in **Fig. 3.1.18 A**. For 600 mm^3 tumor volume, the tumor growth delay and tumor growth delay index (TGI) were found to be 4.4 and 2.1 days, respectively for combination treatment **(Fig. 3.1.18 A)**. Analysis of these results showed that % TGI was significantly higher for MN-OA + radiation (81 ± 1.2 %) as compared to only radiation (59 ± 4.9 %) or MN-OA (26 ± 5.2 %) treatments on day 4. Typically, at day 10, the % TGI reduced to 47.7 ± 6.7 % in mice treated with combination treatment as compared to 23.1 ± 4.2 % in radiation and 5.5 ± 1.5 % in MN-OA treatments **(Fig. 3.1.18 B)**. An image of the representative mouse of various indicated treatments is shown to compare the tumor growth in the right hind leg of mice at day 10 **(Fig. 3.1.18 C)**. Thus, these results further validate the radio-sensitizing ability of MN-OA *in vivo*.

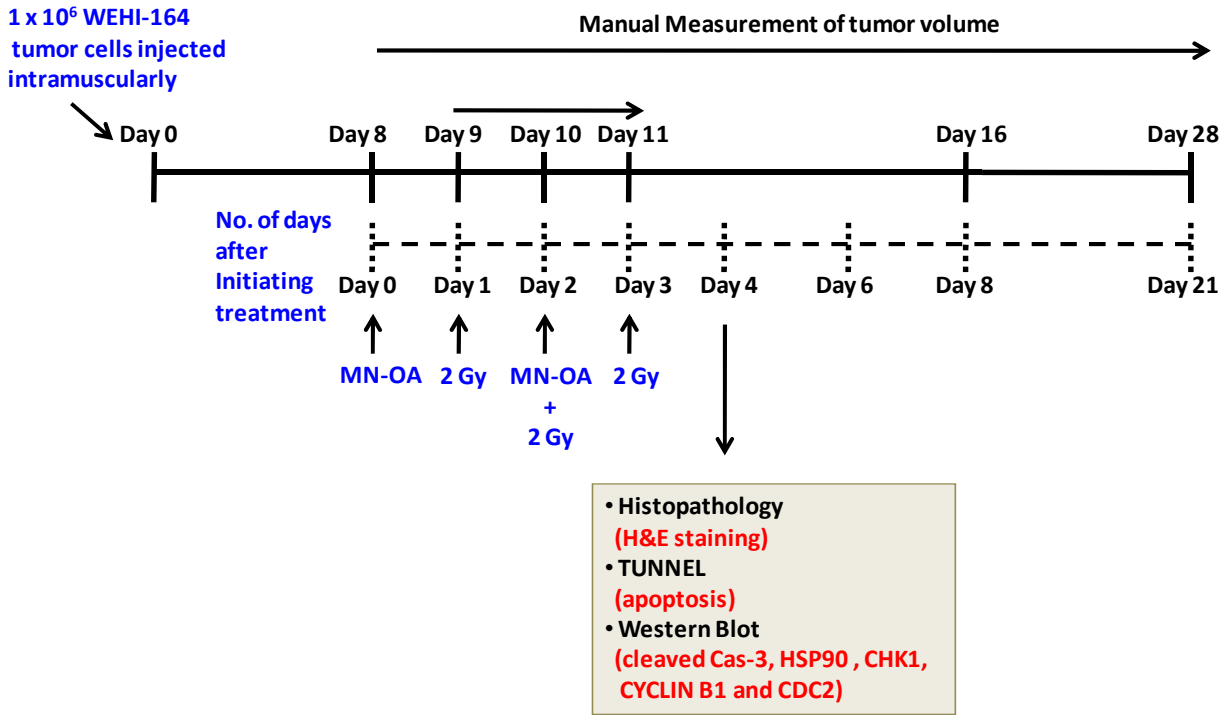

Scheme 3.1.2 *Treatment schedule, sample collection and biological end points of in vivo experiment for determining the radio-sensitization efficacy of MN-OA.*

A.

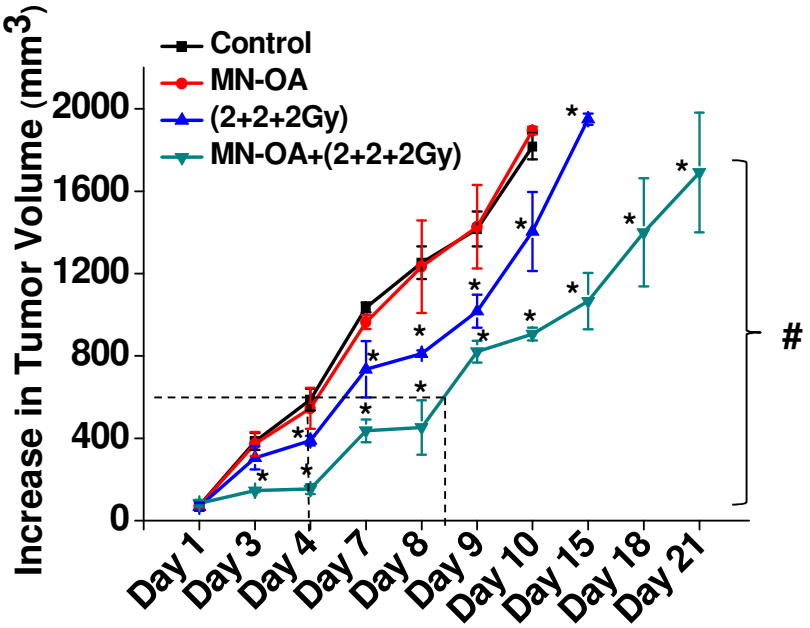

B.

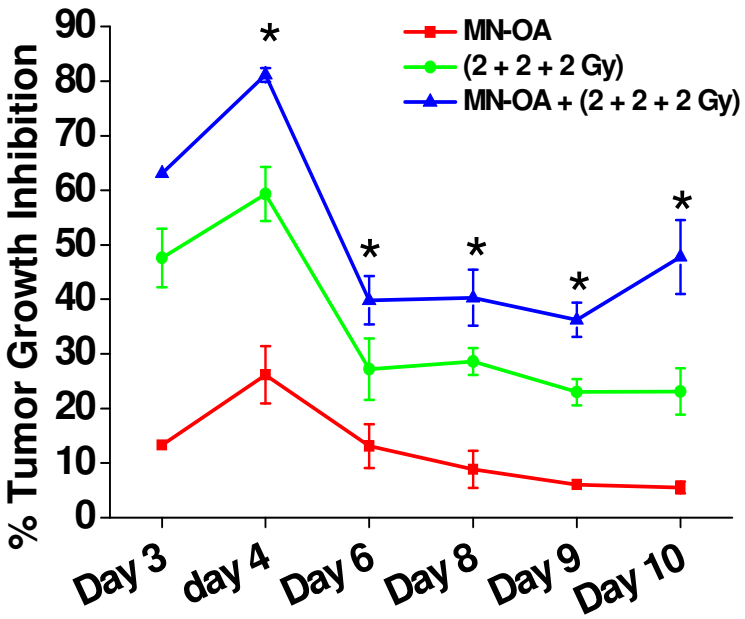

C.

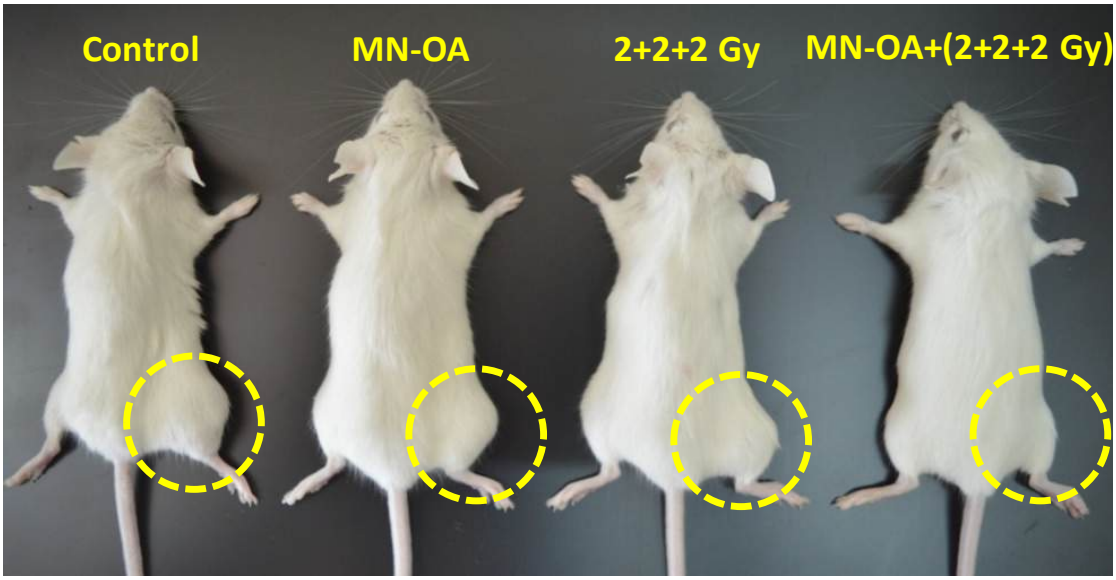

Fig. 3.1.18 *Effect of MN-OA and (3 x 2 Gy) alone and in combination on the tumor growth kinetics of fibrosarcoma tumors.* ***(A)*** *Effect of different treatments on the growth kinetics of fibrosarcoma tumors and* ***(B)*** *% Tumor growth inhibition of fibrosarcoma tumors after treatment with MN-OA and fractionated 6 Gy (3 x 2 Gy) γ radiation alone and/or in combination.* ***(C)*** *Representative images of tumor bearing mice subjected to various treatments. Yellow dotted circles indicate the tumor on the hind leg of mice. * Significantly different at P<0.05 as*

compared to control and # indicates significant difference between MN-OA treated groups with or without 2 Gy.

3.1.5.2 Combination treatment induced severe apoptosis in the tumor tissue

To determine the distribution of MN-OA in tumor tissue, Prussian blue staining was carried out. Results showed uniform distribution of MN-OA within the tumor tissue (**Fig. 3.1.19 A**, black arrows indicate blue spots corresponding to presence of Fe). Furthermore, histopathological studies (H & E staining) showed presence of severe apoptosis in combination treatment group compared to radiation and MN-OA treatments. These samples showed apoptotic tumor cells (indicated by black arrows) visible with fragmented purple stained nuclei surrounded by light pink cytoplasm. **(Fig. 3.1.19 B)**. To further confirm the magnitude of apoptosis in the tumor tissue, TUNEL assay was carried out. Results showed significant ($P<0.05$) increase (~ 4 fold) in the level of apoptosis in combination therapy group (MFI: 1.05 ± 0.07) as compared to control (0.25 ± 0.04), 3 x 2Gy (0.68 ± 0.05) and MN-OA (0.50 ± 0.04) treatments **(Fig. 3.1.19 C & D)**.

A.

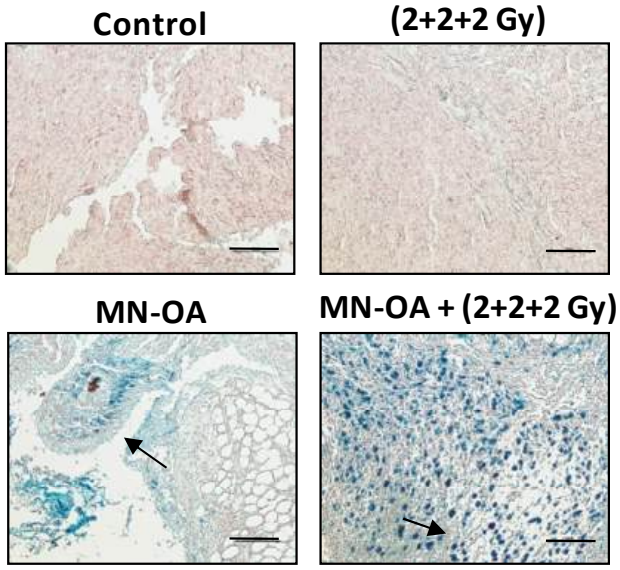

B.

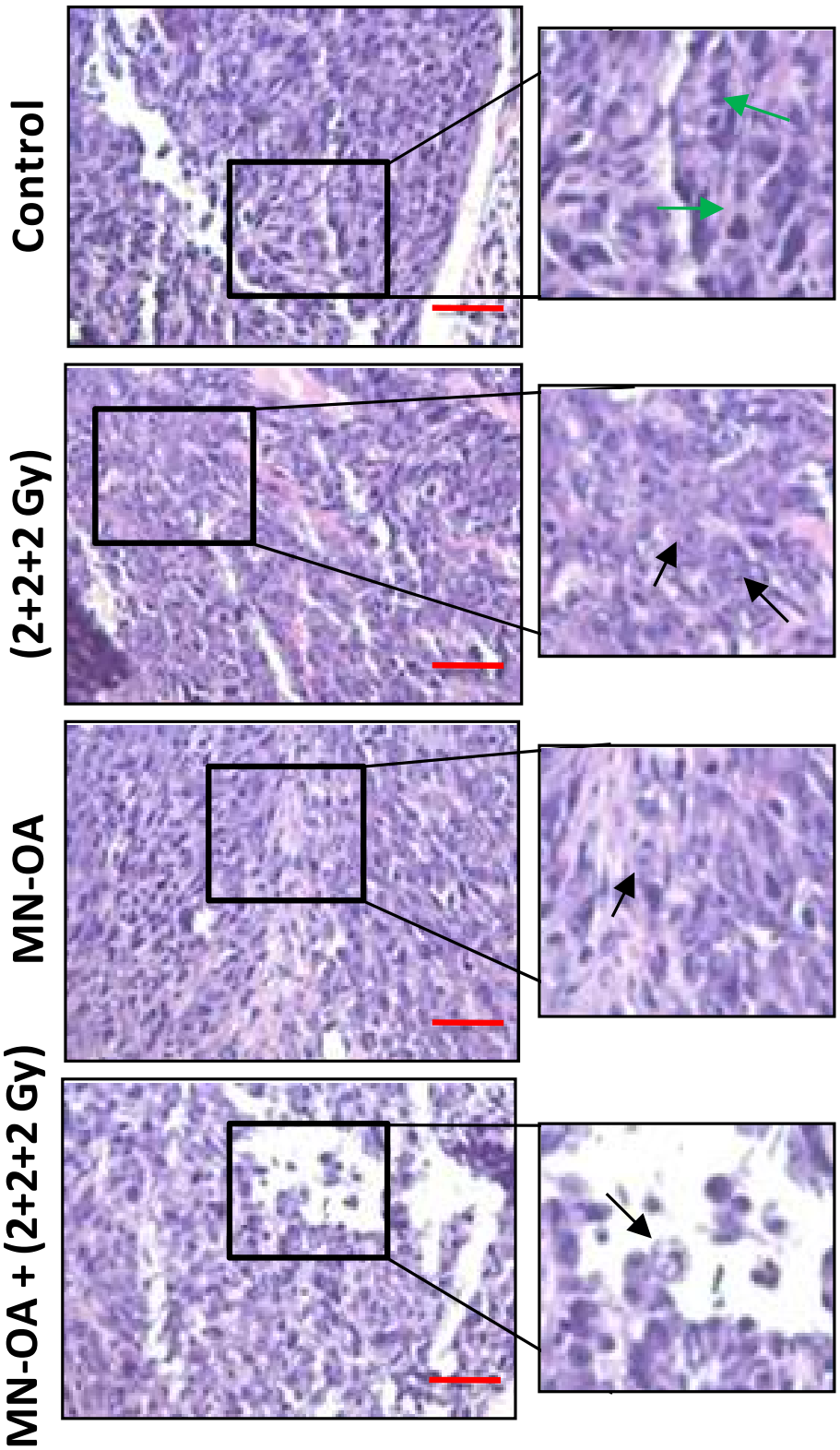

C.

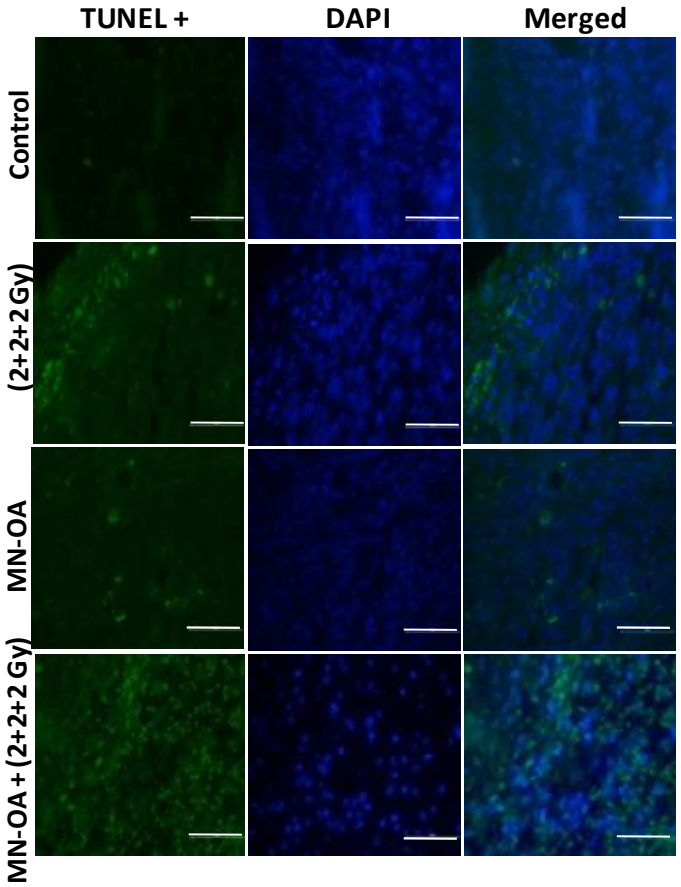

D.

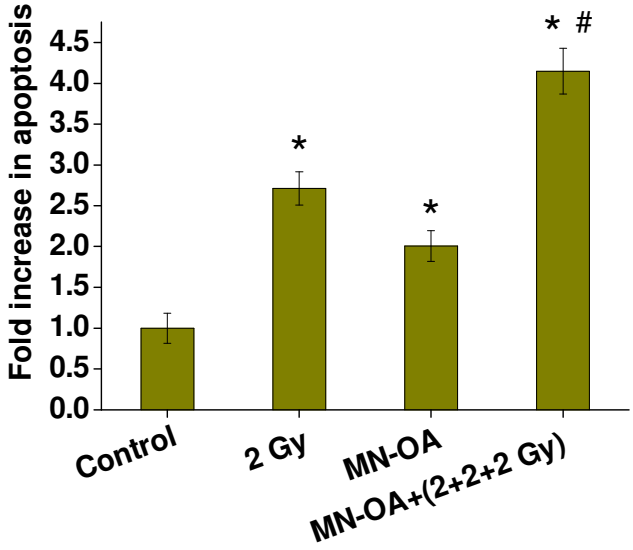

Fig. 3.1.19 *Prussian blue, histopathological and TUNEL analysis of tumor tissue sections.* ***(A)*** *Intra-tumor distribution of MN-OA (Prussian blue staining). Blue spots and arrows correspond to presence of Fe (Magnification: 20 X, Scale bar: 100µm).* ***(B)*** *H&E staining of tumor tissues to*

determine the level of apoptosis. Right panel shows zoomed images (1.7 X) of a part of the image for better visualization of apoptotic features. Non-apoptotic tumor cells show presence of dark blue or purple intact nuclei, whereas, apoptotic tumor cells show presence of fragmented nuclei. Black arrows indicate apoptotic nuclei and green arrows indicate intact nuclei. (Magnification: 40 X, Scale bar: 50 µm). ***(C)*** *Fluorescence microscopic images of tumor sections (TUNEL analysis, Magnification: 60 X, Scale bar: 50µm).* ***(D)*** *Fold change in apoptosis by TUNEL assay on day 4 after treatment. * Significantly different at P<0.05 as compared to control and # significant difference between MN-OA treated groups in combination with or without radiation.*

3.1.5.3 MN-OA down-regulates HSP90 client proteins to induce tumor radio-sensitization

Our *in vitro* results showed that MN-OA induces down-regulation of several client proteins of HSP90, which are involved in cell cycle progression and DNA repair **(Fig. 3.1.10 C, 3.1.12 C and 3.1.16 C)**. Therefore, to validate the role of HSP90 client proteins in the mechanism of MN-OA mediated radio-sensitization under *in vivo* conditions, the levels of the important client proteins of HSP90 were studied in tumor tissue lysates by Western Blotting **(Fig. 3.1.20 A to E)**. Statistical analysis showed a significant ($P<0.05$) down-regulation of client proteins of HSP90 involved in G2-M cell cycle progression (viz. CDC2 and Cyclin B1). Intensity of CHK1 (which plays a crucial role in DNA damage response) was also found to be slightly down-regulated in case of both MN-OA and combination treatments. Interestingly, consistent to the *in vitro* observations, under *in vivo* conditions as well, the levels of HSP90 were found to be significantly ($P<0.05$) higher in case of MN-OA or combination treatment groups.

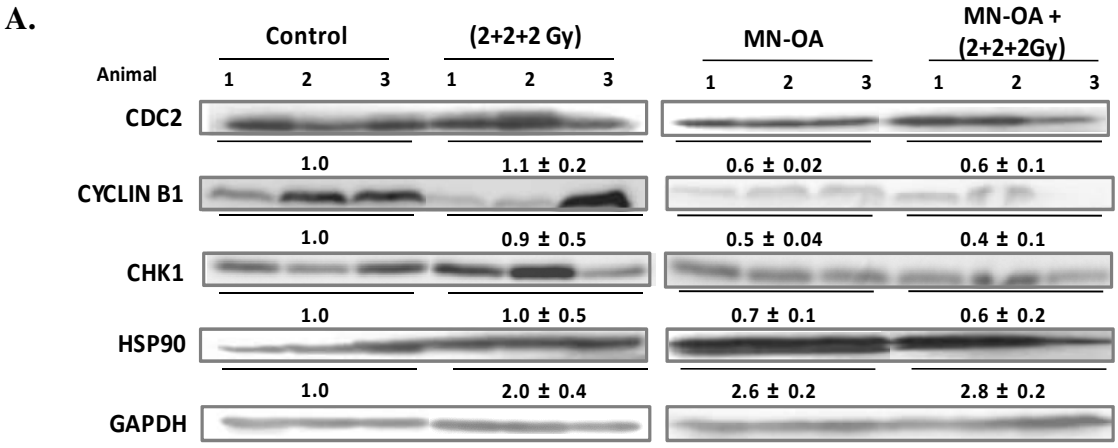
A.
Control
(2+2+2 Gy)
MN-OA
MN-OA + (2+2+2Gy)
Animal
1 2 3 1 2 3 1 2 3 1 2 3
CDC2
1.0 1.1 ± 0.2 0.6 ± 0.02 0.6 ± 0.1
CYCLIN B1
1.0 0.9 ± 0.5 0.5 ± 0.04 0.4 ± 0.1
CHK1
1.0 1.0 ± 0.5 0.7 ± 0.1 0.6 ± 0.2
HSP90
1.0 2.0 ± 0.4 2.6 ± 0.2 2.8 ± 0.2
GAPDH

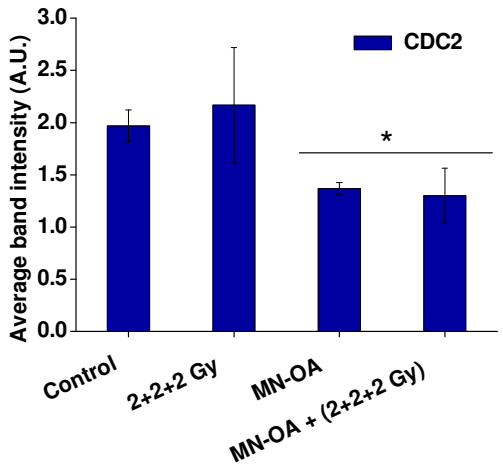
B.
CDC2
Average band intensity (A.U.)
3.0
2.5
2.0
1.5
1.0
0.5
0.0
*
Control
2+2+2 Gy
MN-OA
MN-OA + (2+2+2 Gy)

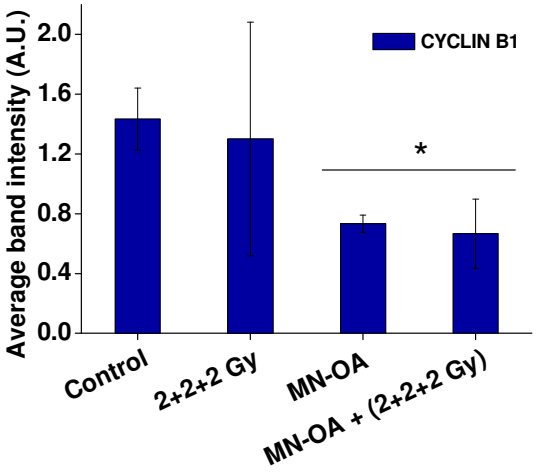
C.
CYCLIN B1
Average band intensity (A.U.)
2.0
1.6
1.2
0.8
0.4
0.0
*
Control
2+2+2 Gy
MN-OA
MN-OA + (2+2+2 Gy)

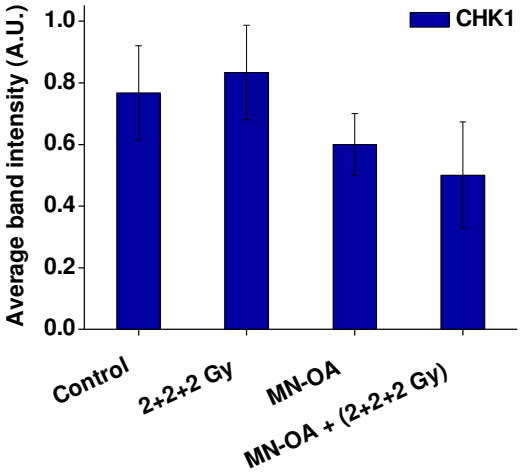
D.
CHK1
Average band intensity (A.U.)
1.0
0.8
0.6
0.4
0.2
0.0
Control
2+2+2 Gy
MN-OA
MN-OA + (2+2+2 Gy)

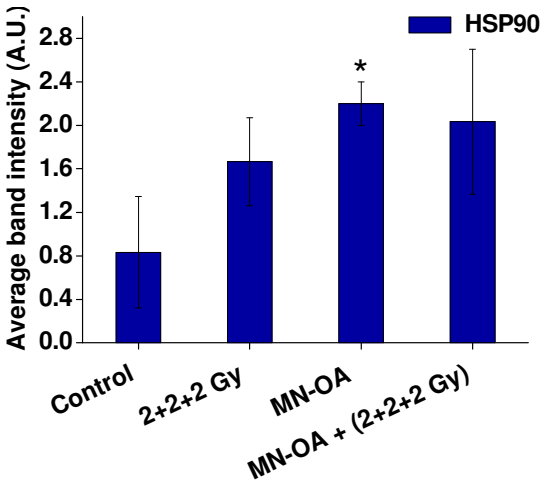
E.
HSP90
Average band intensity (A.U.)
2.8
2.4
2.0
1.6
1.2
0.8
0.4
0.0
*
Control
2+2+2 Gy
MN-OA
MN-OA + (2+2+2 Gy)

Fig. 3.1.20 (A) *Western Blot analysis for the expression of HSP90 and its client proteins in fibrosarcoma tumor. Expression levels of HSP90 client proteins (viz. CHK1, CDC2 and Cyclin B1) were determined. The values are Mean ± SD (n=3) and represent the ratio of band intensities of respective proteins after normalizing with corresponding band intensity for GAPDH.* ***(B to E)*** *Graphs represent the average normalized band intensities for* ***(B)*** *CDC2,* ***(C)*** *Cyclin B1,* ***(D)*** *CHK1 and* ***(E)*** *HSP90. * Significantly different at P<0.05 as compared to control.*

Summary:

Oleic acid coated SPIONs (MN-OA) were synthesized and their efficient magnetic hyperthermia and radio-sensitization efficacy was demonstrated in cancer cells and fiborsarcoma tumor model. MN-OA was found to interact with intra-cellular HSP90 and induce down-regulation of HSP90-client proteins, several of which play important role in cell survival, cell cycle progression and DNA repair. Thus, these results suggest the role of HSP90 modulation and down-regulation of its client proteins as one of the mechanism for enhanced cancer cell killing by MN-OA in combination with magnetic hyperthermia **(Scheme 3.1.3)** and gamma radiation **(Scheme 3.1.4)** .

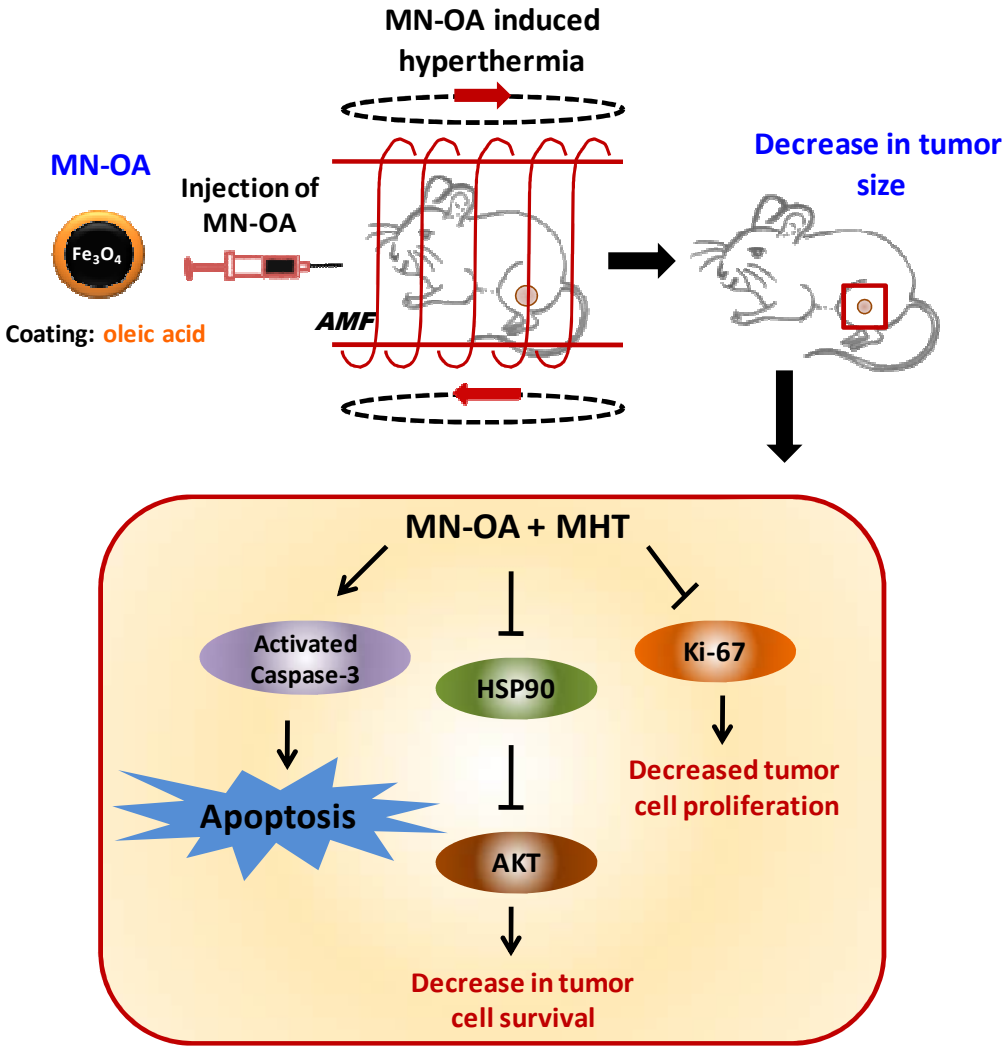

Scheme 3.1.3 *Schematic representation for the key molecular players involved in the MN-OA mediated magnetic hyperthermia therapy induced enhanced inhibition of fibrosarcoma tumors. (Source: Shetake et al, IJH, 2015)*[178].

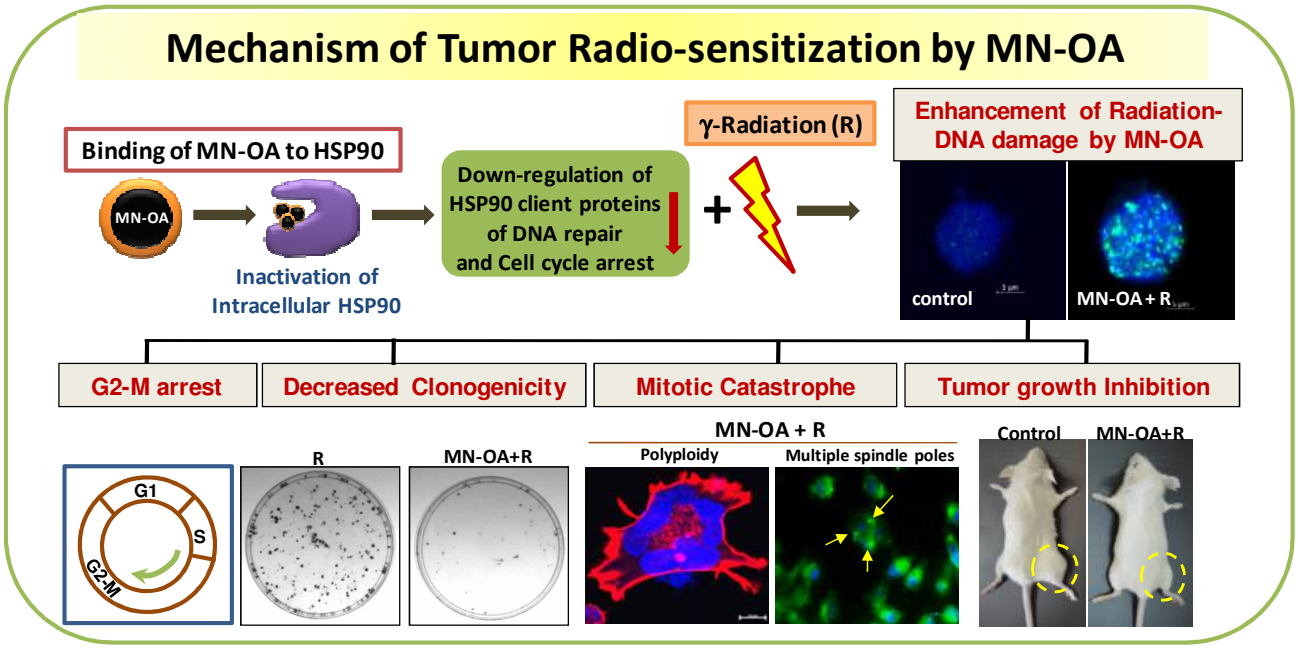

Scheme 3.1.4 *Schematic representation for the mechanism of MN-OA induced radio-sensitization of murine fibrosarcoma cells and its tumor model. (Source: Shetake et al, BBA, 2019)*[169].

CHAPTER 3

RESULTS AND DISCUSSION

Section 3.2 : Synthesis of Targeted Nano-formulation: *In vitro* Efficacy, Toxicity and Mechanism of Combinatorial Cancer Therapy

SECTION 3.2 SYNTHESIS OF TARGETED NANO-FORMULATION: *IN VITRO* EFFICACY, TOXICITY AND MECHANISM OF COMBINATORIAL CANCER THERAPY

As discussed in **Chapter 3, Section 3.1**, MN-OA showed significant potential for magnetic hyperthermia therapy and radio-sensitization of cancer cells. The underlying mechanism of tumor cell killing by MN-OA, both in combination with magnetic hyperthermia therapy (MHT) as well as radiation, has been investigated. MN-OA was found to directly interact with intra-cellular HSP90 and thus inhibit the function of its client proteins. Several of these client proteins play important role in cell survival (AKT), cell cycle progression (Cyclin B1 and CDC2) and DNA repair (BRCA1, RAD51, CHK1). Inspite of the substantial potential of MN-OA for combinatorial MHT and radiation therapy of cancer, the current formulation had certain limitations which needed to be improved for development of MN-OA into a better nano-formulation for targeted cancer therapy. Thus, the present sub-section of the Chapter will discuss the rationale for the design of a tumor targeted liposomal based nano-formulation, its synthesis/characterization using different bio-physical techniques and evaluation of its *in vitro* anti-cancer potential in combination with MHT and radiation.

3.2.1 LIMITATIONS OF MN-OA FOR TARGETED CANCER THERAPY APPLICATIONS:

Major limitation of MN-OA was its non-targeted and hydrophobic nature imparted by its oleic acid coat. Thus, for dispersion in physiological media, MN-OA was initially dispersed in sodium carbonate (0.1 M), followed by dilution in PBS. However, for clinical translation of a nano-

formulation, use of sodium carbonate is not desirable. Moreover, MN-OA was found to agglomerate in presence of serum, which limited its administration by intra-venous (*i.v.)* route and compelled its injection directly at the tumor site. Intra-tumoral mode of injection has the drawbacks of in-homogenous distribution of the nano-particles inside the tumor and non-feasibility of this route of administration for deep seated tumors or metastatic sites. Thus, development of a tumor targeted nano-formulation with better dispersibility and hydrophilicity became crucial.

3.2.2 RATIONALE FOR DESIGN OF TUMOR TARGETED LIPOSOMAL NANO-FORMULATION CO-ENCAPSULATED WITH MN-OA AND DOX (T-LMD):

As discussed in previous **sub-section 3.2.1**, actively targeted nano-formulation of MN-OA was warranted for improved combinatorial cancer therapy application and enhanced therapeutic gain. For this, a liposomal based nano-formulation co-encapsulated with MN-OA and an anti-cancer drug was designed **(Scheme 3.2.1)**. This nano-formulation will enable co-delivery of MN-OA as well as anti-cancer drug to the tumor cells in a targeted manner due to presence of a tumor targeting peptide. In addition, the nano-formulation will be functionalized with polyethylene glycol (PEG), which will enhance its blood circulation time and enable its passive tumor targeting due to enhanced permeability and retention (EPR) effect.

To achieve these features of nano-formulation, appropriate choice of tumor targeting agent, anti-cancer drug and nano-carriers was essential. Thus, the rationale of the chosen targeting agent [cyclic RGD peptide (cRGD)], anti-cancer drug [Doxorubicin (Dox)] and nano-carriers [polyethylene glycol (PEG) coated liposomes (PEG-liposomes)] to develop the tumor

targeted, cRGD-labeled liposomal nano-formulation (co-encapsulated with MN-OA and Dox) referred to as, T-LMD is being discussed below.

Encapsulation of MN-OA

1. As discussed in **Section 3.1**, MN-OA was found to inhibit HSP90's function of folding of its client proteins, thereby resulting in enhanced killing of cancer cells in combination with radiation and MHT.
2. MN-OA due to its hydrophobic nature, can be encapsulated in the membrane region of the liposomes. This will enable better utilization of the hydrophobic and hydrophilic compartment of the liposomes and facilitate higher encapsulation of MN-OA and anti-cancer drug.
3. Oleic acid itself is known to induce apoptosis in cancer cells, which will also contribute towards higher cyto-toxicity to cancer cells[254].
4. MN-OA contains iron oxide which is an established and FDA approved MRI contrast agent[6,257]. Thus, T-LMD can also be used as an MRI contrast agent for cancer diagnosis in future.
5. Owing to the super-paramagnetic behaviour and hyperthermia capabilities of MN-OA, T-LMD will have applicability for MHT of cancer.

A. Dox as an anti-cancer agent

1. Being fluorescent, Dox can be easily monitored for studying its encapsulation efficiency in liposomes and sub-cellular distribution in cancer cells.

2. Due to its predominantly hydrophilic nature, it can be encapsulated in the liposomal core and delivered to the cell interior.
3. Dox is known to damage cancer cells by both direct (DNA intercalation) and indirect (ROS generation) effects[265]. These mechanisms of action of Dox can be exploited for enhancing the efficacy of the nano-formulation when combined with radiation.
4. Dox is known to have severe side effects[258-259] and amelioration of its toxicity by encapsulating it inside liposomal nano-formulation will help to improve its clinical application.

B. <u>Use of PEG and cRGD conjugated liposomes as nano-carrier</u>

1. Due to its neutral charge and associated stearic hindrances, PEG facilitates escape from reticulo-endothelial system, thus enabling longer blood circulation time. It also promotes sustained release of encapsulated drug[260].
2. PEG enables passive targeting of tumor by EPR effect due to leaky tumor neo-vasculature[260].
3. Presence of PEG on the liposome surface makes it amenable for functionalization with targeting agents to reduce normal cell uptake.
4. Due to encapsulation of Dox inside the PEG-liposomes, the toxicity of the free drug (Dox) can be minimized substantially. This will also enable use of higher tolerated doses of Dox for treatment of cancer.
5. cRGD is known to target endothelial cells at neo-vasculature sites[266-267], which makes it a suitable ligand for development of actively targeted nano-formulation.

6. Liposomes are highly bio-compatible and also provide membrane and aqueous compartments for encapsulation of hydrophilic and hydrophobic agents, respectively. These liposomes can be prepared with different sizes and charge providing more options for efficient tumor targeting[267].

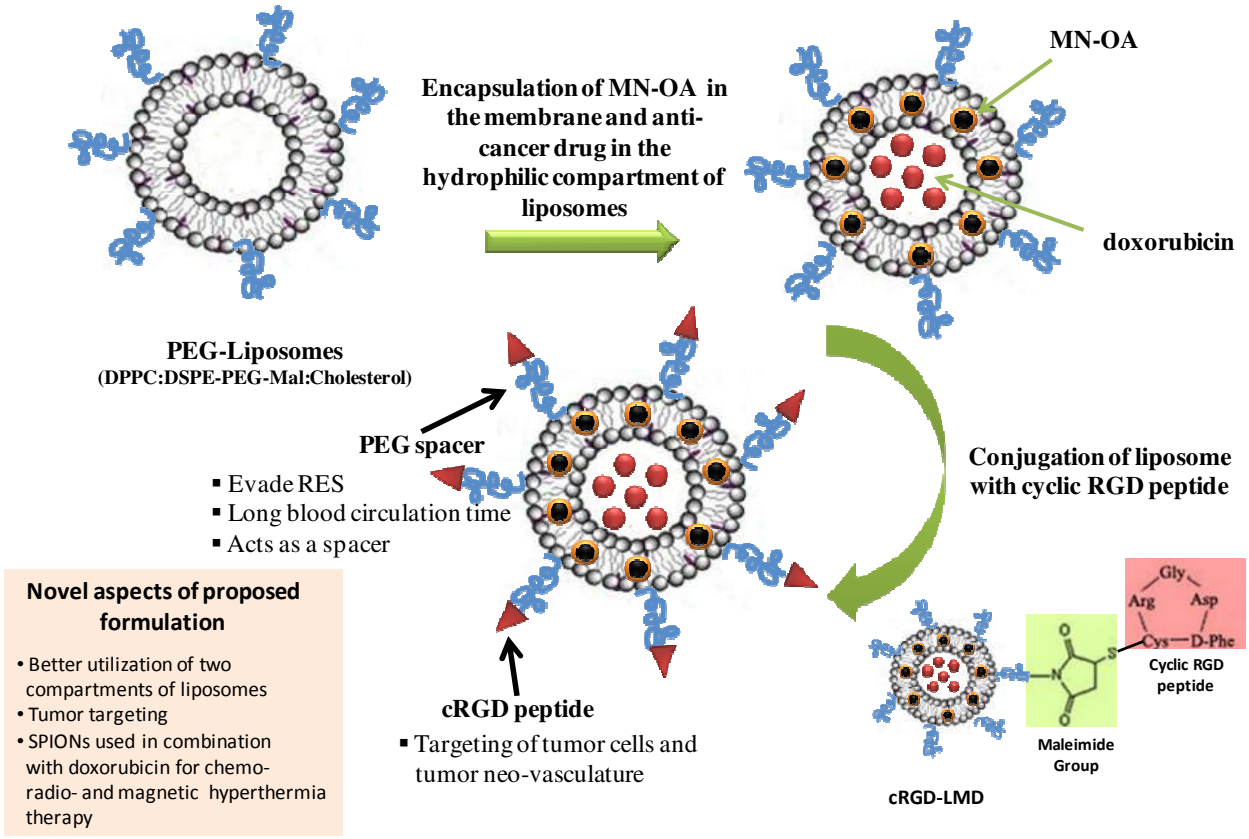

Scheme 3.2.1 *Scheme for design of T-LMD and description of different components.*

3.2.3 SYNTHESIS OF T-LMD

T-LMD was synthesized in two steps:

1. Synthesis and characterization of PEG-Lipo-MN-Dox (**Sections 3.2.3 to 3.2.6**).

2. Conjugation of cRGD peptide to DSPE-PEG-maleimide phospholipid followed by its incorporation during synthesis of cRGD targeted liposomes (**Section 3.2.7**).

3.2.3.1 Synthesis of PEG-liposomes co-encapsulated with MN-OA and Dox (PEG-Lipo-MN-Dox)

The first step towards the development of T-LMD was to synthesize PEG-liposomes co-encapsulated with MN-OA and Dox and to characterize these liposomes for their size, charge and stability by using different bio-physical techniques. PEG-Lipo-MN-Dox was synthesized by thin film hydration method using phospholipids [viz. DPPC, DSPE-PEG and cholesterol in a molar ratio of 6:1:2] and different concentrations of MN-OA (viz. 7, 8 and 9 mg/ml) as mentioned in **Chapter 2, Section 2.4**. The optimum encapsulation of MN-OA was obtained at 8 mg/ml concentration **(Fig. 3.2.1 A)**. Further, liposomes encapsulated with Dox were synthesized and the encapsulation of Dox (100 µM) was carried out by two methods: (A) Thin film hydration and (B) pH gradient. The % encapsulation of Dox by pH gradient method was found to be **97.5 ± 0.5 %,** which was significantly higher than the % encapsulation by thin film hydration method (**40.48 ± 0.83 %).** The details of the two methods of encapsulation are mentioned in **Chapter 2, Section 2.4**.

A.

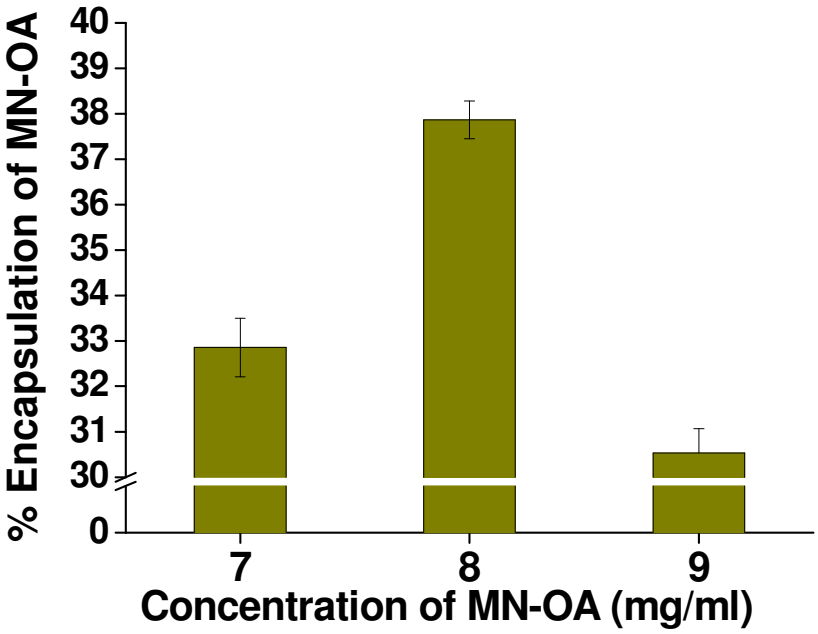

B.

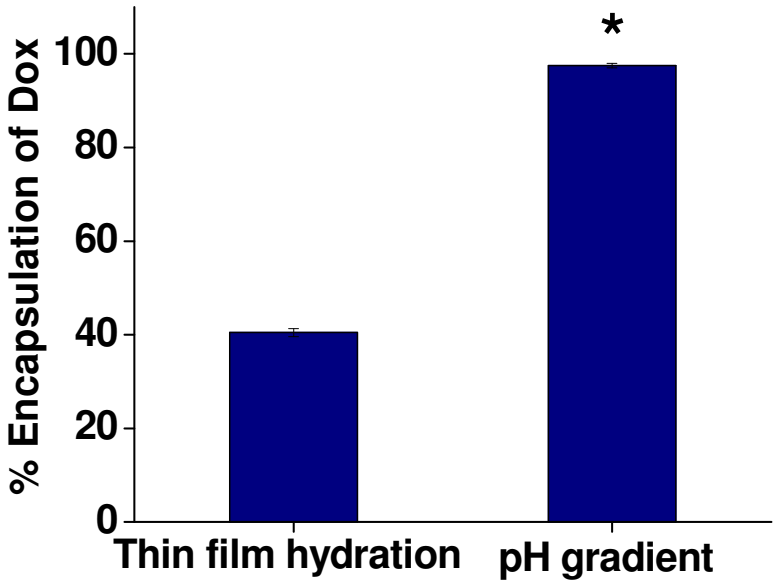

Fig. 3.2.1 *Percentage encapsulation of* ***(A)*** *MN-OA at different concentrations (viz. 7, 8 and 9 mg/ml) and* ***(B)*** *Dox by two different methods, viz. thin film hydration and pH gradient methods, respectively, in PEG-Lipo-MN-Dox. * Significantly different (P<0.05) as compared to control.*

3.2.4 CHARACTERIZATION OF PEG-Lipo-MN-Dox

To confirm the synthesis of liposomes and determine their bio-physical characteristics (such as size, surface charge and distribution of MN-OA in the liposomes), PEG-Lipo-MN-Dox was further characterized by dynamic light scattering (DLS) and zeta potential studies **(Fig. 3.2.2 A & B)**. The average hydrodynamic size was found to be 157.8 nm with a polydispersity index (PDI) of 0.23 (**Fig. 3.2.2 A)**. The average zeta potential of liposomes was found to be -7.3 ± 2.1 mV **(Fig. 3.2.2 B)**. Stability of liposomes was studied by determining the % release of Dox upto 24 h at 37 °C by dynamic dialysis method as discussed in **Chapter 2, Section 2.8**. Briefly, the liposomes were dialysed against PBS (maintained at 37°C in water bath), and an aliquot of 10 µl was removed from the dialysis bag at desired time points (equal volume of PBS was replaced in

the bag to maintain the solution volume). The aliquoted sample of liposomes was lysed with triton X-100 (10 %), followed by measuring its fluorescence intensity after appropriate dilution in a plate reader (Tecan Infinite Pro M200, Switzerland) at 485 nm excitation and 585 nm emission wavelengths, respectively. The increase in the % release of Dox from the liposomes was found to be in-significant (~ 4 ± 0.09 %) upto 24 h measured period as compared to initial incubation period of 10 min **(Fig. 3.2.2 C)**. Transmission electron microscopy (TEM) imaging of liposomes after phosphor-tungstic acid (PTA) staining showed presence of iron deposits mainly in the periphery, suggesting the presence of iron oxide in the liposomal membrane **(Fig. 3.2.2 D)**. Energy dispersive-X-Ray Fluorescence (ED-XRF) confirmed the presence of characteristic peaks for iron (~ 25 Weight % Fe) in the selected field of view (FOV) of TEM **(Fig. 3.2.2 E i - ii)**. These results confirm the synthesis of spherical shaped liposomes co-encapsulated with MN-OA (TEM and ED-XRF analysis) and Dox (based on fluorescence measurements). Results also indicated almost neutral surface charge of PEG-Lipo-MN-Dox formulation with average hydrodynamic size of ~ 150 nm.

A. **B.**

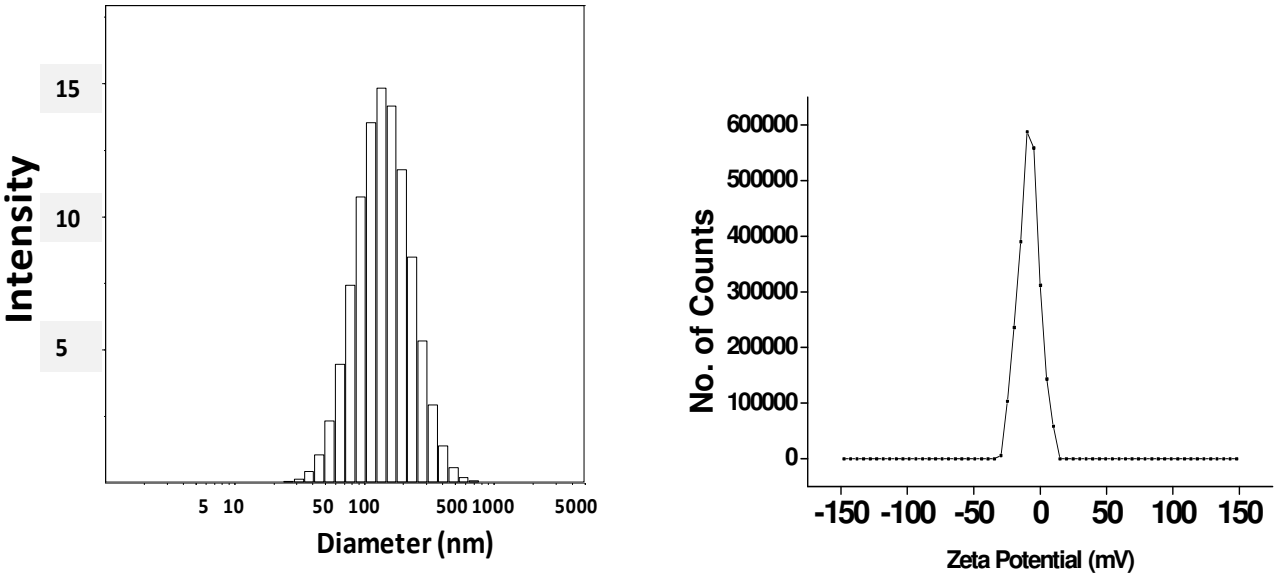

C.

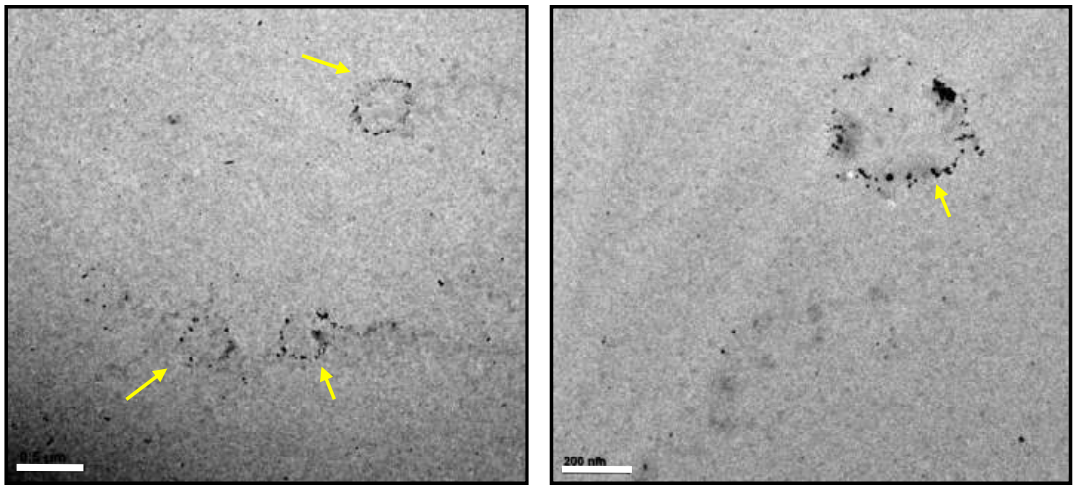

Scale Bar: 500 nm

Scale Bar: 200 nm

D.

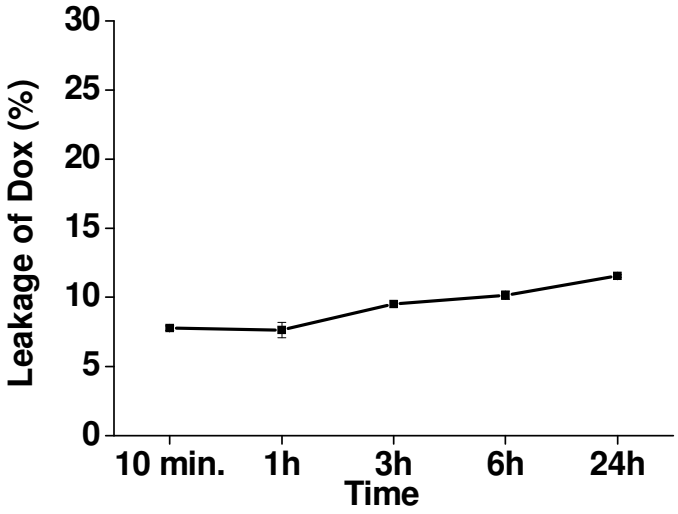

E.

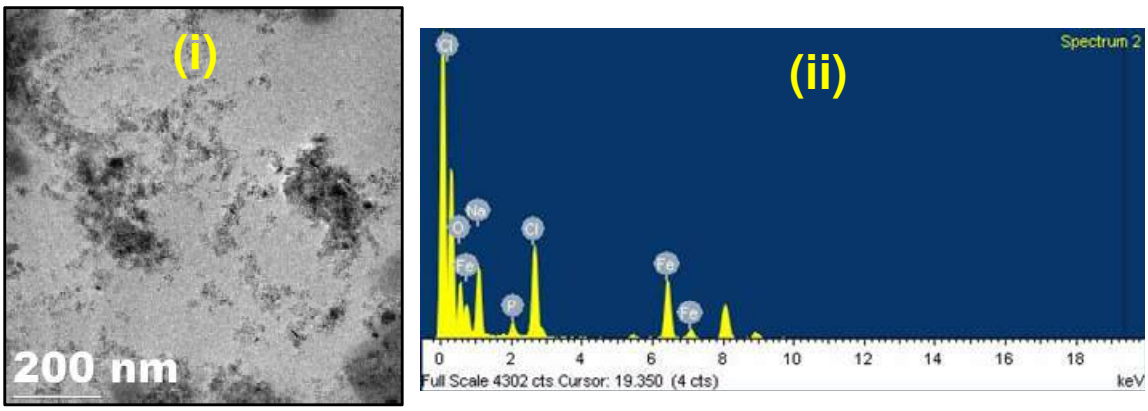

Fig. 3.2.2 *Bio-physical characterization of PEG-Lipo-MN-Dox by* ***(A)*** *Dynamic Light Scattering (DLS),* ***(B)*** *Zeta potential,* ***(C)*** *Stability study of encapsulated Dox in PEG-Lipo-MN-Dox by dynamic dialysis method using fluorescence measurement at Ex: 490 nm and Em : 585 nm,* ***(D)*** *Transmission Electron Microscopy (TEM) of PEG-Lipo-MN-Dox after phosphotungstic acid staining (yellow arrows indicate the dark contrast of iron oxide) and* ***(E-i)*** *TEM of PEG-Lipo-MN-Dox at room temperature and* ***(E-ii)*** *ED-XRF of the selected FOV.*

3.2.5 EVALUATION OF EFFICACY OF PEG-Lipo-MN-Dox AND THEIR RESPECTIVE CONTROLS

To determine the contribution of each component of PEG-Lipo-MN-Dox towards the anti-cancer effect, appropriate controls of each component were synthesized. These controls shall also help to determine whether the therapeutic formulation of PEG-Lipo-MN-Dox is indeed more effective in killing of cancer cells as compared to their individual component controls.

3.2.5.1 Synthesis of liposomes encapsulated with Dox (PEG-Lipo-Dox), MN-OA (PEG-Lipo-MN) or PBS (PEG-Lipo) and determination of their encapsulation efficiency

To evaluate the chemotherapeutic efficacy of PEG-Lipo-MN-Dox, following controls were synthesized **(Scheme 3.2.2)**:

a. Liposomes encapsulated with Dox (PEG-Lipo-Dox)
b. Liposomes encapsulated with MN-OA (PEG-Lipo-MN)
c. Liposomes encapsulated with PBS (PEG-Lipo).

Above three controls were compared with final formulation, PEG-Lipo-MN-Dox. Additionally, PEG-Lipo-MN-Dox formulation was also compared with commercial PEGylated

liposomal formulation (Lippod™, Celon Labs, Hyderabad, India) encapsulated with Dox (2 mg/ml) but without MN-OA. Wherever applicable, the percentage encapsulation of Dox or MN-OA was determined by fluorescence measurement of Dox and Fe estimation of MN-OA by ortho-phenanthroline methods, respectively **(Scheme. 3.2.2)**. Compared to PEG-Lipo-MN (41.9 ± 0.02 %), PEG-Lipo-MN-Dox (38.1 ± 1.3 %) showed lower encapsulation of MN-OA **(Table 3.2.1)**, which may be due to competition of liposomal compartments for Dox and MN-OA. Similar to this, Dox encapsulation was found to be lower in PEG-Lipo-MN-Dox (35.6 ± 2.1 %) as compared to PEG-Lipo-Dox (94.4 ± 2.07 %).

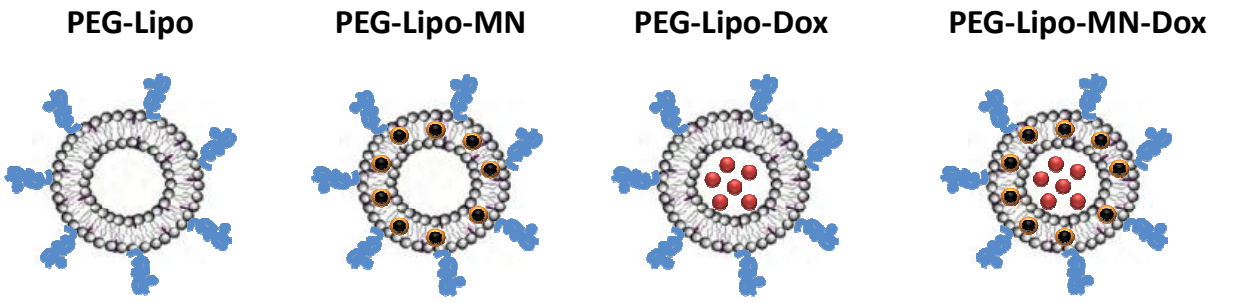

PEG	✓	✓	✓	✓
MN-OA		✓		✓
Dox			✓	✓

Scheme 3.2.2 *Design of individual component controls of PEG-Lipo-MN-Dox, viz. PEGylated liposomes encapsulated with PBS (PEG-Lipo), MN-OA (PEG-Lipo-MN), Dox (PEG-Lipo-Dox) and both MN-OA and Dox (PEG-Lipo-MN-Dox).*

% Encapsulation				
	PEG-Lipo	PEG-lipo-MN	PEG-lipo-Dox	PEG-Lipo-MN-Dox
MN-OA		41.9 ± 0.02		35.67 ± 2.19
Dox			94.4 ± 2.07	38.17 ± 1.32

Table 3.2.1 *Percentage encapsulation of MN-OA or Dox in different liposome controls.*

3.2.5.2. Cyto-toxicity of liposomal nano-formulations in WEHI-164 cells

For determining the chemotherapeutic efficacy, WEHI-164 (murine fibrosarcoma) cells were seeded in 96 well plates and treated with increasing concentrations of the formulations (equivalent to 0.1, 0.2, 0.3 and 0.4 µM Dox and 17.4, 33, 50 and 67 µg/ml of MN-OA) for 24 and 48 h followed by MTT assay. Cancer cells were also treated with Lippod^{TM} (equivalent to 0.1, 0.2, 0.3 and 0.4 µM of Dox).

Results showed significant reduction in the cell viability of WEHI-164 cells after treatment with PEG-Lipo-MN-Dox in a concentration dependent manner as compared to individual treatment controls (viz. PEG-Lipo-Dox or PEG-Lipo-MN) and Lippod^{TM}. At 0.4 µM equivalent Dox concentration, at 24 h, PEG-Lipo-MN-Dox showed significantly lower cell viability (9.3 ± 3.6 %) as compared to PEG-Lipo-Dox (80.7 ± 3.6 %) or PEG-Lipo-MN (54.7 ± 11.6) or PEG-Lipo (95.3 ± 3.4 %) and Lippod^{TM} (88.06 ± 1.8 %), respectively **(Fig. 3.2.3 A-D)**. At 48 h, in all the treatment groups, a further reduction in the cell viability was observed, with PEG-Lipo-MN-Dox treated group having the lowest cell viability of 3.1 ± 0.2 %. These results demonstrated the significant ($P<0.05$) chemotherapeutic efficacy of PEG-Lipo-MN-Dox, which was ~ 7 fold higher than commercially available formulation (Lippod^{TM}). Representative bright field images of WEHI-164 cells treated with various treatments shows the morphological changes (typically cellular fragmentation, cell shrinkage and cell lysis in PEG-Lipo-MN-Dox treatment and increase in cell size after PEG-Lipo-Dox and Lippod^{TM} treatments) associated with different treatments **(Fig. 3.2.3 E)**. The morphological changes followed a concentration dependent pattern similar to toxicity assays for different formulations.

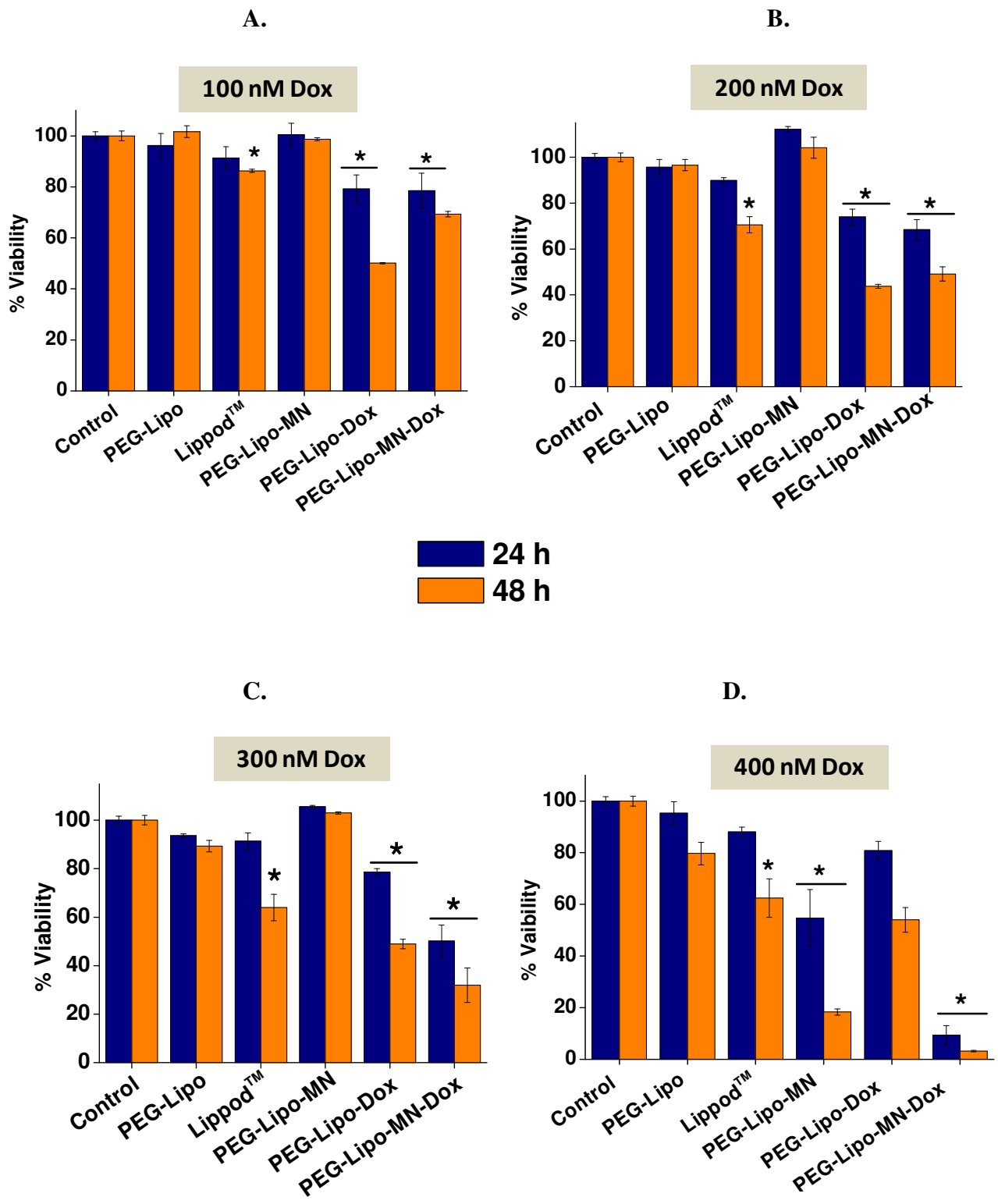
A.
100 nM Dox
% Viability
100
80
60
40
20
0
Control
PEG-Lipo
Lippod™
PEG-Lipo-MN
PEG-Lipo-Dox
PEG-Lipo-MN-Dox
B.
200 nM Dox
% Viability
24 h
48 h
C.
300 nM Dox
% Viability
D.
400 nM Dox
% Vaibility

E.

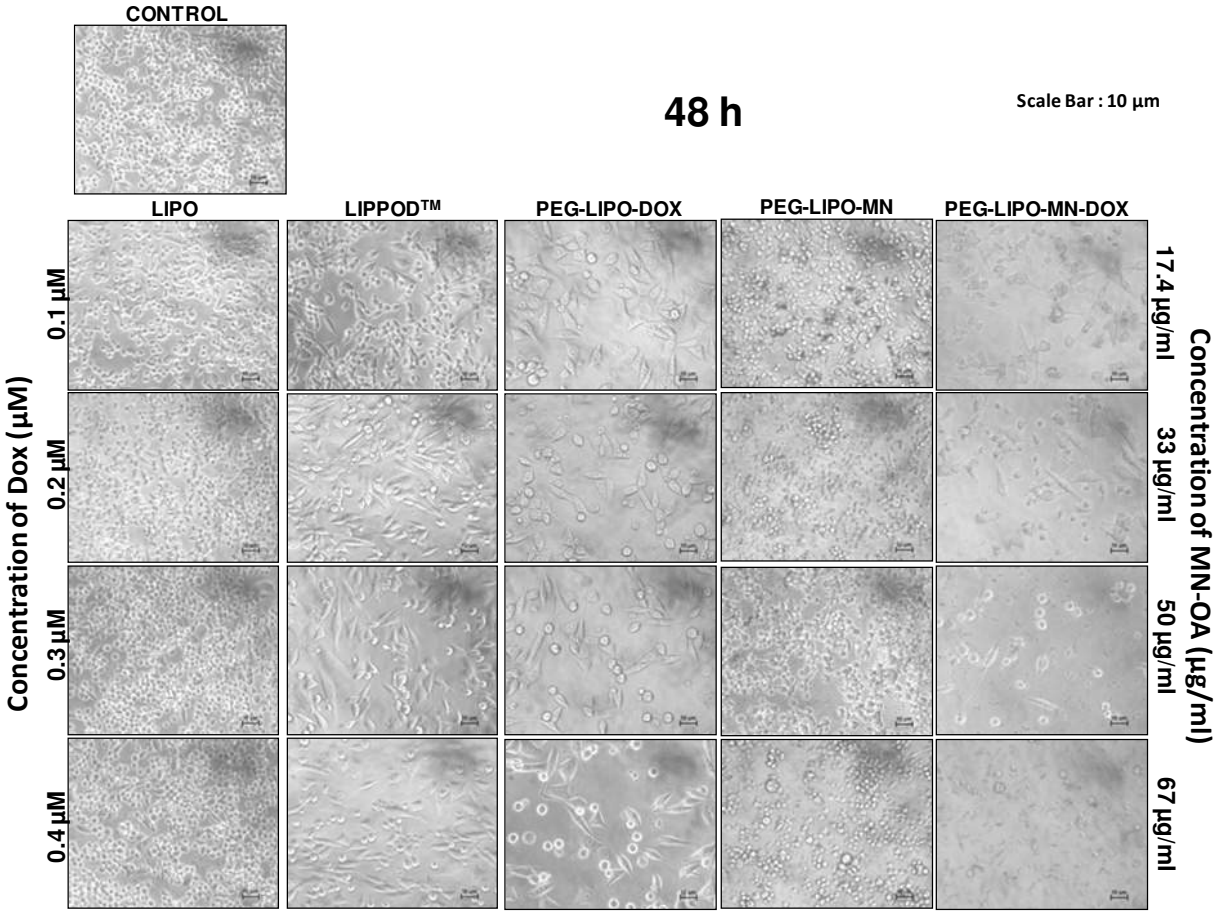

Fig. 3.2.3 (A – D) *Effect of different concentrations, viz. 100, 200, 300 and 400 nM equivalent concentration of Dox and 17.4, 33, 50 and 67 µg/ml equivalent concentration of MN-OA on different liposomes controls and PEG-Lipo-MN-Dox on cell viability of WEHI-164 cells by MTT assay at 24 and 48 h.* Significant at P<0.05 as compared to control.* ***(E)*** *Representative bright field microscopy images of WEHI-164 cells treated with indicated treatments at 48 h. Scale bar =10 µm.*

3.2.6 UPTAKE KINETICS OF PEG-Lipo-MN-Dox IN WEHI-164 CELLS

Since, PEG-Lipo-MN-Dox was found to be most effective in terms of killing of cancer cells as compared to its individual component controls, further experiments were conducted with PEG-

Lipo-MN-Dox. Lippod^{TM} was used as a clinical formulation control to compare its therapeutic efficacy with PEG-Lipo-MN-Dox. The percentage uptake of the non-targeted formulation (PEG-Lipo-MN-Dox) and its sub-cellular distribution were evaluated by flow cytometry, total reflection-X-ray fluorescence spectroscopy (T-XRF), fluorescence microscopy and TEM studies. Moreover, the effect of PEG-Lipo-MN-Dox on cell cycle was studied by PI staining and flow cytometry.

3.2.6.1 Uptake kinetics of PEG-Lipo-MN-Dox in WEHI-164 cells: Flow Cytometry Study

The fluorescent property of Dox was employed to determine the % uptake of PEG-Lipo-MN-Dox inside WEHI-164 cells. WEHI-164 cells were treated with PEG-Lipo-MN-Dox (1 µM: equivalent concentration of Dox) for different time points (viz. 1, 3, 6 and 24 h) and % increase in the fluorescence of Dox inside cells was measured by flow cytometry analysis. Results showed average mean fluorescence intensity (MFI) of 26 ± 2.6 A.U. at 1 h, which increased to 27.5 ± 2.3 A.U. at 3 h and 36 ± 1.3 A.U. at 6 h, respectively and further remained similar at 24h **(Fig. 3.2.4 A & B)**. These results indicate rapid and significant uptake of PEG-Lipo-MN-Dox inside cells at early time points (1 to 6 h), which then seems to saturate upto 24h.

A.

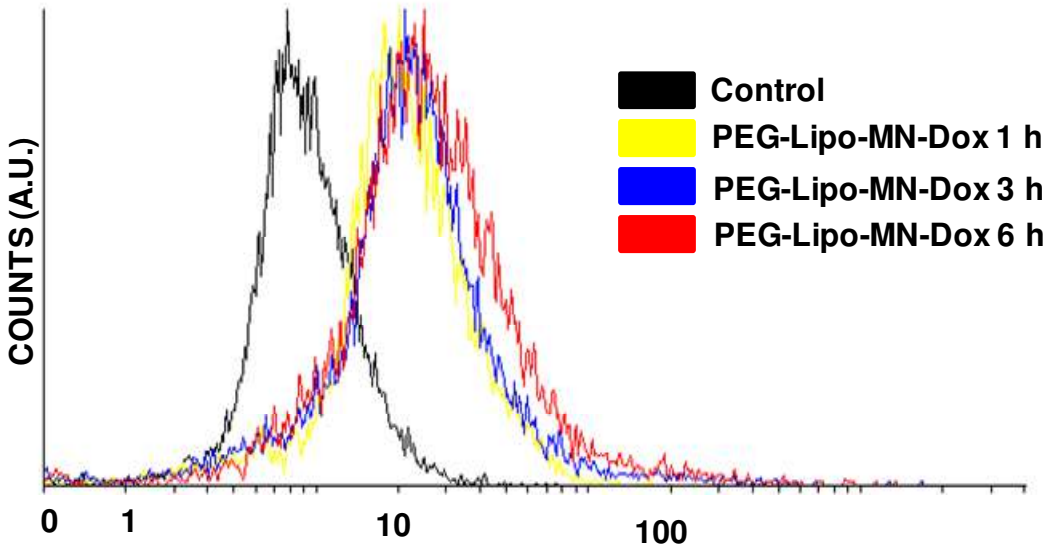

B.

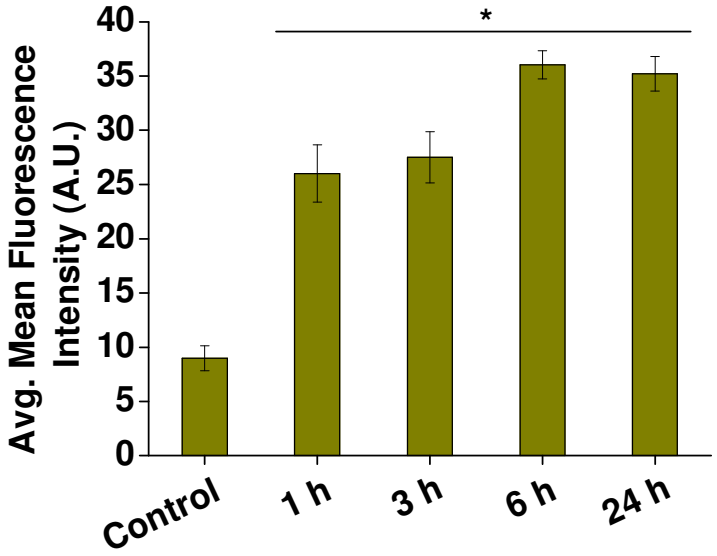

Fig. 3.2.4 (A) *Representative overlay histogram for intra-cellular uptake of PEG-Lipo-MN-Dox in WEHI-164 cells at different time points (viz. 1, 3 and 6 h, note: data for three significant time points are shown for comparison).* ***(B)*** *Average mean fluorescence intensity of fluorescence of PEG-Lipo-MN-Dox treated WEHI-164 cells at different time points (viz. 1, 3, 6 and 24 h). * Significant at P<0.05 as compared to control.(A.U. : Arbitrary unit).*

3.2.6.2 Uptake kinetics of PEG-Lipo-MN-Dox in WEHI-164 cells: Estimation of Cellular Iron (Fe) content by T-XRF analysis

Due to the presence of MN-OA in PEG-Lipo-MN-Dox, the amount of Fe in the formulation could be used as a parameter to study its internalization in the cancer cells. Hence, the results obtained by flow cytometry were further validated by T-XRF, which can sensitively quantify Fe content of MN-OA (upto ppb levels) and thus provide information about the uptake of PEG-Lipo-MN-Dox. As described previously, WEHI-164 cells were treated with PEG-Lipo-MN-Dox (1 µM : equivalent concentration of Dox and 174 µg/ml equivalent concentration of MN-OA) for

different incubation periods, followed by harvesting and digestion of cells in concentrated HCl. The cell-acid digest was heated at 90°C till a clear solution was obtained, followed by dilution in distilled water and processing of samples for T-XRF analysis (as discussed in **Chapter 2, Section 2.12.1**). Results showed a significant increase in Fe content per million cells in a time dependent manner. The % uptake was found to be 5.8 ± 1.8 %, 6 ± 0.8%, 12 ± 1.5%, 14 ± 2.39%, 14 ± 0.6% and 19 ± 1.3% at 30 min, 1h, 2h, 3h, 6h and 24h, respectively **(Fig. 3.2.5)**. These results suggested a rapid uptake of PEG-Lipo-MN-Dox at 30 min, however, maximum uptake was obtained at 24 h.

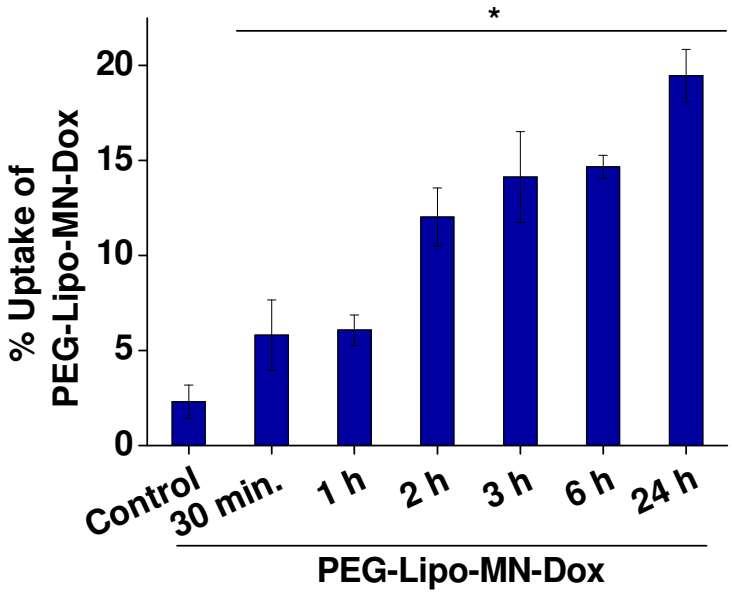

Fig. 3.2.5 *Percentage uptake of PEG-Lipo-MN-Dox in WEHI-164 cells after different time points as determined by Fe content using total reflection-X-Ray fluorescence (T-XRF). * Significant at P<0.05 as compared to control.*

3.2.6.3 Uptake kinetics of PEG-Lipo-MN-Dox in WEHI-164 cells: Fluorescence Microscopy Study

T-XRF analysis indicated significant uptake of PEG-Lipo-MN-Dox inside WEHI-164 cancer cells. The uptake was observed to be rapid as indicated by ~ 6 % uptake at as early as 30 min, which was found to further increase to ~ 14 % at 3 h and was maximum at 24 h (~ 19 %). To further substantiate these results and to determine the sub-cellular distribution of the nano-formulation in WEHI-164 cells, fluorescence microscopy method was used, taking advantage of the red fluorescence of Dox. WEHI-164 cells were treated with PEG-Lipo-MN-Dox (1 µM : equivalent concentration of Dox) for 3, 6 and 24 h, followed by fixing the cells with para-formaldehyde followed by nuclear staining with DAPI and visualization of cells by fluorescence microscopy. Results showed bright red fluorescence of Dox predominantly in the cytosol. At later time points (24 h), co-localization of Dox fluorescence (magenta colour) with nucleus (stained blue with DAPI) could be observed **(Fig. 3.2.6 A)**. The MFI of Dox fluorescence per cell was found to increase from 0.35 ± 0.06 at 3 h to 0.42 ± 0.14 at 6 h and 0.62 ± 0.007 at 24h **(Fig. 3.2.6 B)** suggesting a time dependent increase in the uptake of the nano-formulation in the WEHI-164 cells.

A.

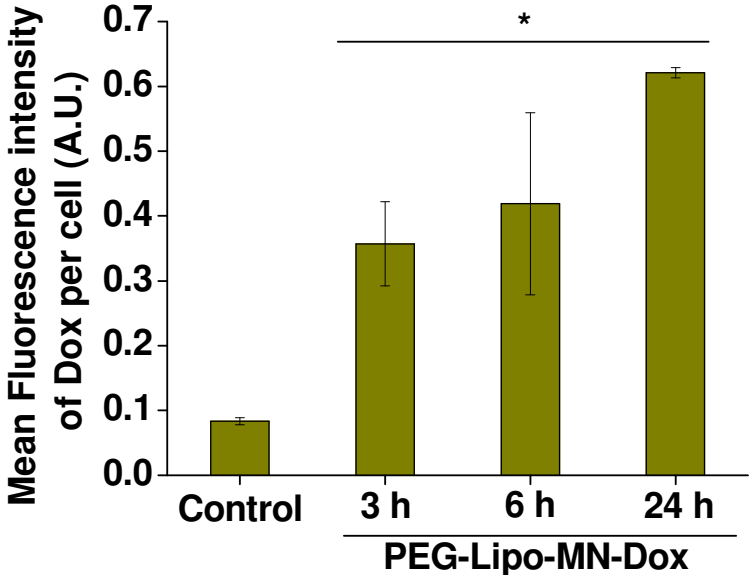

B.

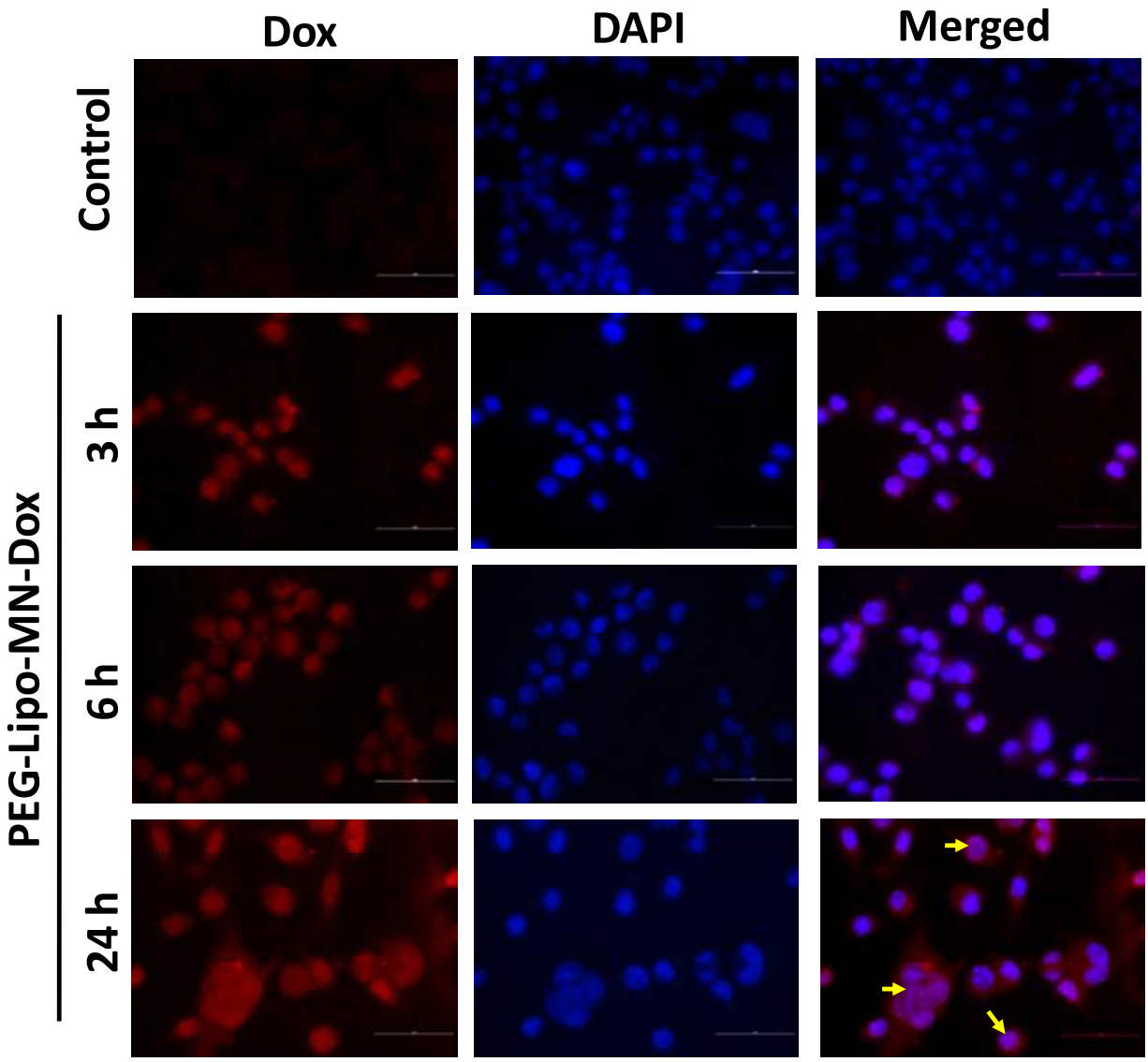

Fig. 3.2.6 ***(A)*** *Kinetics of uptake of PEG-Lipo-MN-Dox in WEHI-164 cells at indicated time points as determined by measurement of MFI of Dox fluorescence per cell (A.U. : Arbitrary units), * Significant at P<0.05 as compared to control and* ***(B)*** *Representative fluorescence microscopy images for sub-cellular distribution of PEG-Lipo-MN-Dox in WEHI-164 cells at different time points (viz. 3, 6 and 24 h). Yellow arrows indicate nuclei showing co-localization (Magenta) of Dox (red) with nuclear stain, DAPI (blue).*

3.2.6.4 TEM analysis validated the sub-cellular localization of PEG-Lipo-MN-Dox mainly in the cytoplasm of WEHI-164 cells

As discussed in **Section 3.2.6.3**, fluorescence microscopy imaging suggested the localization of PEG-Lipo-MN-Dox mainly in the cytosol at early time points (viz. 3 and 6 h), whereas nuclear co-localization was observed at 24 h. This observation was based on the visualization of the red fluorescence of Dox by fluorescence microscopy. To further validate that the intact formulation, i.e. liposomes co-encapsulated with Dox and MN-OA are internalized inside the WEHI-164 cells and the red fluorescence observed is not due to released or leaked Dox from the liposomal formulation, visualization of MN-OA was warranted. Since, iron oxide in MN-OA can be visualized by electron microscopy due to its higher contrast imparted by its atomic weight as compared to other organic cellular components with low atomic weight (viz. carbon, hydrogen, oxygen, etc.), TEM of PEG-Lipo-MN-Dox treated WEHI-164 cells was carried out. Briefly, WEHI-164 cells were treated with PEG-Lipo-MN-Dox (174 µg/ml equivalent concentration of MN-OA and 1 µM equivalent concentration of Dox) at culture conditions for 3 and 24 h. TEM analysis showed significant uptake of the nano-formulation in the cytoplasm as visible from the deposition of high contrast iron (Fe) aggregates. Fe aggregates were found to be deposited in the cytoplasm or inside endocytic vesicles in the cytoplasm **(Fig. 3.2.7 A)**. Treated cells showed significant change in morphology as compared to control cells, such as, shrinkage of nuclei, increase in cell size, change in the number and morphology of mitochondria and increase in number of electron dense vesicles **(Fig. 3.2.7 B).** Interestingly, Fe contrast was not visible in the nucleus of any of the visualized cells. This suggests that the red fluorescence of Dox observed in the nucleus may be due to the Dox released from the internalized liposomal formulation and visible at later time point i.e. 24 h. This hypothesis is further supported by the observed

morphological changes in the treated nuclei (viz. nuclear fragmentation and shrinkage) suggesting interaction of Dox with the cellular nuclei as well. Since, nuclear interaction of Dox is a pre-requisite for manifestation of its cyto-toxicity, these results further corroborate the candidacy of PEG-Lipo-MN-Dox as a potential anti-cancer chemotherapeutic formulation.

A.

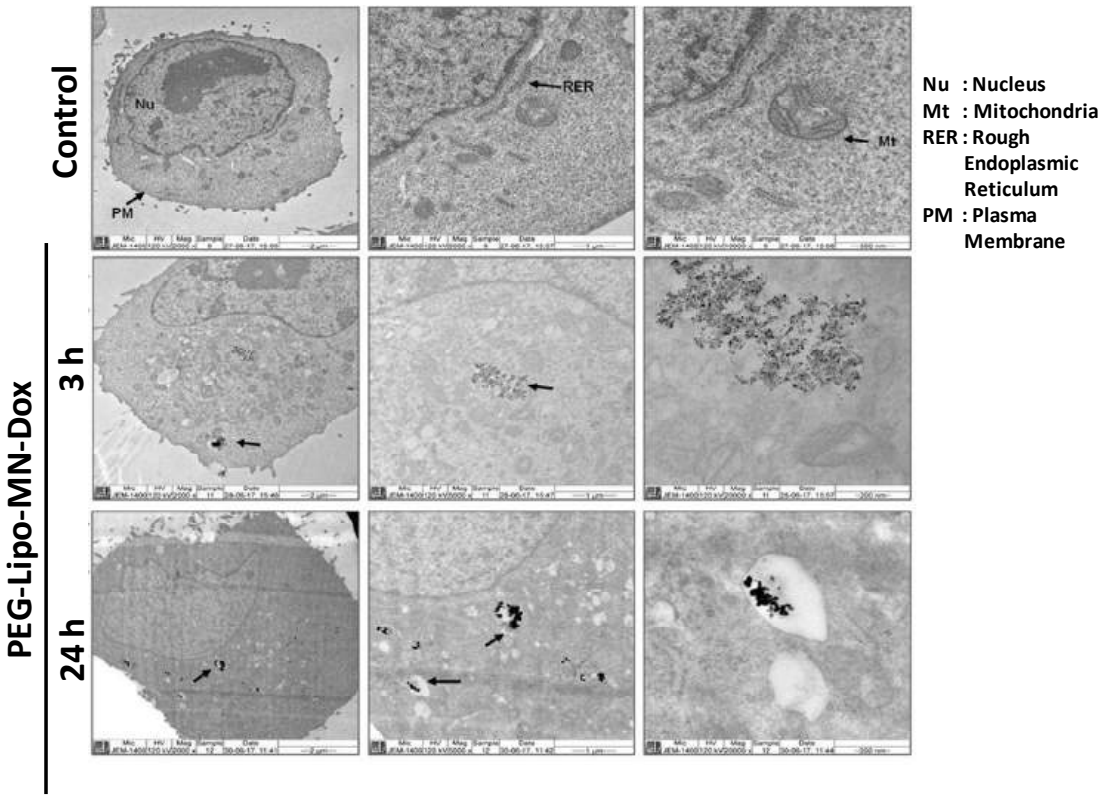

B.

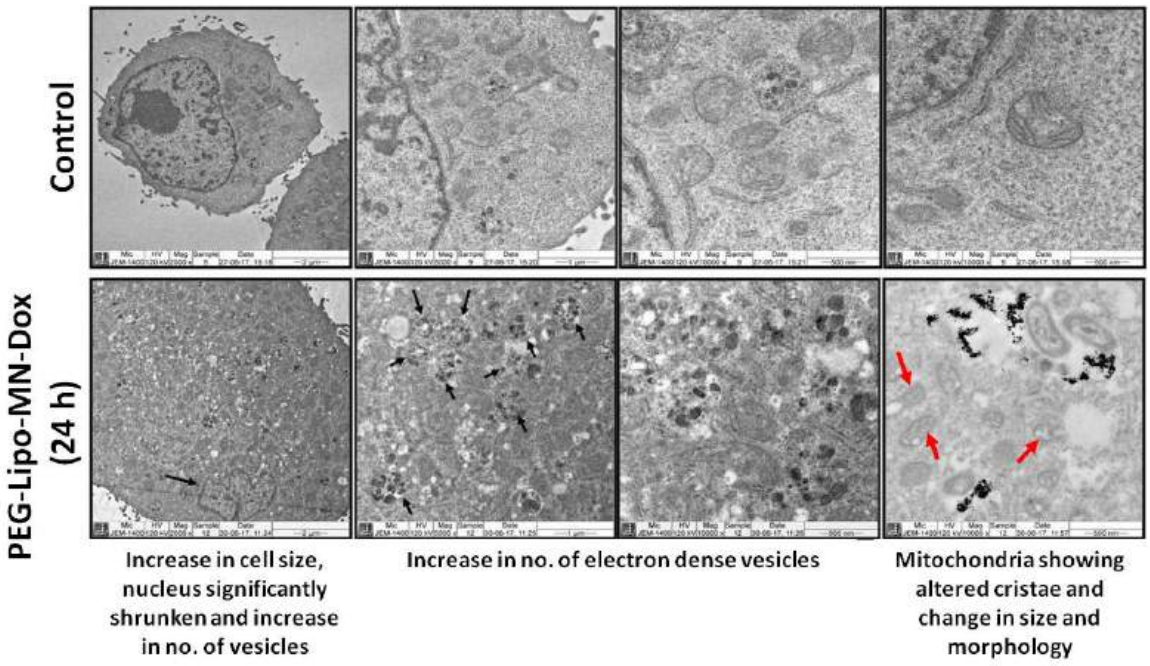

Fig. 3.2.7 *(**A**) TEM analysis of WEHI-164 cells for sub-cellular distribution of PEG-Lipo-MN-Dox at 3h and 24 h. Black arrows indicate the presence of high contrast deposits of iron oxide in cytoplasm and inside cytoplasmic vesicles.* ***(B)*** *Representative images of TEM of WEHI-164 cells for visualization of morphological alterations after treatment with PEG-Lipo-MN-Dox at 24 h. Black arrows indicate presence of electron-dense vesicles and red arrows indicate mitochondria with altered morphology (viz. change in size and altered cristae). Note: Nu: Nucleus, Mt: Mitochondria, RER: Rough Endoplasmic Reticulum and PM: Plasma Membrane.*

3.2.6.5 WEHI-164 cells treated with PEG-Lipo-MN-Dox showed significant increase in the sub-G1 population indicating role of apoptotic cell death

As discussed in **Section 3.2.5.2**, PEG-Lipo-MN-Dox showed a dose dependent increase in the cyto-toxicity in WEHI-164 cells by MTT assay. Moreover, fluorescence microscopy and TEM analysis confirmed significant uptake of PEG-Lipo-MN-Dox in WEHI-164 cells. Nuclear co-

localization of Dox was also observed in the treated cells, which was further corroborated by alterations in the nuclear morphology as observed by TEM. Since, Dox in known to induce apoptotic cell death, sub-G1 analysis (an indicator of apoptotic cell death) was carried out by propidium iodide (PI) staining and flow cytometry. Briefly, WEHI-164 cells were treated with PEG-Lipo-MN-Dox (1µM: equivalent concentration of Dox) followed by harvesting the cells at different time points, viz. 6 h and 24 h. The cells were further fixed with ice cold methanol and processed for PI staining and flow cytometry **(Chapter 2, Section 2.14)**. Results showed a time dependent increase in the sub-G1 population, which increased from 38.06 ± 2.84 % at 6 h to 70.56 ± 5.37 % at 24 h, suggesting an early induction of apoptosis in the treated cells **(Fig. 3.2.8 A & B)**. Whereas the percentage of cells in other phases of cell cycle (viz. G1, S and G2-M) was found to decrease as compared to control at all the time points. These results suggest the role apoptosis as one of the cell death mechanism for cyto-toxicity induced by PEG-Lipo-MN-Dox in WEHI-164 cells.

A.

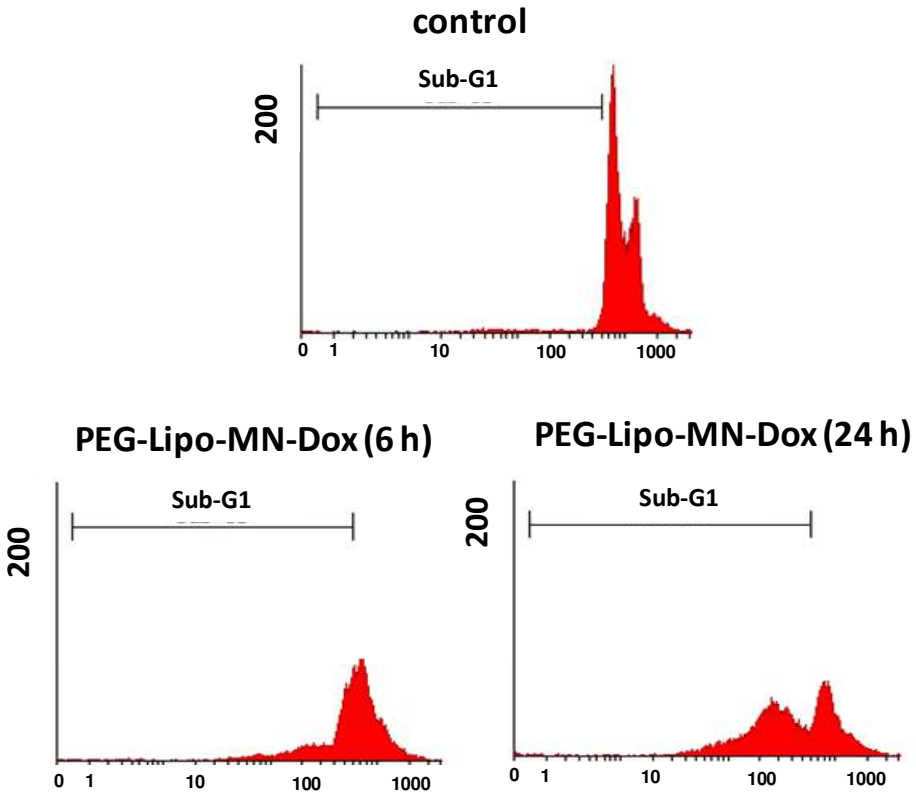

B.

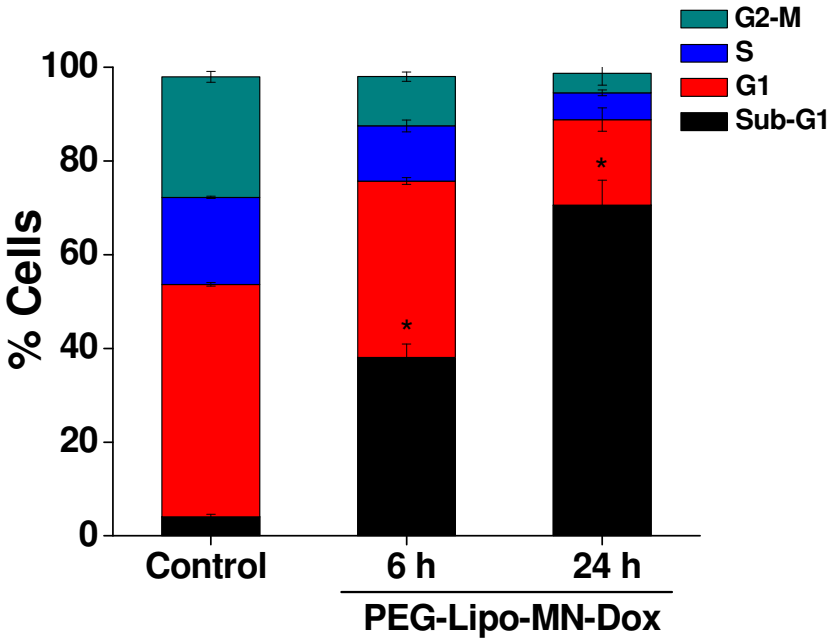

Fig. 3.2.8 (A) *Representative histograms for cell cycle analysis by flow cytometry after PI staining for WEHI-164 cells treated with PEG-Lipo-MN-Dox (1 μM: equivalent concentration of Dox) at different time points (viz. 6 and 24 h). The gated population correspond to cells in Sub-G1 phase.* ***(B)*** *Distribution of WEHI-164 cells in different phases of cell cycle after indicated treatments. Values represent Mean ± SEM and * Significant at P<0.05 as compared to control.*

3.2.7 SYNTHESIS OF cRGD FUNCTIONALIZED PEG-Lipo-MN-Dox

As discussed above, PEG-Lipo-MN-Dox showed significant uptake in WEHI-164 cells as studied by flow cytometry **(Fig. 3.2.4)**, Fe estimation by T-XRF **(Fig. 3.2.5)**, fluorescence microscopy **(Fig. 3.2.6)** and TEM **(Fig. 3.2.7)**. Sub-cellular distribution by fluorescence microscopy and TEM analysis suggested localization of liposomal nano-formulation in the cytoplasm of WEHI-164 cells. Whereas, the liposomal Dox was found to co-localize in the nucleus at 24 h post-treatment. Further, cell cycle analysis after PI staining and flow cytometry showed significant increase in sub-G1 population, suggesting contribution of apoptotic cell

death. These results suggested efficacy of the nano-formulation in terms of significant uptake and cyto-toxicity in cancer cells. Although, PEG-Lipo-MN-Dox was non-targeted, these preliminary results suggested its potential for improved cancer therapy after functionalization with a tumor targeted agent. Thus, for selective targeting of cancer cells, the liposomal nano-formulation needed to be functionalized with a tumor targeting agent, such as a ligand for a tumor specific receptor. For, active tumor targeting, cyclic RGD peptide (cRGD) was chosen mainly due to three reasons, (i) the small molecular weight (~ 300 Da) of the peptide will ensure that the labeled nano-formulation is not bulky, (ii) cRGD will also facilitate the evasion by RES by facilitating higher interaction of cRGD labeled nano-formulation with the tumor cells for internalization and (iii) cRGD specific receptor (i.e. $\alpha v\beta 3$ integrin receptor) is known to be over-expressed on a wide range of tumor cell types as well as on tumor neo-vasculature. The dual targeting of the tumor cells along with its neo-vasculature will help to improve the therapeutic gain of the chemotherapy as reported in literature[266-267]. Thus, the present section discusses the synthesis, characterization and biological evaluation of cRGD labeled PEG-Lipo-MN-Dox, referred to simply as T-LMD, hereafter.

3.2.7.1 Reverse phase - high pressure liquid chromatography (RP-HPLC) and Fourier Transform – Infrared Spectroscopy (FT-IR) analysis confirmed the synthesis of cRGD labeled phospholipid

To synthesize cRGD labeled PEG-Lipo-MN-Dox, a pre-labeling and post-insertion approach was employed[266]. This approach involves the synthesis of a cRGD labeled phospholipid, followed by its incorporation into the liposomal nano-formulation. The synthesis of cRGD labeled phospholipid was carried out by click chemistry using PEGylated-1,2-Distearoyl-

phosphatidyl ethanolamine (DSPE) phospholipid having a maleimide end-group (DSPE-PEG-maleimide) **(Scheme 3.2.3)**. Briefly, DSPE-PEG-maleimide was reacted with thiol group of cRGDfC (cyclic RGD peptide containing additional phenylalanine and cysteine amino acids; the thiol group is provided by cysteine) at 4°C for overnight in a glass bottle in dark (detailed protocol discussed in **Chapter 2 Section 2.5**). The coupling of cRGD to DSPE-PEG-maleimide was confirmed by reverse phase HPLC using water as mobile phase and C8 column as stationary phase. Results showed a significant decrease in the area under the curve for free cRGD from 76786.4 µV.min to 37888.2 µV.min in phospholipid reacted cRGDfC, confirming the conjugation of cRGD to DSPE-PEG-maleimide **(Fig. 3.2.9 A & B)**. To remove the un-reacted cRGD, the reaction mixture was dialyzed against distilled water using dialysis membrane of 3.5 kDa MWCO. HPLC analysis of dialyzed sample showed reduction in the area under the peak to 210.6 µV.min, indicating significant (99.4 %) removal of free cRGD **(Fig. 3.2.9 C)**. Additionally, FT-IR analysis was carried out for free cRGD-SH, DSPE-PEG-maleimide and cRGD conjugated DSPE-PEG-maleimide after dialysis. Results showed the presence of characteristic amide band peaks (amide I and amide II at 1634 and 1545 cm^{-1}, respectively) in cRGD and conjugated lipid, thus confirming the coupling of cRGD to DSPE-PEG. In addition, the Carbonyl stretching vibrations were observed at 1714 cm^{-1} in only lipid and conjugated lipid.

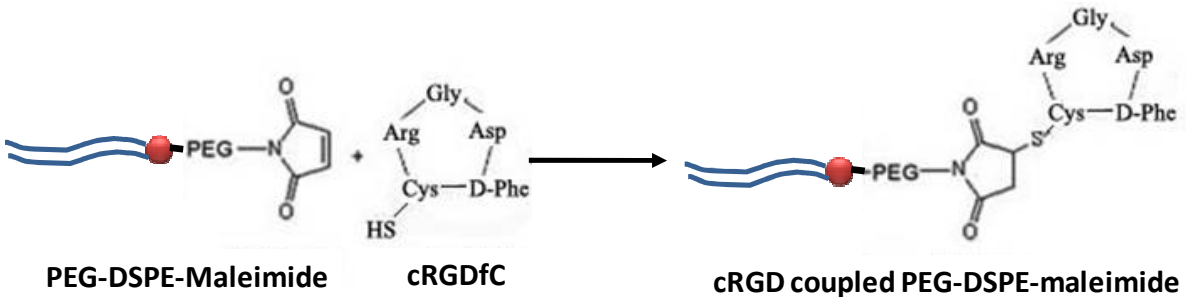

Scheme 3.2.3 *Scheme for reaction between DSPE-PEG-maleimide and cRGDfC peptide.*

A.

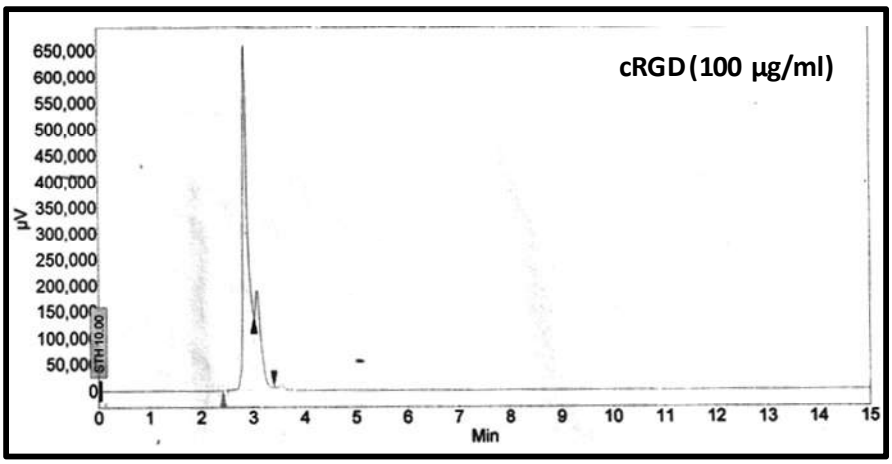
cRGD (100 µg/ml)
µV
650,000
600,000
550,000
500,000
450,000
400,000
350,000
300,000
250,000
200,000
150,000
100,00
50,00
0
STH 10.00
0 1 2 3 4 5 6 7 8 9 10 11 12 13 14 15
Min

B.

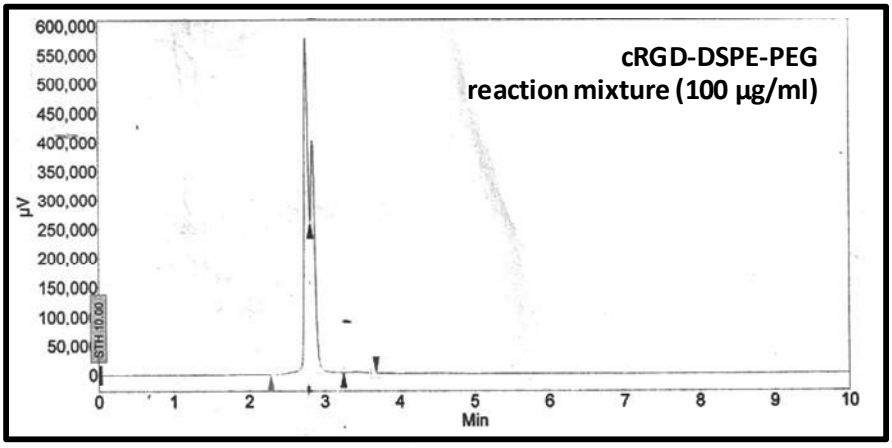
cRGD-DSPE-PEG
reaction mixture (100 µg/ml)
µV
600,000
550,000
500,000
450,000
400,000
350,000
300,000
250,000
200,000
150,000
100,00
50,00
0
STH 10.00
0 1 2 3 4 5 6 7 8 9 10
Min

C.

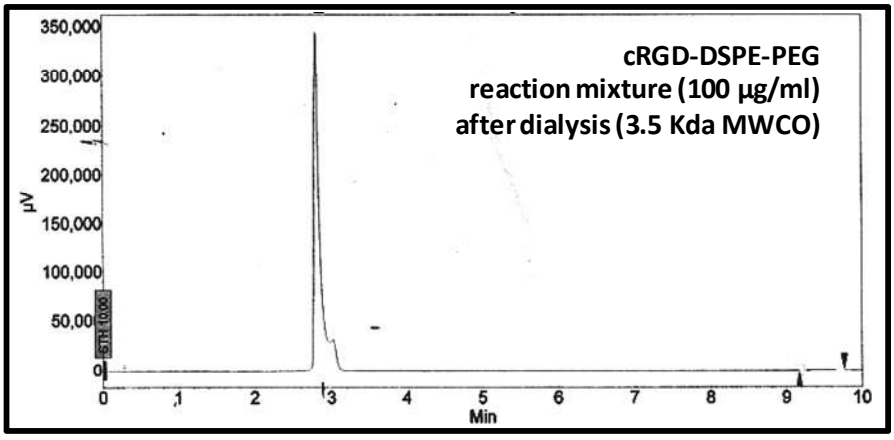
cRGD-DSPE-PEG
reaction mixture (100 µg/ml)
after dialysis (3.5 Kda MWCO)
µV
350,000
300,000
250,000
200,000
150,000
100,000
50,00
0
STH 10.00
0 1 2 3 4 5 6 7 8 9 10
Min

D.

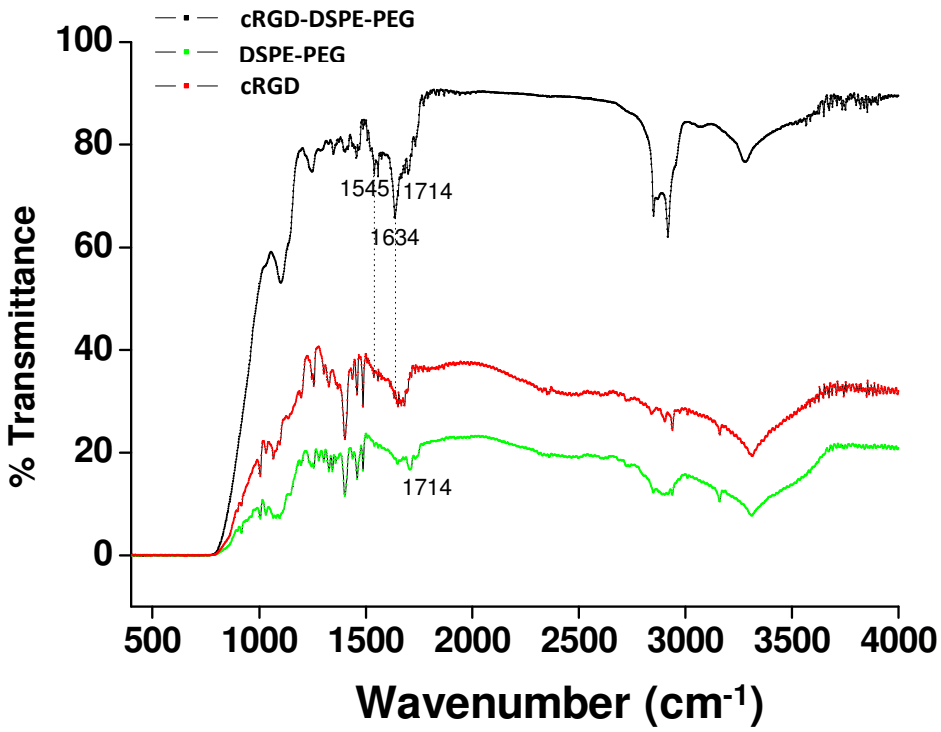

Fig. 3.2.9 *Reverse phase HPLC analysis for* ***(A)*** *cRGD (100 µg/ml),* ***(B)*** *cRGD conjugated PEG-DSPE-maleimide (equivalent to 100 µg/ml cRGD concentration),* ***(C)*** *cRGD conjugated PEG-DSPE-maleimide (equivalent to 100 µg/ml cRGD concentration) after dialysis through 3.5 kDa MWCO membrane and* ***(D)*** *FT-IR analysis of cRGD, DSPE-PEG-maleimide and cRGD conjugated DSPE-PEG-maleimide.*

Sr. No.	SAMPLE	TIME (Min)	Area under the curve (µV.min)
1.	cRGDfC	2.85	76786.4
2.	PEG-DSPE-cRGD reaction mixture	2.75	37888
3.	PEG-DSPE-cRGD after dialysis	2.9	210.6

Table 3.2.2 *Time (in minutes) and area under the curve (μV.min) for HPLC analysis of free cRGD peptide or reaction mixture of cRGD and DSPE-PEG-maleimide, before and after dialysis.*

3.2.7.2 Synthesis of T-LMD and its characterization by different bio-physical techniques

Once, the cRGD labeled phospholipid synthesis was confirmed by HPLC and FT-IR, its incorporation in the liposomal nano-formulation was carried out **(Scheme 3.2.4)**. The synthesis protocol was same as described previously (**Chapter 2, Section 2.4**) with a slight change in the phospholipid composition. The T-LMD consisted of DPPC : DSPE-PEG : DSPE-PEG-cRGD : cholesterol in a molar ratio of 6 : 0.99 : 0.01 : 2. The percentage encapsulation of Dox and MN-OA in this formulation was determined as described previously **(Chapter 2, Section 2.7)**, which were found to be 47.5 ± 0.5 % and 36.76 ± 1.98 %, respectively. DLS analysis showed the hydrodynamic size of T-LMD to be ~ 170 nm with a polydispersity index of 0.2 **(Fig. 3.2.10 A)**. The average zeta potential of the nano-formulation was found to be -21.3 ± 2.5 mV **(Fig. 3.2.10 B)**. Thus, the surface charge of the peptide labeled liposomes (T-LMD) was found to be negative as compared to PEG-Lipo-MN-Dox, which were having an almost neutral surface charge (zeta potential of -7.3 ± 2.1 mV) **(Table 3.2.3)**. Cryo-TEM analysis confirmed the synthesis of spherical vesicles (average size: 166 ± 42 nm) which were pre-dominantly uni-lamellar (~ 70 %) with an average bilayer thickness of 4.58 ± 0.9 nm. The encapsulation of MN-OA was visible as dark aggregates that appeared to be distributed mainly in the liposomal membrane **(Fig. 3.2.10 C, yellow box and arrows)**. The encapsulation of Dox was visible inside the hydrophilic core of liposomes as high contrast lines **(Fig. 3.2.10 C, red box and arrows)**. This pattern of distribution of Dox is in agreement with other reports mentioned in literature, utilizing the citrate

dependent pH gradient method for encapsulation of Dox[268-269]. Thus, cryo-TEM analysis suggested the presence of a mixture of un-encapsulated, Dox and MN-OA encapsulated liposomes. Although, the size distribution and lamellarity of the liposomes appeared to be uniform by cryo-TEM analysis, it needs further validation by more sensitive techniques such as small angle X-ray or neutron scattering. Cryo-TEM analysis of the clinical formulation of PEGylated liposomal Dox (Lippod™) was also carried out for comparison. Cryo-TEM analysis of Lippod™ showed presence of spherical liposomes with slightly smaller size (average size: 133.8 ± 36.6 nm) as compared to T-LMD (average size of 166 ± 42.2 nm). In case of Lippod™ also a mixture of un-encapsulated and Dox encapsulated liposomes was visualized by cryo-TEM analysis.

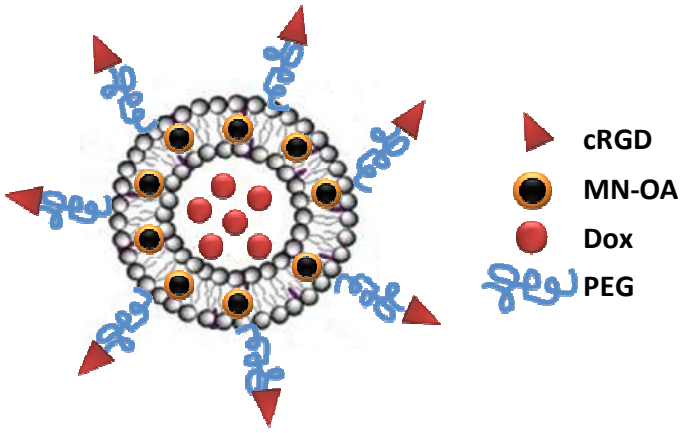

Scheme 3.2.4 *Scheme for the design and composition of T-LMD*

A.

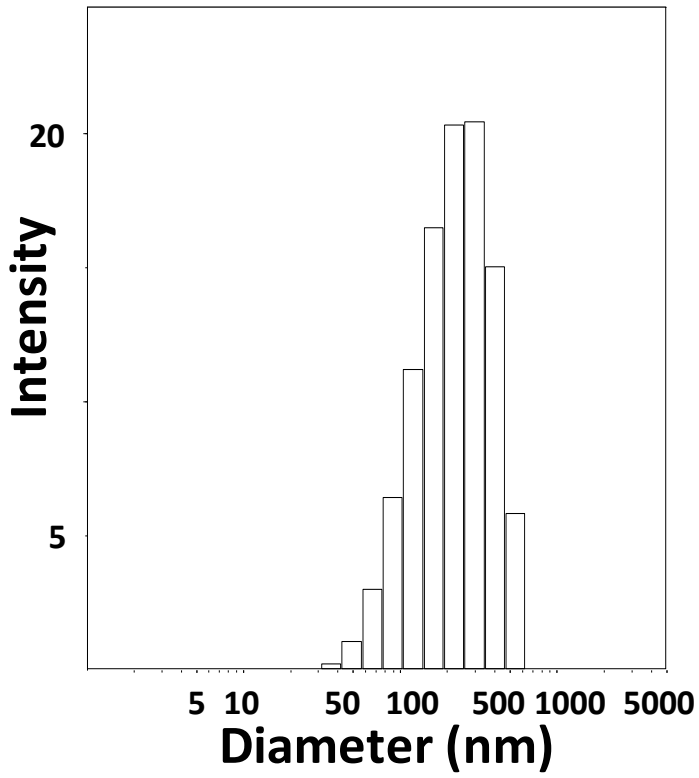
20
Intensity
5
5 10 50 100 500 1000 5000
Diameter (nm)

B.

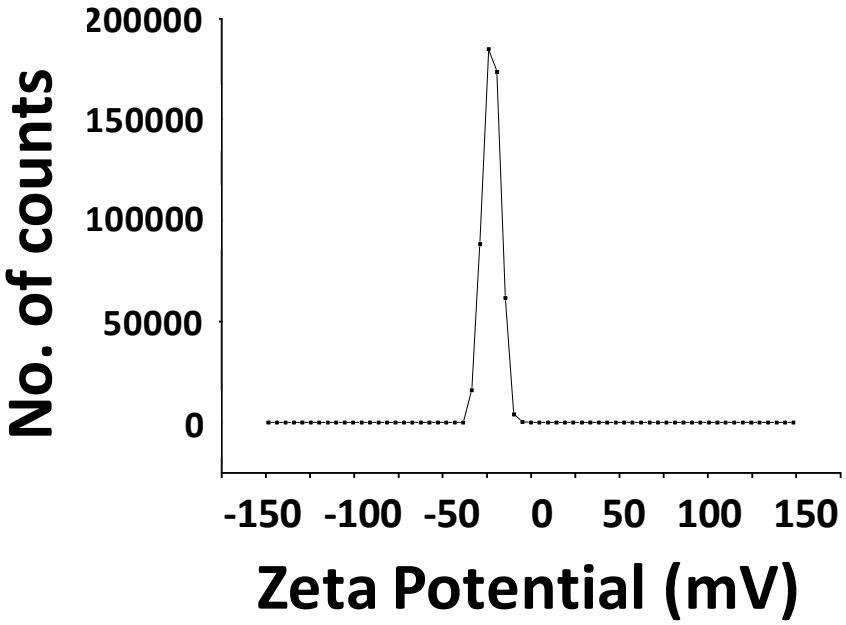
200000
150000
100000
50000
0
No. of counts
-150 -100 -50 0 50 100 150
Zeta Potential (mV)

C.

T-LMD

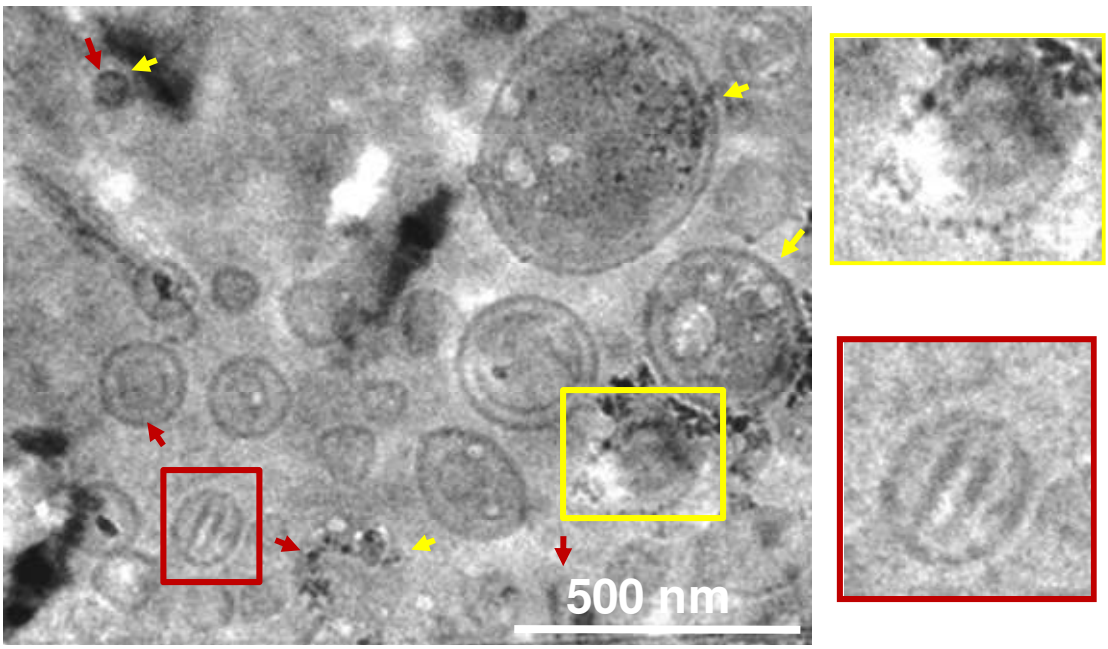

Lippod™

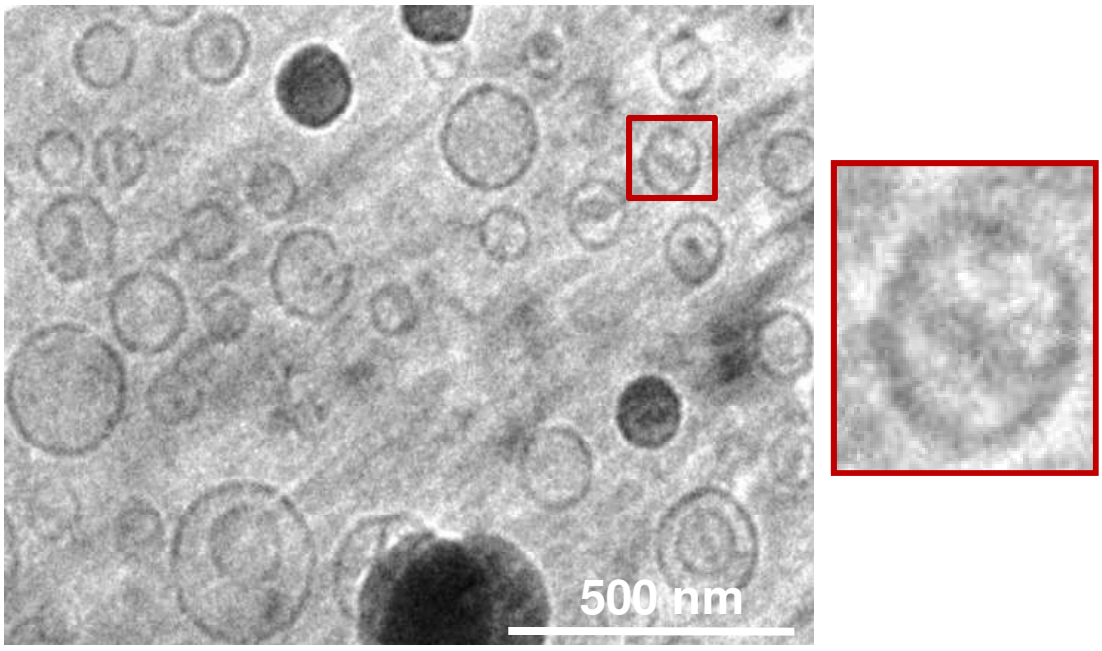

D.

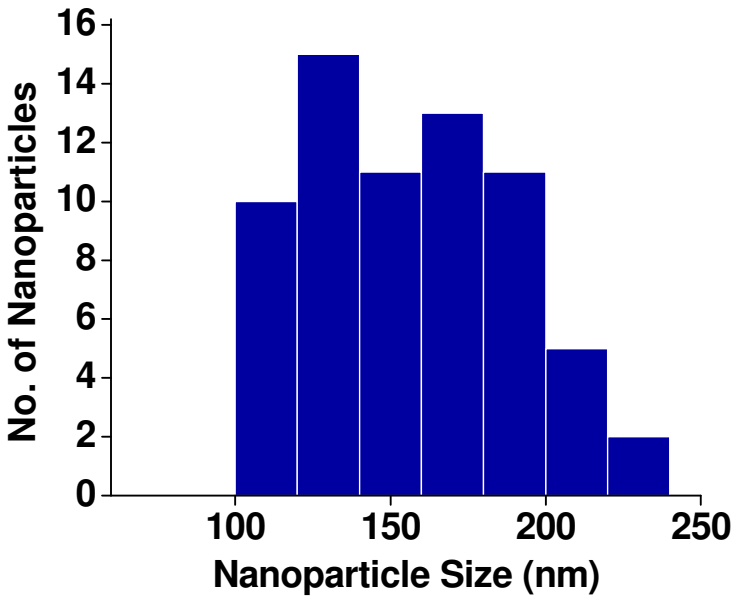

E.

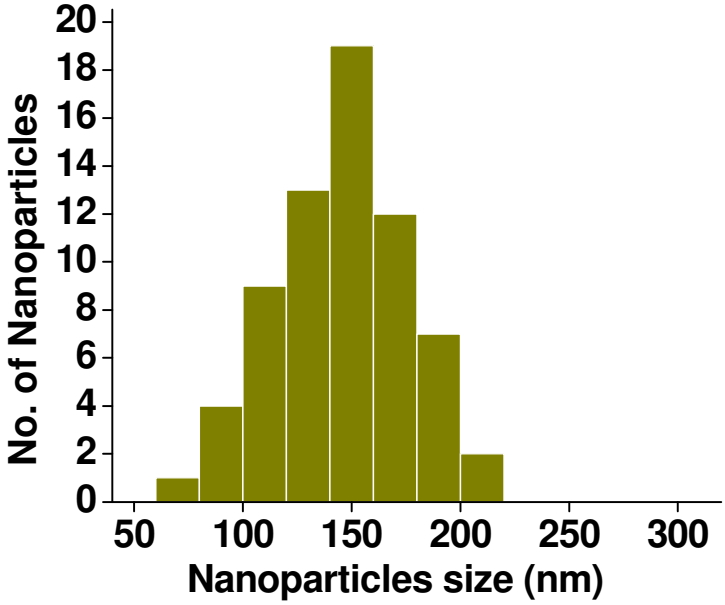

Fig. 3.2.10 *Bio-physical characterization of T-LMD by different methods.* ***(A)*** *Hydrodynamic size distribution of T-LMD as determined by dynamic light scattering (DLS),* ***(B)*** *Surface charge (or zeta potential) of nano-formulation as determined by zeta sizer and* ***(C)*** *Representative images for cryo-TEM analysis of Lippod*^{TM} *and T-LMD. Inset shows magnified image of single liposome with encapsulation of Dox (red box) or MN-OA (yellow box). Size distribution of*

liposomes as determined by statistical analysis of cryo-TEM images (n=100) for ***(D)*** *T-LMD and* ***(E)*** *Lippod*^{TM}.

Sr. No.	Bio-physical characteristics	PEG-Lipo-MN-Dox	T-LMD
1.	**Hydrodynamic size**	157 nm	170 nm
2.	**Polydispersity index**	0.2	0.23
3.	**Surface charge**	-7.3 ± 2.1 mV	-21.3 ± 2.5 mV
4.	**% Encapsulation of Dox**	38.1 ± 1.32	47.5 ± 0.5
5.	**% Encapsulation of MN-OA**	35.6 ± 2.19	36.7 ± 1.98

Table 3.2.3 *Comparison of bio-physical characteristics of PEG-Lipo-MN-Dox and T-LMD.*

3.2.8 T-LMD SHOWED DIFFERENTIAL UPTAKE IN αvβ3 INTEGRIN RECEPTOR OVER-EXPRESSING (U373MG) CELL LINE AS COMPARED TO WEHI-164 CELLS WITH LOW LEVEL EXPRESSION OF THE RECEPTOR

For active tumor targeting, the liposomal nano-formulation was tagged with cRGD peptide. The coupling with cRGD was confirmed by different bio-physical techniques (viz. HPLC and FT-IR **Fig. 3.2.9**). However, to further validate the functional contribution of cRGD for enhanced uptake, intra-cellular uptake studies were carried out in αvβ3 over-expressing U373MG (human glioblastoma) cell line. The status of expression of αvβ3 integrin receptor was determined in U373MG and WEHI-164 (as an immuno-competent tumor model) cell lines using immuno-cytochemistry staining for anti-αvβ3 (Abcam, USA) receptor by flow cytometry. Later, the

uptake of liposomal nano-formulation with or without the cRGD tagging was compared in U373MG and WEHI-164 cells lines by Fe estimation. The results are discussed below:

3.2.8.1 U373MG showed significantly higher (~ 10 fold) expression of αvβ3 integrin receptor as compared to WEHI-164 cell line

As discussed above, based on literature survey, U373MG (an αvβ3 integrin receptor over-expressing) cell line was selected for validating the role of cRGD tagging for active receptor mediated uptake in cancer cells. The status of expression of αvβ3 integrin receptor expression was determined in both U373MG and WEHI-164 cells by flow cytometry analysis after staining with receptor specific antibody. Results showed ~ 10 fold higher expression of integrin receptor in U373MG cells as compared to WEHI-164 **(Fig. 3.2.11)**. Thus, the over-expression of αvβ3 receptor in U373MG and lower expression in WEHI-164 cells was confirmed and validated.

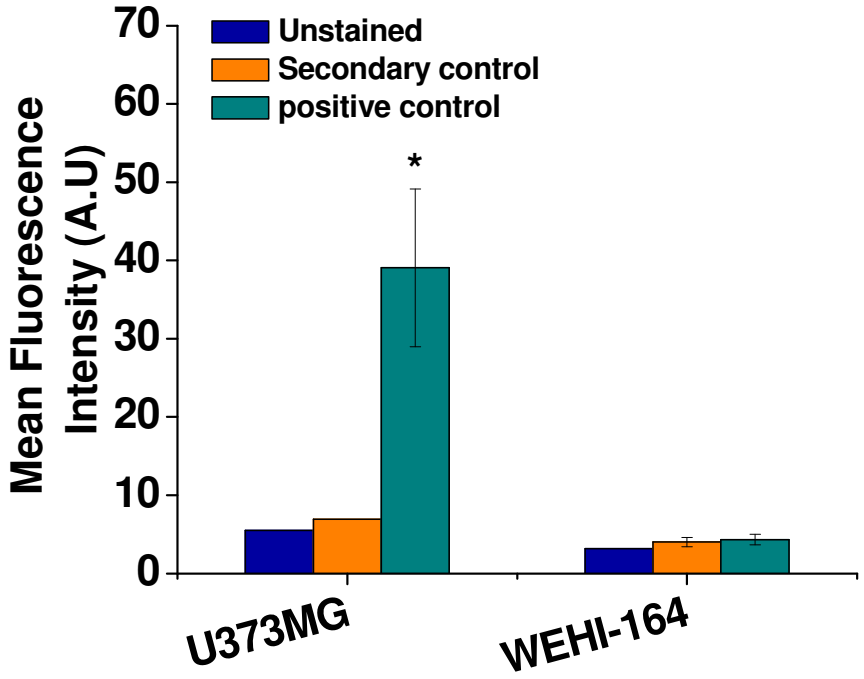

Fig. 3.2.11 *Status of level of expression of αvβ3 integrin receptor in WEHI-164 and U373MG cell lines by flow cytometry, following staining with receptor specific antibody and Alexa Flour 488 labeled secondary antibody.*

3.2.8.2 Flow cytometry showed higher uptake of T-LMD than PEG-Lipo-MN-Dox in U373MG cells

Since, U373MG cells showed higher expression of αvβ3 integrin receptor, the differential uptake of PEG-Lipo-MN-Dox with or without cRGD tagging was further studied in this cell line by flow cytometry. Briefly, the U373MG cancer cells were treated with PEG-Lipo-MN-Dox or T-LMD (0.1 µM: equivalent concentration of Dox and 20 µg/ml equivalent concentration of MN-OA) for 3h followed by processing the cells for flow cytometry analysis. The concentration of Dox in the nano-formulation was very low for flow cytometry studies and it could not be increased due to the observed cyto-toxicity of the formulation at higher concentration of Dox (viz. 1 µM, as discussed in **Section 3.2.6.5**, **Fig. 3.2.8** of this chapter). Thus, SSC (side scatter for granularity) vs FSC (forward scatter for increase in cell size) analysis was carried out, instead of measuring the increase in Dox fluorescence inside the cells. Uptake of the nano-formulation resulted in increase in the granularity of the cells in a concentration dependent manner. Results showed a significant increase in cell population with high SSC in case of PEG-Lipo-MN-Dox (20.6 ± 5.9 %) as compared to control [gated population, Poly-2 (blue), with respect to control]. Whereas, T-LMD showed a further higher increase in SSC (32.4 ± 3.1 %), thus indicating a higher uptake of T-LMD in U373MG cells as compared to only PEG-Lipo-MN-Dox **(Fig. 3.2.12 A & B)**. However, these results needed further validation by other sensitive method of detection.

A.

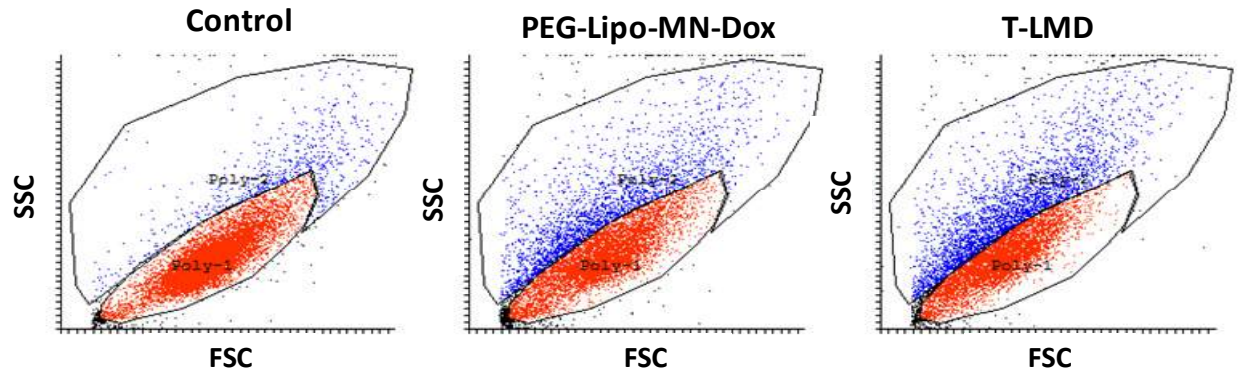

B.

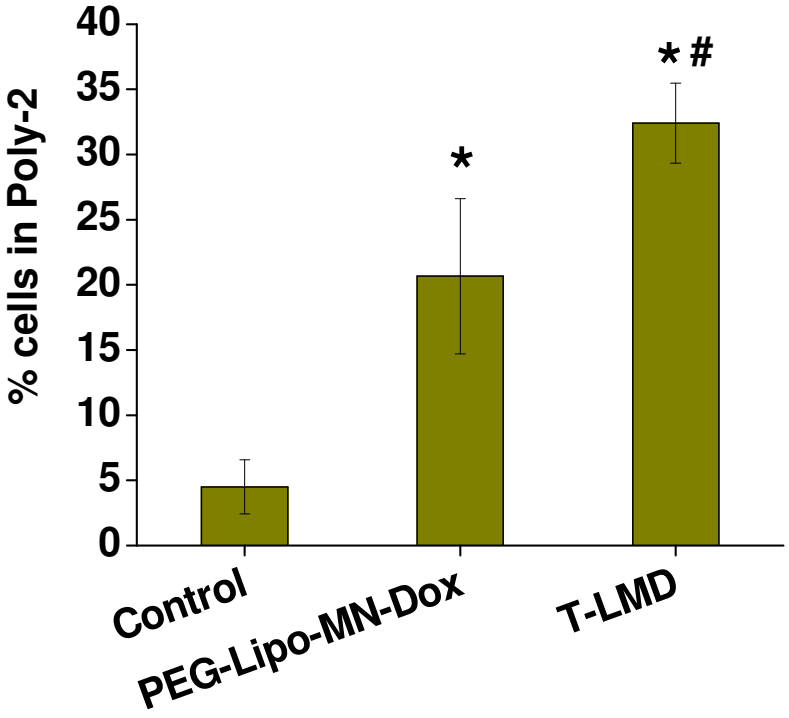

Fig. 3.2.12 (A) *Flow cytometry (FSC vs SSC) analysis of U373MG cells treated with PEG-Lipo-MN-Dox with or without cRGD conjugation at 3 h.* ***(B)*** *U373MG cells (%) with high SSC (gated population poly-2) after treatment with PEG-Lipo-MN-Dox with or without cRGD conjugation at 3 h. * Significant at P<0.05 as compared to control and # indicates significant difference between PEG-Lipo-MN-Dox treated groups with or without cRGD conjugation.*

3.2.8.3 Fe estimation validated the higher uptake of T-LMD in U373MG cells

Flow cytomtery analysis showed a higher SSC (corresponding to increased cellular granularity) in U373MG cells treated with T-LMD as compared to PEG-Lipo-MN-Dox. These results were suggestive of a higher uptake of the T-LMD in U373MG cells. However, to further validate these results and to determine the absolute uptake of the nano-formulation in the cancer cell line, a more sensitive method of Fe estimation by colorimetric assay was employed. As discussed earlier in **Chapter 2, Section 2.12.2**, the presence of MN-OA facilitated the sensitive detection of Fe and thus aided in the estimation of nano-formulation uptake in cancer cells. Although, previously **(Section 3.2.6.2** & **Fig. 3.2.5)** the detection of Fe was done using T-XRF; its use was limited by lengthy sample preparation and assay time (typically each sample requires at least 2 h of preparation and 12 samples can be simultaneously processed in the T-XRF instrument). Moreover, this technique requires high cell number for each sample, which is difficult in case of multiple treatment groups, time points and their replicates. Therefore, colorimetric method with relatively higher throughput, compatible with a plate reader and an ability to process multiple samples simultaneously was devised. To determine the sensitivity, the ortho-phenanthroline method for Fe estimation was standardized using 10 ppm ferrous sulphate as standard. Standard graph showed R-square value of 0.99, and a detection range of 1 ppm to 10 ppm, thus, indicating the efficiency of assay to detect upto 1ppm of Fe in samples **(Fig. 3.2.13 A)**. As discussed in **Chapter 2, Section 2.12**, for determination of nano-formulation uptake in cancer cells, cells treated with PEG-lipo-MN-Dox with or without cRGD conjugation (equivalent to 0.1 µM Dox concentration and 20 µg/ml equivalent concentration of MN-OA) were digested in conc. HCl, followed by heating to decrease the sample volume. A sample volume of 50 µl was used for assay. Results showed 34.8 ± 1.5 % uptake of T-LMD as against 10.2 ± 1.4 % uptake of PEG-

Lipo-MN-Dox in U373MG cells. These results confirm higher uptake of conjugated nano-formulation in U373MG cells. To confirm that the higher uptake is mediated through the interaction of cRGD with its specific αvβ3 integrin receptor, the uptake studies were repeated after a pre-treatment of cells with 10 nM free cRGD peptide for 3h, to block/engage the integrin receptors **(Scheme 3.2.5)**. Results showed a significant decrease in the uptake of T-LMD to 19.1 ± 2.1 % but decline in the uptake was insignificant for unconjugated PEG-Lipo-MN-Dox (8.1 ± 0.54 %) in U373MG cells **(Fig. 3.2.13 B)**. These results confirm that the cRGD conjugated Lipo-MN-Dox shows higher uptake in U373MG cells and that receptor mediated endocytosis appears to be one of the probable mechanisms of uptake.

A.

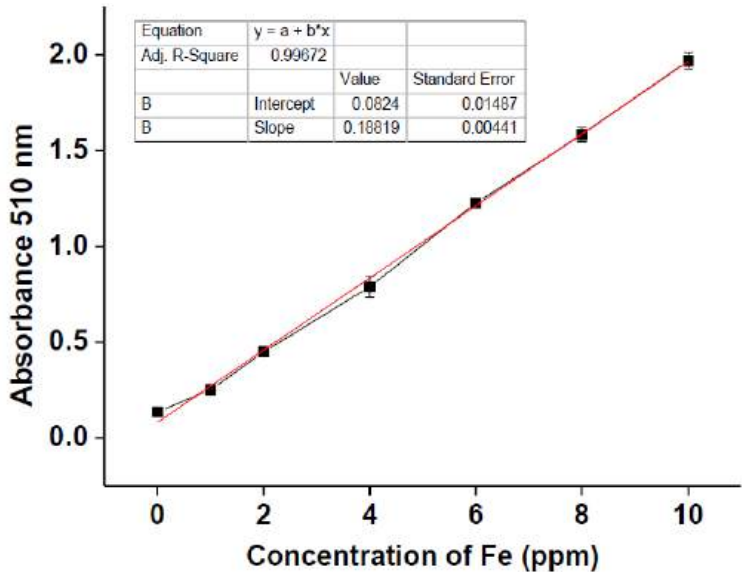

B.

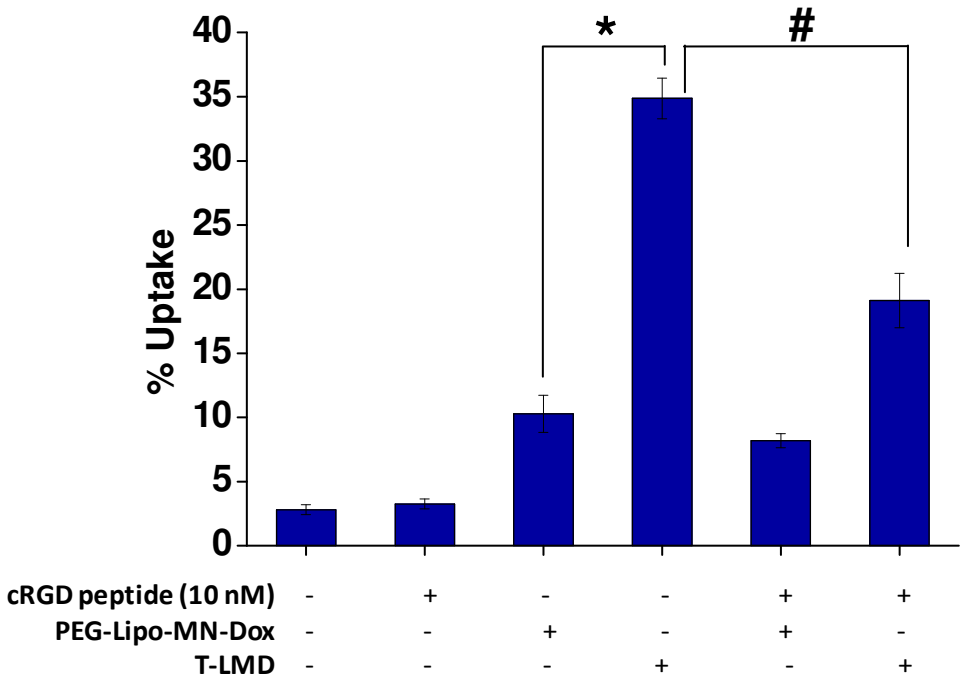

Fig. 3.2.13 *(**A**) Standard graph for Fe estimation by colorimetric detection based ortho-phenanthroline method [inset table indicates the values of correlation co-efficient (R), slope and intercept obtained after linear fitting of the line graph]* ***(B)*** *% Uptake of cRGD conjugated and unconjugated PEG-Lipo-MN-Dox in U373MG cells with or without pre-treatment with free cRGD (blocking) peptide. The Fe content of PEG-Lipo-MN-Dox or T-LMD (equivalent to 20 µg/ml equivalent concentration of MN-OA) was considered as 100 % to determine the % uptake of these nano-formulations in treated U373MG cells. * Significant difference (P<0.05) between PEG-Lipo-MN-Dox and T-LMD treatment groups and # indicates significant difference (P< 0.05) between T-LMD and cRGD pre-treated (cRGD + T-LMD) treatment groups.*

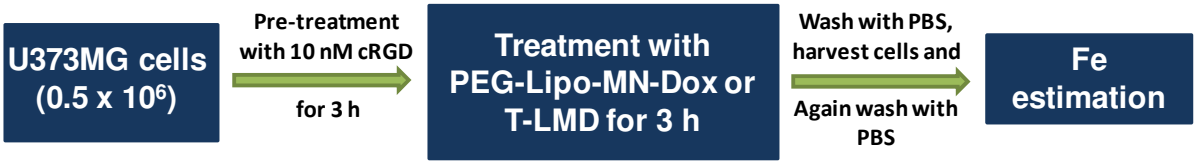

Scheme 3.2.5 *Scheme for treatment of U373MG cells with cRGD peptide (as a blocking peptide) or PEG-Lipo-MN-Dox with or without cRGD conjugation for 3h, followed by the processing of cells for Fe estimation by ortho-phenanthroline method of Fe estimation.*

3.2.8.4 U373MG cells showed higher intra-cellular uptake of T-LMD as compared to WEHI-164 cells

As discussed above, T-LMD showed significantly higher uptake in U373MG cells as compared to its unconjugated counterpart. It intrigued me to determine what would be status of uptake of these nano-formulations in WEHI-164 cells, which showed minimal level of expression of αvβ3 integrin receptor. Therefore, the uptake of PEG-Lipo-MN-Dox conjugated with or without cRGD was compared in mouse fibrosarcoma (WEHI-164) cells and integrin receptor over-expressing human glioblastoma (U373MG) cells. Briefly, cancer cells were treated with T-LMD or PEG-Lipo-MN-Dox (equivalent to 0.1 µM of Dox and 20 µg/ml of MN-OA) for 3 h followed by harvesting the cells and processing them for Fe estimation by ortho-phenanthroline method (as described above and in **Chapter 2, Section 2.12.2**). Results showed a significantly higher uptake (3.4 fold) for T-LMD as compared to un-conjugated formulation in U373MG cells **(Fig. 3.2.14)**. However, WEHI-164 cells showed a marginal increase (1.3 fold) in the uptake of cRGD conjugated PEG-Lipo-MN-Dox (25 ± 2.8 %) as compared to un-conjugated formulation (19 ± 2.3 %). Thus, the cRGD labeling didn't show significant enhancement in the uptake of the liposomal nano-formulation in WEHI-164 cells, probably due to the lower expression of αvβ3 integrin receptors. These results indicate the involvement of some other passive mechanism of uptake of T-LMD in WEHI-164 cells.

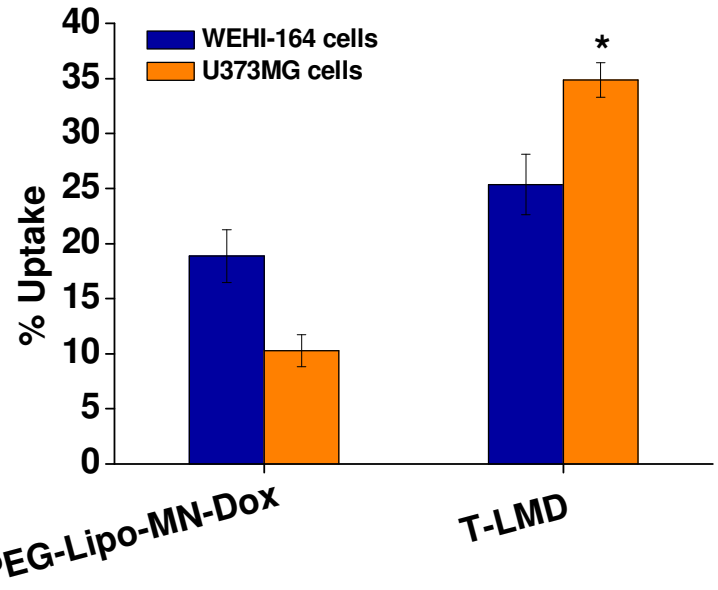

Fig. 3.2.14 *Comparison of percentage uptake of PEG-Lipo-MN-Dox conjugated with or without cRGD in WEHI-164 and U373MG cell lines.* Significant difference (P<0.05) between U373MG cells treated with PEG-Lipo-MN-Dox with or without cRGD conjugation.*

3.2.8.5 Role of receptor mediated endocytosis in uptake of T-LMD in U373MG cells but not in WEHI-164 cells

As discussed in above **Sub-sections** (**3.2.8.3** and **3.2.8.4**), T-LMD was observed to be internalized in U373MG cells via an active mechanism of receptor mediated endocytosis. Whereas, internalization studies with WEHI-164 cells were suggestive of a passive uptake mechanism for the liposomal nano-formulation. Thus, to further validate the role of receptor mediated endocytosis in uptake of T-LMD in U373MG cells, the cancer cells treated with the nano-formulation for different time points (viz. 1 h and 3 h) were treated with antibody specific for early endosomal marker (EEA-1) and processed for confocal microscopy (Leica DMi 8, Germany). Results showed significant increase in the number of endosomes (green foci labeled

with anti-EEA1) in U373MG cells at 1 h post-treatment with T-LMD. Moreover, the red fluorescence of Dox was found to co-localize with the green foci of early endosomes. However, there was a marked decrease in the number of green foci at 3h and the cell morphology was found to be drastically altered showing cell shrinkage **(Fig. 3.2.15 A)**. U373MG cells treated with only Dox showed the red fluorescence of Dox to be localized mainly in the nucleus. On the contrary, WEHI-164 cells treated with T-LMD didn't show any increase in the number of green foci of early endosomes at 1 h or 3 h. In fact, the treated cells showed disappearance of the green foci (visible in untreated control cells) and the red fluorescence of Dox was found to be diffused in the cytoplasm as well as in the nucleus. In WEHI-164 cells also, 3h treatment showed alterations in the cell morphology with significant cell shrinkage **(Fig. 3.2.15 B)**. Analogous to U373MG cells, WEHI-164 cells also showed the localization of only Dox in the nucleus.

A.

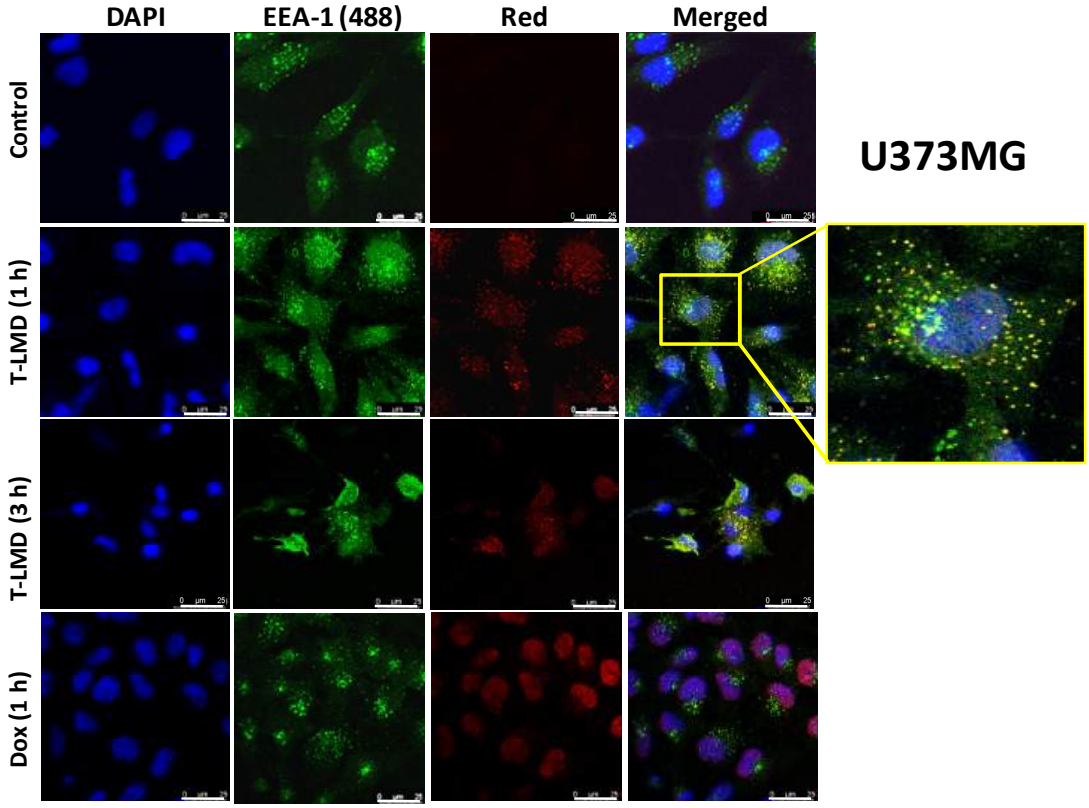

B.

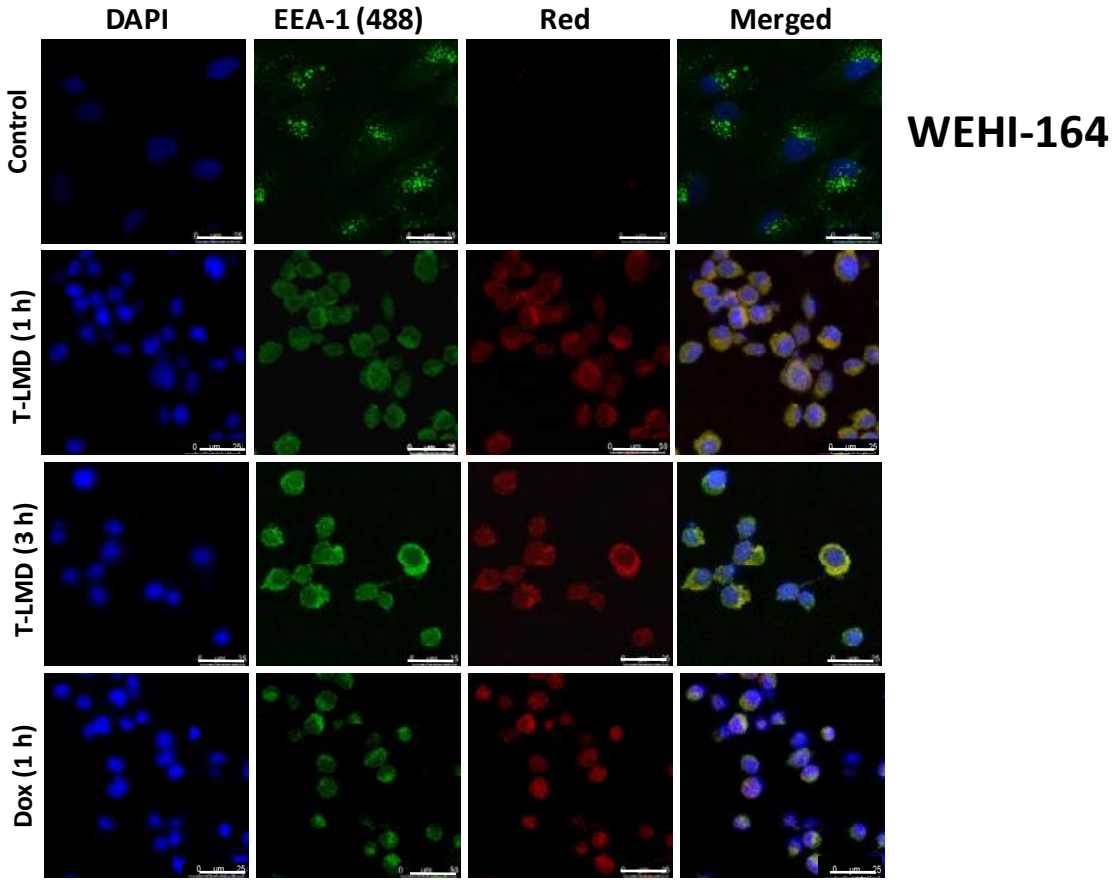

Fig. 3.2.15 *Representative confocal microscopy images of* ***(A)*** *U373MG cells and* ***(B)*** *WEHI-164 cells treated with T-LMD and only Dox for indicated time-points. The green fluorescent foci correspond to early endosomes labeled with early endosomal marker (EEA-1). The red fluorescence corresponds to the distribution of Dox and nuclei are stained blue with DAPI. Scale bar = 25 μm. Inset shows the magnified image of a single U373MG cell demonstrating co-localization (yellow fluorescence in overlay image) of EEA-1 (green fluorescence) and Dox (red fluorescence).*

3.2.9 EVALUATION OF CYTO-TOXICITY OF T-LMD IN MULTIPLE CANCER AND NORMAL CELL LINES

As T-LMD showed higher uptake in both U373MG and WEHI-164 cell lines, the cRGD conjugated nano-formulation was used for further studies. Cell cyto-toxicity experiments in multiple cancer and normal cell lines were carried out to evaluate the anti-cancer efficacy of the targeted liposomal nano-formulation. But before evaluation of the anti-cancer efficacy, the status of the αvβ3 integrin receptor was determined in these cell lines, which is discussed in following Section.

3.2.9.1 U373MG cells showed the highest expression of αvβ3 integrin receptor amongst the studied cancer and normal cell lines

Before evaluating the anti-cancer efficacy of T-LMD in different cancer and normal cell lines, the status of αvβ3 integrin receptor expression on the surface of these cell lines was studied by immuno-cytochemistry using the receptor specific antibody, followed by flow cytometry. For elimination of non-specific signal, all cancer cell lines were also treated with only secondary antibody (secondary antibody control). The receptor status was evaluated in six cancer cell lines, namely, U373MG (human glioblastoma), A549 (human lung carcinoma), MDAMB-231 & MCF-7 (human breast carcinomas), WRL-68 (human hepatoma) and WEHI-164 (murine skin carcinoma) and one normal cell line, WI26VA44 (human normal lung fibroblast). Results showed highest expression of the receptor in U373MG cells (average mean fluorescence intensity 41.9 ± 12.33 A.U.), followed by WI26VA44 (10.6 ± 0.2), A549 (9.7 ± 0.8), MCF-7 (8.9 ± 0.4), MDAMB-231 (8.3 ± 0.2), WRL68 (7.5 ± 0.8) and WEHI-164 (4.3 ± 0.6) cells in the stated order of receptor expression, respectively **(Fig. 3.2.16)**.

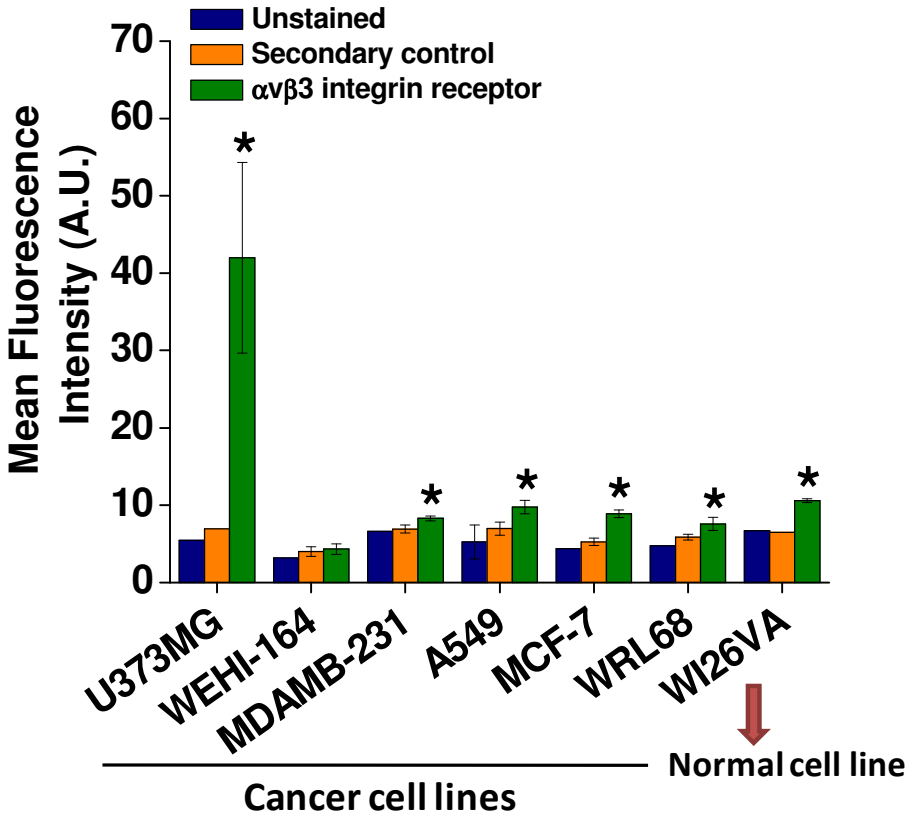

Fig. 3.2.16 *Status of level of expression of αvβ3 integrin receptor in multiple cancer and normal cell lines. * Significantly different at P<0.05 with respect to secondary antibody control. (A.U.: Arbitrary units).*

3.2.9.2 T-LMD showed significant cyto-toxicity in multiple cancer cells lines as compared to Lippod™

Amongst the screened cancer cell lines, U373MG was found to have the highest expression αvβ3 integrin receptor. However, other cell lines also showed moderate expression of the receptor in the stated order (WI26VA44 > A549 > MCF-7 > MDAMB-231 > WRL68). Whereas, WEHI-164 cells showed the lowest signal for the binding of anti-αvβ3 antibody as studied by flow cytometry **(Fig. 3.2.16)**. Therefore, the anti-cancer efficacy of T-LMD was evaluated in these

cell lines. For this, the different cancer (viz. A549, MCF-7, MDAMB-231, WEHI-164, WRL68 and U373MG) and normal (WI26VA44) cell lines were treated with increasing concentrations of T-LMD or Lippod^{TM} (viz. 25, 50, 75, 100, 200, 300 and 400 nM equivalent concentration of Dox) for 48 h followed by determination of cell viability by MTT assay. For ease of comparison, graphs of selected concentrations, viz. 25, 50, 100 and 200 nM equivalent concentration of Dox for T-LMD or Lippod^{TM} are shown in **Fig. 3.2.17 A - D**. Results showed a concentration dependent increase in the cyto-toxicity in all the cancer cell lines. Normal cell line also showed a concentration dependent increase in cyto-toxicity, albeit lower than that observed in case of cancer cell lines. Out of the six cancer cell lines, WEHI-164 and MDAMB-231 were found to be most sensitive to the anti-cancer effect of T-LMD. At 48 h, at 200 nM equivalent concentration of Dox, the viability of WEHI-164 and MDAMB-231 cells was found to be 19.86 ± 3.7 and 17.7 ± 3.1 %, respectively, as compared to U373MG (23.2 ± 2.5 %), A549 (23.08 ± 8.6 %), MCF-7 (31.5 ± 0. %) and WRL-68 (24.14 ± 8.4 %) for T-LMD, respectively **(Fig. 3.2.17 A – D)**. Moreover, the cell viability was significantly higher after treatment with Lippod^{TM} as compared to T-LMD, in all the cancer cell lines (viz. 51.74 ± 1.1, 85.69 ± 3.1, 86.3 ± 2.1, 65.8 ± 0.3, 81.4 ± 1.07 and 87.4 ± 4.6 %, respectively for WEHI-164, U373MG, A549, MCF-7, WRL-68, and MDAMB-231 cell lines). On the contrary, in case of normal cell line, the decrease in cell viability was found to be significantly lower (viz. % viability of 55.06 ± 1.39 and 83.9 ± 3.5 % for T-LMD and Lippod^{TM} at 200 nM concentration of Dox, respectively) in WI26VA44 cells as compared to the cancer cell lines. IC50 value of different cancer and normal cell lines was also determined for all the tested concentrations of T-LMD (viz. 25, 50, 75, 100, 200, 300 and 400 nM equivalent concentration of Dox) by using the software (AAT Bioquest Inc., USA) **(Fig. 3.2.17 E- i to vii)**. **Table 3.2.4** shows the values of IC50 for different cell lines determined at 48

h post-treatment. Thus, based on IC50 values the sensitivity of the cell lines can be considered as follows (most sensitive to least sensitive) : MDAMB-231 > WEHI-164 > MCF-7 > U373MG > WRL68 > A549 > WI26VA44. IC50 values also showed higher toxicity of T-LMD than Lippod^{TM}. Moreover, IC50 values for T-LMD was 1.5 to 2 fold higher for normal cell line as compared to cancer cells. Bright field microscopy imaging of different cell lines at 48 post-treatment showed the presence of cellular debris, cell shrinkage and cells showing apoptotic morphology after T-LMD treatment **(Fig. 3.2.17 F)**.

A.

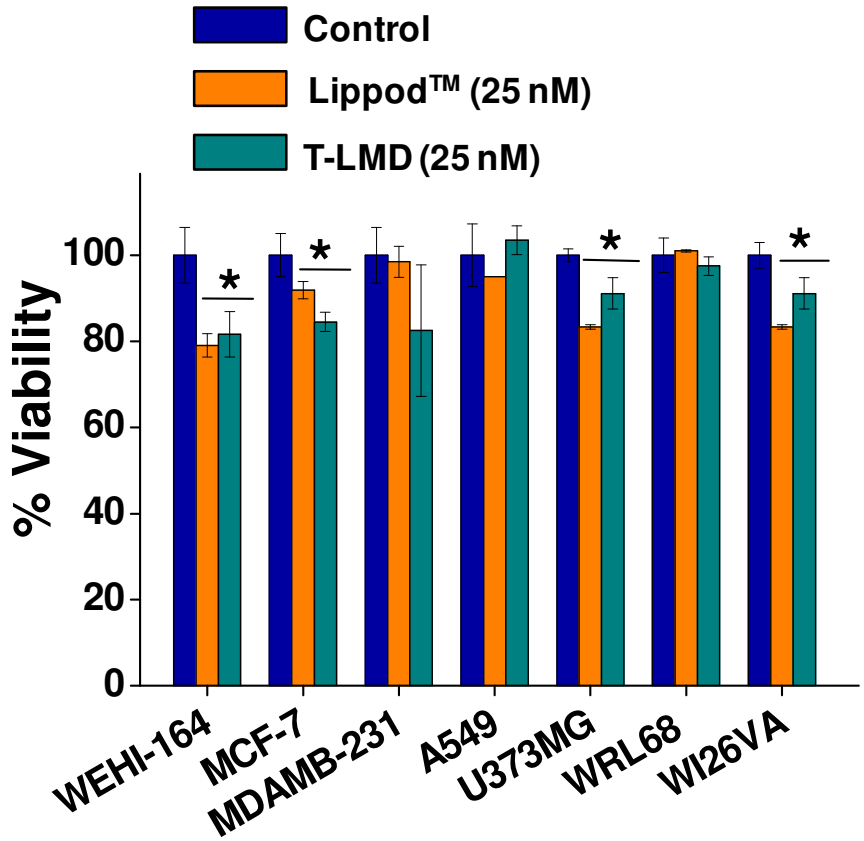

B.

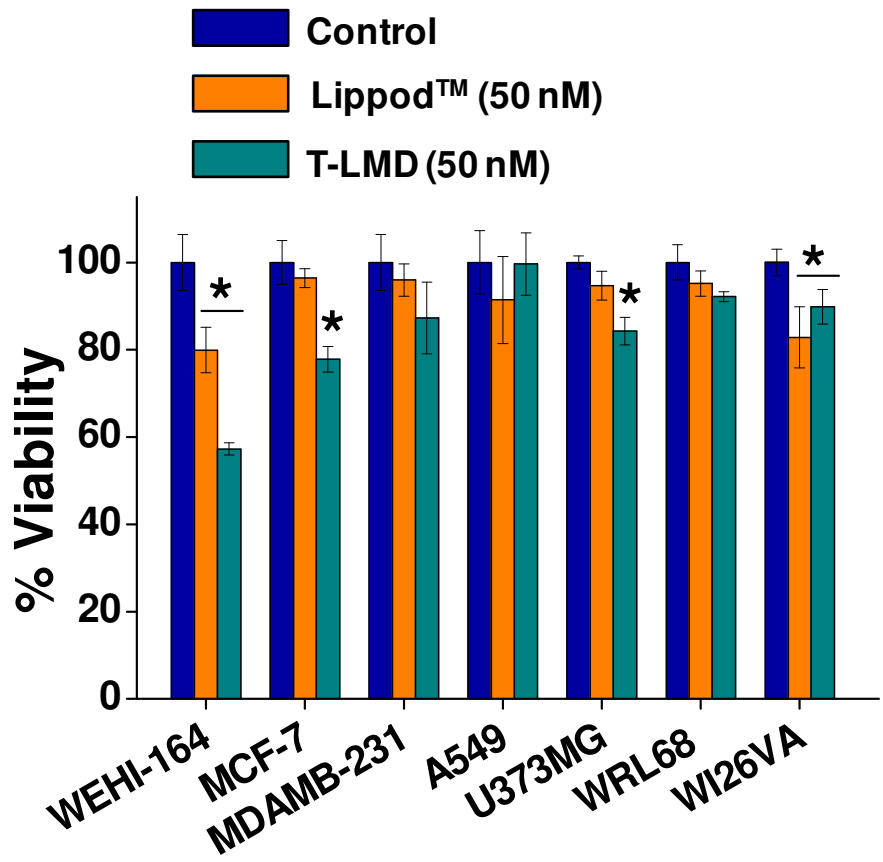
Control
Lippod™ (50 nM)
T-LMD (50 nM)
% Viability
0
20
40
60
80
100
*
WEHI-164
MCF-7
MDAMB-231
A549
U373MG
WRL68
WI26VA

C.

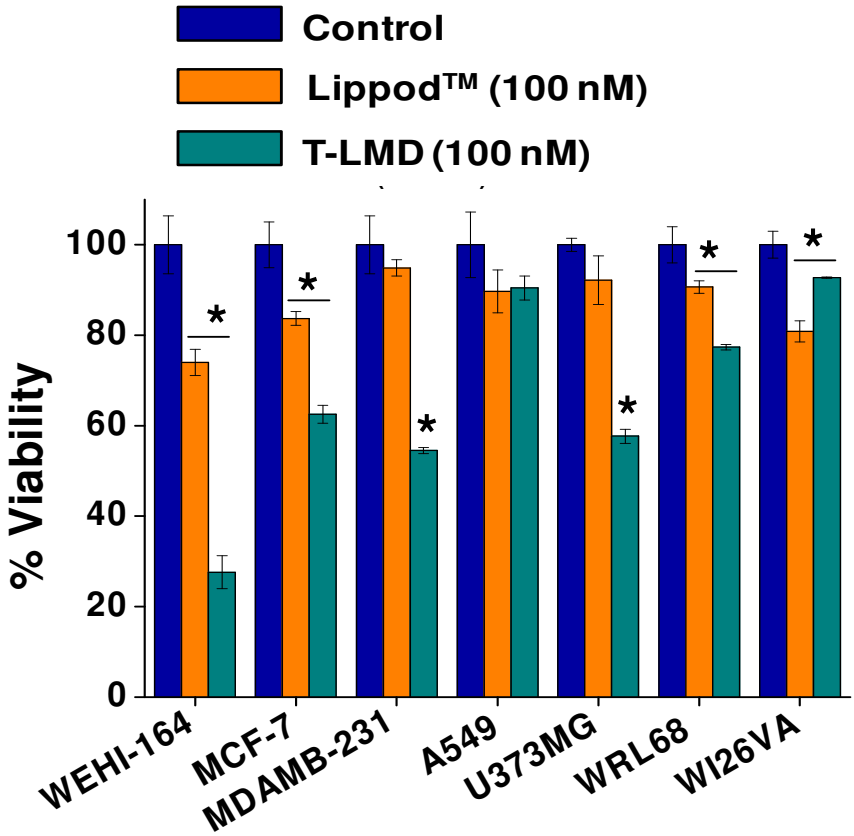
Control
Lippod™ (100 nM)
T-LMD (100 nM)
% Viability
0
20
40
60
80
100
*
WEHI-164
MCF-7
MDAMB-231
A549
U373MG
WRL68
WI26VA

D.

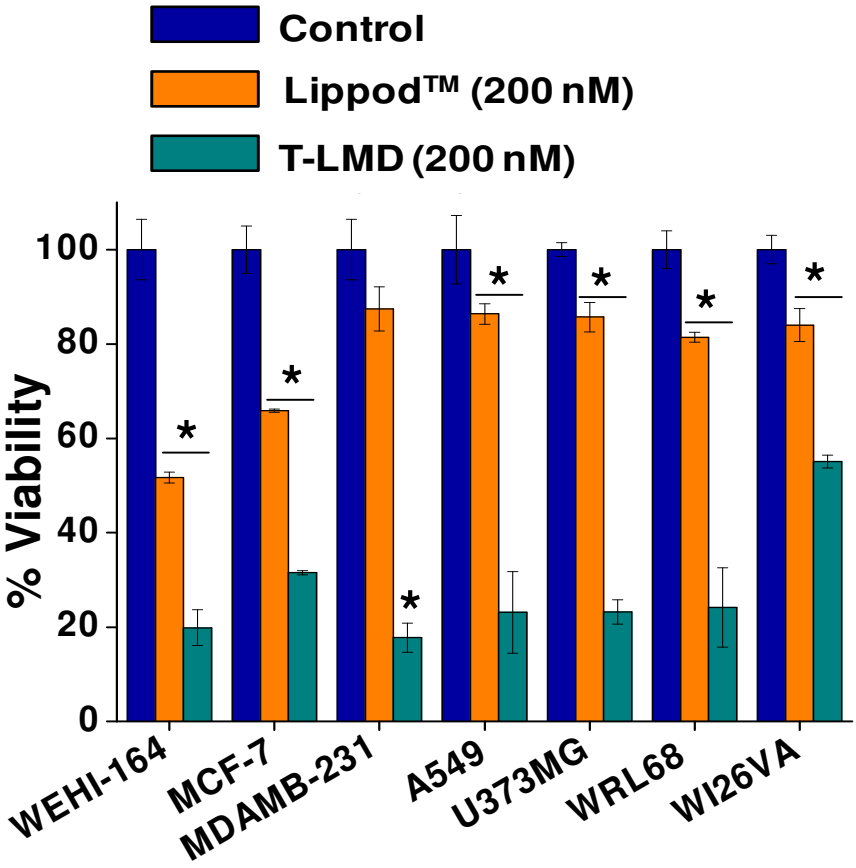
Control
Lippod™ (200 nM)
T-LMD (200 nM)
% Viability
100
80
60
40
20
0
*
WEHI-164
MCF-7
MDAMB-231
A549
U373MG
WRL68
WI26VA

E. **(i)** **(ii)**

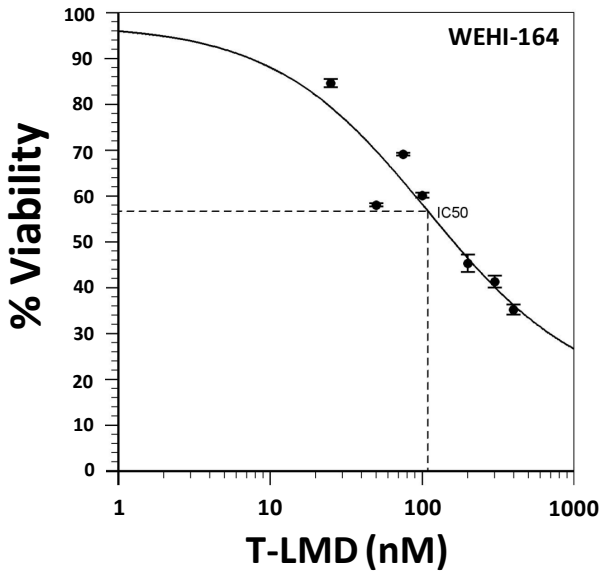
WEHI-164
% Viability
IC50
T-LMD (nM)
1
10
100
1000

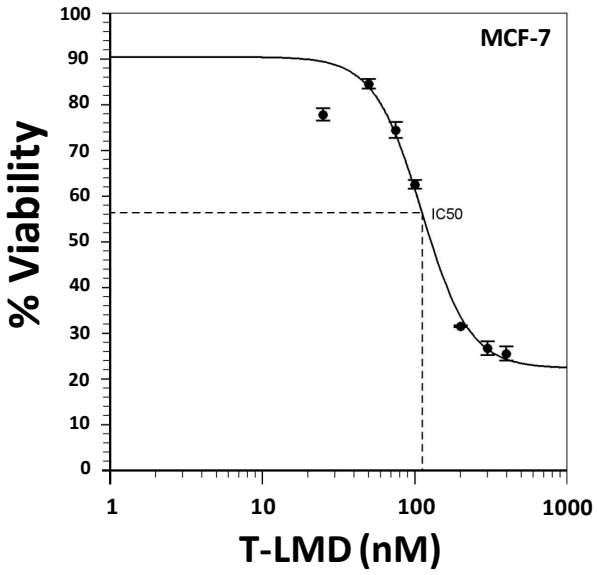
MCF-7
% Viability
IC50
T-LMD (nM)
1
10
100
1000

(iii)

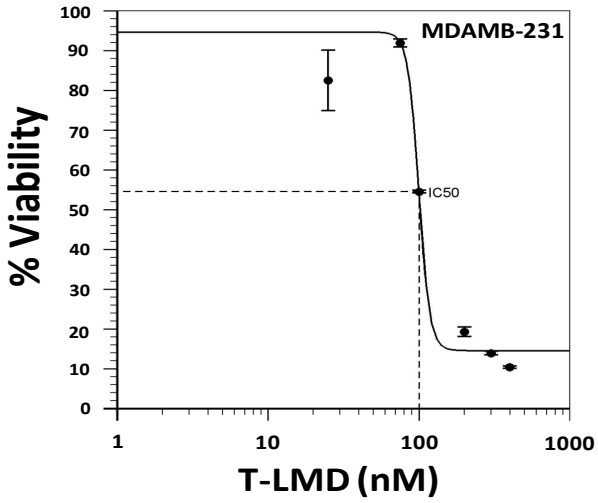

(iv)

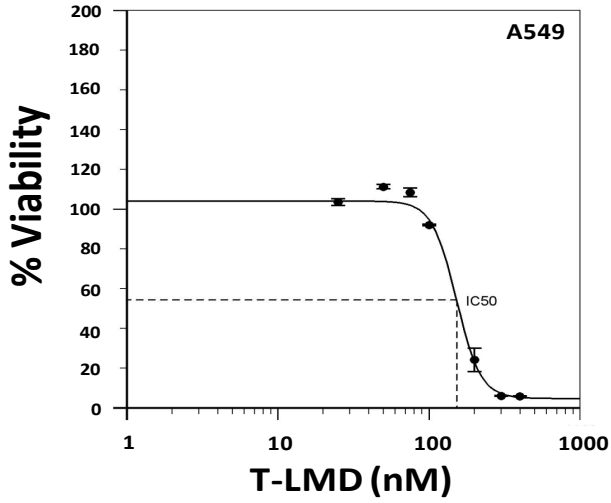

(v)

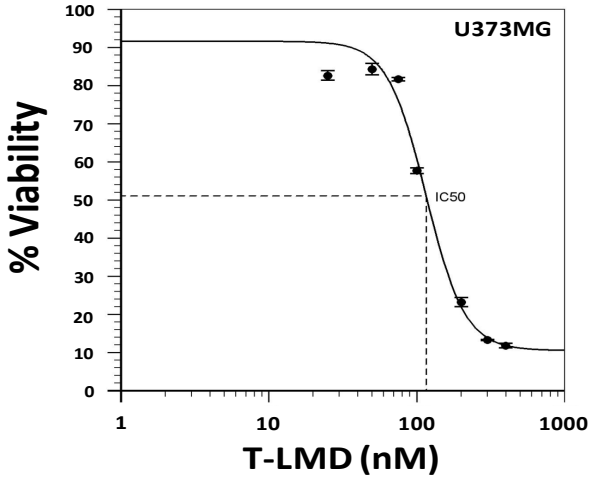

(vi)

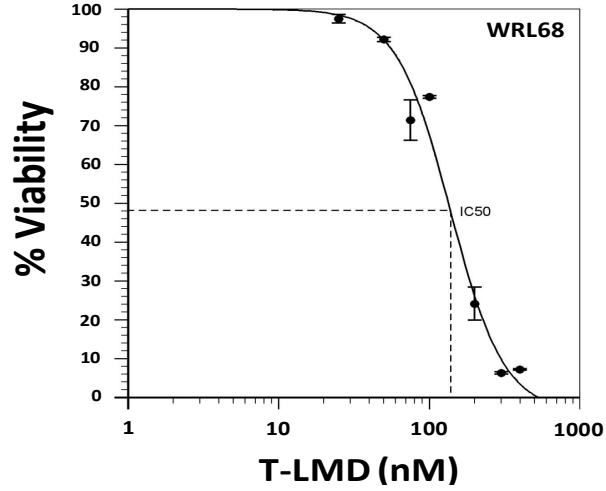

(vii)

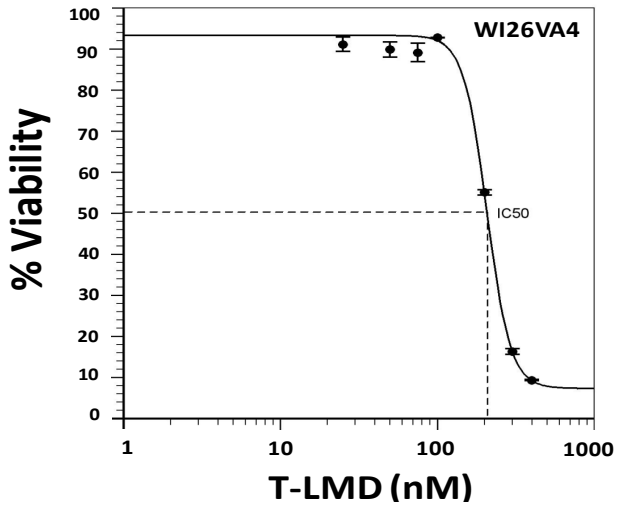

F.

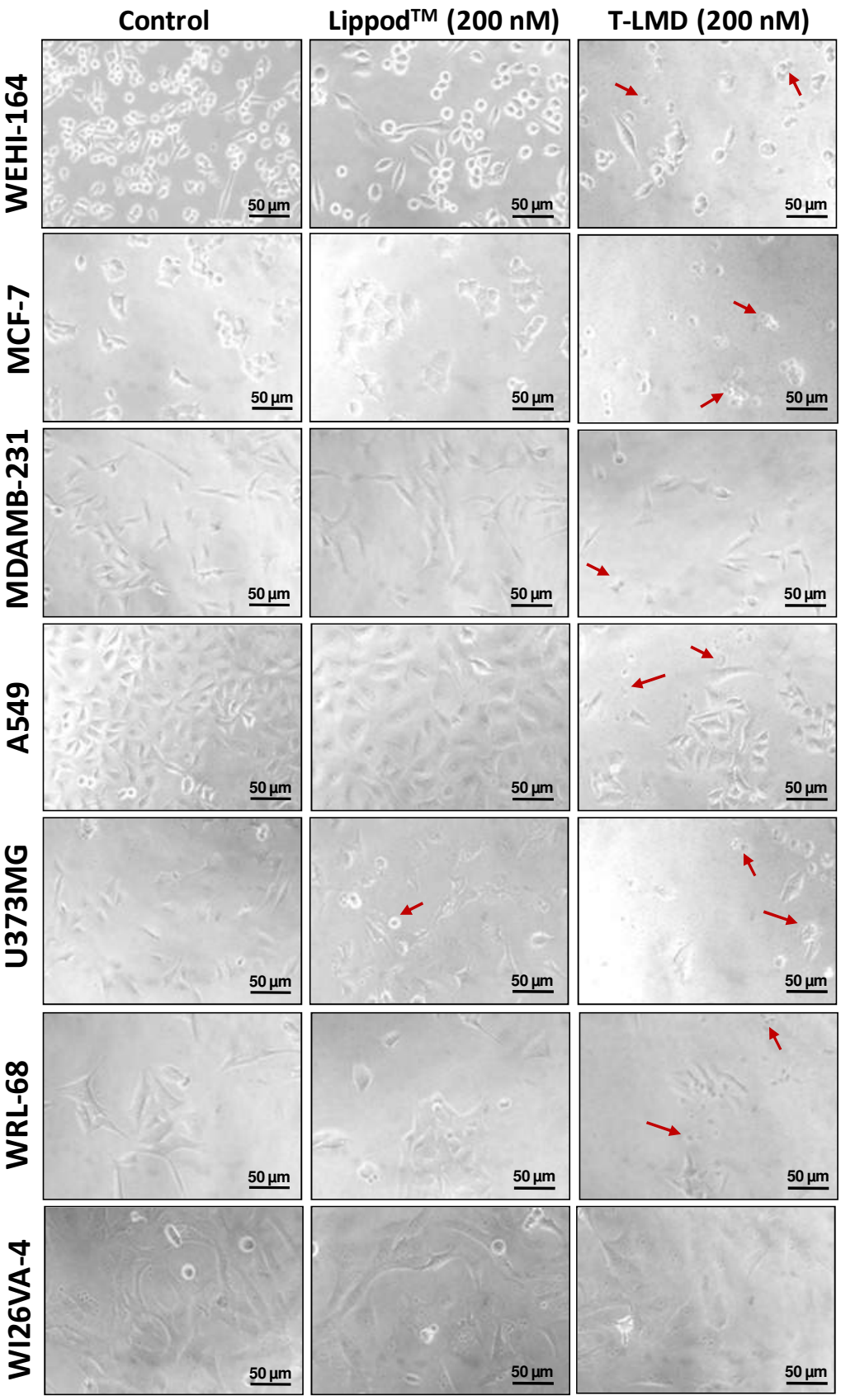
Control
Lippod™ (200 nM)
T-LMD (200 nM)
WEHI-164
MCF-7
MDAMB-231
A549
U373MG
WRL-68
WI26VA-4
50 µm

Fig. 3.2.17 *Percentage cell viability as determined by MTT assay in different cancer (WEHI-164, MCF-7, MDAMB-231, A549 and U373MG) and normal (WI26VA44 and WRL-68) cells lines after treatment with different concentrations of T-LMD or Lippod™ with equivalent concentrations of Dox as 25 nM* ***(A)****, 50 nM* ***(B)****, 100 nM* ***(C)*** *and 200 nM* ***(D)*** *at 48 h. * Significant at P<0.05 as compared to control.* ***(E)*** *IC-50 determination using AAT Bioquest software for* ***(i)*** *WEHI1-64,* ***(ii)*** *MCF-7,* ***(iii)*** *MDAMB-231,* ***(iv)*** *A549,* ***(v)*** *U373MG,* ***(vi)*** *WRL-68 and* ***(vii)*** *WI26VA44 cell lines post-treatment with T-LMD.* ***(F)*** *Representative bright field microscopy images of different cancer and normal cell lines at 48 h post -treatment with 200 nM equivalent Dox concentration of Lippod™ or T-LMD. Scale bar: 50 µm. Red arrows indicate cells with apoptotic morphology.*

Sr. No.	Cell line	IC-50 (µM)	
		T-LMD	Lippod™
1.	MDAMB-231	99.9	> 400 nM
2.	WEHI-164	109.22	334.63
3.	MCF-7	111.96	145.8
4.	U373MG	116.21	> 400 nM
5.	WRL68	138.54	> 400 nM
6.	A549	152.6	> 400 nM
7.	WI26VA44	207.75	> 400 nM

Table 3.2.4 *Table for IC-50 values of different cell lines as determined by MTT, after treatment with increasing concentrations of T-LMD or Lippod™ (equivalent to 25, 50, 100 and 200 µM of Dox concentration) for 48 h.*

3.2.10 EVALUATION OF COMBINATORIAL CANCER THERAPY EFFICACY OF T-LMD IN COMBINATION WITH GAMMA RADIATION AND HYPERTHERMIA THERAPY

As discussed in **Chapter 3, Section 3.1**, a significant enhancement in the anti-cancer efficacy of MN-OA was observed when combined with gamma radiation and hyperthermia therapy. Since, T-LMD contains MN-OA, the radio-sensitizing and hyperthermia efficacy of T-LMD was also evaluated in cancer cells. T-LMD is expected to show better cell killing in combination with radiation and hyperthermia therapy mainly due to two reasons. Firstly, the hyperthermia and radio-sensitizing potential due to MN-OA (demonstrated in **Section 3.1**). Secondly, additional efficacy is expected to be imparted due to presence of Dox, which is also reported to enhance the radiation-induced DNA damage by DNA intercalation and generation of ROS[265]. Hence, experiments were conducted to evaluate the efficacy of the combinatorial cancer therapy for the targeted liposomal nano-formulation (T-LMD).

3.2.10.1 T-LMD showed a dose and time dependent increase in sub-G1 population in WEHI-164 cells in combination with gamma radiation but not in U373MG cells

As discussed in **Section 3.2.9**, T-LMD showed a significant and concentration dependent killing of WEHI-164 and U373MG cells as determined by MTT assay. To further validate these results and also to evaluate the anti-cancer efficacy of this nano-formulation in combination with γ-radiation, cell cycle analysis was performed. Briefly, WEHI-164 and U373MG cells were treated with increasing concentrations of T-LMD (equivalent to 100, 200 and 400 nM of Dox) for 3h followed by irradiation with 2 Gy γ-radiation and further incubation at culture conditions for 24 and 72 h. The effect on different phases of cell cycle in combination with or without gamma

radiation was studied by PI staining and flow cytometry. Results showed a concentration dependent and time dependent increase in the sub-G1 population in WEHI-164 cells. As compared to control (13.79 ± 0.3 %) and 2 Gy (20.8 ± 3.5 %), WEHI-164 cells showed a significant increase in the sub-G1 population after treatment with T-LMD at 200 nM (37.74 ± 1.6 %) and 400 nM (46.16 ± 2.09 %), which was further enhanced to 42.29 ± 5.04 %, 48.33 ± 1.12 % and 54.61 ± 2.04 % respectively, in 100 nM + 2 Gy, 200 nM + 2 Gy and 400 nM + 2 Gy treatments, respectively at 72 h. Interestingly, at 200 nM treatment, WEHI-164 cells showed a significant increase in the G2-M population indicating cell cycle arrest **(Fig. 3.2.18 A & B)**. On the contrary, in case of U373MG cells the sub-G1 population was found to increase slightly to 16.07 ± 0.5 % and 12.24 ± 0.3 % in 200 nM and 400 nM treatment groups at 24 h as compared to control (5.2 ± 0.2 %) and didn't increase further in combination with 2 Gy. Interestingly, at 72 h in case of U373MG cells, although the sub-G1 population did not differ much between the different treatment groups, the G2-M population was found to be significantly higher (37.85 ± 2.29 % and 33.8 ± 4.7 %), respectively, at 200 nM and 400 nM treatments, as compared to control (17.04 ± 0.6 %). However, neither the sub-G1 or G2-M population was found to increase further in combination with 2 Gy **(Fig. 3.2.18 C & D)**.

A. **WEHI-164 cells : 24 h**

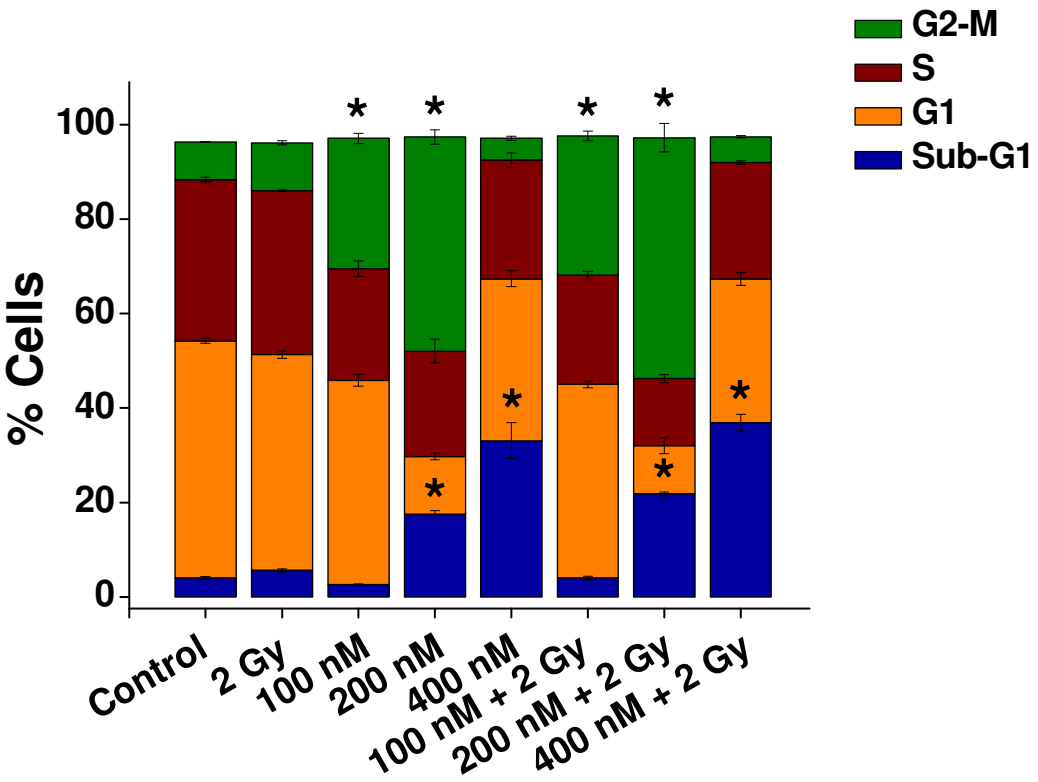

B. **WEHI-164 cells : 72 h**

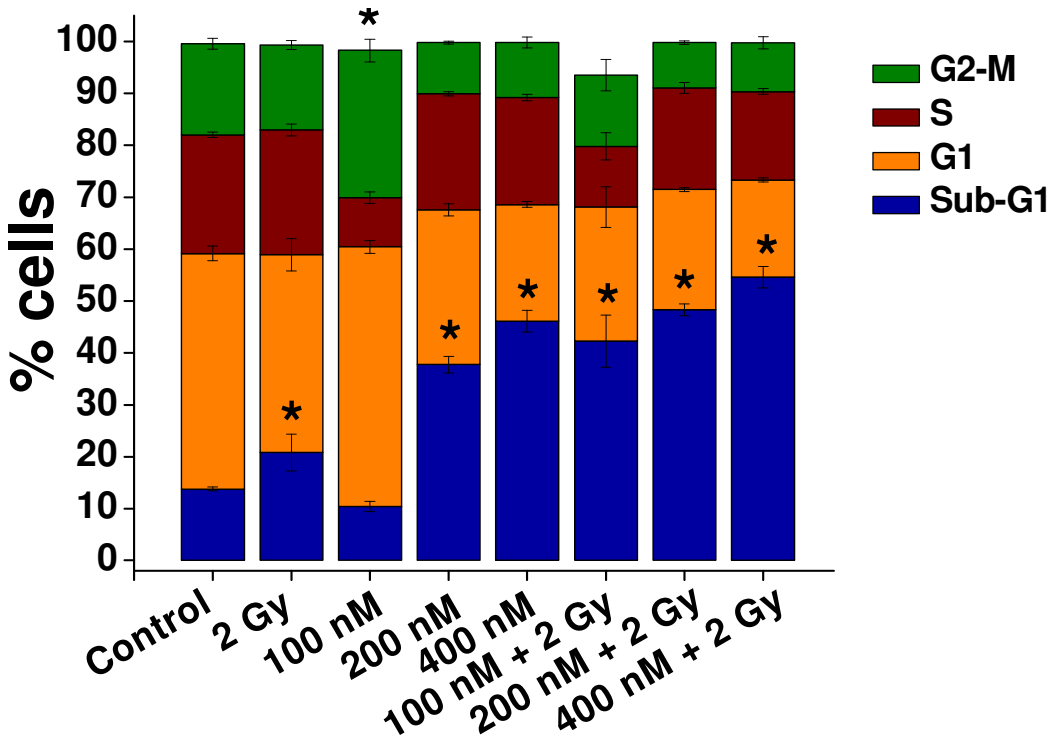

C. U373MG cells : 24 h

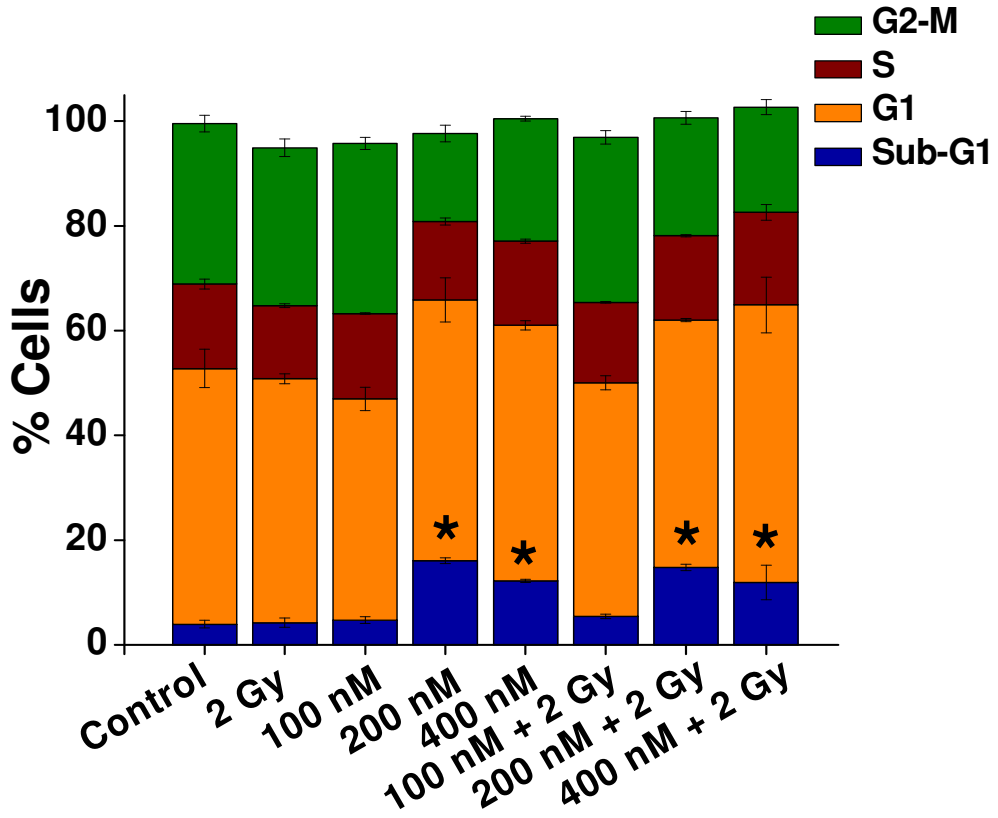

D. U373MG cells : 72 h

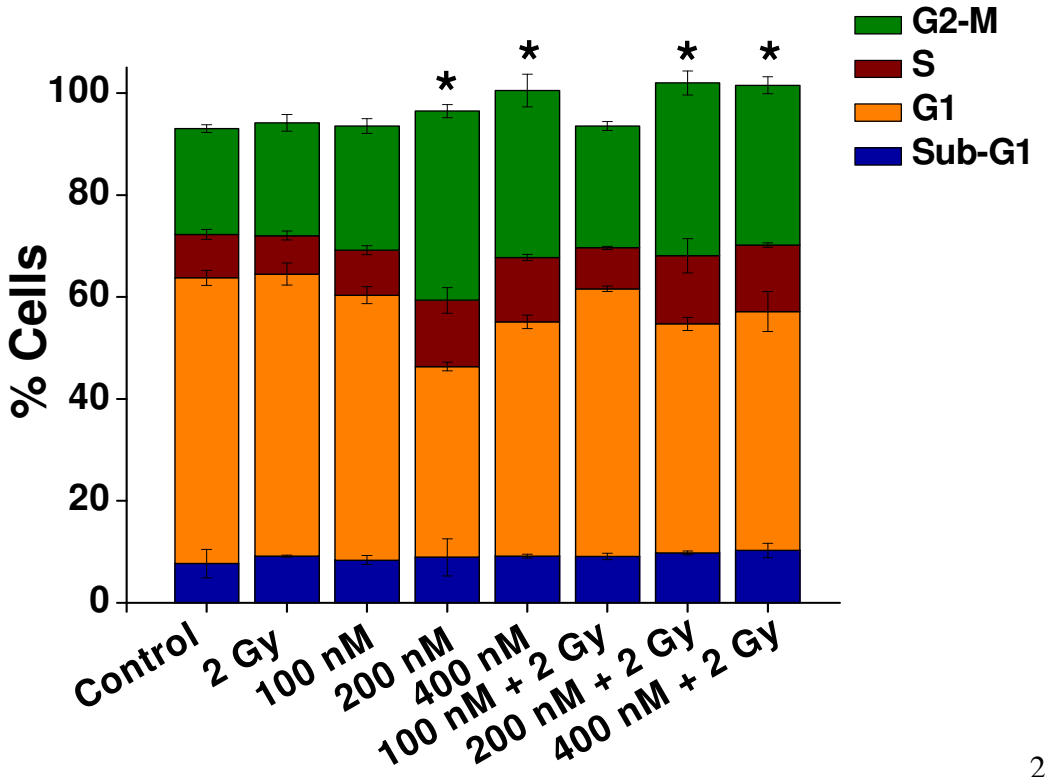

Fig. 3.2.18 *Cell cycle analysis by flow cytometry after PI staining of (A) & (B) WEHI-164 cells at 24 and 72 h, respectively and (C) & (D) U373MG cells at 24 and 72 h, respectively, post-treatment with T-LMD in combination with or without gamma radiation (2 Gy).* Significant at P<0.05 as compared to control.*

3.2.10.2 Clonogenic cell survival assay validated the radio-sensitization efficacy of T-LMD in WEHI-164 cells

As studied by cell cycle analysis **(Section 3.2.10.1)**, WEHI-164 cells showed highest cyto-toxicity after treatment with T-LMD and enhanced killing in combination with gamma radiation. Hence, further experiments were carried out with WEHI-164 cell line. As clonogenic assay is considered to be the gold standard assay to evaluate the radio-sensitization efficacy of any drug or nano-formulation, the effect of the nano-formulation on the clonogenic cell survival was studied in WEHI-164 cells. Results showed that as compared to Lippod^{TM}, T-LMD, showed a concentration dependent decrease in the clonogenic survival of WEHI-164 cells. The % survival of WEHI-164 cells was found to be 76.9 ± 2.4, 64.4 ± 8.1, 42.9 ± 6.7 and 37.9 ± 10.7 %, at 25, 50, 75 and 100 nM equivalent concentration of Dox in T-LMD, respectively *(Note: these concentrations were used as the cell seeding density was 500 for clonogenic assay as compared to 5000 for MTT assay. Also, at the chosen concentrations the combinatorial effect of drug in combination with gamma radiation was clearly visible).* On the contrary, Lippod^{TM} at equivalent concentration of Dox, did not show a concentration dependent decrease in the clonogenic survival of cancer cells **(Fig. 3.2.19 A)**. IC50 of T-LMD by clonogenic cell survival assay was found to be 87.76 μM **(Fig. 3.2.19 B)**. Moreover, in combination with γ-radiation, the % clonogenic survival was found to further decrease to 57.28 ± 15.5, 38.1 ± 8 4.7, 29.2 ± 0.5 and

22.7 ± 3.2 % at 25 nM+ 2Gy, 50 nM+ 2Gy, 75 nM + 2 Gy and 100 nM + 2 Gy, respectively **(Fig. 3.2.19 C & D)**.

A.

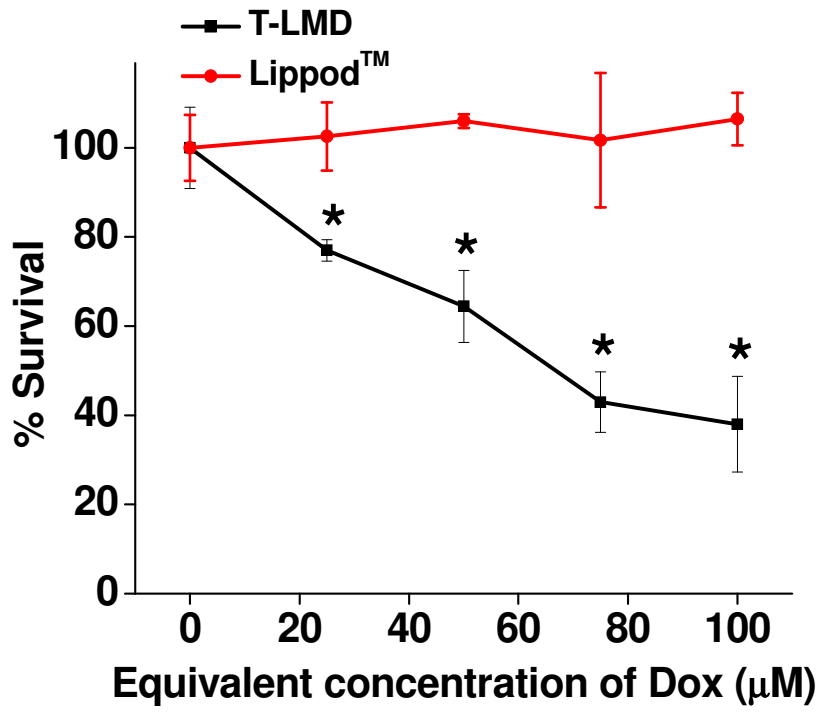

B.

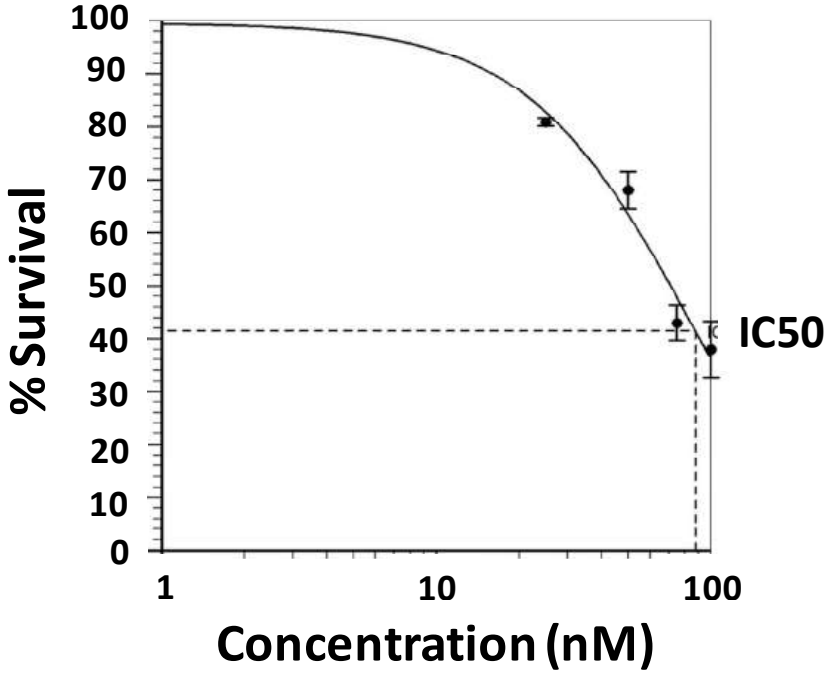

C.

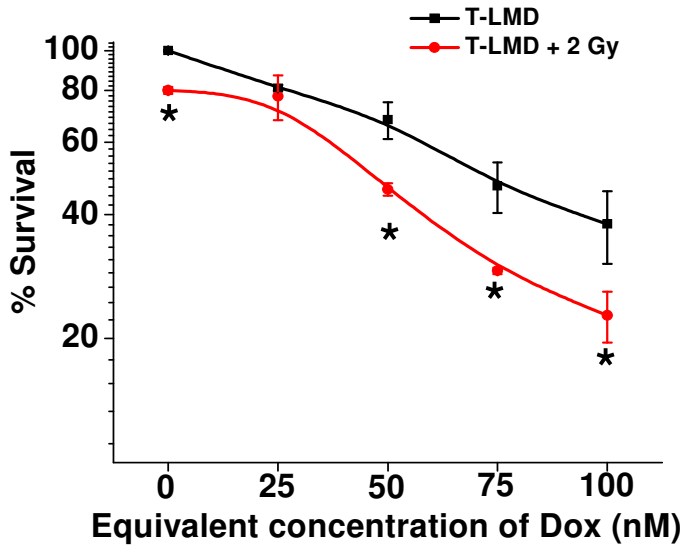

D.

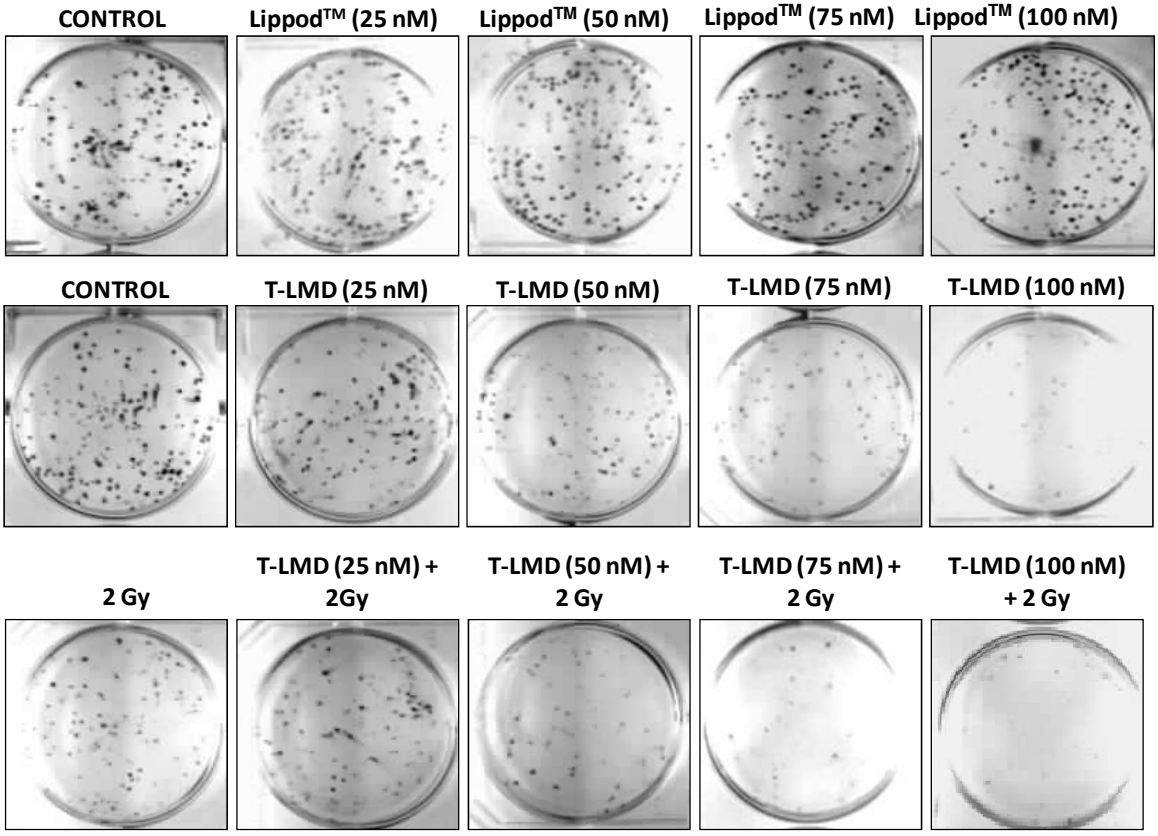

Fig. 3.2.19 ***(A)*** *Percentage clonogenic survival of WEHI-164 cells after treatment with Lippod™ or T-LMD at 25, 50, 75 and 100 nM equivalent concentrations of Dox.* ***(B)*** *Percentage survival of WEHI-164 cells treated with indicated doses of T-LMD either alone or in combination with 2*

*Gy. * Significant at P<0.05 as compared to control and # indicates significant difference between T-LMD treated groups in combination with or without 2 Gy, (C) Representative images of colonies formed during clonogenic cell survival assay of WEHI-164 cells after indicated treatments.*

3.2.10.3 Measurement of intracellular reactive oxygen species (ROS) by DCHFDA in WEHI-164 cells after treatment with T-LMD with or without γ-radiation

Since, WEHI-164 cells showed highest cyto-toxicity after treatment with T-LMD and enhanced killing in combination with gamma radiation, further studies were carried out in these cells to understand the mechanism of anti-cancer effect of nano-formulation. Iron oxide as well as Dox are well reported in literature to induce oxidative stress in cancer cells[265, 270]. Hence, the effect of nano-formulation treatment on the level of intracellular ROS was studied by DCHFDA assay. Since, combinatorial effect was more pronounced at 100 and 200 nM concentrations of T-LMD, these two concentrations were used to measure the levels of ROS in WEHI-164 cells post treatment with the liposomal nano-formulation in combination with or without gamma radiation. Results showed that T-LMD (at 100 and 200 nM equivalent concentrations of Dox) didn't induce significant increase in ROS as compared to control (at 3h). However, in combination with radiation (at 2, 4 and 6 Gy doses), a dose dependent increase in ROS was observed **(Fig. 3.2.20)**. At 200 nM concentration of nano-formulation, the relative fluorescence intensity (RFI) of DCHFDA was found to increase by 1.82 ± 0.03, 3.32 ± 0.23 and 4 ± 0.32 fold respectively in combination with 2, 4 and 6 Gy γ-radiation, respectively. The RFI values were lower for 2 Gy (1.53 ± 0.01), 4 Gy (1.95 ± 0.04) or 6 Gy (3.06 ± 0.3) γ-radiation treatments alone. These results

suggested that increased generation of ROS could be one the contributors for the observed enhanced radio-sensitization by T-LMD in WEHI-164 cells.

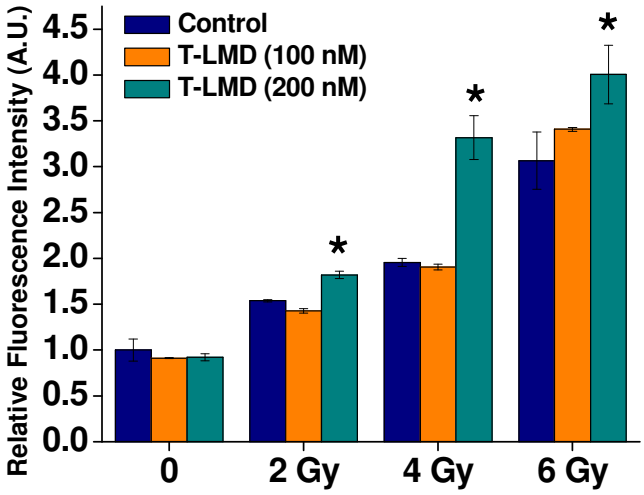

Fig. 3.2.20 *Relative fluorescence intensity of DCHFDA in WEHI-164 cells treated with increasing concentrations of T-LMD (100 and 200 nM) for 3 h, followed by irradiation with different doses of γ-radiation (2, 4 and 6 Gy). A.U.: Arbitrary units.* Significant at P<0.05 as compared to control.*

3.2.10.4 T-LMD showed a significant increase in DNA double strand breaks and a delayed repair of DNA damage in combination with or without 2 Gy

As mentioned in **Section 3.2.10.3**, 200 nM dose of T-LMD was found to be most effective in inducing the generation of ROS when combined with different doses of γ radiation **(Fig. 3.2.20)**. Therefore, further investigations were carried out using 200 nM dose of T-LMD and 2 Gy of radiation dose. As γ radiation is known to cause direct and indirect (through generation of ROS) damage to the DNA, resulting in strand breaks, the level of DNA double strand breaks (DSBs) was determined. The effect of T-LMD (200 nM) or 2 Gy or combination (T-LMD + 2 Gy) treatments, at different time points was determined by immuno-fluorescence staining of the

γH2AX protein (early marker of DSBs). Briefly, WEHI-164 cells were pre-treated with T-LMD for 3 h, followed by irradiation. The cells were fixed with para-formaldehyde (4 %) at desired time points (viz. 5 min, 15 min, 30 min, 1 h, 3 h, 5 h , 24 h, 48 h and 72 h) post-irradiation, followed by processing the cells for immnuno-cytochemical staining of γH2AX as mentioned in **Chapter 2 Section 2.18**. Results showed a time dependent increase in the expression of γH2AX in case of 2 Gy treatment as compared to control **(Fig. 3.2.21 A & B)**. The peak increase in the average MFI per cell of γH2AX was obtained at 30 min for 2 Gy (36.9 ± 2.9 A.U.) treatment group. Interestingly, cancer cells treated with T-LMD and combination therapy (T-LMD + 2 Gy) also showed a time dependent increase in the average MFI of γH2AX, which however, peaked at 3 h (58.4 ± 1.1 and 63.5 ± 2.1 A.U. for T-LMD and combination treatment, respectively). Moreover, combination therapy showed a significantly higher expression of γH2AX (57.3 ± 4.2 and 63.5 ± 2.1 A.U.) as compared to only T-LMD (46.4 ± 5.6 and 58.42 ± 1.1) at 1 and 3 h, respectively. In case of 2 Gy treatment, the expression of γH2AX foci was found to decline from 1 h and was almost equivalent to control after 24 h and upto 72 h. However, in case of T-LMD and combination treatment group, although the γH2AX expression was found to decline from 5 h to 48 h, a sudden increase in the expression level of γH2AX was observed at 72 h. These results suggest that cRGD and combination therapy induces enhanced DSBs and causes slower repair of the DSBs as compared to only 2 Gy. Moreover, these results are in-line with the G2-M arrest observed during sub-G1 analysis of WEHI-164 cells post-treatment with 200 nM T-LMD ± 2 Gy (**Section 3.2.10.1** and **Fig. 3.2.18 A & B**). Thus, the sudden increase in the expression of γH2AX foci at 72 h may be suggestive of generation of new breaks in the DNA of surviving cells, probably due to stalled replication forks as the arrested cells attempt to re-enter mitosis. To further determine the mechanism of enhanced DSBs and its delayed repair due to treatment with

T-LMD ± 2 Gy, Western blot analysis of key proteins, which are known to play a role in DNA damage response (DDR) was evaluated. Results showed a significant up-regulation of P-ATR in T-LMD + 2 Gy group, but P-ATM levels were un-detectable. Elevated P-ATR may be suggestive of induction of DNA damage due to stalled replication forks and is corroborated by the observed enhancement in γH2AX foci at early and late time points **(Fig. 3.2.21 A & B)**, as well as the G2-M arrest observed by sub-G1 analysis **(Fig. 3.2.18 A)**. The levels of total ATM and ATR were found to be slightly elevated in T-LMD group but down-regulated in T-LMD + 2 Gy treatment, suggesting a slightly different mechanism in the two treatment groups. Other DNA repair proteins known to play a role in DDR, viz. P-RAD51 and RAD51, were also found to be elevated in T-LMD and their expression was further enhanced in T-LMD + 2 Gy group. Whereas the levels of down-stream DDR signaling protein CHK1 were found to be down-regulated in both T-LMD and T-LMD + 2 Gy groups. However, P-CHK1 expression was up-regulated in only combination treatment group **(Fig. 3.2. 21 C)**. Thus, the activation of these DDR proteins are suggestive of induction of enhanced DNA damage post-treatment with T-LMD ± 2 Gy.

A.

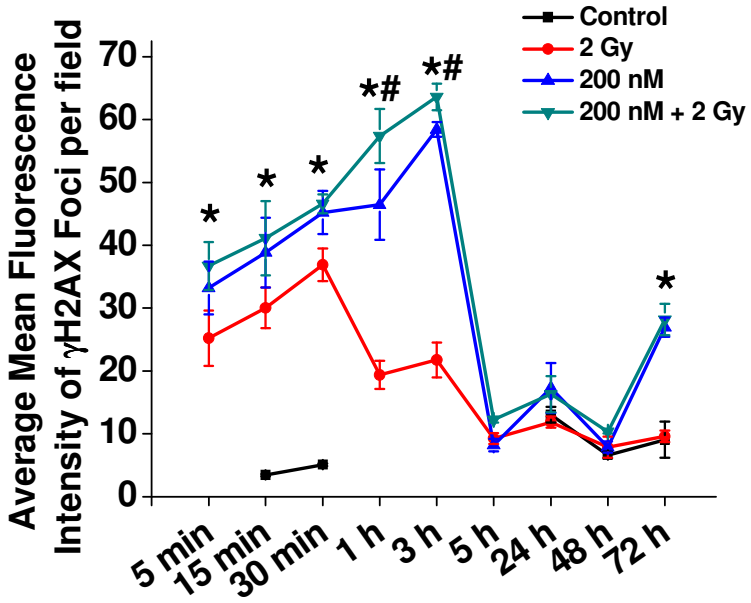

B.

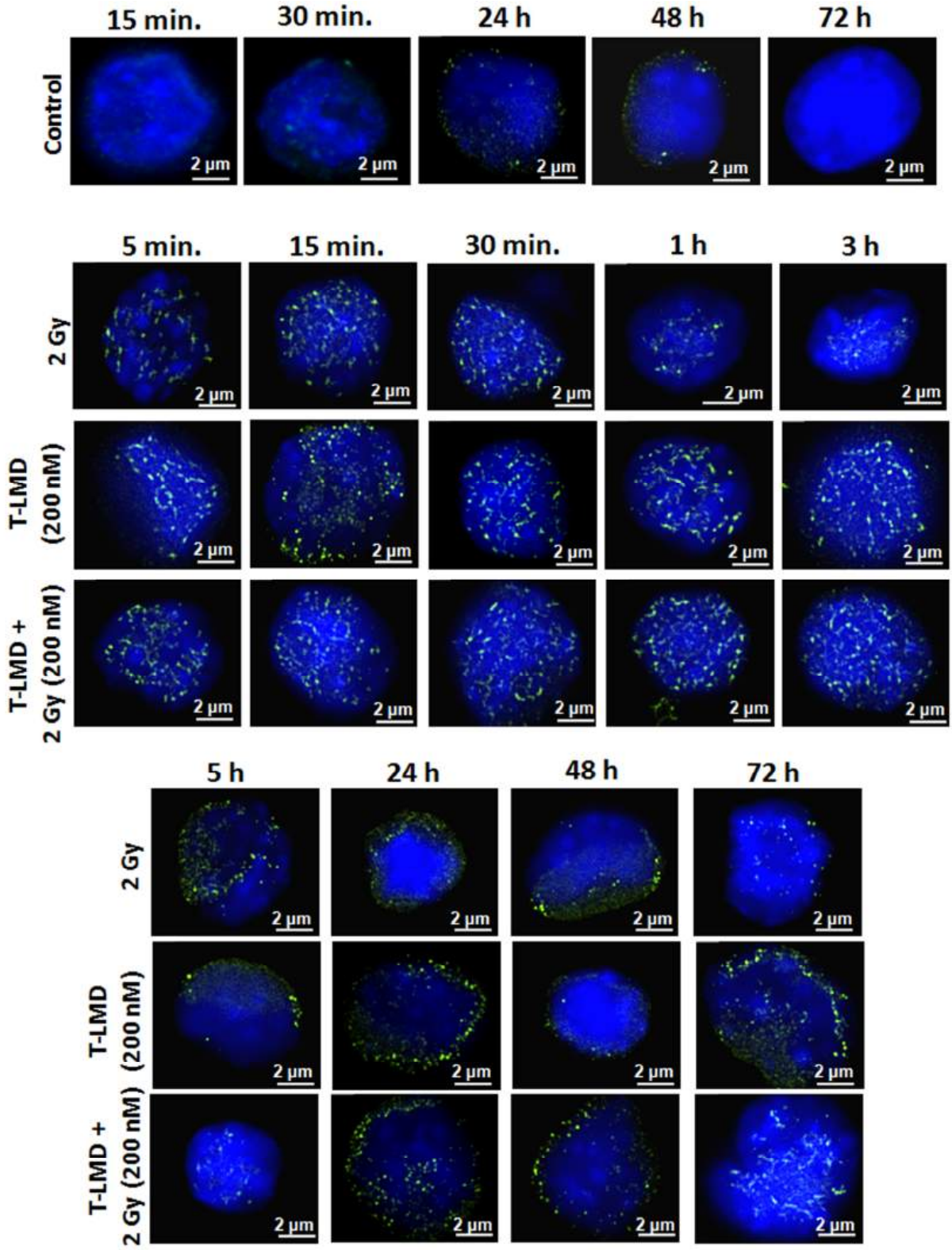
15 min.
30 min.
24 h
48 h
72 h
Control
5 min.
15 min.
30 min.
1 h
3 h
2 Gy
T-LMD (200 nM)
T-LMD + 2 Gy (200 nM)
5 h
24 h
48 h
72 h
2 Gy
T-LMD (200 nM)
T-LMD + 2 Gy (200 nM)
2 µm

C.

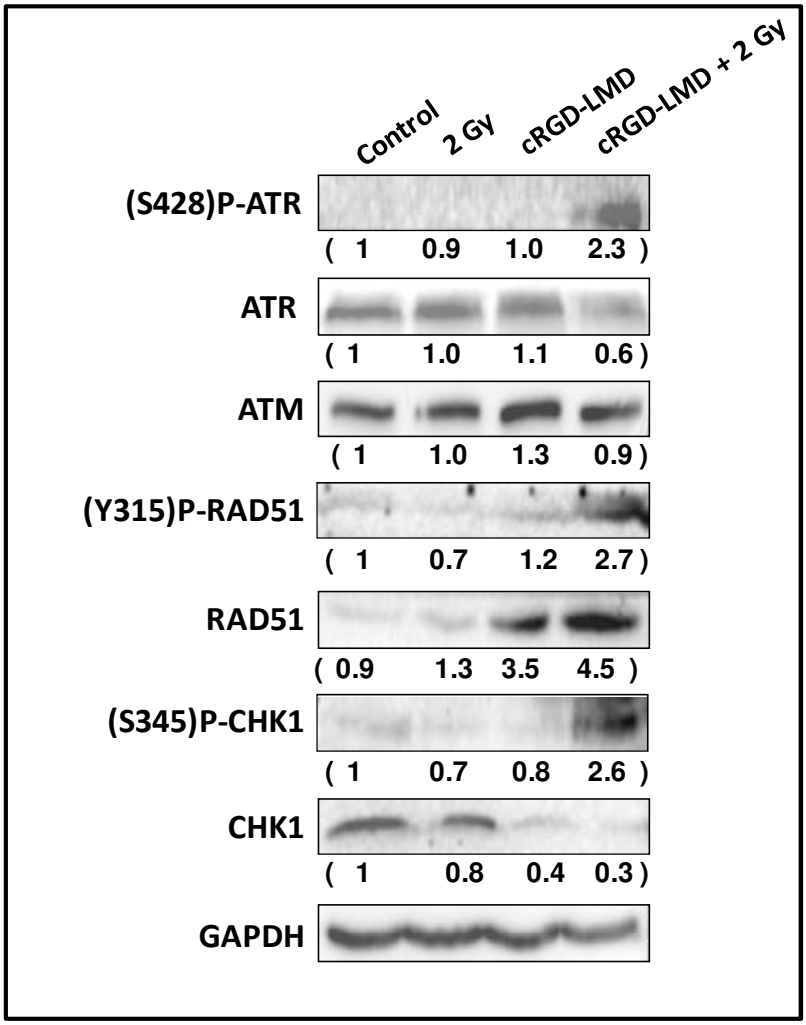

Fig. 3.2.21 (A) *Average mean fluorescence intensity per cell for expression of γH2AX in WEHI-164 cells treated with T-LMD in combination with or without 2 Gy at multiple time points post-irradiation (viz. 5 min, 15 min., 30 min., 1 h, 3 h, 5 h, 24 h, 48 h and 72 h). * Significant at P<0.05 with respect to 2 Gy and # indicates significant difference between T-LMD treated groups in combination with or without 2 Gy,* ***(B)*** *Representative images of γH2AX foci in WEHI-164 cells subjected to indicated treatments and different time points. Scale bar = 2 μm.* ***(C)*** *Western blot images for expression of DDR proteins [(S428)P-ATR, ATR, ATM, (Y315)P-RAD51, RAD51, (S345)P-CHK1 and CHK1)] at 24 h. Values in parenthesis indicate fold change in expression of indicated proteins as compared to control after normalization with GAPDH.*

3.2.10.5 Western blotting analysis suggested role of G2-M arrest, decreased proliferation and increased apoptosis in T-LMD mediated radio-sensitization in WEHI-164 cells

As mentioned in **Section 3.2.10.1**, cell cycle analysis showed an increase in sub-G1 population after treatment with T-LMD either alone or in combination with 2 Gy, suggestive of apoptotic mode of cell death **(Fig. 3.2.18 A-B)**. An increase in G2-M population was also observed at 24 h post-treatment with T-LMD (200 nM) or T-LMD + 2 Gy. To further validate these results, status of key proteins involved in apoptosis, cell proliferation or survival and cell cycle arrest were evaluated by Western blot analysis. Results showed increase in the expression of pro-apoptotic proteins (cleaved PARP, cleaved Cas-3 and BAD) in case of T-LMD and combination treatment group, thereby confirming the induction of apoptosis **(Fig. 3.2.22 B)**. Moreover, expression of P-JNK was found to be up-regulated, whereas the levels of (S112) P-BAD as well as BCL2 were found to be down-regulated in T-LMD and combination treatment group, suggesting induction of apoptosis via activation of JNK pathway and de-phosphorylation of BAD **(Fig. 3.2.22 B)**. Furthermore, the expression of pro-survival proteins (p-AKT, AKT and Survivin) were also found to be down-regulated in the T-LMD and combination treatment group, validating the decrease in cell viability of cells after treatment **(Fig. 3.2.22 A)**. Moreover, a significant increase in the expression of Cyclin B1 and CDC2 and (Y15)P-CDC2 was also observed in T-LMD group and was further enhanced in combination treatment group, thus validating the observed G2-M arrest by cell cycle analysis **(Fig. 3.2.18 C)**. The increased phosphorylation of CDC2 appears to be mediated via decrease in the phosphatase activity of CDC25C via its inactivating phosphorylation on Serine (S216) residue by (S345)P-CHK1, following DDR signaling **(Fig. 3.2.22 C)**. Interestingly, the T-LMD ± 2 Gy treated groups also showed a slight increase in the expression of autophagy marker proteins, Beclin-1 and increased conversion of LC3B(I) to

LC3B (II), suggesting a increase in autophagy processing **(Fig. 3.2.22 D)**. However, these observation needs to be validated by further experiments using specific inhibitors (eg. chloroquine, bafilomycin A1 or 3-methyladenine) to determine the role of autophagic cell death in T-LMD ± 2 Gy induced cyto-toxicity. Since, earlier experiments using MN-OA showed up-regulation of HSP90 due to its inhibition by MN-OA **(Fig. 3.1.7 A)**, we also studied the status of HSP90 expression post-treatment with T-LMD. T-LMD and T-LMD ± 2Gy treatments as well, showed a slightly increased accumulation of HSP90 in WEHI-164 cells. However, on contrary to MN-OA treatment, in case of T-LMD, only some client proteins of HSP90 (viz. AKT, BCL2, CHK1) were found to be down-regulated, whereas some were not (viz. Cyclin B1, CDC2 and RAD51). These results suggest some alternative mechanism which may be playing a role to control the expression of these proteins.

A.

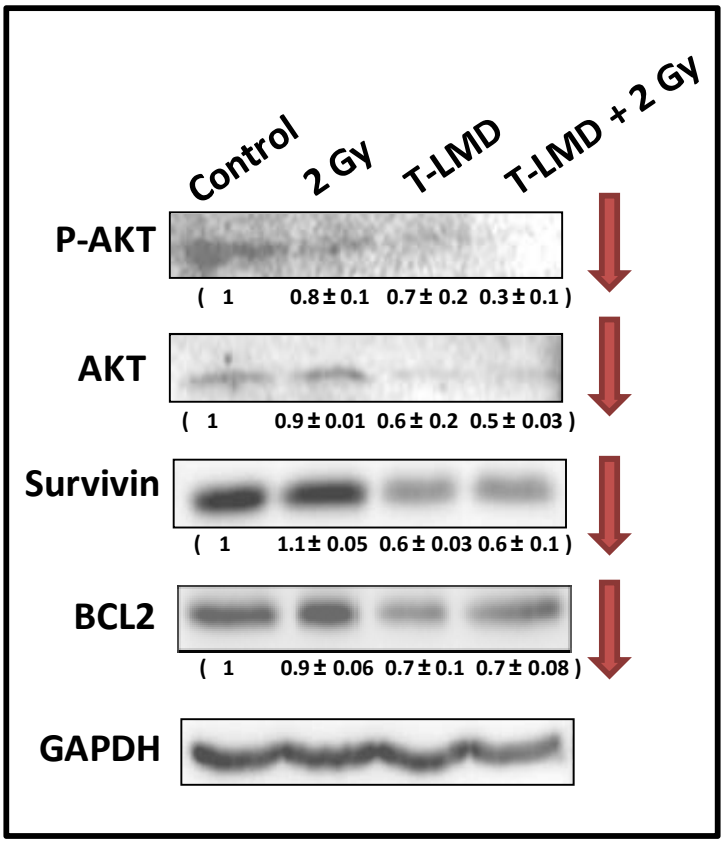

B.

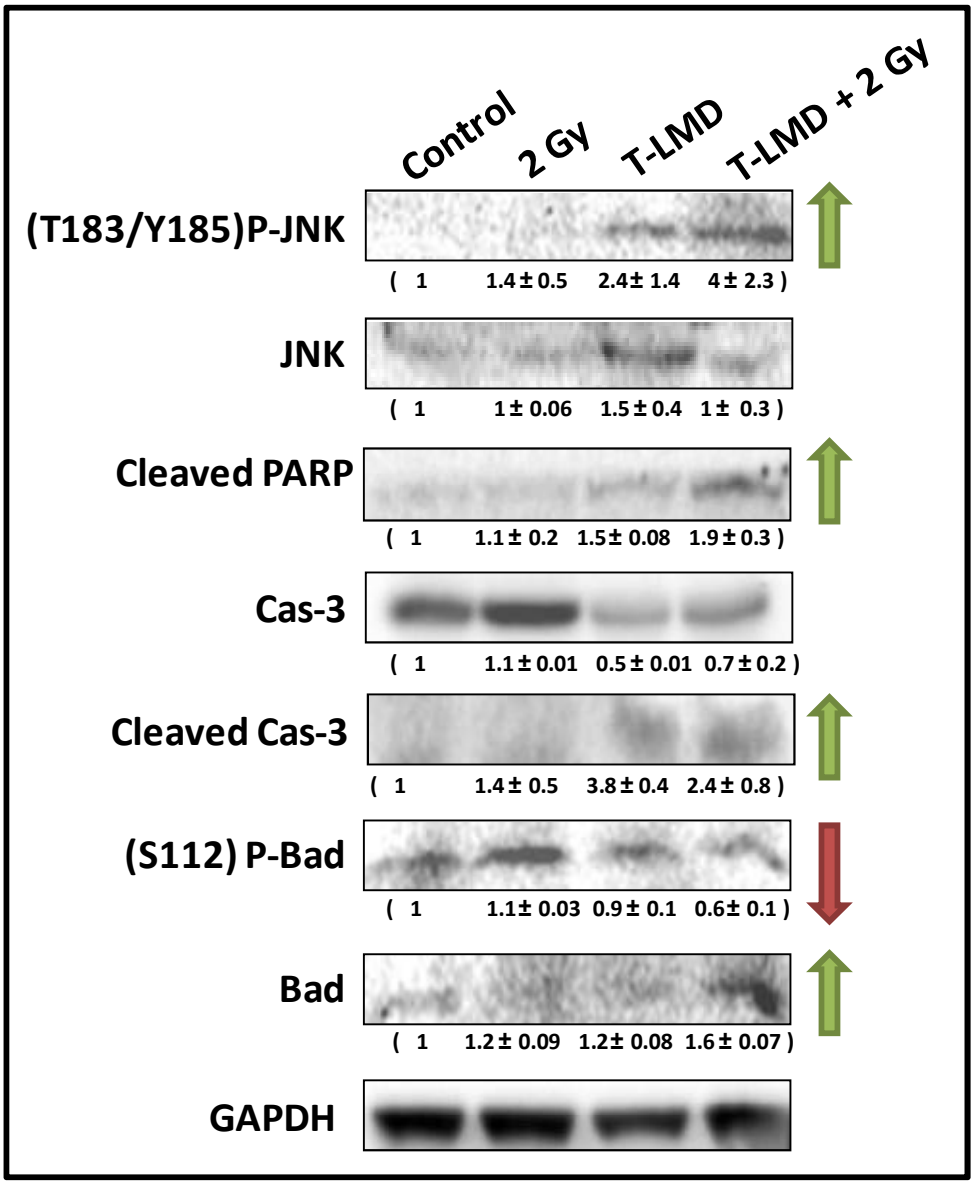
Control
2 Gy
T-LMD
T-LMD + 2 Gy
(T183/Y185)P-JNK
(1 1.4 ± 0.5 2.4 ± 1.4 4 ± 2.3)
JNK
(1 1 ± 0.06 1.5 ± 0.4 1 ± 0.3)
Cleaved PARP
(1 1.1 ± 0.2 1.5 ± 0.08 1.9 ± 0.3)
Cas-3
(1 1.1 ± 0.01 0.5 ± 0.01 0.7 ± 0.2)
Cleaved Cas-3
(1 1.4 ± 0.5 3.8 ± 0.4 2.4 ± 0.8)
(S112) P-Bad
(1 1.1 ± 0.03 0.9 ± 0.1 0.6 ± 0.1)
Bad
(1 1.2 ± 0.09 1.2 ± 0.08 1.6 ± 0.07)
GAPDH

C.

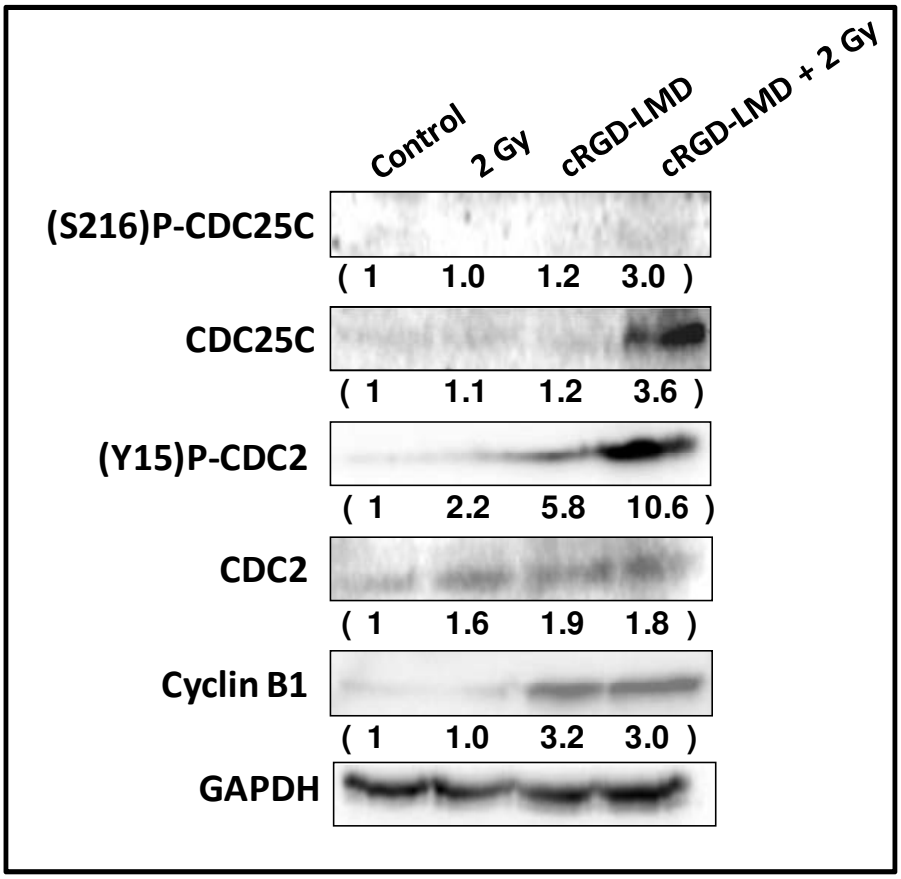
Control
2 Gy
cRGD-LMD
cRGD-LMD + 2 Gy
(S216)P-CDC25C
(1 1.0 1.2 3.0)
CDC25C
(1 1.1 1.2 3.6)
(Y15)P-CDC2
(1 2.2 5.8 10.6)
CDC2
(1 1.6 1.9 1.8)
Cyclin B1
(1 1.0 3.2 3.0)
GAPDH

D.

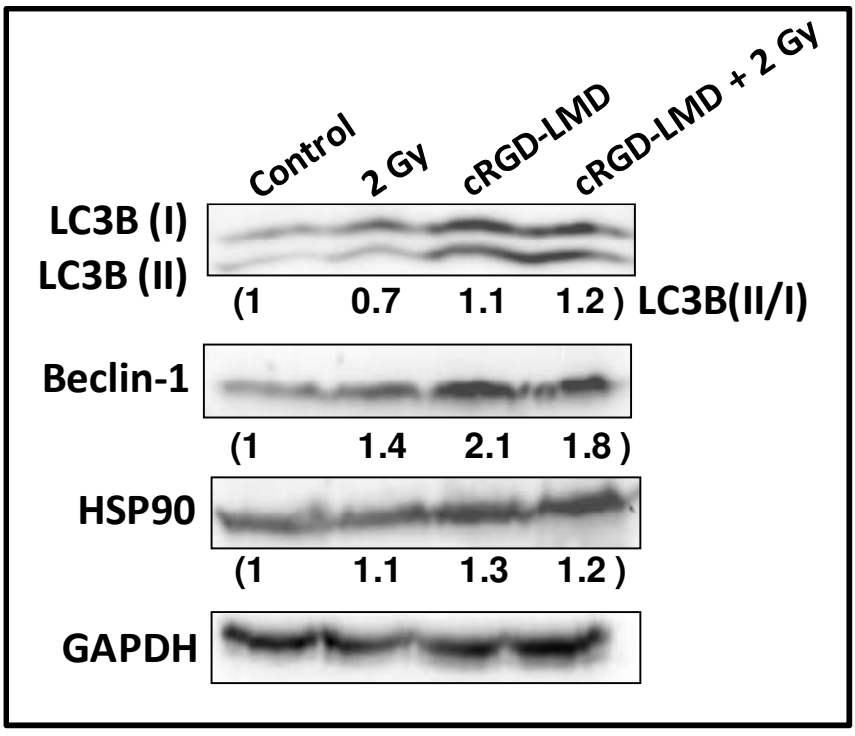
Control
2 Gy
cRGD-LMD
cRGD-LMD + 2 Gy
LC3B (I)
LC3B (II)
(1 0.7 1.1 1.2) LC3B(II/I)
Beclin-1
(1 1.4 2.1 1.8)
HSP90
(1 1.1 1.3 1.2)
GAPDH

Fig. 3.2.22 *Western blot analysis of WEHI-164 cells treated with T-LMD in combination with or without 2 Gy for studying the level of expression of* ***(A)*** *Pro-survival (p-AKT, AKT, survivin and BCL-2) proteins,* ***(B)*** *Pro-apoptotic [P-JNK, JNK, cas-3, cleaved cas-3, cleaved PARP, (S112)P-BAD and BAD] proteins,* ***(C)*** *G2-M arrest specific proteins [(S216)P-CDC25C, CDC25C, (Y15)P-CDC2, CDC2 and Cyclin B1],* ***(D)*** *Autophagy marker proteins [Beclin-1 and LC3B(II)/(I) ratio] and HSP90 chaperone protein. Values in parenthesis represent Mean ± SD values of relative fold change in level of respective proteins as compared to control after normalizing with GAPDH.*

3.2.11 T-LMD IN COMBINATION WITH MAGNETIC HYPERTHERMIA THERAPY (MHT) SHOWED ENHANCED CYTO-TOXICITY IN WEHI-164 CELLS

As mentioned in **Chapter 3.1, Section 3.1.1**, the MHT efficacy of MN-OA was evaluated in cancer cells and animal tumor model. Since, the liposomal nano-formulation consists of MN-OA as one of the active components, the MHT efficacy of T-LMD as well was determined in WEHI-164 cancer cells. To determine the MHT efficacy of T-LMD, firstly its heat generation efficacy under *AC* magnetic field was evaluated. Further cell cyto-toxicity of T-LMD was evaluated in WEHI-164 cells in combination with or without MHT by MTT and PI cell cycle analysis. This was followed by determination of key apoptotic and cell cycle proteins by Western blotting to validate role of apoptosis in the observed enhanced killing of cancer cells by T-LMD in combination with MHT. Thus, the following section discusses the evaluation of hyperthermia therapy efficacy of T-LMD under *in vitro* conditions.

3.2.11.1 T-LMD reached hyperthermic temperature (42 °C) under *AC* magnetic field conditions in 15 min.

For determination of the heat generation efficacy of T-LMD, hyperthermia studies were carried out at 265 kHz radio-frequency, 335 Oe magnetic field intensity, 400 A current for 15 min, using magnetic hyperthermia instrument (DM100 Nanoheating System, NanoScale Biomagnetics, France) in 1 ml of suspension of T-LMD in PBS (equivalent to ~ 3 mg/ml of MN-OA and 40 µM Dox). The temperature was measured using an optical sensor temperature probe (Photon Controls, USA), which was dipped in the middle of nano-formulation suspension. Results showed a rapid increase in the temperature of T-LMD suspension during initial 10 min. The temperature reached from 28.5 °C to 39.7°C in 10 min **(Fig. 3.2.23)**. This was followed by a slower rise in temperature for next five minutes and the suspension reached hyperthermic temperature of 42 °C at 15 min. The SAR was calculated from the time vs temperature curve using the formula as mentioned in **Chapter 2, Section 2.9**. T-LMD showed an SAR of 108.8 Wg^{-1}.

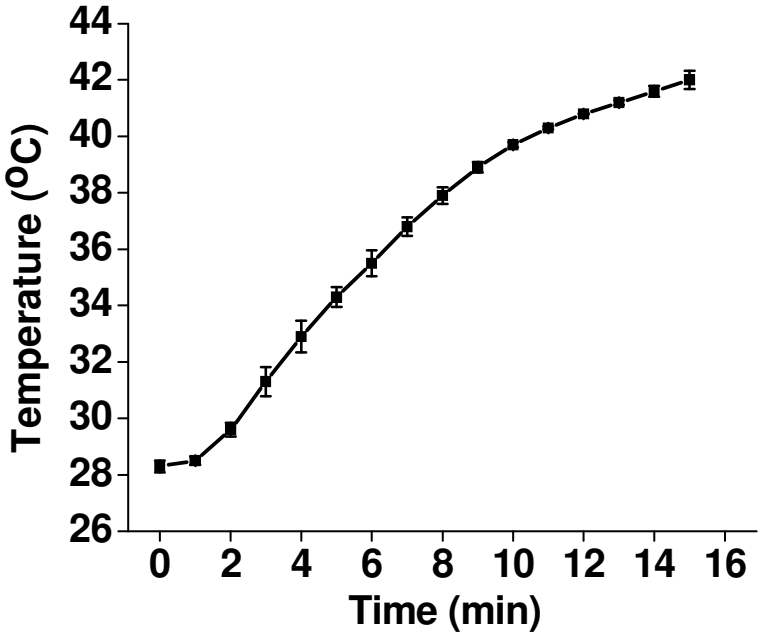

Fig. 3.2.23 *Heat generation by T-LMD (1 ml suspension in PBS corresponding to ~ 3 mg/ml and 40 μM equivalent concentration of MN-OA and Dox, respectively), under AC magnetic field conditions (335 Oe magnetic field intensity, 265 kHz radio-frequency, for 15 min).*

3.2.11.2 MTT assay showed a concentration dependent increase in cell cyto-toxicity in WEHI-164 cancer cells after treatment with T-LMD in combination with or without MHT

To determine the cyto-toxicity of T-LMD in combination with hyperthermia therapy, WEHI-164 cells were treated with increasing concentrations of T-LMD (equivalent to 200 and 400 nM Dox or ~ 40 and 80 μg/ml of MN-OA) for 24 and 48 h, followed by determination of cell viability by MTT assay. Results showed a concentration and time dependent decrease in the cell viability of WEHI-164 cells after treatment with T-LMD alone. The cell viability was found to decrease from 80.8 ± 2.3 % and 65.1 ± 1.6 % at 24 h to 66.5 ± 2.16 % and 39.7 ± 0.15 % at 48 h for 200 and 400 nM T-LMD, respectively **(Fig. 3.2.24)**. Moreover, in combination with MHT, the cell viability was further observed to be decreased in a concentration and time dependent manner. The cell viability was found to be 59.3 ± 3.5 and 54.7 ± 3.3 % at 24 h and 50.8 ± 1.7 and 23.1 ± 1.2 % at 48 h for 200 and 400 nM concentrations of T-LMD in combination with MHT, respectively. These results demonstrate the magnetic hyperthermia efficacy of T-LMD.

A.

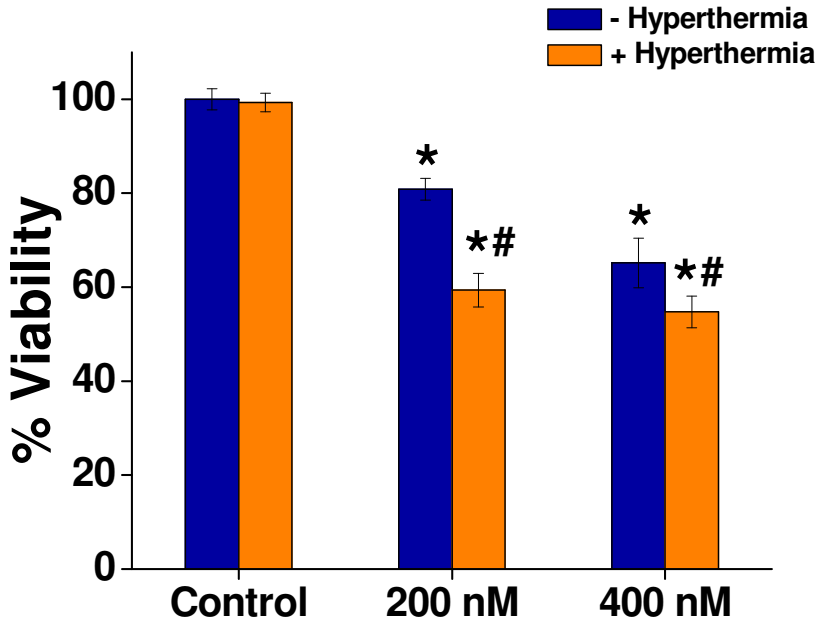

B.

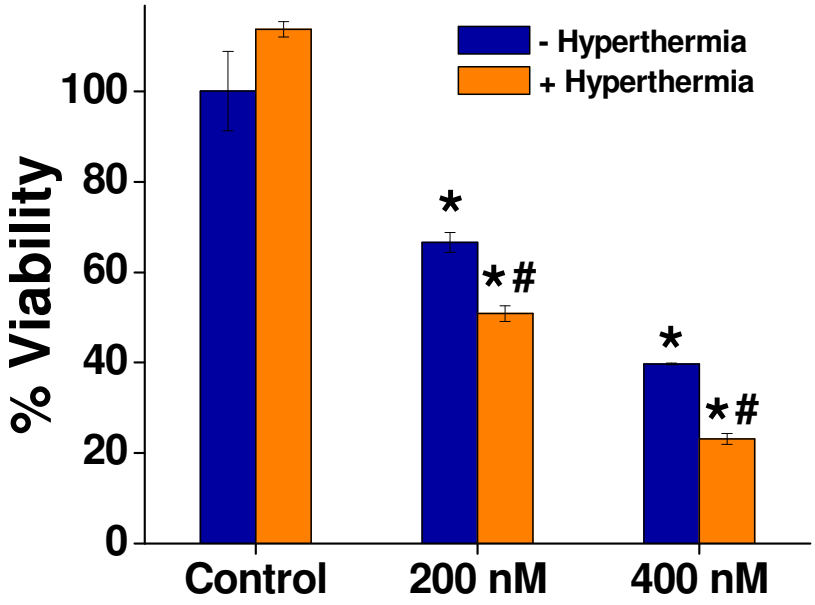

Fig. 3.2.24 *MTT analysis of WEHI-164 cells after treatment with T-LMD (200 and 400 nM equivalent concentrations of Dox and 40 and 80 µg/ml equivalent concentrations of MN-OA) for* ***(A)*** *24 h and* ***(B)*** *48 h. * Significant at P<0.05 as compared to control and # indicates significant difference between T-LMD and T-LMD + hyperthermia group.*

3.2.11.3 T-LMD in combination with MHT showed a concentration dependent increase in sub-G1 population

Cell viability studies by MTT assay suggested significant magnetic hyperthermia efficacy of T-LMD in WEHI-164 cells. To evaluate the role of apoptosis in the T-LMD induced cell death in combination with or without MHT, sub-G1 analysis using PI staining and flow cytometry was carried out. Briefly, WEHI-164 cells were treated with T-LMD (equivalent to 200 and 400 nM Dox or ~ 40 and 80 µg/ml of MN-OA) in combination with or without MHT for 24 and 48 h. Results showed a concentration and time dependent increase in the sub-G1 population in WEHI-164 cells treated with T-LMD (viz. 14.8 ± 0.52 and 20.07 ± 0.99 at 24 h and 27.29 ± 3.7 and 39.2 ± 0.3 % at 48 h for 200 and 400 nM concentration of T-LMD, respectively). However, in combination with MHT, a marginal increase in sub-G1 population was obtained at both the concentrations and time points (viz. 15.9 ± 0.6 and 22.09 ± 1.9 % at 24 h and 29.8 ± 1.3 and 44.1 ± 2.8 % at 48 h for 200 nM + H and 400 nM + H treatments, respectively) **(Fig. 3.2.25 A & B)**. Interestingly, a significant and concentration dependent increase in G2-M population was observed at 24 h, which however increased marginally in case of combination treatment with MHT **(Fig. 3.2.25 A)**. These results were corroborated by a significant increase in expression of Cyclin B1, CDC2 and GADD45α, markers for arrest of cells in G2-M phase of cell cycle. Moreover, the expression of these proteins was found to increase with both the concentration of T-LMD and application of MHT **(Fig. 3.2.25 C)**. The % cells in G2-M phase increased from 23.9 ± 2.28 % and 26.35 ± 3.6 % for 200 nM and 400 nM concentrations of T-LMD to 26.89 ± 2 and 30.23 ± 2.2 % respectively, for 200 nM +H and 400 nM + H treatments.

A.

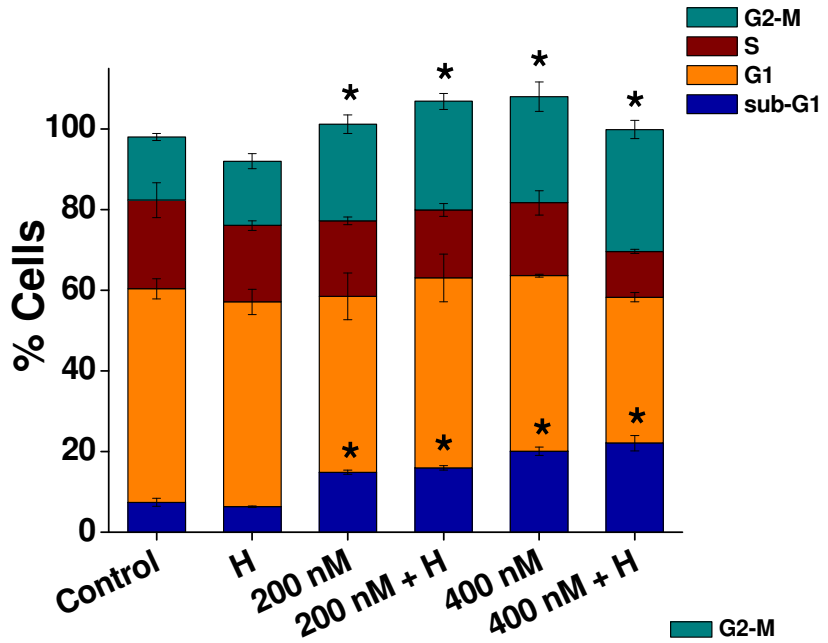
G2-M
S
G1
sub-G1
% Cells
0
20
40
60
80
100
Control
H
200 nM
200 nM + H
400 nM
400 nM + H
*

B.

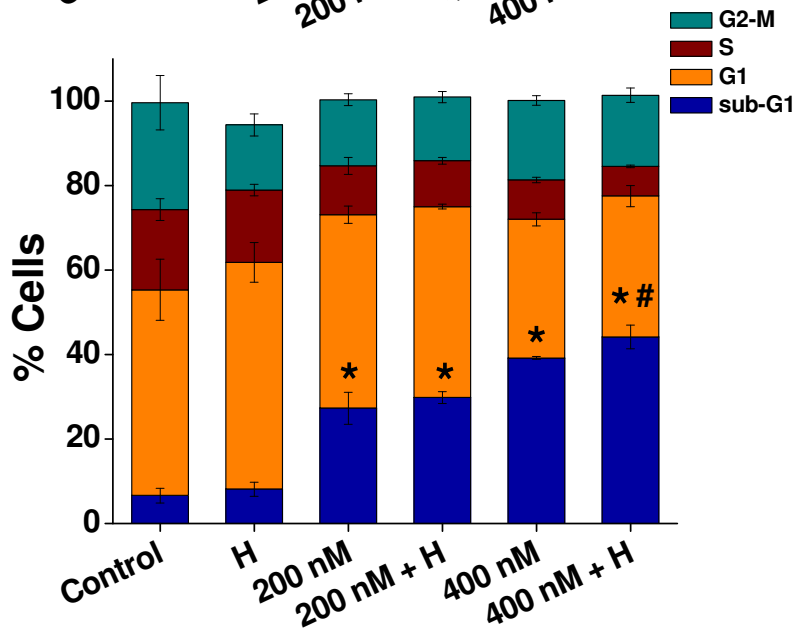
G2-M
S
G1
sub-G1
% Cells
0
20
40
60
80
100
Control
H
200 nM
200 nM + H
400 nM
400 nM + H
*
*#

C.

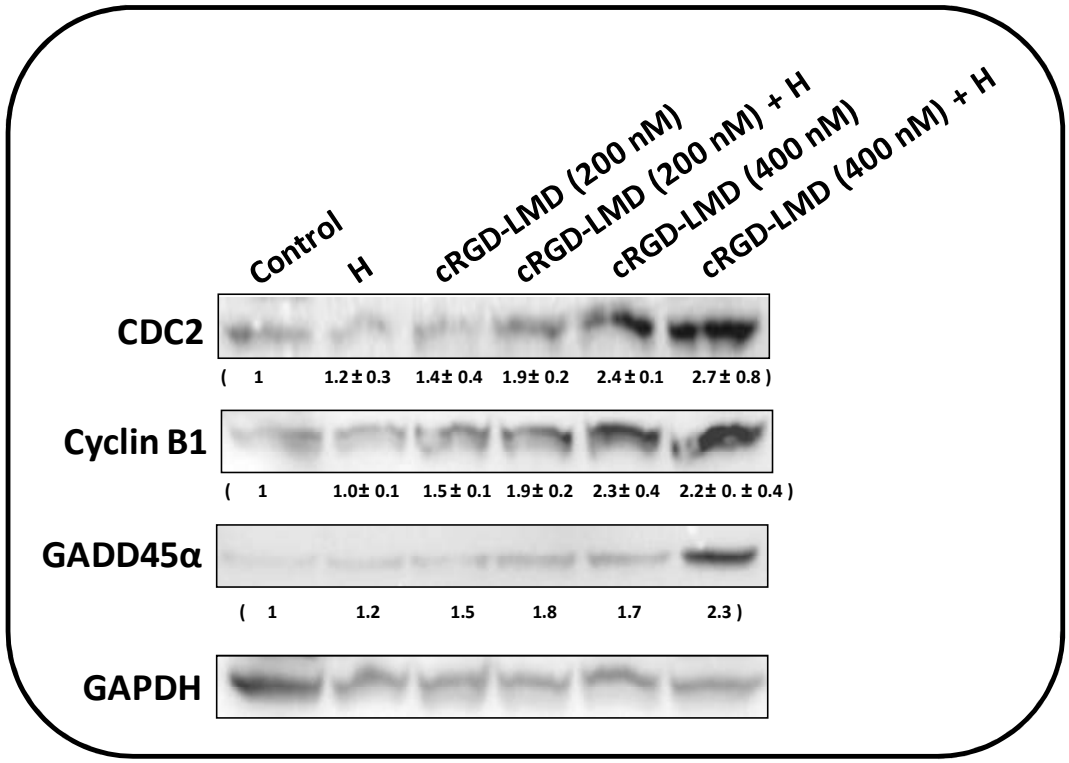

Fig. 3.2.25 *Cell cycle analysis by PI staining and flow cytometry for WEHI-164 cells treated with T-LMD (200 and 400 nM equivalent concentrations of Dox and ~ 12 and 24 µg/ml equivalent concentrations of MN-OA) for* ***(A)*** *24 h and* ***(B)*** *48 h. * Significant at P<0.05 as compared to control and # indicates significant difference between T-LMD and T-LMD + hyperthermia (H) group.* ***(C)*** *Western blot analysis for WEHI-164 cells treated with T-LMD at indicated concentrations in combination with or without MHT (H). Values in parenthesis represent Mean ± SD values of relative fold change in level of respective proteins as compared to control after normalizing with GAPDH.*

3.2.11.4 T-LMD in combination with MHT shows significant up-regulation of pro-apoptotic proteins in WEHI-164 cells

To determine the role of apoptosis in the enhanced cell death induced by T-LMD in combination with or without MHT, Western blot analysis was carried out. Briefly, WEHI-164 cells were treated with different concentrations of T-LMD (equivalent to 200 and 400 nM Dox or ~ 40 and 80 µg/ml of MN-OA) for 24 h, followed by harvesting the cells and processing for Western blotting **(Chapter 2, Section 2.31)**. Results showed a significant increase in expression of pro-apoptotic proteins (viz. cleaved caspase-3 and cleaved PARP) in WEHI-164 cells treated with T-LMD. Moreover, the expression of pro-apoptotic proteins was found to increase in a concentration dependent manner and was further enhanced when combined with MHT **(Fig. 3.2.26)**.

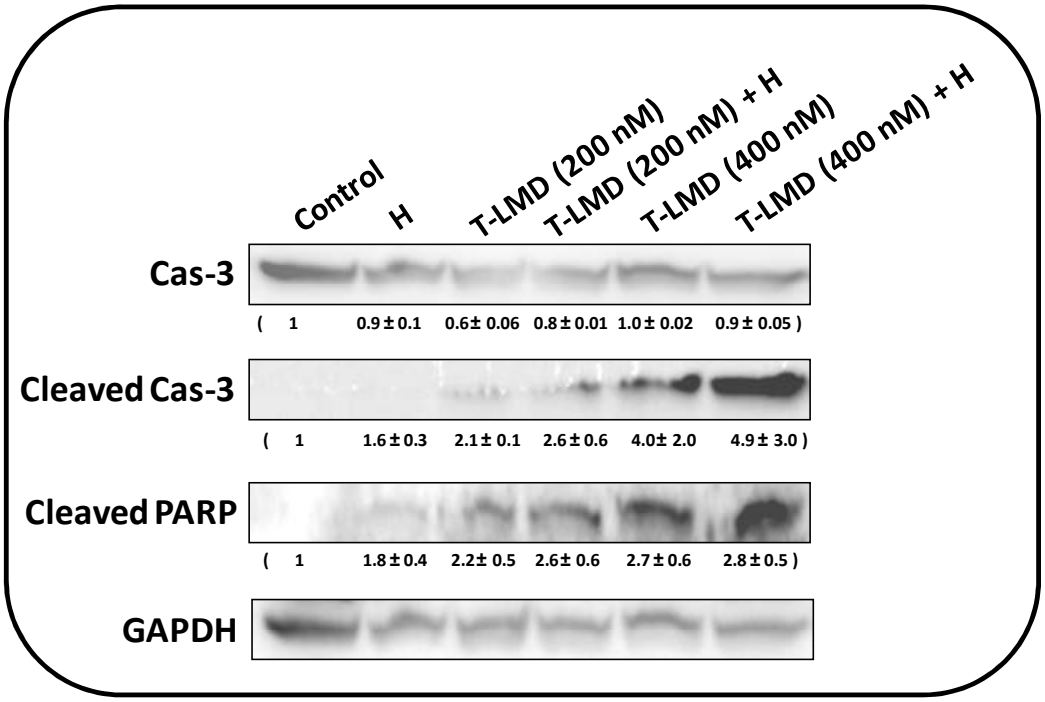

Fig. 3.2.26 *Western blot analysis of WEHI-164 cells treated with T-LMD ± H at 24 h for expression of Pro-apoptotic (Cas-3, Cleaved cas-3 and cleaved PARP) proteins. Values in parenthesis represent Mean ± SD values of relative fold change in level of respective proteins as compared to control after normalizing with GAPDH.*

Summary:

Tumor targeted liposomal nano-formulation (T-LMD) was synthesized and characterized by different bio-physical techniques. T-LMD showed significant uptake by receptor mediated endocytosis in αvβ3 receptor over-expressing cell line (U373MG). T-LMD showed significantly higher (~ 1.6 to 8 fold) anti-cancer efficacy in several cancer cell lines as compared to Lippod^{TM}. Moreover T-LMD showed least cyto-toxicity in normal human lung fibroblasts (WI26VA44) amongst the screened cell lines. T-LMD showed significant magnetic hyperthermia and radio-sensitization efficacy in WEHI-164 cells. The mechanism of enhanced cell death induced by T-LMD ± γ-radiation was found to involve induction of ROS, activation of JNK and up-regulation of pro-apoptotic signalling molecules **(Scheme 3.2.6)**.

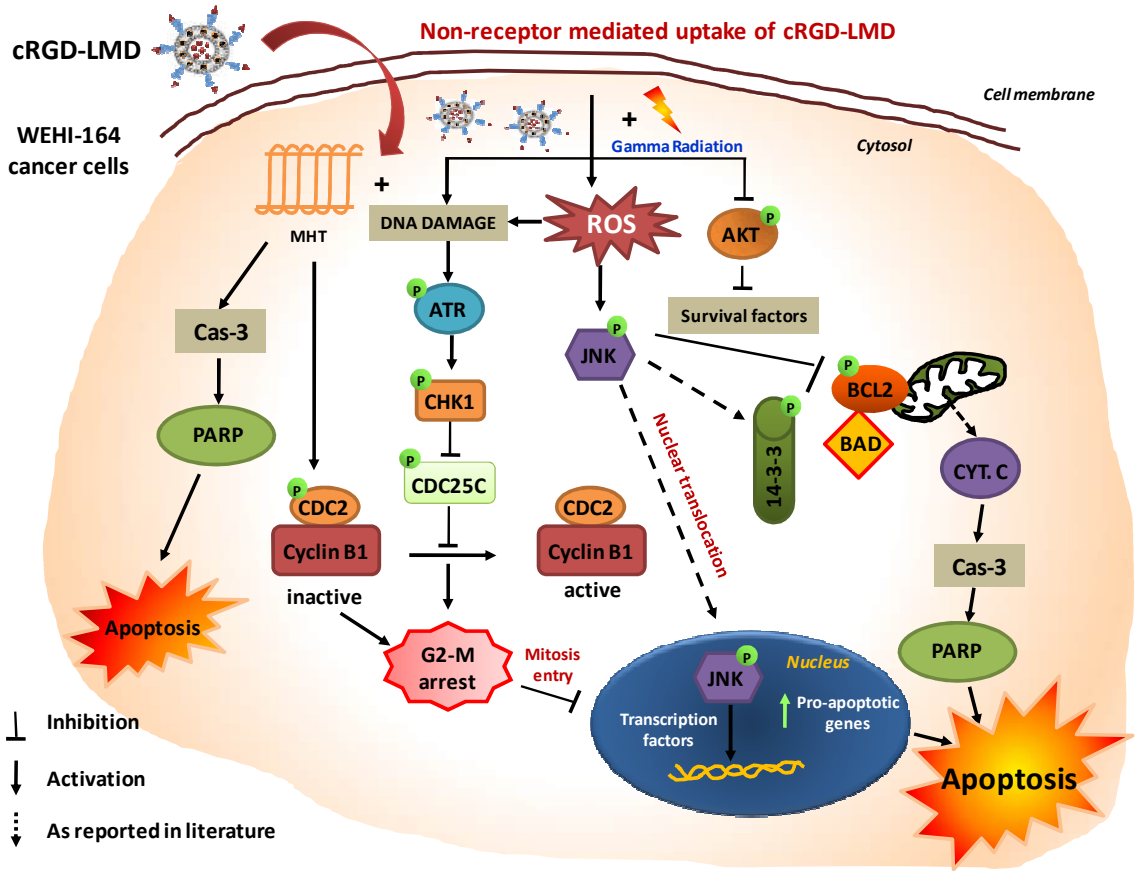

Scheme 3.2.6 *Scheme for the key molecular players involved in the mechanism of T-LMD mediated apoptosis induction in WEHI-164 cells in combination with magnetic hyperthermia and radiotherapy.*

CHAPTER 3

RESULTS AND DISCUSSION

Section 3.3 : Evaluation of Toxicity and Therapeutic efficacy of Targeted Liposomal Nano-formulation (T-LMD) for Combinatorial Cancer Therapy

SECTION 3.3 EVALUATION OF TOXICITY AND THERAPEUTIC EFFICACY OF TARGETED LIPOSOMAL NANO-FORMULATION (T-LMD) FOR COMBINATORIAL CANCER THERAPY

As discussed previously (**Section 3.2.8**), T-LMD showed differential uptake in cancer cells based upon expression of αvβ3 integrin receptor. However, in-spite of the lower uptake in WEHI-164 cells, T-LMD showed significantly higher *in vitro* cyto-toxicity in WEHI-164 cells in a concentration dependent manner **(Fig. 3.2.17)**. Moreover, in combination with γ-radiation, the anti-cancer efficacy of the nano-formulation was found to be further enhanced as confirmed by sub-G1 analysis and clonogenic cell survival assays **(Fig. 3.2.18 and 3.2.19)**. These results demonstrated the radio-sensitization efficacy of T-LMD. Increased generation of ROS and DNA double strand breaks was observed when cells were treated with T-LMD in the combination of γ-radiation **(Fig. 3.2.20 and 3.2.21)**. These results suggested the role of indirect effect of radiation via generation of ROS and increased DNA damage as one of the mechanisms of cyto-toxicity induced by the nano-formulation. In addition, T-LMD was found to exhibit significant MHT efficacy in WEHI-164 cells as determined by MTT assay and cell cycle analysis (**Fig. 3.2.24 and 3.2.25**). To further validate the *in vitro* anti-cancer efficacy of T-LMD at *in vivo* level, an immuno-competent fibrosarcoma tumor model was established in BALB/c mice by intra-muscular injection of WEHI-164 cells. Although the active targeting of T-LMD in WEHI-164 tumor cells is expected to be lower due to poor expression of αvβ3 integrin receptor, passive targeting due to the enhanced permeability and retention (EPR) effect attributable to the leaky vasculature of the tumor, may result in increased accumulation of the nano-formulation at the tumor site. In addition, since the tumor neo-vasculature is known to have higher expression of

αvβ3 integrin receptor, T-LMD may be able to actively target the tumor neo-vasculature and facilitate enhanced accumulation/retention at the tumor site **(Scheme 3.3.1)**.

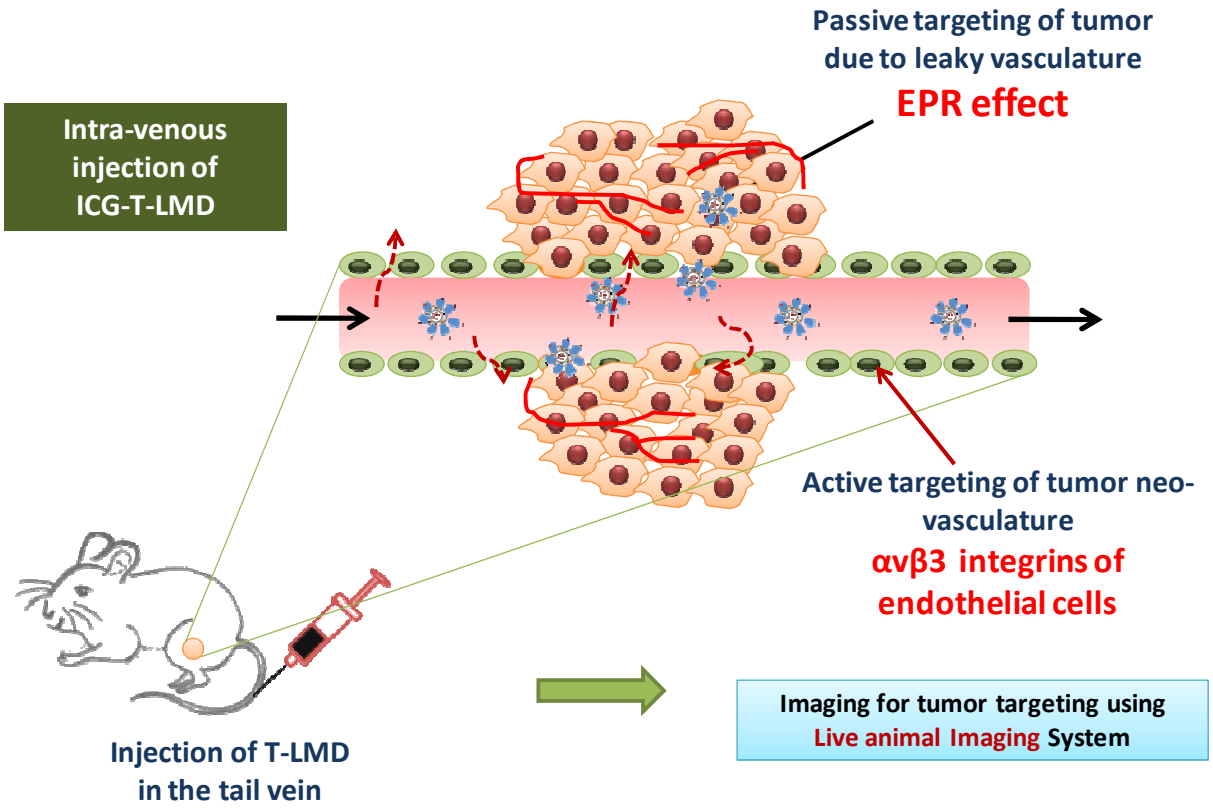

Scheme 3.3.1 *Scheme for the probable mechanism of targeting of fibrosarcoma tumor, post intra-venous administration of T-LMD in immuno-competent BALB/c mice.*

3.3.1 EVALUATION OF THE TUMOR TARGETING EFFICACY OF T-LMD IN MURINE FIBROSARCOMA TUMOR MODEL

Conjugation with cRGD peptide was aimed for targeting of the nano-formulation to the tumor site following intra-venous administration. Thus, to test the efficacy of T-LMD to target and accumulate at the tumor site, murine fibrosarcoma tumor model was selected mainly for two

reasons. (i) Being an immuno-competent tumor model, it more closely simulates the human tumors wherein the immune cells play important decisive role for the success of any chemotherapeutic agent and (ii) T-LMD was found to be most effective in terms of *in vitro* cyto-toxicity in WEHI-164 cells. These observations increase the probability of an effective and successful cRGD-targeted chemotherapy in fibrosarcoma model. Moreover, the immuno-competent model also provides the added advantage of combinatorial therapy in terms of ease of application of radiation and hyperthermia treatments to mice, which otherwise would have been difficult in case of SCID/Nude mice. However, for sensitive and accurate determination of tumor targeting efficacy and bio-distribution of nano-formulation in mice, the liposomal nano-formulation needed further modifications. For this purpose, the liposomal nano-formulation was labeled with a near infrared fluorescent dye, indocyanine green (ICG), which enables depth imaging and sensitive detection of the fluorescent signal in live mice due to its detection range in the near-IR region (Ex: 790 nm and Em: 820 nm). The details of the synthesis of the ICG labeled liposomal nano-formulation and its imaging would be discussed in the following Sections:

3.3.1.1 Synthesis of ICG-labeled T-LMD for evaluation of its tumor targeting efficacy

To evaluate the tumor targeting efficacy of the nano-formulation, a traceable form of T-LMD labeled with ICG was designed. This formulation has potential to be visualized using fluorescence based live animal imaging system in real-time. ICG was encapsulated in the liposomal membrane as described **(Chapter 2, Section 2.6)** and its encapsulation efficacy was found to be 32 ± 1.3 % as determined by fluorescence measurement.

3.3.1.2 Free ICG showed fast elimination mainly via the hepato-biliary route from BALB/c mice by 48 h

Before evaluating the tumor targeting efficacy of ICG labeled T-LMD, the determination of the ICG concentration for sensitive detection by live animal imaging system and its bio-distribution was required. Therefore, free ICG (1 mg per mice) was administered intra-venously into BALB/c mice and the fluorescence intensity was measured using live animal imaging system in both dorsal and ventral positions of animals. Results showed a sharp whole body decline in the fluorescence intensity of free ICG from 5 min to 48 h after intra-venous administration **(Fig. 3.3.1 A & B)**. A maximum increase was found at 30 min, which showed distribution of ICG signal to different organs. It was interesting to observe that higher signal intensity was observed at ventral position, probably due to less attenuation of fluorescence signal due to lesser hair at ventral position. Another reason could be the closer location of the major abdominal/thoracic organs (such as lungs, liver, spleen and intestine) and absence of thoracic bony cage which may partially attenuate the signal in dorsal position. The free ICG signal was almost negligible at 48 h. The fluorescence intensity of different organs dissected out at 48 h showed the highest signal of ICG in intestine followed by liver, lungs and kidneys. Whereas, no detectable signal was observed in the brain, heart and spleen **(Fig. 3.3.1 C)**. These results suggested that ICG binds to plasma proteins in blood and is then metabolized possibly through the hepato-biliary route (viz. the liver → bile → intestine → rectum → feces). These results are in agreement of previous literature of elimination ICG in animal system, following intra-venous administration[271].

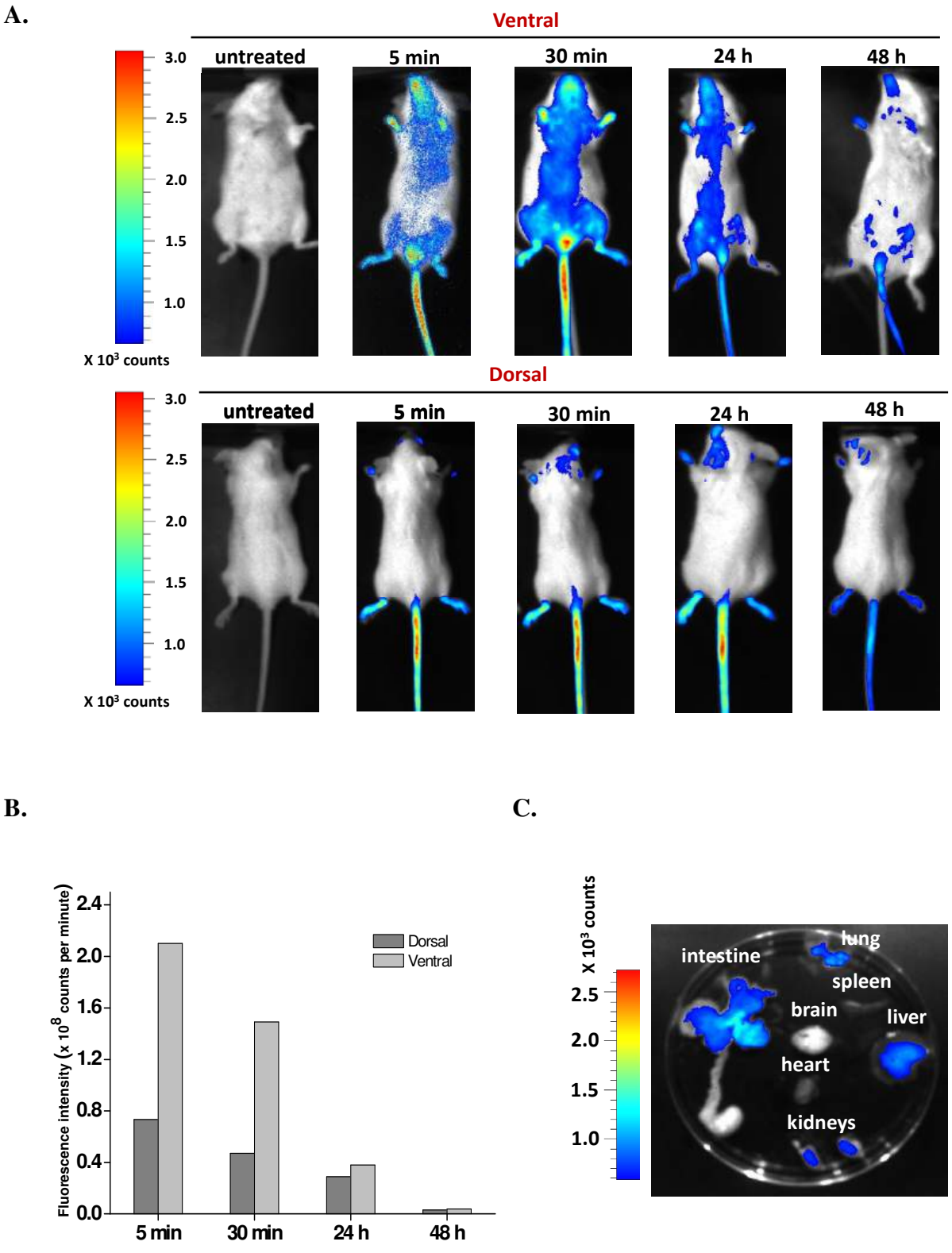

Fig. 3.3.1 ***(A)*** *Representative images of BALB/c mice injected with free ICG (1 mg/mice) intra-venously, at different time points (viz. 5 min, 30 min, 24 h and 48 h).* ***(B)*** *Fluorescence intensity*

of whole body either in dorsal or ventral position at indicated time points as measured by the live animal imaging system (Photon Imager, Biospace Labs, France). ***(C)*** *Representative images of dissected organs of mice injected with free ICG at 48 h post dye administration. Scale shows the color coding for the signal intensity (x 10^3 counts).*

3.3.1.3 ICG labeled T-LMD in fibrosarcoma model showed efficient tumor targeting and significant tumor retention upto day 11 post administration

Since 1 mg free ICG per mice showed detectable fluorescence signal intensity, the ICG labeled T-LMD was also injected at same concentration (i.e. equivalent to 1mg of ICG per mice). The formulation was injected in mice intra-venously followed by animal imaging. Preliminary imaging experiment using mice injected with ICG-T-LMD showed the highest signal in the tumor, ear pinnae, foot paws and the tail vein at 75 min **(Fig. 3.3.2 A)**. The high signal intensity in ear pinnae, paws of feet and tail vein is attributable to the thin layer of skin and absence of hair, resulting in very low signal attenuation compared to signals from internal organs (such as heart, lungs, liver, kidneys, spleen) and tumor. The fluorescence signal of the dissected organs at 3 h post drug administration was also measured. Both the mice showed strong ICG signal in the tumor region (2.54 and 2.98 x 10^8 photons/s/cm^2/Sr in mice no. 1 and 2, respectively). A comparable signal was also visible in the liver and lungs. However, a lower signal was observed in the kidneys, heart and spleen **(Fig. 3.3.2 B & Table 3.3.1)**. These results demonstrated the tumor targeting efficacy of T-LMD. To determine the tumor retention capability of the nano-formulation, the fluorescence intensity of the tumor region was monitored for one remaining mice for upto day 11 after administration of nano-formulation. Results showed a significant retention of the fluorescence signal in the tumor region upto day 11 as evident from the increased

ratio of fluorescence of tumor bearing leg as compared to normal leg (T/N ratio) with time **(Fig. 3.3.2 C & D)**. Thus, these preliminary findings suggested efficient tumor targeting of T-LMD with its enhanced accumulation and retention at the tumor site. For better statistical validation of these observations, further experiments were performed (in subsequent **Section 3.3.1.4**) with more number of fibrosarcoma bearing mice (n=3) followed by comparison of the tumor targeting/bio-distribution efficacy of PEG-Lipo-MN-Dox nano-formulation with or without cRGD labeling.

A.

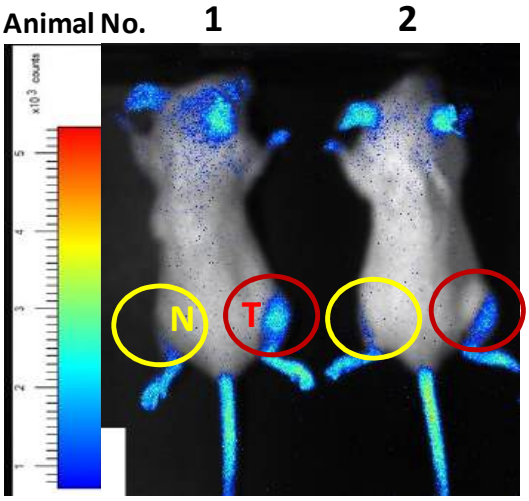

B.

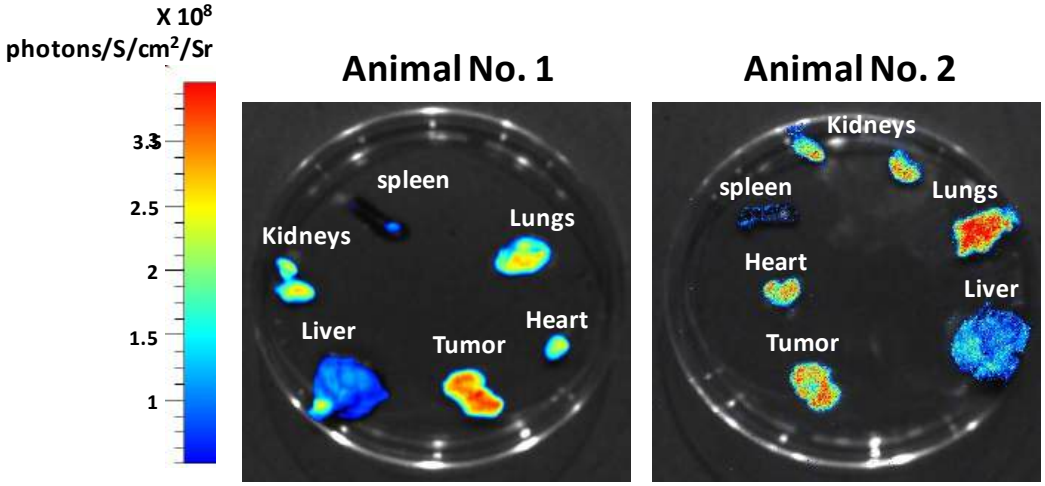

C.

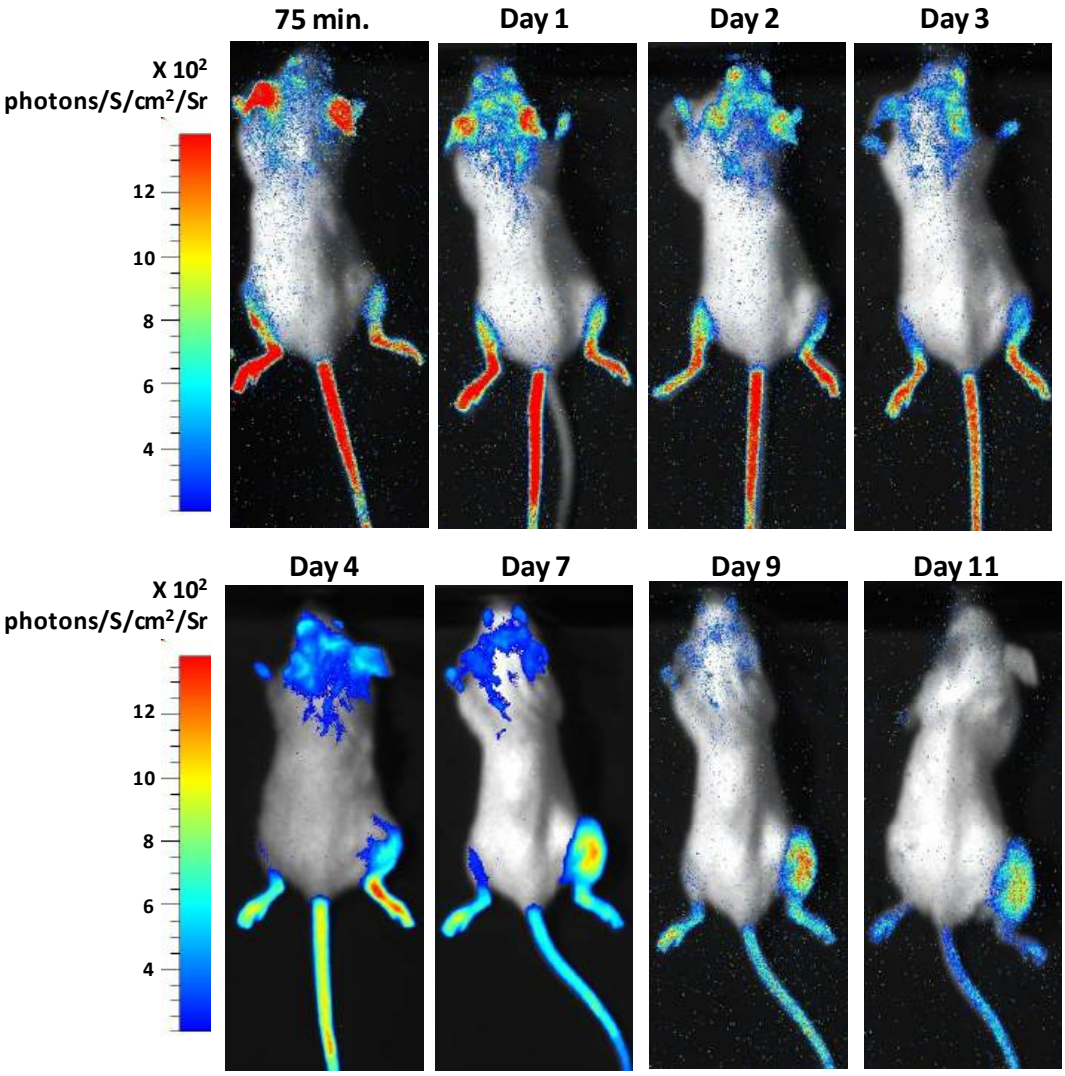
75 min.
Day 1
Day 2
Day 3
X 10²
photons/S/cm²/Sr
12
10
8
6
4
Day 4
Day 7
Day 9
Day 11
X 10²
photons/S/cm²/Sr
12
10
8
6
4

D.

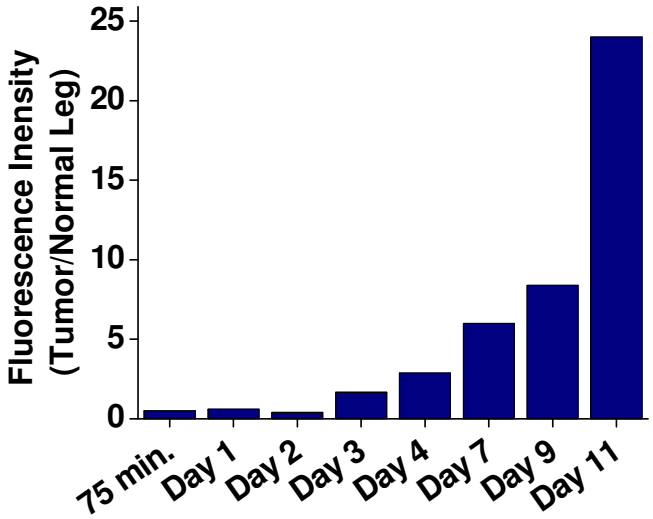
Fluorescence Inensity
(Tumor/Normal Leg)
25
20
15
10
5
0
75 min.
Day 1
Day 2
Day 3
Day 4
Day 7
Day 9
Day 11

Fig. 3.3.2 ***(A)*** *Fluorescence images in near IR range (Ex: 790 nm, Em: 820 nm) for two fibrosarcoma tumor bearing BALB/c mice at 75 min post injection of ICG labeled T-LMD.* ***(B)*** *Representative images of dissected tumor and organs of two mice (animal no.1 and 2) at 48 h post i.v. injection of ICG-T-LMD.* ***(C)*** *Near-IR fluorescence images of fibrosarcoma bearing BALB/c mouse (animal no. 3) at different time points (viz. 75 min. and days 1, 2, 3, 4, 7, 9 and 11) post administration of ICG-T-LMD. Values are for the same mice imaged at different time points following isoflurane based anesthesia.* ***(D)*** *Ratio of fluorescence intensity of tumor bearing and normal leg (T/N) at indicated time points post intravenous administration of ICG-T-LMD.*

Organs	**Fluorescence intensity (x 10^8 Photons/S/cm^2/Sr)**	
	Animal No. 1	**Animal No. 2**
Spleen	**0.07**	**0.28**
Kidneys	**1.04**	**0.85**
Liver	**2.03**	**2.42**
Lungs	**1.67**	**3.24**
Heart	**0.45**	**1.05**
Tumor	**2.54**	**2.98**

Table 3.3.1 *Fluorescence intensity of dissected organs (from Fig. 3.3.2 B) of two BALB/c mice at 3 h post administration of ICG labeled T-LMD.*

3.3.1.4 T-LMD showed significantly better tumor targeting as compared to the un-conjugated nano-formulation

Since the preliminary experiments indicated efficient targeting of T-LMD to the fibrosarcoma tumors, further experiments were performed with 3 mice per group and the tumor targeting efficacy of PEG-Lipo-MN-Dox with or without cRGD labeling was compared. Results showed significantly higher (1.8 fold) tumor targeting efficacy of T-LMD as compared to PEG-Lipo-MN-Dox at 48 h and 168 h as observed by live animal imaging at different time points (viz. 15 min., 30 min., 45 min, 1 h, 3 h, 24 h, 48 h and 168 h) **(Fig. 3.3.3 A)**. The T/N ratio of fluorescence intensity of ICG was found to be higher at most of the time points in mice injected with T-LMD **(Fig. 3.3.3 B)**. To study the bio-distribution of the nano-formulation in tumor and different organs (viz. heart, lungs, liver, kidneys, spleen and intestine), the mice were sacrificed on day 7^{th} post drug administration, the organs were collected and imaged using live animal imaging system. Results showed significantly higher (4.5 fold) fluorescence signal in the tumor of mice injected with T-LMD as compared to PEG-Lipo-MN-Dox **(Fig. 3.3.3 C & D)**. Other organs, however, didn't show much difference in the mean fluorescence intensities. These results suggested that indeed cRGD labeling enabled targeting of the nano-formulation and resulted in higher accumulation of the nano-formulation at the tumor site. Albeit, without cRGD also, PEG-Lipo-MN-Dox is able to target the tumor site passively, probably due to the EPR effect.

A.

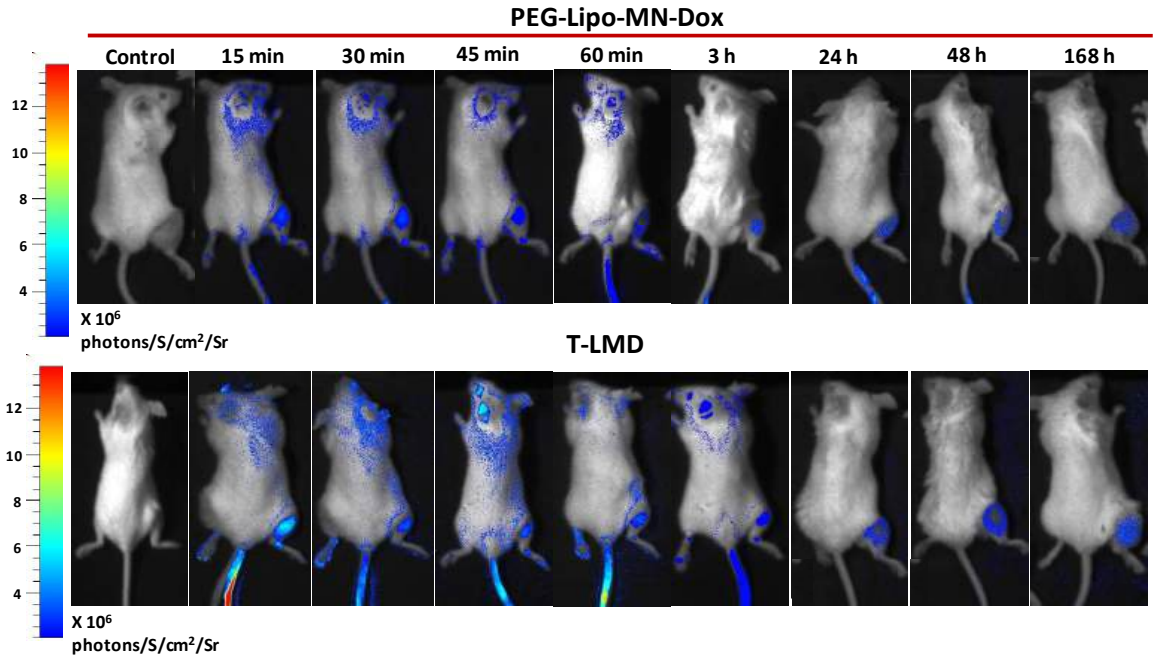
PEG-Lipo-MN-Dox
Control
15 min
30 min
45 min
60 min
3 h
24 h
48 h
168 h
12
10
8
6
4
X 10⁶
photons/S/cm²/Sr
T-LMD
12
10
8
6
4
X 10⁶
photons/S/cm²/Sr

B.

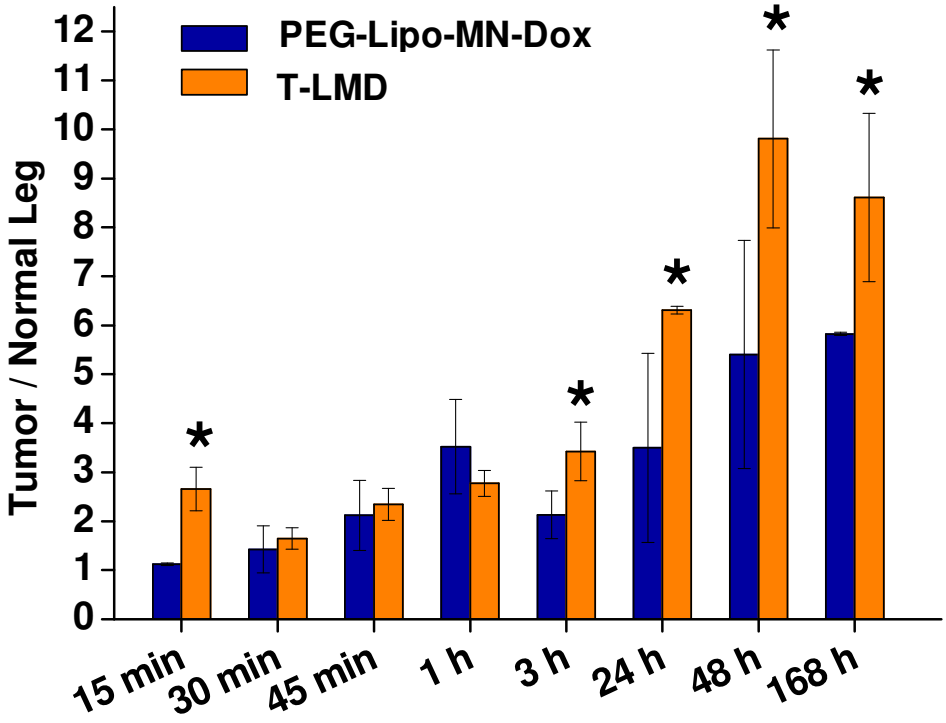
PEG-Lipo-MN-Dox
T-LMD
Tumor / Normal Leg
0
1
2
3
4
5
6
7
8
9
10
11
12
15 min
30 min
45 min
1 h
3 h
24 h
48 h
168 h
*
*
*
*
*

C.

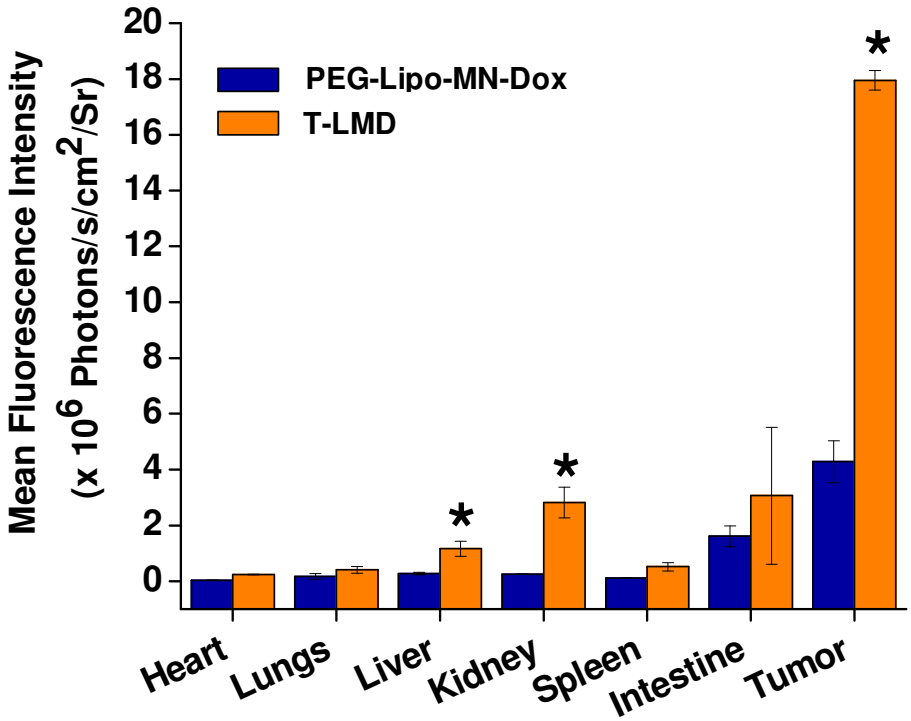

D.

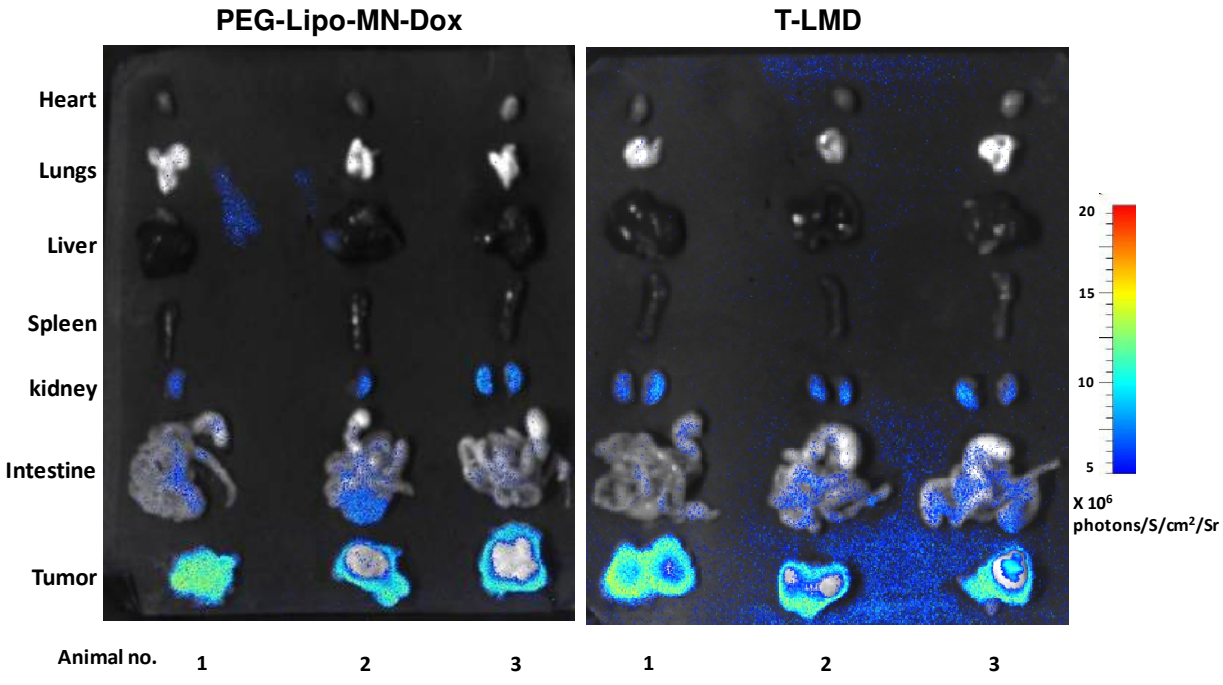

Fig. 3.3.3 *(A) Representative images of mice at selected time points after intra-venous injection of PEG-Lipo-MN-Dox with or without cRGD labeling. Images are captured using live animal*

imaging system (Photon Imager, Biospace Labs, France) under anesthesia (isoflurane) conditions at different time points (viz. 15 min, 30min, 45 min, 1 h, 24 h, 48 h and 168 h).Scale: x 10^6 photons/s/cm^2/Sr. ***(B)*** *Ratio of fluorescence intensity of ICG in tumor bearing and normal leg (T/N) of fibrosarcoma tumor bearing BALB/c mice at indicated time points, post-administration of PEG-Lipo-MN-Dox with or without cRGD conjugation. Values represent Mean ± SD for n=3. * Significant at P<0.05 for PEG-Lipo-MN-Dox treated mice with or without cRGD conjugation* ***(C)*** *Average mean fluorescence intensity of ICG in tumor and different organs (viz. liver, spleen, lungs, heart, kidneys and intestine) for mice on day 7 post-administration of PEG-Lipo-MN-Dox with or without cRGD labeling at indicated time points.* ***(D)*** *Representative images of dissected organs of mice (n=3) at day 7, visualized under live animal imaging system after indicated treatments. Scale: x 10^6 photons/s/cm^2/Sr.*

3.3.2 INFRA-RED (IR) IMAGING SUGGESTED SIGNIFICANT INCREASE IN TUMOR SURFACE TEMPERATURE AFTER MHT

To further corroborate the results of *in vivo* imaging and MHT of tumor, thermal imaging of mice subjected to MHT was carried out using IR camera. If T-LMD has indeed accumulated at the tumor site and is able to locally heat the tumor under AMF conditions, it should lead to a measurable increase in the surface temperature of tumor in mice. Therefore, the tumor surface temperature was measured using an IR based thermal camera prior to placing the mice inside the AMF and immediately after switching off the AMF. Our results showed a significant increase in the tumor surface temperature, especially during the second and third hyperthermia therapy sessions (**Fig. 3.3.4 A-D and Table 3.3.2**). Two out of three mice showed a significant increase in tumor surface temperature of 1 and 1.49 °C at second hyperthermia session (**Fig. 3.3.4 C**).

Whereas, during the third hyperthermia session all three mice showed a rise in the tumor surface temperature of 1.04, 0.5 and 1.04 °C, respectively **(Fig. 3.3.4 D)**. The observed difference in the temperature rise during different hyperthermia sessions may be associated with the change in the concentration and distribution of T-LMD getting accumulated at the tumor site with time. This observation is consistent with the earlier experiment on tumor targeting of nano-formulation studied by ICG labeling, wherein the maximum accumulation of the targeted nano-formulation was observed on day 2 (48 h) post administration of the ICG-T-LMD. Although the temperature rise at the surface is nominal (1.5 °C), the tumor core temperature is expected to be higher due to the poor heat dissipation inside the tumor tissue. Since IR imaging provides only surface temperature of tumor, further studies are needed for more precise and accurate measurement of the temperature at the tumor surface as well inside the tumor core during MHT. This requires the use of advanced techniques such as use of thin optical sensor probes that can be surgically placed inside the tumor core[272] and provide details of temperature as well as oxygen saturation or use of non-invasive MR-thermometry based on proton resonance measurement[273].

A.

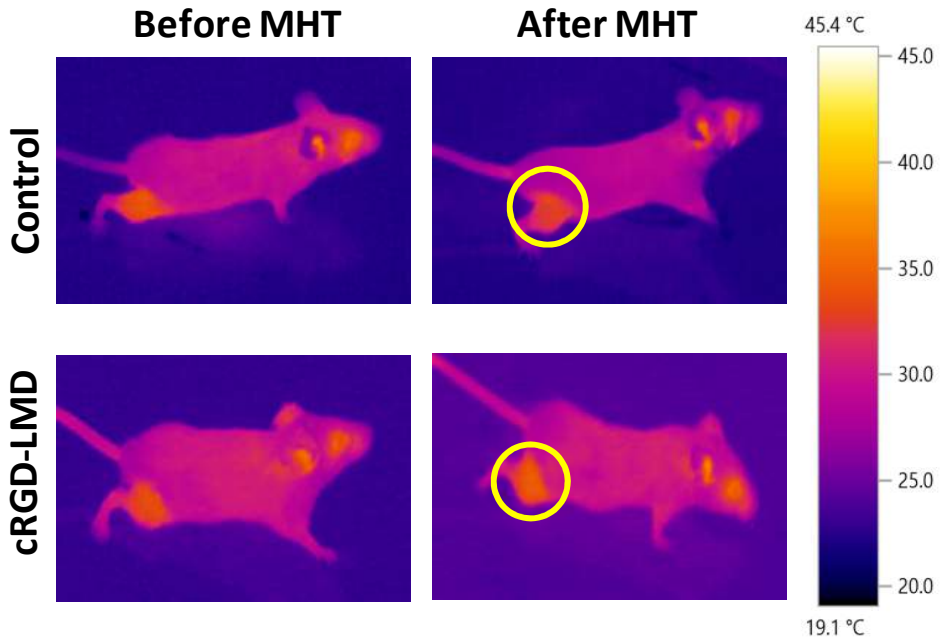

B.

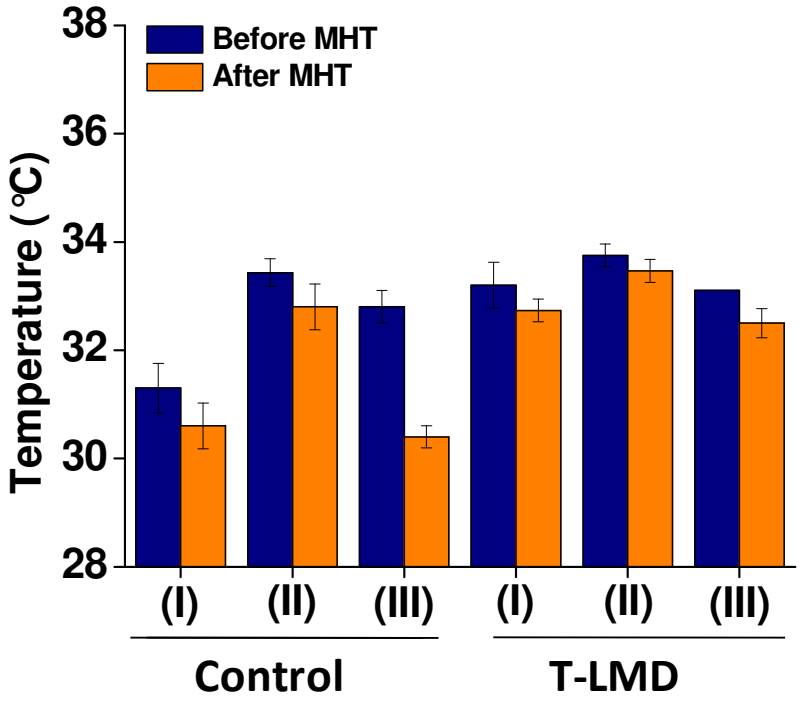
Before MHT
After MHT
Temperature (°C)
38
36
34
32
30
28
(I)
(II)
(III)
(I)
(II)
(III)
Control
T-LMD

C.

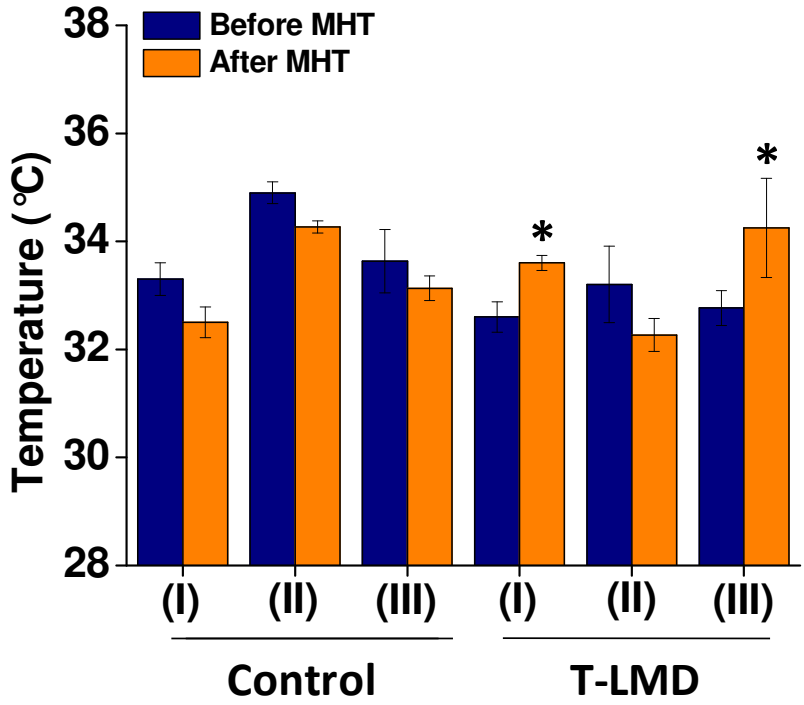
Before MHT
After MHT
Temperature (°C)
38
36
34
32
30
28
*
*
(I)
(II)
(III)
(I)
(II)
(III)
Control
T-LMD

D.

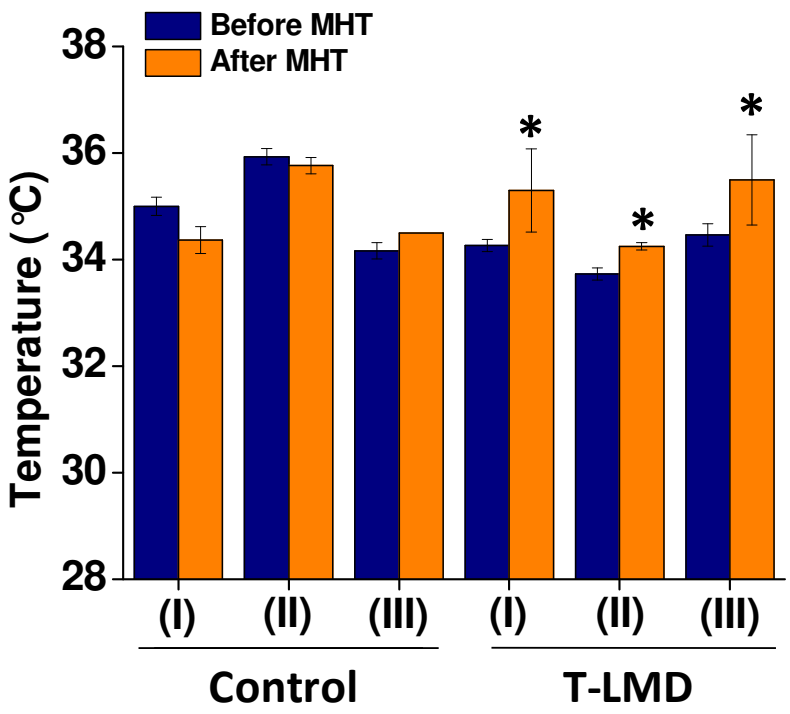

Fig. 3.3.4 *(A) Representative thermal images of fibrosarcoma bearing BALB/c mice captured using IR based thermal imaging camera. The mice were administered with T-LMD, intra-venously and the images were captured on day 2 post nano-formulation administration, just before placing the mice in the AMF and immediately after switching off the AMF. Graphs for increase in tumor surface temperature before and after MHT at* ***(B)*** *first,* ***(C)*** *second and* ***(D)*** *third hyperthermia treatment sessions, respectively. * Significant difference between T-LMD treatment groups before and after MHT at P<0.05. Roman numbers in parenthesis indicate animal number.*

	First Hyperthermia (day 3)					Second Hyperthermia (day 4)					Third Hyperthermia (day 5)				
	Before H		After H		Avg. rise in temp	Before H		After H		Avg. rise in temp	Before H		After H		Avg. rise in temp
	AVG	SD	AVG	SD		AVG	SD	AVG	SD		AVG	SD	AVG	SD	
C + H (I)	31.3	0.45	30.6	0.42	-0.7°C	33.3	0.3	32.5	0.28	-0.8°C	35	0.17	34.36	0.25	-0.6°C
C + H (II)	33.43	0.25	32.8	0.42	-0.6°C	34.9	0.2	34.26	0.11	-0.6°C	35.9	0.15	35.76	0.15	-0.14°C
C + H (III)	32.8	0.3	30.4	0.2	-2.4°C	33.63	0.58	33.13	0.23	-0.5°C	34.16	0.152	34.5	0	0.34°C
cRGD-LMD + H (I)	33.2	0.42	32.73	0.20	-0.4°C	32.6	0.28	33.6	0.14	1.0°C	34.26	0.11	35.3	0.78	1.04°C
cRGD-LMD + H (II)	33.75	0.21	33.46	0.20	-0.29°C	33.2	0.70	32.26	0.30	-0.94°C	33.73	0.11	34.25	0.07	0.52°C
cRGD-LMD + H (III)	33.1	0	32.5	0.26	-0.6°C	32.76	0.32	34.25	0.91	1.49°C	34.46	0.20	35.5	0.84	1.04°C

Table 3.3.2 *Absolute values of the tumor surface temperature measured by thermal (IR based) camera for fibrosarcoma bearing BALB/c mice treated with only AMF (C + H) or T-LMD + AMF (T-LMD + H) just before (Before H) and immediately after (After H) placing the mice under the AMF conditions. Roman numbers in parenthesis indicate animal number.*

3.3.3 T-LMD SHOWED SIGNIFICANT INHIBITION OF TUMOR GROWTH IN COMBINATION WITH HYPERTHERMIA THERAPY

As discussed in **Section 3.3.1**, T-LMD showed significant targeting and accumulation at fibrosarcoma tumor site upto day 11 after intra-venous administration of the nano-formulation. Further to evaluate the combinatorial chemo and hyperthermia therapy efficacy of the nano-formulation, experiments were performed in fibrosarcoma tumor bearing mice using the targeted nano-formulation, T-LMD (as it showed better tumor targeting than unconjugated PEG-Lipo-

MN-Dox). Briefly, the tumor bearing mice were injected with T-LMD (3 mg/kg equivalent concentration of Dox or 2.95 mg/Kg equivalent concentration of MN-OA) and after 24 h the mice were subjected to MHT using the magnetic nano-heating system (DM100 Nano-heating System, NB NanoScale Bio-magnetics, Spain) for three consecutive settings at an interval of 24 h **(Scheme 3.3.2)**. The mice were subjected to *AC* magnetic field (AMF) (magnetic field intensity of 330 Oe, 265 kHz radio-frequency for 10 min. each), by placing them in a plastic restrainer and on an insulated support (as mentioned in **Chapter 2**, **Section 2.10, Scheme 2.6**). Wherever required, tumor volume was determined by measurement of tumor diameters using a digital Vernier caliper (as mentioned in **Chapter 2, Section 2.10**). Results showed that as compared to control, animals treated with AMF (H) didn't show significant decrease in tumor volume. However, animals treated with T-LMD showed a significantly lower tumor volume as compared to control or H, and was further decreased when T-LMD was combined with MHT (H) **(Fig. 3.3.5 A & B)**. Tumor growth delay (TGD) calculated from increase in tumor volume (as discussed in **Chapter 2, Section 2.10**) was increased to 4.4 days in case of combination therapy (T-LMD + H) as compared to 3.2 days in case of treatment with T-LMD **(Fig. 3.3.5 A).**

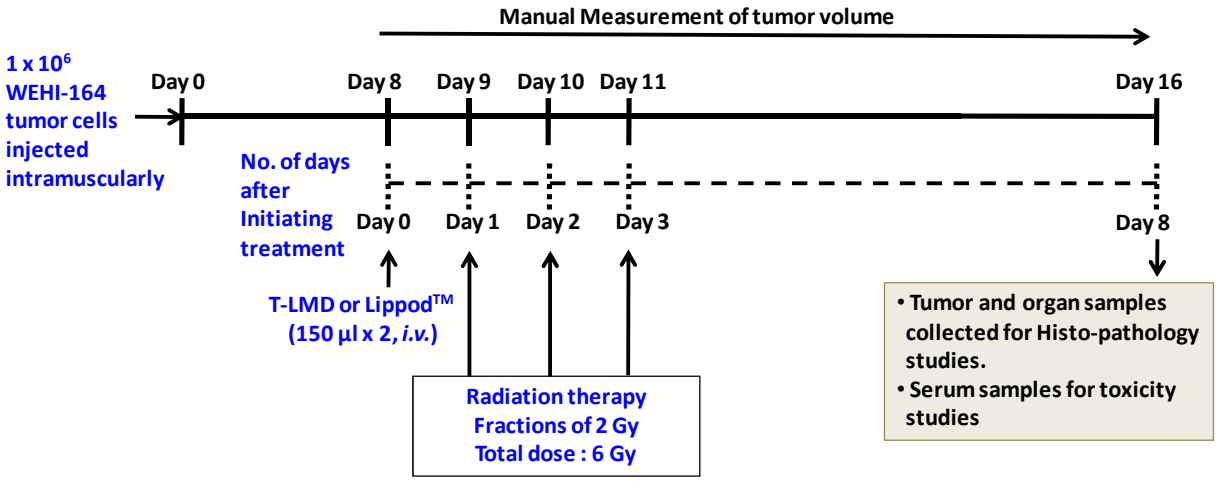

Scheme 3.3.2 *Scheme for treatment schedule of tumor bearing mice with T-LMD and MHT (n=8).*

A.

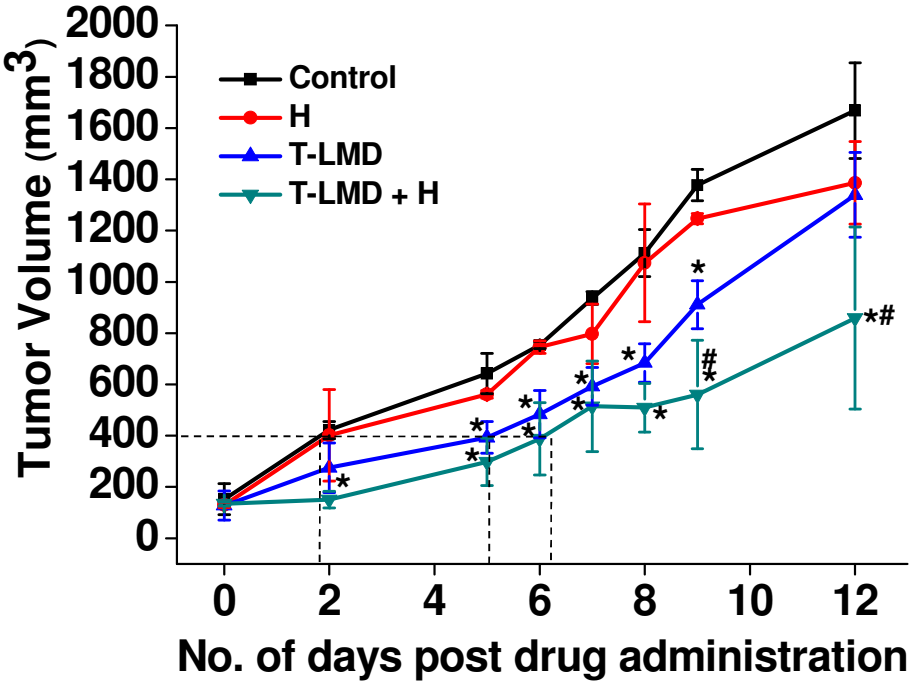

B.

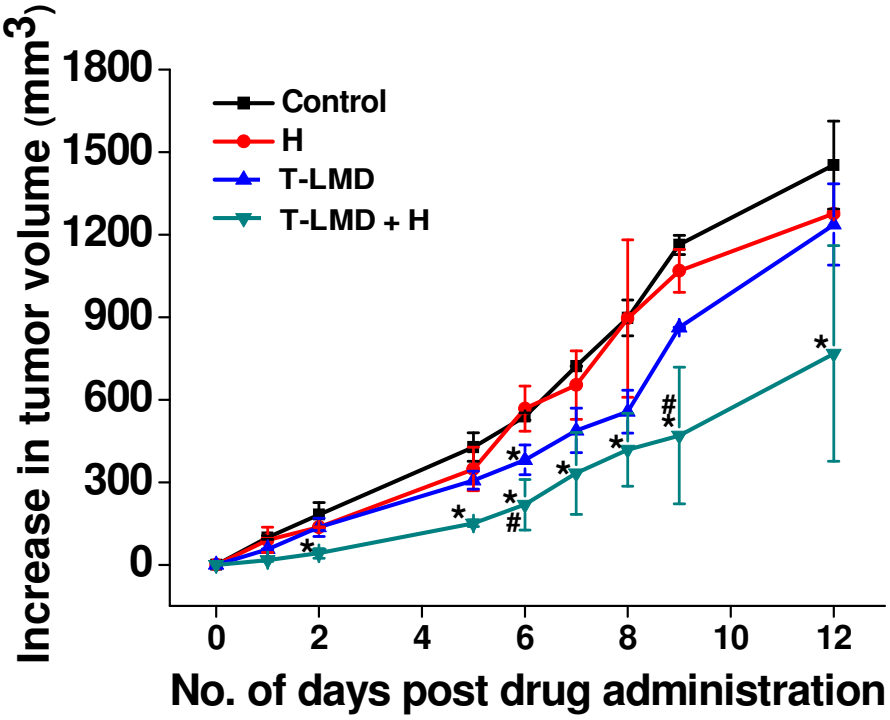

Fig. 3.3.5 (A) *Tumor volume and* ***(B)*** *increase in tumor volume after treatment with T-LMD (3 mg/Kg and 2.95mg/Kg equivalent concentration of Dox and MN-OA, respectively) and magnetic hyperthermia therapy (335 Oe AMF, 265 kHz radio-frequency for 10 min). * Significant at P<0.05 as compared to control and # indicates significant difference between T-LMD treated tumors in combination with or without MHT (H).*

3.3.4 T-LMD EXHIBITED ENHANCED ANTI-TUMOR EFFECT IN COMBINATION WITH GAMMA-RADIATION

As discussed in previous **(Section 3.3.3)**, T-LMD showed significant anti-tumor efficacy in fibrosarcoma tumors in combination with MHT. This ability of the nano-formulation may be attributed to the presence of iron oxide nanoparticles (MN-OA) in the nano-formulation as discussed previously **(Section 3.1.3)**. In addition to MHT, MN-OA was found to induce radio-sensitization in WEHI-164 cancer cells and its tumor model **(Section 3.1.4)**. Moreover, T-LMD also contains doxorubicin, a well reported radio-sensitizing agent in literature[265]. The radio-sensitizing potential of T-LMD has been already established in the *in vitro* experiments **(Section 3.2.10)**. Therefore, I further validated the radio-sensitizing potential of T-LMD, *in vivo* and compared it with Lippod^{TM} (a clinical formulation of liposomal Dox) in murine fibrosarcoma tumor model. A scheme for schedule of treatment is shown in **Scheme 3.3.3**. Briefly, once the tumors were palpable (at day 8 after implantation of WEHI-164 cells), the mice were injected with T-LMD or Lippod^{TM}, intra-venously in two doses of 150 µl each (corresponding to a total dose of 3 mg/Kg and 2.95 mg/kg equivalent concentration of Dox and MN-OA, respectively) on day 0 of treatment. After 24 h (from day 1 to day 3) the mice were subjected to radiation therapy (3 x 2 Gy, total 6 Gy fractionated dose) on three consecutive days at an interval of 24 h. Results

showed a significant inhibition of tumor growth in combination therapy (T-LMD + R) as compared to Lippod^{TM} + R. The TGD was found to be 0.2 and 3.2 days for Lippod^{TM} or T-LMD treatments, respectively. The TGD was found to further increase to 2.2 and 5.5 days in tumors treated with Lippod^{TM} + R or T-LMD + R, respectively **(Fig. 3.3.6 A-B)**. These results show the superior anti-tumor capabilities of targeted nano-formulation, as compared to Lippod^{TM} (clinical formulation of liposomal Dox).

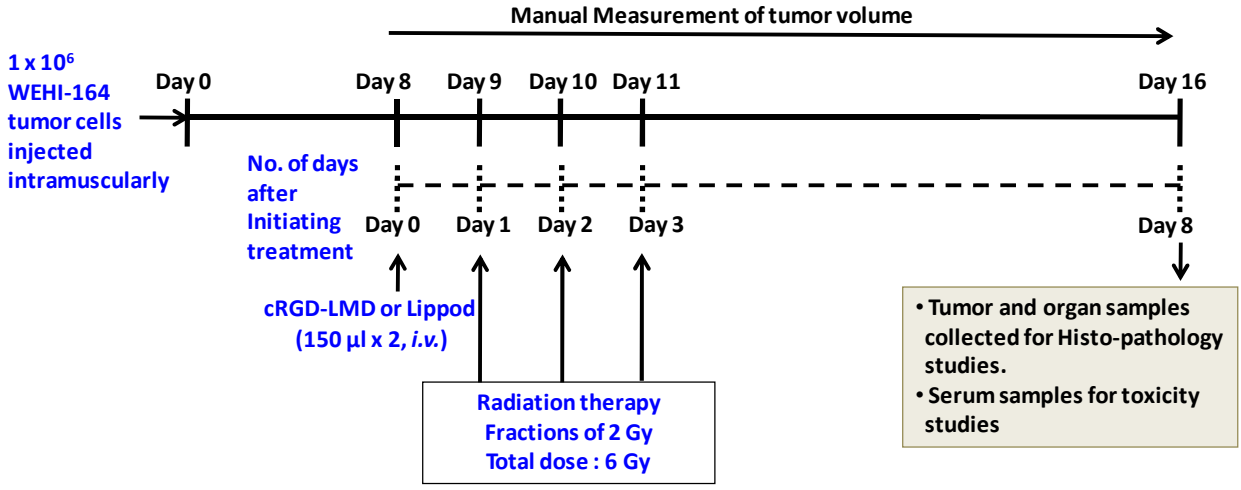

Scheme 3.3.3 *Scheme for treatment schedule of fibrosarcoma tumor bearing BALB/c mice with T-LMD or Lippod^{TM} and γ-radiation (n=8).*

A.

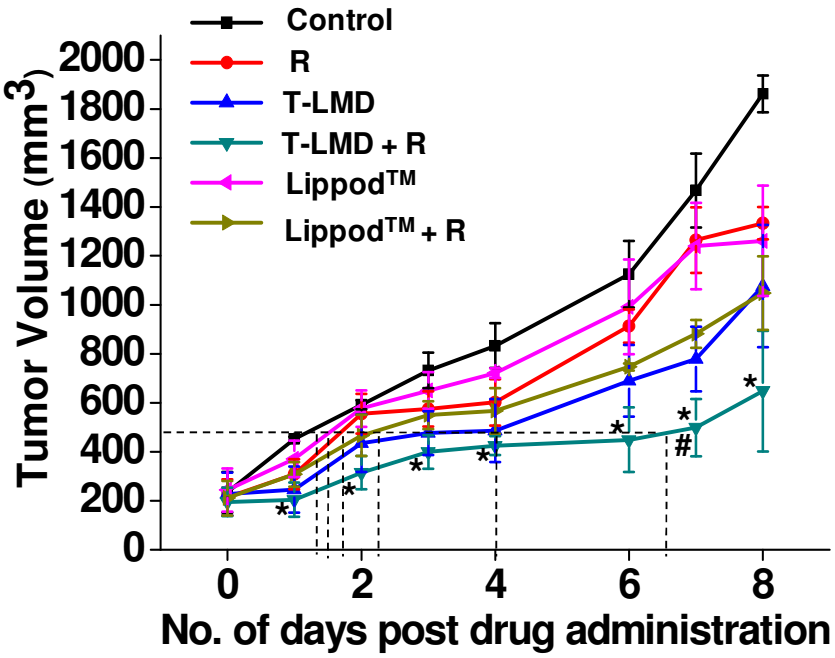

B.

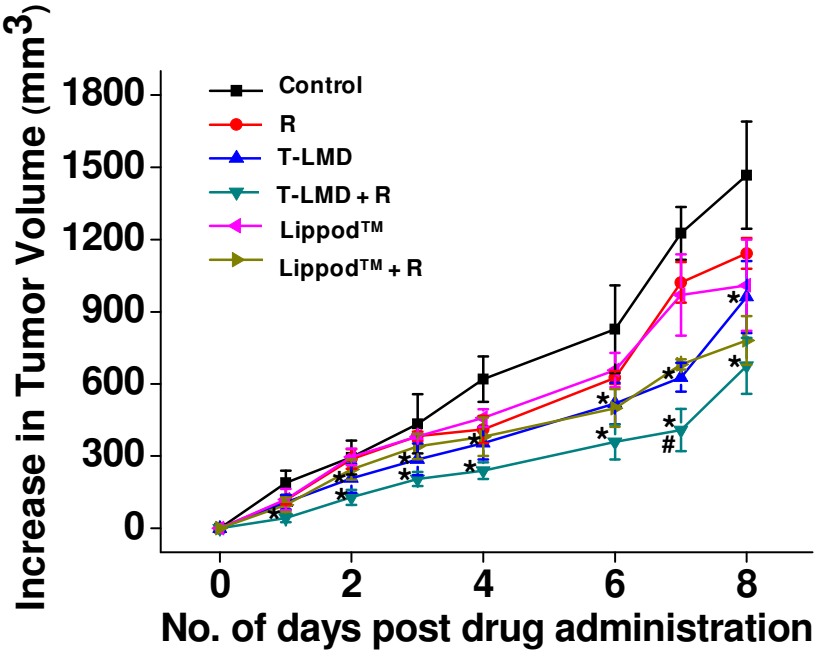

Fig. 3.3.6 *Tumor growth kinetics represented as* ***(A)*** *absolute tumor volume or* ***(B)*** *increase in tumor volume with respect to number of days post indicated treatments. * Significant at P<0.05 as compared to control and # indicates significant difference between T-LMD treated tumors in combination with or without 6 Gy fractionated dose of γ-radiation (R).*

3.3.5 COMBINATORIAL CHEMO-, RADIO- AND HYPERTHERMIA THERAPY INDUCED BY T-LMD SHOWED SUBSTANTIAL INHIBITION OF TUMOR GROWTH

T-LMD showed significant anti-tumor efficacy both in combination with MHT **(Section 3.3.3)** and radiation therapy **(section 3.3.4)**. Clinically, hyperthermia therapy has been demonstrated to enhance the efficacy of radiotherapy mainly by three mechanisms: (i) enhanced oxygenation of the tumor due to vaso-dilation induced by hyperthermic temperature (42 ^{o}C), (ii) enhanced drug accumulation at the tumor site due to the increased blood flow (as a result of vaso-dilation) and (iii) poor heat dissipation at the tumor site due to combined contribution of dis-organized network of blood vessels and high interstitial pressures inside the tumor[274]. However, this is the scenario in case of conventional hyperthermia therapy **(as discussed in Chapter 1, Section 1.4.7)**, wherein the methods of heat delivery are mainly from external heating compared to in situ heating during MHT **(Chapter 1, Section 1.4.8)**. Nevertheless, the *in vitro* and *in vivo* results of T-LMD in WEHI-164 cells, in combination with MHT showed significant killing of tumor cells and inhibition of tumor growth, suggesting the contribution of T-LMD induced MHT for increased tumor control. Therefore, the combinatorial chemo-, radio- and hyperthermia therapy efficacy of T-LMD was evaluated in murine fibrosarcoma tumor model. *(Note: The combinatorial therapy efficacy of T-LMD was not evaluated in vitro, mainly because the mechanism by which hyperthermia contributes to enhancement in chemo-radiotherapy is functional majorly at the tissue level as discussed above).* The treatment protocol followed was same as discussed in case of MHT **(Section 3.3.3)** and radio-therapy **(Section 3.3.4)**. Briefly, following intra-venous injection of T-LMD after 24 h, the mice were first subjected to MHT (H), followed by radiotherapy (R) within 2 h **(Scheme 3.3.4)**. The treatment schedule was repeated on day 2 and day 3 post drug administration. Results showed significantly higher control of tumor

growth in combination therapy (viz. T-LMD + H + R) as compared to T-LMD + H or T-LMD + R or T-LMD treatments. The TGD was found to be 2.9, 3.6, 4.7 and 6.5 days for T-LMD or T-LMD + H or T-LMD + R or T-LMD + H + R treatments, respectively **(Fig. 3.3.7 A & B and Table 3.3.3)**. I also determined the weights of the excised tumors on day 8 post treatment and they were found to be significantly lower for combinatorial treatment (0.93 ± 0.13 g), followed by T-LMD + R (1.3 ± 0.1 g), T-LMD + H (1.9 ± 0.1 g), T-LMD (2.2 ± 0.2 g) and only radiation (2.3 ± 0.2 g) treatments **(Fig. 4.3.7 C)**. The tumor/control (T/C) ratio of tumor volumes at different days post treatment was also calculated. Results showed highest tumor control in the combination therapy group (T-LMD + H + R) followed by T-LMD + R, T-LMD + H and T-LMD treatments as compared to control **(Table 3.3.4)**. T-LMD and R + H treatments showed lower tumor controls as compared to the combination treatments **(Table 3.3.3)**. Thus, these results demonstrate the combinatorial chemo-, radio- and hyperthermia therapy efficacy of T-LMD and establish its candidature as a potential clinical formulation for combinatorial cancer therapy.

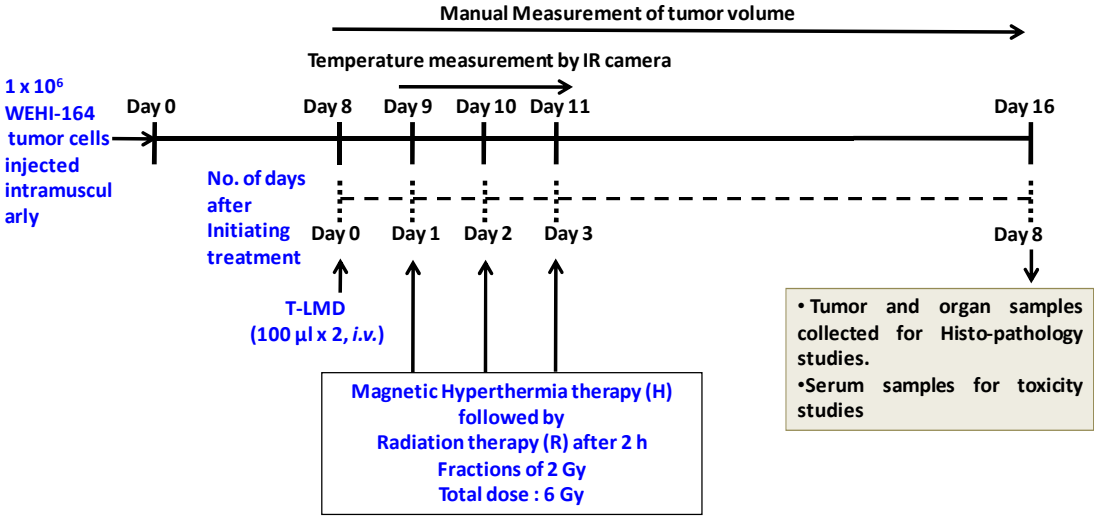

Scheme 3.3.4 *Scheme for schedule of treatment of fibrosarcoma bearing BALB/c mice (n=8) with T-LMD, hyperthermia (H) and radiation therapy (R) either alone or in combination (H+R).*

A.

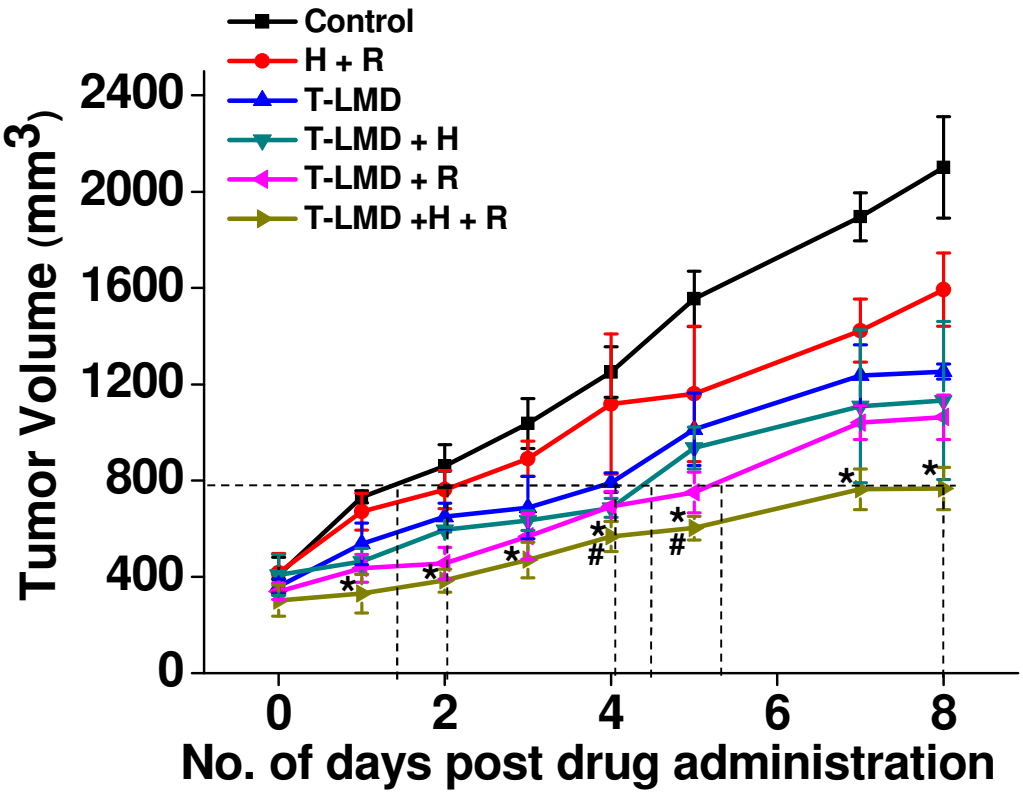
Control
H + R
T-LMD
T-LMD + H
T-LMD + R
T-LMD +H + R
Tumor Volume (mm3)
2400
2000
1600
1200
800
400
0
0
2
4
6
8
No. of days post drug administration

B.

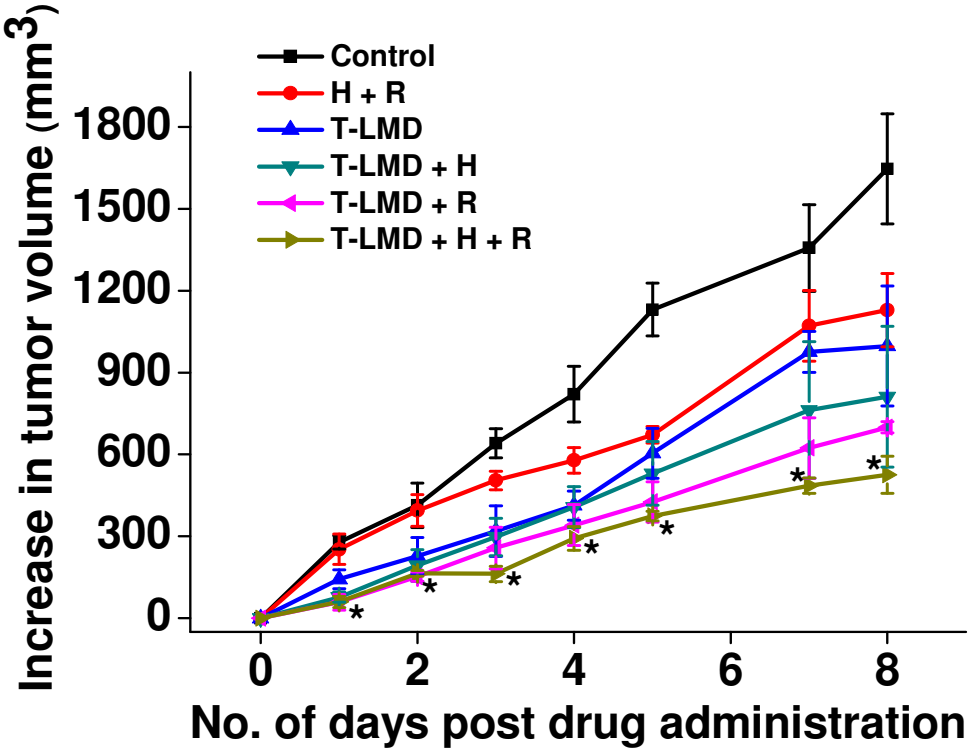
Control
H + R
T-LMD
T-LMD + H
T-LMD + R
T-LMD + H + R
Increase in tumor volume (mm3)
1800
1500
1200
900
600
300
0
0
2
4
6
8
No. of days post drug administration

C.

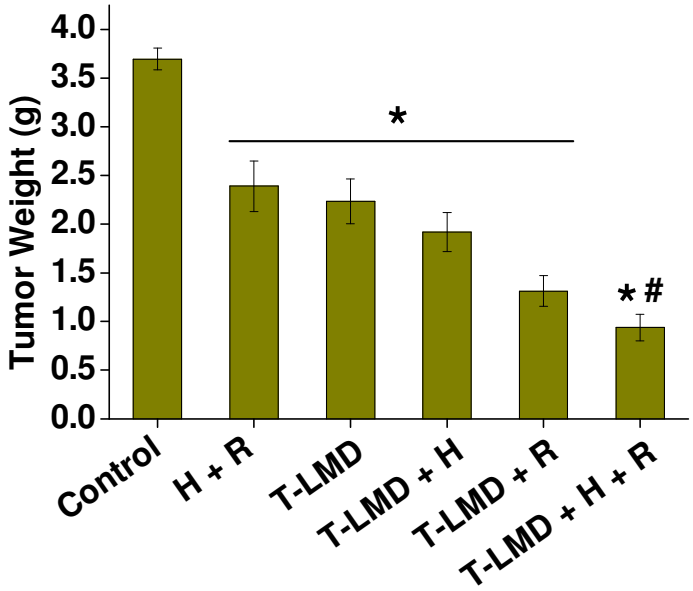

D.

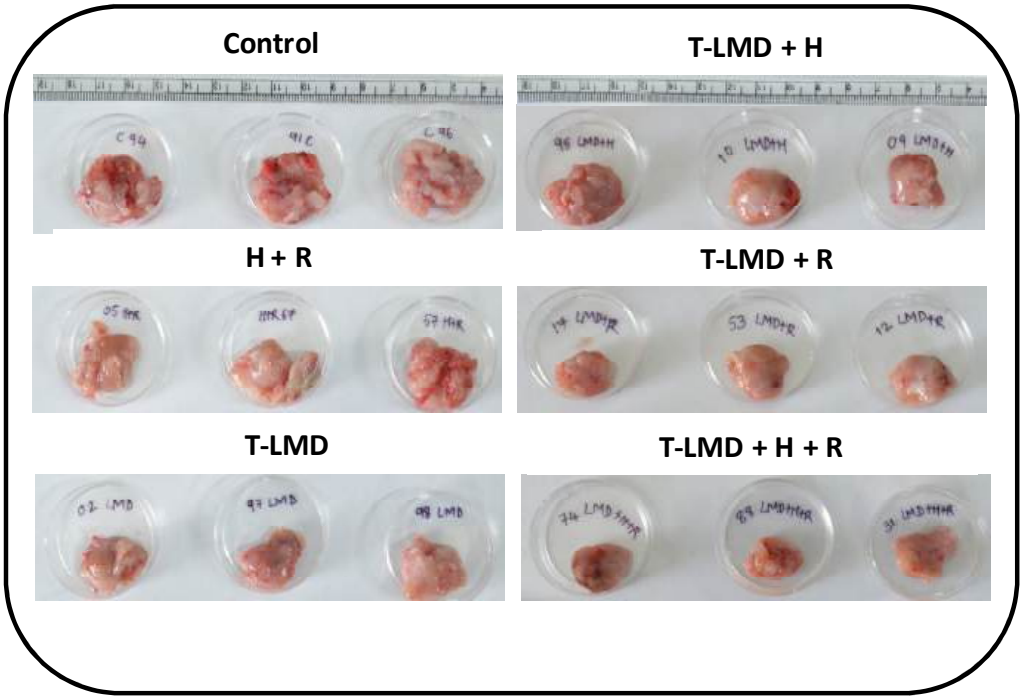

Fig. 3.3.7 *Tumor growth kinetics in terms of* ***(A)*** *absolute tumor volumes and* ***(B)*** *increase in tumor volume at different days post intravenous administration of T-LMD* ***(C)*** *Tumor weights for excised tumors of indicated treatment groups at day 8 after initiation of treatment. * Significant at P< 0.05 as compared to control and # indicates significant difference between combinatorial*

therapy (T-LMD + H + R) as compared to T-LMD + H or T-LMD + R treatments. ***(D)*** *Representative images of excised tumors of indicated treatment groups on day 8.*

	Tumor Growth Delay (TGD) in days
H	**0.75 ± 0.2**
Radiation (R)	**0.7 ± 0.4**
H + R	**0.81**
T-LMD	**2.96 ± 0.4**
T-LMD + R	**4.7 ± 1.13**
T-LMD + H	**3.65 ± 1.06**
T-LMD + H + R	**6.5**
Lippod™	**0.2**
Lippod™ + R	**2.2**

Table 3.3.3 *Values of tumor growth delay (TGD) for indicated treatments.*

	Treated/Control (T/C ratio)				
	Day 1	Day 3	Day 5	Day 7	Day 8
H	0.84 ± 0.3	0.78 ± 0.41	0.87 ± 0.02	0.88 ± 0.07	**0.96 ± 0.2**
Radiation (R)	0.75 ± 0.01	0.78 ± 0.09	0.68 ± 0.1	0.62 ± 0.03	**0.69 ± 0.01**
H + R	1.0 ± 0.02	0.77 ± 0.09	0.62 ± 0.1	0.62 ± 0.08	**0.59 ± 0.01**
T-LMD	0.63 ± 0.1	0.56 ± 0.09	0.56 ± 0.1	0.57 ± 0.01	**0.54 ± 0.09**
T-LMD + R	0.52 ± 0.07	0.45 ± 0.08	0.4 ± 0.07	0.49 ± 0.06	**0.45 ± 0.04**
T-LMD + H	0.54 ± 0.1	0.49 ± 0.08	0.53 ± 0.1	0.50 ± 0.1	**0.53 ± 0.1**
T-LMD + H + R	0.5 ± 0.1	0.44 ± 0.001	0.37 ± 0.01	0.37 ± 0.02	**0.36 ± 0.02**
Lippod™	0.93 ± 0.19	0.96 ± 0.1	0.73 ± 0.16	0.71 ± 0.2	**0.67 ± 0.12**
Lippod™ + R	0.7 ± 0.1	0.75 ± 0.07	0.66 ± 0.01	0.6 ± 0.03	**0.58 ± 0.07**

Table 3.3.4 *Values of ratios of treated/control tumor volumes after indicated treatments at different days post intravenous administration of T-LMD. Note: Shading in red color indicates*

the trend in the value of T/C. Lighter the shading, better the tumor control. The values for H and R are taken from previous experiment ***(Fig. 3.3.5 and 3.3.6)***

3.3.6 TUNEL ANALYSIS AND IMMUNO-FLUORESCENCE STAINING FOR Ki-67 VALIDATED THE SIGNIFICANT TUMOR GROWTH INHIBITION INDUCED BY T-LMD AND COMBINATORIAL THERAPY

As discussed in previous **Section 3.3.5**, T-LMD in combination with or without gamma radiation (R) or MHT (H) or both (H + R) showed significant inhibition of tumor growth. Thus, to determine the contribution of apoptosis to the observed tumor growth inhibition, TUNEL analysis was carried out on control and treated tumor sections on day 8 post-treatment. Results showed significantly higher induction of apoptosis (2.9 ± 0.5 fold) in combinatorial treatment group (T-LMD + H +R) as compared to 2.1 ± 0.1 fold in T-LMD, 2.3 ± 0.2 fold in T-LMD + H, 2.5 ± 0.3 fold in T-LMD + R and 1.6 ± 0.2 and 1.6 ± 0.05 fold in R and H + R groups, respectively **(Fig. 3.3.8 A & C)**. Moreover, the expression of cell proliferation marker (Ki-67) was also determined by immuno-fluorescence staining of tumor tissue sections. Results showed a significant decrease in the expression of Ki-67 in combinatorial treatment group (0.54 ± 0.009 fold) as compared to individual treatments (viz. 0.62 ± 0.1, 0.58 ± 0.03, 0.59 ± 0.02, 0.8 ± 0.12 and 0.8 ± 0.16 fold for T-LMD, T-LMD + H, T-LMD + R, R and H + R treatments, respectively) and control **(Fig. 3.3.8 B & D)**. Thus, these results suggest the role of apoptosis in the observed tumor growth inhibition by T-LMD in combination with or without Radiation (R) or Hyperthermia (H) or both treatments (H + R).

A.

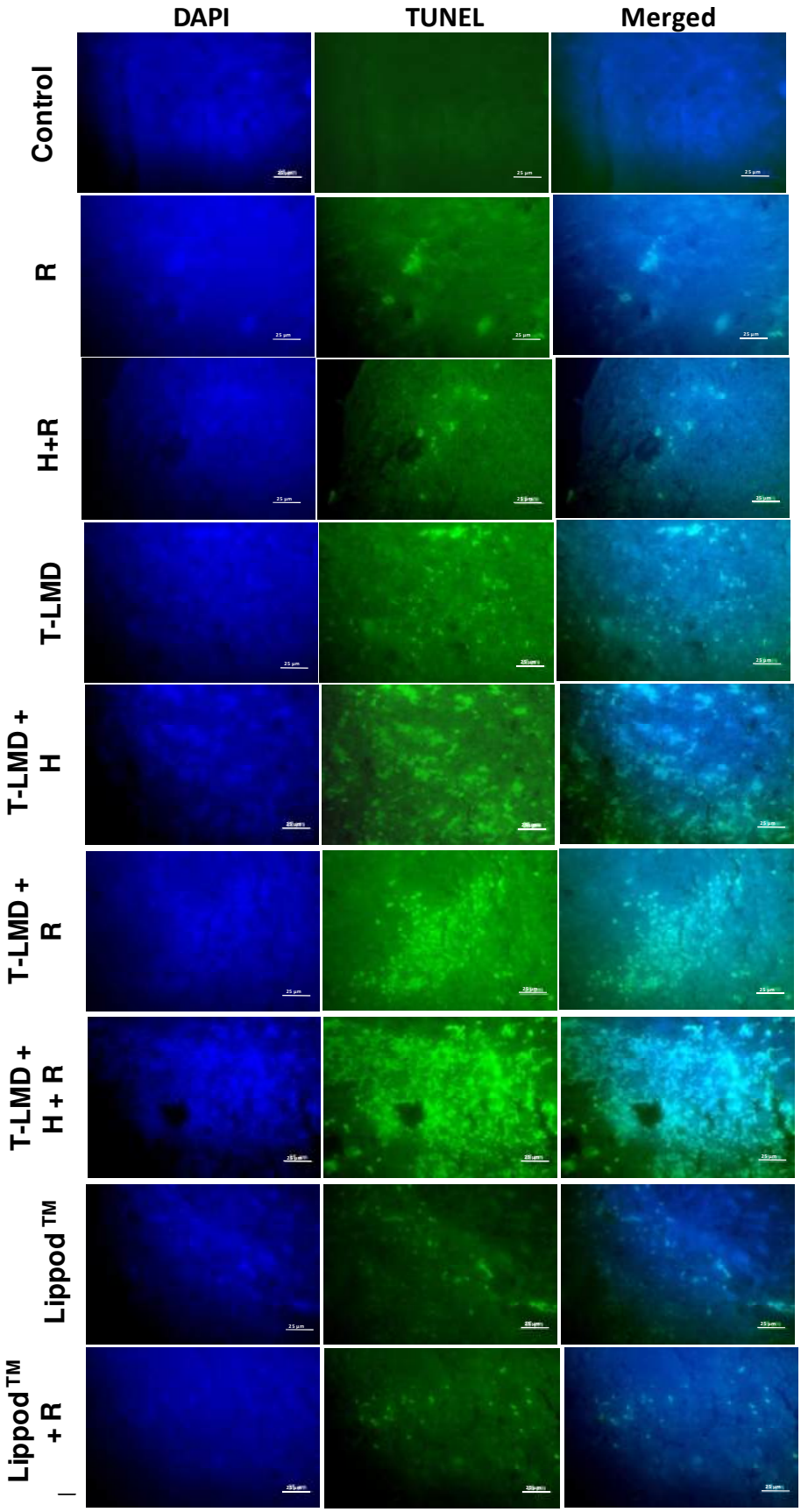
DAPI
TUNEL
Merged
Control
R
H+R
T-LMD
T-LMD + H
T-LMD + R
T-LMD + H + R
Lippod TM
Lippod TM + R

B.

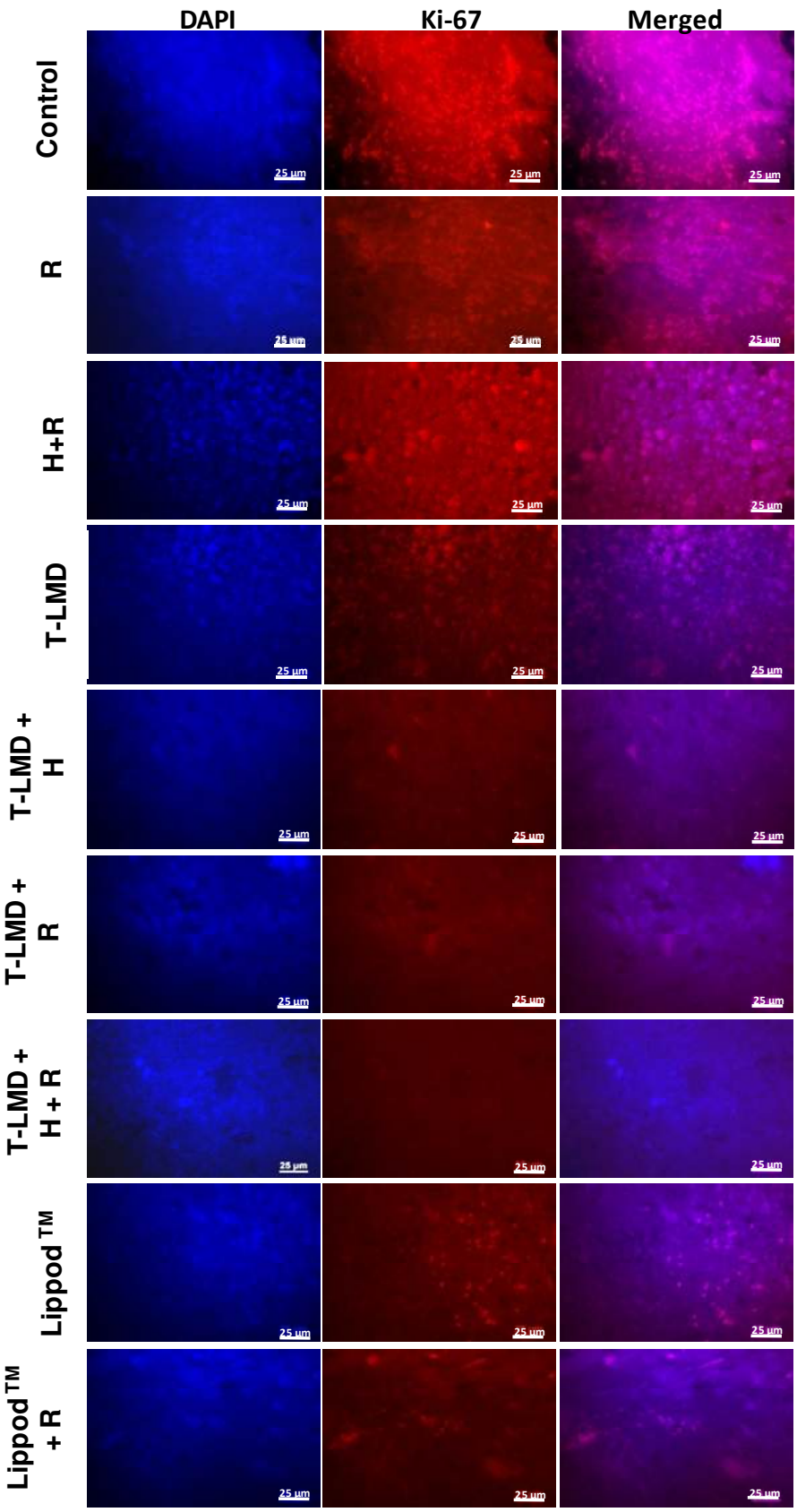
DAPI
Ki-67
Merged
Control
R
H+R
T-LMD
T-LMD + H
T-LMD + R
T-LMD + H + R
Lippod TM
Lippod TM + R
25 µm

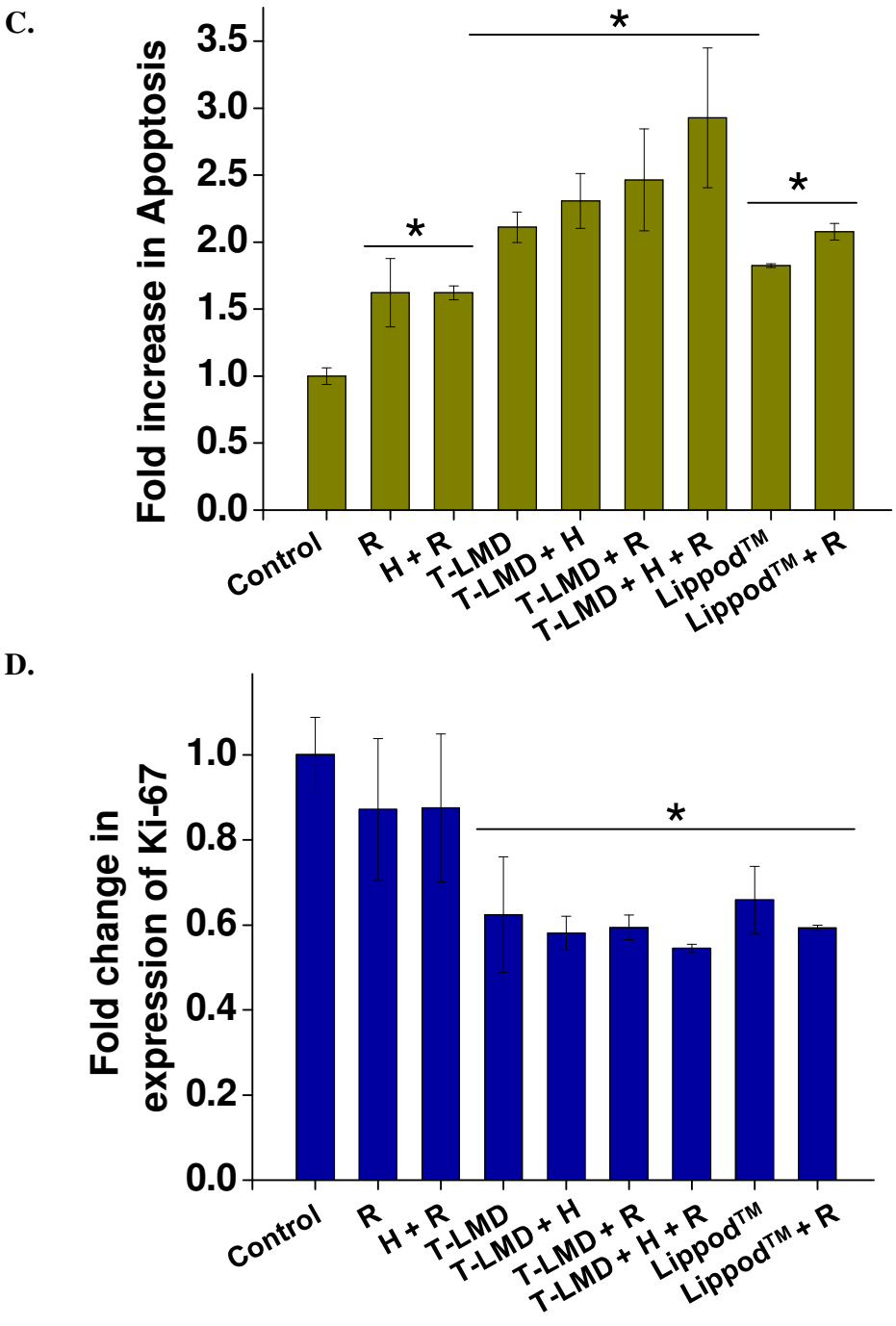

Fig. 3.3.8 *Representative fluorescence microscopy images of tumor of mice subjected to indicated treatments for* ***(A)*** *TUNEL analysis and expression of* ***(B)*** *Ki-67 (proliferation marker),* ***(C)*** *Fold increase in apoptosis in tumor sections of mice subjected to indicated*

treatments and ***(D)*** *Fold change in expression of Ki-67 in tumor sections of mice subjected to indicated treatments. Scale bar : 25 µm.* Significant at P<0.05 as compared to control.*

3.3.7 PRUSSIAN BLUE STAINING CONFIRMED ACCUMULATION OF FE IN TUMORS TREATED WITH T-LMD

Bio-distribution studies using live animal imaging system suggested significant accumulation of T-LMD in tumor region, as visible from the signal of ICG **(Fig. 3.3.3)**. Other organs, viz. kidney, liver and spleen also showed some signal for ICG. To validate that the ICG signal is due to the accumulation of T-LMD and not released or leaked ICG, I carried out Prussian blue staining of sections of tumor and organs (viz. liver, kidney, spleen, lungs and heart), to detect the presence of Fe (Fe is present in the MN-OA encapsulated in T-LMD). Results showed accumulation of Fe in tumor region as visible from the blue colored deposits in tumors treated with T-LMD but not in control **(Fig. 3.3.9)**. Other than tumor, liver, kidney and spleen of T-LMD treated mice also showed few blue colored deposits, suggesting lower accumulation of T-LMD in these organs as compared to tumor. Thus, these results validate the higher accumulation of T-LMD in tumors of treated mice.

A.

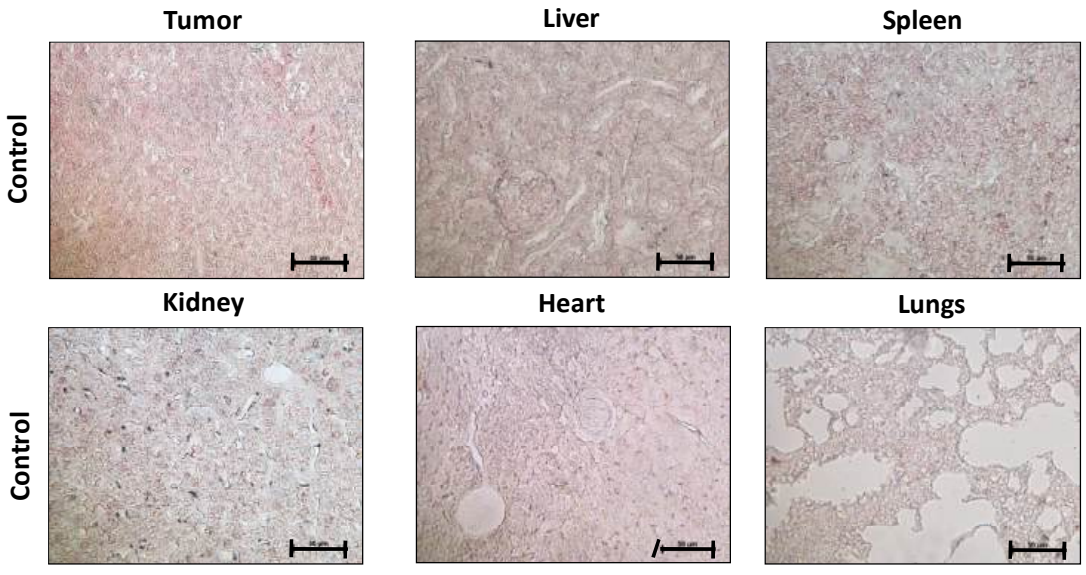

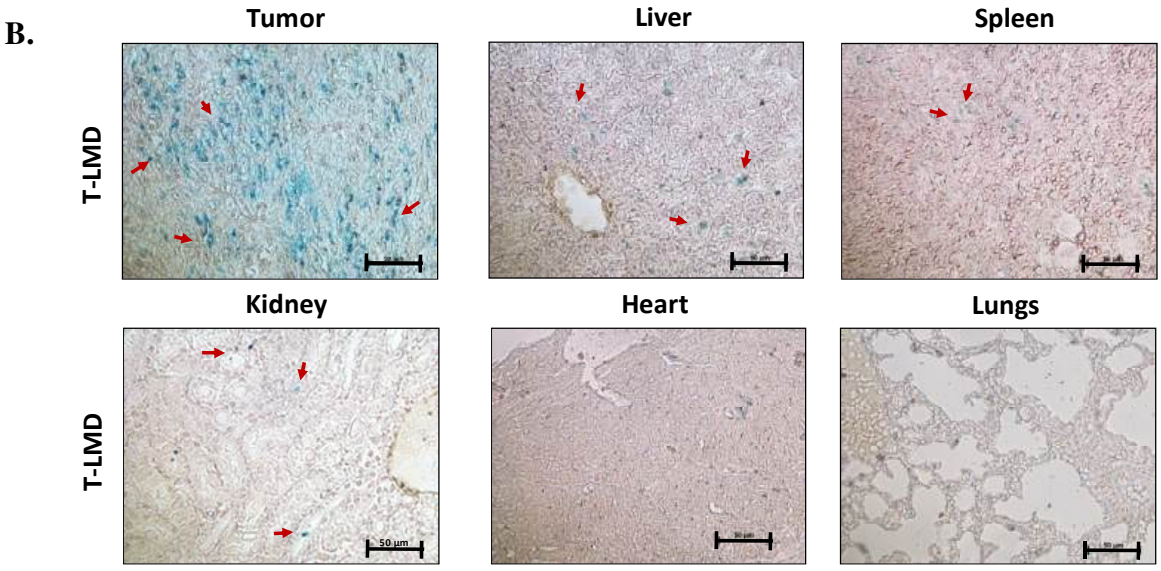

Fig. 3.3.9 *Representative bright field images for Prussian blue staining of tumor and different organs (viz. liver, spleen kidney, heart and lungs) of* ***(A)*** *Control (untreated) or* ***(B)*** *T-LMD treated fibrosarcoma tumor bearing mice. Scale bar = 50 µm. Red arrows indicate blue colored deposits of Fe.*

3.3.8 DETERMINATION OF TOXICOLOGICAL PARAMETERS AFTER TREATMENT WITH T-LMD

For clinical evaluation of any drug, its toxicological and pharmaco-kinetic parameters needs to be evaluated in a suitable animal model, preferably rodents. Hence, to further attest the clinical suitability of T-LMD, its thorough toxicological evaluation was performed in both, fibrosarcoma tumor bearing and healthy BALB/c mice without the tumor. In case of tumor bearing mice, serum or whole blood and tumor or organs samples were collected on day 8, post-administration of the nano-formulation after sacrifice of mice. The details of treatment of healthy mice and sample collection is provided in **Scheme 3.3.5**. The toxicological parameters included determination of serum biochemistry for indicators of organ toxicity [viz. serum alanine

transaminase (ALT), alkaline phosphatase (ALP) as markers of liver function, serum creatinine as marker of kidney function and serum glucose as marker of glucose metabolism]. Complete blood count was also determined to test the effect of treatment of T-LMD on whole blood parameters (viz. RBC, WBC and platelets counts, hemoglobin levels, etc.) **(Table 3.3.6)**. Additionally, tumor and organs were also collected after sacrifice of mice and histopathological studies were carried out to evaluate the presence of any patho-physiological changes (indicative of tissue toxicity) in the organs due to the treatments. Prussian blue staining of tumors and organs was carried out to determine the accumulation of Fe in these tissues and to corroborate the results of bio-distribution of T-LMD as determined by ICG fluorescence **(Fig. 3.3.3)**. Tumor histopathology was also carried out to validate the tumor inhibitory effect of T-LMD in terms of cellular changes such as presence of apoptotic or necrotic regions or to determine the mitotic index of the tumor cells (ratio of circular to spindle shaped cells). These parameters will further substantiate clinical potential of anti-tumor efficacy of the liposomal nano-formulation.

3.3.8.1 Serum biochemistry of fibrosarcoma bearing BALB/c mice subjected to T-LMD and Lippod^{TM} treatments

As discussed, for clinical translation of any nano-formulation, evaluation of its toxicological parameters is a pre-requisite. Therefore, I first evaluated the levels several serum parameters (indicative of the organ function or toxicity) in tumor bearing mice treated with T-LMD either alone or in combination therapy. Herein, Lippod^{TM} was used as a clinical formulation control. Blood samples were collected from various treatment groups (viz. T-LMD, T-LMD + H, T-LMD + R, T-LMD + H + R, H, R, Lippod^{TM}, Lippod^{TM} + R and untreated control) by heart puncture on day 8 post treatment, followed by isolation of serum and measurement of the serum levels of

various enzymes or markers for organ function using the automated serum biochemical analyzer (Rx Daytona +, Randox, USA). Results showed that animals treated with T-LMD, T-LMD + H, T-LMD + R, T-LMD + H + R, didn't show any significant difference in the serum levels of ALT, ALP, creatinine or glucose. Whereas, mice treated with Lippod™ or Lippod™ + R, showed a significant increase in the serum levels of ALT and ALP as compared to control (**Table 3.3.5**). However, creatinine levels were not found to change significantly after Lippod™ or Lippod™ + R treatments. Interestingly, levels of serum glucose were found to be slightly elevated in the Lippod™ + R group, which however needs further investigation.

	Control	H	R	T-LMD	T-LMD + H	T-LMD + R	T-LMD + H + R	Lippod™	Lippod™ + R
ALT (U/L)	41.1 ± 4.5	33.4 ± 3.9	38.07 ± 5.9	30.8 ± 3.12	35.6 ± 5.1	30.3 ± 4.6	43.4 ± 8.6	54.5 ± 3.8 *	55.2 ± 7.2 *
ALP (U/L)	60.9 ± 3.1	65.9 ± 4.2	56.3 ± 4.5	61.1 ± 6.9	64.01 ± 14.9	60.1 ± 7.9	45.6 ± 9.1	75.1 ± 7.08 *	86.45 ± 4.7 *
Creatinine (mg/dL)	0.52 ± 0.04	0.46 ± 0.09	0.41 ± 0.09	0.43 ± 0.07	0.44 ± 0.07	0.54 ± 0.09	0.48 ± 0.06	0.49 ± 0.09	0.53 ± 0.08
Glucose (mg/dL)	156.6 ± 15.3	165.1 ± 9.7	129.4 ± 2.2	165.01 ± 2.6	133.3 ± 9.8	142.8 ± 10.03	183 ± 18.7	175 ± 13.9	173.3 ± 34.1
Total protein (g/dL)	5.4 ± 0.3	5.3 ± 0.3	4.9 ± 0.3	5.3 ± 0.3	5.3 ± 0.2	5.07 ± 0.4	4.7 ± 0.3	5.3 ± 0.3	6.09 ± 0.05
Cholesterol (mg/dL)	92.9 ± 14.6	87.6 ± 5.1	79.9 ± 5.1	71.8 ± 7.3	83.3 ± 5.3	82.7 ± 4.8	82.4 ± 6.5	89.3 ± 8.8	120.4 ± 2.8

Table 3.3.5 *Serum levels of, ALT, ALP, Creatinine, glucose, total protein and cholesterol in fibrosarcoma tumor bearing BALB/c mice on day 8 after indicated treatments. Values are Mean ± SD (n=8). * Significant at P<0.05 as compared to control.*

3.3.8.2 T-LMD showed insignificant change in the whole blood parameters of fibrosarcoma tumor bearing BALB/c mice

The effect of T-LMD on whole blood parameters was also studied by complete blood count using automated blood analyzer (Randox, UK). In case of whole blood analysis, T-LMD didn't show a significant difference in the level of various parameters as compared to control **(Table 3.3.6)**. These results indicate that T-LMD treatment doesn't affect the blood biochemistry of the mice and has insignificant toxicity in tumor bearing BALB/c mice in terms of organ toxicity markers.

	Control		T-LMD	
	Average	SD	Average	SD
WBC (x10³/µl)	5.6	0.3	5.2	1.1
RBC(x10⁶/µl)	7.1	0.8	6.8	0.2
HGB (g/dL)	9.2	1.1	9.05	0.3
MCV (fL)	64.5	1.02	63.7	2.1
MCH (pg)	12.8	0.1	13.2	0.08
MCHC (g/dL)	19.9	0.3	20.7	0.6
RDW (%)	12.6	0.9	13.6	0.6
HDW (g/dL)	1.1	0.3	1.3	0.07
Platelet (x10³/µg)	703.5	237.1	690.7	242.7
% Neutrophiles	43.4	1.06	43.4	4.4
% Lymphocytes	47.8	0.3	46.3	2.5
% Monocytes	1.9	1.05	2.6	1.1
% Eosinophiles	1.7	1.8	2.4	1.1
% Basophiles	1.1	0.2	1.02	0.3
% LUC	4.1	1.3	4.1	1.2

Table 3.3.6 *Whole blood parameters for fibrosarcoma tumor bearing mice at day 8 post treatment with T-LMD.*

3.3.8.3 Histopathological analysis validated the in-significant organ toxicity of T-LMD

To evaluate the effect of T-LMD or Lippod^{TM} treatments on the organ toxicity; heamtoxylin and eosin (H & E) staining of organs of treated tumor bearing mice was carried out **(Chapter 2, Section 2.28)**. Results showed no visible histopathological changes in the organs of BALB/c mice of different treatment groups (viz. R, H, H + R, T-LMD, T-LMD + H, T-LMD + R, T-LMD + H + R, Lippod^{TM} and Lippod^{TM} + R) as compared to control **(Fig. 3.3.10 and Table 3.3.7)**. Whereas, H&E staining of tumor tissue showed presence of increased necrotic regions (N), in tumors treated with Lippod^{TM} ± R or T-LMD ± H or T-LMD ± R and combination treatments as compared to control or R or H or R+H treatment groups **(Table 3.3.7)**. The histopathological analysis was performed by a trained pathologist as mentioned in **Chapter 2, section 2.28**. These results further validate the in-significant organ toxicity of T-LMD.

	Spleen hyperplasia	Tumor			
		Necrosis	Neoplastic cells	Mitotic figures	Neo-vasculature
Control	+	+	++	1-2/5hpf	++
R (2+2+2 Gy)	++	+	++	1-2/5hpf	+
H	+	+	++	1-2/5hpf	+
H+R	++	+	++	1-2/5hpf	+
T-LMD	+	++	+	Nil	+
T-LMD + R	+	+++	++	Nil	+
T-LMD + H	+	++	+	Nil	+
T-LMD + H + R	+	++++	+	1-2/5hpf	+
Lippod™	+	++	++	1-2/5hpf	+
Lippod™ + R	+	++	++	Nil	+

Table 3.3.7 *Histopathological features of tumor and different organ sections after indicated treatments as determined by H & E staining. (hpf: high power fields). Severity of the observed histopathological lesions are graded as +, ++, +++ and ++++ indicating mild (1 - 25 %), moderate (26 - 50 %), moderately severe (51 - 75 %) and severe (76 - 100 %) histopathological changes.*

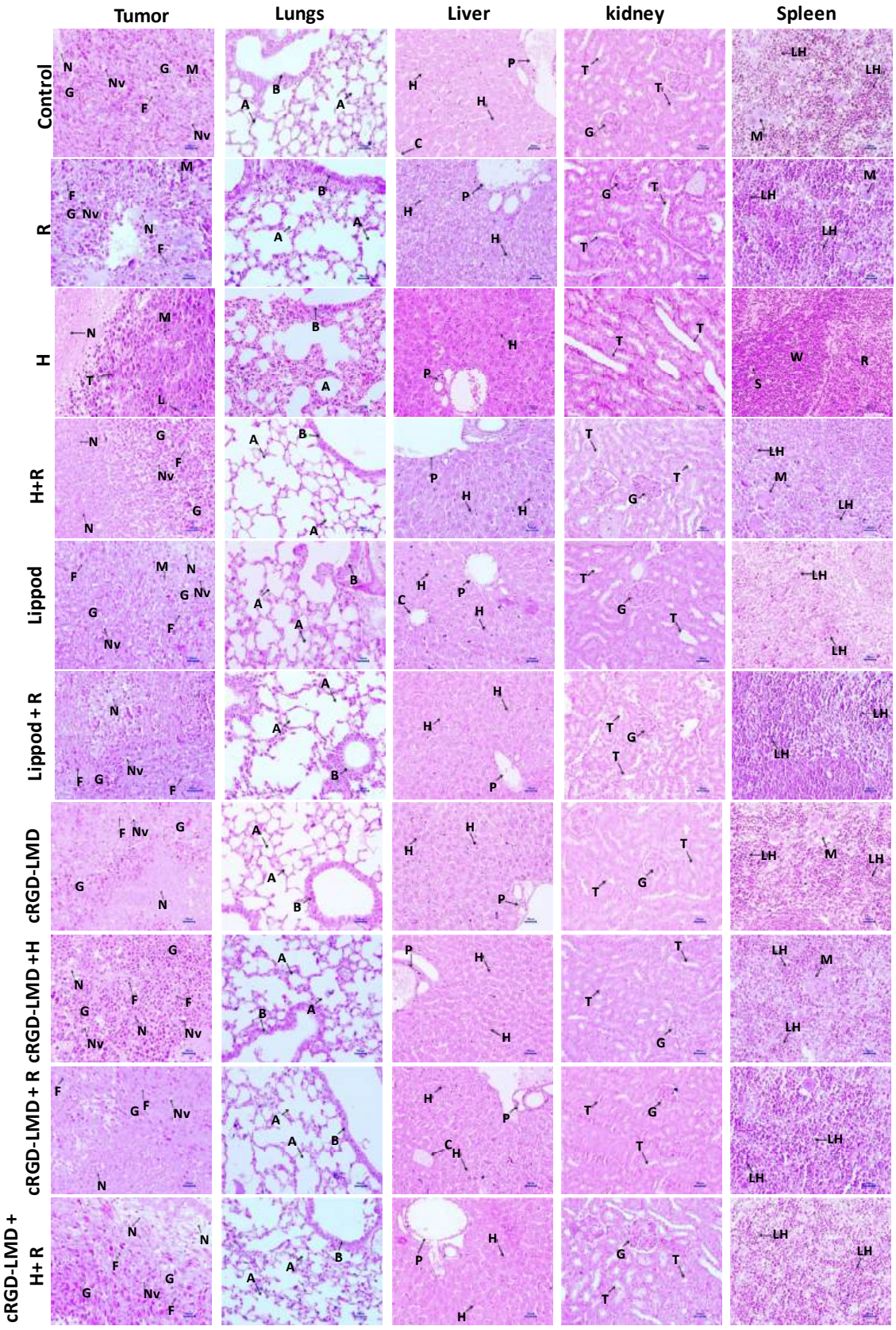
Tumor
Lungs
Liver
kidney
Spleen
Control
R
H
H+R
Lippod
Lippod + R
cRGD-LMD
cRGD-LMD +H
cRGD-LMD + R
cRGD-LMD + H+ R

Fig. 3.3.10 *Representative bright field images of tumor and different organs (viz. liver, kidney, lungs and spleen) of fibrosarcoma tumor bearing mice subjected to indicated treatments. Scale bar : 20 μm. [Liver : portal triad (P), hepatocyte (H), central vein (C); Lungs : alveoli (A), Bronchi (B), Spleen : lymphoid hyperplasia (LH) and megakaryocytosis (M), white pulp (W), red pulp (R), splenic artery (S), Kidney : glomeruli (G), tubules (T) and Tumor : nodular neoplastic growth (G), necrosis (N), neovascularization (Nv), fibrous tissue and collagen deposition (F) and mitoses (M)].*

3.3.9 T-LMD WAS FOUND TO HAVE IN-SIGNIFICANT TOXICITY IN HEALTHY BALB/C MICE

T-LMD was found to have no significant effect on the organ function in tumor bearing BALB/c mice. However, according to Drug Controller General of India (DCGI) and guidelines provided by Central Drugs Standard Control Organization (CDSCO) for 'Evaluation of Nano-pharmaceuticals in India', published in October 2019, testing of toxicity and serum toxicological parameters in healthy rodents is mandatory for consideration of any nano-formulation for clinical application. Therefore, I also studied the toxicological parameters in healthy BALB/c mice. Herein as well, Lippod^{TM} was used as a clinical nano-formulation for comparison. In addition, I also used free drug control [i.e. Dox at equivalent concentration (3 mg/Kg) and high concentrations (20 mg/kg : well reported in literature to be toxic) for comparing the organ toxicity of T-LMD]. The effect of T-LMD on serum biochemistry and whole blood parameters of healthy BALB/c mice was also evaluated using automated systems as discussed in **Section 3.3.8.1- 3.3.8.2**.

3.3.9.1 T-LMD showed in-significant change in the serum parameters as compared to untreated control

To determine the toxicological parameters, T-LMD, Lippod^{TM} and free doxorubicin were injected intravenously in two doses of 150 µl each (with an interval of 6 h) corresponding to a total dose of 3 mg/Kg equivalent concentration of Dox. On day 4 post drug administration, the mice were sacrificed and blood samples were collected by heart puncture **(Scheme 3.3.5)**. Out of 8 mice, 3 mice were used for serum biochemistry analysis, 3 mice for whole blood analysis and rest 2 mice for histopathological studies. Results showed no significant change in the levels of ALT, ALP, creatinine and glucose between control and T-LMD treatment groups. However, in case of mice treated with Lippod^{TM} (3 mg/Kg) and Dox (20 mg/Kg), 1.4 and 1.8 fold increase in the levels of serum ALT was observed **(Table 3.3.8)**. The effect of Lippod^{TM} is consistent with the results observed in tumor bearing BALB/c mice **(Table 3.3.5)**. However, levels of other parameters, namely, serum ALP, creatinine and glucose were not found to change significantly between control and other treatment groups. Since, Dox is well reported in literature to induce cardiac damage, the levels of creatinine Kinase MB (CK-MB), an early serum marker of cardiac damage was also evaluated in different treatment groups. Results showed no significant change in the serum levels of CK-MB between control and T-LMD treatment group. However, in case of Lippod^{TM} (3 mg/kg) and Dox (20 mg/Kg) treatments, 1.5 and 1.9 fold increase in serum CK-MB levels was observed **(Fig. 3.3.11)**. Interestingly, Dox at 3 mg/kg did not induce increase in the levels of CK-MB, which however, needs further investigation. Possible explanation could be related to the plasma clearance time of free Dox and Lippod^{TM}, which is higher for Lippod^{TM} (~ 62 fold slower elimination from blood as compared to free Dox), thus enabling it to stay in circulation for longer times and hence, probably contributed to the observed cardio-toxicity.

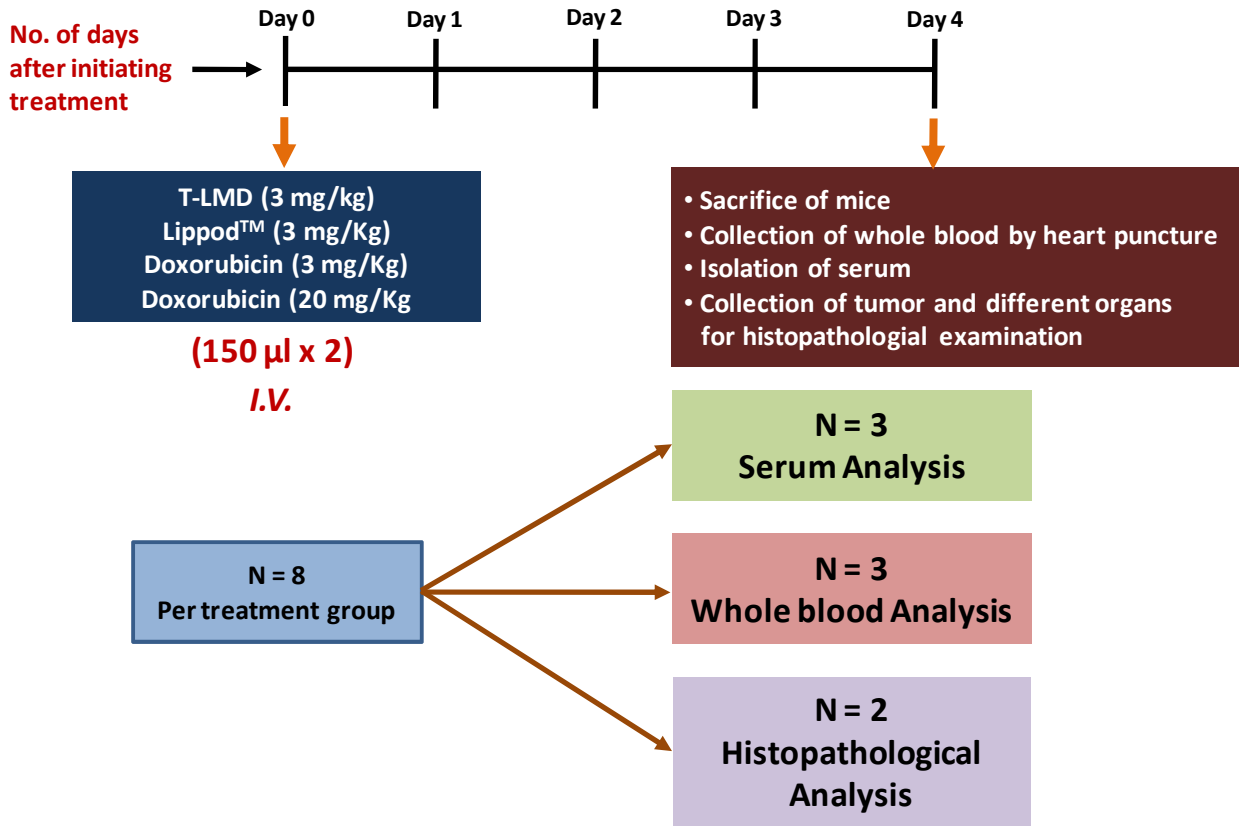

Scheme 3.3.5 *Scheme for treatment of healthy BALB/c mice with indicated treatments via intra-venous route followed by sample collection for evaluation of toxicological parameters.*

	ALT (U/L)	ALP (U/L)	Creatinine (mg/dL)	Glucose (mg/dL)
Control	34.5 ± 0.9	133.0 ± 5.1	0.45 ± 0.06	162.2 ± 9.7
T-LMD (3 mg/Kg)	35.6 ± 1.8	120.9 ± 1.8	0.48 ± 0.05	156.1 ± 6.5
Lippod™ (3 mg/Kg)	48.9 ± 2.5	139.7 ± 3.8	0.43 ± 0.12	157.2 ± 5.6
Dox (3 mg/Kg)	37.5 ± 8.2	139.4 ± 5.9	0.39 ± 0.1	150.2 ± 5.1
Dox (20 mg/Kg)	67.2 ± 0.5	108.9 ± 7.1	0.55 ± 0.1	155.5 ± 1.4

Table 3.3.8 *Serum levels of Creatinine, ALT, ALP and glucose in healthy BALB/c mice on day 4 after indicated treatments. Values are Mean ± SD (n=4). * significant at P<0.05 as compared to control.*

A.

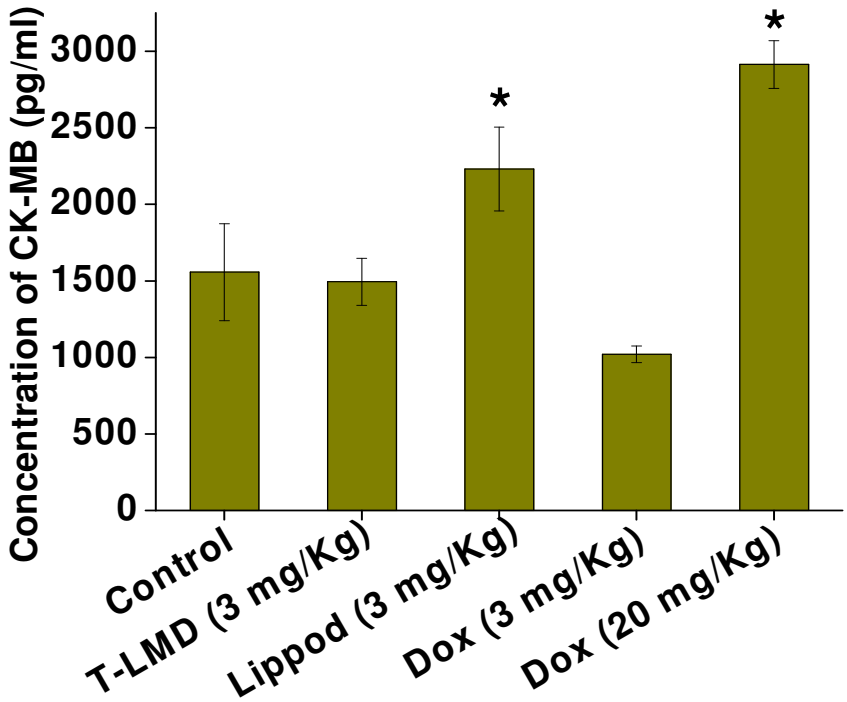

B.

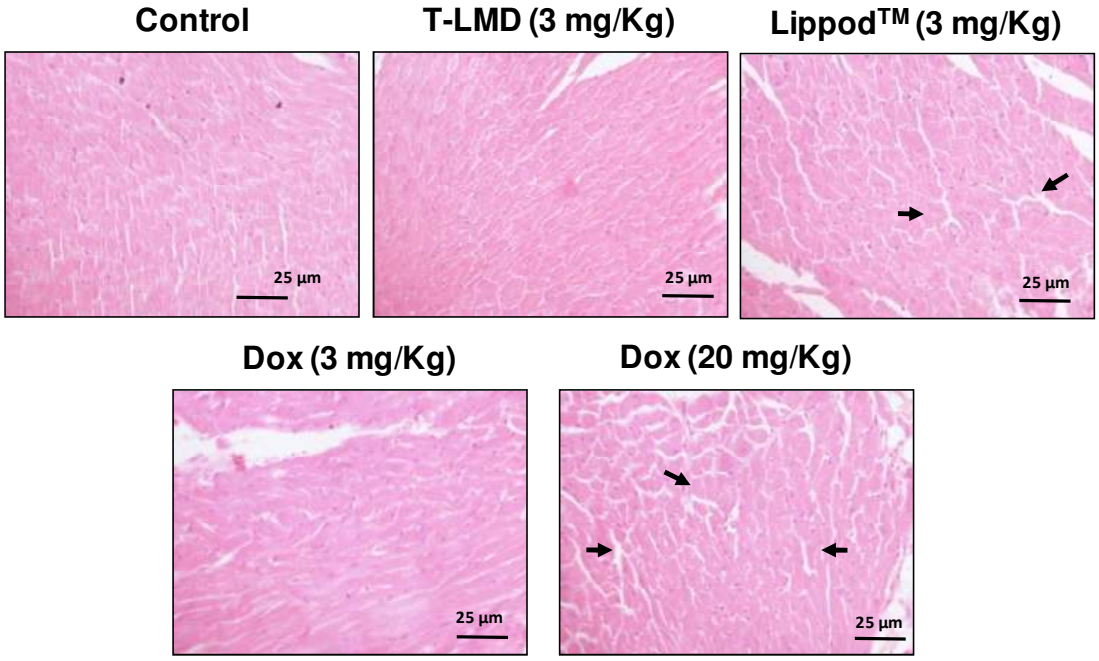

Fig. 3.3.11 ***(A)*** *Serum levels of CK-MB in healthy BALB/c mice on day 4 after indicated treatments. Values are Mean ± SD (n=4). * Significant at P<0.05 as compared to control.* ***(B)*** *Representative bright field microscopy images of heart tissue sections stained with H & E. Scale bar = 25 µm.*

3.3.9.2 T-LMD did not show significant change in the whole blood parameters as compared to free Dox

As discussed in **Section 3.3.9**, as per the recommendation of DCGI and guidelines laid by CDSCO, complete blood count parameters are also required to be studied in healthy rodents as one of the criteria for attesting the candidacy of any nano-formulation to be evaluated for clinical trials. Therefore, whole blood parameters were also studied for BALB/c mice after various treatments [viz. T-LMD (3 mg/Kg equivalent concentration of Dox), Lippod™ (3 mg/Kg equivalent concentration of Dox), Dox (3 mg/Kg) and Dox (20 mg/Kg)]. The whole blood was

collected by heart puncture in a vial containing EDTA solution (0.2 %) on day 4, using automated whole blood analyzer (Randox, UK) **(Scheme 3.3.5)**. Results showed no significant change in the blood parameters between the control, T-LMD and Lippod^{TM} treatment groups **(Table 3.3.9)**. However, in case of free Dox a dose dependent decrease in WBC count was observed **(Fig. 3.3.12)**.

	Control	T-LMD (3 mg/Kg)	Lippod™ (3 mg/Kg)	Dox (3 mg/Kg)	Dox (20 mg/Kg)
WBC	5.6 ± 0.39	5.51 ± 1.78	5.03 ± 0.85	4.13 ± 1.14	2.66 ± 0.34
RBC	8.05 ± 0.36	8.39 ± 0.14	8.44 ± 0.71	8.445 ± 0.4	8.61 ± 0.26
HGB	11.8 ±1.65	11.5 ± 0.14	11.3 ± 0084	11.2 ± 0.7	11.3 ± 0.3
HCT	37.8 ± 1.12	41.7 ± 0.14	40.05 ± 2.75	39.9 ± 2.68	38.9 ± 1.21
MCV	47 ± 1.43	49.7 ± 0.70	47.45 ± 0.63	47.25 ± 0.91	45.16 ± 0.4
MCH	13.76 ± 0.25	13.7 ±0.42	13.4 ± 0.14	13.25 ± 0.21	13.1 ± 0.26
MCHC	28.43 ± 0.55	27.5 ±0.42	28.3 ± 0.14	28.1 ± 0.14	29.06 ± 0.86
CHCM	29.56 ± 0.30	29.1 ±0.28	30.55 ± 0.21	30.8 ± 0.42	31.93 ± 0.25
CH	14.33 ± 0.15	14.45 ± 0.07	14.5 ± 0.14	14.55 ± 0.07	14.46 ± 0. 05
RDW	13.3 ± 0.1	13.05 ± 0.21	12.65 ± 0.21	12.75 ± 0.21	13.03 ± 0.66
HDW	2.07 ± 0.07	1.995 ± 0.26	1.875 ± 0.007	2.09 ± 0.12	1.90 ± 0.06
Platelets	639.66 ± 106.45	716.5 ± 113.84	675 ± 107.48	668 ± 33.94	660.66 ± 141.98
% Neutrophiles	14.93 ± 1.49	14.35 ± 0.21	14.5 ± 2.12	13.05 ± 2.47	20 ± 6.23
% Lymphocytes	79.43 ± 3.87	79.4 ± 1.27	76.85 ±	78.9 ± 2.68	72.5 ± 9.97
% Monocytes	1.7 ± 0.78	0.75 ± 0.07	1.6 ± 0.42	1.25 ± 0.07	0.7 ± 0.34
% Eosinophiles	3.16 ± 1.50	4 ± 1.13	4.9 ± 0.7	5.35 ± 1.2	5.53 ± 3.75
% Basophiles	0.46 ± 0.20	0.85 ± 0.35	0.95 ± 0.49	0.65 ± 0.49	0.46 ± 0.23
% LUC	0.33 ± 0.05	0.6 ± 0.42	1.2 ± 0.84	0.75 ± 0.35	0.8 ± 0.2

Table 3.3.9 *Whole blood parameters for healthy BALB/c mice on day 4 after indicated treatments*

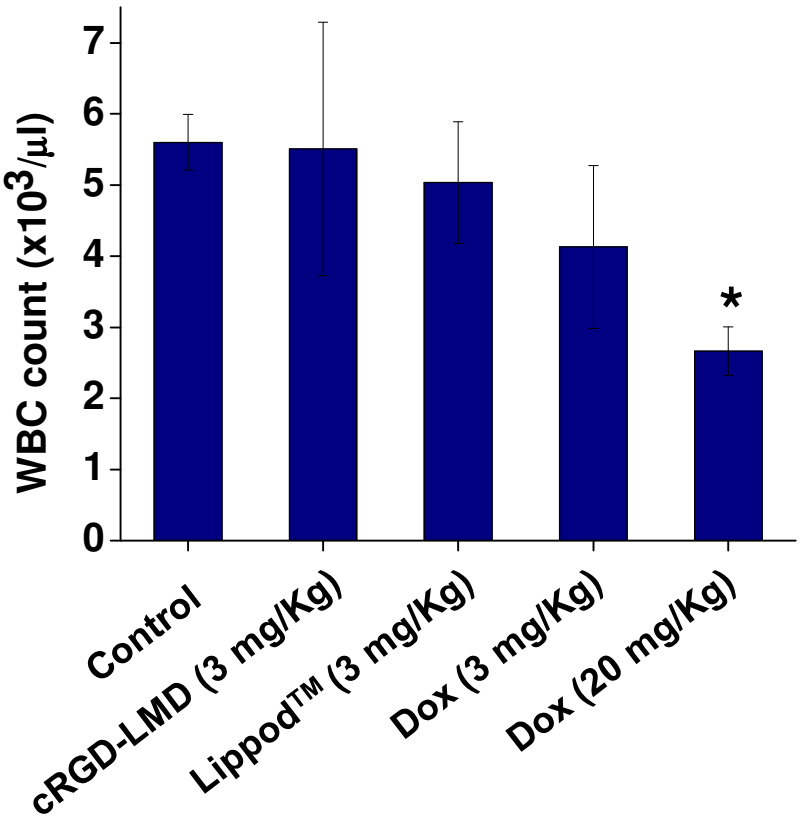

Fig. 3.3.12 *WBC count in healthy BALB/c mice on day 4 after indicated treatments. Values represent Mean ± SD (N = 4). * Significantly different at P<0.05 as compared to control.*

3.3.9.3 Histopathological studies validated the in-significant organ toxicity of T-LMD

To validate the results of serum analysis for organ toxicity, histopathological studies were carried out on different organs by H & E staining of the tissue sections. Results showed no visible histopathological changes in the all the organs of treated mice (all treatment groups), as compared to control except for liver. Histopathological analysis of liver tissue treated with Lippod^{TM} and Dox (20 mg/Kg) showed mild and moderate increase in sinusoidal spaces, suggestive of liver toxicity **(Fig. 3.3.13)**. These results further validate the elevated levels of liver toxicity marker (ALT) in these treatment groups **(Table 3.3.8)**.

A (i)

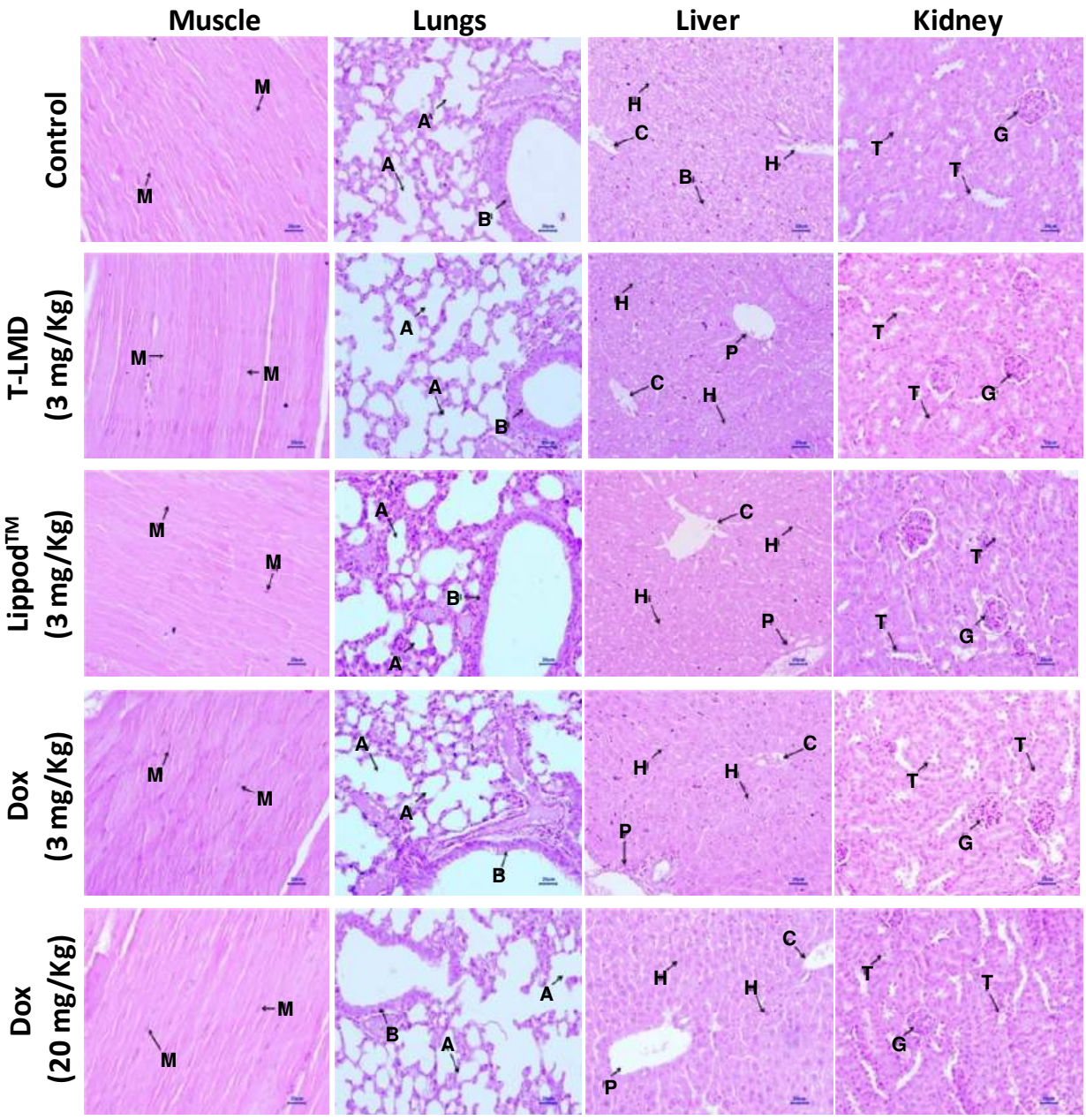
Muscle
Lungs
Liver
Kidney
Control
T-LMD (3 mg/Kg)
Lippod™ (3 mg/Kg)
Dox (3 mg/Kg)
Dox (20 mg/Kg)
M
A
B
H
C
P
T
G

A (ii)

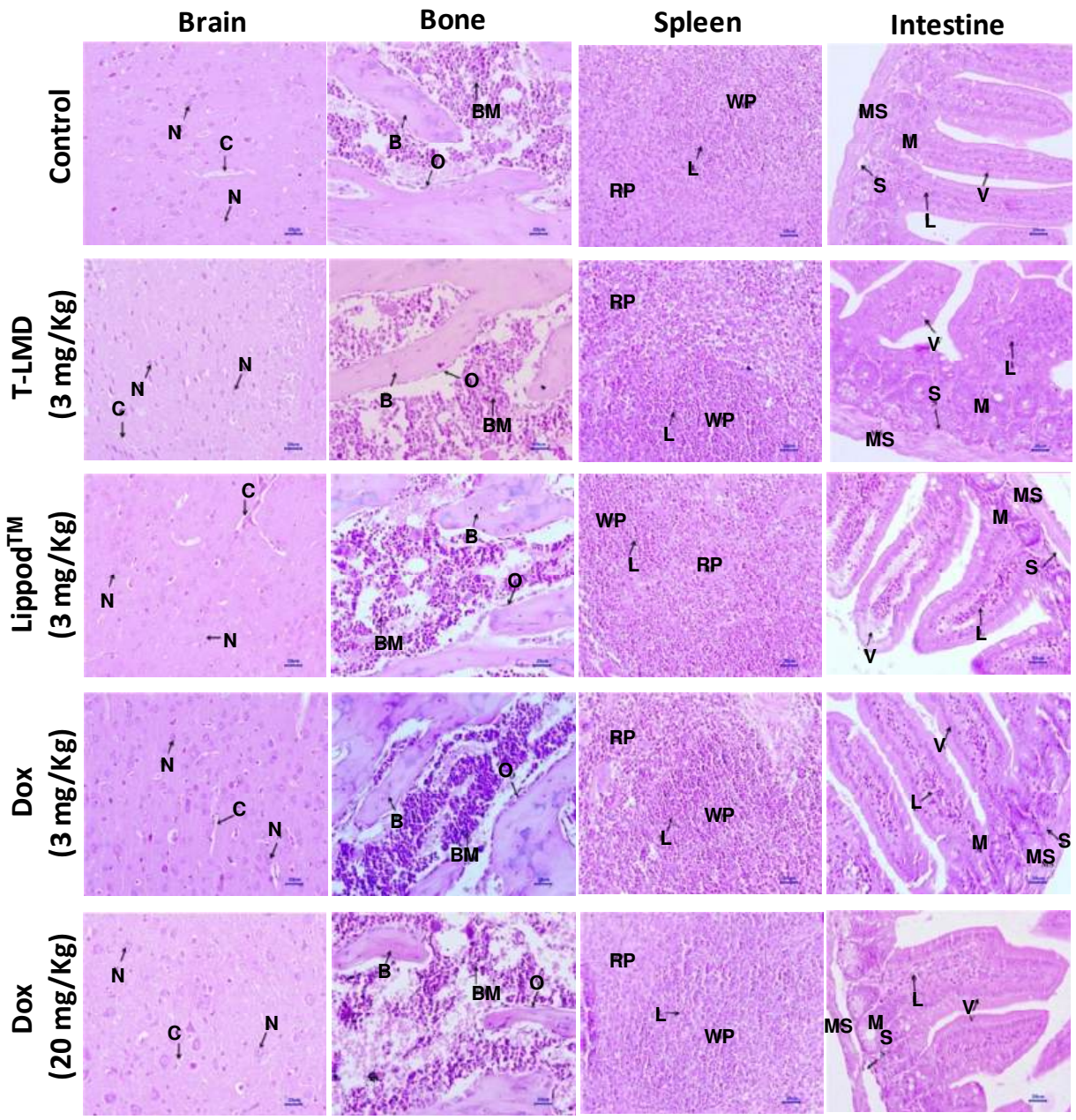

Fig. 3.3.13 *(A) Representative bright field microscopy images of different organs stained with H&E [viz.* ***(i)*** *muscle, lungs, liver, kidney and* ***(ii)*** *brain, bone, spleen and intestine] of healthy BALB/c mice subjected to indicated treatments. Scale bar : 20 µm. [Liver : portal trial (P),*

hepatocyte (H), central vein (C); Lungs : alveoli (A), Bronchi (B), Spleen : lymphoid hyperplasia (LH) and megakaryocytosis (M), Kidney : glomeruli (G), tubules (T), Bone: spongy bone (B), marrow cells (BM), osteoblasts (O), Brain : neuronal cells (N), capillaries (C), Intestine: mucosal epithelium (M), villi (V), submucosa (S), muscularis (MS), lamina propria (L) and Muscle: myocyte (M)].

Summary:

PEG-Lipo-MN-Dox (liposomal nano-formulation without cRGD tagging) or T-LMD were labeled with ICG, near infrared dye and the bio-distribution of these nano-formulations was studied by fluorescence based liver animal imaging in real-time. ICG-T-LMD showed significantly higher (4.5 fold) fluorescence signal in the tumor region as compared to the non-targeted nano-formulation (ICG-PEG-Lipo-MN-Dox). Moreover, other organs (viz. heart, lungs, liver, kidneys, spleen and intestine) showed ~ 6 to 18 fold lower signal of ICG-T-LMD as compared to tumor. Histopathological analysis of organs of tumor bearing and healthy BALB/c mice administered with T-LMD by intra-venous route showed in-significant toxicity. These results were corroborated by analysis of serum markers of liver, kidney and cardio-toxicity, which were found to be similar to control mice, suggesting in-significant to no observable toxicity of T-LMD in mice. Whole blood analysis also confirmed the in-significant toxicity of T-LMD in mice in terms of haematological parameters. Overall, these findings demonstrate the potential of T-LMD to be developed into a pharmacological formulation for tumor targeting and combinatorial chemo- radio- and magnetic hyperthermia therapy agent for cancer.

CHAPTER 4

GENERAL DISCUSSION

GENERAL DISCUSSION

Considering the growing burden of the cancer in India and in the world[1], development of more effective cancer treatment strategies is the need of the hour. Current cancer treatment options (viz. chemo-, radio- and hyperthermia therapy) mainly suffer from the limitations of dose limiting toxicities to normal tissue due to their non-targeted or non-tumor specific nature[2,4]. Secondly, most of the chemo-therapeutic drugs have poor solubility, in-efficient tumor targeting and often suffer the limitation of chemo-resistance. Similarly radio-resistance and thermo-tolerance have been found to hamper the clinical success of radio- and hyperthermia therapies[2-4]. Thus, in order to minimize the side effects of conventional therapies and to attain better therapeutic efficacy, development of tumor specific and more effective anti-cancer strategies has become indispensable.

With the advent of nanotechnology, nanomaterials with radio-sensitizing capabilities (such as gold and iron oxide nanoparticles) have been explored for drug delivery and anti-cancer applications. Amongst these, super-paramagnetic iron oxide nanoparticles (SPIONs) have been found to be most suitable for anti-cancer applications[10]. This is attributed to their super-paramagnetic behavior, high surface area-to-volume ratio and amenability to be conjugated with different functional groups. Liposomes are another class of nanoparticle system and have been extensively utilized clinically for targeted delivery of chemotherapeutic drugs to the tumor site. However, the clinically approved liposomal formulations of Dox (viz. Myocet®, Doxil®, lipo-Dox®, etc) did not show significantly higher anti-tumor efficacy than free Dox; albeit the cardio-toxicity associated with free Dox was substantially reduced by liposomal Dox. Moreover, their efficacy was further limited due to their toxicities (hand and foot syndrome and stomatitis) and

non-targeted nature[275]. On the contrary, most of the SPIONs-based nano-formulations, currently in clinical use are approved for imaging applications (as a MRI contrast agent)[9]. Moreover, very few reports in literature demonstrate the radio-sensitizing and magnetic hyperthermia potential of SPIONs based nano-formulations. Soleymani et al, recently reported the magnetic hyperthermia efficacy of hyaluronic acid coated Fe3O4 nanoparticles (Fe3O4@HA) in breast cancer cells (MDAMB-231). Fe3O4@HA showed preferential targeting and significant killing of MDAMB-231 cells by heating under *AC* magnetic field[279]. Similarly, Kandasamy et al, in a recent report demonstrated the excellent magnetic hyperthermia based anti-cancer efficacy of 3,4-Diaminobenzoinc acid (DABA) coated SPIONs[280]. The radio-sensitizing potential of SPIONs has also been reported and is conjectured principally, due to their high surface-to-volume ratio, which may act as a catalyst for generation of reactive oxygen species (ROS) by involvement of Fe^{2+} in the Fenton's reaction[263,281-282]. However, most of these studies did not elucidate the mechanism by which the SPIONs enhance the cytotoxic effect of ionizing radiation or kill the cancer cells by heat generation under *AC* magnetic field. Moreover, most of these studies use non-targeted formulation of SPIONs and combine them with either chemo- or radio- or hyperthermia but not all three modalities of cancer therapy. Besides, validation of their anti-cancer efficacy in animal models and detailed mechanistic insights are lacking in the literature. Therefore, there is a need to develop better targeted nano-formulation which can be exploited for theranostic applications for cancer and to gain deeper mechanistic understanding by which these nano-formulation result in better therapeutic efficacy. These mechanistic insights may further facilitate the development of a better and efficient anti-cancer nano-formulation.

Thus, in the present thesis, I have synthesized, characterized and evaluated the anti-cancer efficacy of two SPIONs based nano-formulations (viz. MN-OA and T-LMD), using

suitable *in vitro* and *in vivo* models. Moreover, a deeper understanding of the mechanisms by which these nano-formulations exert their anti-cancer effect with identifications of key molecular players (HSP90 or JNK) has been accomplished. Firstly, I synthesized and characterized MN-OA (a non-targeted nano-formulation of SPIONs) and evaluated it's *in vitro* and *in vivo* magnetic hyperthermia (H) and radio-sensitization (2 Gy) efficacy. MN-OA + H showed ~ 5 fold enhanced killing of WEHI-164 cells as compared to ~ 2 fold by MN-OA alone **(Fig. 3.1.6)**. The mechanism of cell killing was observed to be mediated via modulation of HSP90/AKT signaling and induction of caspase-3 dependent apoptosis **(Fig. 3.1.7 & 3.1.10)**. Moreover, in combination with gamma radiation (2 Gy), the anti-cancer efficacy of MN-OA was found to be further enhanced by ~ 9 fold **(Fig. 3.1.11)**. Clonogenic cell survival analysis and linear-quadratic (LQ) fitting of the dose response curve, suggested contribution of potentially lethal damage in MN-OA + 2 Gy treatment (as evident from the increase in the α component) **(Fig. 3.1.11 C and Table 3.1.2)**. A dose enhancement factor (DEF) of 2.1 was observed which is much better than reported values of 1.08 to 1.4 for SPIONs as reported earlier (Esra, K. et al and Khoei, S. et al)[282-283]. Moreover, for the first time, we reported the induction of mitotic catastrophe (MC) by MN-OA and MN-OA + 2 Gy treatments **(Fig. 3.1.15)**. MC was preceded by G2-M arrest **(Fig. 3.1.12)** and resulted in late induction of apoptosis in treated cancer cells (at 96 and 144 h) as confirmed by annexinV/PI staining **(Fig. 3.1.13)**. On similar lines, a recent study by Rivera-Rodriguez, A. et al, reported the induction of MC in MCF-7 cells, but after co-treatment with paclitaxel and SPIONs mediated magnetic hyperthermia therapy[285]. One possible explanation for the MC induced by MN-OA could be its interaction with cellular HSP90 and inhibition of HSP90 client proteins playing important role in cell cycle progression (viz. BRCA1, Cyclin B1). These hypothesis is further corroborated by a similar observation by Zajac, M., et al, in various breast

cancer cells treated with HSP90 inhibitor (17-AAG). These cell lines showed cell death by MC in response to HSP90 inhibition and the MC was found to be induced in a BRCA1 dependent manner[286].

To further understand the mechanism of MN-OA induced radio-sensitization, I studied the effect of MN-OA ± 2 Gy treatment on the status of DNA double strand breaks (DSBs). Interestingly, MN-OA ± 2 Gy was found to induce significantly higher (~ 2 fold) DSBs as indicated by the increased γ-H2AX foci, which were found to be persistent in case of combination treatment (upto 96 h) **(Fig. 3.1.16)**. One of mechanisms of induction of enhanced DSBs by SPIONs is via generation of ROS, mainly catalyzed by Fenton's reaction and Haber-Weiss cycle at the surface of SPIONs, as reported by Voinov et al[263]. Therefore, I also measured the intracellular ROS levels using DCHFDA probe, which, however did not show significant enhancement in ROS in cells treated either with MN-OA (different doses) or combination treatment as against only radiation-treated cells. In fact, the level of ROS was lower in MN-OA + 2 Gy treated cells **(Fig. 3.1.16 C)**. One possible explanation could be the presence of dense oleic acid (OA) coating [29.03 x 10^6 OA molecules per SPION of average crystallite size of 10 nm, Jadhav et al[11]], which could have inhibited the ROS generation at the surface of MN-OA. Another probable mechanism for the observed MN-OA-induced radio-sensitization could be the impairment of DNA repair. Consistent to this, we observed significant down-regulation of DNA repair proteins (RAD51, BRCA1 and CHK1) **(Fig. 3.1.16 D)**. Incidentally, these are well established as client proteins of HSP90[264]. The levels of HSP90, however were found to be elevated in both MN-OA and MN-OA + 2 Gy **(Fig. 3.1.12 C & 3.1.20 A)**. These results suggested inhibition of HSP90 by MN-OA, which in turn triggers more synthesis of HSP90 by feedback mechanism[287]. This observation was corroborated by similar pattern of HSP90 up-

regulation but down-regulation of its client protein (AKT) by known HSP90 inhibitor (17-AAG) **(Fig. 3.1.7 B)**. Furthermore, to confirm the involvement of HSP90-centric mechanism in MN-OA induced radio-sensitization, I studied the radio-sensitizing potential of MN-OA in WEHI-164 transfectants with (~ 50 %) lower expression of HSP90 (SiRNA based knock-down). Results showed a further enhancement (~ 2 fold) in the MN-OA induced radio-sensitivity **(Fig. 3.1.17)**, thereby validating the role of HSP90 in the mechanism of radio-sensitization. Moreover, detection of MN-OA-bound proteins by Western blotting, suggested direct interaction of MN-OA with HSP90 (but not HSP70 or other HSP90-client proteins like RAD51 or CHK1), thus further supporting the HSP90 centric mechanism of action of MN-OA **(Fig. 3.1.16 E)**.

Although, MN-OA may be interacting with a range of proteins, the functional significance of HSP90 combined with its cellular abundance might be making it a plausible target of MN-OA[262,287]. HSP90 has been known to show specificity for proteins with hydrophobic residues scattered over a large surface area[262]. Thus, probably, MN-OA interacts with HSP90, mainly through hydrophobic interactions, owing to the hydrophobicity imparted by its oleic acid coat. It is important to mention that free oleic acid does not show significant cyto-toxicity in WEHI-164 cells, as reported earlier[11]. Thus, in addition to surface hydrophobicity, the specific arrangement of OA on the surface of MN-OA, its nano-size and spherical shape may also be contributing towards its interaction with HSP90. It would be further interesting to characterize the interaction forces involved in the binding of MN-OA to HSP90 using suitable biophysical approaches in future. Furthermore, MN-OA mediated HSP90 inhibition has significance in terms of a higher probability of positive clinical outcomes in magnetic hyperthermia therapy as compared to conventional hyperthermia therapy, wherein HSP90 induced thermo-tolerance has been known to seriously compromise the clinical success of the

latter. Animal experiments further validated the MN-OA induced radio-sensitization and its mechanism in *in vivo* model. The tumor growth delay index (2.1) was found to be similar to the DEF observed in *in vitro* studies **(Fig. 3.1.11 and 3.1.18)**. Similar to *in vitro* experiments, animal experiments also showed down-regulation of CHK1, CDC2 and Cyclin B1 in both MN-OA and combination treatment **(Fig. 3.1.20)** suggesting the contribution of cell cycle arrest and altered DNA damage response (DDR) in the observed anti-tumor effect. Histopathology and TUNEL staining confirmed the role of apoptosis induced by combination treatment **(Fig. 3.1.19)**. Thus, these results advocate the potential of MN-OA for combinatorial cancer therapy.

Although MN-OA showed significant *in vitro* and *in vivo* anti-cancer efficacy, its candidature for further pre-clinical testing was limited by its inability to actively target the cancer cells. Thus, to develop a targeted nano-formulation of MN-OA, it was encapsulated inside PEG-Liposomes, co-encapsulated with Dox and labeled with cRGD (T-LMD) for active targeting of tumor cells and tumor neo-vasculature. There are several reports in literature demonstrating the superior targeting and chemo-radiotherapy potential of cRGD labeled nano-particles[288-290]. However, to best of my knowledge, there are no reports in literature combining the targeting efficacy of cRGD with a liposomal nano-formulation of Dox and SPIONs (encapsulated in liposomal core and membrane, respectively). Thus, to synthesize this novel nano-formulation design, initially I synthesized and characterized the non-targeted liposomal nano-formulation [viz. PEG-liposomes co-encapsulated with MN-OA and Dox (PEG-Lipo-MN-Dox)]. PEG-Lipo-MN-Dox showed an average hydrodynamic size of 150 nm with a polydispersity index of 0.2 and a surface charge of -7.3 **(Fig. 3.2.2)**. TEM analysis showed presence of spherical structures with a peripheral distribution of high contrast aggregates, suggesting the encapsulation of MN-OA in the liposomal membrane **(Fig. 3.2.2 D)**. The presence of Fe in the high contrast aggregates

was confirmed by energy dispersive-X-ray fluorescence analysis **(Fig. 3.2.2 E)**. WEHI-164 cells treated with PEG-Lipo-MN-Dox, showed significant uptake of the nano-formulation as early as 30 min, with maximum uptake obtained at 24 h **(Fig. 3.2.4, 3.2.5 & 3.2.6)**. Sub-cellular distribution studies showed an early distribution of Dox signal in cytosol, which at later time points (24 h) was distributed to nucleus as well **(Fig. 3.2.6 B)**. TEM analysis of T-LMD treated WEHI-164 cells showed presence of high contrast aggregates in cytoplasm and inside vesicles, with significant morphological alterations (nuclear shrinkage, deformed mitochondria and presence of membrane bound electron dense vesicles) suggestive of autophagy dependent or apoptotic cell death **(Fig. 3.2.7 A & B)**. Further, for evaluation of anti-cancer efficacy of PEG-Lipo-MN-Dox, individual component controls were also synthesized and characterized to ensure the higher cyto-toxicity of dual loaded liposomes. Lippod^{TM} (a commercially available PEGylated nano-formulation of liposomal Dox), was used as a comparative control. Cell viability studies showed significant anti-cancer efficacy of PEG-Lipo-MN-Dox in WEHI-164 cells and was ~ 7 fold more effective in killing cancer cells as compared to Lippod^{TM} **(Fig. 3.2.3 A - D)**.

Further, for the development of tumor specific liposomal nano-formulation (T-LMD), the PEG-Lipo-MN-Dox was conjugated with cRGD peptide and the labeling was confirmed by HPLC and FT-IR **(Fig. 3.2.9)**. T-LMD showed a slight increase in hydrodynamic size to ~ 170 nm with a polydispersity index of 0.2 and surface charge of -21.3 mV **(Fig. 3.2.10** and **Table 3.2.3)**. Moreover, cryo-TEM analysis further confirmed the synthesis of shperical liposomes, predominantly uni-lamellar (~ 70 %), with an average bilayer thickness of 4.58 ± 0.9 nm and an average size of 166 ± 42 nm as compared to Lippod^{TM} (133 ± 37 nm) **(Fig. 3.2.10)**. More importantly, encapsulation of Dox was visible as high contrast lines inside the liposomal core,

whereas MN-OA was visible as high contrast aggregates predominantly near the periphery of spherical liposomes **(Fig. 3.2.10 C)**. T-LMD showed significantly higher uptake by receptor-mediated endocytosis (~ 40 %) in the specific receptor ($\alpha_v\beta_3$) over-expressing cell line (U373MG) **(Fig. 3.2.15 A & B)** as compared to WEHI-164 (~ 25 %) **(Fig. 3.2.13)**. The mechanism of uptake of T-LMD in WEHI-164 cells seems to involve non-receptor mediated mechanism, probably due to the lower expression of $\alpha_v\beta_3$ receptor **(Fig. 3.2.11)**, but needs further investigation. Cell cytotoxicity studies in six cancer cells lines (viz. WEHI-164, MCF-7, A549, WRL-68, U373MG and MDAMB-231) and one normal cell line (WI26VA44) showed significant anti-cancer efficacy of T-LMD pre-dominantly in the cancer cell lines **(Fig. 3.2.17)**. The highest IC50 of 207.7 nM was obtained in WI26VA4 (normal lung fibroblast). Whereas cancer cell lines showed a much lower IC50 as follows (in descending order): A549 (152.6 nM) > WRL68 (138.54 nM) > U373MG (116.21 nM) > MCF-7 (111.96 nM) > WEHI-16 (109.2 nM) > MDAMB-231 (99.9 nM) **(Table 3.2.4)**. The different IC50 values for these cell lines may be due to the differences in their inherent sensitivities to the chemotherapeutic agents (viz. Dox and MN-OA).

T-LMD as well, demonstrated significant radio-sensitizing efficacy in WEHI-164 cancer cells and was found to be mediated via induction of G2-M arrest at 24 h. Moreover, a time dependent increase in sub-G1 population **(Fig. 3.2.18 A & B)**, as well as a significant decrease in the clonogenic survival of cancer cells was observed **(Fig. 3.2.19)**. Similar to MN-OA, T-LMD also showed significant increase in γH2AX foci (~ 3 fold higher as compared to 2 Gy at 3 h) **(Fig. 3.2.21 A & B)**. However, unlike MN-OA, which showed peak intensity of γH2AX foci at 30 min. **(Fig. 3.1.16 A & B)**, T-LMD-induced γH2AX foci peaked at 3 h **(Fig. 3.2.21 A)**. This may be attributable to the enhanced DNA damage induced by combination of Dox and MN-OA.

The results are consistent with reports in literature that mention the DSBs inducing ability of Dox[291-292]. The mechanism by which Dox induces DSBs is also well established and is reported to be mediated via DNA intercalation, inhibition of toposiomerase II and generation of oxidative stress owing to its heterocyclic ring structure. The observation that T-LMD alone is able to induce substantial DSBs (2.5 fold as compared to 2 Gy at 3 h), further substantiates the DNA damaging efficacy of T-LMD. Probably, owing to the significantly higher DNA damage inflicted by T-LMD ± 2 Gy, the nano-formulation induces an early G2-M arrest (24 h) **(Fig. 3.2.18 A & B)** and cell death pre-dominantly by apoptosis **(Fig. 3.2.22 A-C)** as against MN-OA ± 2 Gy treatment, that showed late G2-M arrest (48 h) **(Fig. 3.1.12 A & B)** and late killing (at 96 and 144 h) of cells by mitotic catastrophe and apoptosis **(Fig. 3.1.13 & 3.1.15)**.

These results were further validated by the up-regulation of G2-M arrest proteins in T-LMD ± 2 Gy **(Fig. 3.2.22 C)**. Moreover, T-LMD ± 2 Gy showed induction of intrinsic apoptosis pathway via activation of JNK, down-regulation of BCL-2, Survivin, P-AKT, AKT and P-BAD and up-regulation of pro-apoptotic proteins (BAD, cleaved Cas-3 and PARP) **(Fig. 3.2.22 A - B)**. Increased expression of Beclin-1 and LC3B(II) was also observed, suggesting role of autophagy dependent cell death in T-LMD mediated radio-sensitization **(Fig. 3.2.24 D)**. However this observation needs further experimentation to determine the modulation of autophagic flux in combination with inhibitors (3-methly adenine, chloroquine or bafilomycin). Nonetheless, the activation of JNK is well reported to induce autophagy dependent cell death via phosphorylation of BCL2, thereby inhibiting its complexation with Beclin-1 (an important component of autophagosomes), but needs further experimental confirmation[293-294]. Interestingly, T-LMD ± 2 Gy showed increased expression of P-ATR, P-RAD51 and P-CHK1 **(Fig. 3.2.21 C)**, which are the major molecular players in the DDR signalling. It is pertinent to mention that an activation of

P-ATR is suggestive of induction of DSBs due to stalled replication forks[295-296]. This could be one of the possible explanations for the sudden and transient increase in the γH2AX foci at late time points (24 - 72 h) **(Fig. 3.2.21 A & B)**, probably due to aberrant entry of cells into mitosis following a mis-repair or presence of non-repairable DSBs.

Live animal imaging showed significant targeting of tumor by ICG-T-LMD with relatively lower accumulation in other organs **(Fig. 3.3.3 A - D)**. I would like to emphasize here, that T-LMD showed very low accumulation (~ 2 - 4 fold) in organs (viz. liver, kidney and spleen), which is primarily associated with the dose limiting toxicity and clinical success of many targeted or nano-targeted chemotherapeutic agents[297-298]. Although WEHI-164 cells showed lower expression of $\alpha_v\beta_3$ integrin receptor and modest uptake (~ 25 %) of T-LMD in WEHI-164 cells (*in vitro*), the substantially higher accumulation of the nano-formulation at the tumor site, suggests the contribution of tumor neo-vasculature in the uptake of T-LMD **(Fig. 3.3.3)**. Several reports in literature mention the ability of cRGD peptide for targeting of tumor neo-vasculature via the $\alpha_v\beta_3$ integrin receptor[214,290], however, it needs further experimentation using suitable human endothelial cell models or immuno-detection in tumor sections. Thus, these results advocate the superior targeting ability of T-LMD in fibrosarcoma tumor model and substantiates its suitability for further pre-clinical evaluation in other human xenograft models. Moreover, T-LMD showed significantly higher (~ 3 fold) anti-tumor efficacy as compared to Lippod^{TM} **(Fig. 3.3.6)** and was further enhanced when combined with radiation (~ 5 fold) **(Fig. 3.3.6)** or magnetic hyperthermia (~ 4 fold) **(Fig. 3.3.5)** or both (~ 7 fold) **(Fig. 3.3.7)**. The anti-tumor efficacy of T-LMD ± H ± R, was validated by the enhanced expression of TUNEL positive foci (~ 3 fold in T-LMD + H + R) and decreased expression of Ki-67 (~ 2 fold) in the tumor sections **(Fig. 3.3.8)**.

Toxicological evaluation showed in-significant toxicity of T-LMD in healthy mice as evident from the serum markers for liver function (ALT and ALP), kidney (creatinine) and heart (CK-MB) **(Fig. 3.3.11 & Table 3.3.8)**. It is pertinent to mention that Lippod^{TM} at equivalent concentration of Dox (3 mg/Kg), showed measurable cardio-toxicity as indicated by levels of CK-MB (1.5 fold higher than T-LMD or control) **(Fig. 3.3.11 A)** and H & E staining (loss of myofibrils) **(Fig. 3.3.11 B)**. In summary, these results demonstrate the significant tumor targeting and anti-tumor efficacy of T-LMD for combinatorial cancer therapy. Systematic determination of maximum tolerated dose alongwith evaluation of combinatorial cancer therapy efficacy in relevant tumor models is warranted to further establish the candidature of T-LMD as a targeted-combinatorial cancer therapy agent. Toxicological evaluations in suitable rodent models in a GLP lab as per DCGI guidelines also needs to be carried out to process the nano-formulation for further clinical evaluations. Moreover, thorough pharmaco-kinetic studies in tumor and non-tumor models to determine various parameters (such as area under the curve, distribution volumes, elimination times, etc.) are imperative for the translation of T-LMD into a pharmacological formulation. Overall, T-LMD shows tremendous potential to be developed into a pharmacological formulation for tumor targeting in combination with radiation and magnetic hyperthermia therapy.

CHAPTER 5

CONCLUSIONS AND FUTURE DIRECTIONS

Major Conclusions

Two types of SPIONs based nano-formulations, viz. MN-OA and T-LMD were synthesized and characterized by suitable techniques. MN-OA showed excellent radio-sensitizing and magnetic hyperthermia therapy efficacy both, in *in vitro* cultured cells and fibrosarcoma tumor model. The mechanism of MN-OA mediated enhanced cell killing in combination with or without gamma radiation and magnetic hyperthermia was elucidated. HSP90 was identified as a key molecular player in MN-OA mediated cell cyto-toxicity. Further, to improvise the efficacy of MN-OA and to make it tumor specific, T-LMD was designed, synthesized and characterized using suitable techniques. T-LMD showed cancer cell specificity in *in vitro* cell culture and showed interaction with its specific receptor, resulting in enhanced uptake by receptor mediated endocytosis. T-LMD showed significant killing of several cancer cell lines (six types) as compared to normal human lung fibroblasts and was found to be more effective than commercial formulation (Lippod^{TM}). T-LMD showed significant radio-sensitization and magnetic hyperthermia efficacy in cultured cells. It was found to involve the activation of JNK and down-stream activation of pro-apoptotic signalling to induce enhanced cell death. Interestingly, T-LMD was found to induce an enhanced induction of DSBs and their delayed repair as compared to only radiation treatment. T-LMD showed excellent tumor targeting efficacy in fibrosarcoma tumor model with minimum accumulation in other organs. Moreover, T-LMD showed enhanced efficacy for combinatorial chemo-, radio- and magnetic hyperthermia therapy, in fibrosarcoma tumor model as well and was found to significantly more effective than Lippod^{TM}. Evaluation of toxicological parameters using histopathological analysis of tumors and organs of both tumor bearing and healthy BALB/c mice suggested insignificant toxicity of T-LMD. Further, serum and whole blood analysis also suggested the negligible organ toxicity (especially cardio-toxicity) of T-LMD

in healthy mice as compared to Lippod^{TM} or free Dox. Thus, based in these results T-LMD was established as a targeted nano-formulation with potential for enhanced efficacy for tumor targeting and combinatorial chemo-, radiation and hyperthermia therapy of cancer.

Future Directions:

Based on *in vitro* and *in vivo* results, the present thesis opens many new arenas for basic and applied research.

- Mechanistic insights of HSP90 regulation in nano-formulation mediated radio-/thermo-sensitization needs to be established using suitable inhibitors and molecular docking studies.
- A clinical validation of modulation of HSP90 levels in cancer patients would facilitate exploring its prognostic value in hyperthermia therapy.
- Optimization of conditions for freeze-drying/re-constitution and stability parameters is warranted for long term storage/transportation of nano-formulation.
- A thorough evaluation of the toxicity and pharmacokinetics of T-LMD in healthy rodents/pre-clinical animals in GLP laboratory is warranted for its consideration for further clinical testing.
- Validation of anti-tumor efficacy of T-LMD in other human xenograft models is required for its further clinical safety/efficacy evaluation before clinical trials of the nano-formulation.

REFERENCES

OR

BIBLIOGRAPHY

REFERENCES/BIBLIOGRAPHY

1. Bray F, Ferlay J, Soerjomataram I, Siegel RL, Torre LA, Jemal A. Global cancer statistics 2018: GLOBOCAN estimates of incidence and mortality worldwide for 36 cancers in 185 countries. CA: A Cancer Journal for Clinicians. 2018;68(6):394–424.
2. Hosseinzadeh E, Banaee N, Nedaie HA. Cancer and Treatment Modalities. Current Cancer Therapy Reviews. 2017;13(1).
3. Habash RWY, Bansal R, Krewski D, Alhafid HT. Thermal therapy, Part 1: An introduction to thermal therapy. Vol. 34, Critical Reviews in Biomedical Engineering. 2006;34(6):459–89.
4. Dagogo-Jack I, Shaw AT. Tumour heterogeneity and resistance to cancer therapies. Vol. 15, Nature Reviews Clinical Oncology. 2018;15(2):81–94.
5. Xiao Y, Du J. Superparamagnetic nanoparticles for biomedical applications. Vol. 8, Journal of Materials Chemistry B. 2020;8:354–67.
6. Neuberger T, Schöpf B, Hofmann H, Hofmann M, Von Rechenberg B. Superparamagnetic nanoparticles for biomedical applications: Possibilities and limitations of a new drug delivery system. In: Journal of Magnetism and Magnetic Materials. 2005;293(1) 483–96.
7. Patra JK, Das G, Fraceto LF, Campos EVR, Rodriguez-Torres MDP, Acosta-Torres LS, et al. Nano based drug delivery systems: Recent developments and future prospects. Journal of Nanobiotechnology. 2018;16(1):71.
8. Fukuda A, Tahara K, Hane Y, Matsui T, Sasaoka S, Hatahira H, et al. Comparison of the adverse event profiles of conventional and liposomal formulations of doxorubicin using the FDA adverse event reporting system. PLoS One. 2017;12(9).

9. Bobo D, Robinson KJ, Islam J, Thurecht KJ, Corrie SR. Nanoparticle-Based Medicines: A Review of FDA-Approved Materials and Clinical Trials to Date. Vol. 33, Pharmaceutical Research. 2016. p. 2373–87.

10. Janko C, Ratschker T, Nguyen K, Zschiesche L, Tietze R, Lyer S, et al. Functionalized superparamagnetic iron oxide nanoparticles (SPIONs) as platform for the targeted multimodal tumor therapy. Frontiers in Oncology. 2019;9:59.

11. Jadhav N V., Prasad AI, Kumar A, Mishra R, Dhara S, Babu KR, et al. Synthesis of oleic acid functionalized Fe3O4 magnetic nanoparticles and studying their interaction with tumor cells for potential hyperthermia applications. Colloids and Surfaces B: Biointerfaces. 2013;108:158–68.

12. Siegel RL, Miller KD, Jemal A. Cancer statistics, 2018. CA: A Cancer Journal for Clinicians;2018;68(1):7–30.

13. Dhillon PK, Mathur P, Nandakumar A, Fitzmaurice C, Kumar GA, Mehrotra R, et al. The burden of cancers and their variations across the states of India: the Global Burden of Disease Study 1990–2016. The Lancet Oncology. 2018;19(10):1289–306.

14. Smith RD, Mallath MK. History of the growing burden of cancer in India: From antiquity to the 21st century. Journal of Global Oncology. 2019;2019(5):1-15.

15. Saranath D, Khanna A. Current Status of Cancer Burden: Global and Indian Scenario. BioMed Research Journal. 2014;1(1):1.

16. Urruticoechea A, Alemany R, Balart J, Villanueva A, Vinals F, Capella G. Recent Advances in Cancer Therapy: An Overview. Current Pharmaceutical Design. 2009;16(1):3–10.

17. Arruebo M, Vilaboa N, Sáez-Gutierrez B, Lambea J, Tres A, Valladares M, et al. Assessment of the evolution of cancer treatment therapies. Vol. 3, Cancers. 2011. p. 3279–330.

18. Abbas Z, Rehman S. An Overview of Cancer Treatment Modalities. In: Neoplasm. 2018:76558.

19. Raviraj J, Bokkasam VK, Kumar VS, Reddy US, Suman V. Radiosensitizers, radioprotectors, and radiation mitigators. Vol. 25, Indian Journal of Dental Research. 2014;25(1):83–90.

20. Citrin D, Cotrim AP, Hyodo F, Baum BJ, Krishna MC, Mitchell JB. Radioprotectors and Mitigators of Radiation-Induced Normal Tissue Injury. Oncologist. 2010;15(4):360–71.

21. Prasanna PGS, Narayanan D, Hallett K, Bernhard EJ, Ahmed MM, Evans G, et al. Radioprotectors and Radiomitigators for Improving Radiation Therapy: The Small Business Innovation Research (SBIR) Gateway for Accelerating Clinical Translation. Radiation Research. 2015;184(3):235–48.

22. Spalding A, Lawrence T. New and emerging radiosensitizers and radioprotectors. Cancer Investigation. 2006;24:444–56.

23. Wardman P. Chemical Radiosensitizers for Use in Radiotherapy. Clinical Oncology. 2007;19(6):397–417.

24. Weinstein JS, Varallyay CG, Dosa E, Gahramanov S, Hamilton B, Rooney WD, et al. Superparamagnetic iron oxide nanoparticles: Diagnostic magnetic resonance imaging and potential therapeutic applications in neurooncology and central nervous system inflammatory pathologies, a review. Vol. 30, Journal of Cerebral Blood Flow and Metabolism. 2010;30(1):15–35.

25. Çağdaş M, Sezer AD, Bucak S. Liposomes as Potential Drug Carrier Systems for Drug Delivery. In: Application of Nanotechnology in Drug Delivery. 2014:58459.

26. Kalra J, Bally MB. Liposomes. In: Fundamentals of Pharmaceutical Nanoscience. 2013:27–63.

27. Lila ASA, Ishida T. Liposomal delivery systems: Design optimization and current applications. Biological and Pharmaceutical Bulletin. 2017;40:1–10.

28. Nagai H, Kim YH. Cancer prevention from the perspective of global cancer burden patterns. Journal of Thoracic Disease. 2017;9:448–51.

29. GM. C. The Cell: A Molecular Approach. The Development and Causes of Cancer, 2nd edition. Sunderland (MA): Sinauer Associates; 2000.

30. Cavallo F, De Giovanni C, Nanni P, Forni G, Lollini PL. 2011: The immune hallmarks of cancer. In: Cancer Immunology, Immunotherapy. 2011;60(3):319–26.

31. Hanahan D, Weinberg RA. The hallmarks of cancer. Cell. 2000;100(1):57–70.

32. Hanahan D, Weinberg RA. Hallmarks of cancer: The next generation. Cell. 2011;144:646–74.

33. Gabriel J. The Biology of Cancer: Second Edition. 2008:1–204.

34. Nenclares P, Harrington KJ. The biology of cancer. Medicine (United Kingdom). 2020;48(2):67–72.

35. Pardee AB, Stein GS. The Biology and Treatment of Cancer: Understanding Cancer. The Biology and Treatment of Cancer: Understanding Cancer. 2008:1–287.

36. Vineis P, Wild CP. Global cancer patterns: Causes and prevention. The Lancet. 2014;383:549–57.

37. McLaughlin-Drubin ME, Munger K. Viruses associated with human cancer. Biochimica et Biophysica Acta - Molecular Basis of Disease. 2008;1782:127–50.

38. Moore PS, Chang Y. Why do viruses cause cancer? Highlights of the first century of human tumour virology. Nature Reviews Cancer. 2010;10:878–89.

39. Hudnall SD. Viruses and human cancer. 2014:1–386.

40. (IARC) IA for R on C. Latest Global Cancer Data. CA: A Cancer Journal for Clinicians. 2018:13–5.

41. Rajpal S, Kumar A, Joe W. Economic burden of cancer in India: Evidence from cross-sectional nationally representative household survey, 2014. PLoS One. 2018;13(2): e0193320.

42. Uei H, Tokuhashi Y, Maseda M, Nakahashi M, Sawada H, Nakayama E, et al. Clinical results of multidisciplinary therapy including palliative posterior spinal stabilization surgery and postoperative adjuvant therapy for metastatic spinal tumor. Journal of Orthopaedic Surgery and Research. 2018;13:30.

43. Dunne-Daly CF. Principles of radiotherapy and radiobiology. Seminars in Oncology Nursing. 1999;15(4):250–9.

44. Hall EJ. Radiation biology. Cancer. 1985;55:2051-2057.

45. Casas F, Abdel-Wahab S, Filipovic N, Jeremic B. Radiation Therapy. In: International Encyclopedia of Public Health. 2016:260–8.

46. Schulz-Ertner D, Jäkel O, Schlegel W. Radiation Therapy With Charged Particles. Seminars in Radiation Oncology. 2006;16(4):249–59.

47. Durante M, Loeffler JS. Charged particles in radiation oncology. Nature Reviews Clinical Oncology. 2010;7:37–43.

48. Paganetti H. Proton beam therapy. Proton beam therapy. 2017. 1–23 p.

49. Liu H, Chang JY. Proton therapy in clinical practice. Chinese Journal of Cancer. 2011;30:315–26.

50. Moreno AC, Frank SJ, Garden AS, Rosenthal DI, Fuller CD, Gunn GB, et al. Intensity modulated proton therapy (IMPT) – The future of IMRT for head and neck cancer. Oral Oncology. 2019;88:66–74.

51. Therapy R, Cdks B. The Science Behind Radiation Therapy. American Cancer Society. 2014;15.

52. De Los Santos J, Popple R, Agazaryan N, Bayouth JE, Bissonnette JP, Bucci MK, et al. Image guided radiation therapy (IGRT) technologies for radiation therapy localization and delivery. International Journal of Radiation Oncology Biology Physics. 2013;87: 33–45.

53. Smathers JB. The Physics of Radiation Therapy. Journal of Appled Clinical Medical Physics. 2003;4(4):382.

54. Kwekkeboom DJ, Kam BL, Van Essen M, Teunissen JJM, Van Eijck CHJ, Valkema R, et al. Somatostatin receptor-based imaging and therapy of gastroenteropancreatic neuroendocrine tumors. Endocrine-Related Cancer. 2010;17(1):R53-73:.

55. Werner-Wasik M, Rudoler S, Preston PE, Hauck WW, Downes BM, Leeper D, et al. Immediate side effects of stereotactic radiotherapy and radiosurgery. International Journal of Radiation Oncology Biology Physics. 1999;43(2):299–304.

56. Chabner BA, Roberts TG. Chemotherapy and the war on cancer. Nature Reviews Cancer. 2005;5:65–72.

57. DeVita VT, Chu E. A history of cancer chemotherapy. Cancer Research. 2008;68:8643–53.

58. Scholar E. Antimetabolites. In: xPharm: The Comprehensive Pharmacology Reference. 2007:1–4.

59. Tiwari M. Antimetabolites: Established cancer therapy. Vol. 8, Journal of Cancer Research and Therapeutics. 2012:510–9.

60. Peters GJ, Van Der Wilt CL, Van Moorsel CJA, Kroep JR, Bergman AM, Ackland SP. Basis for effective combination cancer chemotherapy with antimetabolites. In: Pharmacology and Therapeutics. 2000:227–53.

61. Mohan K, Jeyachandran R. Alkaloids as anticancer agents. Annals of phytomedicine. 2012;1(1):46–53.

62. Iqbal J, Abbasi BA, Mahmood T, Kanwal S, Ali B, Shah SA, et al. Plant-derived anticancer agents: A green anticancer approach. Asian Pacific Journal of Tropical Biomedicine. 2017;7:1129–50.

63. Pezzuto JM. Plant-derived anticancer agents. Biochemical Pharmacology. 1997;53:121–33.

64. Demain AL, Vaishnav P. Natural products for cancer chemotherapy. Microbial Biotechnology. 2011;4:687–99.

65. Pommier Y. Topoisomerase I inhibitors: Camptothecins and beyond. In: Nature Reviews Cancer. 2006:789–802.

66. Hande KR. Topoisomerase II inhibitors. Update on Cancer Therapeutics. 2008;3:13–26.

67. Chortis V, Taylor AE, Schneider P, Tomlinson JW, Hughes BA, O'Neil DM, et al. Mitotane therapy in adrenocortical cancer induces CYP3A4 and inhibits 5α-reductase, explaining the need for personalized glucocorticoid and androgen replacement. The Journal of Clinical Endocrinology and Metabolism. 2013;98(1):161–71.

68. Terzolo M, Angeli A, Fassnacht M, Daffara F, Tauchmanova L, Conton PA, et al. Adjuvant Mitotane Treatment for Adrenocortical Carcinoma. The New England Journal of Medicine. 2007;356(23):2372–80.

69. Pieters R, Hunger SP, Boos J, Rizzari C, Silverman L, Baruchel A, et al. L-asparaginase treatment in acute lymphoblastic leukemia. Cancer. 2011;117(2):238–49.

70. Covini D, Tardito S, Bussolati O, R. Chiarelli L, V. Pasquetto M, Digilio R, et al. Expanding Targets for a Metabolic Therapy of Cancer: L-Asparaginase. Recent Patents on Anticancer Drug Discovery. 2011;7(1):4–13.

71. Love RR, Leventhal H, Easterling D V., Nerenz DR. Side effects and emotional distress during cancer chemotherapy. Cancer. 1989;63(3):604–12.

72. Regnard C, Kindlen M, Chemotherapy: side effects. In: Supportive and Palliative Care in Cancer. 2019:39–41.

73. Guo ZS. The 2018 Nobel Prize in medicine goes to cancer immunotherapy (editorial for BMC cancer). BMC Cancer. 2018;18(1):1086:.

74. Mukhopadhaya A. Nobel Prize in Physiology or Medicine – 2018. Resonance. 2018;23(12):1359–66.

75. Anusha A, Kumar S, Kaushik S, Jyoti A. Cancer immunotherapy. Journal of Pharmaceutical Sciences and Research. 2017;9(5):662–6.

76. Farkona S, Diamandis EP, Blasutig IM. Cancer immunotherapy: The beginning of the end of cancer? Vol. 14, BMC Medicine. 2016;14:73.

77. Mellman I, Coukos G, Dranoff G. Cancer immunotherapy comes of age. Nature. 2011;480:480–489.

78. Figdor CG, De Vries IJM, Lesterhuis WJ, Melief CJM. Dendritic cell immunotherapy: Mapping the way. Nature Medicine. 2004;10:475–80.

79. Sabado RL, Balan S, Bhardwaj N. Dendritic cell-based immunotherapy. Cell Research. 2017;27:74–95.

80. Cheever MA, Higano CS. PROVENGE (sipuleucel-T) in prostate cancer: The first FDA-approved therapeutic cancer vaccine. Clinical Cancer Research. 2011;17:3520–6.

81. Miliotou AN, Papadopoulou LC. CAR T-cell Therapy: A New Era in Cancer Immunotherapy. Current Pharmaceutical Biotechnology. 2018;19(1):5–18.

82. Fraietta JA, Schwab RD, Maus M V. Improving therapy of chronic lymphocytic leukemia with chimeric antigen receptor T cells. Vol. 43, Seminars in Oncology. 2016;43:291–9.

83. Sha HH, Wang DD, Yan DL, Hu Y, Yang SJ, Liu SW, et al. Chimaeric antigen receptor T-cell therapy for tumour immunotherapy. Bioscience Reports. 2017; 37(1): BSR20160332.

84. News Release F. FDA Approval Brings First Gene Therapy to the United States. Molecular and Cellular Pharmacology. 2017;9(3):17–8.

85. Pehlivan KC, Duncan BB, Lee DW. CAR-T Cell Therapy for Acute Lymphoblastic Leukemia: Transforming the Treatment of Relapsed and Refractory Disease.Current Hematologic Malignancy Reports. 2018;13:396–406.

86. Maude SL, Teachey DT, Porter DL, Grupp SA. CD19-targeted chimeric antigen receptor T-cell therapy for acute lymphoblastic leukemia. Blood. 2015;125(26):4017–23.

87. Scott AM, Wolchok JD, Old LJ. Antibody therapy of cancer. Nature Reviews Cancer. 2012;12:278–87.

88. Kimiz-Gebologlu I, Gulce-Iz S, Biray-Avci C. Monoclonal antibodies in cancer immunotherapy. Molecular Biology Reports. 2018;45:2935–40.

89. Lu RM, Hwang YC, Liu IJ, Lee CC, Tsai HZ, Li HJ, et al. Development of therapeutic antibodies for the treatment of diseases. Journal of Biomedical Science. 2020;27:1.

90. Chames P, Van Regenmortel M, Weiss E, Baty D. Therapeutic antibodies: Successes, limitations and hopes for the future. British Journal of Pharmacology. 2009;157:220–33.

91. Kim SJ, Park Y, Hong HJ. Antibody engineering for the development of therapeutic antibodies. Molecules and Cells. 2005;20:17–29.

92. Kaplon H, Muralidharan M, Schneider Z, Reichert JM. Antibodies to watch in 2020. MAbs. 2020;12(1).

93. Dranoff G. Cytokines in cancer pathogenesis and cancer therapy. Nature Reviews Cancer. 2004;4:11–22.

94. Showalter A, Limaye A, Oyer JL, Igarashi R, Kittipatarin C, Copik AJ, et al. Cytokines in immunogenic cell death: Applications for cancer immunotherapy. Cytokine. 2017;97:123–32.

95. Jiang T, Zhou C, Ren S. Role of IL-2 in cancer immunotherapy. OncoImmunology. 2016; 5(6):e1163462.

96. Rosenberg SA. IL-2: The First Effective Immunotherapy for Human Cancer. Journal of Immunology. 2014;192(12):5451–8.

97. Ben-Ami E, Schachter J. Adjuvant treatment for stage III melanoma in the era of targeted medicine and immunotherapy. Melanoma Management. 2016;3(2):137–47.

98. Sharma P, Allison JP. Immune checkpoint targeting in cancer therapy: Toward combination strategies with curative potential. Cell. 2015;161:205–14.

99. Fessas P, Lee H, Ikemizu S, Janowitz T. A molecular and preclinical comparison of the PD-1–targeted T-cell checkpoint inhibitors nivolumab and pembrolizumab. Seminars in Oncology. 2017;44:136–40.

100. Woller N, Gürlevik E, Ureche CI, Schumacher A, Kühnel F. Oncolytic viruses as anticancer vaccines. Frontiers in Oncology. 2014;4:188.

101. Alemany R. Oncolytic adenoviruses in cancer treatment. Biomedicines. 2014;2:36–49.

102. Pol J, Kroemer G, Galluzzi L. First oncolytic virus approved for melanoma immunotherapy. Oncoimmunology. 2016;5(1):e1115641.

103. Neelapu SS, Tummala S, Kebriaei P, Wierda W, Gutierrez C, Locke FL, et al. Chimeric antigen receptor T-cell therapy-assessment and management of toxicities. Nature Reviews Clinical Oncology. 2018;15:47–62.

104. Le RQ, Li L, Yuan W, Shord SS, Nie L, Habtemariam BA, et al. FDA Approval Summary: Tocilizumab for Treatment of Chimeric Antigen Receptor T Cell-Induced Severe or Life-Threatening Cytokine Release Syndrome. Oncologist. 2018;23(8):943–7.

105. Shah NN, Fry TJ. Mechanisms of resistance to CAR T cell therapy. Nature Reviews Clinical Oncology. 2019;16:372–85.

106. Brudno JN, Kochenderfer JN. Recent advances in CAR T-cell toxicity: Mechanisms, manifestations and management. Blood Reviews. 2019;34:45–55.

107. Lesterhuis WJ, Haanen JBAG, Punt CJA. Cancer immunotherapy-revisited. Nature Reviews Drug Discovery. 2011;10:591–600.

108. Hind D, Ward S, De Nigris E, Simpson E, Carroll C, Wyld L. Hormonal therapies for early breast cancer: Systematic review and economic evaluation. Vol. 11, Health Technology Assessment. 2007;11(26):1-134:.

109. Hellerstedt BA, Pienta KJ. The Current State of Hormonal Therapy for Prostate Cancer. CA: A Cancer Journal for Clinicians. 2002;52(3):154–79.

110. Kokka F, Brockbank E, Oram D, Gallagher C, Bryant A. Hormonal therapy in advanced or recurrent endometrial cancer. Cochrane Database of Systematic Reviews. 2010;2010(12):CD007926.

111. Ruddy KJ, Partridge AH. Adherence with adjuvant hormonal therapy for breast cancer. Annals of Oncology. 2009;20:401–2.

112. Miller WR, Bartlett J, Brodie AMH, Brueggemeier RW, di Salle E, Lønning PE, et al. Aromatase Inhibitors: Are There Differences Between Steroidal and Nonsteroidal Aromatase Inhibitors and Do They Matter? Oncologist. 2008;13(8):829–37.

113. David C, Boinet T. Hormone therapy for prostate cancer. Actualites Pharmaceutiques. 2019;85:13–7.

114. Bolton EM, Lynch T. Are all gonadotrophin-releasing hormone agonists equivalent for the treatment of prostate cancer? A systematic review. BJU International. 2018;122:371–83.

115. Peng J, Sengupta S, Jordan V. Potential of Selective Estrogen Receptor Modulators as Treatments and Preventives of Breast Cancer. Anti-Cancer Agents in Medicinal Chemistry. 2012;9(5):481–99.

116. Westerberg H. Tamoxifen and fluoxymesterone in advanced breast cancer: A controlled clinical trial. Cancer Treatment Reports. 1980;64(1):117–21.

117. Ali A, Khalil MAI, Khan N, Abu Bakar M, Amjad A, Ahmed I, et al. Diethylstilbestrol in the Treatment of Castration-resistant Prostate Cancer: A Lower-middle-income Country Experience. Cureus. 2019; 11(4):e4470.

118. Ziółkowska E, Zarzycka M, Wiśniewski T, Zyromska A. The side effects of hormonal therapy at the patients with prostate cancer. Wspolczesna Onkologia. 2012;16:491–497.

119. Fairchild A, Tirumani SH, Rosenthal MH, Howard SA, Krajewski KM, Nishino M, et al. Hormonal therapy in oncology: A primer for the radiologist. American Journal of Roentgenology. 2015;204:W620–30.

120. Sawyers C. Targeted cancer therapy. Nature. 2004;432:294–7.

121. Gotwals P, Cameron S, Cipolletta D, Cremasco V, Crystal A, Hewes B, et al. Prospects for combining targeted and conventional cancer therapy with immunotherapy. Nature Reviews Cancer. 2017;17:286–301.

122. Padma VV. An overview of targeted cancer therapy. BioMedicine (Netherlands). 2015;5:1–6.

123. Hojjat-Farsangi M. Small-molecule inhibitors of the receptor tyrosine kinases: Promising tools for targeted cancer therapies. International Journal of Molecular Sciences. 2014;15:13768–801.

124. Rader C, Bishop MR. Monoclonal antibodies in cancer therapy. In: General Principles of Tumor Immunotherapy: Basic and Clinical Applications of Tumor Immunology. 2008:453–84.

125. Ferguson FM, Gray NS. Kinase inhibitors: The road ahead. Nature Reviews Drug Discovery. 2018;17:353–76.

126. Arora A, Scholar EM. Role of tyrosine kinase inhibitors in cancer therapy. Journal of Pharmacology and Experimental Therapeutics. 2005;315:971–9.

127. Steelman LS, Martelli AM, Cocco L, Libra M, Nicoletti F, Abrams SL, et al. The therapeutic potential of mTOR inhibitors in breast cancer. British Journal of Clinical Pharmacology. 2016;82(5):1189–212.

128. Onishi H, Katano M. Hedgehog signaling pathway as a therapeutic target in various types of cancer. Cancer Science. 2011;102|:1756–60.

129. Kelleher FC. Hedgehog signaling and therapeutics in pancreatic cancer. Carcinogenesis. 2011;32:445–51.

130. Howell SJ, Johnston SRD, Howell A. The use of selective estrogen receptor modulators and selective estrogen receptor down-regulators in breast cancer. Best Practice and Research: Clinical Endocrinology and Metabolism. 2004;18:47–66.

131. Patel HK, Bihani T. Selective estrogen receptor modulators (SERMs) and selective estrogen receptor degraders (SERDs) in cancer treatment. Pharmacology and Therapeutics. 2018;186:1–24.

132. Waters EA, McNeel TS, Stevens WM, Freedman AN. Use of tamoxifen and raloxifene for breast cancer chemoprevention in 2010. Breast Cancer Research and Treatment. 2012;134(2):875–80.

133. Salem M, Garcia JA. Abiraterone acetate, a novel adrenal inhibitor in metastatic castration-resistant prostate cancer. Current Oncology Reports. 2011;13:92–6.

134. Crawford ED, Schellhammer PF, McLeod DG, Moul JW, Higano CS, Shore N, et al. Androgen Receptor Targeted Treatments of Prostate Cancer: 35 Years of Progress with Antiandrogens. Journal of Urology. 2018;200:956–66.

135. Bose P, Batalo MS, Holkova B, Grant S. Bortezomib for the treatment of non-Hodgkin's lymphoma. Expert Opinion on Pharmacotherapy. 2014;15(16):2443–59.

136. Stewart AK, Rajkumar SV, Dimopoulos MA, Masszi T, Špička I, Oriol A, et al. Carfilzomib, Lenalidomide, and Dexamethasone for Relapsed Multiple Myeloma. The New England Journal of Medicine. 2015;372(2):142–52.

137. Zhang Q, Wang S, Chen J, Yu Z. Histone deacetylases (HDACs) guided novel therapies for T-cell lymphomas. International Journal of Medical Sciences. 2019;16:424–42.

138. Amengual JE, Lichtenstein R, Lue J, Sawas A, Deng C, Lichtenstein E, et al. A phase 1 study of romidepsin and pralatrexate reveals marked activity in relapsed and refractory T-cell lymphoma. Blood. 2018;131(4):397–407.

139. Tsimberidou AM, Giles F, Romaguera J, Duvic M, Kurzrock R. Activity of Interferon-α and Isotretinoin in Patients with Advanced, Refractory Lymphoid Malignancies. Cancer. 2004;100(3):574–80.

140. Bettoli V, Zauli S, Virgili A. Retinoids in the chemoprevention of non-melanoma skin cancers: Why, when and how. Journal of Dermatological Treatment. 2013;24(3):235–7.

141. Krasinskas AM. EGFR Signaling in Colorectal Carcinoma. Pathology Research International. 2011;2011:1–6.

142. Iqbal N, Iqbal N. Human Epidermal Growth Factor Receptor 2 (HER2) in Cancers: Overexpression and Therapeutic Implications. Molecular Biology International. 2014;2014:1–9.

143. Engelhard M. Anti-CD20 antibody treatment of non-Hodgkin lymphomas. Clinical Immunology. 2016;172:101–4.

144. Lipson EJ, Drake CG. Ipilimumab: An anti-CTLA-4 antibody for metastatic melanoma. Clinical Cancer Research. 2011;17:6958–62.

145. Papadopoulos N, Martin J, Ruan Q, Rafique A, Rosconi MP, Shi E, et al. Binding and neutralization of vascular endothelial growth factor (VEGF) and related ligands by VEGF Trap, ranibizumab and bevacizumab. Angiogenesis. 2012;15(2):171–85.

146. DeNardo GL, DeNardo SJ. Turning the heat on cancer. Cancer Biotherapy and Radiopharmaceuticals. 2008;23:671–9.

147. Gas P. Essential facts on the history of hyperthermia and their connections with electromedicine. Przeglad Elektrotechniczny. 2011;87:37–40.

148. Hoption Cann SA, Van Netten JP, Van Netten C. Dr William Coley and tumour regression: A place in history or in the future. Postgraduate Medical Journal. 2003;79:672–80.

149. Hayre DS. 23. Coley's toxin and spontaneous tumour regression. Clinical and Investigative Medicine. 2007;30(4):39.

150. Roussakow S. The History of Hyperthermia Rise and Decline. Conference Papers in Medicine. 2013;2013:1–40.

151. Gao S, Zheng M, Ren X, Tang Y, Liang X. Local hyperthermia in head and neck cancer: Mechanism, application and advance. Oncotarget. 2016;7:57367–78.

152. Lepock JR. Cellular effects of hyperthermia: Relevance to the minimum dose for thermal damage. In: International Journal of Hyperthermia. 2003;19(3):252–266.

153. Hildebrandt B, Wust P, Ahlers O, Dieing A, Sreenivasa G, Kerner T, et al. The cellular and molecular basis of hyperthermia. Critical Reviews in Oncology/Hematology. 2002;43:33–56.

154. Habash RWY, Bansal R, Krewski D, Alhafid HT. Thermal therapy, Part 2: Hyperthermia techniques. Critical Reviews in Biomedical Engineering. 2006;34:491–542.

155. Hager ED. Locoregional Hyperthermia. In: Hyperthermia in Cancer Treatment: A Primer. 2008:167–82.

156. Kok HP, van Haaren PMA, van Dijk JDP, Crezee J. On estimation of the temperature maximum in intraluminal or intracavitary hyperthermia. International Journal of Hyperthermia. 2005;21(4):287–304.

157. Stea B, Kittelson J, Cassady JR, Hamilton A, Guthkelch N, Lulu B, et al. Treatment of malignant gliomas with interstitial irradiation and hyperthermia. International Journal of Radiation Oncology Biology and Physics. 1992;24(4):657–67.

158. Kok HP, Wust P, Stauffer PR, Bardati F, van Rhoon GC, Crezee J. Current state of the art of regional hyperthermia treatment planning: A review. Radiation Oncology. 2015;10:196.

159. Fried SJ, Miller R, Weaver FA, Faddis D. Safe, compact and portable system for regional chemotherapeutic hyperthermic perfusion procedures. Journal of Extra-Corporeal Technology. 1993;25(1):22–6.

160. Pinto A, Pocard M. Hyperthermic intraperitoneal chemotherapy with cisplatin and mitomycin C for colorectal cancer peritoneal metastases: A systematic review of the literature. Pleura and Peritoneum. 2019;4(2):20190006.

161. Franko J, Ibrahim Z, Gusani NJ, Holtzman MP, Bartlett DL, Zeh HJ. Cytoreductive surgery and hyperthermic intraperitoneal chemoperfusion versus systemic chemotherapy alone for colorectal peritoneal carcinomatosis. Cancer. 2010;116(16):3756–62.

162. Frazier N, Payne A, de Bever J, Dillon C, Panda A, Subrahmanyam N, et al. High intensity focused ultrasound hyperthermia for enhanced macromolecular delivery. Journal of Controlled Release. 2016;241:186–93.

163. Andocs G, Rehman MU, Zhao QL, Tabuchi Y, Kanamori M, Kondo T. Comparison of biological effects of modulated electro-hyperthermia and conventional heat treatment in human lymphoma U937 cells. Cell Death Discovery. 2016;2(1):16039.

164. Milligan AJ. Whole-body hyperthermia induction techniques. Cancer Res. 1984;44(10 SUPPL.):4869s-4872s.

165. Samson S, Chretien P. Hyperthermia-induced Cell Death, Thermotolerance, and Heat Shock Proteins in Normal, Respiration-deficient, and Glycolysis-deficient Chinese Hamster Cells. Cancer Research. 1986;46(1):324–7.

166. King YT, Lin CS, Lin JH, Lee WC. Whole-body hyperthermia-induced thermotolerance is associated with the induction of heat shock protein 70 in mice. Journal of Experimental Biology. 2002;205(2):273–8.

167. Bárcena C, Sra AK, Gao J. Applications of magnetic nanoparticles in biomedicine. In: NanoScale Magnetic Materials and Applications. 2009:591–626.

168. Laurent S, Dutz S, Häfeli UO, Mahmoudi M. Magnetic fluid hyperthermia: Focus on superparamagnetic iron oxide nanoparticles. Vol. 166, Advances in Colloid and Interface Science. 2011;166:8–23.

169. Shetake NG, Kumar A, Pandey BN. Iron-oxide nanoparticles target intracellular HSP90 to induce tumor radio-sensitization. Biochimica et Biophysica Acta - General Subjects. 2019;1863(5):857–69.

170. Svaasand LO, Boerslid T, Oeveraasen M. Thermal and optical properties of living tissue: Application to laser-induced hyperthermia. Lasers in Surgery and Medicine. 1985;5(6):589–602.

171. Svaasand LO, Gomer CJ, Morinelli E. On the physical rationale of laser induced hyperthermia. Lasers in Medical Science. 1990;5(2):121–8.

172. Chaplin V, Caskey CF. Multi-focal HIFU reduces cavitation in mild-hyperthermia. Journal of Therapeutic Ultrasound. 2017;5(1):12.

173. Coussios CC, Farny CH, ter Haar G, Roy RA. Role of acoustic cavitation in the delivery and monitoring of cancer treatment by high-intensity focused ultrasound (HIFU). International Journal of Hyperthermia. 2007;23(2):105–20.

174. Shetake N, Balla M., Kumar A, Pandey B. Magnetic hyperthermia therapy: An emerging modality of cancer treatment in combination with radiotherapy. Journal of Radiation and Cancer Research. 2016;7(1):13.

175. Gneveckow U, Jordan A, Scholz R, Brüß V, Waldöfner N, Ricke J, et al. Description and characterization of the novel hyperthermia- and thermoablation-system MFH®300F for clinical magnetic fluid hyperthermia. Medical Physics. 2004;31(6):1444–51.

176. Johannsen M, Gneveckow U, Eckelt L, Feussner A, Waldöfner N, Scholz R, et al. Clinical hyperthermia of prostate cancer using magnetic nanoparticles: Presentation of a new interstitial technique. International Journal of Hyperthermia. 2005;21(7):637–47.

177. Matsubara T, Matsumine A, Kusuzaki K, Asanuma K, Nakamura T, Uchida A, et al. A Minimally Invasive Surgery for Bone Metastases Using the Combination of Photodynamic Therapy and Hyperthermia Treatment. International Journal of Clinical and Experimental Medicine. 2013;04(08):357–63.

178. Shetake NG, Kumar A, Gaikwad S, Ray P, Desai S, Ningthoujam RS, et al. Magnetic nanoparticle-mediated hyperthermia therapy induces tumour growth inhibition by

apoptosis and Hsp90/AKT modulation. International Journal of Hyperthermia. 2015;31(8):909–19.

179. Ghosh R, Pradhan L, Devi YP, Meena SS, Tewari R, Kumar A, et al. Induction heating studies of Fe3O4 magnetic nanoparticles capped with oleic acid and polyethylene glycol for hyperthermia. Journal of Materials Chemistry. 2011;21(35):13388–98.

180. Kumar R, Chauhan A, Jha SK, Kuanr BK. Localized cancer treatment by radio-frequency hyperthermia using magnetic nanoparticles immobilized on graphene oxide: from novel synthesis to *in vitro* studies. Journal of Materials Chemistry B. 2018;6(33):5385–99.

181. Goya GF, Asín L, Ibarra MR. Cell death induced by ac magnetic fields and magnetic nanoparticles: Current state and perspectives. Vol. 29, International Journal of Hyperthermia. 2013;29:810–8.

182. Abenojar EC, Wickramasinghe S, Bas-Concepcion J, Samia ACS. Structural effects on the magnetic hyperthermia properties of iron oxide nanoparticles. Progress in Natural Science: Materials International. 2016;26(5):440–8.

183. Hergt R, Dutz S, Müller R, Zeisberger M. Magnetic particle hyperthermia: Nanoparticle magnetism and materials development for cancer therapy. Journal of Physics: Condensed Matter. 2006;18(38).

184. Bañobre-López M, Teijeiro A, Rivas J. Magnetic nanoparticle-based hyperthermia for cancer treatment. Reports of Practical Oncology and Radiotherapy. 2013;18:397–400.

185. Khan I, Saeed K, Khan I. Nanoparticles: Properties, applications and toxicities. Arabian Journal of Chemistry. 2019;12:908–31.

186. Mohanraj VJ, Chen Y. Nanoparticles - A review. Tropical Journal of Pharmaceutical Research. 2007;5(1).

187. Landauer R. Information is inevitably physical. In: Feynman and Computation. 2018:77–92.

188. Duncan R. Nanomedicine gets clinical. Materials Today. 2005;8(8 SUPPL.):16–7.

189. Webster TJ. Nanomedicine: What's in a definition? International Journal of Nanomedicine. 2006;1:115–6.

190. Brannon-Peppas L, Blanchette JO. Nanoparticle and targeted systems for cancer therapy. Advanced Drug Delivery Reviews. 2012;64:206–12.

191. Alexis F, Pridgen EM, Langer R, Farokhzad OC. Nanoparticle technologies for cancer therapy. Handbook of Experimental Pharmacology. 2010;197:55–86.

192. Wicki A, Witzigmann D, Balasubramanian V, Huwyler J. Nanomedicine in cancer therapy: Challenges, opportunities, and clinical applications. Journal of Controlled Release. 2015;200:138–57.

193. Singh R, Lillard JW. Nanoparticle-based targeted drug delivery. Experimental and Molecular Pathology. 2009;86:215–23.

194. Lombardo D, Kiselev MA, Caccamo MT. Smart Nanoparticles for Drug Delivery Application: Development of Versatile Nanocarrier Platforms in Biotechnology and Nanomedicine. J of Nanomaterials. 2019;2019.

195. Kirtane AR, Kalscheuer SM, Panyam J. Exploiting nanotechnology to overcome tumor drug resistance: Challenges and opportunities. Advanced Drug Delivery Reviews. 2013;65:1731–47.

196. Xue X, Liang XJ. Overcoming drug efflux-based multidrug resistance in cancer with nanotechnology. Chinese Journal of Cancer. 2012;31:100–9.

197. Golombek SK, May JN, Theek B, Appold L, Drude N, Kiessling F, et al. Tumor targeting via EPR: Strategies to enhance patient responses. Advanced Drug Delivery Reviews. 2018;130:17–38.

198. Wang J, Sui M, Fan W. Nanoparticles for Tumor Targeted Therapies and Their Pharmacokinetics. Current Drug Metabolism. 2010;11(2):129–41.

199. Bhatia S, Bhatia S. Nanoparticles Types, Classification, Characterization, Fabrication Methods and Drug Delivery Applications. In: Natural Polymer Drug Delivery Systems. 2016:33–93.

200. Ealias AM, Saravanakumar MP. A review on the classification, characterisation, synthesis of nanoparticles and their application. In: IOP Conference Series: Materials Science and Engineering. 2017;263:032019.

201. Palei NN, Mohanta BC, Sabapathi ML, Das MK. Lipid-based nanoparticles for cancer diagnosis and therapy. In: Organic Materials as Smart Nanocarriers for Drug Delivery. 2018:415–70.

202. García-Pinel B, Porras-Alcalá C, Ortega-Rodríguez A, Sarabia F, Prados J, Melguizo C, et al. Lipid-based nanoparticles: Application and recent advances in cancer treatment. Nanomaterials. 2019;9(4).

203. Ahmed KS, Hussein SA, Ali AH, Korma SA, Lipeng Q, Jinghua C. Liposome: composition, characterisation, preparation, and recent innovation in clinical applications. Journal of Drug Targeting. 2019;27:742–61.

204. Immordino ML, Dosio F, Cattel L. Stealth liposomes: Review of the basic science, rationale, and clinical applications, existing and potential. International Journal of Nanomedicine. 2006;1:297–315.

205. Bulbake U, Doppalapudi S, Kommineni N, Khan W. Liposomal formulations in clinical use: An updated review. Pharmaceutics. 2017;9(2):12.

206. Porfire A, Achim M, Tefas L, Sylvester B. Liposomal Nanoformulations as Current Tumor-Targeting Approach to Cancer Therapy. In: Liposomes. 2017.

207. Chaudhury A, Das S. Folate Receptor Targeted Liposomes Encapsulating Anti-Cancer Drugs. Current Pharmaceutical Biotechnology. 2015;16(4):333–43.

208. Kumar P, Huo P, Liu B. Formulation strategies for folate-targeted liposomes and their biomedical applications. Pharmaceutics. 2019;11(8):381.

209. Song X li, Liu S, Jiang Y, Gu L yan, Xiao Y, Wang X, et al. Targeting vincristine plus tetrandrine liposomes modified with DSPE-PEG2000-transferrin in treatment of brain glioma. European Journal of Pharmaceutical Sciences. 2017;96:129–40.

210. Sun T, Wu H, Li Y, Huang Y, Yao L, Chen X, et al. Targeting transferrin receptor delivery of temozolomide for a potential glioma stem cell-mediated therapy. Oncotarget. 2017;8(43):74451–65.

211. Yan W, Leung SSY, To KKW. Updates on the use of liposomes for active tumor targeting in cancer therapy. Nanomedicine. 2019;15:303–18.

212. Deshpande PP, Biswas S, Torchilin VP. Current trends in the use of liposomes for tumor targeting. Nanomedicine. 2013;8:1509–28.

213. Shi C, Cao H, He W, Gao F, Liu Y, Yin L. Novel drug delivery liposomes targeted with a fully human anti-VEGF165 monoclonal antibody show superior antitumor efficacy in vivo. Biomedicine & Pharmacotherapy. 2015;73:48–57.

214. Dicheva BM, Ten Hagen TLM, Seynhaeve ALB, Amin M, Eggermont AMM, Koning GA. Enhanced Specificity and Drug Delivery in Tumors by cRGD - Anchoring Thermosensitive Liposomes. Pharmaceutical Research. 2015;32(12):3862–76.

215. Lee Y, Thompson DH. Stimuli-responsive liposomes for drug delivery. Wiley Interdisciplinary Reviews: Nanomedicine and Nanobiotechnology. 2017;9(5):10.1002.

216. Yuba E, Osaki T, Ono M, Park S, Harada A, Yamashita M, et al. Bleomycin-loaded pH-sensitive polymer-lipid-incorporated liposomes for cancer chemotherapy. Polymers (Basel). 2018;10(1).

217. Seynhaeve ALB, Amin M, Haemmerich D, van Rhoon GC, ten Hagen TLM. Hyperthermia and smart drug delivery systems for solid tumor therapy. Advanced Drug Delivery Reviews. 2020.

218. Jin Y, Liang X, An Y, Dai Z. Microwave-Triggered Smart Drug Release from Liposomes Co-encapsulating Doxorubicin and Salt for Local Combined Hyperthermia and Chemotherapy of Cancer. Bioconjugate Chemistry. 2016;27(12):2931–42.

219. Tagami T, Ando Y, Ozeki T. Fabrication of liposomal doxorubicin exhibiting ultrasensitivity against phospholipase A2 for efficient pulmonary drug delivery to lung cancers. International Journal of Pharmaceutics. 2017;517(1–2):35–41.

220. Luo D, Nasi L, Carter KA, Lin C, Geng J, Shao S, et al. Rapid Light-Triggered Drug Release in Liposomes Containing Small Amounts of Unsaturated and Porphyrin–Phospholipids. Small. 2016;12(22):3039–47.

221. Dromi S, Frenkel V, Luk A, Traughber B, Angstadt M, Bur M, et al. Pulsed-high intensity focused ultrasound and low temperature - Sensitive liposomes for enhanced targeted drug delivery and antitumor effect. Clinical Cancer Research. 2007;13(9):2722–7.

222. Rękorajska A, Szuplewska A, Rękorajska Joniec A, Pocztańska E, Krysiński P, Dybko A, et al. Magnetic field-assisted selective delivery of doxorubicin to cancer cells using magnetoliposomes as drug nanocarriers. Nanotechnology. 2019;30(31).

223. Rodrigues ARO, Almeida BG, Araújo JP, Queiroz MJRP, Coutinho PJG, Castanheira EMS. Magnetoliposomes for dual cancer therapy. In: Inorganic Frameworks as Smart Nanomedicines. 2018:489–527.

224. Krauss AC, Gao X, Li L, Manning ML, Patel P, Fu W, et al. FDA approval summary: (daunorubicin and cytarabine) liposome for injection for the treatment of adults with high-risk acute myeloid leukemia. Clinical Cancer Research. 2019;25(9):2685–90.

225. Anselmo AC, Mitragotri S. Nanoparticles in the clinic: An update. Bioengineering and Translational Medicine. 2019;4(3).

226. Venkatraman SS, Ma LL, Natarajan J V., Chattopadhyay S. Polymer- and liposome-based nanoparticles in targeted drug delivery. Frontiers in Bioscience - Sch. 2010;2 S(3):801–14.

227. Prasad M, Lambe UP, Brar B, Shah I, J M, Ranjan K, et al. Nanotherapeutics: An insight into healthcare and multi-dimensional applications in medical sector of the modern world. Biomedicine and Pharmacotherapy. 2018;97:1521–37.

228. Thakor AS, Jokerst J V., Ghanouni P, Campbell JL, Mittra E, Gambhir SS. Clinically Approved Nanoparticle Imaging Agents. Journal of Nuclear Medicine. 2016;57(12):1833–7.

229. Gundloori RV, Singam A, Killi N. Nanobased Intravenous and Transdermal Drug Delivery Systems. In: Mohapatra SS, Ranjan S, Dasgupta N, Mishra RK, Thomas S, editors. Applications of Targeted Nano Drugs and Delivery Systems. Elsevier; 2019:551–94.

230. Amin MCIM, Butt AM, Amjad MW, Kesharwani P. Polymeric Micelles for Drug Targeting and Delivery. In: Nanotechnology-Based Approaches for Targeting and Delivery of Drugs and Genes. 2017:167–202.

231. Xiao K, Li Y, Lee JS, Gonik AM, Dong T, Fung G, et al. "OA02" peptide facilitates the precise targeting of paclitaxel-loaded micellar nanoparticles to ovarian cancer In Vivo. Cancer Research. 2012;72(8):2100–10.

232. Teow HM, Zhou Z, Najlah M, Yusof SR, Abbott NJ, D'Emanuele A. Delivery of paclitaxel across cellular barriers using a dendrimer-based nanocarrier. International Journal of Pharmaceutics. 2013;441(1–2):701–11.

233. Karim K, Mandal A, Biswas N, Guha A, Chatterjee S, Behera M, et al. Niosome: A future of targeted drug delivery systems. Journal of Advanced Pharmaceutical Technology and Research. 2010;1:374–80.

234. Deshpande A, Mohamed M, Daftardar SB, Patel M, Boddu SHS, Nesamony J. Solid Lipid Nanoparticles in Drug Delivery: Opportunities and Challenges. In: Emerging Nanotechnologies for Diagnostics, Drug Delivery and Medical Devices. 2017:291–330.

235. Chirio D, Gallarate M, Peira E, Battaglia L, Muntoni E, Riganti C, et al. Positive-charged solid lipid nanoparticles as paclitaxel drug delivery system in glioblastoma treatment. European Journal of Pharmaceutics and Biopharmaceutics. 2014;88(3):746–58.

236. Beloqui A, Solinís MÁ, Rodríguez-Gascón A, Almeida AJ, Préat V. Nanostructured lipid carriers: Promising drug delivery systems for future clinics. Nanomedicine: Nanotechnology, Biology, and Medicine. 2016;12:143–61.

237. Yang X yan, Li Y xia, Li M, Zhang L, Feng L xia, Zhang N. Hyaluronic acid-coated nanostructured lipid carriers for targeting paclitaxel to cancer. Cancer Letters. 2013;334(2):338–45.

238. Li Z, Barnes JC, Bosoy A, Stoddart JF, Zink JI. Mesoporous silica nanoparticles in biomedical applications. Chemical Society Reviews. 2012;41(7):2590–605.

239. Nasab NA, Kumleh HH, Beygzadeh M, Teimourian S, Kazemzad M. Delivery of curcumin by a pH-responsive chitosan mesoporous silica nanoparticles for cancer treatment. Artif Cells, Nanomedicine and Biotechnology. 2018;46(1).

240. Tiwari P, Vig K, Dennis V, Singh S. Functionalized Gold Nanoparticles and Their Biomedical Applications. Nanomaterials. 2011;1(1):31–63.

241. Farooq MU, Novosad V, Rozhkova EA, Wali H, Ali A, Fateh AA, et al. Gold Nanoparticles-enabled Efficient Dual Delivery of Anticancer Therapeutics to HeLa Cells. Scientific Reports. 2018;8(1).

242. Cortajarena AL, Ortega D, Ocampo SM, Gonzalez-García A, Couleaud P, Miranda R, et al. Engineering Iron Oxide Nanoparticles for Clinical Settings. Nanobiomedicine. 2014;1.

243. Guo W, Qiu Z, Guo C, Ding D, Li T, Wang F, et al. Multifunctional Theranostic Agent of Cu2(OH)PO4 Quantum Dots for Photoacoustic Image-Guided Photothermal/Photodynamic Combination Cancer Therapy. ACS Applied Material Interfaces. 2017;9(11):9348–58.

244. Maiti D, Tong X, Mou X, Yang K. Carbon-Based Nanomaterials for Biomedical Applications: A Recent Study. Frontiers in Pharmacology. 2019;9:1401.

245. Karimi M. Mechanism of carbon nanotube uptake by cells. Carbon nanotubes in drug and gene delivery. 2017:5-1 to 5-6.

246. Ji J, Liu M, Meng Y, Liu R, Yan Y, Dong J, et al. Experimental study of magnetic multi-walled carbon nanotube-doxorubicin conjugate in a lymph node metastatic model of breast cancer. Medical Science Monitor. 2016;22:2363–73.

247. Prylutska S, Panchuk R, Gołuński G, Skivka L, Prylutskyy Y, Hurmach V, et al. C60 fullerene enhances cisplatin anticancer activity and overcomes tumor cell drug resistance. Nano Research. 2017;10(2):652–71.

248. Liu J, Cui L, Losic D. Graphene and graphene oxide as new nanocarriers for drug delivery applications. Acta Biomaterialia. 2013;9:9243–57.

249. Pei X, Zhu Z, Gan Z, Chen J, Zhang X, Cheng X, et al. PEGylated nano-graphene oxide as a nanocarrier for delivering mixed anticancer drugs to improve anticancer activity. Scientific Reports. 2020;10(1).

250. Burda C, Chen X, Narayanan R, El-Sayed MA. Chemistry and properties of nanocrystals of different shapes. Chemical Reviews. 2005;105:1025–102.

251. Chen Z, Deng J, Zhao Y, Tao T. Cyclic RGD peptide-modified liposomal drug delivery system: Enhanced cellular uptake *in vitro* and improved pharmacokinetics in rats. International Journal of Nanomedicine. 2012;7:3803–11.

252. Tamura H, Goto K, Yotsuyanagi T, Nagayama M. Spectrophotometric determination of iron(II) with 1,10-phenanthroline in the presence of large amounts of iron(III). Talanta. 1974;21(4):314–8.

253. Rowatt K, Burns RE, Frasca S, Long DM. A combination Prussian blue–hematoxylin and eosin staining technique for identification of iron and other histological features. Journal of Histotechnology. 2018;41(1):29–34.

254. Zhu Y, Schwarz S, Ahlemeyer B, Grzeschik S, Klumpp S, Krieglstein J. Oleic acid causes apoptosis and dephosphorylates Bad. Neurochemistry International. 2005;46(2):127–35.

255. Castedo M, Perfettini JL, Roumier T, Andreau K, Medema R, Kroemer G. Cell death by mitotic catastrophe: A molecular definition. Oncogene. 2004;23:2825–37.

256. Laurent S, Bridot JL, Elst L Vander, Muller RN. Magnetic iron oxide nanoparticles for biomedical applications. Future Medicinal Chemistry. 2010;2:427–49.

257. Peng XH, Qian X, Mao H, Wang AY, Chen ZG, Nie S, et al. Targeted magnetic iron oxide nanoparticles for tumor imaging and therapy. International Journal of Nanomedicine. 2008;3:311–21.

258. Kim SY, Kim SJ, Kim BJ, Rah SY, Sung MC, Im MJ, et al. Doxorubicin-induced reactive oxygen species generation and intracellular Ca2+ increase are reciprocally modulated in rat cardiomyocytes. Experimental & Molecular Medicine. 2006;38(5):535–45.

259. Carvalho C, Santos R, Cardoso S, Correia S, Oliveira P, Santos M, et al. Doxorubicin: The Good, the Bad and the Ugly Effect. Current Medicinal Chemistry. 2009;16(25):3267–85.

260. Milla P, Dosio F, Cattel L. PEGylation of Proteins and Liposomes: a Powerful and Flexible Strategy to Improve the Drug Delivery. Current Drug Metabolism. 2011;13(1):105–19.

261. Rylander, MN, Feng, Y, Bass, J and Diller, KR. Thermally Induced Injury and Heat-Shock Protein Expression in Cells and Tissues. Annals of the New York Academy of Sciences, 2006;1066: 222-242.

262. Travers J, Sharp S, Workman P. HSP90 inhibition: two-pronged exploitation of cancer dependencies. Drug Discov Today. 2012;17(5-6):242-52.

263. Voinov MA, Sosa Pagán JA, Morrison E, Smirnova TI and Smirnov AI. Surface-Mediated

Production of Hydroxyl Radicals as a Mechanism of Iron Oxide Nanoparticle Biotoxicity. Journal of The American Chemical Society. 2010; 133(1):35–41.

264. Wayne N, Mishra P, Bolon DN. Hsp90 and client protein maturation. Methods in Molecular Biology. 2011;787:33-44.

265. Pilco-Ferreto N, Calaf GM. Influence of Dox on apoptosis and oxidative stress in breast cancer cell lines. International Journal of Oncology. 2016;49:753-762.

266. Asati S, Pandey V, and Soni V. RGD Peptide as a Targeting Moiety for Theranostic Purpose: An Update Study. International Journal of Peptide Research and Therapeutics. 2019;25:49–65.

267. Song Z, Lin Y, Zhang X, Feng C, Lu Y, Gao, Y, et al. Cyclic RGD peptide-modified liposomal drug delivery system for targeted oral apatinib administration: enhanced cellular uptake and improved therapeutic effects. International Journal of Nanomedicine. 2017;10(12):1941-1958.

268. Fritze A, Hens F, Kimpfler A, Schubert R, Peschka-Süss R. Remote loading of doxorubicin into liposomes driven by a transmembrane phosphate gradient, Biochimica et Biophysica Acta (BBA) - Biomembranes. 2006;1758(10):1633-1640.

269. Li X, Hirsh DJ, Cabral-Lilly D, Zirkel A, Gruner SM, Janoff AS, et al. Doxorubicin physical state in solution and inside liposomes loaded via a pH gradient. Biochimica et Biophysica Acta . 1998;1415(1):23-40.

270. Ansari MO, Parveen N, Ahmad MF, Wani Al, Afrin S, Rahman Y, et al. Evaluation of DNA interaction, genotoxicity and oxidative stress induced by iron oxide nanoparticles both *in vitro* and *in vivo*: attenuation by thymoquinone. Scientific Reports. 2019;9:6912.

271. Rawashdeh W, Zuo S, Melle A, Appold L, Koletnik S, Tsvetkova Y, et al. Noninvasive Assessment of Elimination and Retention using CT-FMT and Kinetic Whole-body Modeling. Theranostics; 2017;7(6):1499-1510.

272. Roriz P, Silva S, Frazão O, Novais S. Optical Fiber Temperature Sensors and Their Biomedical Applications. Sensors (Basel). 2020;20(7):2113.

273. Fite BZ, Liu Y, Kruse DE, Caskey CF, Walton JH, Lai CY, et al. Magnetic Resonance Thermometry at 7T for Real-Time Monitoring and Correction of Ultrasound Induced Mild Hyperthermia. PLOS ONE. 2012;7(4): e35509.

274. Cheng Y, Weng S, Yu L, Zhu N, Yang M, & Yuan Y. The Role of Hyperthermia in the Multidisciplinary Treatment of Malignant Tumors. Integrative Cancer Therapies. 2019;18:1534735419876345.

275. Chang HI, Yeh MK. Clinical development of liposome-based drugs: formulation, characterization, and therapeutic efficacy. International Journal of Nanomedicine. 2012;7:49-60.

276. Soleymani M, Velashjerdi M, Shaterabadi Z and Barati A. One-pot preparation of hyaluronic acid-coated iron oxide nanoparticles for magnetic hyperthermia therapy and targeting CD44-overexpressing cancer cells. Carbohydrate Polymers. 2020;237:116130.

280. Kandasamy G, Sudame A, Luthra T, Saini K and maity D. Iron Oxide Nanoparticles for Magnetic Fluid Hyperthermia Application in Liver Cancer Treatment. ACS omega, 2018;3(4):3991–4005.

281. Rashid RA, Abidin SZ, Anuar MA, Tominaga T, Akasaka H, Sasaki R, et al. Radiosensitization effects and ROS generation by high Z metallic nanoparticles on human

colon carcinoma cell (HCT116) irradiated under 150 MeV proton beam, OpenNano, 2019;4:100027.

282. Jafari S, Cheki M, Tavakoli MB, Zarrabi A, GhazikhanluSK and Afzalipour R. Investigation of Combination Effect Between 6 MV X-Ray Radiation and Polyglycerol Coated Superparamagnetic Iron Oxide Nanoparticles on U87-MG Cancer Cells. Journal of biomedical physics & engineering. 2020;10(1):15-24.

283. Esra, K. et al., Superparamagnetic iron oxide nanoparticle (SPION) mediated *in vitro* radiosensitization at megavoltage radiation energies. Journal of Radioanalytical and Nuclear Chemistry. 2018;315:595–602.

284. Khoei S, Takan G, Hoca S, Muftuler FZ, Yurt A and Kamer SA. The role of iron oxide nanoparticles in the radiosensitization of human prostate carcinoma cell line DU145 at megavoltage radiation energies, International Journal of Radiation Biology, 2014;90(5):351-356.

285. Rivera-Rodriguez A, Chiu-Lam A, Morozov VM, Ishov AM abd Rinaldi C. Magnetic nanoparticle hyperthermia potentiates paclitaxel activity in sensitive and resistant breast cancer cells. International Journal of Nanomedicine. 2018;13:4771-4779.

286. Zajac M, Moneo MV, Carnero A, Benitez J and Martínez-Delgado B. Mitotic catastrophe cell death induced by heat shock protein 90 inhibitor in BRCA1-deficient breast cancer cell lines. Molecular Cancer Therapeutics. 2008;7(8):2358-66.

287. Camphausen K and Tofilon PJ. Inhibition of Hsp90: a multitarget approach to radiosensitization, Clinical Cancer Research. 2007;13(15):4326–4330.

288. Biscaglia F, Ripani G, Rajendran S, Benna C, Mocellin S, Bocchinfuso G, et al. Gold Nanoparticle Aggregates Functionalized with Cyclic RGD Peptides for Targeting and Imaging of Colorectal Cancer Cells, ACS Applied Nano Materials 2019;2(10):6436-6444.

289. Yadav A, Radharani NN, Gorain M, Bulbule A, Shetti D, Roy G, et al. RGD functionalized chitosan nanoparticle mediated targeted delivery of raloxifene selectively suppresses angiogenesis and tumor growth in breast cancer, NanoScale, 2020;12:10664-10684.

290. Yu X, Song Y, Di Y, He H, Fu D and Jin C. Enhanced tumor targeting of cRGD peptide-conjugated albumin nanoparticles in the BxPC-3 cell line. Scientific Reports. 2016;6:31539.

291. Lu LY, Kerrigan JE, Lin CP, Azarova AM, Tsai YC, Ban Y, et al. Topoisomerase II Mediated DNA Double-Strand Breaks: Implications in Doxorubicin Cardiotoxicity and Prevention by Dexrazoxane. Cancer research. 2007;67: 8839-46.

292. Yang F, Teves SS, kemp CJ and Henikoff S. Doxorubicin, DNA torsion, and chromatin dynamics, Biochimica et Biophysica Acta (BBA) - Reviews on Cancer, 2014;1845(1):84-89.

293. Shimizu S, Konishi A, Nishida Y, Mizuta T, Nishina H, Yamamoto A, et al. Involvement of JNK in the regulation of autophagic cell death. Oncogene. 2010;29:2070–2082.

294. Zhou YY, Li Y, Jiang WQ and Zhou LF. MAPK/JNK signalling: a potential autophagy regulation pathway, Bioscience Reports, 2015;35(3): e00199.

295. Im JS, Keaton M, Lee KY, Kumar P, Park J and Dutta A. ATR checkpoint kinase and CRL1βTRCP collaborate to degrade ASF1a and thus repress genes overlapping with clusters of stalled replication forks. Genes & development. 2014;28(8):875-87.

296. Puigvert JC, Sanjiv k and Helleday T. Targeting DNA repair, DNA metabolism and replication stress as anti-cancer strategies. FEBS J. 2016;283:232-245.

297. Wheler JJ, Tsimberidou AM, Hong DS, Naing A, Falchook GS, Fu s, et al. Risk of serious toxicity in 1181 patients treated in phase I clinical trials of predominantly targeted anticancer drugs: the M. D. Anderson Cancer Center experience. Annals of Oncology, 2012;23:1963- 1967.

298. Sachs JR, Mayawala K, Gadamsetty S, Kang SP and Alwis DP. Optimal Dosing for Targeted Therapies in Oncology: Drug Development Cases Leading by Example, Clinical Cancer Research. 2016;22(6):1318-1324.

PUBLICATIONS AND SCIENTIFIC CONTRIBUTIONS

PUBLICATIONS IN REFEREED JOURNAL

a. Published

1. **Neena G. Shetake**, Amit Kumar, Snehal Gaikwad, Pritha Ray, Sejal Desai, Raghumani Singh Ningthoujam, Rajesh Kumar Vatsa and Badri N. Pandey. Magnetic Nanoparticle mediated Hyperthermia Therapy induces tumor growth inhibition by apoptosis and HSP90/AKT modulation, *International Journal of Hyperthermia* (2015); 31: 909-19.

2. **Neena G. Shetake**, Amit Kumar and B. N. Pandey. Iron-oxide nanoparticles target intracellular HSP90 to induce tumor radio-sensitization. *BBA General Subjects* (2019); 1863: 857-869.

3. **Neena G. Shetake,** B. N. Pandey. Hyperthermia therapy of cancer: Need for deeper biological insights for improved therapeutic outcome. *Journal of Radiation and Cancer Research* (2020); 10(4): 170-173 (*review article).*

b. Manuscript under preparation

1. Neena G. Shetake, Amit Kumar and B. N. Pandey. Targeted Liposomal nano-formulation of SPIONs and doxorubicin showed significant killing of cancer cells by activation of JNK pathway.

2. Neena G. Shetake, Amit Kumar and B. N. Pandey. Liposomal nano-formulation showed targeting and combinatorial chemo-, radio- and hyperthermia therapy efficacy in murine fibrosarcoma model.

AWARDS

1. Neena G. Shetake, Amit Kumar, B. N. Pandey, Magnetic Nanoparticles in combination with gamma radiation induce G2-M arrest and mitotic catastrophe mediated cell death, *ICRR-HHE-2016*, Feb.11-13, 2016, BARC, India. **(Best Oral Presentation Award).**

ABSTRACTS PRESENTED IN INTERNATIONAL CONFERENCES

1. **Neena G. Shetake**, Amit Kumar, B. N. Pandey, Iron oxide based Magnetic Nano-formulation for Improvement of Cancer Radiotherapy, *IAHOM*, Nanavati Hospital, India, Feb 15–16, 2020. **(Invited Talk).**

2. **Neena G. Shetake**, Amit Kumar, B. N. Pandey, Enhancement of Tumor Radio-sensitivity by Iron oxide nanoparticles : role of HSP90, DNA repair and apoptosis *ICRR-HHE 2018*, University of Hyderabad, India Feb, 1-4, 2018. **(Oral Presentation).**

3. **Neena G. Shetake**, Amit Kumar, B. N. Pandey, Iron oxide nanoparticles target intracellular HSP90 to induce tumor radio-sensitization, *(ICN:3I 2017)*, IIT-Roorkee, Dec 6-8 2017. **(Oral Presentation).**

REPRINTS